

UNRAVELLING THE CONSEQUENCES OF AROMATIC CORE-SUBSTITUTION ON REDOX-ACTIVE MOLECULAR TRIANGLES

Fraser Harvey Nicol Arnold

Doctor of Philosophy

University of York

Chemistry

January 2024

ABSTRACT

Electron delocalisation in shape-persistent molecular triangles occurs as a result of cyclic aromatic homoconjugation between the aromatic diimide (ADI) faces, where π -orbital overlap occurs despite being separated by non-conjugating chiral (*R,R*)- or (*S,S*)-*trans*-1,2-diaminocyclohexane linkers and provides the macrocycles with attractive supramolecular and optoelectronic properties. Despite core-functionalised ADIs being well-explored in the literature, core-substitution of the pyromellitic diimide (PMDI) based molecular triangle was not studied until 2023. This Thesis further explores the effect of core-substitution on the structural, dynamic and optoelectronic properties of molecular triangles comprised of functionalised PMDI faces.

In Chapter 2, the presence of bromine atoms in the only previously reported core-functionalised PMDI based molecular triangle is utilised to synthesise a hexa-arylated macrocycle *via* a Suzuki–Miyaura cross-coupling reaction. The structural and optoelectronic properties of the resulting core-functionalised molecular triangles are studied to investigate the influence of core-substitution with six electron-withdrawing or -donating groups. In Chapter 3, the dynamic structural properties of analogous tris-brominated and tris-arylated molecular triangles are studied as well as the role of the cyclic aromatic homoconjugated π -surface in the cavity of the macrocycles in facilitating intra- and intermolecular non-covalent interactions. In Chapter 4, the solution and solid-state emission of brominated PMDI phosphors when incorporated into a rigid macrocycle is studied whilst progress towards the synthesis of emissive core-hydroxylated macrocycles using photochemical and conventional methods is presented. Lastly, Chapter 5 presents initial experiments to study the structural and optoelectronic properties of the five molecular triangles synthesised in Chapters 2 and 4 in thin films to assess their potential for application as organic semiconductors in ion-gated transistors and photovoltaic devices. This Thesis highlights the beneficial supramolecular and optoelectronic properties that can be accessed through the functionalisation of PMDI based molecular triangles to inspire further expansion of the scope of the class of macrocycles in the future.

TABLE OF CONTENTS

ABSTRACT	ii
AUTHOR'S DECLARATION	vi
ACKNOWLEDGEMENTS	vii
<hr/>	
CHAPTER 1 CONJUGATION AND ELECTRON DELOCALISATION IN THREE-DIMENSIONAL MACROCYCLES	1
SYNOPSIS	2
1.1 THROUGH-BOND CONJUGATION	3
1.2 THROUGH-SPACE CONJUGATION	5
1.3. HOMOCONJUGATION: THROUGH-SPACE CONJUGATION SEPARATED BY NON-CONJUGATING GROUPS	8
1.3.1. HOMOCONJUGATION AND HOMOAROMATICITY	8
1.3.2. AROMATIC HOMOCONJUGATION	9
1.3.3. CYCLIC AROMATIC HOMOCONJUGATION IN 3D MACROCYCLES	15
1.3.4 PROPERTIES AND APPLICATIONS FROM CYCLIC AROMATIC HOMOCONJUGATION IN MOLECULAR TRIANGLES	21
1.4. CORE-FUNCTIONALISED AROMATIC DIIMIDES	26
1.5. OVERVIEW	31
1.6. REFERENCES	32
<hr/>	
CHAPTER 2 CORE-SUBSTITUTED MOLECULAR TRIANGLES	43
SYNOPSIS	44
ACKNOWLEDGEMENTS	44
2.1 INTRODUCTION	45
2.2 RESULTS AND DISCUSSION	49
2.2.1 SYNTHESIS AND CHARACTERISATION	49
2.2.2 STRUCTURAL PROPERTIES OF CORE-FUNCTIONALISED MOLECULAR TRIANGLES	52
2.2.3 OPTOELECTRONIC PROPERTIES OF CORE-FUNCTIONALISED MOLECULAR TRIANGLES	58
2.3 CONCLUSIONS	65
2.4 SUPPLEMENTARY INFORMATION	66
2.4.1 MATERIALS AND GENERAL METHODS	66
2.4.2 SYNTHESIS	69

2.4.3 CHARACTERISATION	73
2.4.4 SINGLE X-RAY CRYSTALLOGRAPHY	85
2.4.5 UV-VIS SPECTROSCOPY	92
2.4.6 COMPUTATIONAL STUDIES	94
2.5 REFERENCES	99
CHAPTER 3 DYNAMIC ATROPISOMERISM AND HOST–GUEST BEHAVIOUR OF MOLECULAR TRIANGLES	103
SYNOPSIS	104
ACKNOWLEDGEMENTS	104
3.1 INTRODUCTION	105
3.2 RESULTS AND DISCUSSION	109
3.2.1 THE SYNTHESIS, STRUCTURAL AND OPTOELECTRONIC PROPERTIES OF TRIS-FUNCTIONALISED MOLECULAR TRIANGLES	109
3.2.2 DYNAMIC ATROPISOMERISM OF TRIS-SUBSTITUTED MOLECULAR TRIANGLES	119
3.2.3 HOST-GUEST COMPLEXATION OF MOLECULAR TRIANGLES	126
3.3 CONCLUSIONS	131
3.4 SUPPLEMENTARY INFORMATION	132
3.4.1 MATERIALS AND GENERAL METHODS	132
3.4.2 SYNTHESIS	134
3.4.3 CHARACTERISATION	137
3.4.4 SINGLE X-RAY CRYSTALLOGRAPHY	149
3.4.5 ADVANCED NMR SPECTROSCOPY	157
3.4.6 UV-VIS SPECTROSCOPY	176
3.4.7 COMPUTATIONAL MODELLING	179
3.5 REFERENCES	193
CHAPTER 4 PHOTOACTIVITY OF CORE-SUBSTITUTED MOLECULAR TRIANGLES	198
SYNOPSIS	199
ACKNOWLEDGEMENTS	199
4.1 INTRODUCTION	200
4.2. RESULTS AND DISCUSSION	207
4.2.1. THE PHOTO-ACTIVE BEHAVIOUR OF 6Br IN DMF	207

4.2.2 ROOM-TEMPERATURE PHOSPHORESCENCE OF BROMINATED MOLECULAR TRIANGLES	215
4.2.3. TOWARDS THE SYNTHESIS OF EMISSIVE CORE-HYDROXYLATED MOLECULAR TRIANGLES	220
4.3 CONCLUSIONS	229
4.4 SUPPLEMENTARY INFORMATION	230
4.4.1 MATERIALS AND GENERAL METHODS	230
4.4.2 SYNTHESIS	231
4.4.3 CHARACTERISATION	236
4.4.4 REACTION SCREENING OF TRANSFORMATION OF MONO-BROMINATED 4 TO MONO-HYDROXYLATED 9	239
4.5 REFERENCES	263
CHAPTER 5 REDOX-ACTIVE MACROCYCLES FOR POROUS, THIN-FILM ORGANIC SEMICONDUCTORS	265
SYNOPSIS	266
ACKNOWLEDGEMENTS	266
5.1 INTRODUCTION	267
5.2 RESULTS AND DISCUSSION	270
5.2.1 STRUCTURAL PROPERTIES OF MOLECULAR TRIANGLE THIN FILMS	270
5.2.2. OPTOELECTRONIC PROPERTIES OF MOLECULAR TRIANGLE THIN FILMS	274
5.2.3 DOPING ELECTRON-RICH N-TYPE POLYMERS WITH ELECTRON-DEFICIENT 6Br	280
5.3 CONCLUSIONS	284
5.4 SUPPLEMENTARY INFORMATION	286
5.4.1 MATERIALS AND GENERAL METHODS	286
5.4.2 ASSEMBLY OF CORE-FUNCTIONALISED MOLECULAR TRIANGLES INTO THIN FILMS	287
5.5 REFERENCES	288
CHAPTER 6 SUMMARY AND OUTLOOK	292

AUTHOR'S DECLARATION

I declare that this thesis is a presentation of original work, and I am the sole author. Unless otherwise stated, the work presented in this thesis is the work of the author. This work has not previously been presented for a degree or other qualification at this University or elsewhere. All sources are acknowledged as references.

Signed: F. H. N. Arnold

Date: 02.01.2024

ACKNOWLEDGEMENTS

To Dr Alyssa-Jennifer Avestro, I am incredibly grateful to you for your supervision, support and guidance over the last four years of my PhD. I have learnt so much from your mentoring which has enabled me to develop academically, professionally and personally. The opportunities that I have had during my time in your research group have helped me to grow as a person from being challenged to always consider experimental protocol, results and interpretations critically and in depth, to group jobs and positions of responsibility to develop new skills. I hope I have been a valuable team member and I look forward to seeing the continued research from the Avestro group in the future. Thank you for everything you have done to get me to the position I am in today.

To Dr Nick Rose, I could not have asked for a better office neighbour, lab mate and friend to be by my side during my PhD. We reached the completion of our studies together aided by our frequent lab socials, playing football every Friday and singing and dancing in the lab (especially Paolo hour). You were always able to understand how I was feeling and cheer me up with a dad joke. I was so proud when you finished your PhD and I am excited to see where your career takes you in future. I look forward to our continued friendship and future adventures together.

To the Avestro group – past and present – thank you for making the lab and office a positive environment for productive and fruitful research which has been a pleasure to attend every day. To Grant and Ruhee, thank you for your support and guidance as we have progressed and completed our PhDs together. I am proud of you both for the research you have conducted and I am looking forward to following your careers in the future. To Pavan and Suresh, your mentorship in the lab with continual useful suggestions and ideas to help me to maintain momentum in the various research projects was invaluable.

To the groups in the Molecular Materials section – Spicer, Wilkinson, Bruce, Cowling, Smith and McGonigal groups – thank you for your engagement during joint group meetings, providing valuable questions and feedback during my research presentations. Thank you to all members – past and present – of lab E214 for culturing a communal, positive and fun environment to be a part of during our studies with our regular lab socials and joint lunches by the lake making every day special. Thank you to Dr Iman Khazal for your support and guidance in the lab and your tasty bakes for group events.

To the Department of Chemistry, University of York, thank you for the positive and inclusive environment you provide for all students and staff that walk through the doors. I have thoroughly enjoyed my time being a member of the department and engaging with departmental activities. I am grateful to all academic, technical and research support staff who keep the department moving and enabling undergraduate and postgraduate students to excel in their studies. Thank you to Dr Will Unsworth for being my IPM and providing guidance during my PhD. Thank you to Dr Adrian Whitwood and Theo Tanner for solving the numerous crystal structures. Thank to Heather Fish,

Dr Alex Heyam and Dr Matthew Davy for maintaining the NMR facility and your guidance with advanced experimental design. Thank you to Karl Heaton for running all my MS samples. Lastly thank you to the ChemGrad office for helping make my PhD run smoothly and your informative and reassuring answers to all of my questions.

To funding bodies, thank you to the Royal Society for funding for the first three years of my PhD through the Enhancement Award and the University of York for funding for the fourth year of my postgraduate studies. Thank you to the Japan Society for the Promotion of Science for the opportunity to travel to Japan through the Summer Program Fellowship and conduct research and engage with the culture. Thank you to everyone who supported and welcomed me during my two and a half months in Japan, in particular Dr Masa Akamatsu, Masaki Ishii, Professor Katsuhiko Ariga and the Supramolecules group at the National Institute for Materials Science. I will always cherish my time in Japan especially the memories I was fortunate enough to make.

To the Organics Friday football team – past and present players – every Friday at 5pm I have enjoyed our time on the pitch together. It has been a constant in my life and it has been a pleasure to be a part of the team and contributing to the camaraderie and community spirit through the ups and downs of the results on the pitch!

To my family and friends, thank you for always being there to support, motivate and make me laugh throughout my PhD, education and life, this Thesis is for each and every one of you who have impacted my life. Thank you to my parents, I am eternally grateful for you always being at the end of the phone to provide advice or just listen to my thoughts and feelings. Thank you to my siblings and family for all of the laughs and distractions to keep me going throughout my PhD. Thank you to all of my friends – especially from my undergraduate studies and the Quiz group – for the memories we have made and the fun we have had. Thank you to my flatmate throughout my PhD, David, for listening to my rants after a long day in the lab, helping me to learn to cook and educating me on films and television. Thank you to Aliyah, you have helped me get through the writing process by cheering me up and always putting a smile on my face. To all of you, you have shaped my life and helped morph me into the person I am today, I appreciate every single one of you beyond measure.

CHAPTER 1 |

CONJUGATION AND ELECTRON DELOCALISATION IN THREE-DIMENSIONAL MACROCYCLES

SYNOPSIS

Electronic devices are present in all aspects of life from mobile phones to LEDs and their functions are continually developing towards more advanced technologies. However, with demand and accessibility of electronic devices increasing, there is a requirement for their electro-active materials to be low costing, lightweight and readily available. Such electro-active materials rely on electron delocalisation which can occur via through-bond or through-space conjugation and imparts attractive optoelectronic properties for application in electronic devices and as luminescent materials. In addition to discussing traditional through-bond and through-space conjugation, the less common approach of aromatic homoconjugation is highlighted in this Chapter, with a new term for its role in macrocycles introduced – cyclic aromatic homoconjugation. This Chapter introduces experimental and theoretical techniques to identify electron delocalisation by aromatic homoconjugation including cyclic voltammetry, UV-vis spectroscopy and DFT quantum chemical calculations in triptycenes, 7,7-diphenylnorbornane and poly(phenylene methylene). These techniques are used to highlight other potential systems where aromatic homoconjugation could occur or where rigidification into shape-persistent macrocycles would enhance the electron delocalisation. Cyclic aromatic homoconjugation in a relatively new class of macrocycle – the molecular triangles – is discussed with particular reference to their attractive properties and potential applications that occur as a result of the cyclic delocalisation of electrons between the aromatic diimide (ADI) faces. The cyclic aromatic homoconjugation in molecular triangles influences the assembly of the macrocycle in the solid state through interactions with solvent molecules and electron-rich anions and assists in the formation of emissive donor-acceptor complexes. Furthermore, the redox-active properties of the cyclic aromatic homoconjugated ADI faces in molecular triangles has allowed for the isolation and study of the reduced states and enabled for their utilisation as cathodic materials in lithium-ion batteries. The well-studied influence of core-substitution on the properties of ADIs is discussed with the methods of incorporation of the functionalised small molecules in macrocycles presented. By highlighting the benefits of cyclic aromatic homoconjugation and core-substitution of ADIs on the properties of their respective compounds, this Chapter provides the background for this Thesis which discusses the synthesis, structural and optoelectronic properties of core-functionalised PMDI based molecular triangles.

1.1. THROUGH-BOND CONJUGATION

Conjugation in organic macrocycles has allowed for the development of electro-active materials for application in thin-film transistors and bulk heterojunction photovoltaic cells through their optoelectronic properties.^{1,2} Electron delocalisation around a macrocycle not only allows for their application in electronic devices but also influences the supramolecular assembly through non-covalent interactions (NCIs). Inspiration for new conjugated organic macrocycles can be taken from linear acyclic analogues such as the one-dimensional (1D) halogen-doped polyacetylenes (Figure 1.1). In these conjugated organic polymers, the halogen atoms abstract a single electron each from the conjugated backbone, creating positively charged holes and negatively charged ions enabling higher conductivity. Iodine-doped polyacetylene exhibited 10^7 higher conductivity compared to an un-doped material while AsF_5 -doped *cis*-polyacetylene exhibited a conductivity of $560 \Omega^{-1} \text{ cm}^{-1}$, which was the highest reported conductivity at the time and was comparable to the tetrathiafulvalene-tetracyanoquinodimethane organic metal ($400\text{--}500 \Omega^{-1} \text{ cm}^{-1}$).^{3–6} These discoveries of halogen-doped polyacetylene conductors, led to the 2000 Nobel Prize for Chemistry being awarded to Heeger, MacDiarmid and Shirakawa for “*the discovery and development of conductive polymers*”.

Increasing the dimensionality of organic through-bond conjugated materials from 1D linear chains to 2D planar networks can enable greater electron delocalisation, with the ultimate through-bond conjugated material being graphene (Figure 1.1), which has a zero bandgap and a theoretical charge carrier mobility of $200,000 \text{ cm}^2 \text{ V}^{-1} \text{ s}^{-1}$, at least four orders of magnitude greater than the mobility of the highest organic semiconductors.^{1,7,8} Research momentum into graphene and other 2D synthetic analogues, *i.e.* polyaromatic hydrocarbons (PAHs), was reinvigorated when the 2010 Nobel Prize for Physics was awarded to Geim and Novoselov for “*groundbreaking experiments regarding the two-dimensional material graphene*” due to the remarkable mechanical, thermal and electronic properties of the 2D material.^{2,9} The properties of graphene can be extended in carbon nanotubes (CNTs) where the 2D nanosheet of sp^2 carbons are rolled-up into a cylindrical structure (Figure 1.1). CNTs are strong materials that exhibit charge transport in semiconductors and exceptional thermal conductivity for applications in composites, biosensors, supercapacitors and as scanning probe tips in atomic force and scanning tunnelling microscopy.¹⁰

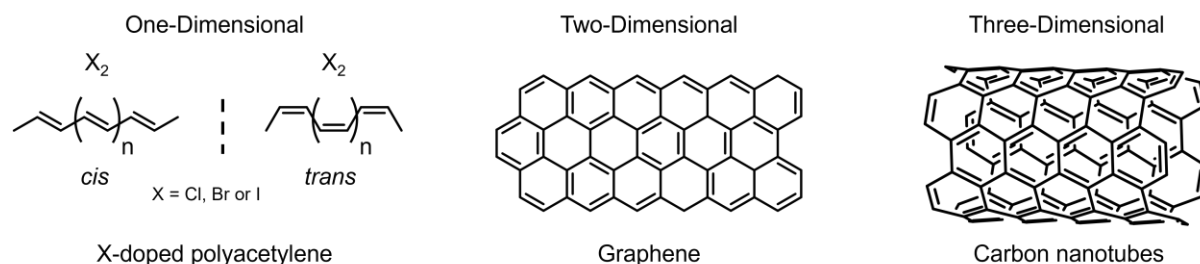


Figure 1.1 Structures of hydrocarbon based through-bond conjugated materials in one-,^{3–6} two-⁹ and three-dimensions.¹⁰

To replicate the remarkable and attractive semiconducting properties of CNTs through efficient electron delocalisation across the sp^2 surface, a large number of studies have been published in the pursuit of conjugated macrocycles through synthetic analogues using a range of different chemical functionality and structural motifs.^{11,12} The simplest analogues of CNTs are molecular nano-belts or -hoops that replicate the shortest portion of the cylindrical structures, such macrocycles that have been synthesised are cycloparaphenylenes (CPPs) where n is the number of benzene units that are directly bonded by *para*-substituted C-C linkers (Figure 1.2a).^{13–15} CPPs (where $n = 5$ to 12) have been shown to have greater conductance by the scanning tunnelling microscope-break junction technique compared with the acyclic analogues on account of the radial overlap of π -orbitals (Figure 1.2b).¹⁶ The radial through-bond conjugation in CPPs has been extended linearly in polymeric CPPs (*e.g.*, polymer **1**) to more closely resemble CNTs with the increased electron delocalisation enhancing the photophysical properties (Figure 1.2c).^{17–19} DFT calculations have also been used to show that different molecular orbitals (MOs) can be delocalised between linear and radial portions of the polymeric CPP.^{18,19} The through-bond conjugation in such polymeric CPPs was tested in optoelectronic devices to utilise the electron and hole mobility *via* electron delocalisation.¹⁷ By varying the structure of CPPs through the substitution of benzene units with aromatic analogues,²⁰ *e.g.*, with hexabenzocoronene as a polyaromatic hydrocarbon (PAH) surface,²¹ or quinone acceptors,²² the optical properties of the CPP analogues can be tuned with different emission colours on account of the extended π -conjugation and donor-acceptor interactions including solvatochromism effects.^{21,22}

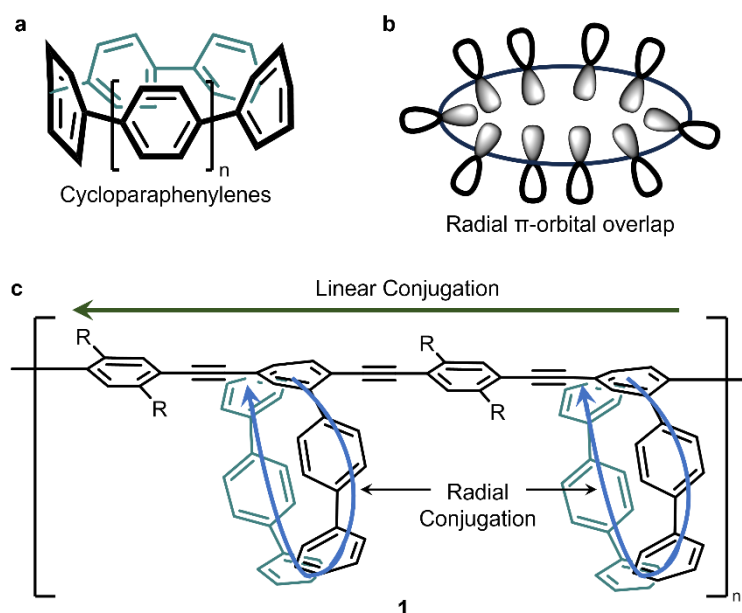


Figure 1.2 (a) General structure ($n = 5–12$) and (b) schematic of radial π -orbital overlap in CPPs.¹³ (c) Combination of linear and radial conjugation in CPP polymer **1** ($R = 2$ -ethylhexyl).¹⁸

The structure of CPPs have been further amended by the inclusion of porphyrin units within the through-bond conjugated macrocycle, *e.g.* compound **2** (Figure 1.3a). Electron delocalisation around the fused porphyrin dimers is not affected despite its inclusion within the strained CPP tape, although

weak conjugation only is observed throughout the macrocycle.²³ However, more efficient through-bond conjugation was present in porphyrin nanorings, where six metallated macrocycles are connected by butadiyne bridges at the meso-position (compound **3**, Figure 1.3b). Extended π -conjugation was observed *via* significant red-shifting in absorption spectra compared with the linear analogue²⁴ with electron delocalisation around the nanoring in the excited state confirmed by time-resolved transient absorption spectroscopy.²⁵ The templated synthesis of such porphyrin nanorings has allowed for larger π -conjugated structures to be synthesised including a 12-membered figure-of-eight nanoring **5**,²⁶ a molecular nanotube containing two, six-membered nanorings (**4**)²⁷ and an oblong-shaped nanoball.²⁸ The efficient through-bond conjugation within the individual nanorings and along the cylinder in the molecular nanotube mean that the electron delocalisation in these porphyrin-based structures provide an additional method towards synthetic analogue of CNTs.²⁷ In addition to potentially exhibiting similar exceptional conductivity properties to CNTs, the incorporation of porphyrin rings into these large structures could allow for biomimetic light harvesting applications on account of their photophysical properties.²⁵

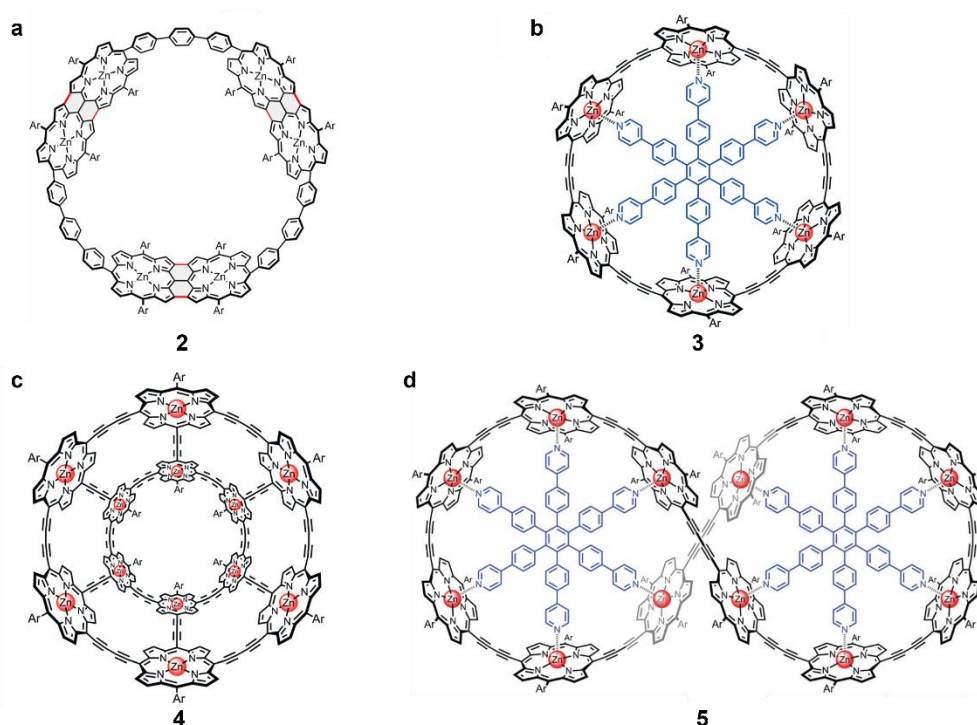


Figure 1.3 Through-bond conjugation and electron delocalisation in porphyrin macrocycles including (a) a CPP containing fused porphyrin dimers, **2**,²³ (b) a six-membered nanoring, **3**,^{24,27} (c) a molecular nanotube **4**²⁷ and (d) a 12-membered figure-of-eight nanoring, **5**.²⁶ Figure reproduced and adapted from References 23, 26 and 27.^{23,26,27}

1.2 THROUGH-SPACE CONJUGATION

An alternative method of electron delocalisation has also been shown to occur – through-space conjugation – where electron density is delocalised not through covalent bonds but instead *via*

overlapping p- and/or π -orbitals on non-covalently bonded atoms. These ‘through-space’ interactions can generally be described in two different contexts (i) intermolecular and (ii) intramolecular.

Intermolecular through-space conjugation occurs when π -surfaces of multiple molecules self-assemble in a supramolecular manner by way of weakly attractive non-covalent forces. Aromatic $\pi\cdots\pi$ interactions can occur in three conformations (i) edge-to-face, (ii) slip-stacked and (iii) face-to-face which can assemble in herringbone, slip-stacked, brick layer stacked and cofacial stacked superstructures (Figure 1.4).²⁹ These three interactions play an important role in the control of (i) the tertiary structure of proteins and subsequent substrate binding,²⁹ (ii) host–guest recognition interactions in supramolecular chemistry²⁹ and (iii) molecular packing of aromatic compounds to facilitate charge transport for organic semiconductors.^{30,31} Such intermolecular ‘ $\pi\cdots\pi$ interactions’ occur as a result of an electron correlation or dispersion effect along with solvent influences and as such are a type of the relatively weak van der Waals interaction.^{32,33}

Increased stability of $\pi\cdots\pi$ interactions can be afforded by covalent fixing of aromatic units intramolecularly within close proximity. The arrangement of phenyl units to optimise through-space π -orbital overlap and thus the facilitation of electron delocalisation can be modulated through the minimisation of steric hinderance such as in hexaarylbenzenes^{34–36}, tetraphenylethylenes^{37,38} and rigid aromatic dimers.³⁹ The efficient through-space conjugation in these aromatic systems can be utilised as molecular wires for multichannel conductance³⁵, organic semiconductors in organic light-emitting diodes (OLEDs)³⁹ and luminescent materials.^{37,38} The increased rigidity that occurs as a result of stabilised through-space interactions and aggregation can reduce non-radiative decay from the excited state *via* vibrational and rotational motion thus enhancing relaxation by fluorescence or phosphorescence or it can ‘turn on’ luminescence through aggregation-induced emission (AIE).³⁸

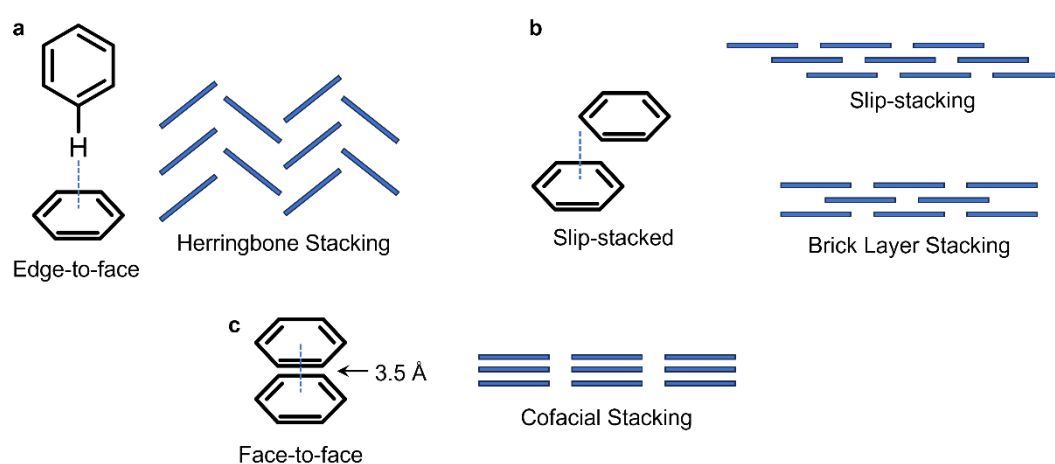


Figure 1.4 $\pi\cdots\pi$ interactions of benzene dimers and superstructures through (a) edge-to-face interactions and herringbone stacking, (b) slip-stacked interactions, slip-stacking and brick layer stacking and (c) face-to-face interactions and cofacial stacking.²⁹

An alternative form of intramolecular through-space conjugation is the incorporation of two or more benzene units where the overlap of π -orbitals are forced into a cofacial geometry in a preorganised macrocycle known as [2,2]-*para*-cyclophanes (Figure 1.5a).^{40–42} In these strained dimers, the distance between the π -surfaces is 3.10 Å which is within the expected distance for the optimal distance for $\pi \cdots \pi$ interactions (≈ 3.5 Å).^{29,43} Red-shifted absorption was observed in a through-bond conjugated polymer containing a through-space interacting cyclophane unit compared with an acyclic monomer. Such red-shifted absorption indicates successful electron delocalisation and subsequent π -extension throughout the polymer chain on account of through-space interactions between the cofacial benzene units in the cyclophane.⁴⁴ The ability for electron density to be shared between the two π -surfaces in macrocyclic cyclophanes has led to the study of their luminescent⁴⁵ and conductive properties.

Larger cyclophanes are also possible with an aromatic surface, where a general definition is the presence of aromatic units incorporated into a macrocycle and linked by an aliphatic chain, where the [2,2]-*para*-cyclophane discussed above is the simplest of the class of compounds.⁴⁶ Therefore, these larger cyclophanes have increased structural and functional group diversity in both the nature and number of π -surfaces and the rigidity of the linker.^{47,48} However, depending on the length of the linker, the π -orbitals are not necessarily preorganised within an optimal distance to allow for efficient overlap for through-space conjugation, although the aromatic cavity can be used as a host for aromatic guests for the formation of inclusion complexes.^{49–51} In a naphthalene diimide (NDI) based dimeric macrocycle **6**, the two naphthalene π -surfaces are in close enough proximity for π -orbital overlap (3.5 Å) (Figure 1.5b). Furthermore, NDIs are well-studied two-electron acceptors, and upon the chemical reduction of both aromatic diimide (ADI) faces with cobaltocene (CoCp₂) to form the dianion, the distance between the two naphthalene surfaces is reduced in the solid state to 3.3 Å. The narrower cavity in the dianion of the NDI cyclophane represents an overcoming of the electronic repulsion and thus shows efficient delocalisation of electrons in the macrocycle.⁵²

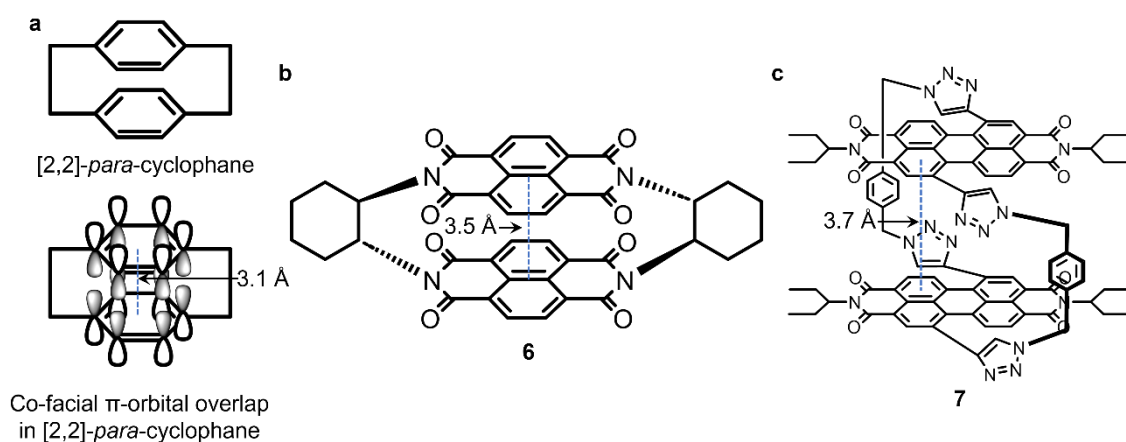


Figure 1.5 Structure of and cofacial π -orbital overlap in (a) [2,2]-*para*-cyclophane,⁴⁶ (b) an NDI-based dimer **6**⁵² and (c) a PDI-based dimer **7**.⁵³

A similar cyclophane dimer **7** composed of perylene diimide (PDI) faces connected at the perylene bay positions by triazole linkers has also been synthesised by Penty *et al.* (Figure 1.5c).⁵³ The bay substitution in this PDI dimer causes a twist in aromatic surface which subsequently induces the formation of two helical enantiomers (*MM* and *PP*) which are stabilised by favourable $\pi \cdots \pi$ interactions (3.7 Å). Such stabilising homochiral aromatic interactions were shown to slow down the rate of interconversion between the enantiomers and thus inducing increased half-lives which allowed for the separation of enantiomers for chiral properties and applications such as circularly polarised luminescence.⁵³

1.3. HOMOCONJUGATION: THROUGH-SPACE CONJUGATION SEPARATED BY NON-CONJUGATING GROUPS

Cofacial $\pi \cdots \pi$ interactions in dimeric cyclophanes are dependent on the rigid linkers to preorganise π -surfaces for optimal π -orbital overlap. To provide the preorganisation for cofacial π -orbital overlap in cyclophanes, high synthetic effort is required to overcome the strain in the dimers. The high synthetic cost of dimerisation can be avoided by utilising lesser-explored non-cofacial through-space interactions, *e.g.* $\neq 180^\circ$. Such through-space conjugation that occurs between p-orbitals despite being separated by a non-conjugating sp^3 centre is called homoconjugation. This electronic communication across non-conjugating groups can be extended to π -orbital overlap between aromatic groups in acyclic (aromatic homoconjugation) and macrocycles (which we term cyclic aromatic homoconjugation).

1.3.1. HOMOCONJUGATION AND HOMOAROMATICITY

In compounds exhibiting homoconjugation, the molecular geometry must be optimised to allow for the overlap of p-orbitals across the non-conjugating group which is often induced by a rigid or cyclic structure. The concept of homoconjugation stems from studies in the mid-1900s into 1,3-allylic interactions which began in 1948 when Winstein and Adams studied the delocalisation of charge between an allyl group and a cation in cholesterol derivatives with the homoallylic resonance affecting the reactivity and consequently the site of attack in substitution reactions (Figure 1.6a).⁵⁴ Subsequently in 1954, Simonetta and Winstein⁵⁵ studied similar 1,3-interactions and homoallylic resonance in a range of similar allylic systems including phenyl cations with the interactions further characterised a year later in 1955 by Winstein *et al.* in 7-norbornyl cations (Figure 1.6b).⁵⁶ These seminal investigations into such 1,3-interactions led to a series of papers coining the terms homoconjugation and homoaromaticity beginning in 1959, following their study on the 3-bicyclo[3.1.0]-hexyl cation – known as the tris-homocyclopropenyl cation (Figure 1.6c).^{57–60}

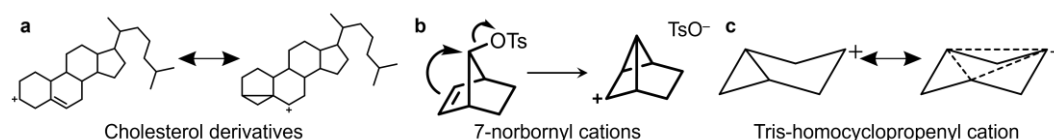


Figure 1.6 Original 1,3-allylic systems studied by Winstein and coworkers in (a) cholesterol derivatives,⁵⁴ (b) the 7-norbornyl cations⁵⁶ and (c) the tris-homocyclopropenyl cation.^{57–60}

Homoaromaticity is where the through-space conjugation across a sp^3 centre (homoconjugation) links within the cyclic delocalisation of $4n+2$ electrons *via* p-orbital overlap, an example being the monohomotropylium cation.⁶¹ If homoaromaticity occurs through homoconjugation an energy stabilisation is expected as well as the other properties that are commonly induced through standard aromaticity (*i.e.* reactivity and magnetic effects).⁶² The concept and influence of homoaromaticity in different compounds has been debated although it is an accepted phenomenon in organic cations with neutral and anionic examples more rare.⁶³ Furthermore, there are examples of cyclic compounds with $4n+2$ electrons that do not show homoaromatic stabilisation despite the homoconjugation of p-orbitals across non-conjugating sp^3 centres such as methylated pericyclynones which bear a resemblance to their analogous through-bond conjugated annulenes.^{64,65}

1.3.2. AROMATIC HOMOCONJUGATION

Homoconjugation can also occur between aromatic rings separated by a non-conjugating centre *via* the overlap of aromatic π -orbitals, with the effects of such aromatic homoconjugation being enhanced within rigid structures such as in polymer chains or highly strained norbornanes. The simplest example of a compound in which aromatic homoconjugation can occur would be in diphenylmethane (DPM) where two benzene rings are separated by a non-conjugating group.⁶⁶ The phenyl rings in DPM are freely rotating, with four representative conformations accessible in solution (Figure 1.7a), where the two phenyl rings are (i) in a planar conformation (DPM-1), (ii) perpendicular to the plane (DPM-2) or (iii) skewed slightly out of plane (DMP-3). The fourth conformation is where one of the phenyl rings remains in plane and the second ring is perpendicular (DPM-4). In DPM-2, π -orbital overlap across the non-conjugating sp^3 centre could occur, although this is restricted when the *ortho*-positions are substituted with the rotation of one of the rings influencing the other through a ‘cogwheeling’ mechanism.^{67–69} However Tu *et al.*,⁷⁰ showed that upon aggregation in the solid state, DPM and its derivatives formed through structural modification underwent clusteroluminescent emission which was attributed to through-space conjugation between the phenyl rings separated by the non-conjugating sp^3 centre. The overlap of π -orbitals prompting aromatic homoconjugation in these compounds was subsequently confirmed in the LUMO (Figure 1.7b) through density functional theory (DFT) calculations indicating that the optimal geometry of DPMs favour aromatic homoconjugation.⁷⁰ Therefore, in order to realise the effects of aromatic homoconjugation on the structural and optoelectronic properties of compounds, the conformation of the DPM motif must be fixed. This can

be achieved either by (i) the incorporation into more rigid and strained systems through structural modification or (ii) reduction of the rotational conformational freedom in the solid state. The promotion of aromatic homoconjugation through the incorporation into rigid and strained systems is more common and has been shown in compounds such as triptycenes⁷¹ and diphenylnorbornanes⁷² and discussed herein.

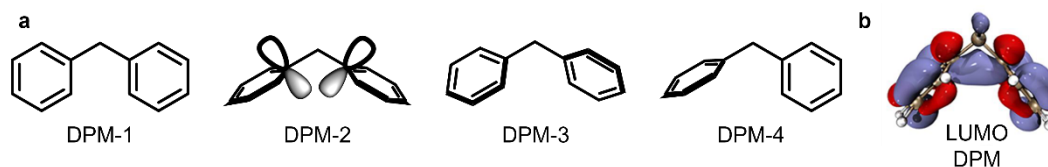


Figure 1.7 (a) Four conformations of DPM in solution: DPM-1, DPM-2, DPM-3 and DPM-4⁶⁸ and (b) π -orbital overlap in the LUMO of the geometry optimised structure of DPM (DFT calculations) – reproduced from Reference 70.⁷⁰

Triptycenes⁷³ are propeller compounds composed of a rigid bicyclic core appended by three phenyl rings separated by angles of 120° (Figure 1.8a). This structural motif is highly rigid and thus a high degree of persistent homoconjugation occurs which has been observed by UV-vis spectroscopy,^{74–76} circular dichroism (CD),^{77,78} photoelectron spectroscopy (PES),^{79–81} and cyclic voltammetry (CV).⁸² In absorption and CD spectra, the presence of lower energy charge-transfer bands indicates through-space conjugation between benzene rings separated by the non-conjugating sp^3 bridge-head carbon of the triptycene backbone.^{74–78} Furthermore, the electronic structure of triptycenes has been studied by PES which determines the ionisation potential of electrons in molecular orbitals (MOs). Theoretical calculations using the linear combination bonding orbital (LCBO) model has been used to predict the ionisation energies of π -orbitals based on aromatic homoconjugation, with the results correlating with the spectral features of the PES experiment, thus confirming the presence of through-space interactions between adjacent π -systems separated by a non-conjugating sp^3 linker.⁸¹ Lastly, aromatic homoconjugation in electroactive triptycenes can be evidenced using cyclic voltammetry, where delocalisation of electrons around the rigid bicyclic framework allows for multiple accessible redox-active states. In a triptycene containing three oxidisable methoxy substituted benzene propellers, delocalisation of the electrons between π -systems allows for three accessible oxidation states. This is evidence for aromatic homoconjugation, as upon the oxidation of the first di-methoxybenzene unit, the resulting radical cation is delocalised around the triptycene structure with the subsequent oxidation of the other two di-methoxy-benzene units forming the di-radical cation and tris-radical cation respectively.⁸³

Despite significant research and subsequent evidence for aromatic homoconjugation in triptycenes as discussed in the previous paragraph, the presence of electron delocalisation between the three propeller units in triptycene compounds is not universal across all of its derivatives.⁸⁴ For example, Gu and Lai⁸⁵ have shown that through-space conjugation between π -systems of the triptycene framework does not occur thus not contributing towards electron delocalisation between through-bond conjugated

bis(fluorenyl)-based oligomers. Nonetheless, aromatic homoconjugation in triptycenes has been shown to contribute towards properties for various applications, which include their use as luminescent materials for use in organic light emitting diodes (OLEDs) *via* thermally-activated delayed fluorescence (TADF).⁷¹

Through-space aromatic homoconjugation in triptycenes has been shown to enhance the TADF of twisted donor–acceptor (D–A) systems (Figure 1.8b).^{86–91} Traditionally, the emission in D–A TADF systems is encouraged by a small energy gap between the singlet (S_1) and triplet (T_1) excited states (ΔE_{ST}) allowing for reverse intersystem crossing (rISC) as well as limited orbital overlap between spatially separate HOMO and LUMOs on D and A moieties respectively.⁹² The inherent aromatic homoconjugation in the triptycene framework can be used as a suitable motif to allow for – whilst also minimising – the overlap of D–A MOs and reducing the ΔE_{ST} to promote rISC. Through the use of a variety of different D and A moieties used around the propellor structure of the triptycene framework, emission *via* TADF can be tuned at a wide range of colours and wavelengths across the electromagnetic spectrum. The triptycene backbone has been used to separate donor (triphenylamine,⁸⁶ 1,4-dimethoxybenzene,⁸⁸ carbazole,^{89,90} phenothiazine⁸⁹ or phenoxazine⁹¹) and acceptor (dicyanoquinoxaline,⁸⁶ dicyanopyrazine,⁸⁶ coumarin,⁸⁸ naphthilimide,⁸⁹ bromonaphthilimide⁸⁹ or quinoxaline^{90,91}) moieties (Figure 1.8c–f) or as part of a fused carbazole – triazine D–A fluorophore (Figure 1.8g).⁸⁷ As a result of the TADF properties of these D–A triptycene luminophores, their application in OLEDs can be studied through the incorporation of the bicyclic compound into thin films and subsequent fabrication into devices.^{86,87,91}

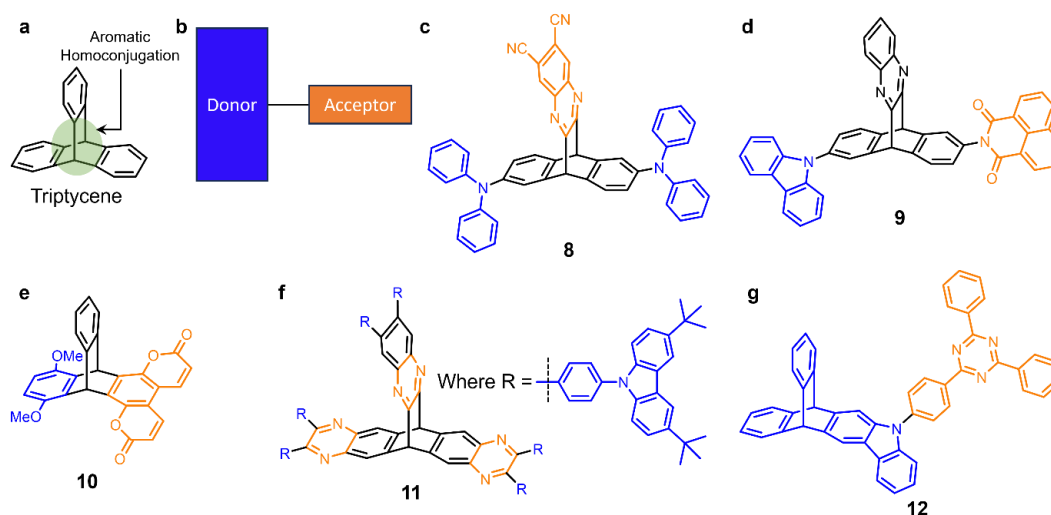


Figure 1.8 (a) Aromatic homoconjugation in the triptycene backbone⁸⁶ and (b) generic twisted donor-acceptor structure for TADF emitters.⁹² Different types of donor-acceptor structures for TADF emission containing a triptycene framework for using (c) diphenyl amine donor and dicyanoquinoxaline acceptor (**8**),⁸⁶ (d) carbazole donor and naphthalimide acceptor (**9**),⁸⁹ (e) dimethoxybenzene donor and coumarin acceptor (**10**),⁸⁸ (f) 3,6-di-tert-butylcarbazole donor and quinoxaline acceptor (**11**)⁹⁰ and (g) a fused triptycene carbazole donor and triazine acceptor (**12**).⁸⁷

The norbornane bicyclic framework can also be used to provide the required rigidity in diphenyl methane derivatives. In 1993,⁷² the synthesis of 7,7-diphenylnorbornane (DPN) was reported, where

the phenyl moieties are separated by a non-conjugated sp^3 centre in the 7-position of the bicyclic backbone (Figure 1.9a). Steric repulsions between the *ortho*-substituents of the benzene rings and the *exo*-hydrogens of the norbornane skeleton hinders the rotation of the phenyl units which enforces an apical cofacial alignment of the aromatic groups and thus promotes a geometry that allows for through-space π -orbital mixing.⁹³ Energy barriers of 16.2–17.2 kcal mol⁻¹ are observed when the *ortho*-positions are substituted with fluorine atoms and a variety of *para*-substituents,⁹³ although the rotation is less hindered when the *ortho*-hydrogen atoms only are present (6.0–7.9 kcal mol⁻¹).⁹⁴ UV-vis spectroscopy has been used to demonstrate the presence of aromatic homoconjugation in DPNs, where a new absorption at 228 nm is observed that is absent in the non-conjugated diphenylpropane analogue.⁷² The presence of aromatic homoconjugation was further confirmed when multiple DPN motifs were either directly bonded or linked by phenyl units (**13**) (Figure 1.9b), with the absorption linked to π -orbital overlap red-shifted to 290 nm (from 228 nm) and plateauing towards 4 to 5 DPN groups⁹⁵ indicating increasing π -conjugation.^{95–98} Furthermore, in asymmetric DPNs where the two phenyl units are asymmetrically substituted with donor (D) or acceptor (A) groups, additional charge-transfer absorption peaks are present in UV-vis spectra indicating electron transfer across the non-conjugated sp^3 centre.^{99–101} Theoretical density functional theory (DFT) calculations can also be used to visualise the π -orbital overlap between adjacent phenyl rings separated by the non-conjugating sp^3 norbornane carbon in the isosurface of the unoccupied molecular orbitals *e.g.* LUMO+1 (Figure 1.9c).¹⁰⁰

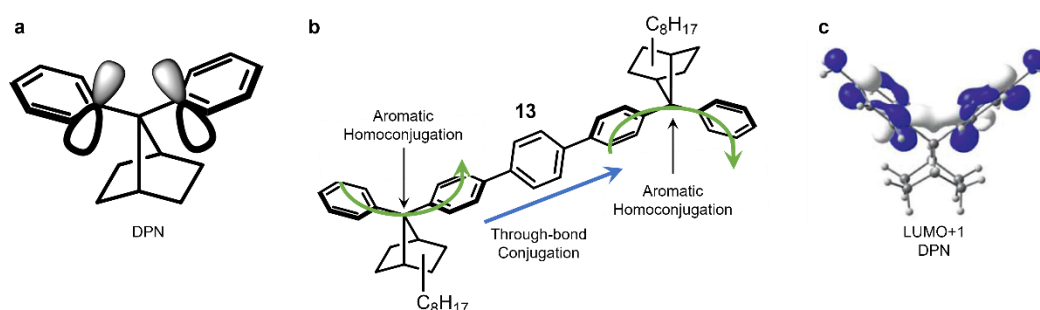


Figure 1.9 Aromatic homoconjugation in 7,7-diphenylnorbornane (DPN) compounds showing (a) π -orbital overlap across the non-conjugating sp^3 centre in the norbornane framework,⁷² (b) through-space and through-bond conjugation in a DPN dimer with a phenyl linker⁹⁸ and (c) delocalisation of the LUMO+1 across the non-conjugating sp^3 centre modelled by DFT calculations (replicated and adapted from reference 100).¹⁰⁰

Electron delocalisation as a result of aromatic homoconjugation in DPNs as well as the rigid, preorganised structure of the bicyclic framework has made these compounds attractive candidates as (i) hosts for cationic^{102,103} and aromatic¹⁰⁴ guests and (ii) metallocene ligands for catalytic polymerisation reactions.^{105–107} The preorganised structure of macrocycles containing two aromatic homoconjugated DPN units, linked by ethene motifs with an electron-rich aromatic cavity allows for the encapsulation of one cationic silver (I) ion,¹⁰² whereas the preferred conformation of a separate acyclic DPN containing three of the bicyclic motifs can selectively bind NH_4^+ over K^+ .

More recently, the phenomenon of aromatic homoconjugation has been used to provide an explanation for the photophysical properties of compounds previously considered to be non-conjugated. For example, poly(phenylene methylene), PPM, is a fluorescent polymer containing repeat units of the benzyl functional group ($\text{C}_6\text{H}_5\text{CH}_2-$) (Figure 1.10a) with the origin of its luminescence originally hypothesised to be as a result of the formation of a 9,10-diphenyl anthracene side-product in the polymerisation reaction.¹⁰⁸ In 2017, Caseri and coworkers,¹⁰⁹ revisited the fluorescence of PPM (Figure 1.10c) and its substituted derivatives: (i) poly(2-methyl phenylene methylene) (PMPM) and (ii) poly(2,4,6-trimethyl phenylene methylene) (PTMPM), and show that the similar emission profiles of the three polymers is likely to be as a result of π -extension through aromatic homoconjugation.

In the study by Caseri and coworkers,¹⁰⁹ potential other causes for the solution- and solid-state fluorescence of PPM were considered, including: (i) AIE, aggregation-caused quenching (ACQ) or excimer formation on account of $\pi \cdots \pi$ interactions and (ii) the formation of 9,10-diphenyl anthracene. The authors argue that fluorescence of PPM in dilute and concentration solutions and in the solid state exclude potential AIE or ACQ effects while the well-resolved vibronic structure of the emission spectrum and ground-state absorption of emissive species remove the possibility of excimer formation. Furthermore, in considering the required conditions for the potential synthesis of the emissive 9,10-diphenyl anthracene side-product, the authors were able to disprove the hypothesis that the presence of the small molecule contaminant caused the luminescence of PPM.¹⁰⁹

With the potential alternatives to aromatic homoconjugation considered and proven to be flawed, the possibility of through-space conjugation and subsequent delocalisation of π -electrons was probed. DFT calculations of a PPM chain containing three phenyl groups were completed which showed that the lowest energy conformation existed with a dihedral angle across the sp^3 centre of 56° . Furthermore, in a similar fashion to the aromatic homoconjugation in 7,7-diphenylnorbornanes, orbital overlap was observed visually in the LUMO of the PPM chain providing evidence for electron delocalisation *via* through-space conjugation across sp^3 centres (Figure 1.10b). A last observation that provided evidence for aromatic conjugation was a 25% increase in the absorbance of PPM in thin films after annealing above the T_g of the polymer. The increase in absorbance indicates that upon annealing, the more-ordered conformation of polymer chains allows for more homoconjugative interactions. Whereas the lower absorbance prior to annealing, shows that the increased disorder in the polymer chains is not conducive to the optimal geometry of the DPM units to maximise π -orbital overlap.¹⁰⁹ The discovery of aromatic homoconjugation in PPM has led to additional investigations into the origins of the luminescent properties including under increased pressure.¹¹⁰

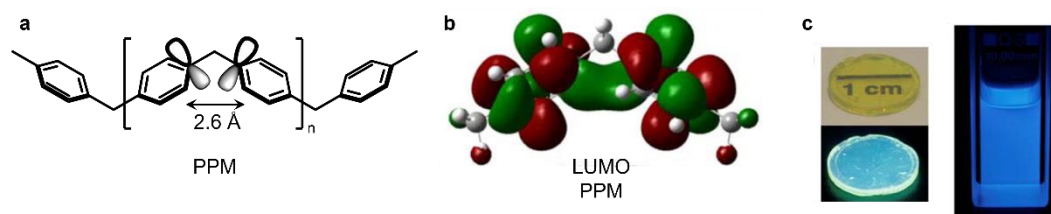


Figure 1.10 Aromatic homoconjugation in poly(phenylene methylene) (PPM) showing (a) π -orbital overlap across the non-conjugating CH_2 sp^3 centre, (b) delocalisation of the LUMO across the non-conjugation sp^3 centre and (c) solid- and solution-state emission of PPM.¹⁰⁹ Figure replicated and adapted from reference 109.¹⁰⁹

In the examples of aromatic homoconjugation discussed above (diphenylmethane, triptycenes, 7,7-diphenylnorbornane and poly(phenylene methylene)), it was shown that the overlap of π -orbitals was maximised when the aromatic rings were incorporated into rigid systems. Therefore, using the structural motifs and characterisation of the delocalisation of electrons in such aromatic homoconjugated systems, other systems where through-space conjugation across insulating sp^3 centres could occur can be proposed. For example, molecular clips and tweezers with ‘non-conjugating’ aromatic groups have been shown as receptors for aromatic substrates through non-covalent interactions (NCIs) such as $\text{C-H}\cdots\pi$ and $\pi\cdots\pi$ interactions.¹¹¹ Such preorganised aromatic receptors commonly contain bicyclic linkers between aromatic surfaces, where the belt-like structure remains flexible enough to expand and contract where necessary during the complexation process.¹¹¹ Such rigid bicyclic linkers,^{112–117} could be considered to be similar to triptycenes and 7,7-diphenylnorbornanes where aromatic homoconjugation is known. Therefore, if aromatic homoconjugation were to be observed in molecular clips and tweezers, the delocalisation of electrons in the electron-rich host could assist in its complexation with electron-deficient guests through NCIs. In fact, intramolecular interactions in aromatic molecular clips with a central quinone moiety, *e.g.* **14**, (Figure 1.11a) have been observed through UV-vis spectroscopy with broad, low energy absorption peaks observed which are similar to the long wavelength transitions present as a result of aromatic homoconjugation in DPNs.¹¹⁸ These broad absorption bands have been attributed to configuration interactions in the excited state between π -orbitals of aromatic side walls and central quinone moiety and as the orbital mixing occurs over the non-conjugating sp^3 bridging atom it is indeed a homoconjugative interaction.¹¹⁸ Therefore, these proof-of-concept homoconjugative interactions between aromatic side-walls and central quinone unit in the excited state indicate that aromatic homoconjugation could be possible in these molecular tweezer and clips structures and influence the ability of the receptors to complex with aromatic guests.

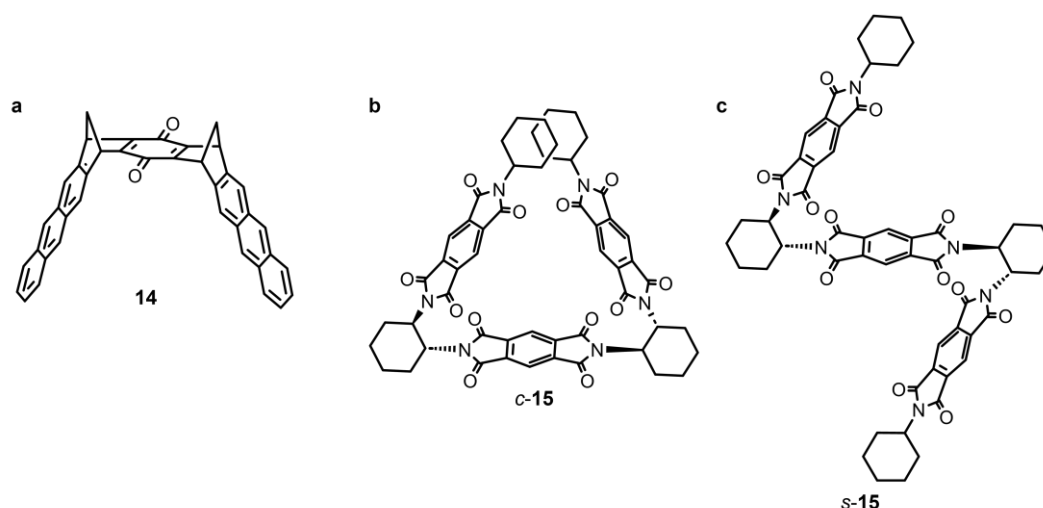


Figure 1.11 Proposed structures that could exhibit aromatic homoconjugation on account of exciton coupling in circular dichroism in a (a) molecular clip¹¹⁸ and (b) ‘C’ shaped isomer and (c) ‘S’ shaped isomer of PMDI trimers.¹¹⁹

In a similar manner to the excited-state intramolecular interaction in molecular clips discussed previously,¹¹⁸ exciton coupling in multi-chromophoric compounds has been shown using CD through the study of Cotton effects and their signs which also allowed for the determination of the absolute configuration of such structures.^{119–123} Exciton coupling, where the excited-state is delocalised across multiple chromophores, was observed in compounds containing different combinations of two or more aromatic diimide units (*N*-phthalimides (PI),^{120–122} 1,8-naphthalimides (NPI),¹²¹ pyromellitic diimides (PMDI)^{119,122,123} and naphthalene diimides (NDI)¹²³) separated by non-conjugating enantiomerically pure (*R,R*)- or (*S,S*)-1,2-*trans*-diaminocyclohexane linkers. The acyclic trimer, **15**, can exist in two conformations, ‘C’ or ‘S’ as a result of different dihedral angles around the N-C-C-N bonds at the diaminocyclohexane linkers (Figure 1.11b and c). The torsional angles for the ‘C’ conformer in a calculated geometry optimised and X-ray crystal structure are -44.3 and -44.0° respectively.¹¹⁹ As a result of these dihedral angles as well as the evidence that the aromatic diimide chromophores interact in the excited-state *via* exciton coupling, intramolecular through-space conjugation between adjacent π -surfaces in the ground-state of the acyclic dimers and trimers could be visualised to potentially occur.

1.3.3. CYCLIC AROMATIC HOMOCONJUGATION IN 3D MACROCYCLES

In addition to the acyclic trimer **15** that can adopt two conformations (‘C’ and ‘S’) discussed above, Gawroński *et al.*¹¹⁹ also incorporated three PMDI units into a rigid macrocycle **16**. In the acyclic trimer, **15**, the outer PMDI units are capped with cyclohexylamine groups, whereas in cyclic trimer **16**, instead of the capping groups, the outer diimides are also linked by a *trans*-1,2-diaminocyclohexane group to create a helical, macrocyclic structure. The CD spectrum of the rigid macrocycle **16** provided in depth insight into its electronic structure compared with the mixture of ‘C’ and ‘S’ isomers of the acyclic **15**. Furthermore, as a result of the rigid macrocyclic structure of **16**, hetero coupling of different electronic transitions at similar energies was possible in the excited state which was not observed in the acyclic analogues.¹¹⁹ The synthesis and study of the chiroptical properties of the PMDI-based macrocycle, **16**

in 2002 was the first of a series of investigations into such ‘molecular triangles’ where three aromatic diimides (ADIs), such as PMDI, NDI or perylene diimide (PDI) are separated by a non-conjugating enantiomerically pure (*R,R*)- or (*S,S*)-diaminocyclohexane linker (Figure 1.12).¹²⁴

In 2013, Stoddart and coworkers¹²⁵ followed the seminal work of Gawroński *et al.*¹¹⁹ (PMDI-based macrocycle, **16**) by synthesising the NDI-based molecular triangle, **17**. Interestingly, DFT calculations of the NDI-based molecular triangle, **17**, showed that the LUMO was delocalised around the macrocycle *via* through-space communication between adjacent π -surfaces (Figure 1.13a).¹²⁵ The π -orbital overlap in **17** occurs between NDI surfaces at 60° that are separated between two sp^3 centres in the diaminocyclohexane linker and is therefore a form of aromatic homoconjugation. Furthermore, as the through-space conjugation between NDI units in **17** occurs in a macrocycle to complete cyclic electron delocalisation, we further classify this electronic communication as cyclic aromatic homoconjugation. Such cyclic aromatic homoconjugation, where electron delocalisation occurs *via* through-space electronic communication, around the molecular triangle framework provides a suitable comparison with the CPPs discussed in Section 1.1 where the electron delocalisation instead occurs throughout the macrocycle *via* through-bond conjugation.

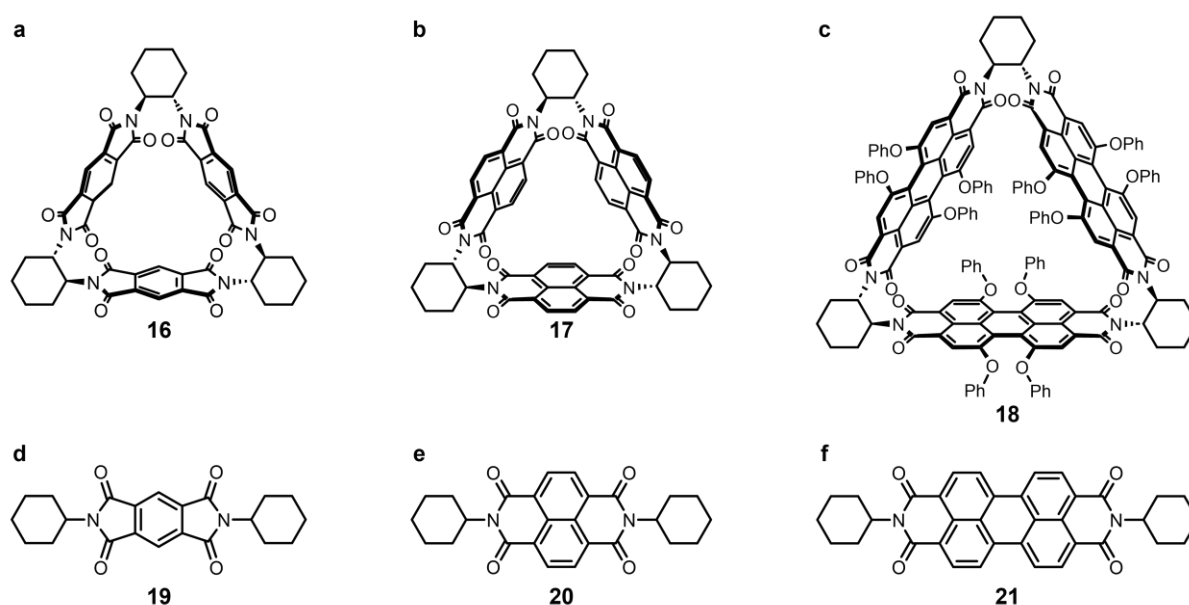


Figure 1.12. Molecular triangles which exhibit cyclic aromatic homoconjugation consisting of three aromatic diimides (ADIs) using (a) pyromellitic diimide (PMDI),^{119,126} **16** (b) naphthalene diimide (NDI),¹²⁵ **17** and (c) perylene diimide (PDI) **18**.¹²⁷ Acyclic monomeric model compounds using (d) PMDI,^{119,126} **19**, (e) NDI,¹²⁵ **20** and (f) PDI, **21**.¹²⁷

The redox-active nature of the NDI faces allowed Stoddart and coworkers¹²⁵ to further confirm the through-space electronic communication between aromatic π -surfaces using CV (Figure 1.13b) in the same way as shown for aromatic homoconjugation in triptycenes. Each NDI is a two-electron acceptor, therefore, the incorporation of three units into the molecular triangle allows for up to six reductions to occur. As a result of the electronic communication between the two-electron acceptors, upon the addition of the first electron to the macrocycle, it is delocalised around the ring. Consequently, the

subsequent five electron reductions occur step wise with the increasing electron-density of the macrocycle making it more difficult to reduce the molecular triangle further. Therefore, during electrochemical reduction using CV, six reduction peaks are observed allowing for up to six individually accessible reduced states. If there was no electronic communication between the redox-active faces, the first reduction of each of the three NDI units would occur at the same potential to form a tris-radical anion, $[17]^{3-}$. The addition of the second electron to each NDI unit would subsequently occur at a more negative potential to form the hexa-anion ($[17]^{6-}$).¹²⁵

Cyclic aromatic homoconjugation in NDI-based molecular triangle, **17**, was also proven through electronic studies of the mono-radical anion of **17**, $[17]^{-}$ which was formed by the chemical reduction with one equivalent of cobaltocene (CoCp_2). Studies of the mono-radical anion by continuous wave (*cw*) electron paramagnetic resonance (EPR) and electron-nuclear double resonance (ENDOR) spectroscopies showed that the electron in the free radical was delocalised across the three NDI units in the macrocycle (Figure 1.13c and d). Comparisons between the *cw*-EPR and *cw*-ENDOR spectra of $[17]^{-}$ and the mono-radical anion of the analogous NDI monomer reference compound **20**, showed the expected differences for evidence of electronic communication. The linewidth of the splitting in the EPR spectrum of $[17]^{-}$ are decreased by a factor of 1.75 compared with the monomeric $[20]^{-}$ which is in agreement with the convention that the linewidth scales with the reciprocal of \sqrt{n} where n is the number of units by which the electron is shared ($\sqrt{3} = 1.73$). Further evidence was provided in the *cw*-ENDOR spectrum where the hyperfine splitting of $[17]^{-}$ was also decreased by a factor of three compared with $[20]^{-}$ on account of electron communication between three NDI units.¹²⁵

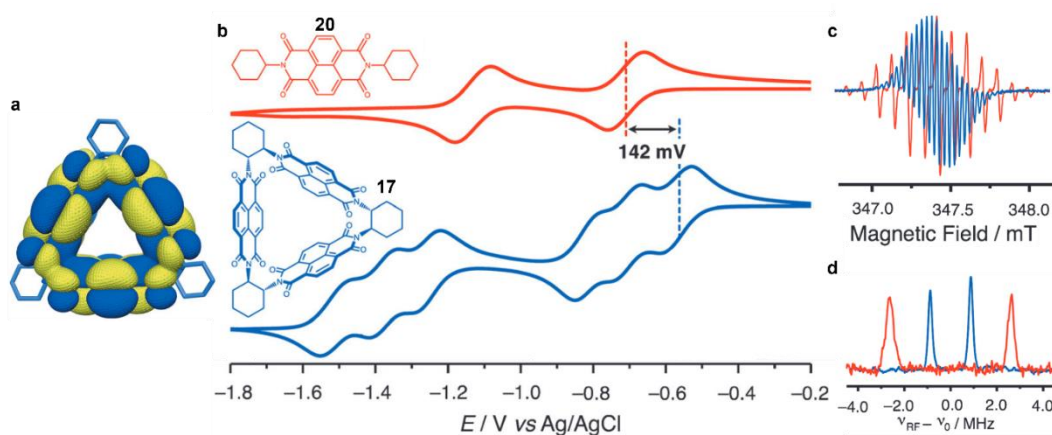


Figure 1.13 Evidence of cyclic aromatic homoconjugation in NDI-based molecular triangle, **17** through (a) delocalisation of the LUMO around the macrocycle in DFT calculations, (b) the presence of six accessible reduced states in the cyclic voltammogram of **17** compared with monomeric NDI **20** and narrower line widths in (c) *cw*-EPR and (d) *cw*-ENDOR spectra of $[17]^{-}$ compared with $[20]^{-}$. Figure replicated and adapted from reference 125.¹²⁵

Stoddart and coworkers¹²⁷ expanded the scope of molecular triangles to further investigate the non-cofacial through-space conjugation between ADIs by synthesising a rigid equilateral macrocycle composed of three PDI units which contained phenoxy-substituents on the aromatic core (**18**) to improve solubility. They also synthesised the PMDI-based molecular triangle, **16**, previously studied

by Gawroński *et al.* using a slightly adapted chromatography free method.¹²⁶ Cyclic aromatic homoconjugation was exhibited in **18** using *cw*-EPR and *cw*-ENDOR in the same manner as for NDI-based **17**. Upon chemical reduction of the macrocycle to the mono-radical anion ($[\mathbf{18}]^{\cdot-}$) spectral narrowing was observed in the *cw*-EPR spectrum compared with the monomeric PDI analogue. Furthermore, a decrease by a factor of three in the hyperfine coupling between $[\mathbf{21}]^{\cdot-}$ and $[\mathbf{18}]^{\cdot-}$ occurred on account of electron delocalisation between all three redox-active faces.¹²⁷ Whereas in **16**, electronic communication was evidenced using differential pulse voltammetry (DPV) where six accessible reduced states were observed on account of delocalisation of the electrons around the rigid molecular triangle.¹²⁶

In addition to equilateral triangles comprising three faces of the same ADI, Stoddart and coworkers^{128,129} have also synthesised asymmetric isosceles triangles containing combinations of two different ADIs (PMDI, NDI and PDI), **22–25** (Figure 1.14). In these isosceles triangles, aromatic homoconjugation does not occur around the whole macrocycle although some electron delocalisation does occur between adjacent NDI and PDI faces as shown by *cw*-EPR and *cw*-ENDOR experiments. In the asymmetric macrocycles containing two PMDI faces (**22** or **23**) no through-space conjugation occurs with the electron in the mono-radical anion residing on the NDI and PDI face as the *cw*-EPR and *cw*-ENDOR spectra resemble the monomeric NDI and PDI reference compounds, **20** and **21** respectively.^{128,129} Whereas, in the macrocycle containing two NDI faces and one PMDI face, **24**, the hyperfine splitting of the *cw*-ENDOR spectrum decreases by a factor of two which indicates delocalisation of the mono-radical anion between the two NDI units.¹²⁸ Furthermore, in an isosceles triangle containing two NDI units and one PDI face, **25** a decrease in the linewidths in *cw*-EPR and *cw*-ENDOR spectra compared with the reference PDI **21** were observed, although not as much to represent full delocalisation of the mono-radical anion, but nevertheless indicating a small amount of electronic communication.¹²⁹

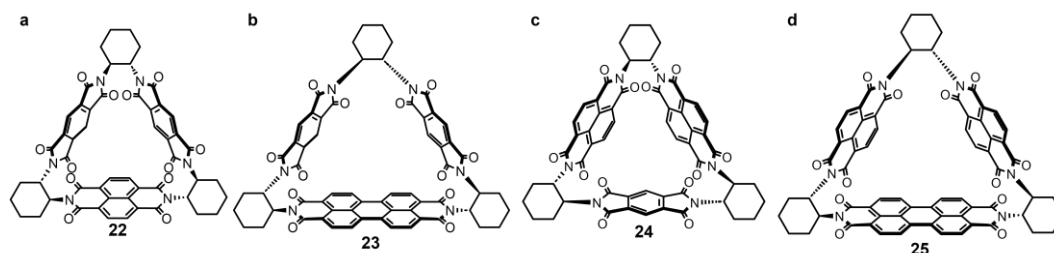


Figure 1.14 Isosceles triangles containing two PMDI faces and (a) one NDI unit,¹²⁸ **22** and (b) one PDI unit, **23** and two NDI faces¹²⁹ and (c) one PMDI unit, **24**¹²⁸ and (d) one PDI unit, **25**.¹²⁹

The incorporation of NDIs into non-triangular macrocycles has also been studied, where although the geometry of the redox-active faces are non-optimal for efficient orbital overlap, electron hopping has still been shown to occur.^{130,131} A square-shaped macrocycle, **26**, composed of four NDI faces connected by four (*S,S*)-*trans*-1,2-diaminocyclohexane linkers was synthesised by Stoddart and co-workers¹³⁰ which was structurally similar to the dimers⁵² and molecular triangles¹²⁵ discussed previously (Figure

1.15a). The synthesis of the square-shaped macrocycle induces strain in the NDI faces and diaminocyclohexane linkers *via* bending and puckering respectively. As a result of the redox-active faces being almost perpendicular to each other in the square-shaped macrocycle limited π -orbital overlap occurs across the non-conjugated cyclohexane sp^3 carbon atoms. Despite limited through-space conjugation, studies of the mono-radical anion (formed by chemical reduction with 1 equiv. CoCp_2) by *cw*-EPR and *cw*-ENDOR spectroscopies showed a decrease in the isotropic hyperfine coupling in the respective spectra indicating that the free radical was delocalised around the macrocycle. As a result of the absence of cyclic aromatic homoconjugation the delocalisation of electrons must therefore occur *via* hopping between the aromatic π -surfaces.¹³⁰

Electron hopping was also exhibited in the mono-radical anion of a chiral covalent organic cage containing three NDI faces, **27**, (Figure 1.15b) where in *cw*-EPR spectra, decreased isotropic hyperfine couplings were observed at elevated temperatures (350 K). At 295 K the free radical is localised on one NDI unit in the trimeric cage, where weak electronic coupling between the redox-active faces occurs as a result of the redox-active NDI faces being separated by a distance of 9.9 Å.¹³¹

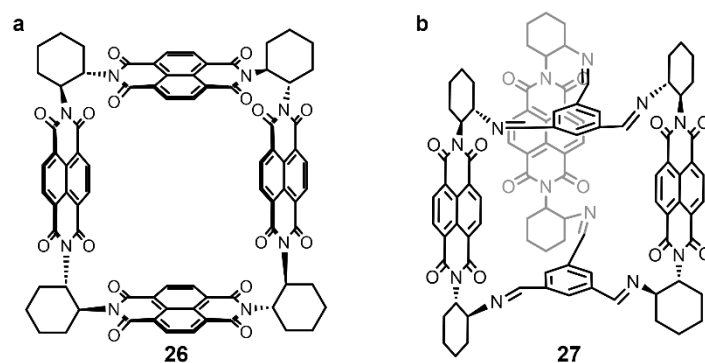


Figure 1.15 Structures of NDI-based compounds where electronic communication can occur (a) a molecular square **26**¹³⁰ and (b) organic cage **27**.¹³¹

Another series of preorganised macrocycles that have begun to be investigated for aromatic homoconjugation and subsequent electron delocalisation are pillar[n]arenes, where *n* is the number of 1,4-disubstituted benzene units that are linked by methylene (CH_2) groups and the aromatic groups are separated by an obtuse angle ($>90^\circ$). Electron delocalisation by through-space conjugation has been observed in pillar[5]arenes with the benzene units substituted with phenylethynyl substituents (macrocycle **28**) *via* red-shifted absorption and emission peaks with respect to the acyclic monomer (1,4-bis(phenylethynyl)benzene) (Figure 1.16a).¹³² Such red-shifted absorption and emission is similar to the observations for aromatic homoconjugation in the 7,7-diphenylnorbornanes discussed in Section 1.3.2.⁹⁵ However, whether the delocalisation of the electrons is as a result of aromatic homoconjugation between diphenyl motifs in the pillar[5]arene backbone or longer-range through-space interactions between the phenylethynyl substituents is unclear. Despite the uncertainty of whether aromatic homoconjugation occurs in the 1,4-bis(phenylethynyl) substituted pillar[5]arene, it was subsequently

confirmed in pillar[5]arenes where non-aromatic ethylene glycol substituents were used.¹³³ For example, 1,4-dimethoxy substituted pillar[5]arene **29** was shown to be inherently fluorescent as a result of aromatic homoconjugation and aggregation effects in AIE (Figure 1.16b). The fluorescence of the pillar[5]arene macrocycle was then utilised for sensing of n-alkane solvents where upon adsorption of the alkane chains in the cavity, the emission was quenched.¹³³ The potential for electronic communication *via* through-space conjugation in pillar[n]arenes ($n = 5$ or 6) has been further confirmed in macrocycles where two or more disubstituted benzene units are replaced by redox-active quinone groups.^{134,135} As was discussed for redox-active triptycenes⁸³ and molecular triangles^{125,126}, electrochemical experiments (CV and DPV) can be used to provide evidence of through-space conjugation as a result of delocalisation of electrons in each reduced state. Indeed, in pillar[n]arenes containing more than two quinone units (compounds **30–33**) resolution of the consequential reductions was observed by square-wave voltammetry (SWV) indicating electronic communication between adjacent redox-active centres (Figure 1.16c). Where, the redox-active quinones are not adjacent, the electrons are localised on the respective electron-acceptor.^{134,135} The aromatic homoconjugation between adjacent quinone groups has also been exhibited by DFT calculations where the LUMO is delocalised across the non-conjugating CH_2 sp^3 centre.^{134,135} Furthermore, anisotropic current intensity density (AICD) calculations show electron delocalisation *via* through-space conjugation in 5- and 6-membered pillar[n]arene macrocycles containing more than two quinone groups replacing the standard 1,4-disubstituted benzene units.¹³⁵

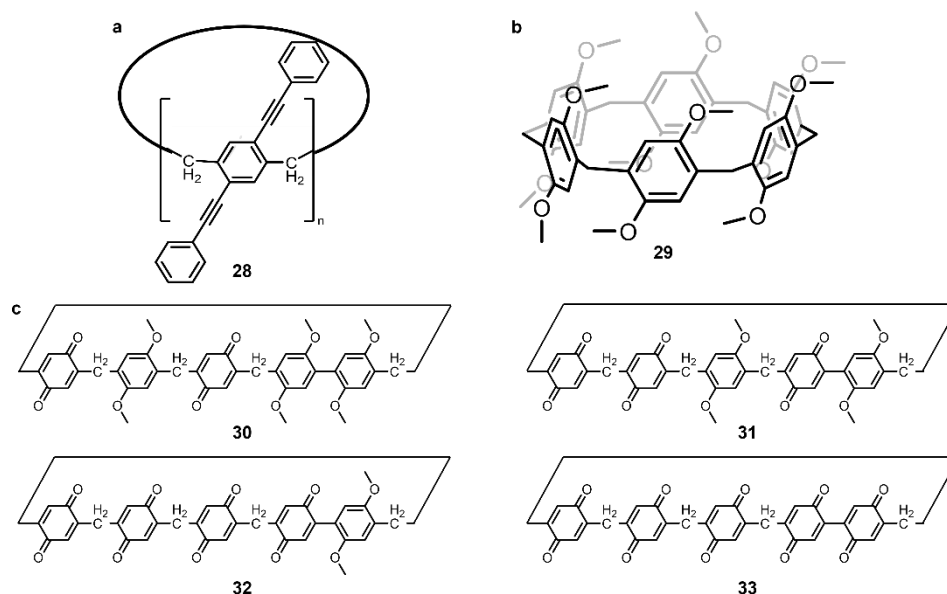


Figure 1.16 Pillar[n]arene compounds that exhibit through-space communication with (a) phenylethynyl (**28**)¹³² and (b) dimethoxy (**29**)¹³³ substituents and (c) benzene units replaced with 2–5 quinone groups (**30–33**).¹³⁴

1.3.4 PROPERTIES AND APPLICATIONS FROM CYCLIC AROMATIC HOMOCONJUGATION IN MOLECULAR TRIANGLES

The utilisation of cyclic aromatic homoconjugation in pillar[n]arenes for use as a fluorescence sensor¹³³ shows that electron delocalisation in macrocycles can impart additional functionality and properties for applications in supramolecular chemistry. Indeed, the delocalisation of electrons in molecular triangles, in addition to the inherent nature of the three electron-deficient, redox-active ADI faces, provides the macrocycles with attractive properties.¹²⁴ These properties include supramolecular assembly,^{136–138} host–guest complexation and co-crystallisation,^{125,139–142} charge and electron-transport^{126,143} and radical anion formation^{144–147} which allow for the aromatic macrocycles to be studied for applications in supramolecular gels,¹³⁷ two-photon absorption,¹⁴⁰ upconversion-emission,¹⁴² non-linear optics,^{141,148,149} cathodes in Li-ion batteries,^{126,143} and organic spintronic devices.¹⁴⁴ Notably, most of the properties and applications of molecular triangles have been studied with respect to the NDI-based macrocycle **17**.

The supramolecular assembly of NDI-based molecular triangle **17**, can be tuned by the presence of different guest molecules and solvent molecules to interact non-covalently with the macrocycle especially within the electron-deficient cavity in the presence of three, cyclic aromatic homoconjugated π -surfaces. Halogenated solvents are able to be encapsulated within the cavity of the macrocycle *via* favourable halogen $\cdots\pi$ interactions. Furthermore, when haloalkanes are used as the solvent, $X\cdots X$ ($X = \text{Cl}$ or Br) NCIs also occur to template the formation of 1D chains of macrocycle.^{136,137} The formation of 1D channels of macrocycle **17** has been proven by studies of the X-ray diffraction pattern of single-crystals of enantiomerically pure **17** (using (*R,R*)-*trans*-1,2-diaminocyclohexane (**17-R**) or (*S,S*)-1,2-*trans*-diaminocyclohexane (**17-S**) linkers) grown *via* vapour diffusion of hexane into a solution of the molecular triangle in 1,2-dibromoethane (Figure 1.17a and b). In the crystal structure, the 1D channels are shown to be composed of stacked dimers of the molecular triangle with one macrocycle in the dimer rotated 60° compared with the other. In addition, the two macrocycles in the dimer are non-covalently bonded by three pairs of $\text{C-H}\cdots\text{O}$ interactions. When the analogous 1,2-dichloroethane solvent was used, 1D channels were indeed formed, however, the macrocycles are rotated by 62.7° , with the formation of helical tetramers instead (Figure 1.17c). The screw axis of the helical tetramer is induced by the chirality of the (*R,R*)- or (*S,S*)-1,2-*trans*-diaminocyclohexane linker, where if the opposite enantiomer was used, the opposite *m*- or *p*- helix forms. The absence of the helical 1D channels when $\text{BrCH}_2\text{CH}_2\text{Br}$ and other analogues (1-chloro-2-bromoethane and 1-chloro-2-iodoethane) were used as crystallisation solvents suggests that the length of the chlorinated alkane and subsequent $\text{Cl}\cdots\text{Cl}$ interactions are optimal to allow the cooperative $\text{C-H}\cdots\text{O}$ interactions to translate the molecular chirality to the supramolecular scale.¹³⁶

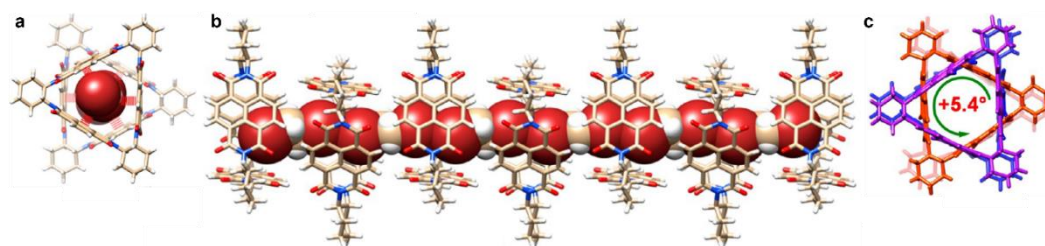


Figure 1.17 Crystal structures showing the assembly of NDI-based macrocycle to form supramolecular nanotubes with 1,2-dibromoethane from (a) top view and (b) side view. (c) Assembly with 1,2-dichloroethane forms a helical chain with an additional 5.4° twist. Figure replicated and adapted from reference 136.¹³⁶

The influence of the size of and geometry of the halogenated solvent was also exhibited when the *cis*-isomer of 1,2-dichloroethene was dissolved in **17-R**, where an organogel was formed composed of nanofibers which assemble into intertwined nanoribbons.¹³⁶ An organogel is formed in this scenario as a result of increased flexibility in the 1D channels of triangle molecules where alkene $\cdots\pi$ interactions occur between solvent (1,2-dichloroethene) and the electron-deficient cavity of **17** in addition to longer (and thus weaker) Cl \cdots Cl NCIs. Although, organogels are not formed when enantiomerically pure **17** (*-R* or *-S*) is dissolved in saturated halogenated alkane solvents, when a 1:1 racemic mixture of **17-R** and **17-S** is dissolved in 1,2-dichloroethane a gelled network of interwoven fibrillar chains is formed.¹³⁷ The formation of the fibrils is templated by (i) Cl $\cdots\pi$ (between solvent and **17**) and (ii) Cl \cdots Cl interactions (between solvent molecules) as discussed for the 1D chains in the crystalline state above. As no gelation occurs when enantiomerically pure samples of NDI-based triangle **17** (**17-R** or **17-S**) are dissolved in ClCH₂CH₂Cl, the preference of the racemic mixture to form 1D fibrils was attributed to the greater cooperativity of the two opposite enantiomers of the macrocycle for 12 intermolecular C-H \cdots O interactions compared with two molecular triangle molecules of the same chirality (6 C-H \cdots O NCIs).¹³⁷ Although organogels do not form when racemic mixtures of **17** are dissolved in other halogenated solvents (CH₂Cl₂, CHCl₃, ClCH₂CH₂Br, ClCH₂CH₂I and BrCH₂CH₂Br) they do form precipitates, with the BrCH₂CH₂Br solid assembling into 1D fibres in a similar manner to the organogel although in the brominated solvent more rigid, thicker and straighter structures are formed which potentially influences its ability to form a gelled structure.¹³⁷

The supramolecular packing of molecular triangles can also be tuned through the growth of single crystals using host–guest mixtures or co-crystallisations utilising the cyclic aromatic homoconjugation in molecular triangles for interactions with the electron-deficient delocalised π -surface. For example, NDI-based macrocycle **17** also forms helical 1D chains in the solid state when complexed with an electron-rich triiodide anion guest (Figure 1.18).¹²⁵ Host–guest complexes between **17** and I₃[−] (**17**⊃I₃[−]) have been observed in a 1:1 ratio in the crystalline solid state enabled by anion $\cdots\pi$ interactions between macrocycle and anion. In the structure, the guest anion is encapsulated within the electron-deficient cyclic aromatic homoconjugated aromatic cavity with the tetrabutylammonium counter cation being charge-separated. In CD₂Cl₂ solution, a binding constant of $25 \pm 2 \text{ M}^{-1}$ was measured by ¹H NMR spectroscopy and in the solid state, the supramolecular packing of the molecular triangles form *p*- or

m-helical chains depending on which chiral linker is used, (*R,R*)- or (*S,S*)-1,2-*trans*-diaminocyclohexane respectively. The assembly of 1D helical chains of **17**⊃I₃[−] is enabled by intermolecular $\pi\cdots\pi$ interactions between adjacent macrocycles. Such aromatic interactions are ‘turned on’ upon incorporation of an electron-rich guest within the cavity of the macrocycle, with no $\pi\cdots\pi$ interactions observed in the absence of I₃[−].¹²⁵ Although, subsequent crystal engineering of NDI based macrocycle **17** at a range of concentrations in MeCN did show different supramolecular packing into a honeycomb and hexagonal pattern of nanotube like structures *via* $\pi\cdots\pi$ and C-H \cdots O interactions with encapsulated diethyl ether anti-solvent molecules in the cavity of the molecular triangle.¹³⁸

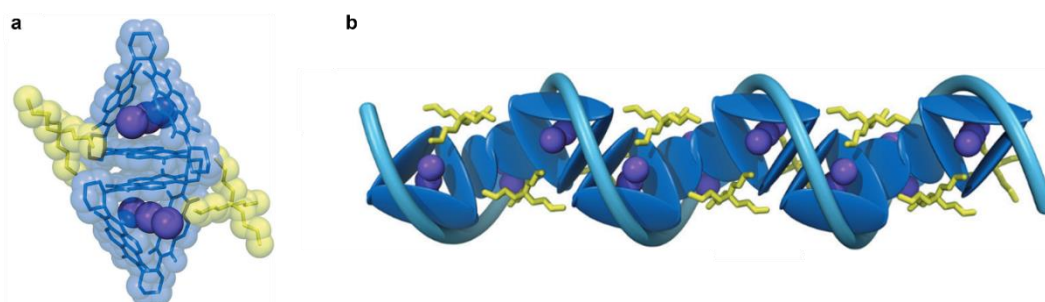


Figure 1.18 Host–guest complex of **17**⊃I₃[−] where encapsulation of the triiodide anion (a) ‘turns on’ $\pi\cdots\pi$ interactions between macrocycles in the unit cell and (b) induces the formation of helical nanotubes where the chirality of the helix is dependent on the presence of (*R,R*)- or (*S,S*)-*trans*-1,2-diaminocyclohexane in the molecular triangle. Figure replicated and adapted from reference 125.¹²⁵

Alternatively, a range of different supramolecular packing arrangements form when **17** is co-crystallised with the electron-rich tetrathiafulvalene (TTF) small molecule.¹³⁸ Three polymorphs of **17**⊃TTF charge-transfer (CT) cocrystals form depending on the solvents used and the crystallisation method, *e.g.*, slow evaporation in MeCN, vapour diffusion of hexane into CHCl₃ and either vapour diffusion of diethylether or hexane into a CH₂Cl₂ solution or slow evaporation of a CH₂Cl₂ solution. The single crystal grown in MeCN contains dimers of **17** that form on account of C-H \cdots O interactions with a disordered bridging TTF molecule encapsulated within the cavity of both macrocycles. The encapsulation of the TTF molecule within the macrocycle is enabled by face-to-face $\pi\cdots\pi$ and end-to-face S $\cdots\pi$ interactions between the TTF molecule and the cyclic aromatic homoconjugated electron-deficient π -surface in the cavity. Outside of the cavity of the macrocycle, the two molecular triangle units interact with a further two TTF molecules each with the third NDI surface interacting *via* $\pi\cdots\pi$ contacts with an adjacent molecule of **17**. The various intermolecular contacts between triangle molecules and triangle and TTF molecules leads to the formation of a 2D network of CT interactions (Figure 1.19a).¹³⁸

Conversely, when **17** is co-crystallised with TTF in halogenated solvents (CHCl₃ and CH₂Cl₂), the electron-rich molecule is unable to fill the cavity of the macrocycle as it faces competition with solvent molecules which can interact *via* Cl $\cdots\pi$ contacts between solvent and the through-space conjugated π -surface. In the crystal structure with encapsulated CHCl₃ molecules, there are two macrocycles in the unit cell, rotated by 60° to maximise intermolecular C-H \cdots O interactions and allowing for the formation

of supramolecular nanotubes. The two triangle molecules in the dimer represent two layers of ordered structure in the supramolecular packing in the single crystal. In one of the layers, each of the **17** macrocycles interact with three TTF molecules through $\pi \cdots \pi$ contacts with the NDI surface as well as C-H $\cdots\pi$ interactions between the cyclohexane protons of the molecular triangle and the TTF guest (Figure 1.19b and d). The regular pattern of the layer is also facilitated by Cl \cdots S interactions between CHCl₃ and TTF molecules. Whereas in the second layer, the triangle molecules interact with CHCl₃ molecules (*via* Cl $\cdots\pi$ interactions) only with no involvement of TTF molecules. The solvent molecules present in this second layer are also interacting with each other through Cl \cdots Cl interactions to provide additional order to the layer through the formation of a hexagonal grid of solvent. In both of the layers of the crystal described above, the macrocycles are assembled in a vertex to edge manner which leads to a tiling effect of the molecular triangles.¹³⁸ A slightly different scenario is observed when the cavity of the macrocycle is filled with a CH₂Cl₂ solvent molecule (single crystals grown either by vapour diffusion of Et₂O or hexane or slow evaporation of CH₂Cl₂ solutions). As has been observed in other crystal structures of **17**, the macrocycles interact *via* complementary C-H \cdots O contacts to form 1D channels of supramolecular nanotubes. Furthermore, the unit cell contains a single molecular triangle with an encapsulated CH₂Cl₂ molecule inside the cavity and three external TTF molecules that coordinate with the macrocycle through $\pi \cdots \pi$ interactions. The packing within the crystal structure is assisted by additional S \cdots S interactions between TTF units in addition to the occurrence of $\pi \cdots \pi$ interactions between macrocycle and small molecule. These S \cdots S interactions between TTF molecules occur in a cyclic manner to form a triangular structure which is similar in size to a **17** molecular triangle and subsequently leads to a tessellated pattern of molecular triangles and coordinated TTF supramolecular triangles (Figure 1.19c and e).¹³⁸

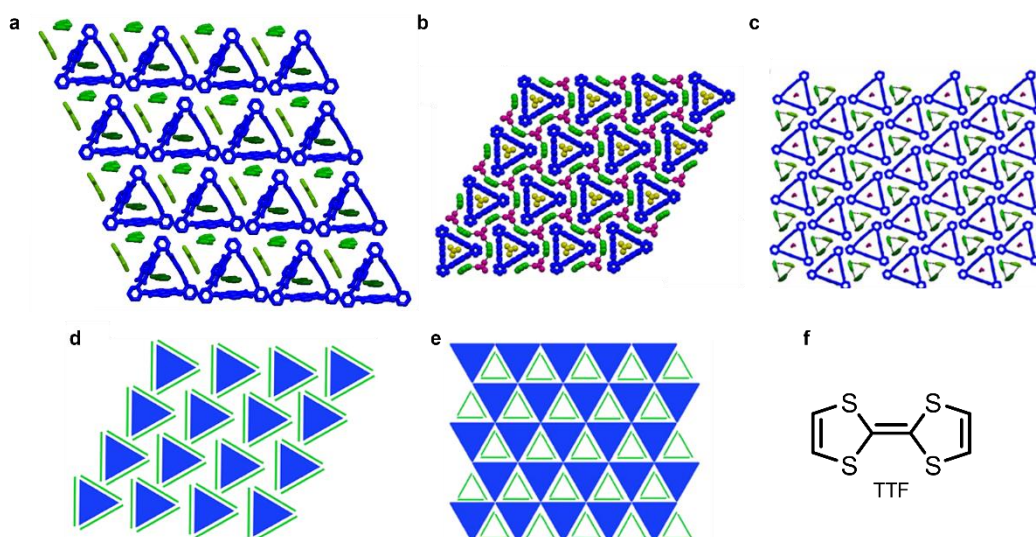


Figure 1.19 Supramolecular tessellation in the solid state of **17** with TTF in (a) MeCN, (b) CHCl₃ and (c) CH₂Cl₂. General schematics of the 2D pattern of **17** and TTF in (d) CHCl₃ and (e) CH₂Cl₂. (f) Structure of tetrathiafulvalene (TTF). Figure replicated and adapted from reference 138.¹³⁸

The co-crystals between **17** and TTF discussed earlier were prepared to investigate the potential application of the CT interactions between the electron deficient, cyclic aromatic homoconjugated π -surface and the electron-rich donor for charge and electron transport in organic semiconductor devices.¹³⁸ Other co-crystals of molecular triangles have been prepared *via* D–A $\pi\cdots\pi$ interactions between electron-rich aromatic donors (coronene (Cor)),^{140,141} 9,10-dichloroanthracene (DCA)¹⁴² or 1-chloronaphthalene (CN)¹⁴² and electron-deficient **17** for non-linear optical applications. These co-crystals^{140,142} present similar structural features as discussed for **17**⊃TTF¹³⁸ where complementary C–H \cdots O interactions between molecular triangles at 60° rotations to form 1D channels of acceptor macrocycles and donors in **17**⊃Cor,¹⁴⁰ **17**⊃DCA¹⁴² and **17**⊃CN.¹⁴² In the solid state, coronene prefers to assemble with macrocycle **17** through face-to-face $\pi\cdots\pi$ interactions with the crystals emitting red light under a fluorescent microscope, compared with green emission from the respective donor or acceptor crystals alone and confirmed by fluorescence spectroscopy. Furthermore, the **17**⊃Cor co-crystals also exhibited greater two-photon absorption compared with the individual donor or acceptor crystals on account of the π -orbital overlap between the coronene donor and molecular triangle acceptor facilitating electron delocalisation and subsequent supramolecular electronic polarisation.^{140,141} In a similar manner to **17**⊃Cor, D–A co-crystals (**17**⊃DCA and **17**⊃CN) exhibit red-shifted emission (red and yellow luminescence respectively) compared with crystals containing the individual D or A components. The supramolecular packing of **17**⊃DCA forms a hexagonal superstructure with each DCA donor molecule interacting with two macrocycles of **17** through $\pi\cdots\pi$, Cl $\cdots\pi$ and Cl \cdots H–C contacts. Conversely, **17**⊃CN, forms a vertex-to-edge tiling superstructure which is enabled by $\pi\cdots\pi$ and C–H $\cdots\pi$ interactions between NDI-based molecular triangle **17** and 1-chloronaphthalene. The red and yellow emission of **17**⊃DCA and **17**⊃CN respectively in co-crystals are replicated in their crystalline thin films. As a result of stronger binding between macrocycle **17** with CN than DCA, upon exposure of **17**⊃DCA with solvent vapour of CN, the emission colour changes from red to yellow representing the formation of co-crystals of **17**⊃CN with the transformation being reversible. The co-crystals also exhibited two-photon absorption and excited fluorescence which combined with the possible interconversion between **17**⊃DCA and **17**⊃CN could allow for application as a non-linear optical switch with dual-colour emission.¹⁴²

The inherent properties of the redox-active nature of NDI and PMDI based molecular triangles **17** and **16** respectively have allowed them to be utilised as cathodic materials in lithium-ion batteries, taking advantage of the high number of accessible reduced states (up to six electron reductions) for such relatively small molecules. Such properties include (i) the cyclic aromatic homoconjugation enabling the efficient delocalisation of electrons around the macrocycle, (ii) the porous nature of the molecular triangle allowing for the diffusion of Li⁺ ions and (iii) decreased solubility in battery solvents providing the electrode increased stability.^{124,126,143} The molecular triangles maintain a high capacity performance after a large number of cycles, *e.g.*, after 300 cycles at a current rate of 10 C, **17** maintains a performance

of 71.1 mAh g⁻¹ compared with a theoretical maximum capacity of 154.8 mAh g⁻¹ (46%). The exceptional performance of **17** in Li-ion batteries shows a considerable improvement compared with the acyclic, monomeric NDI reference compound (**20**) which exhibits a rapid loss of discharge capacity (mAh g⁻¹) with the majority of the capacity lost after 10 cycles at a current rate of 1 C.¹⁴³ Similarly, the PMDI based molecular triangle **16**, exhibits exceptional performance compared with the analogous monomeric reference compound, **19**. The initial capacity of macrocycle **16** was calculated to be 163 mAh g⁻¹ which reduced to 86 mAh g⁻¹ (64%) after 50 cycles at a current rate of 5 C. The high solubility of the acyclic monomer **19** means it has poor performance in cathodic materials with the discharge capacity reduced to less than 10 mAh g⁻¹ (from an initial capacity of 94 mAh g⁻¹).¹²⁶

Upon chemical reduction of molecular triangle **17** with one equivalent of cobaltocene (CoCp₂), the mono-radical anion ([**17**]^{•-}) was formed and studies of the free radical through *cw*-EPR and *cw*-ENDOR experiments confirmed the delocalisation of electrons around the macrocycle *via* cyclic aromatic homoconjugation.¹²⁵ Mono-radical anions of **17** in the crystalline solid state formed electrochemically (with a range of electrolytes: Rb•ClO₄,¹⁴⁵ NH₄•ClO₄,¹⁴⁵ TBA•ClO₄,^{145,147} and MePy•PF₆,¹⁴⁵) have been shown to assemble into a packing structure that resembles the elusive K₄ polymorph of carbon *via* supramolecular intermolecular $\pi\cdots\pi$ interactions between macrocycles. Further electrochemical preparations of the mono-radical anion of **17** where the free electron is delocalised around the macrocycle in the presence of multidentate ligands (18-crown-6, 15-crown-5 and 2,2,2-cryptand) and electrolyte salts (Na•ClO₄, K•ClO₄, Rb•ClO₄ and Cs•ClO₄) revealed cubic or tetragonal space groups with extensive supramolecular packing.¹⁴⁶ Consequently, upon further reduction to the tris-radical anion ([**17**]^{3•-}) which was confirmed by X-ray crystallography, a doublet spin state is observed at 7 K which then transitions to a quartet state above 15 K. Further studies by EPR spectroscopy and of magnetic susceptibility confirm an antiferromagnetic intramolecular superexchange in the tris-radical anion *via* three cobaltocenium counter anions as well as the tris-radical anion exhibiting spin frustration.¹⁴⁴

Thus far, the influence of electron delocalisation *via* cyclic aromatic homoconjugation on the structural and optoelectronic properties of rigid, shape-persistent molecular triangles has been shown. Furthermore, the ability of the electron-deficient through-space conjugated macrocycles to interact with solvents and electron-rich guests to (i) enable supramolecular packing into nanotubes or tessellated 2D nanosheets and (ii) to form D–A charge-transfer complexes to access optically active two-photon absorption and dual-emissive materials has been discussed. The redox-active nature of the molecular triangles to accept electrons has also prompted their study as cathodic materials in Li-ion batteries alongside characterisation of the radical-anion reduced states.

1.4. CORE-FUNCTIONALISED AROMATIC DIIMIDES

Molecular triangles have been known for over 20 years since the seminal synthesis of the PMDI based macrocycle **16** by Gawroński *et al.*¹¹⁹ in 2002. Subsequently, it has been shown that cyclic aromatic

homoconjugation around the macrocycle imparts attractive structural and optoelectronic properties in the molecular triangles for potential applications in optical devices and lithium-ion batteries. Despite the extensive study of the properties of molecular triangles, the influence of core-functionalisation of ADI faces in the macrocycles has only recently begun to be explored.¹⁵⁰ Although the PDI based molecular triangle **18** contained 12 phenoxy-substituents on the aromatic core (four substituents per ADI face), this was to improve the solubility of the macrocycle and the effect of the functionalisation on the properties of the compound was not investigated.¹²⁷

The lack of exploration of core-functionalised molecular triangles is surprising given that core-substituted ADIs, in particular NDIs and PDIs, have been extensively studied and reviewed in the literature.^{151–155} Core-functionalisation of NDIs and PDIs usually begins with the halogenation of the aromatic core of the parent anhydride which can then be converted to diimides by condensation with a wide range of amines.¹⁵⁶ The presence of the aromatic C-X (X = Cl or Br) bonds allows for the access of a large scope of products through various reaction types including (i) nucleophilic substitution (S_NAr),^{157,158} (ii) Buchwald-Hartwig¹⁵⁹ and (iii) Suzuki-Miyaura^{160,161} couplings (Figure 1.20). Upon the addition of electron-donating or -withdrawing substituents to the aromatic core in NDIs or PDIs the optoelectronic properties can be tuned to vary the absorption and emission wavelengths and reduction potentials of the two-electron acceptors.¹⁶²

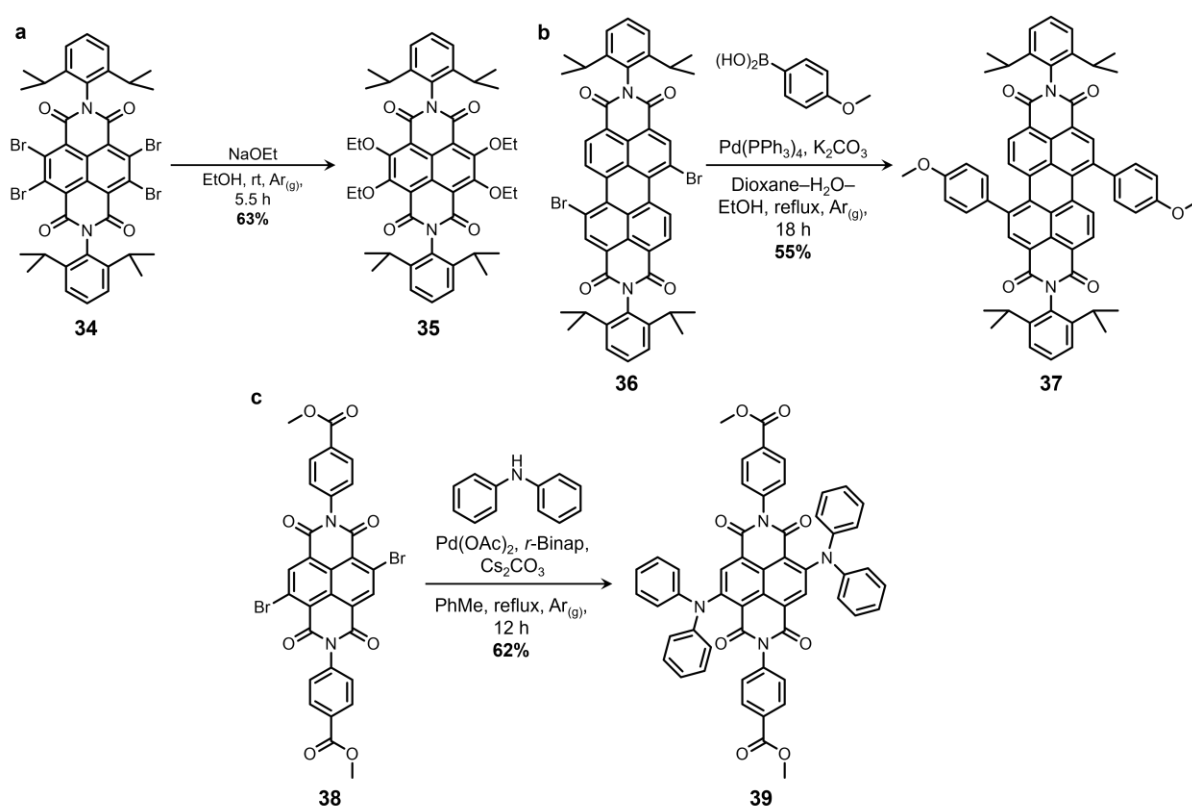


Figure 1.20 Examples of the synthesis of core-functionalised ADIs including (a) S_NAr of NDI **34**,¹⁵⁸ (b) Suzuki-Miyaura coupling of PDI **36**¹⁶¹ and (c) Buchwald-Hartwig coupling of NDI **38**.¹⁵⁹

Although NDIs are not inherently luminescent, their emission can be ‘turned on’ upon core-functionalisation of the electron-deficient π -surface with electron-rich alkylamines or alkoxy substituents.¹⁶³ Furthermore, the emission of NDIs can be tuned towards delayed fluorescence (DF) and room-temperature phosphorescence (RTP) upon core-functionalisation with electron-rich carbazoles in **40** and **41** (Figure 1.21a and b), where the D–A interaction with the electron-deficient π -surface allows for triplet harvesting by narrowing the energy gap between the singlet and triplet excited states.¹⁶⁴ Alternatively, core-functionalisation with two *N*-benzyl-4-aminopiperidine substituents **42** (Figure 1.21c) enables the NDI based small molecule to be used as a pH sensor where the emission is sensitive to the presence of H^+ cations on account of the protonation of the piperidine nitrogen in **43**. The emission is blue-shifted in the protonated form with increased quantum yield compared with the neutral form with interconversion between the two states being reversible upon addition of trifluoroacetic acid and triethylamine respectively.¹⁶⁵ The redox-active nature of electron-deficient NDI small molecules to accept electrons makes them attractive materials for charge transport in organic semiconductors (OSCs). Furthermore, the ability to tune the energies of the frontier molecular orbitals of NDIs through functionalisation of the aromatic core can improve the air stability of the compounds in the anionic state. Most commonly, NDIs are utilised as *n*-type materials on account of the transport of electrons being favourable *via* the electron-deficient π -surface which can be enhanced through core-functionalisation with electron-withdrawing substituents, *e.g.* 2-(1,3-dithiol-2-ylidene)malonitrile moieties in **44** (Figure 1.21c).¹⁶⁶ However, when the naphthalene core is fused with electron-rich carbazole donors in **45** (Figure 1.21d), the charge transport can be tuned towards the movement of holes in *p*-type OSCs. The inclusion of bulky 1,3-diisopropylaniline end-groups prevent cofacial $\pi\cdots\pi$ interactions of the π -surfaces, with intermolecular slip-stacked interactions between carbazole donors on adjacent NDI molecules promoting transport of holes.¹⁶⁶

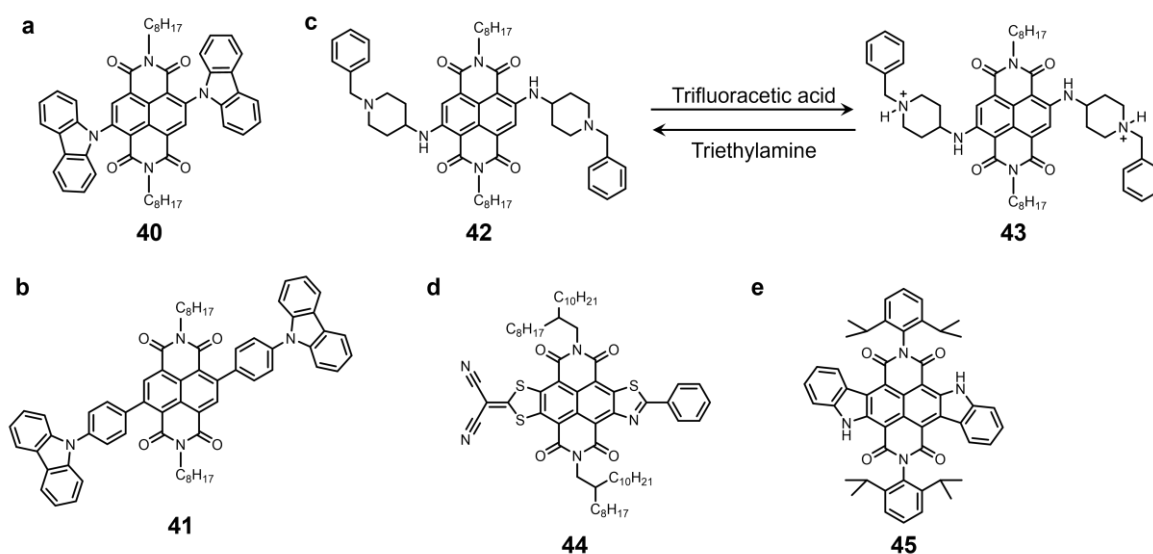


Figure 1.21 Examples of core-functionalised NDIs substituted with (a) carbazole¹⁶⁴ and (b) phenyl carbazole for DF and RTP emission,¹⁶⁴ (c) piperidine derivatives for use as fluorescent pH sensors,¹⁶⁵ (d) 2-(1,3-dithiol-2-ylidene)malonitrile for use as an *n*-type OSC¹⁶⁶ and (e) fused carbazole for *p*-type OSCs.¹⁶⁶

In addition to influencing the optoelectronic properties, core-functionalisation of NDIs and PDIs can be used to tune the supramolecular assembly of the compounds. The inclusion of methoxytriethylene glycol chains on aromatic core-substituents in **46** induces supramolecular assembly of the NDIs into spherical vesicles which were observed by transmission electron microscopy and confirmed by dynamic light scattering to have an average size of 90 nm (Figure 1.22a).¹⁶⁷ Furthermore, the aggregation of NDIs was tuned by inverting alkyl and peptide functionality in *N*-substituted end-group and aromatic core-substituents in **47** and **48** (Figure 1.22b). When the peptide-based substituent is located on the aromatic core and *N*-alkyl imide end-group, $\pi \cdots \pi$ interactions are dominant to form an H-aggregated state in n-hexane. Whereas when the substituents are inverted with *N*-peptide imide end-groups and alkylated aromatic core, intermolecular hydrogen-bonding between amino acids is preferred towards a J-aggregated state in n-hexane.¹⁶⁸ Core-functionalisation of PDIs has also been shown to enable dimerisation as shown earlier in Section 1.2 by Penty *et al.*⁵³ where click reactions were used to generate macrocycle **7** (Figure 1.5). Alternatively, Ball *et al.*¹⁶⁹ used a Stille reaction to synthesise a through-bond conjugated PDI dimer **49**, where the helicity of the perylene aromatic core means that a mixture of interconvertible (*R,R*), (*S,S*) and (*S,R*) conformations are isolated. These conformers can interconvert at room temperature and the authors showed that a pure sample of the (*S,S*) isomer interconverted to the equilibrium mixture with the (*R,R*) isomer and achiral (*S,R*) forms within two hours.¹⁶⁹

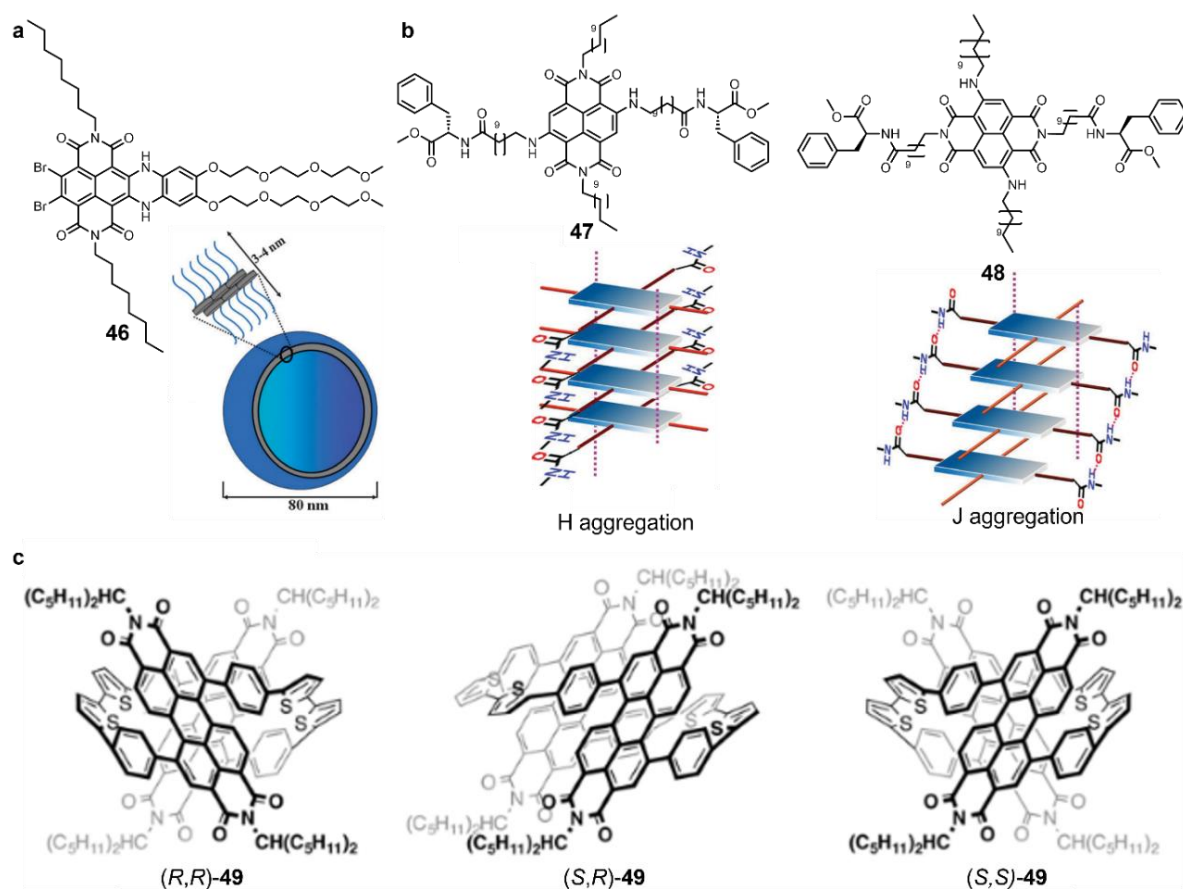


Figure 1.22 Structure of core-functionalised NDIs to influence the supramolecular assembly into (a) spherical vesicles (**46**)¹⁶⁷ and (b) H-aggregates (**47**) and J-aggregates (**48**).¹⁶⁸ (c) Core-functionalisation of PDI to generate a through-bond conjugated macrocycle **49** in (*R,R*), (*S,R*) and (*S,S*) conformations.¹⁶⁹ Figures reproduced from References 167, 168 and 169.^{167–169}

Although dimerisation *via* core-functionalisation has been shown in PDI dimers, macrocyclisation is more commonly achieved through end-group substitution for example in the NDI dimer **6** which exhibited cofacial π -orbital overlap.⁵² Macrocycles containing two or more PMDI units have also been synthesised by end-group substitution *e.g.* **50–54**. The presence of core-halogenated PMDI faces in these dimers and trimers provides functional handles *via* cross-coupling reactions towards carbon nanotube like structures, where the oligomerisation could be capped by the macrocycles containing asymmetric mono-functionalised PMDI units. Indeed, the core-brominated macrocycles have been π -extended *via* Sonogashira coupling with phenylethynyl substituents to provide a proof-of-concept towards future carbon nanotube like structures (Figure 1.23a).^{170–172} The PMDI trimers, **51–53**, bear a resemblance to the rigid shape-persistent molecular triangle **16**, which until recently, no core-functionalised analogues of had been prepared. In 2023, Wang and Zhao¹⁵⁰ presented the first example of a core-functionalised, cyclic aromatic homoconjugated PMDI based molecular triangle through the addition of six bromine atoms, **55** (Figure 1.23b). They showed that core-bromination of the PMDI based molecular triangle influences the supramolecular assembly of the macrocycle to form a crystalline, porous hydrogen-bonded organic framework which can be reversibly converted to and from its amorphous form upon the removal and addition of solvent molecules.¹⁵⁰ Apart from the influence of core-bromination on the supramolecular assembly of the molecular triangle in the solid state, no other properties or applications of the functionalised macrocycle were explored which is despite the wide range of properties and applications that have been studied for both unsubstituted molecular triangles and core-functionalised ADIs discussed in this Chapter.

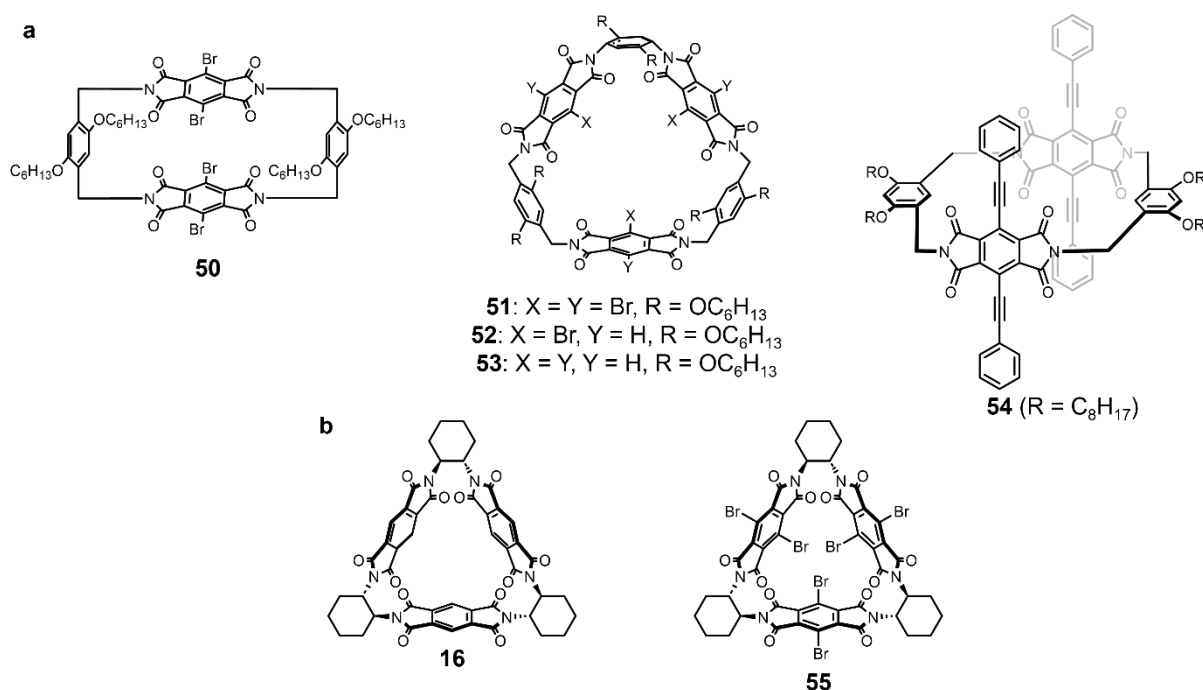


Figure 1.23 (a) Examples of core-functionalised PMDI macrocycles **50–54** through end-group linkages^{170–172} and (b) PMDI based molecular triangle **16**^{119,126} and its core-brominated derivative **55**.¹⁵⁰

1.5. OVERVIEW

As discussed in this Chapter, cyclic aromatic homoconjugation in molecular triangles comprised of aromatic diimides (ADIs) provides the macrocycles with a vast array of structural and optoelectronic properties. It is surprising therefore that until 2023, the influence of core-functionalisation of the ADI faces in molecular triangles had not been explored, despite substitution of the aromatic core being shown to also affect the structural and optoelectronic properties of the small molecules. Therefore, it was envisioned that the π -electronics of cyclic aromatic homoconjugated molecular triangles could be tuned through the introduction of either electron-withdrawing or -donating substituents to the aromatic core of the ADI faces in the macrocycle.

In Chapter 2, the first report of a core-substituted PMDI-based molecule triangle (**55**) by Wang and Zhao¹⁵⁰ is discussed and the structural and optoelectronic properties of the core-brominated macrocycle is investigated in addition to further post-synthetic functionalisation to yield a hexa-arylated molecular triangle. The core-functionalised molecular triangles (Figure 1.24) synthesised and studied in Chapter 2 present the first steps towards triangular nanoprisms of covalently bonded molecular triangles. The functionalisation of the PMDI based molecular triangle in this and future Chapters is selected on account of its reduced number of sites for aromatic substitution providing greater selectivity compared with the analogous NDI and PDI macrocycles. In Chapter 3, analogous tris-brominated and -arylated molecular triangles (Figure 1.24) are presented which exist as a mixture of atropisomers. Consequently, the role of the electron-deficient cyclic aromatic homoconjugated π -surface in the cavity of the macrocycle through intra- and intermolecular halogen $\cdots\pi$ interactions is investigated.

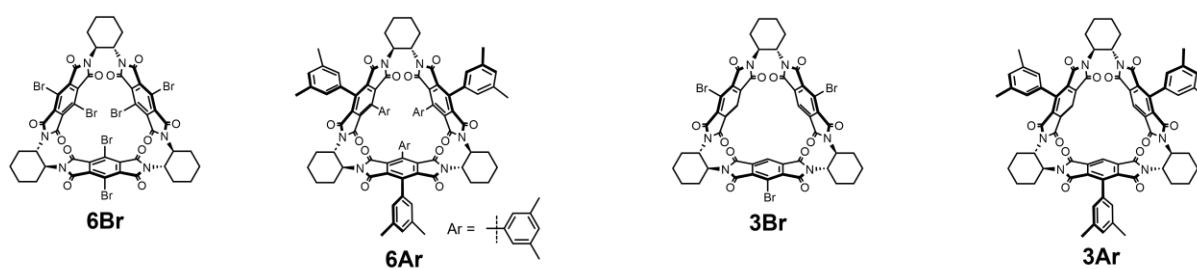


Figure 1.24 Structures of core-functionalised PMDI based molecular triangles synthesised and studied in this Thesis.

Chapter 4 discusses the influence of core-functionalisation of molecular triangles on the solution- and solid-state luminescent properties of the macrocycles. Furthermore, synthetic efforts to pursue core-hydroxylated molecular triangles are presented to access their potential as luminescent compounds through excited-state intramolecular proton transfer. Lastly, in Chapter 5, the potential application of core-functionalised molecular triangles as *n*-type organic semiconducting materials is discussed through the fabrication and electrochemical reduction of macrocyclic thin films. Additionally, the potential of an electron-deficient hexa-brominated molecular triangle as a dopant for electron-rich *p*-type polymers as bulk heterojunctions in photovoltaic cells is investigated. This Thesis expands the scope of molecular

triangles through the core-functionalisation of the PMDI core with three or six bromine atoms and 3,5-dimethylbenzene groups. Thus, synthetic methods for progress towards triangular nanoprisms of covalently bonded molecular triangles are provided in addition to the inherent interesting dynamic structural and optoelectronic properties of the core-functionalised macrocycles.

1.6. REFERENCES

- (1) Luo, H.; Yu, C.; Liu, Z.; Zhang, G.; Geng, H.; Yi, Y.; Broch, K.; Hu, Y.; Sadhanala, A.; Jiang, L.; Qi, P.; Cai, Z.; Sirringhaus, H.; Zhang, D. Remarkable Enhancement of Charge Carrier Mobility of Conjugated Polymer Field-Effect Transistors upon Incorporating an Ionic Additive. *Sci. Adv.* **2016**, *2*, e1600076.
- (2) Wu, J.; Pisula, W.; Müllen, K. Graphenes as Potential Material for Electronics. *Chem. Rev.* **2007**, *107*, 718–747.
- (3) Shirakawa, H.; Louis, E. J.; MacDiarmid, A. G.; Chiang, C. K.; Heeger, A. J. Synthesis of Electrically Conducting Organic Polymers: Halogen Derivatives of Polyacetylene, (CH)_x. *J. Chem. Soc. Chem. Commun.* **1977**, 578–580.
- (4) Chiang, C. K.; Druy, M. A.; Gau, S. C.; Heeger, A. J.; Louis, E. J.; MacDiarmid, A. G.; Park, Y. W.; Shirakawa, H. Synthesis of Highly Conducting Films of Derivatives of Polyacetylene, (CH)_x. *J. Am. Chem. Soc.* **1978**, *100*, 1013–1015.
- (5) Audenaert, M.; Gusman, G.; Deltour, R. Electrical Conductivity of I₂-Doped Polyacetylene. *Phys. Rev. B* **1981**, *24*, 7380–7382.
- (6) Kholmanov, I. N.; Magnuson, C. W.; Aliev, A. E.; Li, H.; Zhang, B.; Suk, J. W.; Zhang, L. L.; Peng, E.; Mousavi, S. H.; Khanikaev, A. B.; Piner, R.; Shvets, G.; Ruoff, R. S. Improved Electrical Conductivity of Graphene Films Integrated with Metal Nanowires. *Nano Lett.* **2012**, *12*, 5679–5683.
- (7) Odom, S. A.; Caruso, M. M.; Finke, A. D.; Prokup, A. M.; Ritchey, J. A.; Leonard, J. H.; White, S. R.; Sottos, N. R.; Moore, J. S. Restoration of Conductivity with TTF-TCNQ Charge-Transfer Salts. *Adv. Funct. Mater.* **2010**, *20*, 1721–1727.
- (8) Yavari, F.; Kritzinger, C.; Gaire, C.; Song, L.; Gulapalli, H.; Borca-Tasciuc, T.; Ajayan, P. M.; Koratkar, N. Tunable Bandgap in Graphene by the Controlled Adsorption of Water Molecules. *Small* **2010**, *6*, 2535–2538.
- (9) Allen, M. J.; Tung, V. C.; Kaner, R. B. Honeycomb Carbon: A Review of Graphene. *Chem. Rev.* **2010**, *110*, 132–145.
- (10) Rathinavel, S.; Priyadharshini, K.; Panda, D. A Review on Carbon Nanotube: An Overview of Synthesis, Properties, Functionalization, Characterization, and the Application. *Mater. Sci. Eng. B* **2021**, *268*, 115095.
- (11) Mirzaei, S.; Castro, E.; Hernández Sánchez, R. Conjugated Molecular Nanotubes. *Chem. – Eur. J.* **2021**, *27*, 8642–8655.
- (12) Iyoda, M.; Yamakawa, J.; Rahman, M. J. Conjugated Macrocycles: Concepts and Applications. *Angew. Chem. Int. Ed.* **2011**, *50*, 10522–10553.
- (13) E. Lewis, S. Cycloparaphenylenes and Related Nanohoops. *Chem. Soc. Rev.* **2015**, *44*, 2221–2304.

- (14) Jasti, R.; Bhattacharjee, J.; Neaton, J. B.; Bertozzi, C. R. Synthesis, Characterization, and Theory of [9]-, [12]-, and [18]Cycloparaphenylene: Carbon Nanohoop Structures. *J. Am. Chem. Soc.* **2008**, *130*, 17646–17647.
- (15) Takaba, H.; Omachi, H.; Yamamoto, Y.; Bouffard, J.; Itami, K. Selective Synthesis of [12]Cycloparaphenylene. *Angew. Chem. Int. Ed.* **2009**, *48*, 6112–6116.
- (16) Lv, Y.; Lin, J.; Song, K.; Song, X.; Zang, H.; Zang, Y.; Zhu, D. Single Cycloparaphenylene Molecule Devices: Achieving Large Conductance Modulation via Tuning Radial π -Conjugation. *Sci. Adv.* **2021**, *7*, eabk3095.
- (17) Huang, Q.; Zhuang, G.; Zhang, M.; Wang, J.; Wang, S.; Wu, Y.; Yang, S.; Du, P. A Long π -Conjugated Poly(Para-Phenylene)-Based Polymeric Segment of Single-Walled Carbon Nanotubes. *J. Am. Chem. Soc.* **2019**, *141*, 18938–18943.
- (18) Peters, G. M.; Grover, G.; Maust, R. L.; Colwell, C. E.; Bates, H.; Edgell, W. A.; Jasti, R.; Kertesz, M.; Tovar, J. D. Linear and Radial Conjugation in Extended π -Electron Systems. *J. Am. Chem. Soc.* **2020**, *142*, 2293–2300.
- (19) Peterson, E.; Maust, R. L.; Jasti, R.; Kertesz, M.; Tovar, J. D. Splitting the Ring: Impact of Ortho and Meta π Conjugation Pathways through Disjointed [8]Cycloparaphenylene Electronic Materials. *J. Am. Chem. Soc.* **2022**, *144*, 4611–4622.
- (20) Wang, J.; Zhang, X.; Jia, H.; Wang, S.; Du, P. Large π -Extended and Curved Carbon Nanorings as Carbon Nanotube Segments. *Acc. Chem. Res.* **2021**, *54*, 4178–4190.
- (21) Lu, D.; Wu, H.; Dai, Y.; Shi, H.; Shao, X.; Yang, S.; Yang, J.; Du, P. A Cycloparaphenylene Nanoring with Graphenic Hexabenzocoronene Sidewalls. *Chem. Commun.* **2016**, *52*, 7164–7167.
- (22) Kuwabara, T.; Orii, J.; Segawa, Y.; Itami, K. Curved Oligophenylenes as Donors in Shape-Persistent Donor–Acceptor Macrocycles with Solvatofluorochromic Properties. *Angew. Chem. Int. Ed.* **2015**, *54*, 9646–9649.
- (23) Stawski, W.; Van Raden, J. M.; Patrick, C. W.; Horton, P. N.; Coles, S. J.; Anderson, H. L. Strained Porphyrin Tape–Cycloparaphenylene Hybrid Nanorings. *Org. Lett.* **2023**, *25*, 378–383.
- (24) Hoffmann, M.; Kärnbratt, J.; Chang, M.-H.; Herz, L. M.; Albinsson, B.; Anderson, H. L. Enhanced π Conjugation around a Porphyrin[6] Nanoring. *Angew. Chem. Int. Ed.* **2008**, *47*, 4993–4996.
- (25) Bressan, G.; Peeks, M. D.; Anderson, H. L.; Meech, S. R.; Heisler, I. A. Time-Resolved Structural Dynamics of Extended π -Electron Porphyrin Nanoring. *J. Phys. Chem. C* **2019**, *123*, 27222–27229.
- (26) O’Sullivan, M. C.; Sprafke, J. K.; Kondratuk, D. V.; Rinfrey, C.; Claridge, T. D. W.; Saywell, A.; Blunt, M. O.; O’Shea, J. N.; Beton, P. H.; Malfois, M.; Anderson, H. L. Vernier Templating and Synthesis of a 12-Porphyrin Nano-Ring. *Nature* **2011**, *469*, 72–75.
- (27) Neuhaus, P.; Cnossen, A.; Gong, J. Q.; Herz, L. M.; Anderson, H. L. A Molecular Nanotube with Three-Dimensional π -Conjugation. *Angew. Chem. Int. Ed.* **2015**, *54*, 7344–7348.
- (28) Cremers, J.; Haver, R.; Rickhaus, M.; Gong, J. Q.; Favereau, L.; Peeks, M. D.; Claridge, T. D. W.; Herz, L. M.; Anderson, H. L. Template-Directed Synthesis of a Conjugated Zinc Porphyrin Nanoball. *J. Am. Chem. Soc.* **2018**, *140*, 5352–5355.
- (29) Meyer, E. A.; Castellano, R. K.; Diederich, F. Interactions with Aromatic Rings in Chemical and Biological Recognition. *Angew. Chem. Int. Ed.* **2003**, *42*, 1210–1250.
- (30) Coropceanu, V.; Cornil, J.; da Silva Filho, D. A.; Olivier, Y.; Silbey, R.; Brédas, J.-L. Charge Transport in Organic Semiconductors. *Chem. Rev.* **2007**, *107*, 926–952.

- (31) Yao, Z.-F.; Wang, J.-Y.; Pei, J. Control of π - π Stacking via Crystal Engineering in Organic Conjugated Small Molecule Crystals. *Cryst. Growth Des.* **2018**, *18*, 7–15.
- (32) Martinez, C. R.; Iverson, B. L. Rethinking the Term “Pi-Stacking.” *Chem. Sci.* **2012**, *3*, 2191–2201.
- (33) Grimme, S. Do Special Noncovalent π - π Stacking Interactions Really Exist? *Angew. Chem. Int. Ed.* **2008**, *47*, 3430–3434.
- (34) Rosokha, S. V.; Neretin, I. S.; Sun, D.; Kochi, J. K. Very Fast Electron Migrations within P-Doped Aromatic Cofacial Arrays Leading to Three-Dimensional (Toroidal) π -Delocalization. *J. Am. Chem. Soc.* **2006**, *128*, 9394–9407.
- (35) Zhen, S.; Mao, J.-C.; Chen, L.; Ding, S.; Luo, W.; Zhou, X.-S.; Qin, A.; Zhao, Z.; Tang, B. Z. Remarkable Multichannel Conductance of Novel Single-Molecule Wires Built on Through-Space Conjugated Hexaphenylbenzene. *Nano Lett.* **2018**, *18*, 4200–4205.
- (36) Rios, C.; Salcedo, R. Computational Study of Electron Delocalization in Hexaarylbenzenes. *Molecules* **2014**, *19*, 3274–3296.
- (37) Shen, P.; Zhuang, Z.; Jiang, X.-F.; Li, J.; Yao, S.; Zhao, Z.; Tang, B. Z. Through-Space Conjugation: An Effective Strategy for Stabilizing Intramolecular Charge-Transfer States. *J. Phys. Chem. Lett.* **2019**, *10*, 2648–2656.
- (38) Liu, J.; Zhang, H.; Hu, L.; Wang, J.; Lam, J. W. Y.; Blancafort, L.; Tang, B. Z. Through-Space Interaction of Tetraphenylethylene: What, Where, and How. *J. Am. Chem. Soc.* **2022**, *144*, 7901–7910.
- (39) Shen, P.; Liu, H.; Zhuang, Z.; Zeng, J.; Zhao, Z.; Tang, B. Z. Through-Space Conjugated Electron Transport Materials for Improving Efficiency and Lifetime of Organic Light-Emitting Diodes. *Adv. Sci.* **2022**, *9*, 2200374.
- (40) Brown, C. J.; Farthing, A. C. Preparation and Structure of Di-p-Xylylene. *Nature* **1949**, *164*, 915–916.
- (41) Cram, D. J.; Steinberg, H. Macro Rings. I. Preparation and Spectra of the Paracyclophanes. *J. Am. Chem. Soc.* **1951**, *73*, 5691–5704.
- (42) Cram, D. J.; Allinger, N. L.; Steinberg, H. Macro Rings. VII. The Spectral Consequences of Bringing Two Benzene Rings Face to Face1. *J. Am. Chem. Soc.* **1954**, *76*, 6132–6141.
- (43) Li, J.; Shen, P.; Zhao, Z.; Tang, B. Z. Through-Space Conjugation: A Thriving Alternative for Optoelectronic Materials. *CCS Chem.* **2019**, *1*, 181–196.
- (44) Morisaki, Y.; Lin, L.; Chujo, Y. Through-Space Conjugated Polymer Containing [2.2]Paracyclophane and Dithiafulvene Units in the Main Chain. *Polym. Bull.* **2009**, *62*, 737–747.
- (45) Spuling, E.; Sharma, N.; Samuel, I. D. W.; Zysman-Colman, E.; Bräse, S. (Deep) Blue through-Space Conjugated TADF Emitters Based on [2.2]Paracyclophanes. *Chem. Commun.* **2018**, *54*, 9278–9281.
- (46) Majerz, I.; Dziembowska, T. What Is the Main Feature Distinguishing the Through-Space Interactions in Cyclophanes from Their Aliphatic Analogues? *ACS Omega* **2020**, *5*, 22314–22324.
- (47) Roy, I.; David, A. H. G.; Das, P. J.; Pe, D. J.; Stoddart, J. F. Fluorescent Cyclophanes and Their Applications. *Chem. Soc. Rev.* **2022**, *51*, 5557–5605.
- (48) Spenst, P.; Würthner, F. Photo- and Redoxfunctional Cyclophanes, Macrocycles, and Catenanes Based on Aromatic Bisimides. *J. Photochem. Photobiol. C Photochem. Rev.* **2017**, *31*, 114–138.

- (49) Tominaga, M.; Kondo, S.; Hyodo, T.; Kawahata, M.; Yamaguchi, K. Structure Analysis of Inclusion Crystals of Diimide-Based Macrocycles with Halocarbons. *CrystEngComm* **2022**, *24*, 3165–3171.
- (50) Jazwinski, J.; Blacker, A. J.; Lehn, J.-M.; Cesario, M.; Guilhem, J.; Pascard, C. Cyclo-Bisintercalands: Synthesis and Structure of an Intercalative Inclusion Complex, and Anion Binding Properties. *Tetrahedron Lett.* **1987**, *28*, 6060.
- (51) Tominaga, M.; Nanbara, S.; Hyodo, T.; Kawahata, M.; Yamaguchi, K. Orientation of Carbonyl Groups in Inclusion Crystals Formed from Ketones with Aromatic Diimide-Based Macrocycles. *CrystEngComm* **2023**, *25*, 1295–1300.
- (52) Wu, Y.; Frasconi, M.; Gardner, D. M.; McGonigal, P. R.; Schneebeil, S. T.; Wasielewski, M. R.; Stoddart, J. F. Electron Delocalization in a Rigid Cofacial Naphthalene-1,8:4,5-Bis(Dicarboximide) Dimer. *Angew. Chem. Int. Ed.* **2014**, *53*, 9476–9481.
- (53) Penty, S. E.; Zwijnenburg, M. A.; Orton, G. R. F.; Stachelek, P.; Pal, R.; Xie, Y.; Griffin, S. L.; Barendt, T. A. The Pink Box: Exclusive Homochiral Aromatic Stacking in a Bis-Perylene Diimide Macrocycle. *J. Am. Chem. Soc.* **2022**, *144*, 12290–12298.
- (54) Winstein, S.; Adams, R. The Role of Neighboring Groups in Replacement Reactions. XIV. The 5,6-Double Bond in Cholesteryl p-Toluenesulfonate as a Neighboring Group. *J. Am. Chem. Soc.* **1948**, *70*, 838–840.
- (55) Simonetta, M.; Winstein, S. Neighboring Carbon and Hydrogen. XVI. 1,3-Interactions and Homoallylic Resonance. *J. Am. Chem. Soc.* **1954**, *76*, 18–21.
- (56) Winstein, S.; Shatavsky, M.; Norton, C.; Woodward, R. B. 7-NORBORNENYL AND 7-NORBORNYL CATIONS. *J. Am. Chem. Soc.* **1955**, *77*, 4183–4184.
- (57) Winstein, S.; Sonnenberg, J.; De Vries, L. THE TRIS-HOMOCYCLOPROPENYL CATION1. *J. Am. Chem. Soc.* **1959**, *81*, 6523–6524.
- (58) Winstein, S. HOMO-AROMATIC STRUCTURES. *J. Am. Chem. Soc.* **1959**, *81*, 6524–6525.
- (59) Winstein, S.; Sonnenberg, J. Homoconjugation and Homoaromaticity. III.1 The 3-Bicyclo [3.1.0]Hexyl System2,3. *J. Am. Chem. Soc.* **1961**, *83*, 3235–3244.
- (60) Winstein, S.; Sonnenberg, J. Homoconjugation and Homoaromaticity. IV. The Trishomocyclopropenyl Cation. A Homoaromatic Structure1,2. *J. Am. Chem. Soc.* **1961**, *83*, 3244–3251.
- (61) Paquette, L. A. The Realities of Extended Homoaromaticity. *Angew. Chem. Int. Ed. Engl.* **1978**, *17*, 106–117.
- (62) Williams, R. V. Homoaromaticity. *Chem. Rev.* **2001**, *101*, 1185–1204.
- (63) Tran Ngoc, T.; Grabicki, N.; Irran, E.; Dumele, O.; Teichert, J. F. Photoswitching Neutral Homoaromatic Hydrocarbons. *Nat. Chem.* **2023**, *15*, 377–385.
- (64) Scott, L. T. Cyclic Homoconjugation in Neutral Organic Molecules. *Pure Appl. Chem.* **1986**, *58*, 105–110.
- (65) Spitler, E. L.; Johnson, C. A.; Haley, M. M. Renaissance of Annulene Chemistry. *Chem. Rev.* **2006**, *106*, 5344–5386.
- (66) Barnes, J. C.; Paton, J. D.; Damewood, J. R.; Mislow, K. Crystal and Molecular Structure of Diphenylmethane. *J. Org. Chem.* **1981**, *46*, 4975–4979.

- (67) Weissensteiner, W. Correlated Rotation of Aryl Substituents in Diarylmethyl-, Diarylphosphine- and Related Fragments. An Empirical Force Field Study. *Monatshefte Für Chem. Chem. Mon.* **1992**, 123, 1135–1147.
- (68) Montaudo, G.; Caccamese, S.; Finocchiaro, P. Conformational Preferences of Bridged Aromatic Compounds. I. o-Substituted Diphenylmethanes. *J. Am. Chem. Soc.* **1971**, 93, 4202–4207.
- (69) Montaudo, G.; Finocchiaro, P.; Caccamese, S.; Bottion, F. Conformational Preferences of Bridged Aromatic Compounds. II. Substituted Dibenzylbenzenes. *J. Am. Chem. Soc.* **1971**, 93, 4208–4213.
- (70) Tu, W.; Xiong, Z.; Zhang, Z.; Zhang, J.; Wang, L.; Xie, Y.; Wang, Y.; Zhang, H.; Sun, J. Z.; Tang, B. Z. Manipulation of the Through-Space Interactions in Diphenylmethane. *Smart Mol.* **2023**, 1, e20220006.
- (71) Mistry, J.-R.; Montanaro, S.; Wright, I. A. Homoconjugation Effects in Triptycene Based Organic Optoelectronic Materials. *Mater. Adv.* **2023**, 4, 787–803.
- (72) Martínez, A. G.; Barcina, J. O.; Albert, A.; Cano, F. H.; Subramanian, L. R. 7,7-Diphenylnorbornane: The First Cofacial Diphenylmethane Derivative. *Tetrahedron Lett.* **1993**, 34, 6753–6756.
- (73) Bartlett, P. D.; Ryan, M. J.; Cohen, S. G. Triptycene1 (9,10-o-Benzenoanthracene). *J. Am. Chem. Soc.* **1942**, 64, 2649–2653.
- (74) Nakazawa, T.; Murata, I. The 9,10-Dihydro-9,10-(1,2-Tropylio)Anthracene Tetrafluoroborate. Transannular .Pi.-Pi. Interaction between Tropylium Ion and Remote Benzene Rings. *J. Am. Chem. Soc.* **1977**, 99, 1996–1997.
- (75) Yamamura, K.; Nakasuji, K.; Murata, I.; Inagaki, S. Substituent Effects on the Charge-Transfer Band Shifts in 9,10-Dihydro-9,10-o-Benzenoanthracene-1,4-Diones : Further Confirmation of the Charge-Transfer Transition for a Symmetry-Forbidden Charge-Transfer Interaction. *J. Chem. Soc. Chem. Commun.* **1982**, 396–397.
- (76) Harada, N.; Uda, H.; Nakasuji, K.; Murata, I. Interchromophoric Homoconjugation Effect and Intramolecular Charge-Transfer Transition of the Triptycene System Containing a Tetracyanoquinodimethane Chromophore. *J. Chem. Soc. Perkin Trans. 2* **1989**, 1449–1453.
- (77) Harada, N.; Tamai, Y.; Takuma, Y.; Uda, H. Absolute Stereochemistry and Chiroptical Properties of Chiral Tribenzotriptycene and Benzotriptycenes. *J. Am. Chem. Soc.* **1980**, 102, 501–506.
- (78) Harada, N.; Tamai, Y.; Uda, H. Circular Dichroic Power of Chiral Triptycenes. *J. Am. Chem. Soc.* **1980**, 102, 506–511.
- (79) Martin, H.-D.; Mayer, B. Proximity Effects in Organic Chemistry—The Photoelectron Spectroscopic Investigation of Non-Bonding and Transannular Interactions. *Angew. Chem. Int. Ed. Engl.* **1983**, 22, 283–314.
- (80) Martin, H.-D.; Mayer, B.; Gleiter, R.; Schäfer, W.; Vögtle, F. Photoelektronenspektroskopische Untersuchung transannularer π -, σ - und n-Wechselwirkungen in brückenkopfsubstituierten Triptycenen. *Chem. Ber.* **1983**, 116, 2546–2553.
- (81) Kobayashi, T.; Kubota, T.; Ezumi, K. Intramolecular Orbital Interactions in Triptycene Studied by Photoelectron Spectroscopy. *J. Am. Chem. Soc.* **1983**, 105, 2172–2174.
- (82) Doerner, T.; Gleiter, R.; Neugebauer, F. A. On the Homoconjugation of Two Acceptor Groups. *Eur. J. Org. Chem.* **1998**, 1998, 1615–1623.
- (83) Talipov, M. R.; Navale, T. S.; Rathore, R. The HOMO Nodal Arrangement in Polychromophoric Molecules and Assemblies Controls the Interchromophoric Electronic Coupling. *Angew. Chem. Int. Ed.* **2015**, 54, 14468–14472.

- (84) Chou, H.-H.; Shih, H.-H.; Cheng, C.-H. Triptycene Derivatives as High- T_g Host Materials for Various Electrophosphorescent Devices. *J. Mater. Chem.* **2010**, *20*, 798–805.
- (85) Gu, X.; Lai, Y.-H. Triptycene: No Homoconjugation Effect for Extending Optical Properties of π -Conjugated Oligomers. *Org. Lett.* **2010**, *12*, 5200–5203.
- (86) Kawasumi, K.; Wu, T.; Zhu, T.; Chae, H. S.; Van Voorhis, T.; Baldo, M. A.; Swager, T. M. Thermally Activated Delayed Fluorescence Materials Based on Homoconjugation Effect of Donor–Acceptor Triptycenes. *J. Am. Chem. Soc.* **2015**, *137*, 11908–11911.
- (87) Huang, W.; Einzinger, M.; Zhu, T.; Chae, H. S.; Jeon, S.; Ihn, S.-G.; Sim, M.; Kim, S.; Su, M.; Teverovskiy, G.; Wu, T.; Van Voorhis, T.; Swager, T. M.; Baldo, M. A.; Buchwald, S. L. Molecular Design of Deep Blue Thermally Activated Delayed Fluorescence Materials Employing a Homoconjugative Triptycene Scaffold and Dihedral Angle Tuning. *Chem. Mater.* **2018**, *30*, 1462–1466.
- (88) Qian, R.; Tong, H.; Huang, C.; Li, J.; Tang, Y.; Wang, R.; Lou, K.; Wang, W. A Donor–Acceptor Triptycene–Coumarin Hybrid Dye Featuring a Charge Separated Excited State and AIE Properties. *Org. Biomol. Chem.* **2016**, *14*, 5007–5011.
- (89) Lei, P.; Zhang, S.; Zhang, N.; Yin, X.; Wang, N.; Chen, P. Triptycene-Based Luminescent Materials in Homoconjugated Charge-Transfer Systems: Synthesis, Electronic Structures, AIE Activity, and Highly Tunable Emissions. *ACS Omega* **2020**, *5*, 28606–28614.
- (90) Montanaro, S.; Congrave, D. G.; Etherington, M. K.; Wright, I. A. Homoconjugation Enhances the Photophysical and Electrochemical Properties of a New 3D Intramolecular Charge Transfer Iptycene Displaying Deep Blue Emission. *J. Mater. Chem. C* **2019**, *7*, 12886–12890.
- (91) Montanaro, S.; Pander, P.; Mistry, J.-R.; Elsegood, M. R. J.; Teat, S. J.; Bond, A. D.; Wright, I. A.; Congrave, D. G.; Etherington, M. K. Simultaneous Enhancement of Thermally Activated Delayed Fluorescence and Photoluminescence Quantum Yield via Homoconjugation. *J. Mater. Chem. C* **2022**, *10*, 6306–6313.
- (92) Uoyama, H.; Goushi, K.; Shizu, K.; Nomura, H.; Adachi, C. Highly Efficient Organic Light-Emitting Diodes from Delayed Fluorescence. *Nature* **2012**, *492*, 234–238.
- (93) Martínez, A. G.; Barcina, J. O.; Cerezo, A. de F.; Rivas, R. G. Hindered Rotation in Diphenylmethane Derivatives. Electrostatic vs Charge-Transfer and Homoconjugative Aryl–Aryl Interactions. *J. Am. Chem. Soc.* **1998**, *120*, 673–679.
- (94) Casarini, D.; Grilli, S.; Lunazzi, L.; Mazzanti, A. Conformational Studies by Dynamic NMR. 97.1 Structure, Conformation, Stereodynamics and Enantioseparation of Aryl Substituted Norbornanes. *J. Org. Chem.* **2004**, *69*, 345–351.
- (95) Herrero-García, N.; Fernández, I.; Osío Barcina, J. Electron Delocalization in Homoconjugated 7,7-Diarylnorbornane Systems: A Computational and Experimental Study. *Chem. – Eur. J.* **2011**, *17*, 7327–7335.
- (96) Martínez, A. G.; Barcina, J. O.; Cerezo, A. de F.; Schlüter, A.-D.; Frahn, J. Synthesis of Poly[p-(7-Phenylene-7-(2',5'-Dihexyl-4-Biphenylene))Norbornane]: The First Soluble Polymer with Alternating Conjugation and Homoconjugation. *Adv. Mater.* **1999**, *11*, 27–31.
- (97) Caraballo-Martínez, N.; del Rosario Colorado Heras, M.; Blázquez, M. M.; Barcina, J. O.; García Martínez, A.; del Rosario Torres Salvador, M. Synthesis of Homoconjugated Oligomers Derived from 7,7-Diphenylnorbornane. *Org. Lett.* **2007**, *9*, 2943–2946.
- (98) Osío Barcina, J.; Colorado Heras, M. del R.; Mba, M.; Gómez Aspe, R.; Herrero-García, N. Efficient Electron Delocalization Mediated by Aromatic Homoconjugation in 7,7-Diphenylnorbornane Derivatives. *J. Org. Chem.* **2009**, *74*, 7148–7156.

- (99) Osío Barcina, J.; Herrero-García, N.; Cucinotta, F.; De Cola, L.; Contreras-Carballada, P.; Williams, R. M.; Guerrero-Martínez, A. Efficient Photoinduced Energy Transfer Mediated by Aromatic Homoconjugated Bridges. *Chem. – Eur. J.* **2010**, *16*, 6033–6040.
- (100) Herrero-García, N.; del Rosario Colorado Heras, M.; del Rosario Torres, M.; Fernández, I.; Osío Barcina, J. A Joint Experimental and Computational Investigation on Homoconjugated Push-Pull Chromophores Derived from 7,7-Diphenylnorbornane. *Eur. J. Org. Chem.* **2012**, *2012*, 2643–2655.
- (101) Martínez, A. G.; Barcina, J. O.; de Fresno Cerezo, A.; Rojo, G.; Agulló-López, F. 7,7-Diarylnorbornanes: Novel Nonclassical NLO-Active Chromophores. *J. Phys. Chem. B* **2000**, *104*, 43–47.
- (102) García Martínez, A.; Osío Barcina, J.; del Rosario Colorado Heras, M.; de Fresno Cerezo, Á.; del Rosario Torres Salvador, M. Complexation Behavior of a Highly Preorganized 7,7-Diphenylnorbornane-Derived Macrocycle: Towards the Design of Molecular Clocks. *Chem. – Eur. J.* **2003**, *9*, 1157–1165.
- (103) Rueda-Zubiaurre, A.; Herrero-García, N.; del Rosario Torres, M.; Fernández, I.; Osío Barcina, J. Rational Design of a Nonbasic Molecular Receptor for Selective NH_4^+/K^+ Complexation in the Gas Phase. *Chem. – Eur. J.* **2012**, *18*, 16884–16889.
- (104) García Martínez, A.; Osío Barcina, J.; de Fresno Cerezo, Á. Influence of Highly Preorganised 7,7-Diphenylnorbornane in the Free Energy of Edge-to-Face Aromatic Interactions. *Chem. – Eur. J.* **2001**, *7*, 1171–1175.
- (105) Lobón-Poo, M.; Barcina, J. O.; Martínez, A. G.; Expósito, M. T.; Vega, J. F.; Martínez-Salazar, J.; Reyes, M. L. Meso-[Norbornane-7,7-Bis(Indenyl)]Titanium Dichloride: A Highly Active Catalyst for Ethylene–Styrene Copolymerization. *Macromolecules* **2006**, *39*, 7479–7482.
- (106) Expósito, M. T.; Vega, J. F.; Martínez-Salazar, J. Molecular Structure and Properties of Ethylene-Co-Styrene Polymers Obtained from [Norbornane-7,7-Bis(1-Indenyl)]Titanium Dichloride Catalyst System. *J. Appl. Polym. Sci.* **2007**, *106*, 1421–1430.
- (107) Expósito, M. T.; Vega, J. F.; Ramos, J.; Osío-Barcina, J.; García-Martínez, A.; Martín, C.; Martínez-Salazar, J. Highly Active Ethylene/Hydroxyl Comonomers Copolymerization Using Metallocene Catalysts. *J. Appl. Polym. Sci.* **2008**, *109*, 1529–1534.
- (108) Ellis, B.; White, P. G.; Young, R. N. The Fluorescence of Polybenzyl. *Eur. Polym. J.* **1969**, *5*, 307–314.
- (109) Braendle, A.; Perevedentsev, A.; Cheetham, N. J.; Stavrinou, P. N.; Schachner, J. A.; Mösch-Zanetti, N. C.; Niederberger, M.; Caseri, W. R. Homoconjugation in Poly(Phenylene Methylene)s: A Case Study of Non- π -Conjugated Polymers with Unexpected Fluorescent Properties. *J. Polym. Sci. Part B Polym. Phys.* **2017**, *55*, 707–720.
- (110) Perevedentsev, A.; Francisco-López, A.; Shi, X.; Braendle, A.; Caseri, W. R.; Goñi, A. R.; Campoy-Quiles, M. Homoconjugation in Light-Emitting Poly(Phenylene Methylene)s: Origin and Pressure-Enhanced Photoluminescence. *Macromolecules* **2020**, *53*, 7519–7527.
- (111) Klärner, F.-G.; Kahlert, B. Molecular Tweezers and Clips as Synthetic Receptors. Molecular Recognition and Dynamics in Receptor–Substrate Complexes. *Acc. Chem. Res.* **2003**, *36*, 919–932.
- (112) Kearney, P. C.; Mizoue, L. S.; Kumpf, R. A.; Forman, J. E.; McCurdy, A.; Dougherty, D. A. Molecular Recognition in Aqueous Media. New Binding Studies Provide Further Insights into the Cation- π Interaction and Related Phenomena. *J. Am. Chem. Soc.* **1993**, *115*, 9907–9919.
- (113) Petti, M. A.; Shepodd, T. J.; Barrans, R. E.; Dougherty, D. A. “Hydrophobic” Binding of Water-Soluble Guests by High-Symmetry, Chiral Hosts. An Electron-Rich Receptor Site with a

General Affinity for Quaternary Ammonium Compounds and Electron-Deficient .Pi. Systems. *J. Am. Chem. Soc.* **1988**, *110*, 6825–6840.

(114) Hardouin-Lerouge, M.; Hudhomme, P.; Sallé, M. Molecular Clips and Tweezers Hosting Neutral Guests. *Chem. Soc. Rev.* **2010**, *40*, 30–43.

(115) Marchioni, F.; Juris, A.; Lobert, M.; Seelbach, U. P.; Kahlert, B.; Klärner, F.-G. Luminescent Host–Guest Complexes Involving Molecular Clips and Tweezers and Tetracyanobenzene. *New J. Chem.* **2005**, *29*, 780–784.

(116) Klärner, F.-G.; Kahlert, B.; Boese, R.; Bläser, D.; Juris, A.; Marchioni, F. Synthesis and Supramolecular Properties of Molecular Clips with Anthracene Sidewalls. *Chem. – Eur. J.* **2005**, *11*, 3363–3374.

(117) Klärner, F.-G.; Madenci, S.; Kuchenbrandt, M. C.; Bläser, D.; Boese, R.; Fukuhara, G.; Inoue, Y. Donor/Acceptor-Substituted Chiral Molecular Clips – Synthesis and Host–Guest Complex Formation. *Eur. J. Org. Chem.* **2012**, *2012*, 3385–3395.

(118) Jansen, G.; Kahlert, B.; Klärner, F.-G.; Boese, R.; Bläser, D. Intramolecular Electronic Interactions between Nonconjugated Arene and Quinone Chromophores. *J. Am. Chem. Soc.* **2010**, *132*, 8581–8592.

(119) Gawroński, J.; Brzostowska, M.; Gawrońska, K.; Koput, J.; Rychlewska, U.; Skowronek, P.; Nordén, B. Novel Chiral Pyromellitdiimide (1,2,4,5-Benzenetetracarboxydiimide) Dimers and Trimers: Exploring Their Structure, Electronic Transitions, and Exciton Coupling. *Chem. – Eur. J.* **2002**, *8*, 2484–2494.

(120) Gawronski, J.; Kazmierczak, F.; Gawronska, K.; Rychlewska, U.; Nordén, B.; Holmén, A. Excited States of the Phthalimide Chromophore and Their Exciton Couplings: A Tool for Stereochemical Assignments. *J. Am. Chem. Soc.* **1998**, *120*, 12083–12091.

(121) Gawroński, J.; Gawrońska, K.; Skowronek, P.; Holmén, A. 1,8-Naphthalimides as Stereochemical Probes for Chiral Amines: A Study of Electronic Transitions and Exciton Coupling. *J. Org. Chem.* **1999**, *64*, 234–241.

(122) Gawronski, J.; Gawronska, K.; Grajewski, J.; Kacprzak, K.; Rychlewska, U. Folding of Aromatic Oligoimides of Trans-1,2-Diaminocyclohexane. *Chem. Commun.* **2002**, 582–583.

(123) Gawroński, J.; Brzostowska, M.; Kacprzak, K.; Kołbon, H.; Skowronek, P. Chirality of Aromatic Bis-Imides from Their Circular Dichroism Spectra. *Chirality* **2000**, *12*, 263–268.

(124) Wang, Y.; Wu, H.; Stoddart, J. F. Molecular Triangles: A New Class of Macrocycles. *Acc. Chem. Res.* **2021**, *54*, 2027–2039.

(125) Schneebeli, S. T.; Frascioni, M.; Liu, Z.; Wu, Y.; Gardner, D. M.; Strutt, N. L.; Cheng, C.; Carmieli, R.; Wasielewski, M. R.; Stoddart, J. F. Electron Sharing and Anion– π Recognition in Molecular Triangular Prisms. *Angew. Chem. Int. Ed.* **2013**, *52*, 13100–13104.

(126) Kim, D. J.; Hermann, K. R.; Prokofjevs, A.; Otley, M. T.; Pezzato, C.; Owczarek, M.; Stoddart, J. F. Redox-Active Macrocycles for Organic Rechargeable Batteries. *J. Am. Chem. Soc.* **2017**, *139*, 6635–6643.

(127) Wu, Y.; Young, R. M.; Frascioni, M.; Schneebeli, S. T.; Spenst, P.; Gardner, D. M.; Brown, K. E.; Würthner, F.; Stoddart, J. F.; Wasielewski, M. R. Ultrafast Photoinduced Symmetry-Breaking Charge Separation and Electron Sharing in Perylenediimide Molecular Triangles. *J. Am. Chem. Soc.* **2015**, *137*, 13236–13239.

(128) Nalluri, S. K. M.; Liu, Z.; Wu, Y.; Hermann, K. R.; Samanta, A.; Kim, D. J.; Krzyaniak, M. D.; Wasielewski, M. R.; Stoddart, J. F. Chiral Redox-Active Isosceles Triangles. *J. Am. Chem. Soc.* **2016**, *138*, 5968–5977.

- (129) Mohan Nalluri, S. K.; Zhou, J.; Cheng, T.; Liu, Z.; Nguyen, M. T.; Chen, T.; Patel, H. A.; Krzyaniak, M. D.; Goddard, W. A. I.; Wasielewski, M. R.; Stoddart, J. F. Discrete Dimers of Redox-Active and Fluorescent Perylene Diimide-Based Rigid Isosceles Triangles in the Solid State. *J. Am. Chem. Soc.* **2019**, *141*, 1290–1303.
- (130) Wu, Y.; Nalluri, S. K. M.; Young, R. M.; Krzyaniak, M. D.; Margulies, E. A.; Stoddart, J. F.; Wasielewski, M. R. Charge and Spin Transport in an Organic Molecular Square. *Angew. Chem. Int. Ed.* **2015**, *54*, 11971–11977.
- (131) Šolomek, T.; Powers-Riggs, N. E.; Wu, Y.-L.; Young, R. M.; Krzyaniak, M. D.; Horwitz, N. E.; Wasielewski, M. R. Electron Hopping and Charge Separation within a Naphthalene-1,4:5,8-Bis(Dicarboximide) Chiral Covalent Organic Cage. *J. Am. Chem. Soc.* **2017**, *139*, 3348–3351.
- (132) Ogoshi, T.; Umeda, K.; Yamagishi, T.; Nakamoto, Y. Through-Space π -Delocalized Pillar[5]Arene. *Chem. Commun.* **2009**, 4874–4876.
- (133) Feng, X.; Wu, J.; Liao, P.; Guo, J.; Li, Z.; Lin, R.; Chi, Z.; Zhang, J.; James, S. L. Pillararene for Fluorescence Detection of N-Alkane Vapours. *Mater. Chem. Front.* **2021**, *5*, 7910–7920.
- (134) Avei, M. R.; Kaifer, A. E. Through-Space Communication Effects on the Electrochemical Reduction of Partially Oxidized Pillar[5]Arenes Containing Variable Numbers of Quinone Units. *J. Org. Chem.* **2017**, *82*, 8590–8597.
- (135) Rashvand Avei, M.; Etezadi, S.; Captain, B.; Kaifer, A. E. Visualization and Quantitation of Electronic Communication Pathways in a Series of Redox-Active Pillar[6]Arene-Based Macrocycles. *Commun. Chem.* **2020**, *3*, 1–15.
- (136) Liu, Z.; Liu, G.; Wu, Y.; Cao, D.; Sun, J.; Schneebeli, S. T.; Nassar, M. S.; Mirkin, C. A.; Stoddart, J. F. Assembly of Supramolecular Nanotubes from Molecular Triangles and 1,2-Dihaloalkanes. *J. Am. Chem. Soc.* **2014**, *136*, 16651–16660.
- (137) Liu, Z.; Sun, J.; Zhou, Y.; Zhang, Y.; Wu, Y.; Nalluri, S. K. M.; Wang, Y.; Samanta, A.; Mirkin, C. A.; Schatz, G. C.; Stoddart, J. F. Supramolecular Gelation of Rigid Triangular Macrocycles through Rings of Multiple C–H \cdots O Interactions Acting Cooperatively. *J. Org. Chem.* **2016**, *81*, 2581–2588.
- (138) Beldjoudi, Y.; Narayanan, A.; Roy, I.; Pearson, T. J.; Cetin, M. M.; Nguyen, M. T.; Krzyaniak, M. D.; Alsubaie, F. M.; Wasielewski, M. R.; Stupp, S. I.; Stoddart, J. F. Supramolecular Tessellations by a Rigid Naphthalene Diimide Triangle. *J. Am. Chem. Soc.* **2019**, *141*, 17783–17795.
- (139) Nagurniak, G. R.; Piotrowski, M. J.; Muñoz-Castro, À.; Cascaldi, J. B. S.; Parreira, R. L. T.; Caramori, G. F. What Is the Driving Force behind Molecular Triangles and Their Guests? A Quantum Chemical Perspective about Host–Guest Interactions. *Phys. Chem. Chem. Phys.* **2020**, *22*, 19213–19222.
- (140) Wang, Y.; Wu, H.; Li, P.; Chen, S.; Jones, L. O.; Mosquera, M. A.; Zhang, L.; Cai, K.; Chen, H.; Chen, X.-Y.; Stern, C. L.; Wasielewski, M. R.; Ratner, M. A.; Schatz, G. C.; Stoddart, J. F. Two-Photon Excited Deep-Red and near-Infrared Emissive Organic Co-Crystals. *Nat. Commun.* **2020**, *11*, 4633.
- (141) Wang, L.; Liu, Y.-L.; Wang, M.-S. The Organic Co-Crystals Formed Using Naphthalenediimide-Based Triangular Macrocycles and Coronene: Intermolecular Charge Transfers and Nonlinear Optical Properties. *Phys. Chem. Chem. Phys.* **2022**, *24*, 29747–29756.
- (142) Wang, Y.; Wu, H.; Jones, L. O.; Mosquera, M. A.; Stern, C. L.; Schatz, G. C.; Stoddart, J. F. Color-Tunable Upconversion-Emission Switch Based on Cocrystal-to-Cocrystal Transformation. *J. Am. Chem. Soc.* **2023**, *145*, 1855–1865.

- (143) Chen, D.; Avestro, A.-J.; Chen, Z.; Sun, J.; Wang, S.; Xiao, M.; Erno, Z.; Algaradah, M. M.; Nassar, M. S.; Amine, K.; Meng, Y.; Stoddart, J. F. A Rigid Naphthalenediimide Triangle for Organic Rechargeable Lithium-Ion Batteries. *Adv. Mater.* **2015**, *27*, 2907–2912.
- (144) Wu, Y.; Krzyaniak, M. D.; Stoddart, J. F.; Wasielewski, M. R. Spin Frustration in the Triradical Trianion of a Naphthalenediimide Molecular Triangle. *J. Am. Chem. Soc.* **2017**, *139*, 2948–2951.
- (145) Mizuno, A.; Shuku, Y.; Suizu, R.; Matsushita, M. M.; Tsuchiizu, M.; Reta Mañeru, D.; Illas, F.; Robert, V.; Awaga, K. Discovery of the K4 Structure Formed by a Triangular π Radical Anion. *J. Am. Chem. Soc.* **2015**, *137*, 7612–7615.
- (146) Mizuno, A.; Shuku, Y.; Suizu, R.; Tsuchiizu, M.; Awaga, K. 3D Supramolecular Chiral Crystal Structures of Radical Anion Salts of (–)-NDI- Δ and Possible Magnetic Phase Diagrams. *CrystEngComm* **2021**, *23*, 5053–5059.
- (147) Mizuno, A.; Shuku, Y.; Matsushita, M. M.; Tsuchiizu, M.; Hara, Y.; Wada, N.; Shimizu, Y.; Awaga, K. 3D Spin-Liquid State in an Organic Hyperkagome Lattice of Mott Dimers. *Phys. Rev. Lett.* **2017**, *119*, 057201.
- (148) Wang, L.; Liu, Y.-L.; Wang, M.-S. Effects of Atypical Hydrogen Bonds and π – π Interactions on Nonlinear Optical Properties: Dimers of Triangular Structures Based on Perylene, Naphthalene, and Pyromellitic Diimides. *Langmuir* **2023**, *39*, 357–366.
- (149) Wang, L.; Liu, Y.-L.; Li, Q.-J.; Chen, S.-H.; He, D.; Wang, M.-S. Assembling of Perylene, Naphthalene, and Pyromellitic Diimide-Based Materials and Their Third-Order Nonlinear Optical Properties. *J. Phys. Chem. A* **2022**, *126*, 870–878.
- (150) Wang, D.; Zhao, Y. Rigid-Flexible Hybrid Porous Molecular Crystals with Guest-Induced Reversible Crystallinity. *Angew. Chem. Int. Ed.* **2023**, *62*, e202217903.
- (151) Insuasty, A.; Maniam, S.; Langford, S. J. Recent Advances in the Core-Annulation of Naphthalene Diimides. *Chem. – Eur. J.* **2019**, *25*, 7058–7073.
- (152) Kumar, S.; Shukla, J.; Kumar, Y.; Mukhopadhyay, P. Electron-Poor Arylenediimides. *Org. Chem. Front.* **2018**, *5*, 2254–2276.
- (153) Bhosale, S. V.; Bhosale, S. V.; Bhargava, S. K. Recent Progress of Core-Substituted Naphthalenediimides: Highlights from 2010. *Org. Biomol. Chem.* **2012**, *10*, 6455–6468.
- (154) Sakai, N.; Mareda, J.; Vauthey, E.; Matile, S. Core-Substituted Naphthalenediimides. *Chem. Commun.* **2010**, *46*, 4225–4237.
- (155) Würthner, F. Perylene Bisimide Dyes as Versatile Building Blocks for Functional Supramolecular Architectures. *Chem Commun* **2004**, 1564–1579.
- (156) Suraru, S.-L.; Würthner, F. Strategies for the Synthesis of Functional Naphthalene Diimides. *Angew. Chem. Int. Ed.* **2014**, *53*, 7428–7448.
- (157) Yue, W.; Jiang, W.; Böckmann, M.; Doltsinis, N. L.; Wang, Z. Regioselective Functionalization of Core-Perfluorinated Perylene Diimides. *Chem. – Eur. J.* **2014**, *20*, 5209–5213.
- (158) Röger, C.; Würthner, F. Core-Tetrasubstituted Naphthalene Diimides: Synthesis, Optical Properties, and Redox Characteristics. *J. Org. Chem.* **2007**, *72*, 8070–8075.
- (159) Shukla, J.; Ajayakumar, M. R.; Mukhopadhyay, P. Buchwald-Hartwig Coupling at the Naphthalenediimide Core: Access to Dendritic, Panchromatic NIR Absorbers with Exceptionally Low Band Gap. *Org. Lett.* **2018**, *20*, 7864–7868.

- (160) Bhosale, S. V.; Kalyankar, M. B.; Bhosale, S. V.; Langford, S. J.; Reid, E. F.; Hogan, C. F. The Synthesis of Novel Core-Substituted Naphthalene Diimides via Suzuki Cross-Coupling and Their Properties. *New J. Chem.* **2009**, *33*, 2409–2413.
- (161) Pagoaga, B.; Giraudet, L.; Hoffmann, N. Synthesis and Characterisation of 1,7-Di- and Inherently Chiral 1,12-Di- and 1,6,7,12-Tetraarylperylene-tetracarbox-3,4:9,10-Diimides. *Eur. J. Org. Chem.* **2014**, *2014*, 5178–5195.
- (162) Chopin, S.; Chaignon, F.; Blart, E.; Odobel, F. Syntheses and Properties of Core-Substituted Naphthalene Bisimides with Aryl Ethynyl or Cyano Groups. *J. Mater. Chem.* **2007**, *17*, 4139–4146.
- (163) Würthner, F.; Ahmed, S.; Thalacker, C.; Debaerdemaeker, T. Core-Substituted Naphthalene Bisimides: New Fluorophors with Tunable Emission Wavelength for FRET Studies. *Chem. – Eur. J.* **2002**, *8*, 4742–4750.
- (164) Kuila, S.; Ghorai, A.; Samanta, P. K.; Siram, R. B. K.; Pati, S. K.; Narayan, K. S.; George, S. J. Red-Emitting Delayed Fluorescence and Room Temperature Phosphorescence from Core-Substituted Naphthalene Diimides. *Chem. – Eur. J.* **2019**, *25*, 16007–16011.
- (165) Cox, R. P.; Higginbotham, H. F.; Graystone, B. A.; Sandanayake, S.; Langford, S. J.; Bell, T. D. M. A New Fluorescent H⁺ Sensor Based on Core-Substituted Naphthalene Diimide. *Chem. Phys. Lett.* **2012**, *521*, 59–63.
- (166) Chen, X.; Wang, J.; Zhang, G.; Liu, Z.; Xu, W.; Zhang, D. New Core-Expanded Naphthalene Diimides with Different Functional Groups for Air-Stable Solution-Processed Organic n-Type Semiconductors. *New J. Chem.* **2013**, *37*, 1720–1727.
- (167) Bhosale, S. V.; Jani, C. H.; Lalander, C. H.; Langford, S. J.; Nerush, I.; Shapter, J. G.; Villamaina, D.; Vauthey, E. Supramolecular Construction of Vesicles Based on Core-Substituted Naphthalene Diimide Appended with Triethyleneglycol Motifs. *Chem. Commun.* **2011**, *47*, 8226–8228.
- (168) Gayen, K.; Hazra, S.; Pal, A. K.; Paul, S.; Datta, A.; Banerjee, A. Tuning of the Optoelectronic Properties of Peptide-Appended Core-Substituted Naphthalenediimides: The Role of Self-Assembly of Two Positional Isomers. *Soft Matter* **2021**, *17*, 7168–7176.
- (169) Ball, M.; Fowler, B.; Li, P.; Joyce, L. A.; Li, F.; Liu, T.; Paley, D.; Zhong, Y.; Li, H.; Xiao, S.; Ng, F.; Steigerwald, M. L.; Nuckolls, C. Chiral Conjugated Corrals. *J. Am. Chem. Soc.* **2015**, *137*, 9982–9987.
- (170) Halim, Md. E.; Bandyopadhyay, A.; Hossain, Md. E.; Shinmyozu, T. A Study on the Synthesis, Characterization, Structural Optimization, and Conformational Behaviors of Bromo-Substituted Pyromelliticdiimide-Based [2+2] Macrocycle as Structural Units of Covalently Linked Molecular Tubes. *J. Mol. Struct.* **2020**, *1213*, 128164.
- (171) Ershad Halim, Md.; Bandyopadhyay, A.; Sun, L.; Tao, K.; Sangvikar, Y. S.; Miyazaki, T.; Watanabe, M.; Ideta, K.; Matsumoto, T.; Goto, K.; Shinmyozu, T. Synthesis of Bromo- and Iodo-Substituted Pyromellitic Diimide-Based [2+2]- and [3+3]Macrocycles, and Their Absorption Spectra and Electrochemical and Inclusion Properties. *Tetrahedron Lett.* **2015**, *56*, 6970–6974.
- (172) Kato, S.; Nonaka, Y.; Shimasaki, T.; Goto, K.; Shinmyozu, T. Novel Pyromellitic Diimide-Based Macrocycle with a Linear π -Electronic System and Bis(Phenylethynyl)Pyromellitic Diimide: Syntheses, Structures, Photophysical Properties, and Redox Characteristics. *J. Org. Chem.* **2008**, *73*, 4063–4075.

CHAPTER 2 |

CORE-SUBSTITUTED MOLECULAR TRIANGLES

SYNOPSIS

Molecular triangles, composed of three aromatic diimide (ADI) units connected by three chiral (*R,R*)- or (*S,S*)-*trans*-1,2-diaminocyclohexane linkers, have been developed over the last 22 years and studied extensively for their ability to (i) act as macrocyclic hosts, (ii) accept electrons and (iii) undergo supramolecular assembly. More recently, in 2023, a molecular triangle containing core-substitution of pyromellitic diimide (PMDI) faces with six bromine atoms was synthesised and studied for its adsorption properties in the solid state where it forms a crystalline hydrogen-bonded framework. However, the influence of core-bromination of the PMDI based molecular triangle on its host–guest capabilities and optoelectronic properties were not explored. In this Chapter, an alternative synthesis of the core-brominated molecular triangle **6Br** is presented and subsequently exploited as a functional handle to introduce new functional groups *i.e.* six 3,5-dimethylbenzene groups *via* a Suzuki–Miyaura cross-coupling reaction to yield a core-arylated macrocycle **6Ar**. The structural and optoelectronic properties of the molecular triangles upon the addition of six electron-withdrawing (**6Br**) and electron-donating (**6Ar**) groups are studied and compared with the unsubstituted molecular triangle **6H**. Analysis of X-ray crystal structures of **6H**, **6Br** and **6Ar** show how core-substitution influences the supramolecular packing of the macrocycle and the structural properties of the rigid shape-persistent molecular triangle backbone. In addition, the impact of the introduction of electron-donating and -withdrawing substituents on the aromatic core of molecular triangles on the energy of the frontier molecular orbitals (FMOs) is presented by modelling **6H**, **6Br** and **6Ar** with DFT calculations and studying the compounds by UV-vis spectroscopy and electrochemical experiments. The results of this Chapter demonstrate an expanded scope of molecular triangles where core-functionalisation can tune the optoelectronic properties of the macrocycle. The fundamental understanding of the structural and optoelectronic properties of core-functionalised molecular triangles gained in this Chapter, lead to further studies on the host-guest chemistry (Chapter 3) and emission (Chapter 4) of the macrocycles as well as beginning to explore their application as organic semiconductors (Chapter 5).

ACKNOWLEDGEMENTS

FHNA acknowledges support from (i) William Glover-Humphreys for assistance in the synthesis of **6Ar** and key precursors, (ii) Dr Neil Scott for valuable discussions about conditions for Suzuki–Miyaura coupling reactions, (iii) Dr Adrian Whitwood and Theo Tanner for solving X-ray crystal structures, (iv) Grant Brown for Hirschfeld analysis of X-ray crystal structures, (v) Ruhee Dawood for completing DFT calculations, (vi) Ruhee Dawood and Shana Noureen for assistance in UV-vis spectroscopy, (vii) Dr Suresh Mothika for guidance and assistance in electrochemical and chemical reduction experiments and (viii) Professor Victor Chechik for completing EPR spectroscopy experiments.

2.1 INTRODUCTION

Electron-deficient, two-electron acceptor aromatic diimides (ADIs), *e.g.*, pyromellitic, naphthalene, and perylene diimides (PMDI, NDI and PDI), respectively (Figure 2.1a), are attractive functional molecules for applications in anion- π catalysis,¹ lithium-ion batteries,² dyes and pigments³ and as *n*-type organic semiconductors.⁴ Functionalisation of the aromatic core of ADIs is also a useful tool for tuning the optoelectronic properties of the chromophores,⁵ stabilising the formation of persistent radical anions and cations,⁶ and influencing the self-assembly of the π -surfaces.⁷ Core-substitution of the smallest ADI, PMDI, is favourable due to its limited sites of substitution providing greater selectivity for further functionalisation compared with the larger NDIs and PDIs. The introduction of coordinating atoms or functional groups (halogen atoms, carboxylic acid groups or pyridine rings) onto the PMDI core allows the molecule to participate in non-covalent interactions, *e.g.* intermolecular halogen \cdots O=C interactions in compounds **1** and **2**⁸ (Figure 2.1b). The ability of core-substituted PMDI molecules to participate in intermolecular bonding means they can be incorporated into metal-organic frameworks (**3**)⁹ (Figure 2.1c) and coordinating networks (**4**) (Figure 2.1d).¹⁰

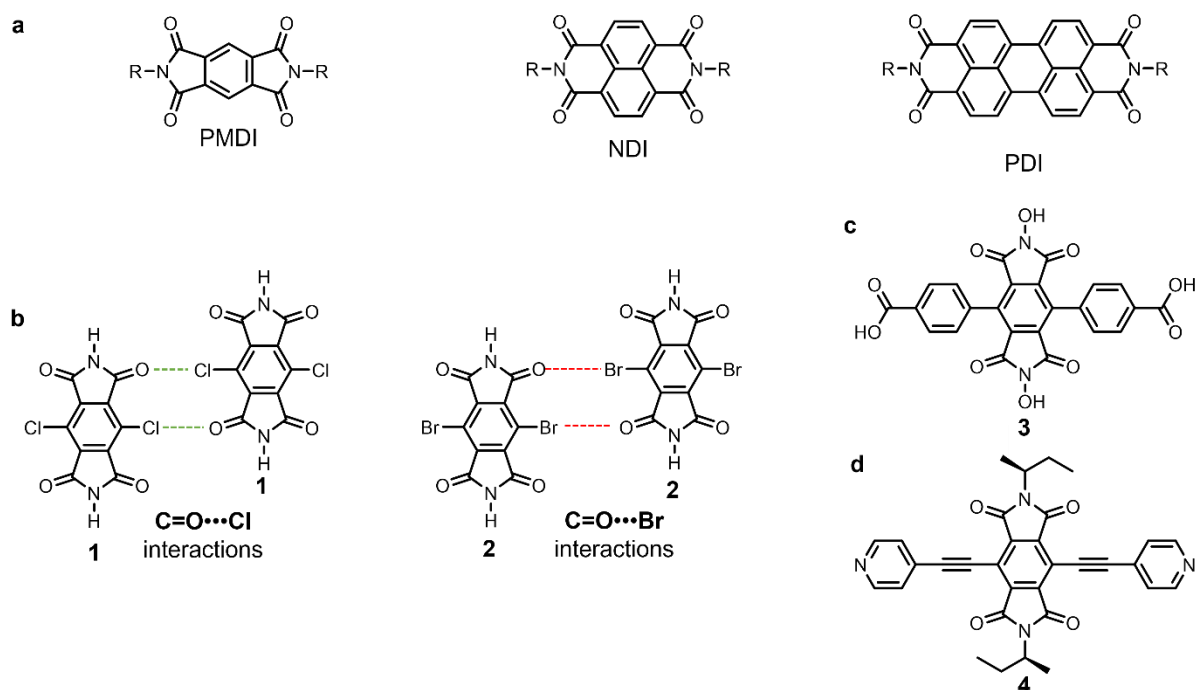


Figure 2.1 (a) Aromatic diimides **PMDI**, **NDI** and **PDI** (generalised R-group). (b) Halogen \cdots carbonyl interactions in **1** and **2**⁸. PMDI molecules that are core-functionalised with (c) carboxylic acids⁹ and (d) pyridine rings¹⁰ to interact with metal ions for incorporation into metal-organic frameworks and 2D coordination polymers respectively.

The presence of halogen atoms on the PMDI core introduces additional reactivity in the molecule for core-extension *via* metal-catalysed cross-couplings (*e.g.* Ullman¹¹, Suzuki-Miyaura¹² and Sonogashira¹³) (Figures 2.2a–c). The properties of the resulting core-extended PMDI molecules have been studied showing localisation of polyradicals in oligomer chain **7** maintaining high spin multiplicity¹¹ and tuning of the aggregation-induced emission of conjugated luminophores, *e.g.* PMDI

9.¹² Guo and Watson¹³ showed that the introduction of electron-rich phenyl-alkyl substituents influenced the optical properties of the donor-acceptor systems due to lower energy electronic transitions and narrowing of the band gap. In addition, their DFT models show that the HOMO was delocalised around the core-substituent with the LUMO residing on the PMDI scaffold **10**. Furthermore, metal catalysed cross-coupling reactions have also been used to synthesise polymers containing core-functionalised PMDI molecules, *e.g.* Sonogashira¹³ (polymer **11**) and Stille,^{14,15} for applications as *n*-type organic semiconductors (OSCs) in photovoltaic devices,¹⁴ and field-effect transistors¹⁵ and as cathodic materials for Li- and Na-ion batteries, with favourable interactions between sodium ions and polymer chain.¹⁶

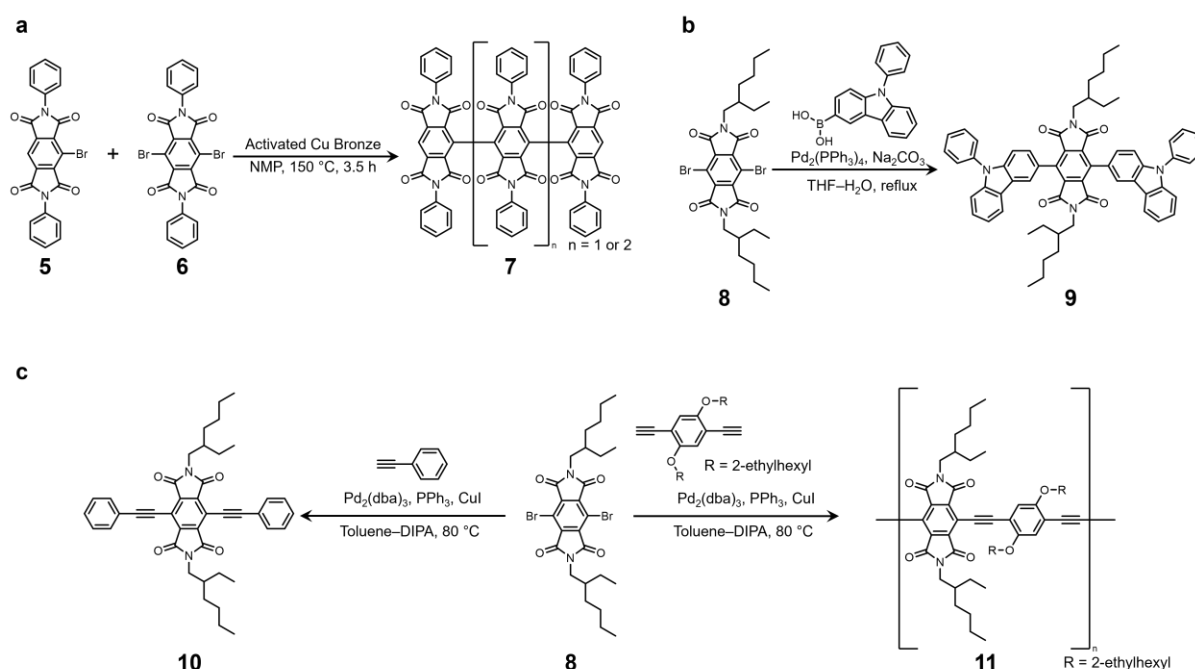


Figure 2.2 Synthesis of core-extended PMDI molecules *via* (a) Ullman,¹¹ (b) Suzuki-Miyaura¹² and (c) Sonogashira¹³ cross-coupling reactions.

In addition to aromatic core-substitution, variation in the *N*-position of PMDI small molecules increases their synthetic versatility and makes them suitable for incorporation into macrocycles for molecular recognition¹⁷ and as precursors towards carbon nanotube like structures such as in compounds **12** and **13** (Figure 2.3a).^{18–20} Despite core-functionalised PMDI small molecules and polymers being studied extensively for a range of applications, the incorporation of core-substituted PMDI units in the molecular triangle, *e.g.* **6H** was not achieved until 2023.²¹

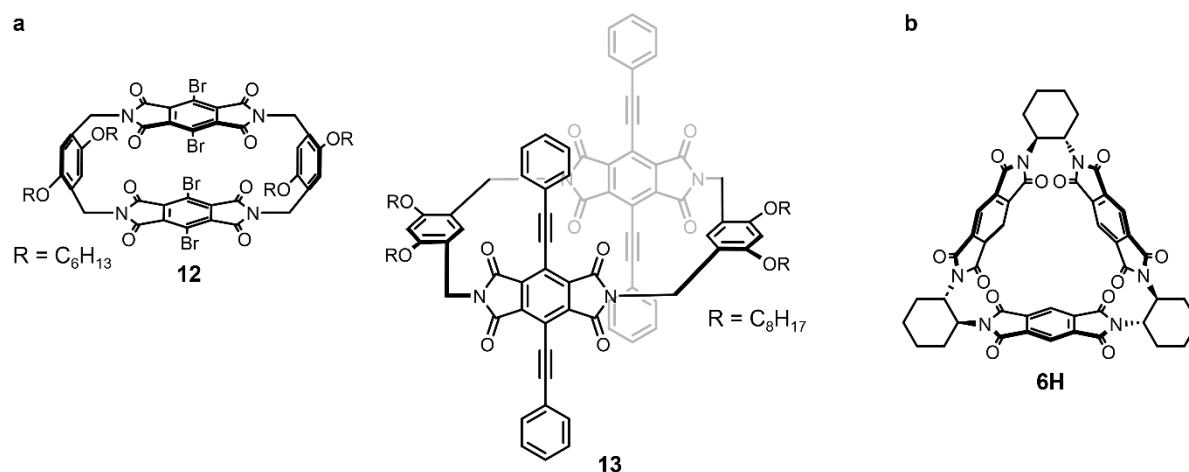


Figure 2.3 (a) Macrocycles **12** and **13** containing core-functionalised PMDI units^{18–20} and (b) PMDI based molecular triangle **6H**.

Zhao and Wang²¹ recently reported the synthesis of a hexa-brominated PMDI-based molecular triangle, **6Br**, (Figure 2.4) *via* a chromatography-free method originally developed by Kim *et al.*²² for **6H**. The resulting core-halogenated molecular triangle, **6Br**, crystallised in non-coordinating THF solvent forming a hydrogen-bonded organic framework (HOF-1) through C=O \cdots H–C interactions. The porous, supramolecular crystalline material that formed showed uptake of n-hexane in the pores of the HOF. The crystallinity of the hexane-soaked HOF was monitored by powder X-ray diffraction (pXRD) whilst being exposed to air and after 24 hours the structure became disordered due to desolvation. However, upon soaking in n-hexane again the crystallinity returned with this cycle being repeated up to three times. These results show a self-repairing mechanism with the crystalline structure reforming upon the addition of n-hexane after previous collapse of the ordered structure due to desolvation. This result is significant because no reformation of the crystalline structure upon resolution of single crystals of **6H** was observed. Furthermore, HOF-1 was used to separate benzene from cyclohexane on account of the potential for $\pi\cdots\pi$ interactions between PMDI side units and the aromatic solvent to lead to favourable uptake in the cavity of the macrocycles within the crystalline material. Indeed, benzene uptake by the crystal was around seven times greater than that of cyclohexane with negligible results for the non-aromatic solvent.²¹

This first report of a core-substituted PMDI-based molecular triangle by Zhao and Wang²¹ explores the differences in the crystalline properties of the brominated molecular triangle, **6Br**, compared with **6H** as well as the potential for reversible uptake and separation of solvent molecules. However, the work by Zhao and Wang²¹ does not explore how core-bromination influences the optoelectronic properties of molecular triangles. For instance, *how does the introduction of bromine atoms affect (i) the cyclic aromatic homoconjugation of molecular triangles, (ii) the electronics and redox-active behaviour of the macrocycle, (iii) the optical and emissive properties of the chromophores and (iv) the reactivity towards cross-coupling reagents for post-synthetic functionalisation?* These investigations are of interest to provide a direction for second-generation molecular triangles such as the incorporation of the

macrocycles in more complex structures such as triangular nanoprisms through oligomerisation. Such chains of molecular triangles would be attractive due to their electron-deficient channel composed of the cavities of each macrocycle. Supramolecular interactions have been shown to facilitate the formation of nanotubes²³ and tessellated, 2D nanosheets²⁴ of the NDI based molecular triangle (macrocycle 17 *c.f.* Figure 1.12 *vide supra*). The decreased solubility of covalently bonded molecular triangle polymers, coupled with its ability to accept $6n$ electrons (where n is number of macrocycles) could provide enhanced stability as cathodic materials in Li-ion batteries for greater capacity performance.²⁵

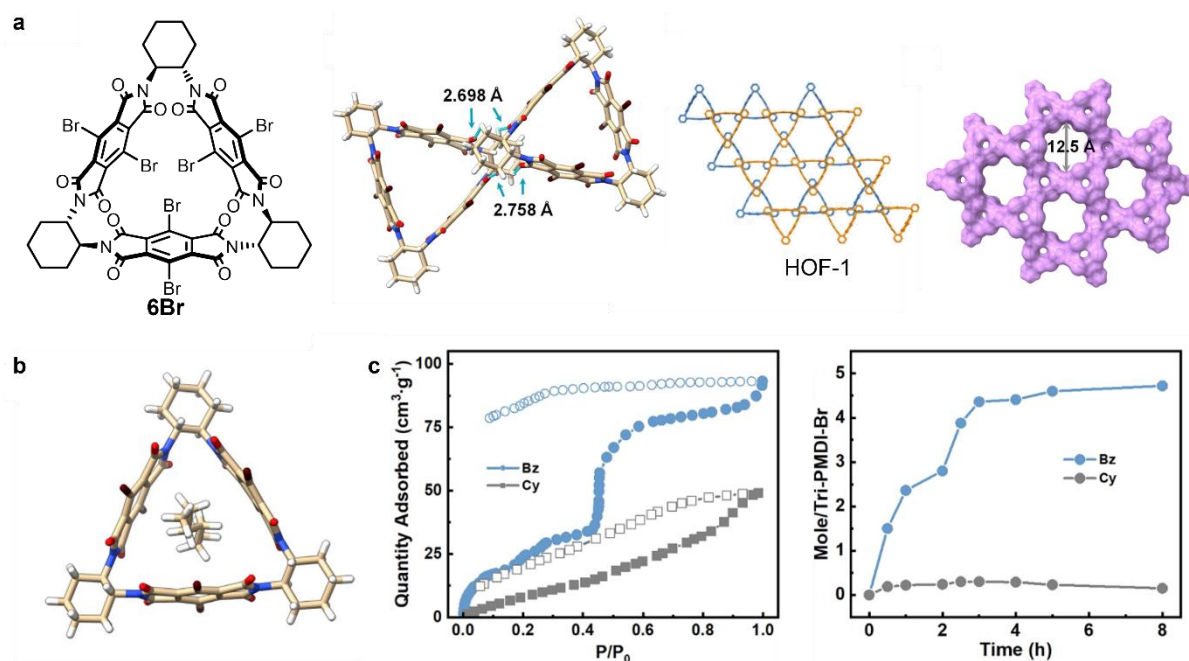


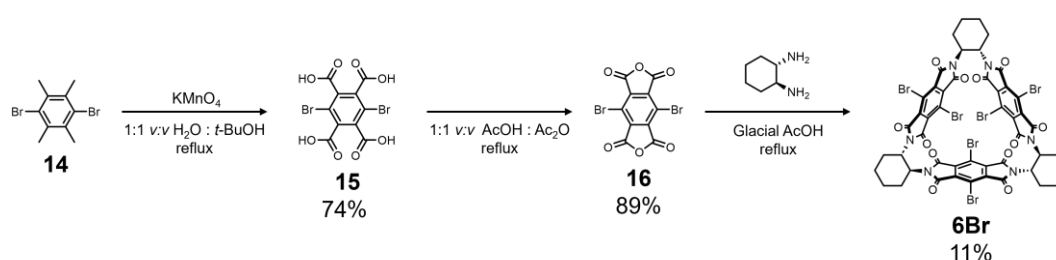
Figure 2.4 (a) Chemical structure, solid state X-ray crystal structure and supramolecular packing of **6Br** into the porous HOF-1. (b) Crystal structure of **6Br** with an encapsulated n-hexane molecule in the cavity. (c) Adsorption and separation of benzene (Bz) from cyclohexane (Cy) via favourable interactions with HOF-1.²¹ Figure reproduced from reference 21.²¹

This Chapter describes the investigations into the effect of core-bromination on the structural and optoelectronic properties of the molecular triangle through comparison of **6Br** with **6H**. The post-synthetic Suzuki–Miyaura cross-coupling of the brominated macrocycle with an aryl boronic acid is also shown to synthesise a hexa-arylated molecular triangle **6Ar**, to make progress towards the overall goal of triangular nanoprisms. The fundamental experimental and theoretical investigations that are discussed in this Chapter provide a background for serendipitous discoveries that are explored more deeply with advanced techniques in later chapters to unravel the consequences of core-substitution on the structural (Chapter 3) and optical (Chapter 4) properties of molecular triangles towards potential applications as organic semiconductors (Chapter 5).

2.2 RESULTS AND DISCUSSION

2.2.1 SYNTHESIS AND CHARACTERISATION

The synthesis of brominated molecular triangle **6Br** was achieved by adapting literature procedures in a three-step synthesis composed of (i) oxidation,^{8,11,22} (ii) ring-closing^{8,11,22} and (iii) macrocyclisation.²⁶ In order to prepare the key brominated PMDA precursor **16**, tetramethylbenzene **14** was first oxidised with excess KMnO_4 (up to 2.5 equiv. per methyl group) to tetraacid **15** (74%) before the formation of anhydride **16** (89%) by refluxing in an equal volume mixture of glacial AcOH and Ac_2O . Full synthetic procedures and characterisation can be found in the Supplementary Information (Sections 2.4.2 and 2.4.3).



Scheme 2.1 Synthesis of brominated molecular triangle **6Br** via tetraacid **15** and anhydride **16** precursors.

The condensation reaction of anhydride **16** with (*S,S*)-*trans*-1,2-diaminocyclohexane to synthesise macrocycle **6Br** followed an adapted 2002 procedure²⁶ from Gawroński *et al.* which was originally used for **6H**. Molecular triangle **6Br** was isolated following purification using automated column chromatography (SiO_2 : 0–100% Me_2CO in CH_2Cl_2) in a yield of 11% and characterised using ^1H and ^{13}C NMR spectroscopy and high-resolution mass spectrometry (Supplementary Information, Sections 2.4.2 and 2.4.3).

Molecular triangle **6H** was also synthesised following the procedure developed by Gawroński *et al.*²⁶ to assist in the characterisation of **6Br**. In the ^1H NMR spectrum of **6H** in CDCl_3 (Figure 2.5a), the chemical shift for the aromatic proton (H^1) is represented as a singlet at 8.03 ppm, the cyclohexane proton adjacent to the imide unit (H^4) as a multiplet between 5.23–5.11 ppm and the cyclohexane protons (H^5 and H^6) as overlapping multiplets in regions between 2.13–1.88 and 1.63–1.51 ppm. The cyclohexane proton environment adjacent to the diimide (H^4) is used as an indicator to confirm successful condensation of the (*S,S*)-*trans*-1,2-diaminocyclohexane linker with the anhydride, as upon diimide formation, the chemical shift for the proton is more deshielded and moves downfield, to a shift of around 5 ppm. The aromatic proton (H^1) and cyclohexane proton (H^4) have equal integration (6:6), with protons (H^5 and H^6) integrating to a total of 24 as expected for synthesis for **6H** macrocycle with three PMDI side units and three cyclohexane linkers. The cyclohexane proton environments in the ^1H NMR spectrum, Figure 2.5b, of **6Br** is similar to **6H** with the peak representing H^4 between 5.23–5.09 ppm and H^5 and H^6 represented by peaks at 2.03–1.88 and 1.58–1.50 ppm. The absence of any aromatic

proton environments provides further evidence of full functionalisation of the PMDI core of the macrocycle.

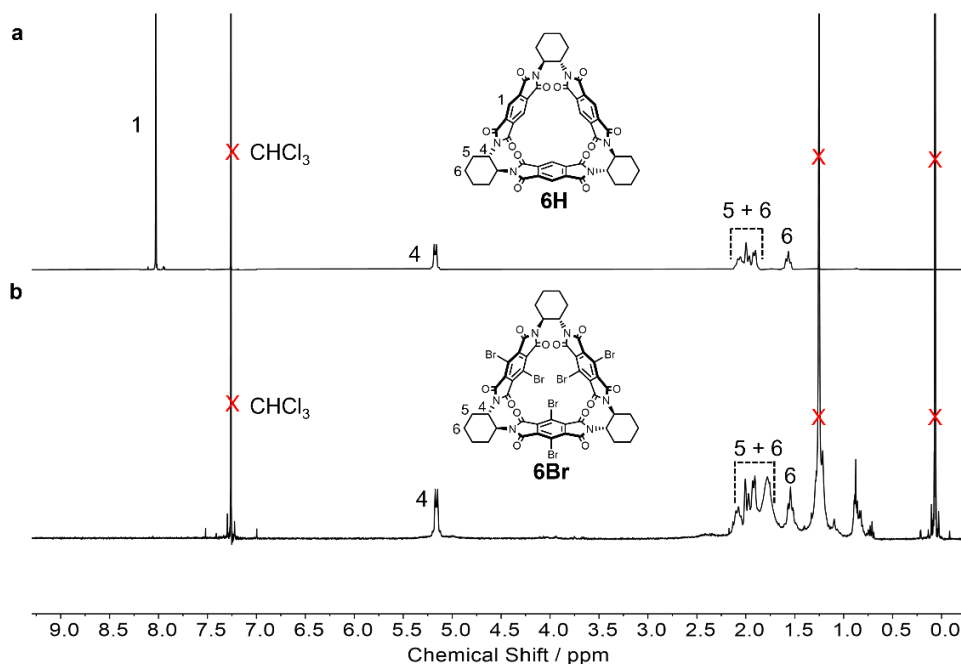


Figure 2.5 Stacked ^1H NMR (400 MHz, CDCl_3 , 298 K) spectra of (a) **6H** and (b) **6Br**.

Furthermore, the ^{13}C NMR spectra (Figure 2.6) for the two synthesised macrocycles are similar with the three cyclohexane carbon environments (4, 5 and 6) present below 60 ppm and the core aromatic carbon where substitution occurs (1) at 119.08 and 114.7 ppm for **6H** and **6Br** respectively. The change in shift of the carbons directly bonded to the hydrogen or bromine atoms shows the influence of core-substitution on the electronics of the environment, with the presence of heavy halogen atoms increasing the shielding of the carbon leading to an upfield resonance shift. The carbon environments for carbons 2 and 3 are split into two peaks (2 & 2' and 3 & 3'). The presence of two carbon peaks despite the symmetric X_2PMDI unit ($\text{X} = \text{H}$ or Br) is due to the helical nature of the macrocycle which is induced through the use of chiral (*S,S*)-*trans*-1,2-diaminocyclohexane linkers with the separate peaks representing carbon atoms on the same end of the PMDI unit (Figure 2.6). As a result of the inverse symmetry of the chiral linker at the opposite end of the PMDI unit, the carbon environments for 2 & 2' and 3 & 3' are equivalent diagonally across the PMDI face. These symmetry effects of two distinct carbon environments are also observed for the NDI-based molecular triangle.²⁷

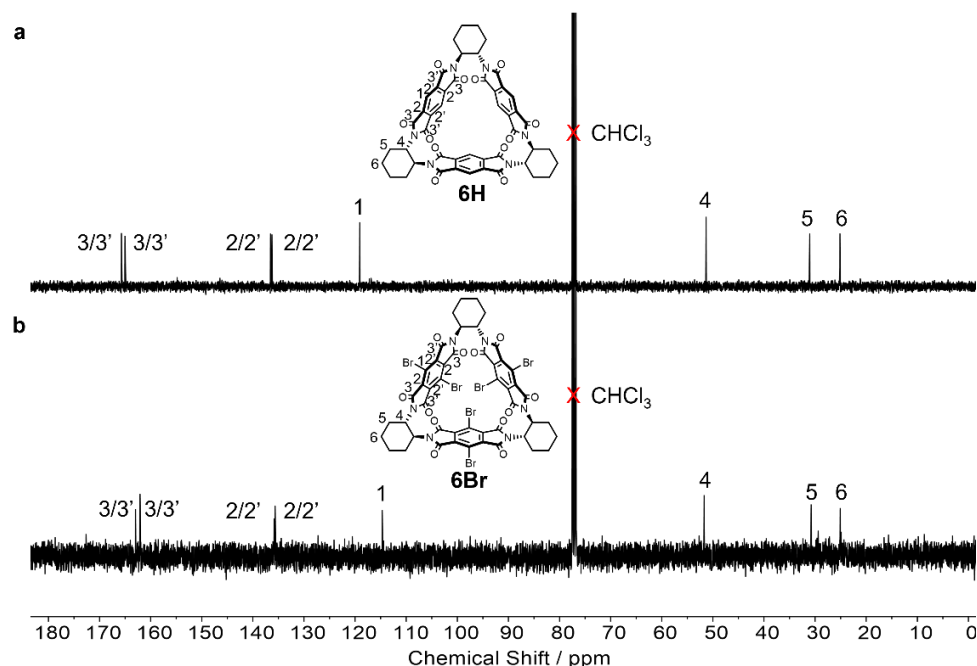
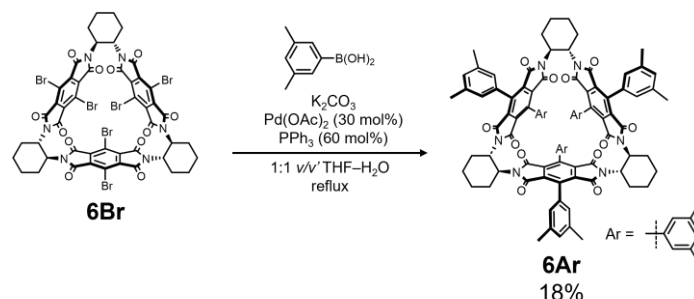


Figure 2.6. Stacked ^{13}C NMR (101 MHz, CDCl_3 , 298 K) spectra of (a) **6H** and (b) **6Br**.

With the brominated molecular triangle **6Br** in hand, a Suzuki–Miyaura cross-coupling reaction with 3,5-dimethylbenzene boronic acid was achieved to synthesise a hexa-arylated macrocycle, **6Ar** (Scheme 2.2). Such post-synthetic functionalisation of a core-substituted molecular triangle provides the potential for covalently bonded macrocycles towards triangular nanoprisms. Successful synthesis of **6Ar** was achieved using 5 mol% catalyst ($\text{Pd}(\text{OAc})_2$) loading per bromine atom in a yield of 18% following purification *via* automated column chromatography (SiO_2 : 0–100% EtOAc in *n*-hexane). The desired product **6Ar** was separated from side-products that could include partially arylated molecular triangles in addition to unreacted boronic acid, triphenylphosphine and triphenylphosphine oxide.



Scheme 2.2 Synthesis of aryl-substituted molecular triangle **6Ar** through a Suzuki–Miyaura coupling of 3,5-dimethylbenzene boronic acid with **6Br**.

The arylated macrocycle **6Ar** was characterised by ^1H and ^{13}C NMR spectroscopy (Supplementary Information, Sections 2.4.2 and 2.4.3) with the aid of 2D NMR spectroscopy techniques (COSY (Figure S2.10, HMQC (Figure S2.11) and HMBC (Figure S2.12)) to assign proton and carbon environments. The ^1H NMR spectrum of **6Ar** (Figure 2.7) revealed the diagnostic cyclohexane proton environments (H^4) between 5.00–4.81 that are shifted upfield relative to **6H** and **6Br** on account of the increased electron density due to the electron-donating aryl substituents. The cyclohexane proton environments

between 2.13–1.76 ppm and at 1.34 ppm for H⁵ and H⁶ are observed in similar regions to **6H** and **6Br**. In addition, the 3,5-dimethylbenzene protons H⁸ and H¹⁰ are separated into two distinct environments which could be due to the steric crowding and rigid nature of core-substituted aryl groups around the 3D macrocycle. The crystal structure of **6Ar** allows for the methyl protons H¹⁰ and H^{10'} to be distinguished and discussed below (Section 2.2.2). In the ¹³C spectrum of **6Ar** (Figures S2.8 and S2.9, Section 2.4.3), carbons 2 and 3 are also split into individual environments similar to **6H** and **6Br**, on account of the 3D nature of the core-functionalised molecular triangle.

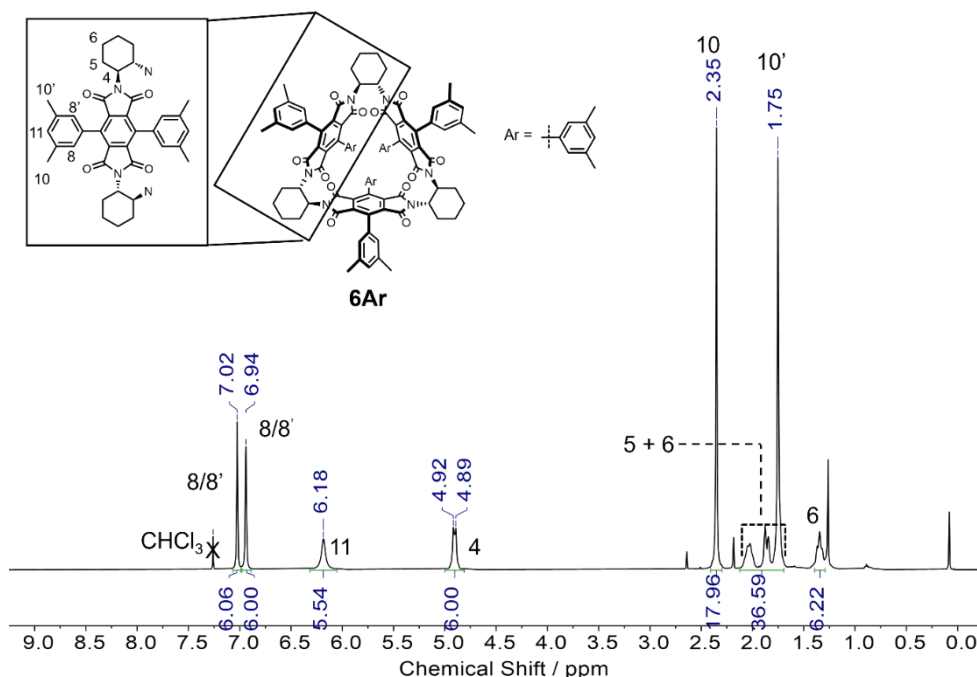


Figure 2.7 ¹³C NMR (101 MHz, CDCl₃, 298 K) spectrum of **6Ar**.

Upon increasing the core-functionalisation of the PMDI based molecular triangle from **6H** to **6Br** to **6Ar**, the solubility in polar aprotic solvents increases. Core-substituted molecular triangles **6H** and **6Br** are most soluble in chlorinated (dichloromethane and chloroform) and amide based (*N,N*-dimethylformamide (DMF), 1-methyl-2-pyrrolidinone (NMP) and *N,N*-dimethylacetamide (DMAc)) solvents. Whereas, upon core-functionalisation with 3,5-dimethylbenzene substituents, the molecular triangle becomes more readily soluble in more solvents including tetrahydrofuran (THF) and ethyl acetate.

2.2.2 STRUCTURAL PROPERTIES OF CORE-FUNCTIONALISED MOLECULAR TRIANGLES

Absolute structure confirmation and a resulting study of the solid-state packing of synthesised compounds **6H**, **6Br** and **6Ar** were achieved through growing single crystals and analysis of crystal structures obtained through X-ray diffraction. Single crystals were grown *via* vapour diffusion of a non-polar solvent (hexane and pentane) into a solution of compound in polar solvent (acetone and

CH_2Cl_2). Tabulated crystallographic data for all structures are provided in the Supplementary Information (Section 2.4.4).

A new polymorph of the previously studied literature compound, **6H**, was discovered by growing a single crystal through the vapour diffusion method with hexane into an acetone solution. Previously, **6H** has been shown by Gawroński *et al.*²⁶ in 2002 to crystallise with benzene molecules in a P6_3 space group (**6H**:2002, Figure 2.8a), or as shown by Stoddart and coworkers in 2017,²² with two triangle molecules in an unit cell of space group P1 (1) with NMP solvent molecules (**6H**:2017, Figure 2.8b).²² Herein, we present a third polymorph of **6H** in a monoclinic system with a P2_1 space group, with two triangle molecules (**6H**• Me_2CO (1) and **6H**• Me_2CO (2)) in the unit cell of the crystal structure (Figure 2.8c). Subsequent Hirschfeld analysis of the P2_1 unit cell does not reveal any close non-covalent contacts influencing the supramolecular packing of the macrocycles with Van der Waals interactions between hydrogen atoms being most common (Figure 2.8.d).

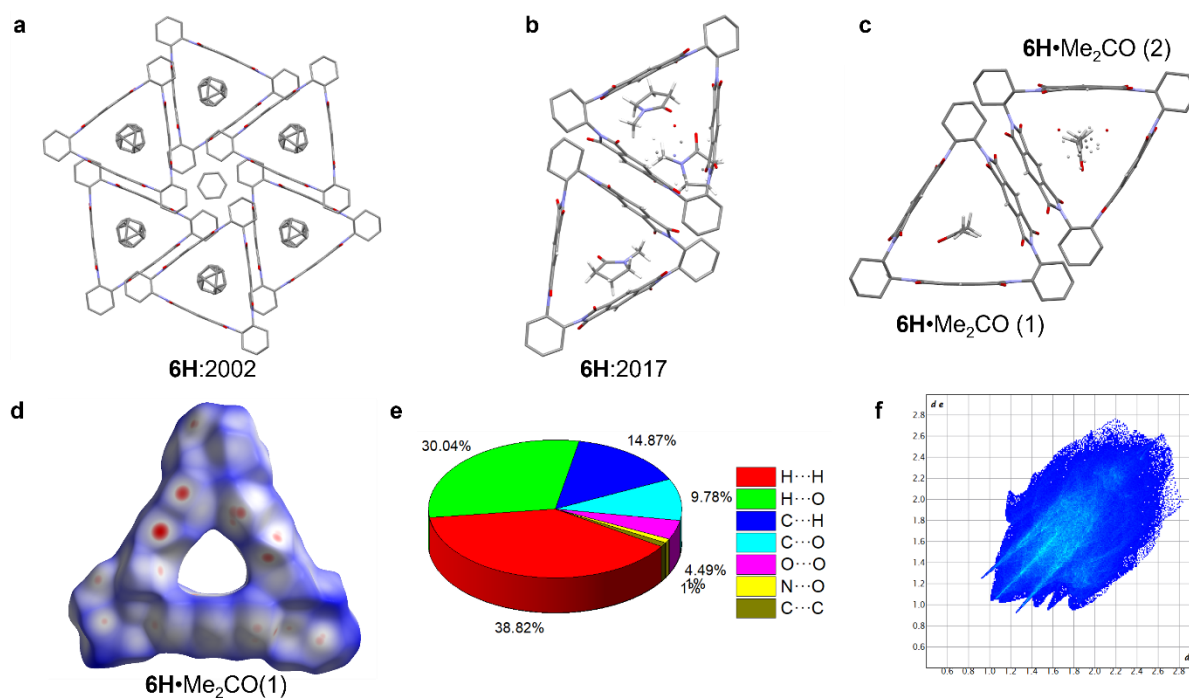


Figure 2.8. Different crystal structure polymorphs of **6H**. (a) Supramolecular packing of **6H**:2002 in P6_3 space group with benzene solvate molecules shown by Gawroński *et al.*²⁶ (b) Unit cell of **6H**:2017 in P1 (1) space group with NMP solvent molecules as shown by Stoddart and coworkers.²² (c) Monoclinic unit cell of **6H** in P2_1 space group with acetone solvent inside cavity of macrocycle grown in this study and two triangle molecules (**6H** (1) and **6H** (2)). Hirschfeld analysis of molecule **6H** (1) in monoclinic unit cell with (d) Hirschfeld surface of triangle molecule, (e) the percentage of reciprocal internal interactions higher than 1% and (f) the accompanying fingerprint plot for all interactions. Cyclohexane protons have been omitted for clarity.

Two polymorphs of the hexa-brominated triangle **6Br** have been discovered depending on whether the crystal is solvated or not. When a non-coordinating solvent was used to dissolve the macrocycle (CH_2Cl_2), a desolvated crystal structure (hexagonal, P6_3) was obtained with the same framework structure (Figure S2.16) as reported by Wang and Zhao²¹ in 2023 and discussed in Section 2.1. Hirschfeld analysis indicates that Van der Waals interactions and $\text{H}\cdots\text{O}$ hydrogen bonds contribute to

the formation of the crystalline HOF structure (Figure S2.17). Conversely, when **6Br** was crystallised with coordinating acetone solvent (**6Br**•Me₂CO), a trigonal crystal structure (R32) was found containing a hexagonal array of triangles forming 1D channels (Figure 2.9). The channels are formed due to the presence of a crown of acetone molecules with carbonyls facing towards triangle units in both directions. The C=O bonds of the acetone molecules are interacting non-covalently with bromine atoms of the triangle through C=O⋯Br halogen bonding interactions with two triangle units interacting cooperatively with one crown of acetone molecules. Furthermore, Hirshfeld analysis of the crystal structure indicates that all interactions between carbonyl groups (C=O) and bromine atoms occur *via* halogen bonding between macrocycle and acetone molecules rather than between adjacent molecular triangle units (Figures S2.14 and S2.15).

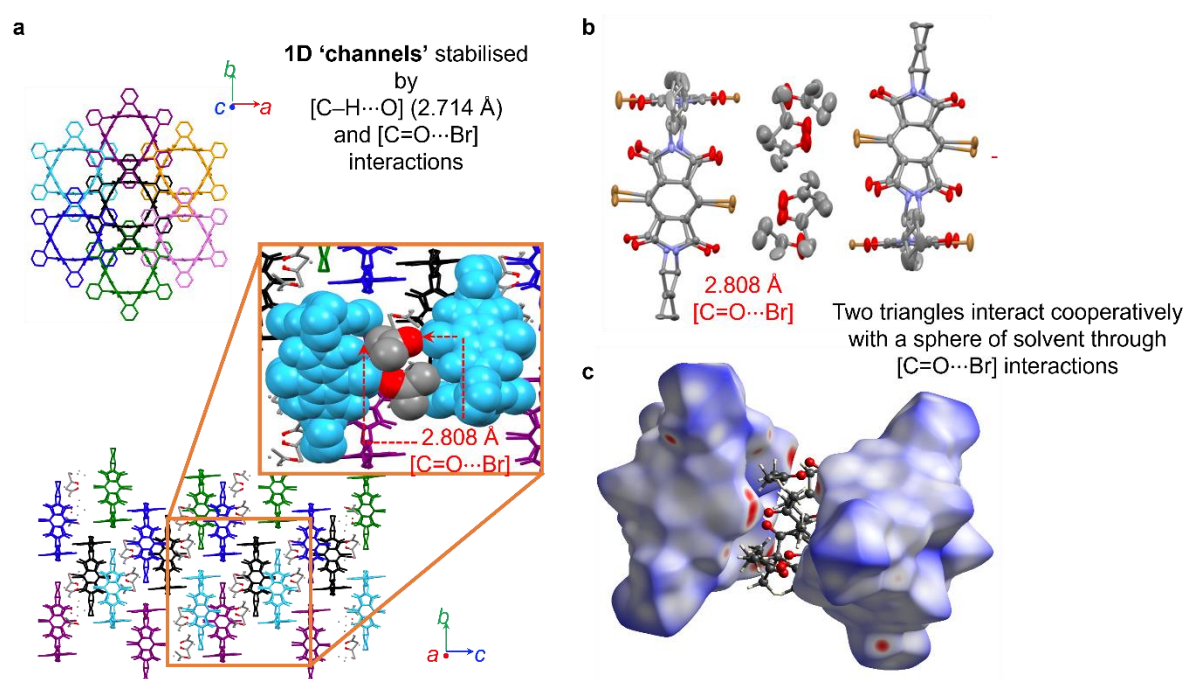


Figure 2.9 (a) Supramolecular packing of **6Br**•Me₂CO forming a hexagonal array of 1D channels. (b) Two triangle molecules interact with a crown of acetone molecules with (c) Hirshfeld analysis revealing that C=O⋯Br interactions occur solely between acetone solvent and triangle molecules.

Two different polymorphs of **6Ar** were discovered depending on the crystallisation conditions used and the quantity of solvated acetone molecules present, **6Ar**•2Me₂CO and **6Ar**•3Me₂CO. In both crystal structures of **6Ar**, solvated acetone molecules are present and the 3,5-dimethylbenzene groups are all twisted away from the PMDI face at dihedral angles between 52.7° and 59.3°, to minimise the steric hindrance of the bulky substituents. Furthermore, the two 3,5-dimethylbenzene substituted on the same PMDI unit are twisted in opposite directions. In addition to minimising steric repulsion, the rotation of 3,5-dimethylbenzene substituents positions a methyl group (–CH₃) facing towards the π-surface of an adjacent aryl group prompting potential C–H⋯π interactions. The donation of electron density from a methyl group to a π-surface would deshield the methyl protons towards higher shifts in the ¹H NMR spectrum for **6Ar** which allows for the assignment of protons H¹⁰ and H^{10'} (Figure 2.7). Looking along

and perpendicular to the macrocyclic cavity, the arylated molecular triangle begins to resemble carbon nanotube like-structures and thus allows for the visualisation of triangular nanoprisms *via* the oligomerisation of the macrocycle units (Figure 2.10).

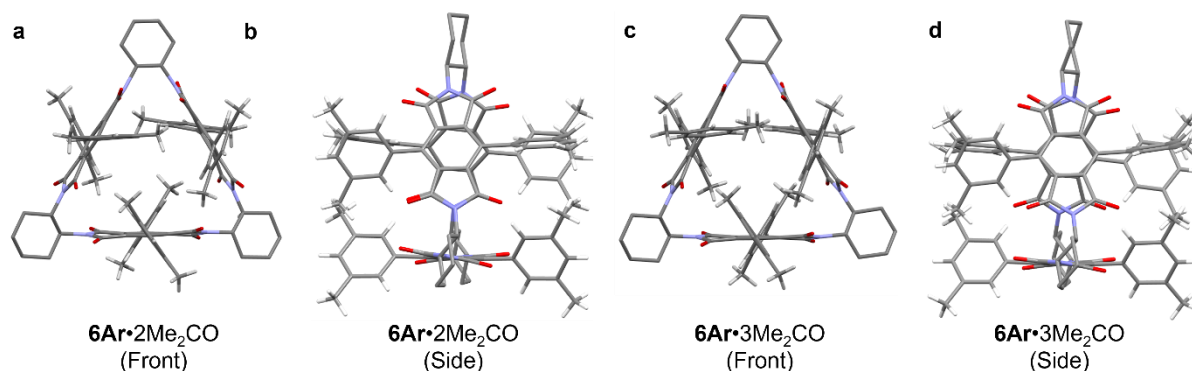


Figure 2.10 X-ray crystal structures of **6Ar** with acetone solvent molecules and cyclohexane hydrogens omitted for clarity for (a) **6Ar**•**2Me₂CO**, front view, (b) **6Ar**•**2Me₂CO**, side view, (c) **6Ar**•**3Me₂CO**, front view and (d) **6Ar**•**3Me₂CO** side view.

The structural parameters of all molecular triangles in the solid-state (cavity distances 1, 2 and 3, angles a, b and c between PMDI-units and bend within PMDI-units, (i–vi)) have been measured using Mercury software from X-ray crystal structures and shown in Figure 2.11. Measurements were made for each crystal structure obtained (**6H**•**Me₂CO**, **6Br**•**Me₂CO**, **6Br**, **6Ar**•**2Me₂CO** and **6Ar**•**3Me₂CO**), where in the crystal structure of **6H**•**Me₂CO** with two triangle molecules present in the unit cell, parameters were taken for both macrocycles, **6H**•**Me₂CO** (1) and **6H**•**Me₂CO** (2). These measurements reveal that core-substitution does not significantly impact the cavity distance between the centre of a PMDI-unit and opposite cyclohexane linker ranging between 9.26 and 9.80 Å in all crystal structures. There is some variation in distances 1–3 within a molecular triangle however the measured distances are consistently relatively close. The angles between PMDI-units in the molecular triangles are close to 60° as would be expected for equilateral triangles with a range of angles between 57.4 and 64.5° in the crystal structures of **6H**, **6Br** and **6Ar**. Lastly, a slight bend in the PMDI-unit is observed (angles i–vi) in molecular triangles in the solid-state between 3.2° and 6.5°.

The unit cells for different polymorphs of the triangles contain one or two triangle molecules with slightly different structural parameters (distances 1, 2 and 3, angles a, b and c and bends i–vi) highlighting effects of solvent encapsulation. For example, in the unit cell of **6H**, there are two macrocycles with varied distance and angular parameters. This could be due to the presence of acetone solvent molecules inside the molecular triangles thus impacting the geometry of the structure in the solid-state. Such variability in structural parameters is also observed in the two crystal structures obtained for **6Ar** in the presence of acetone molecules. Conversely, in the two crystal structures for **6Br**, with and without acetone, the structural parameters are symmetrical as would be expected for equilateral triangles. In the absence of solvent molecules in the unit cell (**6Br**, Figure 2.11e) equal cavity heights and angles are measured, the bends within the PMDI units do vary on either side of the benzene

core, although this is repeated throughout the macrocycle. However, for **6Br**•Me₂CO (Figure 2.11d) the absence of variability in the structural parameters is more surprising given the interacting solvent molecules. The symmetrical structural parameters could be attributed to supramolecular packing in the crystal where a ‘crown’ of solvent molecules interacts cooperatively with two macrocycles.

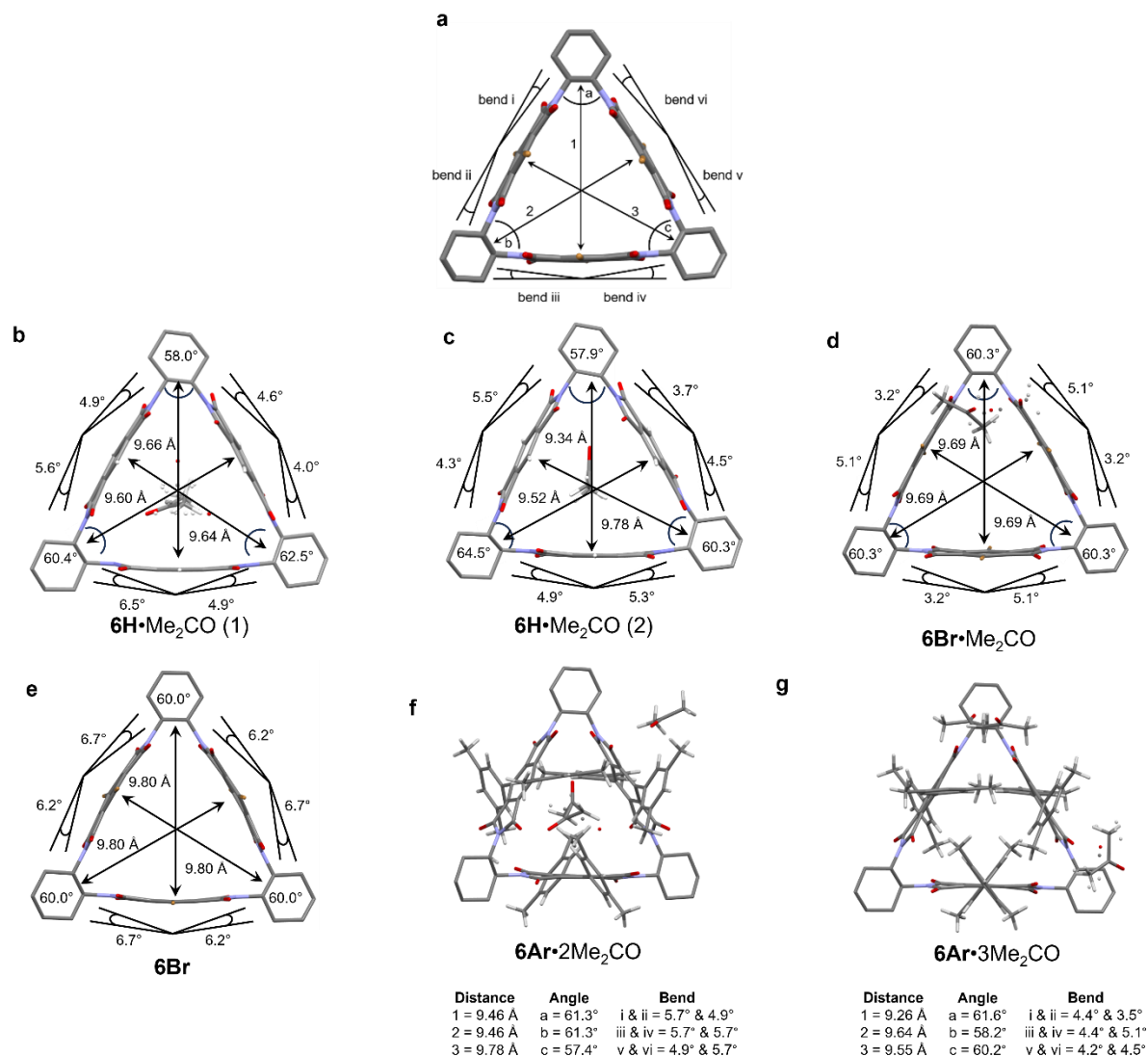


Figure 2.11 Crystal structures showing (a) structural parameters of general macrocyclic structure for (b) **6H**•Me₂CO (1), (c) **6H**•Me₂CO (2), (d) **6Br**•Me₂CO, (e) **6Br**, (f) **6Ar**•2Me₂CO and (g) **6Ar**•3Me₂CO.

The structural properties of molecular triangles, **6H**, **6Br** and **6Ar**, in the solid-state (Figure 2.11) were compared with geometry optimised structures from density functional theory (DFT) calculations at the B3LYP-D3(BJ)/def2svp/PCM (Solvent = CH₂Cl₂) level of theory (Figure 2.12). The cavity distances (1–3) of macrocycles **6H**, **6Br** and **6Ar** in the optimised structures are very similar (within 0.04 Å) which are consistent with the cavity distances measured in X-ray crystal structures for **6H** and **6Br** (Figure 2.11.) although more variable distances are observed in the experimental data for **6Ar**. The angles between PMDI-units in the geometry optimised structures of **6H**, **6Br** and **6Ar** are comparable with experimental values, which are close to the expected 60° for equilateral triangles. Despite the

optimised structures exhibiting a slight bend in the PMDI-units, the calculated values for **6H** and **6Br** (0.9 – 1.2°) are smaller compared to the experimental values measured in the solid-state (3.2 – 6.7°). The bends in the PMDI units for geometry optimised **6Ar** (1.7 – 4.3°) are larger compared to the theoretical values for **6H** and **6Br** which could be due to the influence of the sterically bulky 3,5-dimethylbenzene substituents. Furthermore, the bends in PMDI units in the geometry optimised structure for **6Ar** are in a similar range to the experimental data (3.5 – 5.7°) (Figure 2.11). The dihedral angles between the 3,5-dimethylbenzene substituents and the PMDI core were also measured from the geometry optimised structure of **6Ar** with a variable range (53.4 – 67.1°) observed which was comparable to the experimental values (52.7 – 59.3°). In a similar manner to the experimental data, the aryl-substituents are twisted in the geometry optimised structure of **6Ar** to minimise steric repulsion.

The structural parameters that have been measured experimentally in the solid-state through XRD measurements and theoretically through geometry optimisation DFT calculations are largely in agreement. However, the experimental values tend to be more variable which can be attributed to the more complex nature of the single crystals used to measure the experimental values, with other factors playing an important role including solvation, non-covalent interactions and packing effects. In the DFT calculations, electronic and steric effects are modelled along with a solvent model. As there are fewer external factors influencing the structure of the molecular triangle in the calculated structures, less variability in the structural parameters is observed, although the values are comparable to the experimental data.

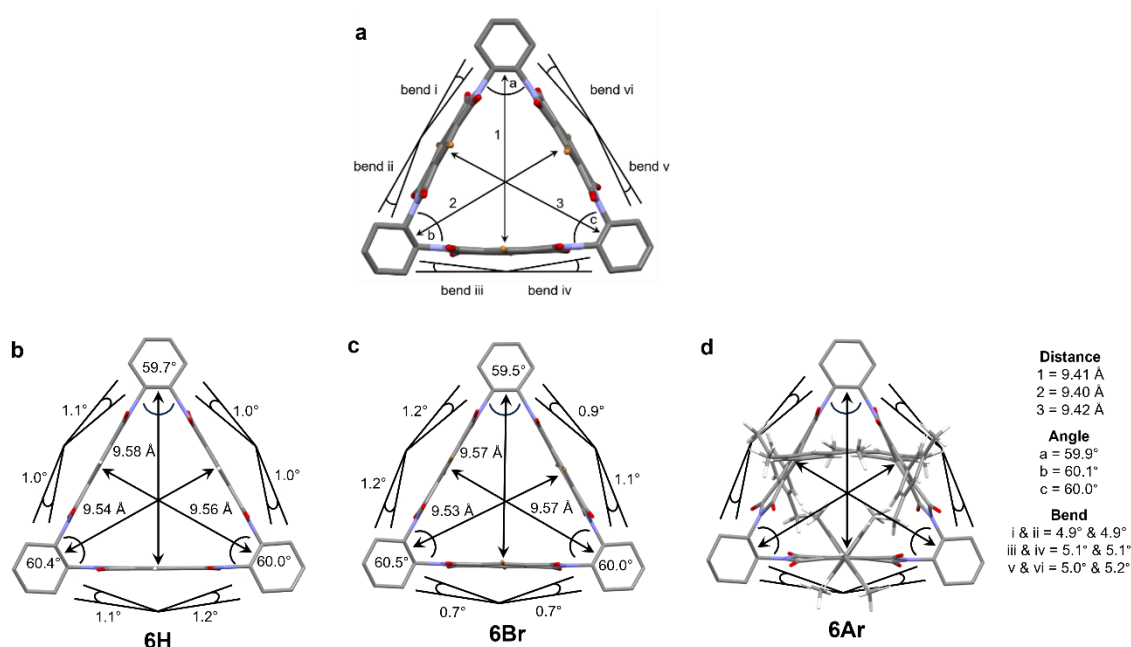


Figure 2.12 Geometry optimised DFT structures showing (a) structural parameters of general macrocyclic structure for (b) **6H**, (c) **6Br**, (d) **6Ar**. (e) Table showing dihedral angles of 3,5-dimethylbenzene substituents and PMDI core for **6Ar**. (B3LYP-D3(BJ)/def2svp/PCM (Solvent = CH_2Cl_2)).

2.2.3 OPTOELECTRONIC PROPERTIES OF CORE-FUNCTIONALISED MOLECULAR TRIANGLES

In addition to allowing for the evaluation of the structural features of core-substituted macrocycles, DFT calculations provided an insight into the electronic structure of molecular triangles **6H**, **6Br** and **6Ar** (Figure 2.13). DFT calculations at the B3LYP-D3(BJ)/def2svp/PCM (Solvent = CH₂Cl₂) level of theory were completed, where PCM is the polarisable continuum model which treats the solvent implicitly as a dielectric continuum medium rather than explicit methods which instead model the solvent molecules directly. Upon core-bromination of **6H** to **6Br**, both stabilisation of the LUMO and destabilisation of the HOMO is observed (HOMO: -7.70 to -7.48 eV and LUMO: -3.42 to -3.65 eV). These energy level changes lead to a narrowing of the bandgap (E_g) from 4.28 eV in **6H** to 3.83 eV in **6Br**. Furthermore, addition of six electron-donating 3,5-dimethylbenzene groups to the PMDI core of molecular triangles also influences the electronics of the macrocycle compared to **6H**, with a destabilisation of both the HOMO and LUMO, where the effect on the energy of the HOMO is more significant than the LUMO leading to a narrower band gap for **6Ar** (3.11 eV).

In Figure 2.13, the HOMO, HOMO-1, HOMO-2, LUMO, LUMO+1 and LUMO+2 energy levels are plotted due to degeneracies seen in the energy levels. In **6H**, the HOMO and HOMO-1 are doubly degenerate (-7.70 eV) with the HOMO-2 0.1 eV lower in energy (-7.80 eV). Similar degeneracy is observed in the LUMO and LUMO+1, with the energies doubly degenerate (-3.42 eV) and LUMO+2 at -3.32 eV. The same degeneracy of the LUMO and LUMO+1 is observed in **6Br** (-3.65 eV) with the LUMO+2 also 0.1 eV higher in energy (-3.55 eV). In contrast to **6H**, the HOMO of **6Br** is non-degenerate ($E_{\text{HOMO}} = -7.48$ eV), with the slightly lower energy HOMO-1 and HOMO-2 doubly degenerate (-7.51 eV). Lastly, the HOMO, HOMO-1 and HOMO-2 of **6Ar** are all non-degenerate with energies of -6.40 , -6.47 and -6.53 eV respectively. However, the LUMO and LUMO+1 of **6Ar** are degenerate (-3.29 eV) with the LUMO+2 higher in energy (-3.17 eV).

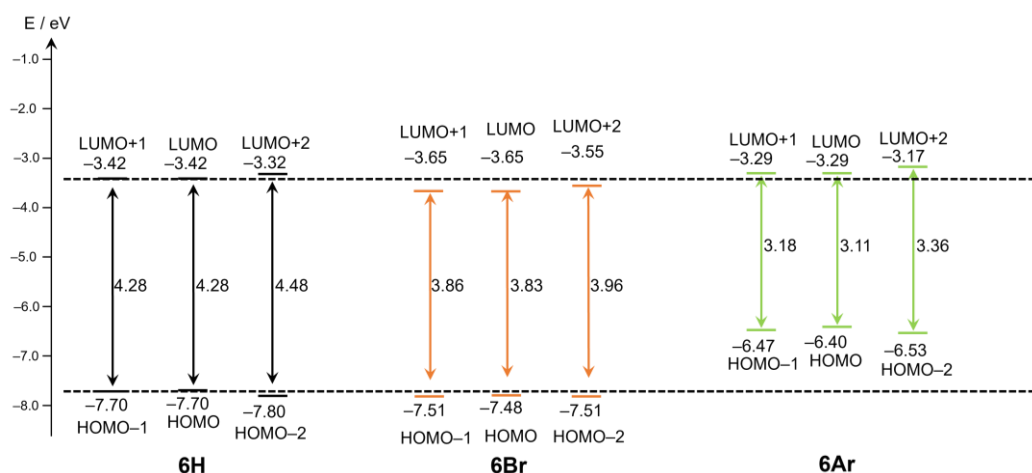


Figure 2.13 Energy levels of the HOMO, HOMO-1, HOMO-2, LUMO, LUMO+1 and LUMO+2 for (a) **6H**, (b) **6Br** and (c) **6Ar**, from DFT calculations (B3LYP-D3(BJ)/def2svp/PCM (Solvent = CH₂Cl₂)). The dotted lines represent the HOMO and LUMO energy levels of the unsubstituted **6H** for comparison.

In the seminal work by Stoddart and co-workers²⁷ on the NDI-based macrocycle, a symmetric LUMO with cyclic aromatic homoconjugation around the macrocycle was observed in the visual depiction of the theoretically modelled MO. It was hypothesised that through-space conjugation between PMDI units would also be observed in the MO depictions of molecular triangles **6Br** and **6Ar** (Figure 2.14). Interestingly, the symmetric or asymmetric nature of the visual depictions of the frontier molecular orbitals (HOMO, HOMO–1, HOMO–2, LUMO, LUMO+1 and LUMO+2) correlate with the degeneracy of the respective energy levels as discussed above. For **6H**, **6Br** and **6Ar**, the LUMO, LUMO+1 and LUMO+2 reside solely on the PMDI macrocycle core only and not on the core-substituent. This explains why the doubly degenerate LUMO and LUMO+1, and slightly higher energy non-degenerate LUMO+2 of **6H** are also observed in **6Br** and **6Ar**. The density of the doubly degenerate LUMO and LUMO+1 is asymmetric, with aromatic homoconjugation between adjacent PMDI units observed in a similar manner to that shown by Stoddart and coworkers²⁷ in the LUMO of the NDI based molecular triangle. Despite the density of the non-degenerate LUMO+2 being symmetric no aromatic homoconjugation is observed. Visual depictions of the LUMO, LUMO+1 and LUMO+2 of **6Ar** are shown as representative examples in Figure 2.14 (**6H** and **6Br** shown in Supplementary Information, Section 2.4.6, Figure S2.23).

The symmetry of the visual depictions of the HOMO, HOMO–1 and HOMO–2 of **6H**, **6Br** and **6Ar** are also correlated with the degeneracy of the respective energy levels, where a doubly degenerate HOMO, HOMO–1 or HOMO–2 is represented by asymmetric and non-degenerate energy level symmetric MOs respectively. Notably, the electron density of the MOs resides on both the macrocycle and core-substituent, either bromine atoms or 3,5-dimethylbenzene groups which explains why the degeneracy of the HOMO, HOMO–1 and HOMO–2 is different in **6H**, **6Br** or **6Ar** upon core-bromination or -arylation. Figure 2.14 shows representative examples of the HOMO, HOMO–1 and HOMO–2 from **6Ar** from a front and side view (visual depictions for **6H** and **6Br** shown in Supplementary Information, Section 2.4.6, Figure S2.23).

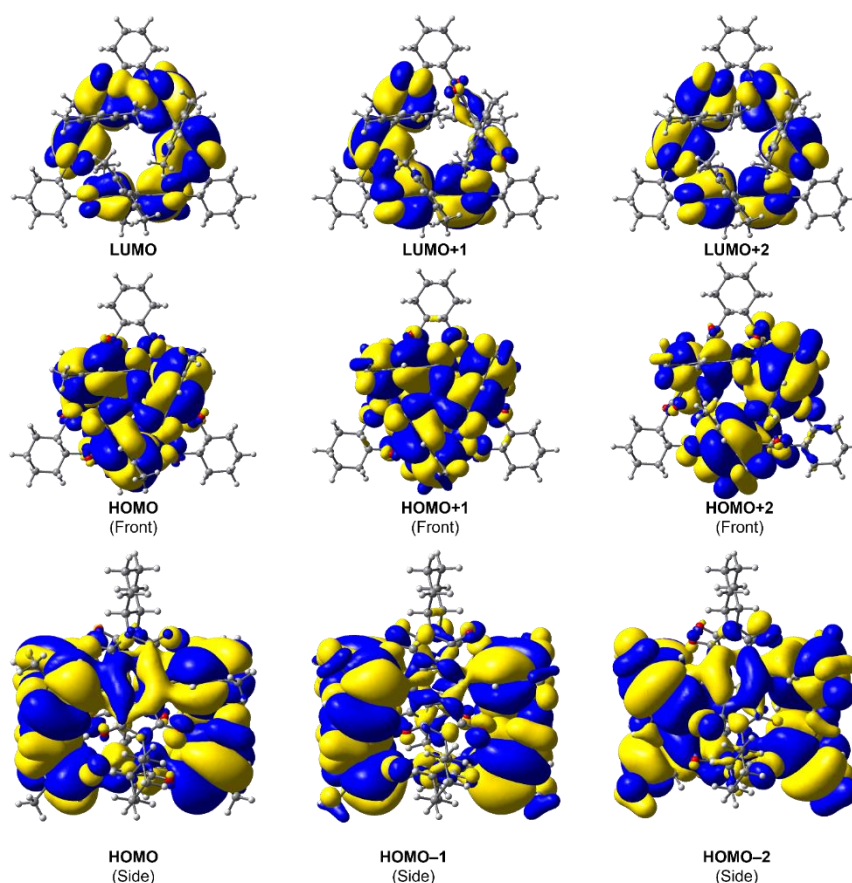


Figure 2.14 Visual depictions of the LUMO, LUMO+1 and LUMO+2 and front and side views of HOMO, HOMO-1 and HOMO-2 of **6Ar**. Isovalue = 0.05.

The effect of core-substitution on the electronic structure of molecular triangles was studied in the absorption spectra of **6H**, **6Br** and **6Ar** in CHCl_3 , DMF and THF, Figure 2.15. The absorption of ADI chromophores in molecular triangles typically occurs as a result of π - π^* electronic transitions.²⁶ For **6H** and **6Br** the π - π^* electronic transitions show vibronic fine structure between 310–320 and 350–370 nm respectively with no significant change in wavelength between CHCl_3 , THF and DMF. The red shift of absorption from **6H** to **6Br** is further extended to longer wavelengths for **6Ar**. A broad absorption peak at 390 nm (CHCl_3 and DMF) and 380 nm (THF) is observed for the π - π^* electronic transition of **6Ar**. Furthermore, an additional π - π^* electronic transition for **6Ar** is observed at 295 nm (CHCl_3 and DMF) and 290 nm in THF. The featureless nature of the absorptions for **6Ar** is due to the population of a greater number of vibrational energy levels in **6Ar** on account of the 3,5-dimethylbenzene substituents that are able to rotate in solution. Whereas, in the shape-persistent molecular triangles, **6H** and **6Br**, where the PMDI core is substituted with hydrogen or bromine atoms, there is increased rigidity in the absence of the flexible aryl groups. Excited state TD-DFT calculations could be completed in the future to potentially confirm the electronic transitions related to each absorption peak.

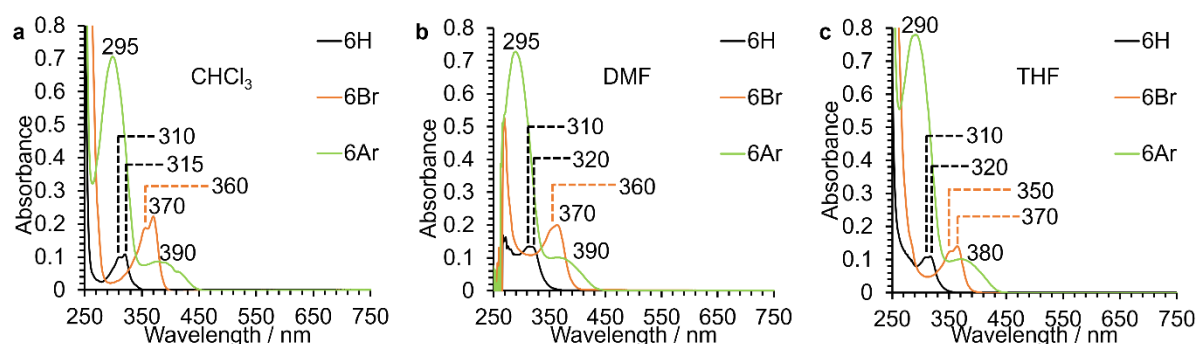


Figure 2.15 UV-vis spectra of **6H**, **6Br** and **6Ar** (25 μ M) in (a) CHCl_3 , (b) DMF and (c) THF.

The optical bandgap for **6H**, **6Br** and **6Ar** was calculated experimentally using the onset wavelength of the lowest energy transition in the absorption spectra in THF. A red shift in absorption for the π - π^* electronic transition was observed from **6H** to **6Br** to **6Ar**, thus giving optical bandgaps ($E_{\text{g,opt}}$) of 3.68, 3.25 and 2.76 eV respectively. The trend of decreasing bandgaps upon core-bromination and subsequent arylation is in agreement with the bandgaps calculated by DFT calculations (4.28, 3.83 and 3.11 eV for **6H**, **6Br** and **6Ar** respectively), although the theoretical values are greater in magnitude.

UV-vis spectra of molecular triangles **6H**, **6Br** and **6Ar** were also recorded in CH_2Cl_2 at a range of concentrations (Figure S2.20–22, Section 2.4.5, Supplementary Information). Using the Beer-Lambert law, the molar absorption coefficient was calculated at the λ_{max} , giving values of 5830, 10700 and 35600 $\text{M}^{-1} \text{cm}^{-1}$ for **6H**, **6Br** and **6Ar** respectively. Core-bromination (**6Br**) and subsequent arylation (**6Ar**) increases the molar absorptivity of the molecular triangles two- and six-fold respectively compared with the unsubstituted macrocycle (**6H**). This was visually observed with **6Ar** being a bright yellow solid and forming relatively intense yellow solutions whereas **6H** and **6Br** are white, and pale-yellow solids respectively. The greater extinction coefficient of core-functionalised molecular triangles, **6Br** and **6Ar** compared with **6H** indicates that the π - π^* electronic transitions are more populated. The influence of bromine and 3,5-dimethylbenzene substituents on the transition dipole moment and thus the extinction coefficient could be as a result of vibronic coupling of the electronic states leading to the relaxation of selection rules for absorption.^{28,29}

DFT calculations revealed that changes in core-substituent on molecular triangles affect the MO energy levels with **6Br** stabilising and **6Ar** destabilising the LUMO energy respectively. As molecular triangles are six-electron acceptors due to the presence of three PMDI two-electron acceptors units, the LUMO energy levels of **6H**, **6Br** and **6Ar** were calculated from experimental cyclic voltammetry (CV) and differential pulse voltammetry (DPV) data (Figure 2.16). The voltage at which each PMDI unit is reduced depends on the energy of the LUMO and thus the nature of the core-substituent (electron-donating or -withdrawing). Therefore, based on the DFT calculated energy levels, it was hypothesised that **6Br** ($E_{\text{LUMO}} = -3.65$ eV) and **6Ar** ($E_{\text{LUMO}} = -3.29$ eV) would be reduced at the least and most negative potentials respectively. The hypothesis was indeed observed experimentally *via* CV and DPV with the first reduction occurring at -0.47 , -0.78 and -0.84 V vs Ag/AgCl (CV) (Figure 2.16a)

and -0.485 , -0.760 and -0.805 V vs Ag/AgCl (DPV) (Figure 2.16b) for **6Br**, **6H** and **6Ar** respectively. Furthermore, experimental LUMO energies were calculated from the cyclic voltammograms for **6H**, **6Br** and **6Ar** as -3.65 , -3.94 and -3.60 eV respectively. The trend of the decrease in energy of the LUMO from **6Ar** to **6H** to **6Br** is consistent with the DFT calculations, although the theoretical values are all between 0.23 – 0.31 eV higher in energy.

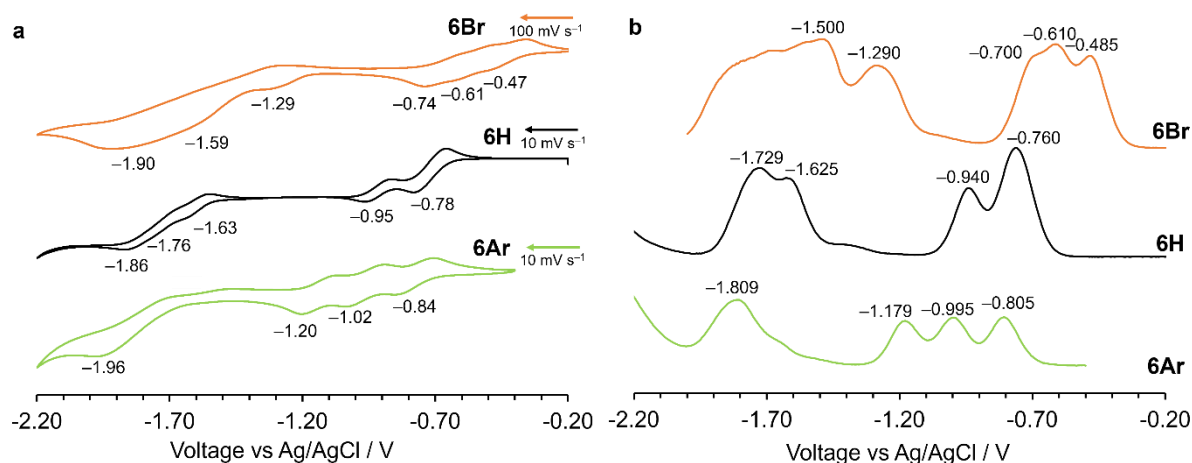


Figure 2.16 (a) CV and (b) DPV of **6H**, **6Br** and **6Ar** in anhydrous, degassed THF (1 mM) with TBAPF₆ (0.1 M) as supporting electrolyte.

As discussed in Chapter 1, evidence for cyclic aromatic homoconjugation in molecular triangles can be shown using CV and DPV, where electronic communication between overlapping π -orbitals leads to the occurrence of six single-electron reductions, as opposed to two, three-electron processes. Indeed, in the cyclic voltammograms (Figure 2.16a), the first reduction of each PMDI unit in **6Br** and **6Ar** are split into three peaks, whereas the lack of well-resolved peak splitting for the subsequent second reduction of **6Ar** can be attributed to the slow kinetics of charge transfer at the electrode.²² The cyclic voltammogram of **6Br** was measured at a scan rate of 100 mV s^{-1} (10 mV s^{-1} for **6H** and **6Ar**), with resolution of six accessible reduced states evidence for cyclic aromatic homoconjugation in the macrocycle. In the cyclic voltammogram of **6H**, the first reduction of each PMDI unit was split into two peaks with the second reduction showing three single-electron processes. The differential pulse voltammograms provided further evidence of electron delocalisation around the molecular triangles. The area under a peak in the voltammogram in DPV represents the number of electrons in a redox-process, and as such the first reductions observed for **6Br** and **6Ar** show three relatively equal height reductions which could therefore be single-electron processes. This would indicate that the more intense peak in the differential pulse voltammogram at -0.760 eV for **6H** could represent two overlapping single-electron reduction processes. Furthermore, the broader peaks at more negative potentials (< -1.29 eV) for **6H**, **6Br** and **6Ar** could also represent three successive overlapping one-electron reduction processes.

Table 2.1 shows experimental values that can be obtained from absorption spectroscopy (λ_{max} (nm), ϵ ($\text{M}^{-1} \text{cm}^{-1}$) and $E_{\text{g,opt}}$ (eV)) and CV ($E_{1/2}$ (eV) and E_{LUMO} (eV)) with comparisons to theoretical MO energy levels. Using the experimental band gap ($E_{\text{g,opt}}$) and LUMO, experimental estimation of the HOMO energy levels was calculated, with the values showing the same trend as in DFT calculations of successive destabilisation of the MO upon core-substitution from **6H** to **6Br** to **6Ar**.

Table 2.1 Experimental and theoretical values from UV-vis spectroscopy, cyclic voltammetry and DFT calculations for molecular triangles **6H**, **6Br** and **6Ar**.

	6H	6Br	6Ar
^a λ_{max} / nm	320	368	302
^b ϵ / $\text{M}^{-1} \text{cm}^{-1}$	5830	10700	35600
^c $E_{\text{g,opt}}$ / eV	3.68	3.25	2.76
^d $E_{1/2}$ / V	-0.72	-0.42	-0.78
^e E_{LUMO} (CV) / eV	-3.65	-3.94	-3.60
^f E_{HOMO} (Exp) / eV	-7.33	-7.19	-6.36
^g E_{LUMO} (DFT) / eV	-3.42	-3.65	-3.29
^g E_{HOMO} (DFT) / eV	-7.70	-7.48	-6.40
^g $E_{\text{g,DFT}}$ / eV	4.28	3.83	3.11

^aWavelength of maximum absorption in CH_2Cl_2 . ^bMolar absorption coefficient in CH_2Cl_2 calculated at the λ_{max} . ^cOptical bandgap measured through onset wavelength of lowest energy transition in UV-vis spectrum of compound in THF. ^dHalf wave potential of first reductions of compounds in THF (V vs Ag/AgCl). ^eThe LUMO energy level was calculated from the onset of the first reduction potential in CV, using the equation $E_{\text{LUMO}} = [-e[E_{\text{onset, red}} - 0.50 + 4.8]]$ eV, where the oxidation potential of Fc/Fc^+ against Ag/AgCl in THF with TBAPF₆ was found to be 0.50 V and 4.8 eV is the energy level of ferrocene below the vacuum level. ^fCalculated from $E_{\text{HOMO}} = E_{\text{LUMO}} - E_{\text{g,opt}}$. ^gValues from DFT calculations B3LYP-D3(BJ)/def2svp/PCM(solvent = CH_2Cl_2).

Following successful characterisation of the electronic structure of the neutral states of **6H**, **6Br** and **6Ar** by UV-vis spectroscopy, the electronic structure of the reduced states of **6H** and **6Br** using spectroelectrochemistry and chemical reduction were studied (Figure 2.17). Upon electrochemical reduction of the molecular triangles by the application of a potential (0 to -2.0 V), a new set of red-shifted peaks formed at 669 and 713 nm and 637 and 679 nm representing the formation of tris-radical anions [**6H**]^{3•-} and [**6Br**]^{3•-} respectively. Upon further reduction, these two peaks decrease in intensity, with two additional higher energy peaks forming at 526 and 555 nm for [**6H**]⁶⁻. Unfortunately, the hexa-anion of the brominated macrocycle, [**6Br**]⁶⁻ was not observed. The inability to observe [**6Br**]⁶⁻ could have been as a result of the increased reactivity of electron-deficient **6Br** in the electron-rich DMF solvent as discussed in Chapter 4.

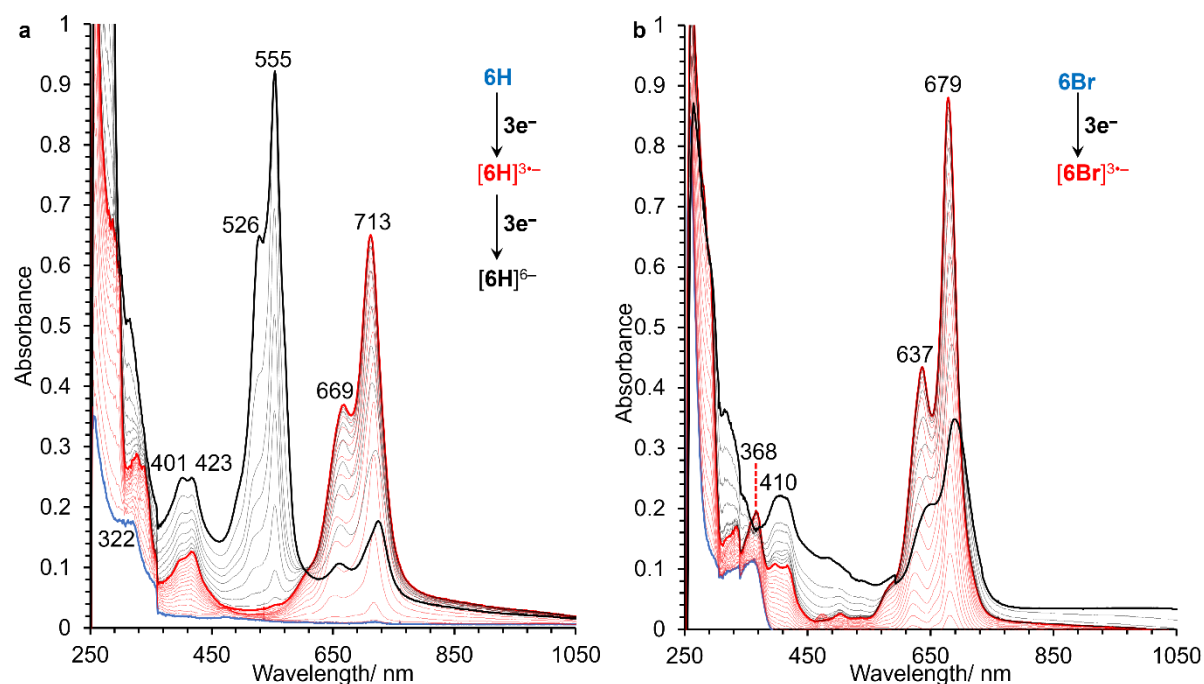


Figure 2.17 Spectroelectrochemical data of (a) **6H** and (b) **6Br** generated by electrochemical reduction using CV (0 to -2.0 V) in anhydrous, degassed DMF (1 mM) with TBAPF₆ (0.1 M) as supporting electrolyte.

As the hexa-anion of **6Br** was unable to be generated using spectroelectrochemistry, chemical reduction of **6H** and **6Br** with decamethyl cobaltocene (CoCp^*_2) was carried out with the reduced states studied using UV-vis spectroscopy (Figure 2.18). Upon the addition of up to three equivalents of CoCp^*_2 two new lower energy peaks were present at 665 and 715 nm and 640 and 680 nm representing tris-radical anions $[6H]^{3\bullet-}$ and $[6Br]^{3\bullet-}$ respectively. The wavelengths of these new species match the peaks for the tris-radical anions $[6H]^{3\bullet-}$ and $[6Br]^{3\bullet-}$ generated using spectroelectrochemistry (Figure 2.17). To prove that the new species formed were indeed the tris-radical anions, the solutions were studied with electroparamagnetic resonance (EPR) spectroscopy (Figure 2.18a and c (inset)). A signal was observed in response to the change in the magnetic field, providing evidence for the presence of free radical species *e.g.* $[6H]^{3\bullet-}$ and $[6Br]^{3\bullet-}$. The subsequent addition of an excess of CoCp^*_2 initiated a decrease in intensity of the peaks at 665 and 710 nm and 640 and 680 nm for the tris-radical anions and new broad peaks formed at 545 and 550 nm representing the hexa-anions, $[6H]^{6-}$ and $[6Br]^{6-}$. This is in agreement with the absorption spectrum of **6H** upon reduction after applying a potential (Figure 2.17). Two well-resolved peaks for $[6H]^{6-}$ are present upon electrochemical reduction (Figure 2.17a), whereas the resolution of the peaks is absent in the absorption spectrum for the chemically reduced sample, with a broad featureless absorption observed instead. The colour change upon chemical reduction would be useful for the characterisation of the radical anion and hexa-anion states. However, the dark purple colour of the CoCp^*_2 reductant in DMF masked any colour change upon chemical reduction of the molecular triangle.

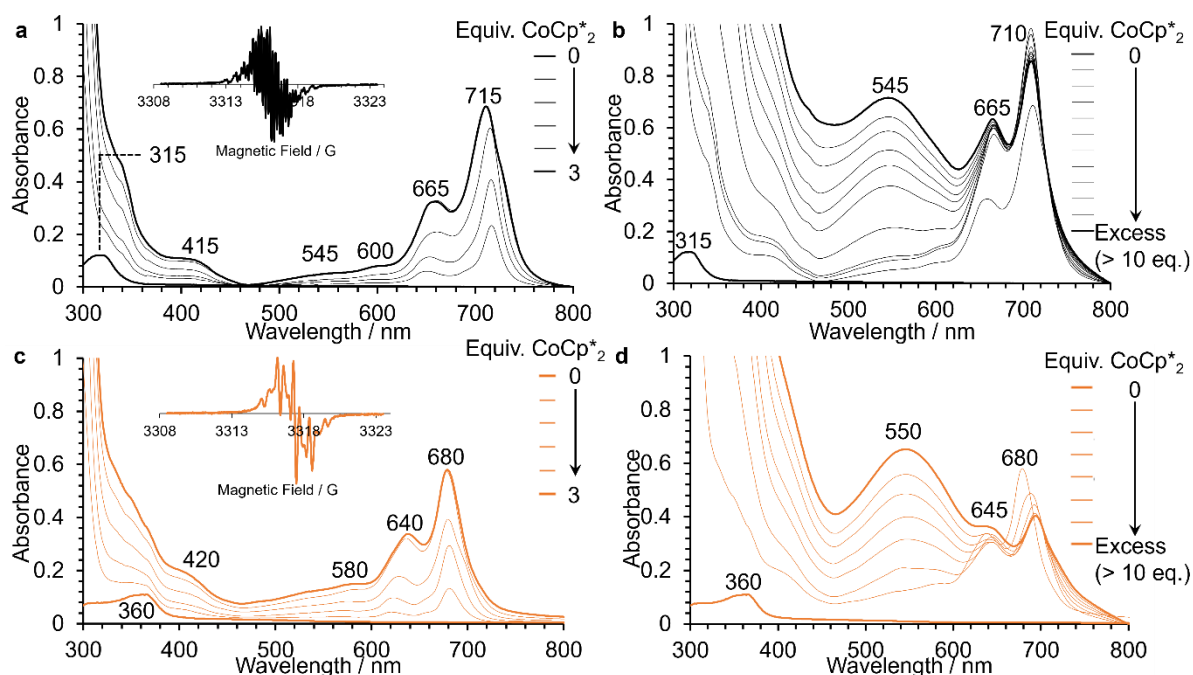


Figure 2.18 UV-vis spectra of reduced states of (a) **6H** (0–3 eq. CoCp^*_2), (b) **6H** (0–>10 eq. CoCp^*_2), (c) **6Br** (0–3 eq. CoCp^*_2) and (d) **6Br** (0–>10 eq. CoCp^*_2) generated by chemical reduction with CoCp^*_2 in DMF. Inset: EPR spectra of tris-radical anions of (a) **6H** and (c) **6Br**.

2.3 CONCLUSIONS

This Chapter detailed the synthesis and comprehensive structural, electronic and electrochemical analysis of three PMDI based molecular triangles, functionalised at the aromatic core with hydrogen atoms (**6H**), bromides (**6Br**) or bulky aryl (**6Ar**) substituents to understand the fundamental impact of these structural modifications. Molecular triangles, **6H** and **6Br**, were previously known in the literature,^{21,22,26} whereas the novel synthesis of **6Ar** was achieved by reacting **6Br** with 3,5-dimethylbenzene boronic acid *via* a Suzuki-Miyaura coupling reaction. It was found that in the crystalline solid-state, **6Br** interacts with a crown of acetone molecules *via* $\text{C-Br}\cdots\text{O}=\text{C}$ interactions leading to the formation of a supramolecular, hexagonal array of 1D channels. Whereas the bulky aryl-substituents in **6Ar** are twisted to minimise steric repulsion and maximise van der Waals interactions. Notably, core-functionalisation of PMDI based molecular triangles does not significantly influence the structural features of the rigid, shape-persistent macrocycle, with the cavity distance and angles between X_2PMDI ($\text{X} = \text{H}, \text{Br}$ or 3,5-dimethylbenzene) side units being similar in **6H**, **6Br** and **6Ar** as measured experimentally in X-ray crystal structures and theoretically from DFT calculated geometry optimised models. The influence of core-functionalisation on the energy levels of the frontier molecular orbitals of **6H**, **6Br** and **6Ar** have been calculated theoretically (DFT calculations) and experimentally (UV-vis spectroscopy and cyclic voltammetry). The HOMO of **6H** is destabilised upon the introduction of bromide (**6Br**) and aryl (**6Ar**) substituents, although more significantly by the latter. Conversely, the LUMO of the macrocycle is stabilised upon core-bromination (**6Br**) and slightly destabilised by the introduction of electron-rich 3,5-dimethylbenzene groups (**6Ar**). These effects lead

to a narrowing of the bandgap in both **6Br** (3.83 eV (DFT) and 3.25 (UV)) and **6Ar** (3.11 eV (DFT) and 2.76 eV (UV)) compared with **6H** (4.28 eV (DFT) and 3.68 eV (UV)). The molar absorption coefficient of the macrocycles increases upon core-bromination and -arylation, 5830, 10700 and 35600 M⁻¹ cm⁻¹ for **6H**, **6Br** and **6Ar** respectively. Furthermore, core-functionalisation of molecular triangles does not disrupt cyclic aromatic homoconjugation, with electronic communication around the macrocycles evidenced by the splitting of redox events in CV and DPV showing more than three accessible reduced states. The electronic structure of the globally reduced states (tris-radical anion and hexa-anion) of **6H** and **6Br** were studied by absorption spectroscopy after reduction electrochemically with an applied voltage and chemically with CoCp*₂. These experiments revealed red-shifted peaks above 600 nm representing [**6H**]^{3•-} and [**6Br**]^{3•-}, with subsequent reduction peaks blue-shifted to around 550 nm for [**6H**]⁶⁻ and [**6Br**]⁶⁻.

Ultimately, this work has shown that core-functionalisation of molecular triangles with electron-withdrawing and -donating bromide and aryl groups respectively influences the optical and electrochemical properties which is a direct result of the stabilisation and destabilisation of the FMOs and subsequent narrowing of the band gap. The tuning of these properties *via* the core-functionalisation of molecular triangles could be utilised for application in electronic devices such as *n*-type organic semiconductors which is investigated in Chapter 5. Furthermore, the presence of bromide reactive handles in **6Br** allows for post-synthetic functionalisation to expand the class of molecular triangles even further, beginning with the Suzuki-Miyaura coupling with 3,5-dimethylbenzene to yield **6Ar**. This represents the first step on the journey towards triangular nanoprisms through cross-linking molecular triangles.

2.4 SUPPLEMENTARY INFORMATION

2.4.1 MATERIALS AND GENERAL METHODS

All chemicals and reagents were purchased from commercial suppliers (Sigma Aldrich, Fisher Scientific, Alfa Aesar, Fluorochem, Apollo Scientific or Tokyo Chemical Industry) and used without further purification unless otherwise stated. Anhydrous solvents were obtained from a neutral alumina Solvent Purification System under nitrogen and stored over activated (>250 °C at 0.01 mbar overnight) 3 Å molecular sieves under a dry Ar atmosphere.

Analytical thin-layer chromatography (TLC) was performed on silica gel 60 plates pre-loaded with F254 indicator (Sigma Aldrich) and visualised under UV light irradiation (254 and 365 nm). Automated flash column chromatography was performed using a Teledyne ISCO Combiflash NextGen 300+ with detectors using broad range UV-vis (200–800 nm) and evaporative light scattering (ELS) through N₂ gas and loaded on pre-filled RedisepTM Gold cartridges (normal phase: SiO₂) by dry loading from adsorbed celite. Nuclear magnetic resonance (NMR) spectra were recorded on a JEOL ECS400D

spectrometer (working frequency of 400 and 101 MHz for ^1H and ^{13}C nuclei respectively). Chemical shifts (δ) are reported in ppm relative to the signals corresponding to residual non-deuterated solvents (CDCl_3 : δ_{H} 7.26 ppm, δ_{C} 77.16 ppm, $(\text{CD}_3)_2\text{SO}$: δ_{H} 2.50 ppm, δ_{C} 39.52 ppm, $(\text{CD}_3)_2\text{CO}$: δ_{H} 2.05 ppm, δ_{C} 206.62 ppm, 29.84 ppm). Coupling constants (J) are reported in Hertz (Hz) and ^1H multiplicities are reported in accordance with the following convention: s = singlet, d = doublet, t = triplet, q = quadruplet, p = pentet, m = multiplet. Assignment of ^1H and ^{13}C NMR signals were accomplished with the aid of DEPT-135 and two-dimensional COSY, HSQC and HMBC NMR spectroscopies. NMR spectra were processed using MestReNova software, Version 14. High-resolution mass spectrometry (HR-MS) was completed using a Bruker compact time-of-flight mass spectrometer using an atmospheric-pressure chemical ionisation (APCI) source.

Diffraction data were collected at 110 K (cooled with liquid N_2 using an Oxford Instruments Cryojet) on an Oxford Diffraction Supernova diffractometer ($\text{CuK}\alpha$ λ = 1.54184 Å) using a Cannon EOS CCD camera. A suitable crystal was selected and mounted (oil on 100 μm mount) on a SuperNova Dual, Cu at home/near, Eos diffractometer. Diffractometer control, data collection, initial unit cell determination, frame integration and unit cell refinement were carried out with 'CrysAlisPro'.³⁰ Face-indexed absorption corrections were applied using spherical harmonics implemented in SCALE3 ABSPACK scaling algorithm.³¹ OLEX2 was used for overall structure solution, refinement and preparation of computer graphics and publication data.³² Within OLEX2, the structures were solved with the Superflip Structure solution program using 'charge flipping'³³ or with the ShelXS/ShelXT structure solution programs using Direct Methods.³⁴ Refinement by full-matrix least-squares used the SHELXL-97 algorithm within OLEX2. All non-hydrogen atoms were refined anisotropically and hydrogen atoms were placed using a 'riding model' and included in the refinement at calculated positions. Visualisation, exploration, distance and angle measurement and image capture of crystal structures were completed using Mercury.³⁵ Hirschfeld analysis and energy framework calculations of crystal structures were performed using CrystalExplorer17.5 software employing the TONTO utility for theoretical calculations carried out at the DFT/B3LYP/6-31g(d,p) level of theory.³⁶ For energy framework calculations, a molecular shell with a 3.8 Å radius was generated around a central molecule, and the interaction energies (electrostatic, dispersion and total) between the molecular pairs were calculated. The scale factors for benchmarked energies used for the construction of energy models were taken from Mackenzie *et al.*³⁷ The lattice energy was calculated as the halved sum of the interaction energies between the given molecule and all the surrounding molecules within 25 Å radius.³⁷

Solution-state absorption spectra were recorded using an Agilent Technologies Cary 5000 Series UV-Vis-NIR spectrophotometer or Shimadzu UV 1800 spectrophotometer using standard 10 mm path length UV-vis quartz cuvettes at room temperature using samples prepared in dry solvents.

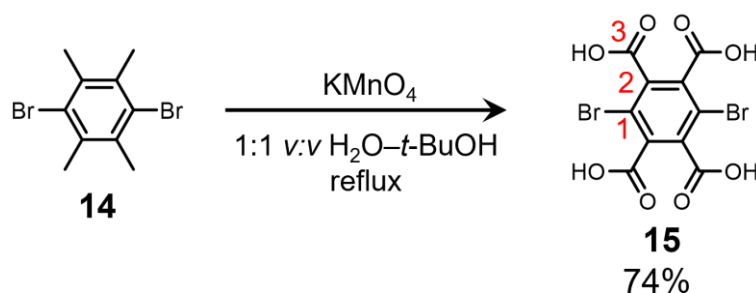
Solution-state electrochemical experiments (cyclic voltammetry (CV) and differential pulse voltammetry (DPV)) were carried out using a Gamry Reference 3000 Potentiostat at room temperature with a standard three-electrode setup using Ar-purged, freeze-pump-thawed sample solutions in anhydrous THF. Tetrabutylammonium hexafluorophosphate (TBAPF₆; 0.1 M) was recrystallized from hot EtOH and used as the supporting electrolyte. A glassy carbon working electrode (BASi; 0.071 cm²) was used where the electrode surface was polished routinely with 0.05 µm alumina–water slurry on a felt surface immediately before each use. A platinum wire counter electrode was used with an aqueous Ag/AgCl reference electrode which was routinely stored in an aqueous 3 M KCl solution. Spectroelectrochemistry (SEC) experiments were performed at room temperature using an optically transparent thin-layer electrochemical (OTTLE) cell (path length approx. 0.2 mm with two CaF₂ windows separated by PTFE spacers) fitted with a Pt wire mesh working electrode, Pt wire counter electrode and an Ag wire pseudo-reference electrode. All SEC samples were prepared as Ar-purged freeze-pump-thawed solutions in anhydrous DMF containing TBAPF₆ (0.1 M) as the supporting electrolyte and analysed with a sweeping voltage from 0 to –2.0 V.

Chemical reduction experiments were performed in an argon atmosphere using an MBraun UniLab Pro glove box (<0.1 ppm O₂ and H₂O content). Decamethylcobaltocene (CoCp*₂) was used as a single-electron reductant ($E_{1/2}(\text{CoCp}^*_2) = -1.3 \text{ V vs Fc}^+/\text{Fc}$) and titrated into analyte solutions prepared under a dry Ar atmosphere and using anhydrous, thoroughly degassed DMF solutions.

Electron paramagnetic spectroscopy (EPR) spectra were recorded at X-band on a Bruker EMX-Micro spectrometer using 0.1 G modulation amplitude. EPR samples were prepared and stored in an anaerobic glove box (MBraun UniLab Pro) under a dry Ar atmosphere in anhydrous and thoroughly degassed DMF solutions.

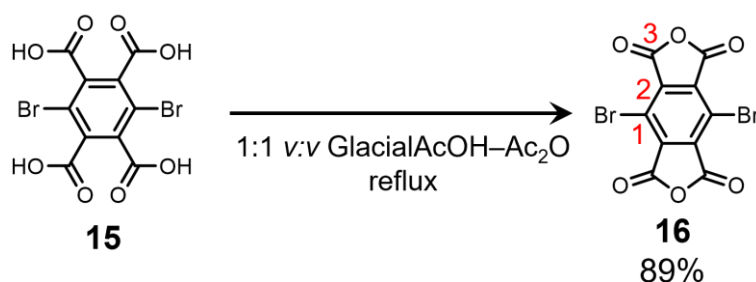
Theoretical density functional theory (DFT) ground state geometry optimisation and frequency calculations were performed using Gaussian 16 software,³⁸ on the Viking High Performance Computer facility provided by the University of York. The calculations were carried out using Becke's three-parameter exchange functional³⁹ with the gradient-corrected correlation formula of Lee, Yang and Parr (B3LYP)⁴⁰ paired with the double zeta valence plus polarisation def2svp basis set,⁴¹ PCM solvation model (CH₂Cl₂) and dispersion corrections (D3BJ).⁴² Ground state geometries were verified by convergence to a minimum stationary point and no negative vibrational frequencies observed.

2.4.2 SYNTHESIS

1,4-DIBROMOBENZENE-2,3,5,6-TETRACARBOXYLIC ACID (**15**)

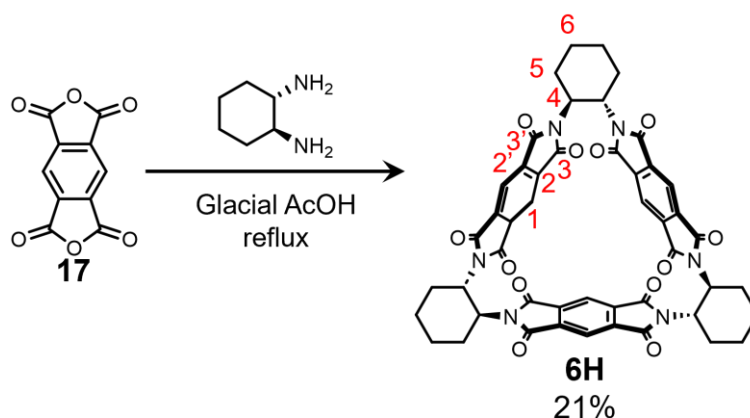
1,4-Dibromo-2,3,5,6-tetramethylbenzene **14**, (20.00 g, 68.5 mmol, 1.0equiv.) was suspended in $t\text{-BuOH-H}_2\text{O}$ (1:1 v/v, 308 mL) and stirred. Potassium permanganate (54.00 g, 342 mmol, 4.99 equiv.) was added and the reaction mixture heated at reflux for 4 h at which point the pink colour remained. The solution was cooled to rt and a second equal portion of potassium permanganate (54.00 g, 342 mmol, 4.99 equiv.) was added to the reaction mixture, which was then heated to reflux overnight. Upon cooling the reaction mixture below 60 °C, absolute EtOH (200 mL) was added and the mixture heated to 80 °C to quench any remaining KMnO_4 . The resulting mixture was cooled to rt, filtered to remove insoluble MnO_2 salts, the filtrate was concentrated *in vacuo* and the resulting residue was dried at 80 °C in a vacuum oven (10^{-3} mbar) overnight. The dried crude material was re-dissolved in water (80 mL) and conc. HCl (15 mL) added to the solution, at pH = 2 a precipitate formed. Additional water (100 mL) was added to fully dissolve solid and conc. HCl (5 mL) was added to until pH = 1. The acidic solution was concentrated *in vacuo*, the resulting residue suspended in acetone and any insoluble salts were removed by filtration. The filtrate was concentrated *in vacuo* to give a light brown solid. The insoluble salts were re-dissolved in water and acidified to pH = 1 with conc. HCl and worked up as previously to afford additional light brown solid. The light brown solids were combined and dried on the high vacuum to give the desired product, **15**, (21.00 g, 51.0 mmol, 74%).

^{13}C NMR (101 MHz, $(\text{CD}_3)_2\text{CO}$, 298 K): δ_{C} 165.9 (**3**), 138.4 (**2**), 116.5 (**1**). Spectroscopic data are consistent with the literature.⁸

1,4-DIBROMOBENZENE-2,3,5,6-TETRACARBOXYLIC ANHYDRIDE (16)

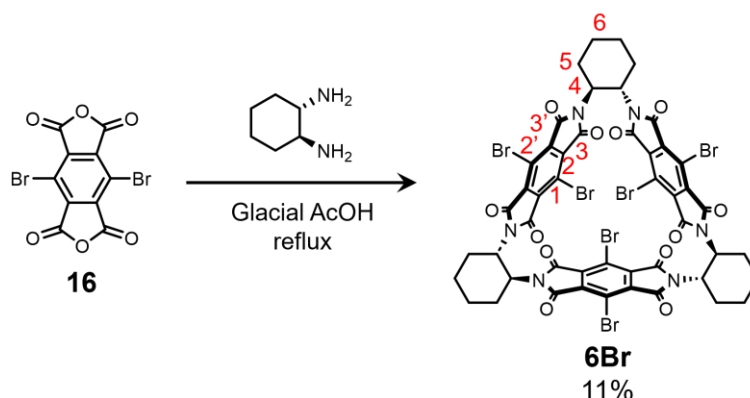
1,4-Dibromobenzene-2,3,5,6-tetracarboxylic acid **15**, (20.00 g, 48.55 mmol) was stirred in glacial AcOH–Ac₂O (1:1 v/v, 122 mL) and heated to reflux overnight. The reaction mixture was cooled to rt and the precipitate isolated by filtration, washed with H₂O and dried on the high vacuum to give **16** (13.16 g, 35.0 mmol, 72%) as a light brown solid.

¹³C NMR (101 MHz, (CD₃)₂CO, 298 K): δ_C 159.0 (3), 138.6 (2), 117.3 (3). Spectroscopic data are consistent with the literature.⁸

MOLECULAR TRIANGLE 6H

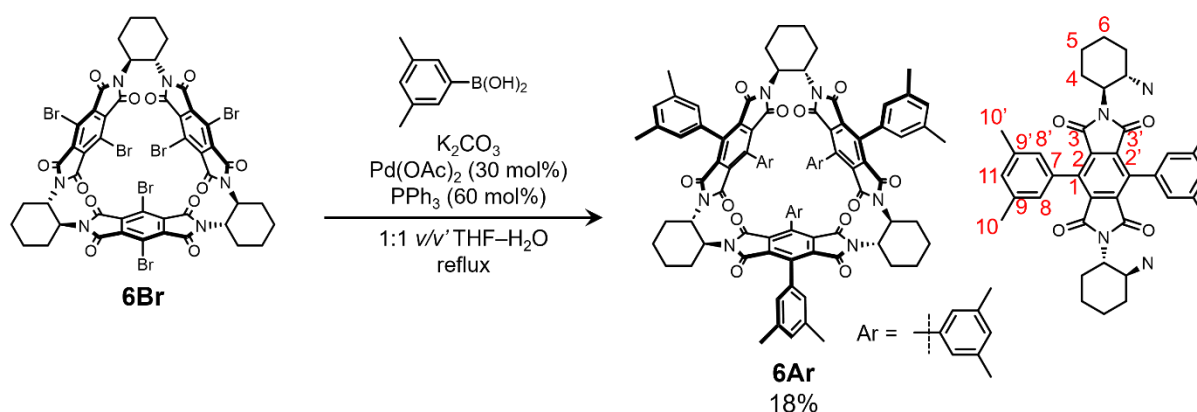
A solution of (*S,S*)-*trans*-1,2-diaminocyclohexane (0.26 g, 2.29 mmol, 1.00 equiv.) in glacial AcOH (9 mL) was added to a stirring solution of **17** (0.50 g, 2.29 mmol, 1.00 equiv.) in glacial AcOH (9.36 mL) and refluxed for 4 h. The reaction mixture was cooled to rt and concentrated *in vacuo* to give a grey solid which was refluxed in CH₂Cl₂ (50 mL) for 2 h. The suspension was cooled to rt and the unwanted polymeric solid removed by filtration. The filtrate was concentrated *in vacuo* and the solid subjected to column chromatography (SiO₂: 0–100% Me₂CO in CH₂Cl₂) to give **6H** (0.14 g, 0.16 mmol, 21%) as a colourless solid.

¹H NMR (400 MHz, CDCl₃, 298 K): δ_H 8.03 (s, 6H¹), 5.23–5.10 (m, 6H⁴), 2.13–1.88 (m, 18H⁵⁺⁶), 1.61–1.50 (m, 6H⁶). ¹³C NMR (101 MHz, CDCl₃, 298 K): δ_C 165.7 (3/3'), 165.0 (3/3'), 136.6 (2/2'), 136.3 (2/2'), 119.1 (1), 51.3 (4), 31.1 (5), 25.1 (6). APCI-MS (+ve, CH₂Cl₂): calcd for [M+H]⁺ *m/z* = 889.2464, found 889.2453. Spectroscopic data are consistent with the literature.^{22,26}

MOLECULAR TRIANGLE **6Br**

A solution of (*S,S*)-*trans*-1,2-diaminocyclohexane (0.15 g, 1.34 mmol, 1.01 equiv.) in AcOH (5.66 mL) was added to a stirring solution of **16** (0.50 g, 1.33 mmol, 1.00 equiv.) in glacial AcOH (5 mL) and refluxed for 4 h. The reaction mixture was cooled to rt and concentrated *in vacuo* to give a brown solid which was refluxed in CH₂Cl₂ (50 mL) for 2 h. The suspension was cooled to rt and the unwanted polymeric solid removed by filtration. The filtrate was concentrated *in vacuo* and the orange solid subjected to column chromatography (Si)₂: 0–100% Me₂CO in CH₂Cl₂ to give **6Br** (70 mg, 0.05 mmol, 11%) as a yellow solid.

¹H NMR (400 MHz, CDCl₃, 298 K): δ_H 5.23–5.10 (m, 6H⁴), 2.13–1.88 (m, 18H⁵⁺⁶), 1.56–1.48 (m, 6H⁶). ¹³C NMR (101 MHz, CDCl₃, 298 K): δ_C 163.0 (3/3'), 162.1 (3/3'), 135.9 (2/2'), 135.7 (2/2'), 114.7 (1), 51.7 (4), 30.8 (5), 25.1 (6). APCI-MS (+ve, CH₂Cl₂): calcd for [M+H]⁺ *m/z* = 1356.7095, found 1356.7027. Spectroscopic data are consistent with the literature.²¹

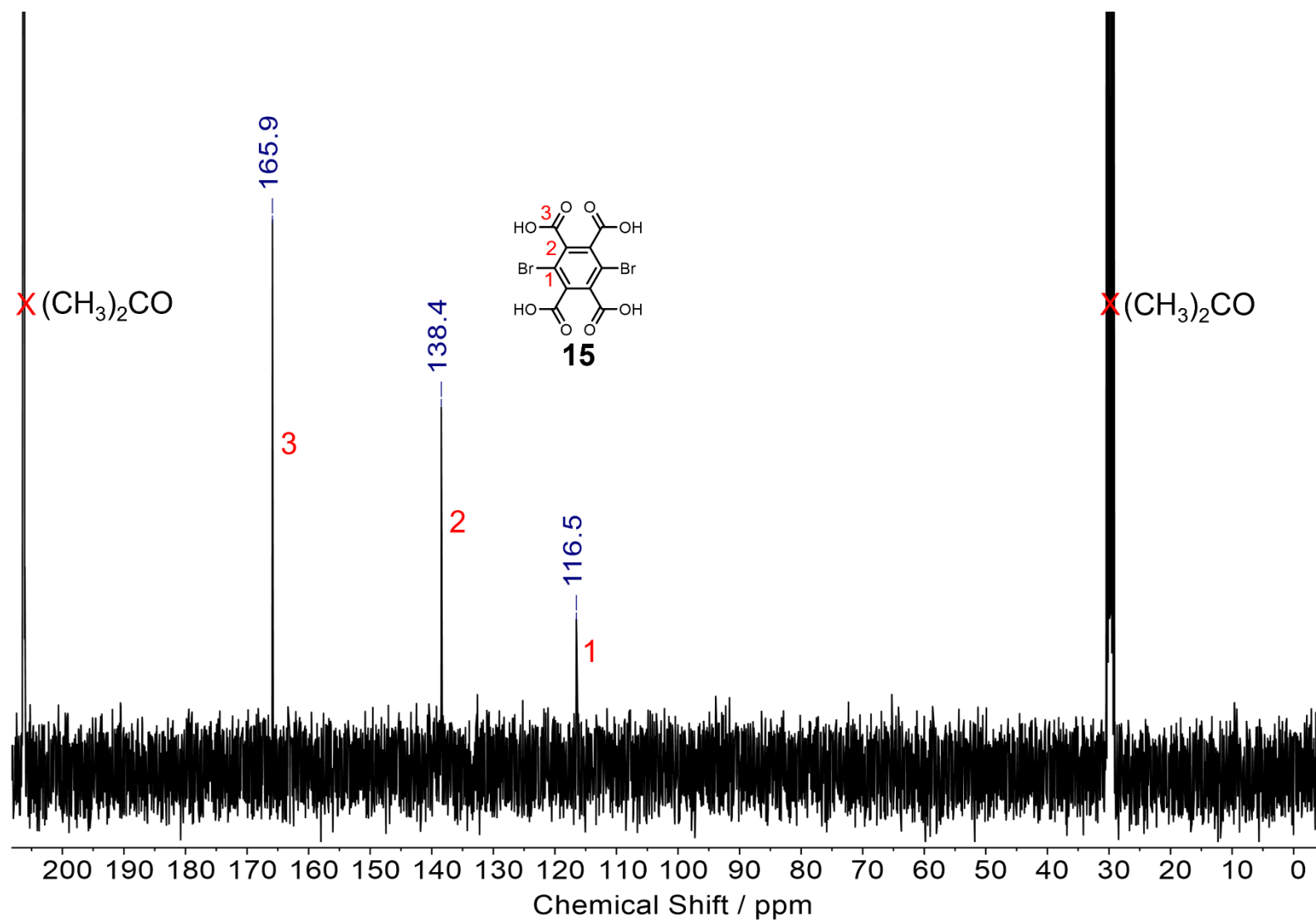
MOLECULAR TRIANGLE **6Ar**

A round bottom flask was charged with **6Br** (250 mg, 0.18 mmol, 1.0 equiv.), 3,5-dimethylbenzene boronic acid (167 mg, 1.11 mmol, 6.07 equiv.), K₂CO₃ (76 mg, 0.55 mmol, 3.00 equiv.), Pd(OAc)₂ (13.2 mg, 0.059 mmol, 0.32 equiv.) and PPh₃ (28 mg, 0.11 mmol, 0.58 equiv.) and cycled under N₂ atmosphere three times. A 1:1 v/v mixture of THF–H₂O (5.4 mL) was degassed under N₂ and transferred

to the reaction flask to dissolve the reagents before being heated to reflux overnight. The reaction mixture was then cooled to rt before adding sat. NaHCO_3 (100 mL) and extracting the aqueous phase with CH_2Cl_2 (3 x 100 mL). The organic layers were combined, dried (Na_2SO_4), filtered and the filtrate concentrated *in vacuo*. The resulting solid was purified by automated flash chromatography (SiO_2 : 0–100% EtOAc in n-hexanes) to afford **6Ar** (49 mg, 0.03 mmol, 18%) as a yellow solid.

^1H NMR (400 MHz, CDCl_3 , 298 K): δ_{H} 7.02 (s, $6\text{H}^{8/8'}$), 6.94 (s, $6\text{H}^{8/8'}$), 6.18 (s, 6H^{11}), 4.99–4.81 (m, 6H^4), 2.35 (s, 18H^{10}), 2.13–1.69 (m, 18H^{5+6}), 1.75 (s, $18\text{H}^{10'}$), 1.39–1.29 (m, 6H^6). **^{13}C NMR** (101 MHz, CDCl_3 , 298 K): δ_{C} 164.6 ($3/3'$), 164.0 ($3/3'$), 138.1 (7), 137.8 ($9/9'$), 137.0 ($9/9'$), 134.1 ($2/2'$), 133.3 ($2/2'$), 131.3 ($8/8'$), 129.8 (1), 127.5 (11), 126.9 ($8/8'$), 50.9 (4), 30.1 (5), 25.0 (6), 21.5 (10), 20.5 ($10'$). **APCI-MS** (+ve, CH_2Cl_2): calcd for $[\text{M}+\text{H}]^+$ m/z = 1513.6220, found 1513.6163.

2.4.3 CHARACTERISATION

Figure S2.1 ^{13}C NMR (101 MHz, $(\text{CD}_3)_2\text{CO}$, 298 K) spectrum of **15**.

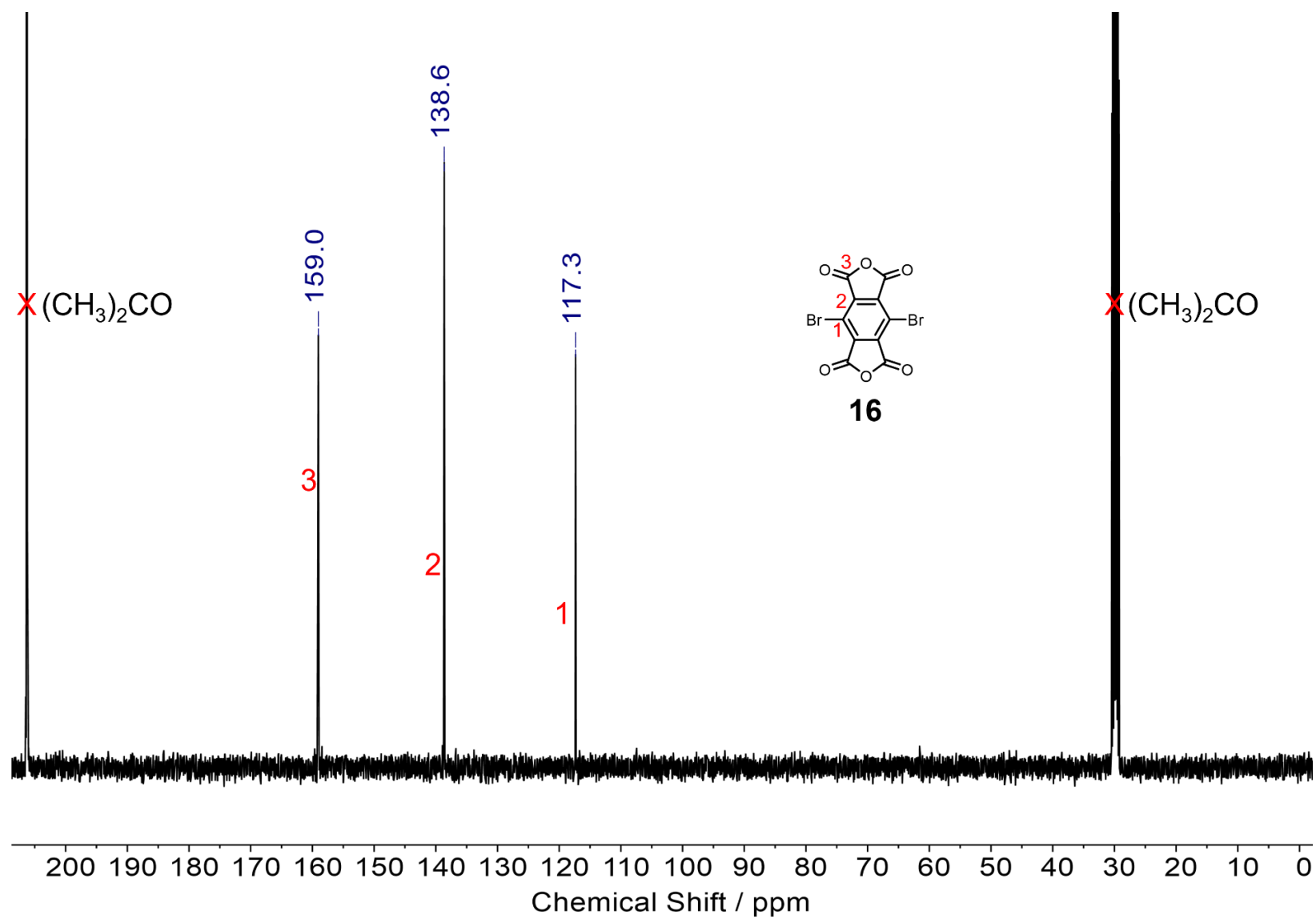
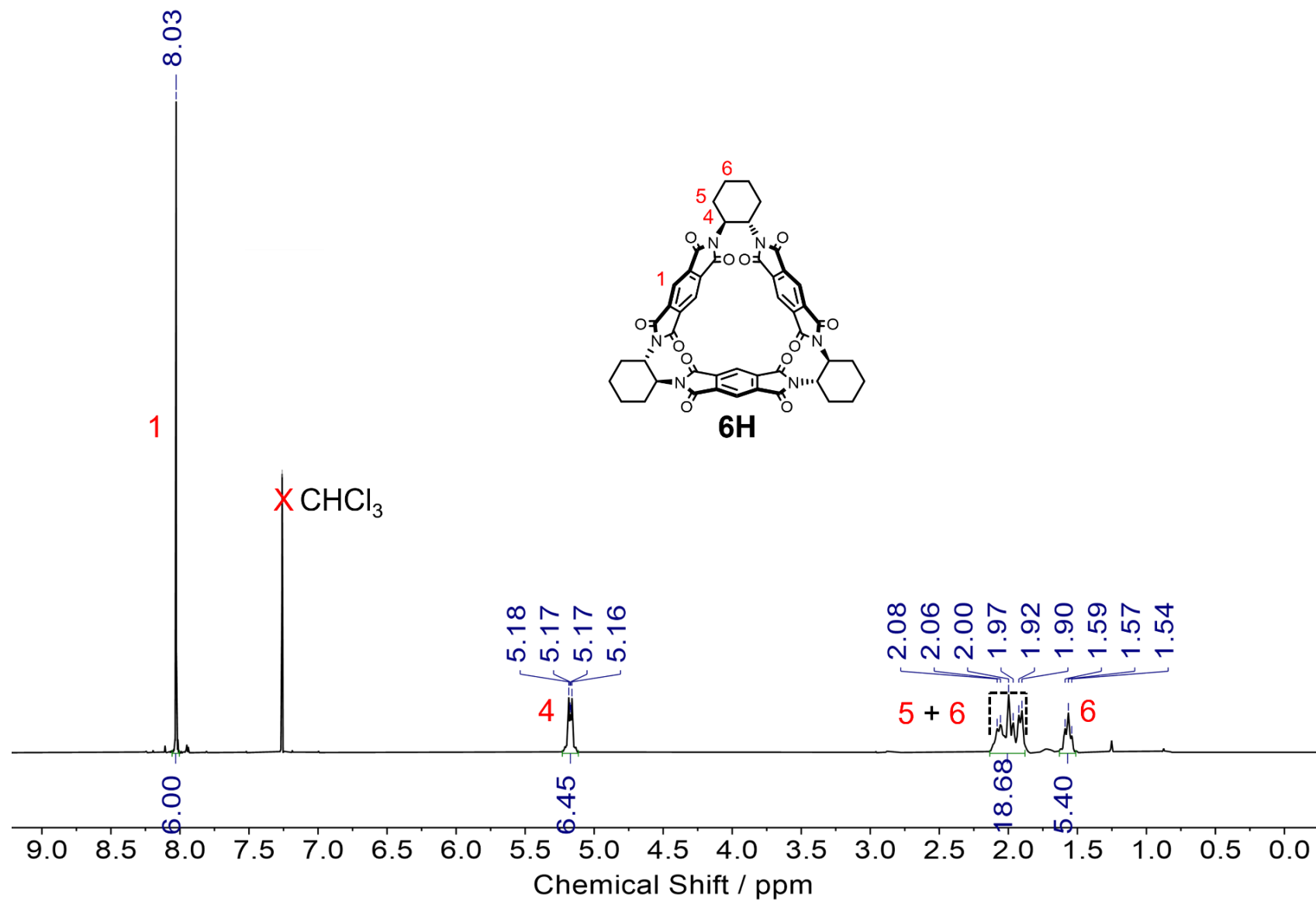
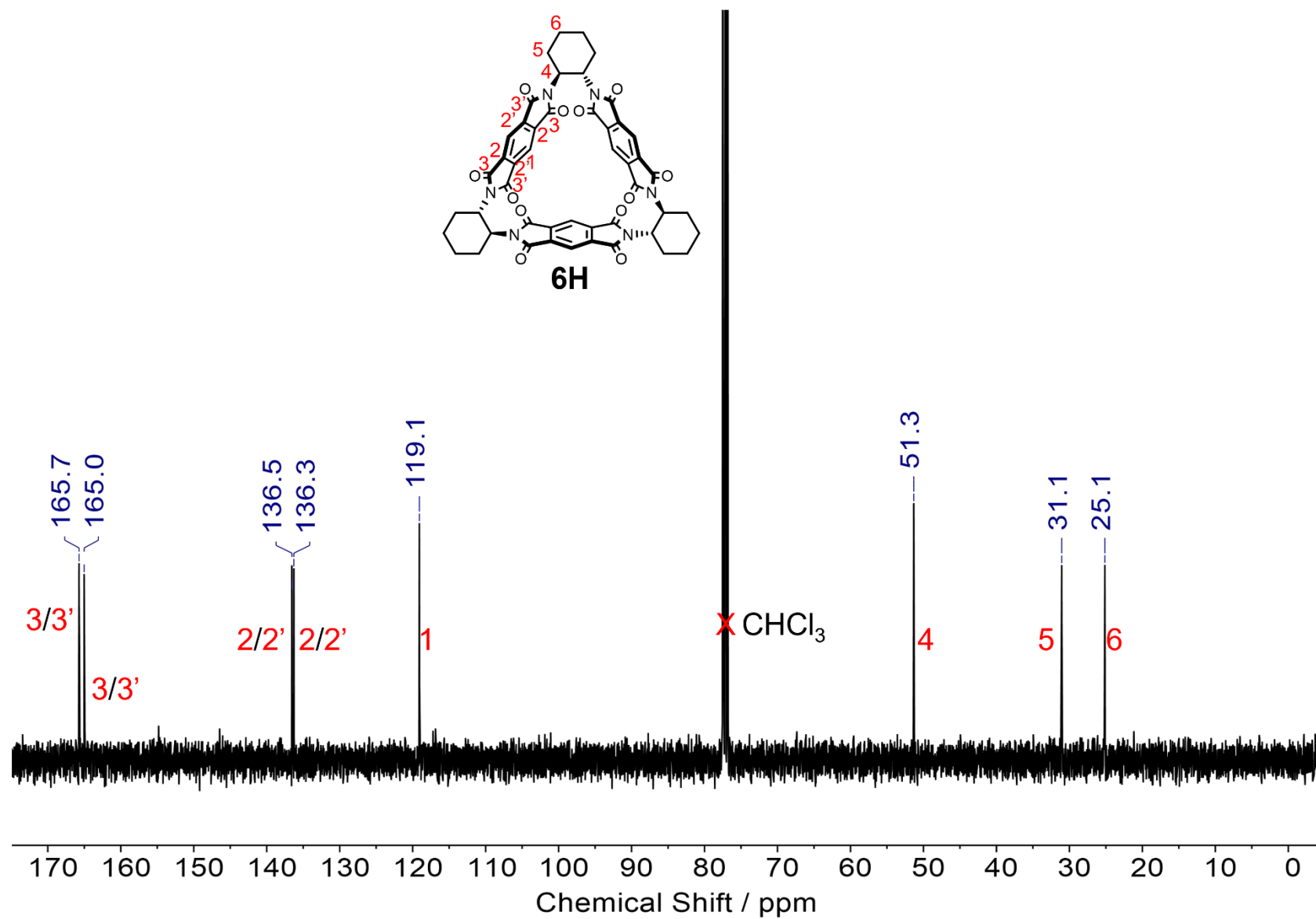
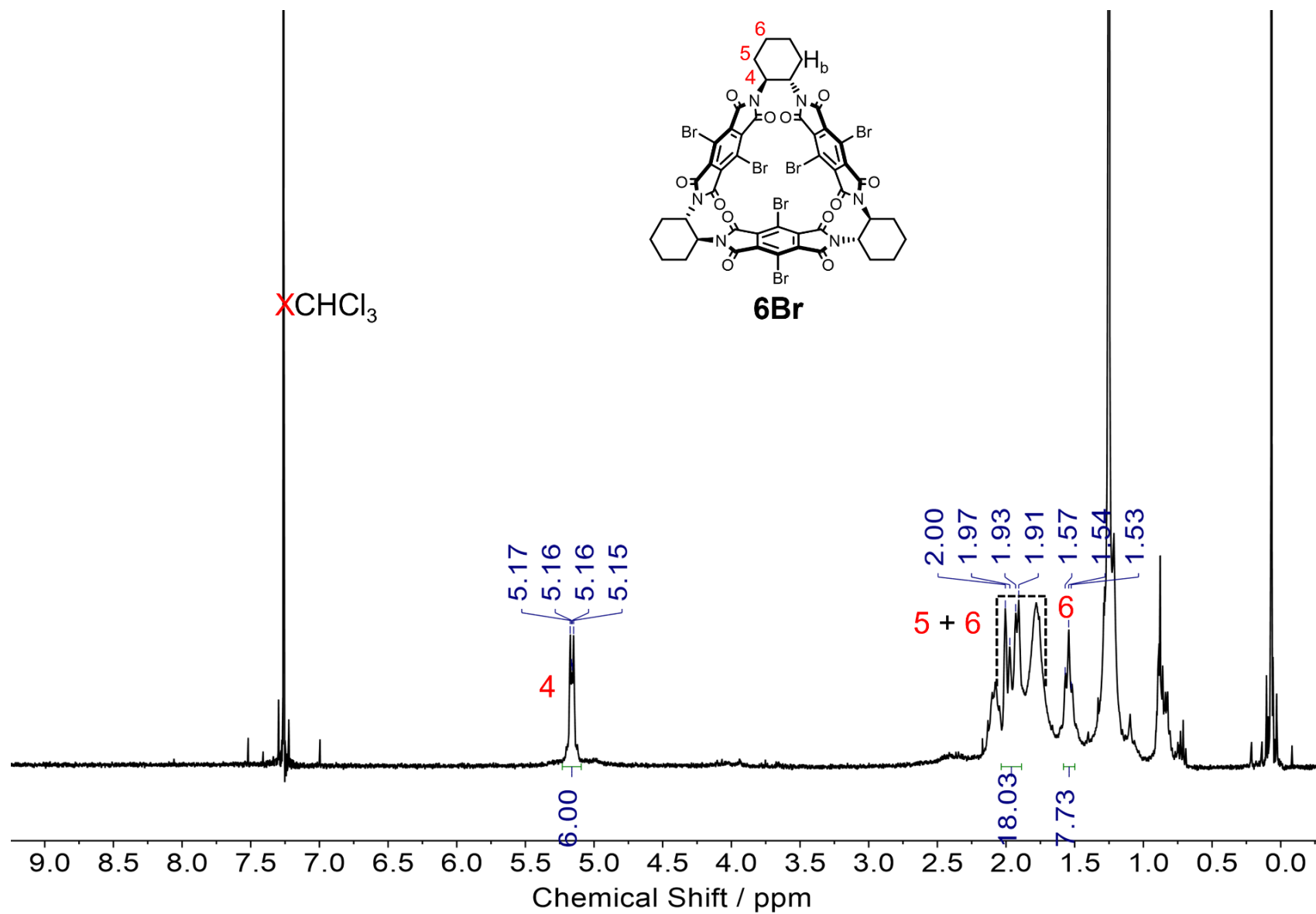


Figure S2.2 ^{13}C NMR (101 MHz, $(\text{CD}_3)_2\text{CO}$, 298 K) spectrum of **16**.

Figure S2.3 ^1H NMR (400 MHz, CDCl_3 , 298 K) spectrum of **6H**.

Figure S2.4 ^{13}C NMR (101 MHz, CDCl_3 , 298 K) spectrum of **6H**.

Figure S2.5 ^1H NMR (400 MHz, CDCl_3 , 298 K) spectrum of **6Br**.

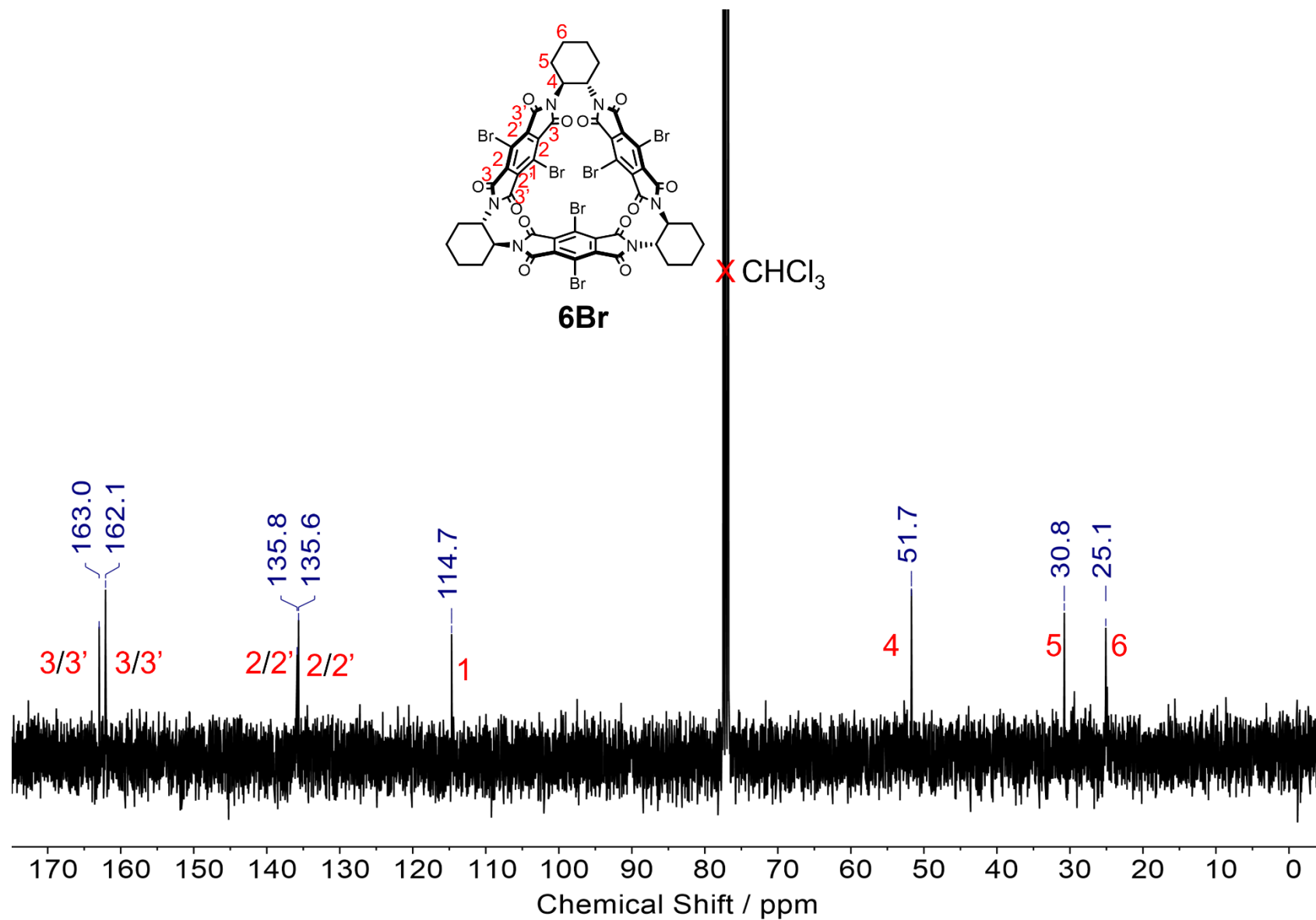
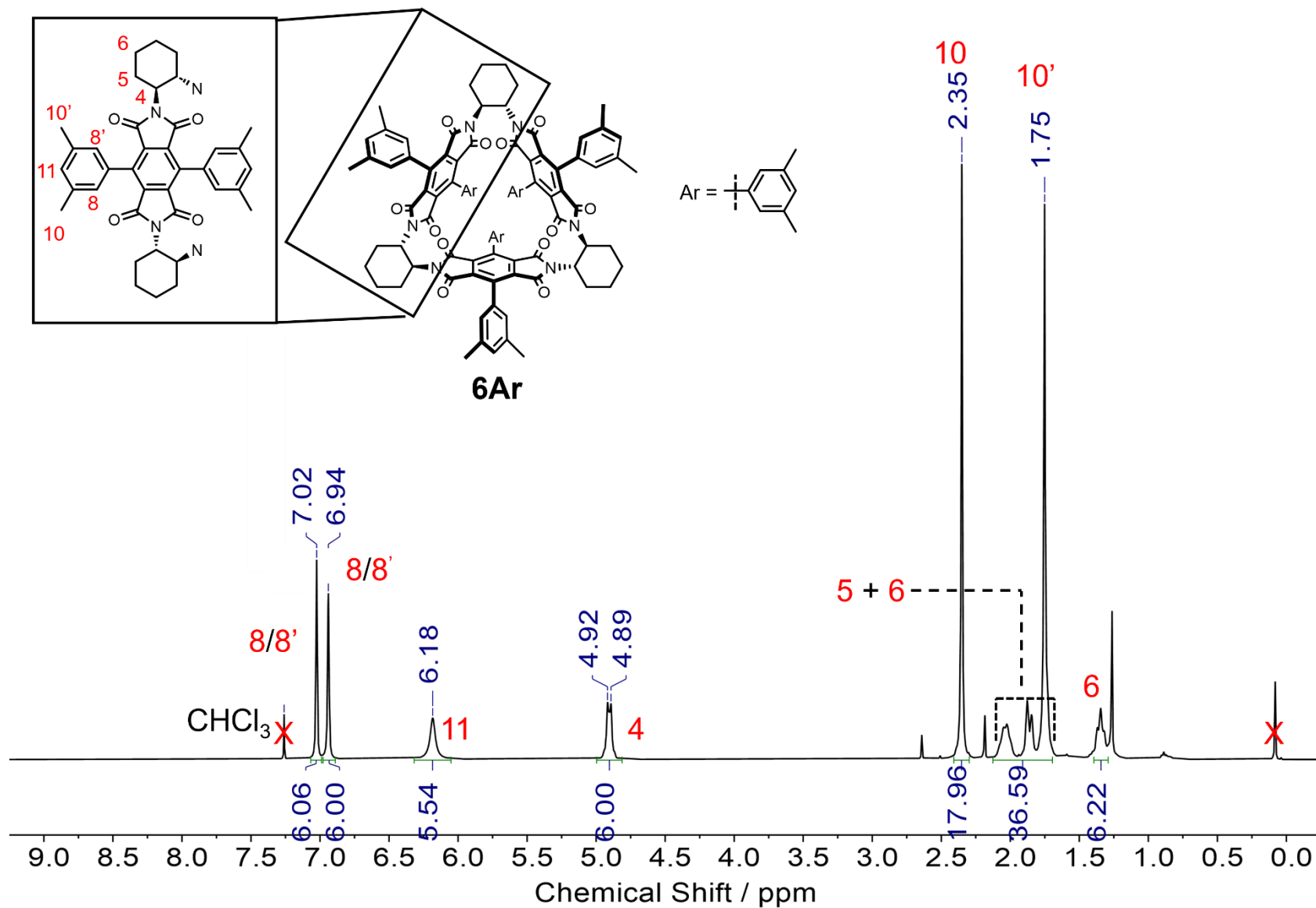
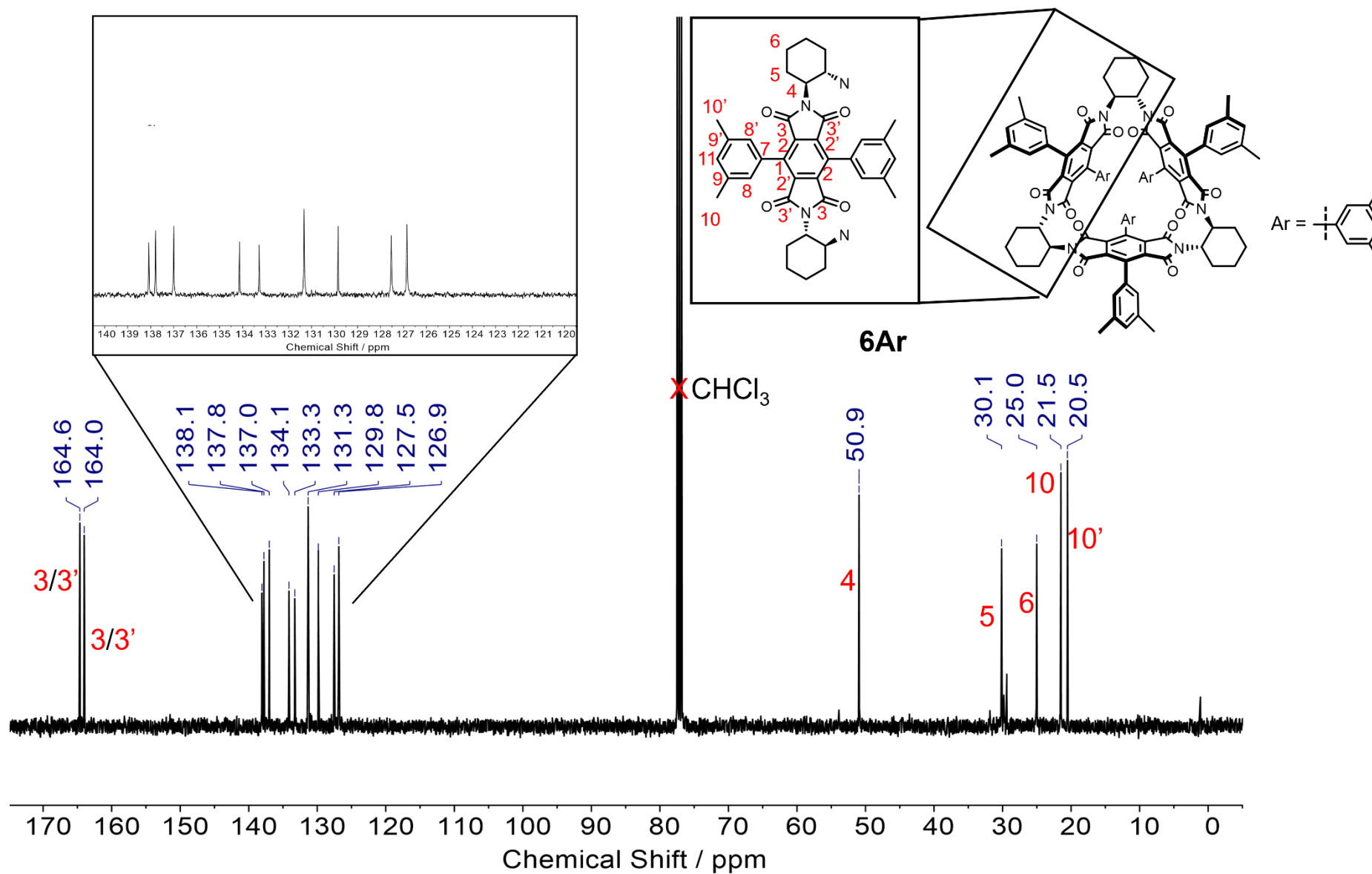
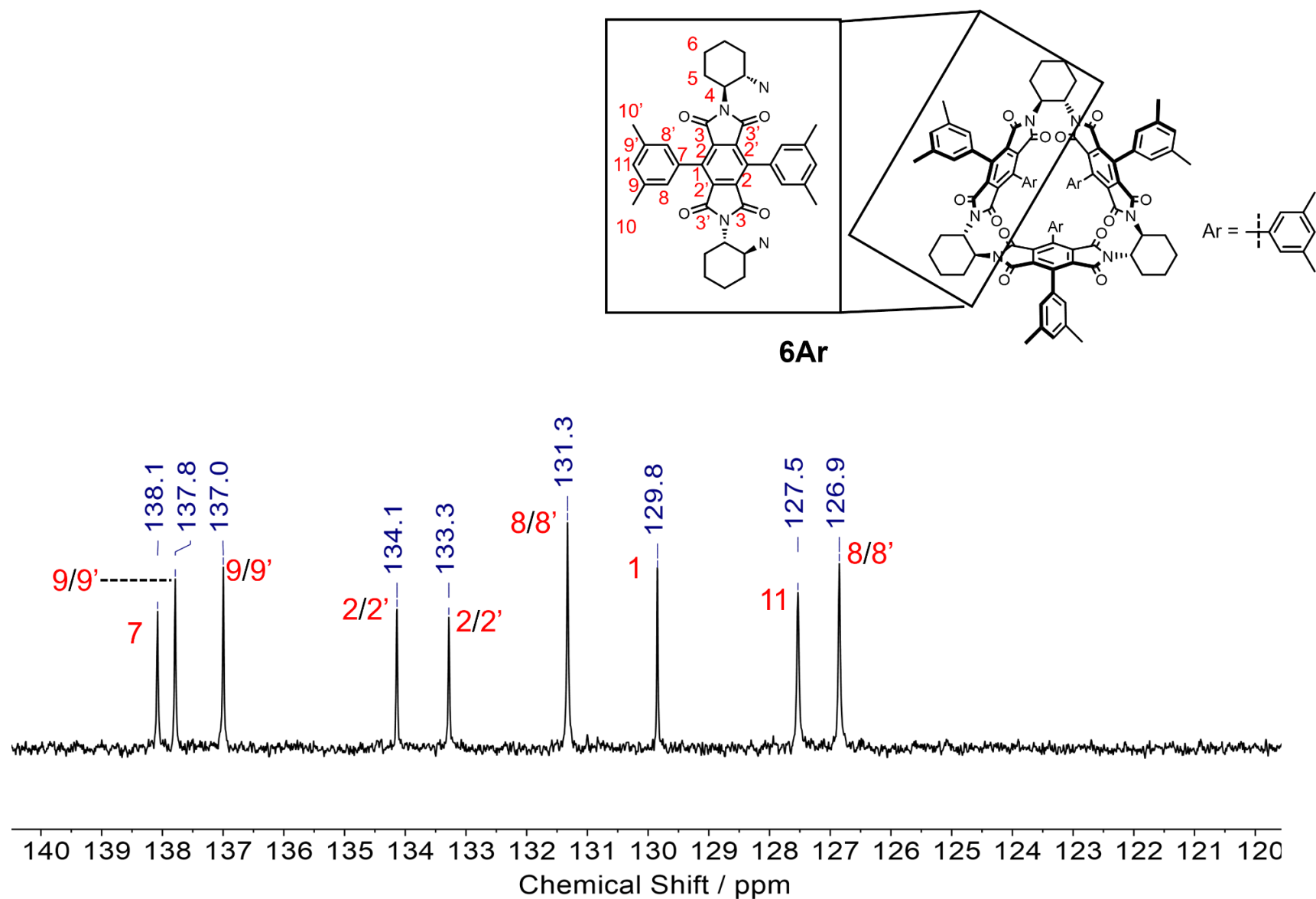


Figure S2.6 ^{13}C NMR (101 MHz, CDCl_3 , 298 K) spectrum of **6Br**.

Figure S2.7 ^1H NMR (400 MHz, CDCl_3 , 298 K) spectrum of **6Ar**.


 Figure S2.8 ^{13}C NMR spectrum (101 MHz, CDCl_3 , 298 K) of **6Ar**.

Figure S2.9 Inset of ^{13}C NMR (101 MHz, CDCl_3 , 298 K) spectrum of **6Ar**.

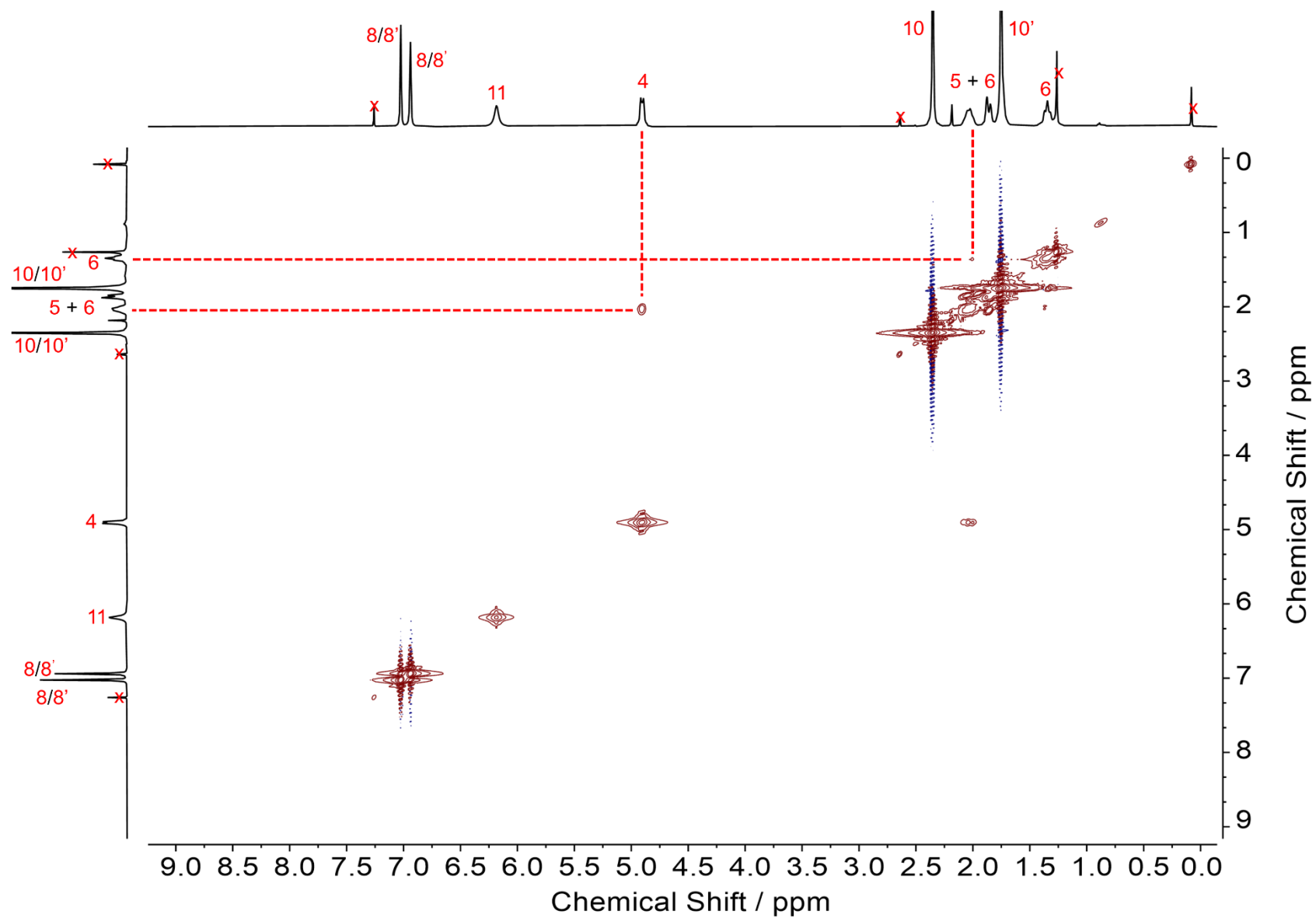


Figure S2.10 Annotated ^1H - ^1H COSY NMR (400 MHz, CDCl_3 , 298 K) spectrum of **6Ar**.

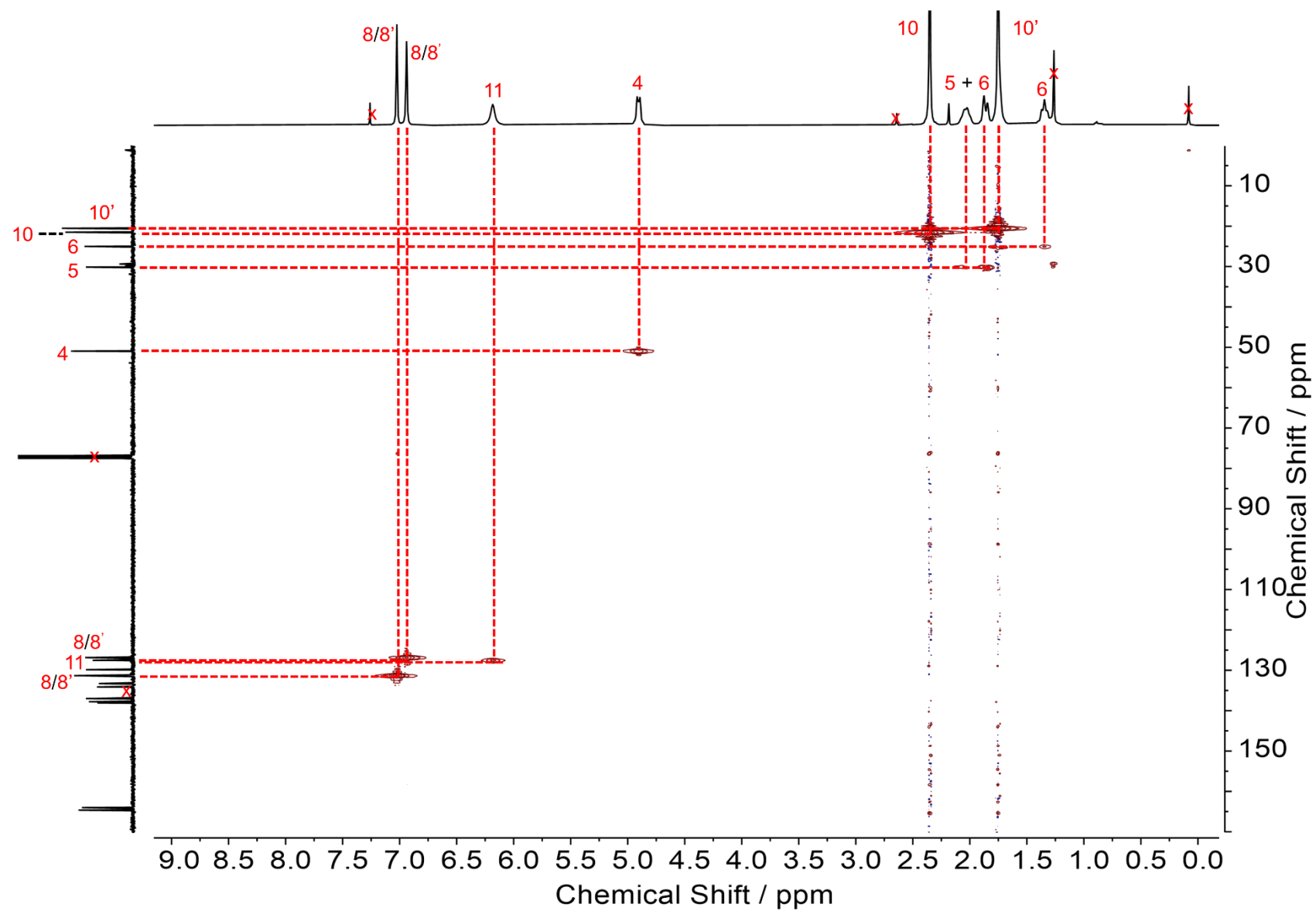


Figure S2.11 Annotated ^1H - ^{13}C HSQC NMR (400 MHz, CDCl_3 , 298 K) spectrum of **6Ar**.

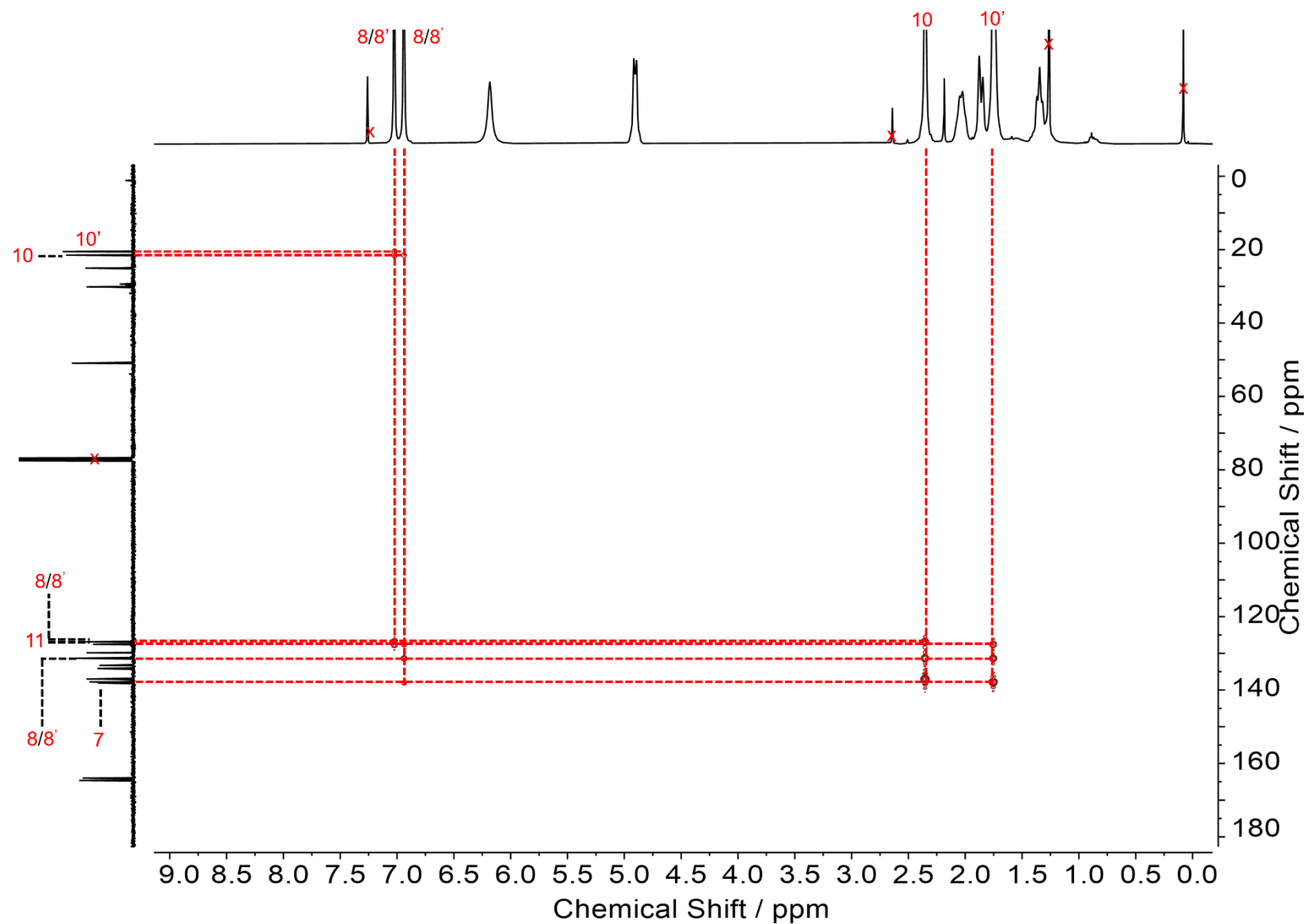


Figure S2.12 Annotated ^1H - ^{13}C HMBC NMR (400 MHz, CDCl_3 , 298 K) spectrum of **6Ar**.

2.4.4 SINGLE X-RAY CRYSTALLOGRAPHY

2.4.4.1 CRYSTAL STRUCTURE OF **6H**

6H•(CH₃)₂O

Single crystals of **6H**•(CH₃)₂CO suitable for X-ray diffraction were grown by solvent vapour diffusion of n-hexane into a solution of **6H** (0.47 mg mL⁻¹) in acetone. Crystal data for C₅₁H₄₂N₆O₁₃ ($M = 946.90$ g mol⁻¹): monoclinic, space group P2₁, $a = 18.4875(6)$ Å, $b = 7.5954(2)$ Å, $c = 32.8636(14)$ Å, $\alpha = 90^\circ$, $\beta = 102.305(4)^\circ$, $\gamma = 90^\circ$, $V = 4508.7(3)$ Å³, $Z = 4$, $T = 110.00(10)$ K, $\mu(\text{Cu K}\alpha) = 0.852$ mm⁻¹, $\rho_{\text{calc}} = 1.395$ g cm⁻³, 27856 reflections measured ($8.11^\circ \leq 2\theta \leq 134.128^\circ$), 12313 independent reflections ($R_{\text{int}} = 0.0968$, $R_{\text{sigma}} = 0.1103$) which were used in all calculations. The final R_1 was 0.0549 ($I > 2\sigma(I)$) and wR_2 was 0.1151 (all data).

The unit cell contains two molecules of **6H** with a single molecule of acetone encapsulated within the cavity of each macrocycle. One of the acetone molecules was disordered and modelled in three positions with refined occupancies of 0.448(4):0.339(4):0.212(4). Within this acetone molecule, C-C bond lengths were restrained to be equal and the C=O bond lengths restrained to be 1.21 Å. The atomic displacement parameter (ADP) of C99, C99A and C99B were constrained to be equal and C99 and C99a were constrained to have the same coordinates. The ADPs of C97B, C98, C98A and C98B were restrained to be approximately isotropic.

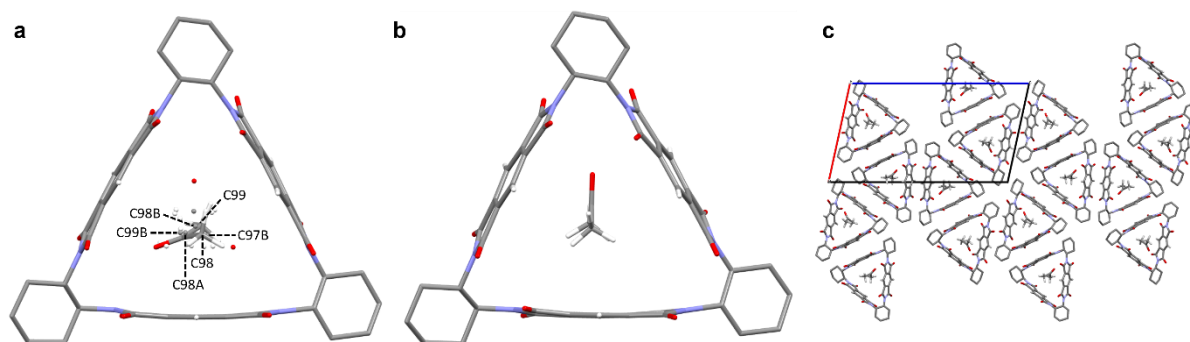


Figure S2.13 X-ray crystal structure of **6H** showing (a) triangle 1 in unit cell (with relevant solvent atom labels for restraints made in crystal structure determination), (b) triangle 2 in unit cell and (c) supramolecular packing of unit cell. Cyclohexane hydrogen atoms have been removed for clarity.

2.4.4.2 CRYSTAL STRUCTURES OF **6Br**

Two polymorphs of **6Br** in the solid state have been discovered depending on the crystallisation conditions and solvated nature of the crystal structure.

6Br•(CH₃)₂CO

Single crystals of **6Br**•(CH₃)₂CO suitable for X-ray diffraction were grown by solvent vapour diffusion of pentane into a solution of **6Br** (≈ 4.00 mg mL⁻¹) in acetone. Crystal data for C₅₇H₄₈Br₆N₆O₁₅ ($M = 1536.47$ g mol⁻¹): trigonal, space group R3₂, $a = 19.5827(2)$ Å, $b = 19.5827(2)$ Å, $c = 29.0126(3)$ Å,

$\alpha = 90^\circ$, $\beta = 90^\circ$, $\gamma = 120^\circ$, $V = 9635.2(2) \text{ \AA}^3$, $Z = 6$, $T = 110.00(10) \text{ K}$, $\mu(\text{Cu K}\alpha) = 5.078 \text{ mm}^{-1}$, $\rho_{\text{calc}} = 1.589 \text{ g cm}^{-3}$, 17061 reflections measured ($8.02^\circ \leq 2\theta \leq 134.104^\circ$), 3840 independent reflections ($R_{\text{int}} = 0.0413$, $R_{\text{sigma}} = 0.0246$) which were used in all calculations. The final R_1 was 0.0475 ($I > 2\sigma(I)$) and wR_2 was 0.1142 (all data).

The crystal contained solvent channels filled with disordered solvent, two per unit cell. These channels run parallel to the c-axis. Around the edge of the channel, it was possible to model acetone molecules disordered over two positions with one acetone per asymmetric unit of equal occupancy. For these acetones, the C–C bond lengths were restrained to be 1.52 Å, the C=O bond length restrained to be 1.21 Å and the CH₃–O distances restrained to be equal. The ADPs of the pairs O5 & O6 and C19 & C22 were constrained to be equal. The ADPs of O5, O6, C17, C19, C21 & C22 were restrained to be approximately isotropic. The remainder of the solvent in the channels was too disordered to produce a discrete atom model and so was accounted for using a solvent mask. Each void was estimated to contain 129 electrons per unit cell which is equivalent to 3 pentane molecules.

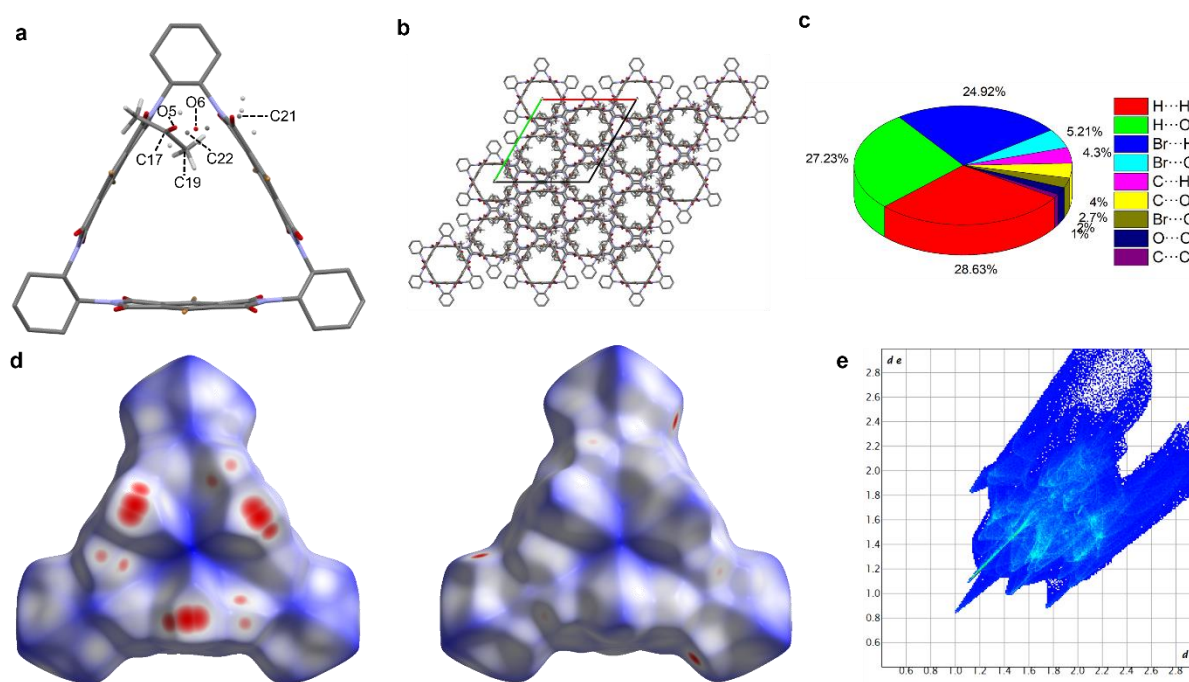


Figure S2.14 X-ray crystal structure of **6Br•**(CH₃)₂CO showing (a) unit cell of X-ray crystal structure of **6Br•** (with relevant solvent atom labels for restraints made in crystal structure determination) and (b) supramolecular packing, cyclohexane hydrogen atoms omitted for clarity. Hirschfeld analysis of **6Br•**(CH₃)₂CO showing (c) the percentage of reciprocal intermolecular interactions higher than 1%, (d) front and back surfaces of triangle molecules mapped with d_{norm} and (e) accompanying fingerprint plot for all interactions.

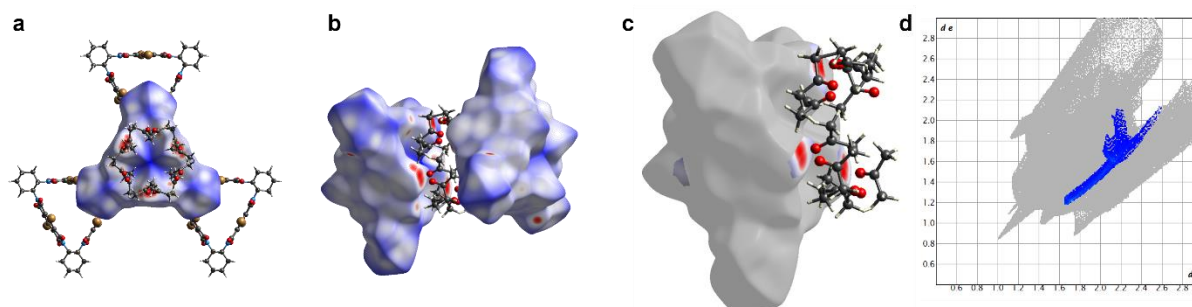


Figure S2.15 Hirshfeld analysis of **6Br**•(CH₃)₂CO showing (a) the front side of the surface of a **6Br** molecule surrounded by acetone molecules, (b) interactions between disordered Me₂CO molecules and Hirshfeld surfaces of two **6Br** molecules, (c) Hirshfeld surface with highlighted regions showing only Br···O interactions between **6Br** molecule and accompanying Me₂CO molecules only and (d) finger print region focusing on Br···O interactions only.

6Br

A single crystal of **6Br** suitable for X-ray diffraction was grown by solvent vapour diffusion of n-hexane into a solution of **6Br** in CH₂Cl₂. Channels of electron density through the structure were modelled using a SQUEEZE solvent mask. Crystal data for C₄₈H₃₀Br₆N₆O₁₂ ($M = 1362.24 \text{ g mol}^{-1}$): hexagonal, space group P6₃, $a = 20.1757(3) \text{ \AA}$, $b = 20.1757(3) \text{ \AA}$, $c = 11.39170(10) \text{ \AA}$, $\alpha = 90^\circ$, $\beta = 90^\circ$, $\gamma = 120^\circ$, $V = 4015.84(12) \text{ \AA}^3$, $Z = 2$, $T = 110.00(10) \text{ K}$, $\mu(\text{Cu K}\alpha) = 3.975 \text{ mm}^{-1}$, $\rho_{\text{calc}} = 1.127 \text{ g cm}^{-3}$, 9614 reflections measured ($8.766^\circ \leq 2\theta \leq 142.942^\circ$), 3735 independent reflections ($R_{\text{int}} = 0.022$, $R_{\text{sigma}} = 0.0287$) which were used in all calculations. The final R_1 was 0.0515 ($I > 2\sigma(I)$) and wR_2 was 0.2063 (all data).

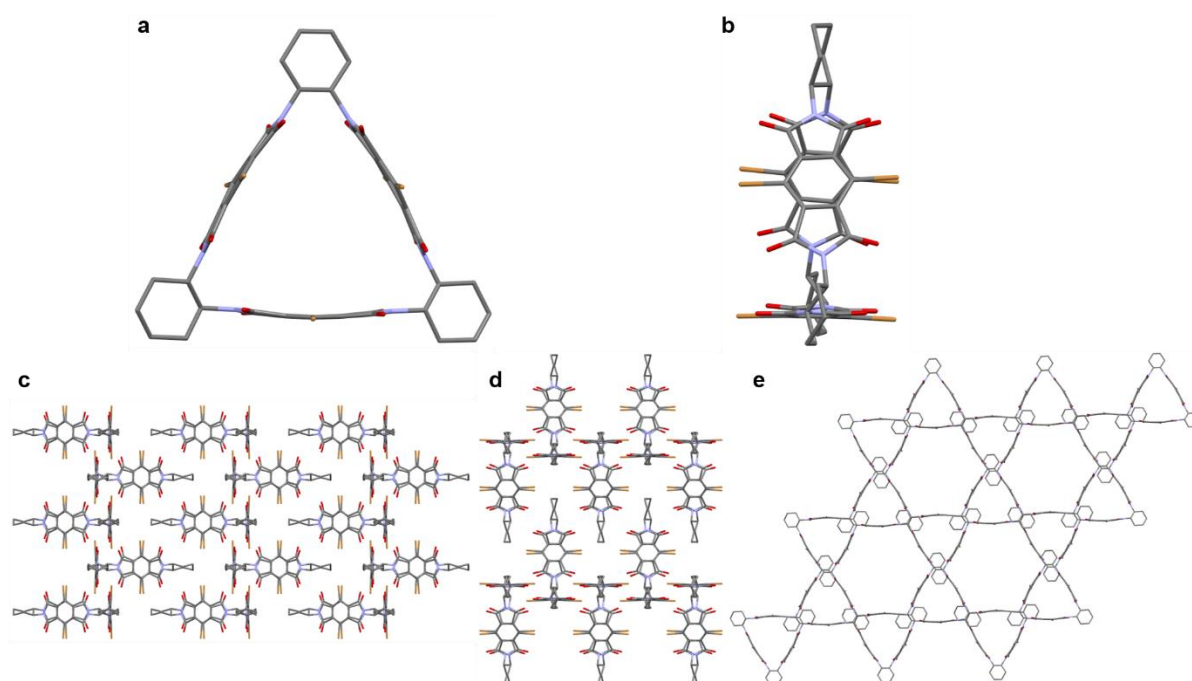


Figure S2.16. Unit cell of solvent-free X-ray crystal structure of **6Br** from (a) front-view and (b) side-view. (c), (d) and (e) solvent-free supramolecular packing of **6Br** in 3-dimensions. Cyclohexane hydrogen atoms have been omitted for clarity.

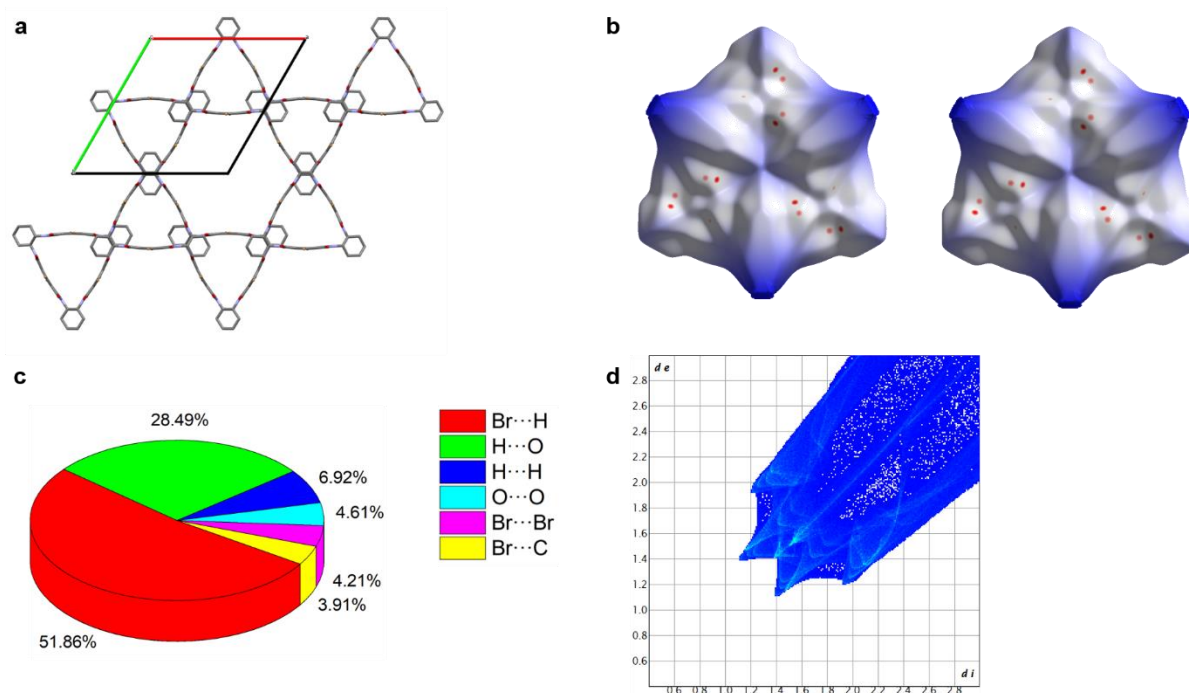


Figure S2.17. a) Supramolecular packing of **6Br** with unit cell highlighted, looking along c axis, cyclohexane hydrogen atoms omitted for clarity. Hirshfeld analysis of **6Br** showing (b) front and back surfaces mapped with d_{norm} , (c) the percentage of reciprocal intermolecular interactions higher than 1% and (d) accompanying fingerprint plot for all interactions.

2.4.4.3 CRYSTAL STRUCTURES OF 6Ar

Two polymorphs of **6Ar** in the solid state have been discovered, both contain solvated acetone molecules, however, the difference between structures occurs due to number of solvated acetone molecules in the crystal structure.

6Ar•2(CH₃)₂CO

Single crystals of **6Ar**•2(CH₃)₂CO suitable for X-ray diffraction were grown by solvent vapour diffusion of *n*-hexane into a solution of **6Ar** ($\approx 4 \text{ mg mL}^{-1}$) in acetone. Crystal data for C_{103.23}H_{96.74}N₆O_{14.48} ($M = 1653 \text{ g mol}^{-1}$): orthorhombic, space group C222₁, $a = 16.7079(3) \text{ \AA}$, $b = 21.4320(4) \text{ \AA}$, $c = 28.0256(4) \text{ \AA}$, $\alpha = 90^\circ$, $\beta = 90^\circ$, $\gamma = 90^\circ$, $V = 10035.5(3) \text{ \AA}^3$, $Z = 4$, $T = 110.00(10) \text{ K}$, $\mu(\text{Cu K}\alpha) = 0.589 \text{ mm}^{-1}$, $\rho_{\text{calc}} = 1.094 \text{ g cm}^{-3}$, 17180 reflections measured ($7.414^\circ \leq 2\theta \leq 134.15^\circ$), 8376 independent reflections ($R_{\text{int}} = 0.0317$, $R_{\text{sigma}} = 0.0381$) which were used in all calculations. The final R_1 was 0.0347 ($I > 2\sigma(I)$) and wR_2 was 0.0979 (all data).

The crystal contained disordered, partially occupied acetone molecules. One acetone molecule was partially occupied with a refined occupancy of 0.758(5). The acetone molecule in the cavity of the macrocycle was modelled in three positions (two of which were related by a mirror plane) with refined occupancies of 0.379(6), 0.379(6) and 0.204(7). For this encapsulated solvent molecule, C-C bond lengths were restrained to be 1.52 \AA and the ADPs of C53 and C53a constrained to be equal. The rest

of the solvent was too disordered to model with a discrete atom model and so was modelled using a solvent mask which predicted 33 electrons per asymmetric unit which would be one acetone molecule.

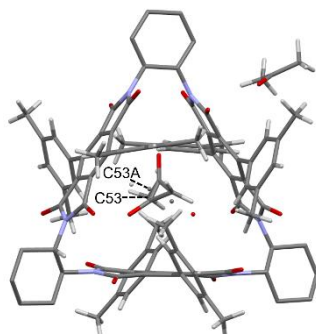


Figure S2.18. Unit cell of **6Ar•2(CH₃)₂CO** from X-ray crystal structure with relevant solvent atom labels for restraints made in crystal structure determination. Cyclohexane hydrogen atoms have been omitted for clarity.

6Ar•3(CH₃)₂CO

Single crystals of **6Ar•3(CH₃)₂CO** suitable for X-ray diffraction were grown by solvent vapour diffusion of n-hexane into a solution of **6Ar** ($\approx 4 \text{ mg mL}^{-1}$) in acetone. Crystal data for $\text{C}_{105}\text{H}_{102}\text{N}_6\text{O}_{15}$ ($M = 1687.92 \text{ g mol}^{-1}$): monoclinic, space group $P2_1$, $a = 13.38115(13) \text{ \AA}$, $b = 16.20734(15) \text{ \AA}$, $c = 23.8522(2) \text{ \AA}$, $\alpha = 90^\circ$, $\beta = 100.5894(11)^\circ$, $\gamma = 90^\circ$, $V = 5084.80(9) \text{ \AA}^3$, $Z = 2$, $T = 109.95(10) \text{ K}$, $\mu(\text{Cu K}\alpha) = 0.594 \text{ mm}^{-1}$, $\rho_{\text{calc}} = 1.102 \text{ g cm}^{-3}$, 33029 reflections measured ($7.076^\circ \leq 2\theta \leq 134.15^\circ$), 14050 independent reflections ($R_{\text{int}} = 0.0344$, $R_{\text{sigma}} = 0.0427$) which were used in all calculations. The final R_1 was 0.0372 ($I > 2\sigma(I)$) and wR_2 was 0.1003 (all data).

The crystal contained disordered solvent molecules. One acetone molecule was modelled in two positions of equal occupancy with common sites for the methyl carbon atoms. The ADPs of two pairs of disordered atoms were constrained to be equal (C97 & C97A, O13 & O13A). For the remainder of the disordered solvent, a discrete atom model could not be achieved so this was modelled with a solvent mask. There was evidence of acetone in the cavity of the macrocycle, but this was of low occupancy and clearly disordered. The occupancy was estimated as 25% based on the electron count predicted by the solvent mask. The other disordered solvent was in a cavity, had a predicted electron count of 66 electrons and is therefore likely to contain two acetone molecules.

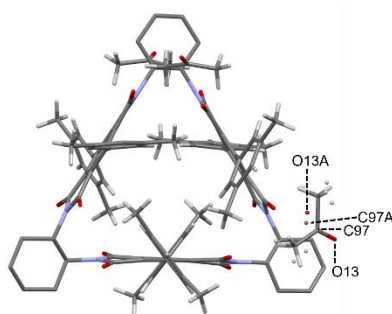


Figure S2.19. Unit cell of **6Ar•3(CH₃)₂CO** from X-ray crystal structure with relevant solvent atom labels for restraints made in crystal structure determination. Cyclohexane hydrogen atoms have been omitted for clarity.

Table S2.1 Crystal structure data for molecular triangles **6H** and **6Br**.

	6H •Me ₂ CO	6Br •Me ₂ CO	6Br
Empirical Formula	C ₅₁ H ₄₂ N ₆ O ₁₃	C ₅₇ H ₄₈ Br ₆ N ₆ O ₁₅	C ₄₈ H ₃₀ Br ₆ N ₆ O ₁₂
Formula Weight / g mol ⁻¹	946.90	1536.47	1362.24
Temperature (<i>T</i>) / K	110.00(10)	110.00(10)	110.00(10)
Crystal System	Monoclinic	Trigonal	Hexagonal
Space Group	P2 ₁	R32	P6 ₃
<i>a</i> / Å	18.4875(6)	19.5827(2)	20.1757(3)
<i>b</i> / Å	7.5954(2)	19.5827(2)	20.1757(3)
<i>c</i> / Å	32.8636(14)	29.0126(3)	11.39170(10)
α / °	90	90	90
β / °	102.305(4)	90	90
γ / °	90	120	120
Volume (<i>V</i>) / Å ³	4508.7(3)	9635.2(2)	4015.84(12)
<i>Z</i>	4	6	2
ρ_{calc} / g cm ⁻³	1.395	1.589	1.127
μ / mm ⁻¹	0.852	5.078	3.975
F(000)	1976.0	4572.0	1332.0
Crystal Size / mm ³	0.208 x	0.237 x	0.18 x
	0.029 x	0.199 x	0.11 x
	0.023	0.091	0.8
Radiation	Cu K α	Cu K α	Cu K α
	(λ = 1.54184)	(λ = 1.54184)	(λ = 1.54184)
2 θ range for data collection / °	8.11 to 134.128	8.02 to 134.104	8.766 to 142.942
Index Ranges	-21 ≤ <i>h</i> ≤ 22	-23 ≤ <i>h</i> ≤ 20	-23 ≤ <i>h</i> ≤ 18
	-9 ≤ <i>k</i> ≤ 3	-16 ≤ <i>k</i> ≤ 23	-24 ≤ <i>k</i> ≤ 15
	-38 ≤ <i>l</i> ≤ 39	-34 ≤ <i>l</i> ≤ 26	-10 ≤ <i>l</i> ≤ 13
Reflections Collected	27856	17061	9614
	12313	3840	3735
Independent Reflections	R _{int} = 0.0968	R _{int} = 0.0413	R _{int} = 0.022
	R _{sigma} = 0.1103	R _{sigma} = 0.0246	R _{sigma} = 0.0287
Data/Restraints/Parameters	12313 /44 /1317	3840 /50 /281	3735 /1 /217
Goodness-of-fit on F ²	0.981	1.093	1.208
Final R Indexes (<i>I</i> ≥ 2 σ (<i>I</i>))	R ₁ = 0.0549	R ₁ = 0.0475	R ₁ = 0.0515
	wR ₂ = 0.0997	wR ₂ = 0.1140	wR ₂ = 0.1978
Final R Indexes (all data)	R ₁ = 0.0960	R ₁ = 0.0478	R ₁ = 0.0590
	wR ₂ = 0.1151	wR ₂ = 0.1142	wR ₂ = 0.2063
Largest diff. peak/hole / e Å ⁻³	0.22 / -0.23	0.80 / -0.83	1.65 / -0.52
Flack Parameter	0.0(2)	0.00(3)	0.00(2)

Table S2.2 Crystal structure data for molecular triangle **6Ar**.

	6Ar•2Me₂CO	6Ar•3Me₂CO
Empirical Formula	C _{103.23} H _{96.74} N ₆ O _{14.48}	C ₁₀₅ H ₁₀₂ N ₆ O ₁₅
Formula Weight / g mol ⁻¹	1653.00	1687.92
Temperature (<i>T</i>) / K	110.00(10)	109.95(10)
Crystal System	Orthorhombic	Monoclinic
Space Group	C222 ₁	P2 ₁
<i>a</i> / Å	16.7079(3)	13.38115(13)
<i>b</i> / Å	21.4320(4)	16.20734(15)
<i>c</i> / Å	28.0256(4)	23.8522(2)
α / °	90	90
β / °	90	100.5894(11)
γ / °	90	90
Volume (<i>V</i>) / Å ³	10035.5(3)	5084.80(9)
<i>Z</i>	4	2
ρ_{calc} / g cm ⁻³	1.094	1.102
μ / mm ⁻¹	0.589	0.594
F(000)	3496.0	1788.0
Crystal Size / mm ³	0.369 x	0.164 x
	0.181 x	0.137 x
	0.11	0.021
Radiation	Cu K α	Cu K α
	(λ = 1.54184)	(λ = 1.54184)
2 θ range for data collection / °	7.414 to 134.15	7.076 to 134.15
Index Ranges	-16 ≤ <i>h</i> ≤ 19	-14 ≤ <i>h</i> ≤ 15
	-22 ≤ <i>k</i> ≤ 25	-19 ≤ <i>k</i> ≤ 13
	-33 ≤ <i>l</i> ≤ 19	-28 ≤ <i>l</i> ≤ 28
Reflections Collected	17180	33029
	8376	14050
Independent Reflections	R _{int} = 0.0317	R _{int} = 0.0344
	R _{sigma} = 0.0381	R _{sigma} = 0.0427
Data/Restraints/Parameters	8376 / 2 / 602	14050 / 1 / 1160
Goodness-of-fit on F ²	1.070	1.024
Final R Indexes (<i>I</i> ≥ 2 σ (<i>I</i>))	R ₁ = 0.0347	R ₁ = 0.0372
	wR ₂ = 0.0967	wR ₂ = 0.0975
Final R Indexes (all data)	R ₁ = 0.0364	R ₁ = 0.0422
	wR ₂ = 0.0979	wR ₂ = 0.1003
Largest diff. peak/hole / e Å ⁻³	0.21 / -0.17	0.39 / -0.18
Flack Parameter	0.01(8)	0.12(11)

2.4.5 UV-VIS SPECTROSCOPY

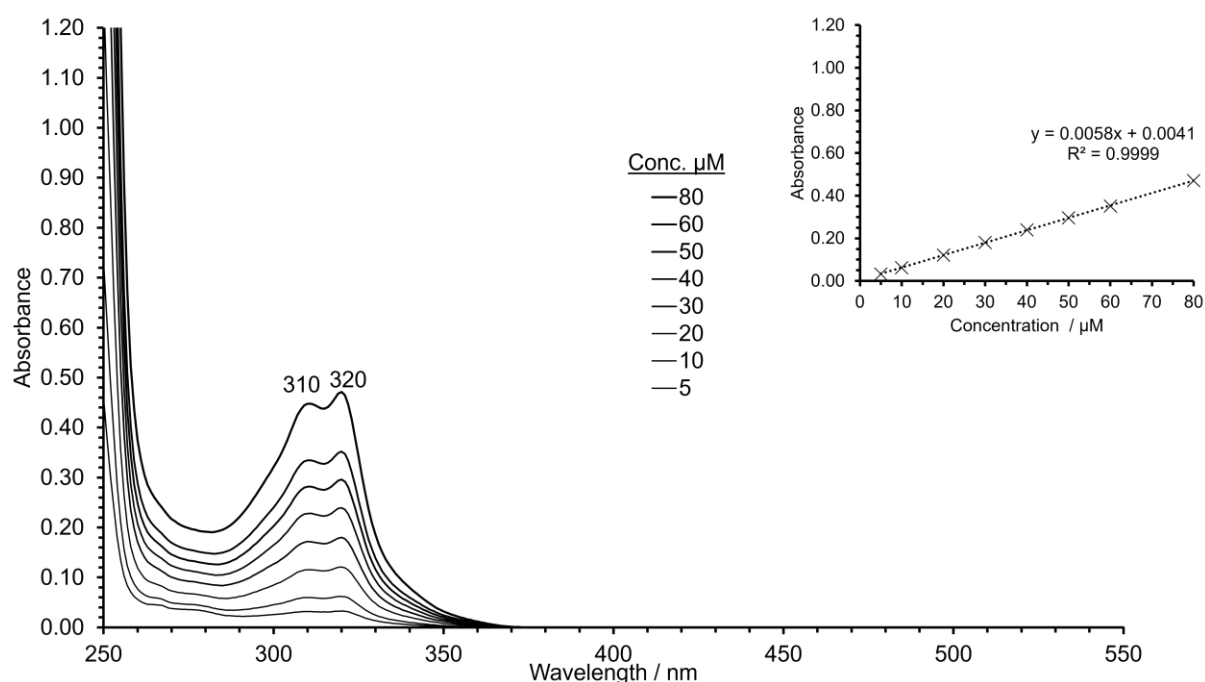


Figure S2.20 Concentration-dependent UV-vis spectrum of compound **6H** in CH_2Cl_2 (5–80 μM). **Inset.** Beer-Lambert plot at 320 nm.

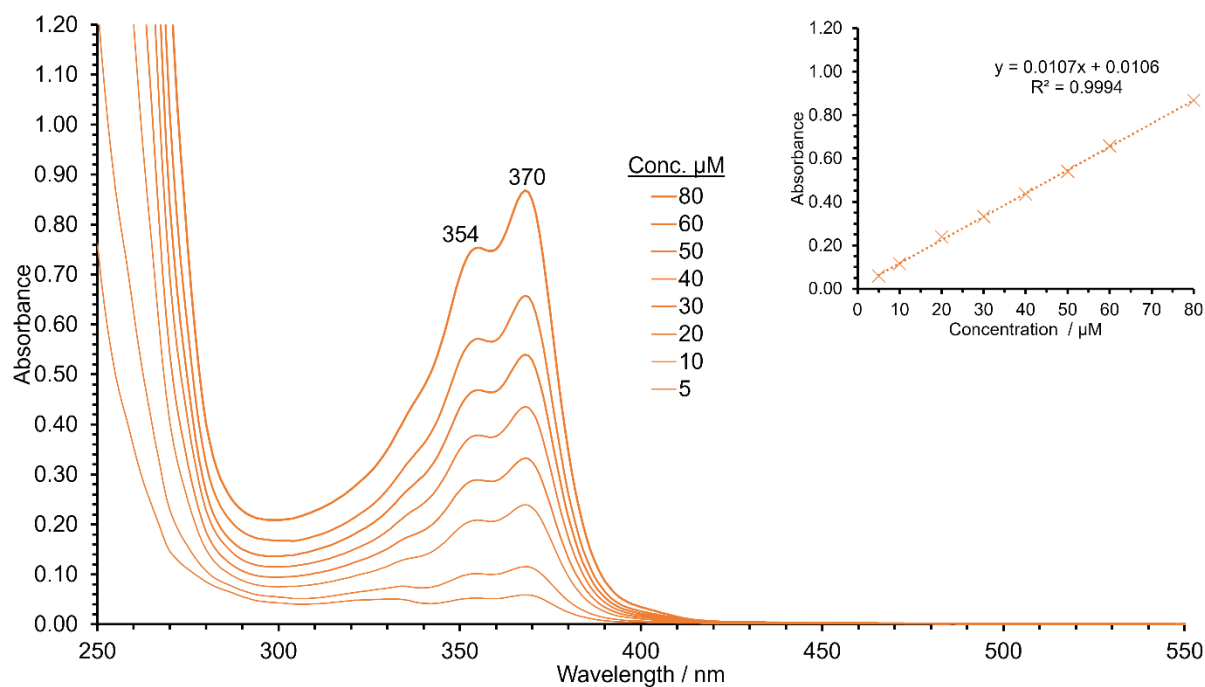


Figure S2.21 Concentration-dependent UV-vis spectrum of compound **6Br** in CH_2Cl_2 (5–80 μM). **Inset.** Beer-Lambert plot at 368 nm.

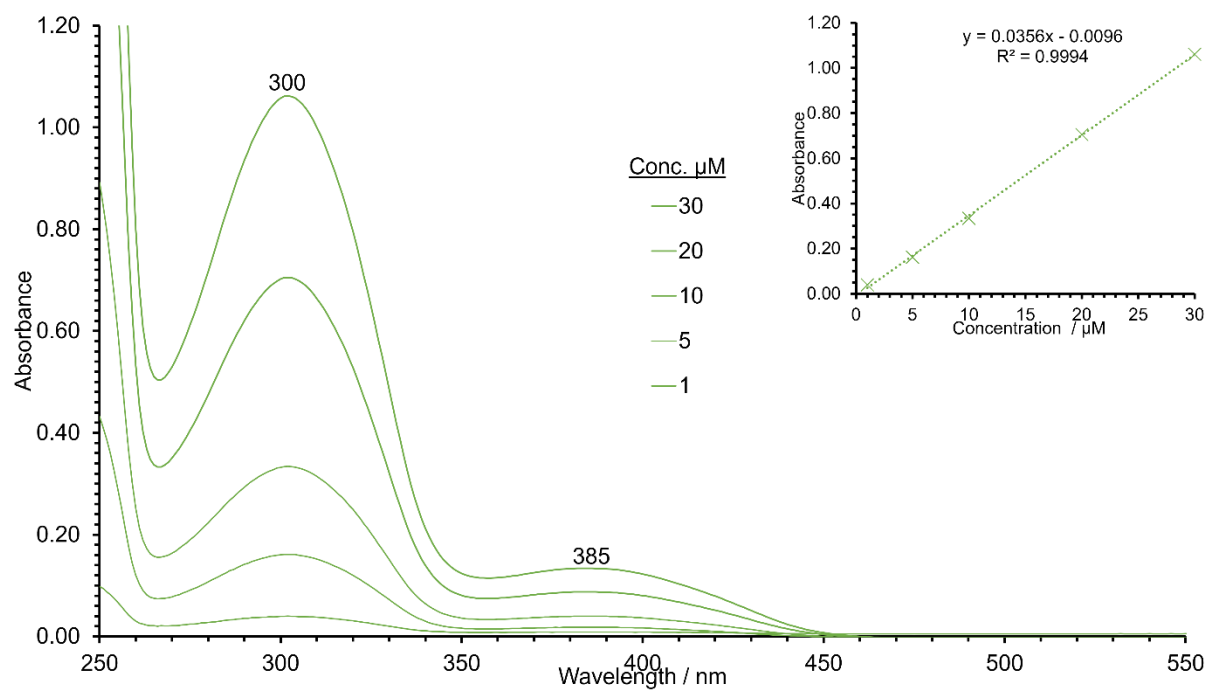


Figure S2.22 Concentration-dependent UV-vis spectrum of compound **6Ar** in CH_2Cl_2 (1–30 μM). **Inset.** Beer-Lambert plot at 302 nm.

2.4.6 COMPUTATIONAL STUDIES

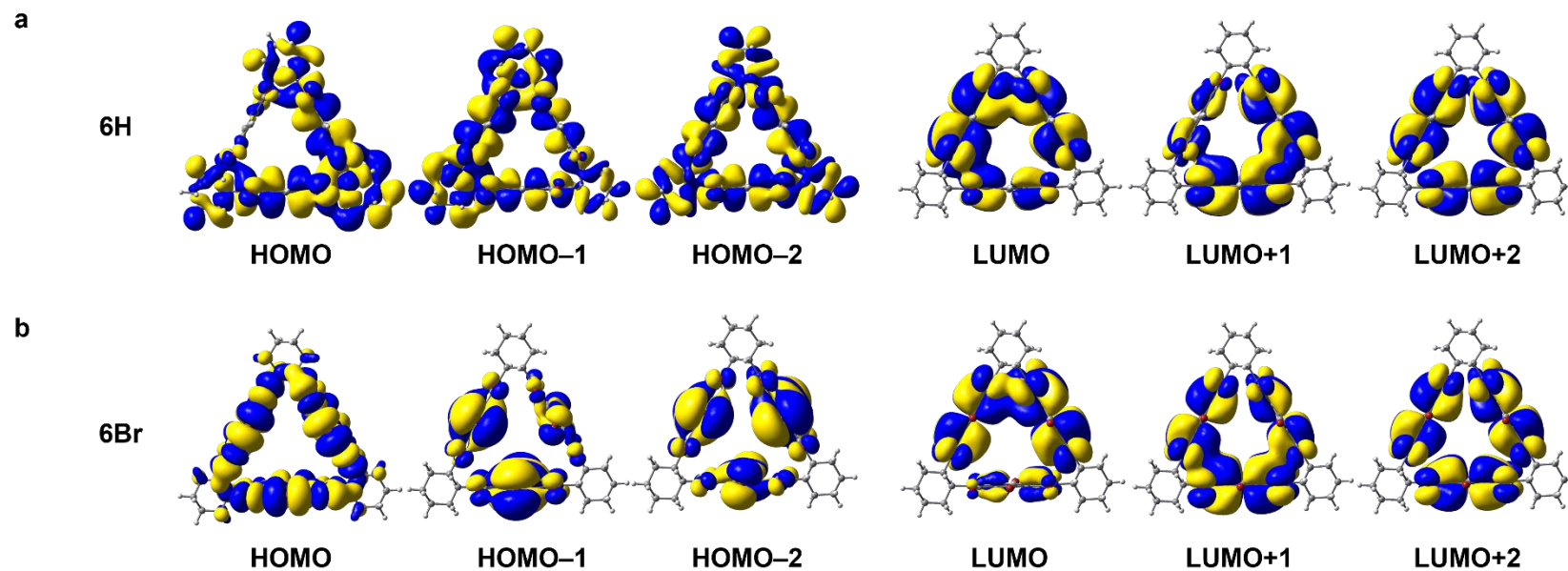


Figure S2.23 Visual depictions of the LUMO, LUMO+1, LUMO+2, HOMO, HOMO-1 and HOMO-2 of (a) **6H** and (b) **6Br**. Isovalue = 0.05.

2.4.6.1 CARTESIAN COORDINATES

Table S2.3 Cartesian coordinates of DFT geometry-optimised **6H** at the B3LYP-D3(BJ)/def2svp level of theory in CH₂Cl₂ (PCM solvent model).

C	5.62768	-8.15073	17.44009	C	6.644305	-8.03482	11.52563
H	5.420887	-9.22326	17.5527	C	7.043005	-9.14848	10.78885
C	4.843335	-7.62914	16.21712	C	7.598568	-9.2214	9.399977
H	5.023213	-6.54993	16.12413	N	7.872423	-10.5739	9.166101
C	7.914625	-9.17959	17.46813	N	5.340344	-8.18945	14.9652
C	9.297316	-8.71314	17.14066	O	7.584079	-12.5879	10.29347
C	10.50169	-9.41365	17.17883	O	5.26701	-10.4659	15.44314
C	11.62115	-8.67862	16.79328	O	5.578014	-6.17936	13.81885
C	13.05587	-9.10072	16.71359	O	7.780909	-8.31301	8.62126
C	12.91785	-6.87888	16.03823	C	7.454032	-11.1367	6.77419
C	11.54041	-7.33722	16.39634	H	6.533676	-11.6517	7.089816
C	10.33807	-6.63307	16.37023	H	7.181487	-10.0973	6.527014
C	9.218973	-7.36786	16.7566	C	8.071303	-11.8287	5.555124
C	7.78676	-6.94106	16.84824	H	7.363041	-11.8025	4.71217
N	7.071238	-8.07803	17.24119	H	8.240176	-12.8936	5.793792
N	13.75617	-7.99161	16.22455	C	9.401515	-11.1826	5.155224
O	7.560396	-10.2686	17.85259	H	9.214868	-10.1534	4.800959
O	13.535	-10.1728	17.00652	H	9.855974	-11.7286	4.31367
O	13.27258	-5.78588	15.66575	C	10.38041	-11.1349	6.33254
O	7.320412	-5.84514	16.63311	H	11.3048	-10.6085	6.049202
C	15.67036	-9.09162	15.06526	H	10.6634	-12.1563	6.636247
H	15.56316	-10.0314	15.62306	C	16.02498	-7.89077	17.25184
C	15.19079	-7.93315	15.96529	H	15.8622	-8.82244	17.81843
H	15.33144	-6.98987	15.42103	H	15.66941	-7.05841	17.87848
C	14.2792	-10.5162	13.54266	C	17.511	-7.72317	16.92017
C	13.45356	-10.2778	12.31891	H	18.10329	-7.7223	17.84864
C	12.68663	-11.176	11.57914	H	17.66422	-6.73777	16.44574
C	12.01624	-10.6191	10.4919	C	18.00333	-8.82224	15.97338
C	11.11192	-11.2751	9.494967	H	17.9614	-9.79613	16.49235
C	11.24975	-9.01372	8.966769	H	19.05771	-8.65308	15.70404
C	12.10671	-9.2589	10.16779	C	17.14837	-8.89599	14.70456
C	12.8846	-8.36337	10.89965	H	17.25677	-7.97002	14.11611
C	13.55485	-8.9201	11.98725	H	17.4715	-9.73168	14.06495
C	14.46172	-8.26543	12.98329	C	5.165649	-7.42162	18.70806
N	14.8203	-9.26709	13.89282	H	5.401298	-6.34876	18.61373
N	10.67018	-10.2538	8.646266	H	5.734147	-7.80877	19.56765
O	14.46584	-11.5534	14.13294	C	3.661445	-7.61847	18.91993
O	10.8104	-12.4449	9.41857	H	3.335273	-7.06825	19.81645
O	11.07172	-7.97926	8.368997	H	3.462744	-8.68725	19.11447
O	14.82438	-7.11116	13.01605	C	2.857696	-7.16926	17.69558
C	8.444802	-11.1309	7.945244	H	2.962481	-6.07691	17.57151
H	8.689017	-12.169	8.207401	H	1.785066	-7.36853	17.84608
C	9.746308	-10.4136	7.528682	C	3.34125	-7.8649	16.41938

H	9.49662	-9.3862	7.232326	H	2.800326	-7.48454	15.53923
C	7.493967	-11.3841	10.25074	H	3.150865	-8.9491	16.47957
C	6.970538	-10.4524	11.29671	H	6.420037	-11.7515	12.96345
C	6.48176	-10.7355	12.57078	H	12.95936	-7.3056	10.64329
C	6.082752	-9.62194	13.30725	H	12.61294	-12.234	11.83462
C	5.520762	-9.55042	14.6932	H	6.704437	-7.01902	11.13232
C	5.678179	-7.38226	13.86507	H	10.56292	-10.4592	17.48434
C	6.167774	-8.31667	12.80476	H	10.27716	-5.58681	16.06728

Table S2.4 Cartesian coordinates of DFT geometry-optimised **6Br** at the B3LYP-D3(BJ)/def2svp level of theory in CH₂Cl₂ (PCM solvent model).

C	5.615218	-8.15079	17.44701	C	6.686677	-8.03862	11.54311
H	5.406933	-9.22342	17.55368	C	7.063786	-9.15319	10.78625
C	4.833812	-7.6203	16.22628	C	7.615274	-9.23362	9.388166
H	5.019891	-6.54203	16.13615	N	7.870942	-10.5852	9.154988
C	7.891631	-9.1936	17.42521	N	5.333202	-8.18004	14.97388
C	9.282928	-8.72379	17.1067	O	7.562655	-12.5993	10.25704
C	10.49425	-9.42424	17.11407	O	5.185281	-10.4446	15.44156
C	11.62876	-8.68558	16.76125	O	5.636991	-6.16679	13.86846
C	13.07239	-9.10384	16.68514	O	7.80523	-8.33593	8.602004
C	12.94086	-6.86934	16.05791	C	7.450662	-11.1454	6.76001
C	11.5527	-7.33165	16.40147	H	6.527852	-11.6565	7.07446
C	10.34133	-6.63118	16.39434	H	7.183109	-10.1055	6.510118
C	9.209513	-7.3646	16.76651	C	8.069052	-11.8432	5.544522
C	7.771882	-6.93538	16.88609	H	7.363758	-11.8148	4.699275
N	7.059295	-8.08087	17.24384	H	8.230873	-12.9085	5.786179
N	13.77014	-7.98708	16.22351	C	9.404255	-11.2058	5.146891
O	7.522983	-10.2889	17.77064	H	9.224595	-10.1772	4.787643
O	13.56077	-10.1735	16.96305	H	9.858521	-11.7579	4.30933
O	13.31037	-5.77507	15.71068	C	10.38048	-11.1583	6.326764
O	7.297891	-5.83679	16.71819	H	11.30733	-10.636	6.044139
C	15.68997	-9.07955	15.06727	H	10.65843	-12.1794	6.635282
H	15.59191	-10.0218	15.62183	C	16.03794	-7.89171	17.26037
C	15.20699	-7.92664	15.97195	H	15.87809	-8.82803	17.81995
H	15.34857	-6.97986	15.43463	H	15.67968	-7.06471	17.89241
C	14.29696	-10.5071	13.55616	C	17.52333	-7.7159	16.92888
C	13.45156	-10.2709	12.33633	H	18.11593	-7.72152	17.85704
C	12.67176	-11.1644	11.59367	H	17.67221	-6.7254	16.46396
C	11.99793	-10.6196	10.49532	C	18.02047	-8.80396	15.97163
C	11.09594	-11.2795	9.487505	H	17.98515	-9.78255	16.48204
C	11.23382	-9.02109	8.953331	H	19.07337	-8.62598	15.70252
C	12.08674	-9.25814	10.16815	C	17.16501	-8.87271	14.70246
C	12.8633	-8.36377	10.91353	H	17.26753	-7.94216	14.12046
C	13.54867	-8.91132	12.00354	H	17.49155	-9.70266	14.05727
C	14.46646	-8.2561	13.00066	C	5.156323	-7.42835	18.71951
N	14.83256	-9.25828	13.89963	H	5.395959	-6.356	18.63344
N	10.66117	-10.2614	8.63855	H	5.722009	-7.82467	19.57671

O	14.5038	-11.5385	14.14586	C	3.650831	-7.6208	18.92708
O	10.79056	-12.4455	9.401221	H	3.326121	-7.07575	19.82717
O	11.05514	-7.9974	8.341412	H	3.446824	-8.69002	19.11321
O	14.83188	-7.10509	13.04418	C	2.851038	-7.15811	17.70509
C	8.440043	-11.1431	7.931794	H	2.962637	-6.06568	17.58842
H	8.680265	-12.1818	8.193591	H	1.777182	-7.35197	17.85326
C	9.743292	-10.429	7.515985	C	3.330488	-7.84896	16.42465
H	9.496659	-9.40342	7.212195	H	2.793004	-7.45951	15.54646
C	7.482911	-11.3963	10.23035	H	3.133372	-8.932	16.47839
C	6.966227	-10.4603	11.28673	Br	12.52507	-12.9875	12.05432
C	6.46425	-10.7314	12.56453	Br	6.343251	-12.4877	13.24102
C	6.067955	-9.61815	13.31367	Br	10.58953	-11.2552	17.55657
C	5.481013	-9.53994	14.69734	Br	12.96854	-6.53022	10.48375
C	5.705633	-7.37072	13.89219	Br	6.857827	-6.27856	10.88708
C	6.186601	-8.30961	12.82165	Br	10.23909	-4.81329	15.90304

Table S2.5 Cartesian coordinates of DFT geometry-optimised **6Ar** at the B3LYP-D3(BJ)/def2svp level of theory in CH₂Cl₂ (PCM solvent model).

C	5.467761	-8.12687	17.3064	C	7.579472	-14.3448	13.40366
H	5.259665	-9.19666	17.43693	H	8.621961	-12.6041	12.68386
C	4.764011	-7.64194	16.02098	C	5.18745	-14.0429	13.84509
H	4.932364	-6.5616	15.92266	H	4.40524	-12.0785	13.41167
C	7.748403	-9.14736	17.43903	C	6.335671	-14.8431	13.82353
C	9.136131	-8.71551	17.04326	H	6.262455	-15.8877	14.14041
C	10.35272	-9.41617	17.15873	C	7.026654	-6.68852	10.89018
C	11.48049	-8.6483	16.81001	C	8.299137	-6.27728	10.46734
C	12.93163	-9.04755	16.77758	C	5.931773	-5.83191	10.72366
C	12.77935	-6.86304	16.00323	C	8.485547	-5.03409	9.855475
C	11.39333	-7.32375	16.34698	H	9.154848	-6.94339	10.59101
C	10.17679	-6.63371	16.20874	C	6.091083	-4.57702	10.12299
C	9.056656	-7.38603	16.60345	H	4.941132	-6.15125	11.05203
C	7.629703	-6.93279	16.75051	C	7.368452	-4.20353	9.684378
N	6.91586	-8.05335	17.17403	H	7.499958	-3.23126	9.199879
N	13.62988	-7.93931	16.29068	C	10.04211	-5.24706	15.69794
O	7.36667	-10.1902	17.91443	C	9.181941	-4.98845	14.62045
O	13.44326	-10.0997	17.08923	C	10.70728	-4.18514	16.32205
O	13.1458	-5.79873	15.56113	C	8.957959	-3.6815	14.17827
O	7.151722	-5.83392	16.58377	H	8.656236	-5.81252	14.13461
C	15.63412	-9.01605	15.26267	C	10.51015	-2.86668	15.89297
H	15.52806	-9.9499	15.82977	H	11.37583	-4.38512	17.16123
C	15.07701	-7.85606	16.11585	C	9.62467	-2.63489	14.83236
H	15.22865	-6.91888	15.56443	H	9.45215	-1.60672	14.49999
C	14.30187	-10.4758	13.72627	C	10.40678	-10.8253	17.62214
C	13.41851	-10.239	12.52892	C	9.596361	-11.7951	17.00883
C	12.69865	-11.1705	11.75558	C	11.21544	-11.1905	18.70412
C	12.07977	-10.6051	10.62417	C	9.566309	-13.109	17.48185
C	11.21278	-11.2636	9.584861	H	8.961351	-11.5172	16.16614

C	11.29568	-8.99296	9.104008	C	11.22525	-12.5078	19.18305
C	12.13645	-9.23288	10.32349	H	11.84276	-10.44	19.18717
C	12.83717	-8.30056	11.10767	C	10.39284	-13.4482	18.56531
C	13.49648	-8.876	12.20794	H	10.38257	-14.4766	18.93868
C	14.46705	-8.23061	13.15816	C	12.63264	-12.608	12.11907
N	14.82893	-9.22421	14.06736	C	12.24641	-12.9841	13.41579
N	10.79151	-10.2447	8.726467	C	13.00775	-13.5949	11.20034
O	14.56434	-11.5029	14.30555	C	12.26055	-14.3247	13.80843
O	10.90495	-12.4289	9.471028	H	11.95573	-12.22	14.13861
O	11.0585	-7.95651	8.527667	C	13.00512	-14.9498	11.55853
O	14.90625	-7.10335	13.15776	H	13.31256	-13.307	10.19321
C	8.635232	-11.1678	7.871587	C	12.63582	-15.2938	12.86433
H	8.878812	-12.2055	8.133764	H	12.64243	-16.3473	13.15927
C	9.947346	-10.4211	7.548501	C	12.89682	-6.8422	10.84098
H	9.694891	-9.39763	7.242049	C	12.53269	-5.94071	11.85212
C	7.626383	-11.4405	10.14665	C	13.37632	-6.35423	9.619583
C	7.155476	-10.4999	11.22501	C	12.66492	-4.56158	11.66694
C	6.613824	-10.796	12.49103	H	12.16421	-6.31677	12.80799
C	6.164372	-9.66035	13.19158	C	13.51134	-4.97725	9.403178
C	5.56264	-9.56865	14.56812	H	13.66109	-7.05446	8.832433
C	5.775893	-7.40842	13.74153	C	13.16397	-4.10084	10.43962
C	6.286705	-8.35194	12.69242	H	13.2792	-3.02372	10.28493
C	6.847998	-8.05555	11.43871	C	3.864242	-14.582	14.32681
C	7.250486	-9.19484	10.72014	H	3.886979	-15.6764	14.43029
C	7.731358	-9.28131	9.29745	H	3.603791	-14.1565	15.31086
N	8.003762	-10.6299	9.068565	H	3.047849	-14.3176	13.63622
N	5.358477	-8.20843	14.81403	C	8.784949	-15.2447	13.33258
O	7.674211	-12.6476	10.13738	H	9.715378	-14.6686	13.24834
O	5.297097	-10.4562	15.34755	H	8.857491	-15.8956	14.217
O	5.718984	-6.20061	13.7245	H	8.725536	-15.9016	12.44809
O	7.843463	-8.40485	8.470798	C	8.634385	-14.1259	16.87679
C	7.719679	-11.172	6.642207	H	7.769158	-14.2997	17.53888
H	6.790526	-11.707	6.892209	H	8.242344	-13.7901	15.90805
H	7.446028	-10.1345	6.391083	H	9.13267	-15.0966	16.73247
C	8.428033	-11.8388	5.458394	C	12.1287	-12.8912	20.32773
H	7.777561	-11.813	4.569998	H	11.8884	-13.8918	20.71509
H	8.598293	-12.9041	5.69496	H	13.18422	-12.8991	20.00692
C	9.771785	-11.1679	5.153941	H	12.05084	-12.1718	21.15827
H	9.591809	-10.1374	4.800111	C	11.93094	-14.7151	15.22524
H	10.28779	-11.6965	4.336987	H	12.85469	-14.9008	15.79949
C	10.67346	-11.1183	6.391975	H	11.37937	-13.9216	15.74587
H	11.60449	-10.5729	6.173162	H	11.33289	-15.638	15.26297
H	10.954	-12.1383	6.702338	C	13.37559	-16.003	10.54522
C	15.83632	-7.77471	17.44537	H	13.54926	-16.9789	11.02117
H	15.66708	-8.70206	18.01692	H	12.57003	-16.1307	9.802141
H	15.42889	-6.94231	18.03984	H	14.28421	-15.7231	9.989314
C	17.33364	-7.57395	17.18836	C	13.98959	-4.45373	8.072701

H	17.87668	-7.54679	18.1462	H	13.14252	-4.33509	7.374898
H	17.4864	-6.59045	16.70983	H	14.47082	-3.46969	8.174628
C	17.90457	-8.67015	16.28238	H	14.70527	-5.14324	7.600053
H	17.86133	-9.6386	16.81148	C	12.26206	-3.59847	12.75182
H	18.96708	-8.47467	16.06814	H	12.2548	-4.08133	13.73859
C	17.12074	-8.78338	14.97076	H	12.9394	-2.73137	12.7886
H	17.23307	-7.86304	14.37515	H	11.24665	-3.20935	12.57358
H	17.49883	-9.6188	14.36153	C	9.855481	-4.59611	9.410462
C	4.91997	-7.36781	18.52005	H	10.51571	-5.45559	9.230258
H	5.150015	-6.29555	18.4112	H	9.803896	-3.99197	8.491743
H	5.434154	-7.72522	19.42552	H	10.33775	-3.97396	10.18156
C	3.406999	-7.58107	18.6356	C	4.918449	-3.64011	9.981241
H	3.012475	-7.01103	19.49142	H	4.804286	-3.02108	10.88807
H	3.209988	-8.64692	18.84749	H	5.049089	-2.95458	9.13074
C	2.679602	-7.17967	17.34781	H	3.975406	-4.19004	9.842732
H	2.775735	-6.08943	17.20045	C	8.034913	-3.40959	13.02037
H	1.602459	-7.3929	17.43368	H	7.333986	-4.23981	12.85873
C	3.256087	-7.89915	16.12363	H	7.456021	-2.48669	13.17942
H	2.769078	-7.5472	15.20109	H	8.604434	-3.27759	12.08628
H	3.077053	-8.98445	16.19766	C	11.25954	-1.73003	16.54056
C	6.521556	-12.1868	13.00135	H	10.71422	-0.7794	16.44477
C	7.661652	-13.0067	13.01043	H	11.43985	-1.92103	17.60924
C	5.29387	-12.7114	13.42068	H	12.24566	-1.59344	16.0636

2.5 REFERENCES

- (1) Zhao, Y.; Cotellet, Y.; Liu, L.; López-Andarias, J.; Bornhof, A.-B.; Akamatsu, M.; Sakai, N.; Matile, S. The Emergence of Anion- π Catalysis. *Acc. Chem. Res.* **2018**, *51*, 2255–2263.
- (2) Li, L.; Wang, J.; Chen, M.; Chen, Y.; Xiao, W.; Chen, D.; Lin, M. The Impact of Vertical π -Extension on Redox Mechanisms of Aromatic Diimide Dyes. *Chin. Chem. Lett.* **2019**, *30*, 2254–2258.
- (3) Langhals, H.; Karolin, J.; Johansson, L. B.-Å. Spectroscopic Properties of New and Convenient Standards for Measuring Fluorescence Quantum Yields. *J. Chem. Soc. Faraday Trans.* **1998**, *94*, 2919–2922.
- (4) Gsänger, M.; Bialas, D.; Huang, L.; Stolte, M.; Würthner, F. Organic Semiconductors Based on Dyes and Color Pigments. *Adv. Mater.* **2016**, *28*, 3615–3645.
- (5) V. Bhosale, S.; V. Bhosale, S.; K. Bhargava, S. Recent Progress of Core-Substituted Naphthalenediimides: Highlights from 2010. *Org. Biomol. Chem.* **2012**, *10*, 6455–6468.
- (6) Ajayakumar, M. R.; Asthana, D.; Mukhopadhyay, P. Core-Modified Naphthalenediimides Generate Persistent Radical Anion and Cation: New Panchromatic NIR Probes. *Org. Lett.* **2012**, *14*, 4822–4825.
- (7) Al Kobaisi, M.; Bhosale, S. V.; Latham, K.; Raynor, A. M.; Bhosale, S. V. Functional Naphthalene Diimides: Synthesis, Properties, and Applications. *Chem. Rev.* **2016**, *116*, 11685–11796.
- (8) Cao, D.; Hong, M.; Blackburn, A. K.; Liu, Z.; Holcroft, J. M.; Stoddart, J. F. Two-Point Halogen Bonding between 3,6-Dihalopyromellitic Diimides. *Chem. Sci.* **2014**, *5*, 4242–4248.

- (9) Wang, M.; Liang, G.; Wang, Y.; Fan, T.; Yuan, B.; Liu, M.; Yin, Y.; Li, L. Merging N-Hydroxyphthalimide into Metal-Organic Frameworks for Highly Efficient and Environmentally Benign Aerobic Oxidation. *Chem. – Eur. J.* **2021**, *27*, 9674–9685.
- (10) Larpent, P.; Jouaiti, A.; Kyritsakas, N.; Hosseini, M. W. Molecular Tectonics: Homochiral Coordination Networks Based on Combinations of a Chiral Neutral Tecton with Hg(II), Cu(II) or Ni(II) Neutral Complexes as Metallatectons. *Dalton Trans.* **2013**, *43*, 2000–2006.
- (11) Wu, Y.; Han, J.-M.; Hong, M.; Krzyaniak, M. D.; Blackburn, A. K.; Fernando, I. R.; Cao, D. D.; Wasielewski, M. R.; Stoddart, J. F. X-Shaped Oligomeric Pyromellitimide Polyradicals. *J. Am. Chem. Soc.* **2018**, *140*, 515–523.
- (12) Liu, X.; Yang, J.; Liu, H.; Yuan, X.; Liu, G.; Pu, S. Pyromellitic Diimide-Based Luminophors: Tunable Aggregation-Induced Emission (AIE) and Reversible Mechanofluorochromism Characteristics. *J. Photochem. Photobiol. Chem.* **2021**, *417*, 113344.
- (13) Guo, X.; Watson, M. D. Pyromellitic Diimide-Based Donor–Acceptor Poly(Phenylene Ethynylene)s. *Macromolecules* **2011**, *44*, 6711–6716.
- (14) Luo, C.; Meng, X.; Han, L.; Sun, S.; Lin, T.; Sun, J.; Peng, H.; Chu, J. N-Type Pyromellitic Diimide-Benzodithiophene-Containing Conjugated Polymers for All-Polymer Solar Cells with High Open-Circuit Voltage. *Synth. Met.* **2014**, *196*, 110–116.
- (15) Shao, J.; Chang, J.; Dai, G.; Chi, C. Pyromellitic Diimide-Based Copolymers for Ambipolar Field-Effect Transistors: Synthesis, Characterization, and Device Applications. *J. Polym. Sci. Part Polym. Chem.* **2014**, *52*, 2454–2464.
- (16) Zindy, N.; Blaskovits, J. T.; Beaumont, C.; Michaud-Valcourt, J.; Saneifar, H.; Johnson, P. A.; Bélanger, D.; Leclerc, M. Pyromellitic Diimide-Based Copolymers and Their Application as Stable Cathode Active Materials in Lithium and Sodium-Ion Batteries. *Chem. Mater.* **2018**, *30*, 6821–6830.
- (17) Nakagaki, T.; Shin-ichiro, K.; Harano, A.; Shinmyozu, T. Molecular Recognition of Polymethoxybenzenes by Host Molecule Comprised of Two Pyromellitic Diimides and Two Dialkoxynaphthalenes. *Tetrahedron* **2010**, *66*, 976–985.
- (18) Halim, Md. E.; Bandyopadhyay, A.; Hossain, Md. E.; Shinmyozu, T. A Study on the Synthesis, Characterization, Structural Optimization, and Conformational Behaviors of Bromo-Substituted Pyromelliticdiimide-Based [2+2] Macrocycle as Structural Units of Covalently Linked Molecular Tubes. *J. Mol. Struct.* **2020**, *1213*, 128164.
- (19) Ershad Halim, Md.; Bandyopadhyay, A.; Sun, L.; Tao, K.; Sangvikar, Y. S.; Miyazaki, T.; Watanabe, M.; Ideta, K.; Matsumoto, T.; Goto, K.; Shinmyozu, T. Synthesis of Bromo- and Iodo-Substituted Pyromellitic Diimide-Based [2+2]- and [3+3]Macrocycles, and Their Absorption Spectra and Electrochemical and Inclusion Properties. *Tetrahedron Lett.* **2015**, *56*, 6970–6974.
- (20) Kato, S.; Nonaka, Y.; Shimasaki, T.; Goto, K.; Shinmyozu, T. Novel Pyromellitic Diimide-Based Macrocycle with a Linear π -Electronic System and Bis(Phenylethynyl)Pyromellitic Diimide: Syntheses, Structures, Photophysical Properties, and Redox Characteristics. *J. Org. Chem.* **2008**, *73*, 4063–4075.
- (21) Wang, D.; Zhao, Y. Rigid-Flexible Hybrid Porous Molecular Crystals with Guest-Induced Reversible Crystallinity. *Angew. Chem. Int. Ed.* **2023**, *62*, e202217903.
- (22) Kim, D. J.; Hermann, K. R.; Prokofjevs, A.; Otley, M. T.; Pezzato, C.; Owczarek, M.; Stoddart, J. F. Redox-Active Macrocycles for Organic Rechargeable Batteries. *J. Am. Chem. Soc.* **2017**, *139*, 6635–6643.

- (23) Liu, Z.; Liu, G.; Wu, Y.; Cao, D.; Sun, J.; Schneebeli, S. T.; Nassar, M. S.; Mirkin, C. A.; Stoddart, J. F. Assembly of Supramolecular Nanotubes from Molecular Triangles and 1,2-Dihaloalkanes. *J. Am. Chem. Soc.* **2014**, *136*, 16651–16660.
- (24) Beldjoudi, Y.; Narayanan, A.; Roy, I.; Pearson, T. J.; Cetin, M. M.; Nguyen, M. T.; Krzyaniak, M. D.; Alsubaie, F. M.; Wasielewski, M. R.; Stupp, S. I.; Stoddart, J. F. Supramolecular Tessellations by a Rigid Naphthalene Diimide Triangle. *J. Am. Chem. Soc.* **2019**, *141*, 17783–17795.
- (25) Chen, D.; Avestro, A.-J.; Chen, Z.; Sun, J.; Wang, S.; Xiao, M.; Erno, Z.; Algaradah, M. M.; Nassar, M. S.; Amine, K.; Meng, Y.; Stoddart, J. F. A Rigid Naphthalenediimide Triangle for Organic Rechargeable Lithium-Ion Batteries. *Adv. Mater.* **2015**, *27*, 2907–2912.
- (26) Gawroński, J.; Brzostowska, M.; Gawrońska, K.; Koput, J.; Rychlewska, U.; Skowronek, P.; Nordén, B. Novel Chiral Pyromellitdiimide (1,2,4,5-Benzenetetracarboxydiimide) Dimers and Trimers: Exploring Their Structure, Electronic Transitions, and Exciton Coupling. *Chem. – Eur. J.* **2002**, *8*, 2484–2494.
- (27) Schneebeli, S. T.; Frasconi, M.; Liu, Z.; Wu, Y.; Gardner, D. M.; Strutt, N. L.; Cheng, C.; Carmieli, R.; Wasielewski, M. R.; Stoddart, J. F. Electron Sharing and Anion- π Recognition in Molecular Triangular Prisms. *Angew. Chem. Int. Ed.* **2013**, *52*, 13100–13104.
- (28) Perkampus, H.-H. *UV-VIS Spectroscopy and Its Applications*; Springer: Berlin, Heidelberg, 1992.
- (29) Herzberg, G. *Molecular Spectra and Molecular Structure Volume III - Electronic Spectra and Electronic Structure of Polyatomic Molecules*, 2nd ed.; R.E. Krieger Pub. Co.: Malabar, Fla., 1989.
- (30) CrysAlisPro. CrysAlisPro, Oxford Diffraction Ltd. Version 1.171.34.40.
- (31) Empirical Absorption Correction Using Spherical Harmonics, Implemented in SCALE3 ABSPACK Scaling Algorithm within CrysAlisPro Software. Scale3, Oxford Diffraction Ltd. Version 1.171.34.40.
- (32) Dolomanov, O. V.; Bourhis, L. J.; Gildea, R. J.; Howard, J. a. K.; Puschmann, H. OLEX2: A Complete Structure Solution, Refinement and Analysis Program. *J. Appl. Crystallogr.* **2009**, *42* (2), 339–341. <https://doi.org/10.1107/S0021889808042726>.
- (33) Sheldrick, G. M. A Short History of SHELX. *Acta Crystallogr. A* **2008**, *64* (1), 112–122. <https://doi.org/10.1107/S0108767307043930>.
- (34) Sheldrick, G. M. SHELXT – Integrated Space-Group and Crystal-Structure Determination. *Acta Crystallogr. Sect. Found. Adv.* **2015**, *71*, 3–8.
- (35) Macrae, C. F.; Sovago, I.; Cottrell, S. J.; Galek, P. T. A.; McCabe, P.; Pidcock, E.; Platings, M.; Shields, G. P.; Stevens, J. S.; Towler, M.; Wood, P. A. Mercury 4.0: From Visualization to Analysis, Design and Prediction. *J. Appl. Crystallogr.* **2020**, *53*, 226–235.
- (36) Spackman, M. A.; Jayatilaka, D. Hirshfeld Surface Analysis. *CrystEngComm* **2009**, *11*, 19–32.
- (37) Mackenzie, C. F.; Spackman, P. R.; Jayatilaka, D.; Spackman, M. A. CrystalExplorer Model Energies and Energy Frameworks: Extension to Metal Coordination Compounds, Organic Salts, Solvates and Open-Shell Systems. *IUCrJ* **2017**, *4*, 575–587.
- (38) Frisch, M. J.; Trucks, G. W.; Schlegel, H. B.; Scuseria, G. E.; Robb, M. A.; Cheeseman, J. R.; Scalmani, G.; Barone, V.; Petersson, G. A.; Nakatsuji, H.; Li, X.; Caricato, M.; Marenich, A. V.; Bloino, J.; Janesko, B. G.; Gomperts, R.; Mennucci, B.; Hratchian, H. P.; Ortiz, J. V.; Izmaylov, A. F.; Sonnenberg, J. L.; Williams, D.; Ding, F.; Lipparini, F.; Egidi, F.; Goings, J.; Peng, B.; Petrone, A.; Henderson, T.; Ranasinghe, D.; Zakrzewski, V. G.; Gao, J.; Rega, N.; Zheng, G.; Liang, W.; Hada, M.; Ehara, M.; Toyota, K.; Fukuda, R.; Hasegawa, J.; Ishida, M.; Nakajima, T.; Honda, Y.; Kitao, O.;

Nakai, H.; Vreven, T.; Throssell, K.; Montgomery Jr., J. A.; Peralta, J. E.; Ogliaro, F.; Bearpark, M. J.; Heyd, J. J.; Brothers, E. N.; Kudin, K. N.; Staroverov, V. N.; Keith, T. A.; Kobayashi, R.; Normand, J.; Raghavachari, K.; Rendell, A. P.; Burant, J. C.; Iyengar, S. S.; Tomasi, J.; Cossi, M.; Millam, J. M.; Klene, M.; Adamo, C.; Cammi, R.; Ochterski, J. W.; Martin, R. L.; Morokuma, K.; Farkas, O.; Foresman, J. B.; Fox, D. J. Gaussian 16 Rev. A.03, 2016.

(39) Becke, A. D. Density-functional Thermochemistry. III. The Role of Exact Exchange. *J. Chem. Phys.* **1993**, 98, 5648–5652.

(40) Lee, C.; Yang, W.; Parr, R. G. Development of the Colle-Salvetti Correlation-Energy Formula into a Functional of the Electron Density. *Phys. Rev. B* **1988**, 37, 785–789.

(41) Weigend, F. Accurate Coulomb-Fitting Basis Sets for H to Rn. *Phys. Chem. Chem. Phys.* **2006**, 8, 1057.

(42) Grimme, S.; Ehrlich, S.; Goerigk, L. Effect of the Damping Function in Dispersion Corrected Density Functional Theory. *J. Comput. Chem.* **2011**, 32, 1456–1465.

CHAPTER 3 |

DYNAMIC ATROPISOMERISM AND
HOST–GUEST BEHAVIOUR OF
MOLECULAR TRIANGLES

SYNOPSIS

Organic molecular balances have been used to measure the strength of non-covalent interactions (NCIs) through the stabilisation of favourable conformations upon hindered rotation. Such restricted rotation can also lead to atropisomerism (isomers exist with half-lives > 1000 s) and/or planar chirality in macrocycles containing aromatic rings such as pillar[n]arenes. In these systems, the rate of rotation is influenced by substituents on the rotating unit through steric hinderance or favourable NCIs. In this Chapter, the effect of intra- and intermolecular NCIs in core-substituted molecular triangles is investigated *via* dynamic atropisomerism and host–guest chemistry. Tris-functionalised molecular triangles, **3Br** and **3Ar**, are synthesised and their structural and optoelectronic properties studied and compared with the hexa-functional macrocyclic analogues, **6H**, **6Br** and **6Ar** (Chapter 2). Notably, **3Br** and **3Ar** exist as a mixture of *syn*- and *anti*-atropisomers in solution evidenced by ^1H NMR spectroscopy and in the solid state (X-ray diffraction). Further studies using variable temperature (VT) ^1H - ^1H EXSY NMR spectroscopy and internal reaction coordinate (IRC) density functional theory (DFT) calculations show that **3Br** and **3Ar** can interconvert through rotation of PMDI side walls. For **3Br** the rate of interconversion between isomers is enhanced when the rotation goes *via* a pathway with an intra-annular bromine rather than a hydrogen substituent, despite the increased van der Waals radius of the halogen atom. Favourable intramolecular $\text{Br}\cdots\pi$ interactions stabilise the intra-annular bromine transition state by 2.9 kcal mol^{-1} , with this system bearing a resemblance to ground state molecular balances. In a separate example, intermolecular anion $\cdots\pi$ interactions between the electron-rich triiodide anion and electron-deficient **6Br** macrocycle lead to host–guest complexes where the structure of the molecular triangle adapts to maximise the binding ($61 \pm 5\text{ M}^{-1}$, CDCl_3). The results from this Chapter therefore highlight the influence that intra- and intermolecular NCIs on the structure of rigid, shape-persistent macrocycles which bear similarities with the behaviour of enzymes in the induced-fit binding model.

ACKNOWLEDGEMENTS

FHNA acknowledges support from (i) William Glover-Humphreys for assistance in the synthesis of **3Ar** and key precursors, (ii) Dr Neil Scott for valuable discussions about conditions for Suzuki–Miyaura coupling reactions, (iii) Dr Adrian Whitwood and Theo Tanner for solving X-ray crystal structures, (iv) Heather Fish, Dr Alex Heyam and Dr Matthew Davy for assistance in the design and completion of advanced NMR spectroscopy experiments, (v) Mariia Kuznetsova for assistance with host-guest chemistry studies, (vi) Dr Paul McGonigal and Ruhee Dawood for completing DFT calculations, (vii) Ruhee Dawood and Shana Noureen for assistance in UV-vis spectroscopy, (viii) Dr Suresh Mothika for guidance with electrochemical and chemical reduction experiments and (ix) Professor Victor Chechik for completing EPR spectroscopy experiments.

3.1 INTRODUCTION

The importance of catalysis is prevalent in nature, in particular through enzymes, where the presence and activity of the biological catalyst enhances the rate of reaction, with such processes vital for the survival of all biological life.¹ Non-covalent interactions (NCIs) such as hydrogen-bonds, electrostatics, van der Waals, $\pi \cdots \pi$, cation $\cdots \pi$ and anion $\cdots \pi$ are crucial in determining the tertiary structure of proteins and the relative strengths of these interactions are crucial to allowing conformational change for the specific binding of substrates in enhancing catalytic activity.^{2,3} The strength of such intramolecular NCIs have been quantified and measured in synthetic model compounds experimentally through the development of molecular balances.^{4,5} A range of molecular balances which are all structurally rigid with restricted rotation have been developed (Figure 3.1), including but not limited to; Wilcox's arylestes,⁶ Motherwell's bicyclononanes,⁷ Shimizu's *N*-arylimides,⁸ and Cockroft's diarylformamides.^{9,10} These respective studies have allowed for the strength of NCIs to be calculated using the population ratio of favourable/unfavourable conformers. Many different NCIs have been characterised using these molecular balances including $\text{CH} \cdots \pi$,¹¹ $\text{OH} \cdots \pi$,¹² $\text{S} \cdots \pi$,¹³ halogen $\cdots \pi$,^{14,15} $\text{C}=\text{O} \cdots \pi$,^{16,17} $\pi \cdots \pi$,¹⁸ and chalcogen bonding,¹⁹ as well as the role of solvent in understanding the preference for certain conformational isomers.^{20,21} Notably, these studies have shown that halogen $\cdots \pi$ interactions require an optimal distance between halogen atom and π -surface to avoid steric repulsion, however if this is achieved successfully then the interaction can be stabilising by up to -5.0 kJ mol^{-1} .¹⁵ Furthermore, $\text{C}=\text{O} \cdots \pi$ interactions have been shown to aid in the rotation between conformers by stabilising transition state structures.¹⁷ When considering potential intramolecular interactions in molecular balances, the role of different solvent molecules must also be accounted for, *e.g.*, different functional groups and polarities, which can influence the equilibrium between different rotational states.^{20,21}

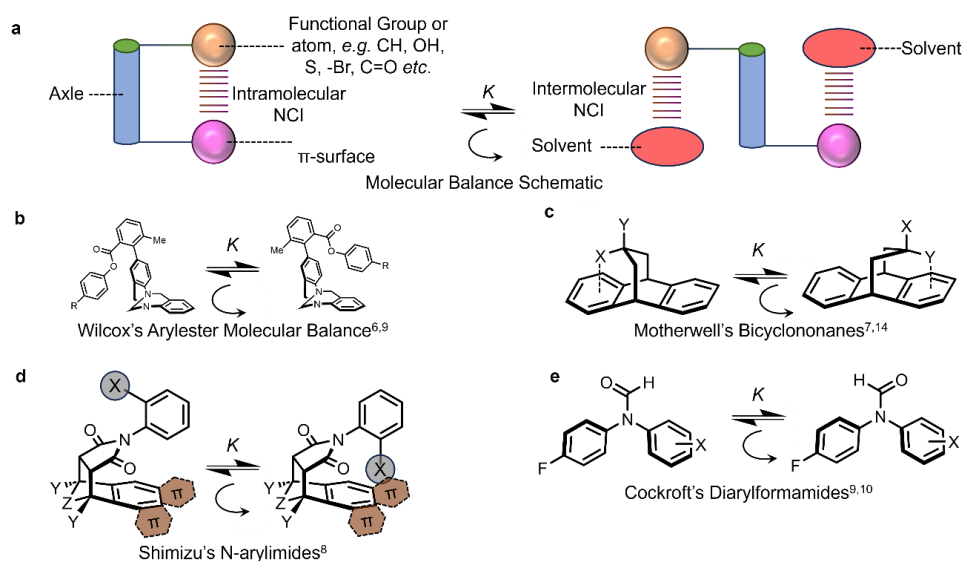


Figure 3.1 (a) General scheme for molecular balances with competing solvent molecules and examples: (b) Wilcox's arylestes,^{6,9} (c) Motherwell's bicyclononanes,^{7,14} (d) Shimizu's *N*-arylimides,⁸ and (e) Cockroft's diarylformamides^{9,10}.

The sterically hindered rotation in molecular balances is a form of atropisomerism which Oki²² classified formally as occurring when isomers exist with half-lives of above 1000 seconds ($\Delta G^\ddagger > 25 \text{ kcal mol}^{-1}$). Atropisomers can be found in natural products (*e.g.* vancomycin, flavomannins and abyssomicin C), and synthetic compounds (sterically hindered acyclic and cyclic molecules) with applications in asymmetric catalysis and as pharmaceutical drug candidates.^{23,24} The potential for drug candidates to rotate between atropisomers could lead to biologically active enantiomers with differing and potentially dangerous properties and thus is an important property to be studied during the development of new pharmacological compounds.^{25,26}

In addition to being a required consideration in drug development, the restricted rotation of dynamically active atropisomers has been exploited in a molecular rotor system by Leigh and co-workers²⁷ through the utilisation of the hindered rotation of a pyrrole-2-carboxylic acid (Figure 3.2a). They were able to control the unidirectional rotation of this molecular motion through the use of enantiomerically pure fuel (carbodiimide) and an anhydride hydrolysis catalyst, such that, if the opposite enantiomer of the catalyst was used the rotation would occur in the opposite direction.²⁷ Another example of where atropisomerism has been put to use is in the synthesis of macrocycles. The favoured *syn*-isomer of an atropisomeric NDI molecule, *syn*-**3**, with restricted rotation was utilised with the preorganisation of the major isomer allowing for efficient, high-yielding cyclisation without the need for common macrocyclisation methods such as templation (Figure 3.2b).²⁸

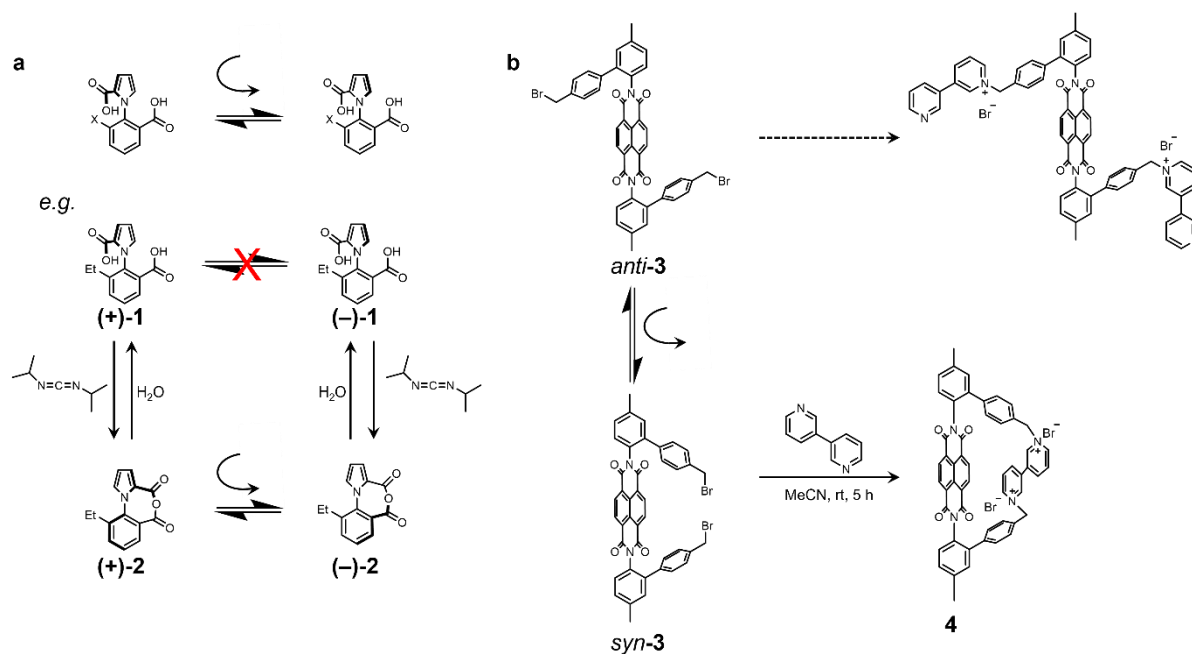


Figure 3.2 (a) Leigh's autonomous molecular motor for unidirectional rotation²⁷ and (b) atropisomerism in an NDI molecule where the preference for *syn*-**3** provides preorganisation for the synthesis of macrocycle **4**.²⁸

Rotation within a macrocycle has been observed and studied in pillar[n]arenes (Figure 3.3a),^{29,30} which were first reported in 2008 by Ogoshi and co-workers,³¹ with interconversion being enabled by intramolecular hydrogen-bonds and occurring faster than the NMR timescale at room temperature.³²

Pillar[n]arenes consist of [n] number of 1,4-disubstituted alkoxy aryls linked by methylene bridges and can exist as two planar chiral enantiomers *pR* and *pS*, due to the regiochemical positioning of the alkoxy groups on the benzene rings (Figure 3.3b).³³ A range of alkoxy-substituted pillar[5]arenes with varying lengths of alkyl chains have been synthesised and as the length of the alkyl chain increases, interconversion between the two enantiomers becomes more hindered and thus occurs at a slower rate, although separation of the enantiomers was still not possible.³² Upon the introduction of larger bulkier groups such as cyclohexane and phenyl rings separation of *pR* and *pS* enantiomers of pillar[5]arene was possible.³³ Conversely, for pillar[6]arene, even the addition of cyclohexylmethylene ($R = \text{CH}_2\text{Cy}$) substituents did not prevent rotation due to the larger cavity size (7.5 Å) of the macrocycle compared with pillar[5]arene, with covalent bridging across one side of the macrocycle instead being used to fix the conformation.³⁴ Another strategy to slow the rate of interconversion of planar chiral enantiomers of pillar[n]arenes is the formation of host-guest complexes with cationic guests being encapsulated in the electron-rich cavity of the 5-unit macrocycle (5 Å diameter).³⁵ The achievement of the separation of the planar chiral enantiomers of pillar[n]arenes has enabled the *pR* and *pS* isomers to be used in chiral applications such as chiral switches, enantioselective recognition, chirality sensing and circularly polarised luminescent (CPL) materials.³⁶

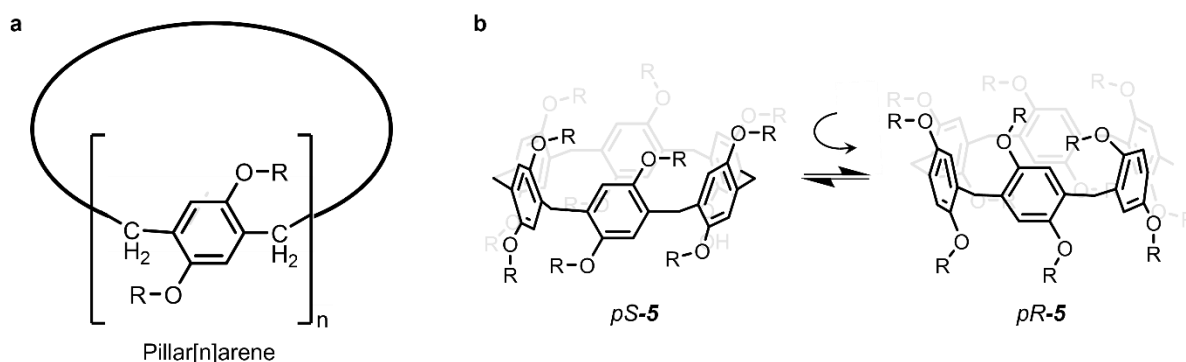


Figure 3.3 (a) General schematic for the structure of pillar[n]arenes³² and (b) rotation between planar chiral isomers (*pS* and *pR*) of pillar[6]arene **5**, where even when the R groups were large bulky cyclohexylmethylene substituents rotation occurred.³⁴

Pillar[n]arenes, as a type of cyclophane, are therefore similar to molecular triangles, with the cavity sizes on the same order of magnitude (Figure 3.4a). Consequently, it could be envisioned that rotation would also occur in molecular triangles, although the increased rigidity in the shape-persistent macrocycle could hinder rotation. Indeed, rotation has been investigated by variable temperature ^1H NMR spectroscopy in an isosceles triangle containing two PMDI-side units with an additional NDI wall, macrocycle **6** (Figure 3.4b). The protons present on the PMDI-core are represented as two peaks due to the decreased (C_2) symmetry in the macrocycle compared to the equilateral triangles (D_3 symmetry).^{37,38} The two inequivalent proton environments of the PMDI-core, H_A and $H_{A'}$, coalesced at a temperature of 426 K which relates to an energy barrier to interconversion of 23 kcal mol⁻¹.³⁷ The higher temperature of coalescence in the rigid isosceles molecular triangle indicates that rotation is more hindered compared with pillar[n]arenes (where ΔG^\ddagger is between 11 ($R = \text{C}_2\text{H}_5$) and 15 ($R = \text{C}_{12}\text{H}_{25}$) kcal

mol^{-1} when $n = 5$).³² The restricted rotation of PMDI units around a $\text{C-N}\cdots\text{N-C}$ axle in the isosceles triangles differs to the interconversion in planar chiral pillar[n]arenes by the angle between repeating units in the macrocycles. In molecular triangles, the angle between aromatic diimide side-units linked by diaminocyclohexane vertices is acute at around 60° , whereas in pillar[n]arenes with $n = 5$ and 6 being most common, the angle between 1,4-alkoxybenzene repeating units is obtuse ($>90^\circ$), therefore rotation in molecular triangles is more sterically hindered.

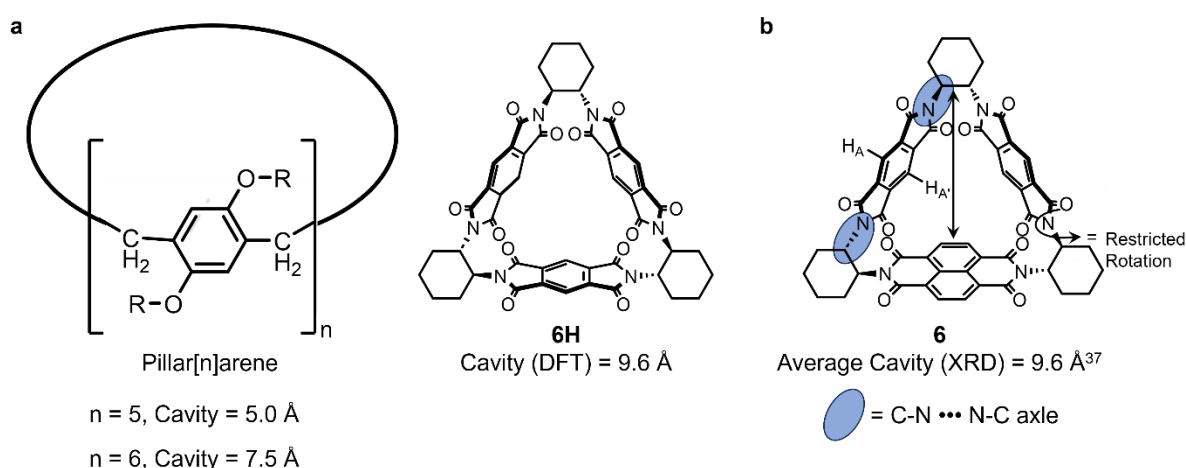


Figure 3.4 (a) Comparison of the cavity size of pillar[n]arenes ($n = 5$ or 6)^{34,35} and PMDI based molecular triangle **6H** (Chapter 2). (b) Structure of 2PMDI-NDI isosceles molecular triangle **6** with average distance of cavity measurement shown and PMDI protons H_A and $\text{H}_{A'}$ labelled.³⁷

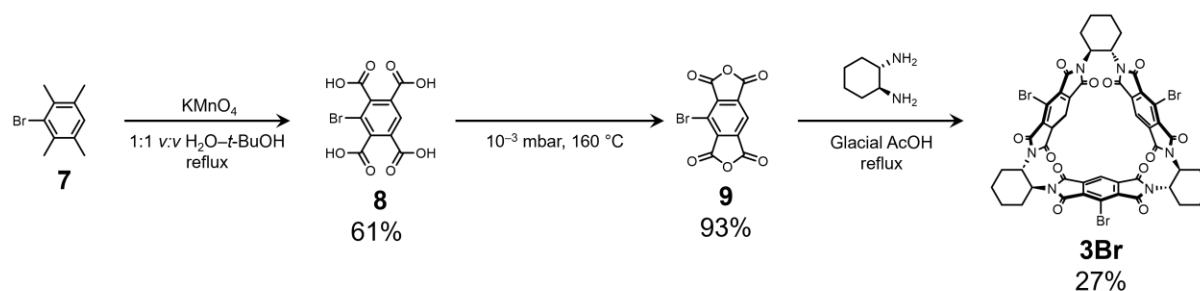
In this Chapter, the synthesis of tris-substituted molecular triangles **3Br** and **3Ar** are described and their structural and optoelectronic properties compared with the hexa-substituted macrocycles **6H**, **6Br** and **6Ar** introduced in Chapter 2. The tris-functionalised molecular triangles are found to exist as a mixture of *syn*- and *anti*-isomers and interconversion between these isomers is possible *via* rotation of mono-substituted PMDI side walls. Investigations into the energy barrier and mechanism of this atropisomerism between *syn*- and *anti*-isomers of **3Br** and **3Ar** were completed using VT ^1H and ^1H - ^1H EXSY NMR spectroscopy and transition (TS) and IRC-DFT calculations. As hypothesised, steric hinderance arising from the carbonyl groups and from bulky (aryl) substituents acts to slow down or prevent rotation pathways. Surprisingly however, the presence of a large bromine substituent in the place of a hydrogen atom leads to an increase in rate of rotation, which can be attributed to stabilising $\text{Br}\cdots\pi$ interactions developing at the modelled transition state, akin to a transition state molecular balance.¹⁷ In addition to intramolecular transition state halogen $\cdots\pi$ interactions, intermolecular anion $\cdots\pi$ interactions between electron-deficient molecular triangles and an electron-rich trihalide anion (I_3^-) have also been studied. Out of the five molecular triangles synthesised and characterised in Chapters 2 and 3, **6Br** exhibited the greatest binding with I_3^- ($61 \pm 5 \text{ M}^{-1}$ in CDCl_3) as determined by ^{13}C NMR spectroscopy host–guest titrations which is almost three times greater than NDI based molecular triangle **10** ($25 \pm 2 \text{ M}^{-1}$ in CD_2Cl_2 determined by ^1H NMR spectroscopy).³⁹ These results show that intermolecular halogen $\cdots\pi$ interactions between electron-rich anions and electron-deficient

molecular triangles are greater in the core-brominated PMDI based macrocycle (**6Br**) than in the unsubstituted NDI based macrocycle **10**, despite a smaller aromatic π -surface. The enhanced binding in **6Br** could have potential implications for the supramolecular assembly of macrocycles towards non-covalently bonded triangular nanoprisms or for sensing applications of electron-rich small molecules.

3.2 RESULTS AND DISCUSSION

3.2.1 THE SYNTHESIS, STRUCTURAL AND OPTOELECTRONIC PROPERTIES OF TRIS-FUNCTIONALISED MOLECULAR TRIANGLES

In Chapter 2, the synthesis, structural and optoelectronic properties of molecular triangles (**6H**, **6Br** and **6Ar**) composed of symmetric PMDI faces with aromatic core substitution with hydrogen atoms, bromine atoms or 3,5-dimethylbenzene groups were discussed. Subsequently, the synthesis of tris-substituted molecular triangle **3Br** was pursued using adapted literature procedures (Scheme 3.1).^{40,41} The synthesis of macrocycle **3Br** began with the oxidation of mono-bromo-tetramethylbenzene **7** with KMnO_4 to synthesise tetracarboxylic acid **8** (61%) followed by the formation of anhydride **9** (93%) by dehydration at 160 °C under reduced pressure (10^{-3} mbar).



Scheme 3.1 Synthesis of brominated molecular triangle **3Br** via tetra-acid **8** and anhydride **9** precursors.

The condensation reaction of anhydride **9** with (*S,S*)-*trans*-1,2-diaminocyclohexane to synthesise macrocycle **3Br** followed an adapted procedure from Gawroński *et al.*⁴² which was used for **6H** and **6Br** in Chapter 2. Macrocycle **3Br** was isolated following purification using automated column chromatography (SiO_2 : 0–100% Me_2CO in CH_2Cl_2) in a yield of 27% and characterised using ^1H and ^{13}C NMR spectroscopy and high-resolution mass spectrometry (Supplementary Information, Sections 3.4.2 and 3.4.3).

In the ^1H NMR spectrum for **3Br** (Figure 3.5a), proton environments were observed in similar regions to the hexa-substituted molecular triangles **6H**, **6Br** and **6Ar** (Chapter 2), however, unexpected additional peaks are also present. Four equal intensity aromatic peaks (H^2), which are independent environments as confirmed by ‘pureshift’ yielded chirp excitation (PSYCHE) ^1H NMR spectroscopy (Figure 3.5b), are observed at 8.02, 7.99, 7.98 and 7.97 ppm respectively. Furthermore, the four overlapping cyclohexane peaks between 5.35–5.00 ppm (H^7) are four independent proton environments.

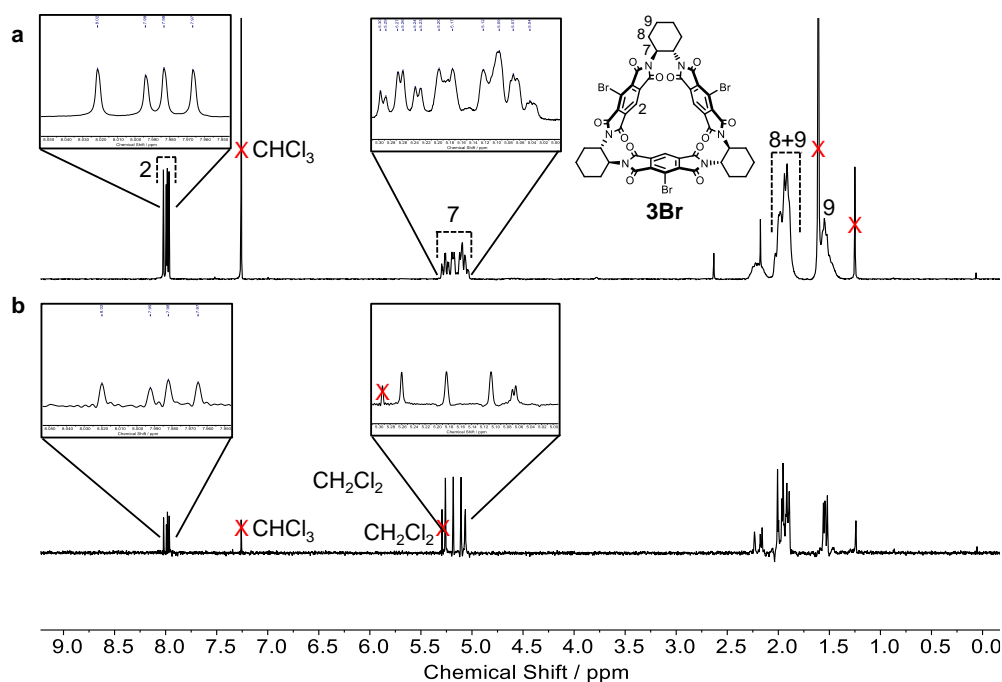


Figure 3.5 (a) ^1H NMR (400 MHz, CDCl_3 , 298 K) spectrum of **3Br** and (b) PSYCHE ^1H NMR (500 MHz, CDCl_3 , 298 K) spectrum of **3Br**.

The aromatic proton (H^2) (8.02–7.97 ppm) and cyclohexane proton (H^7) (5.30–5.00 ppm) regions integrate in a 1:2 ratio respectively which is the expected values for **3Br**. Therefore, it was conceivable that the additional proton peaks that were present in the ^1H NMR spectrum (Figure 3.5a) were due to the presence of a related macrocycle. Due to the 3D nature of molecular triangles, the substituents on the PMDI core face into opposite planes and thus this led to a hypothesis that **3Br** could exist as a mixture of *syn*-isomer, where either all three bromine atoms point into the same plane and *anti*-isomer, where two bromines point into the same plane with the third in the opposite direction (Figure 3.6). It was hypothesised that one of the aromatic proton environments represents the *syn*-isomer, with the other three environments representing the PMDI protons of the *anti*-isomer. As the four aromatic protons integrate to equal values, this would indicate a ratio of *syn:anti* of 1:3 in a solution of **3Br** in CDCl_3 .

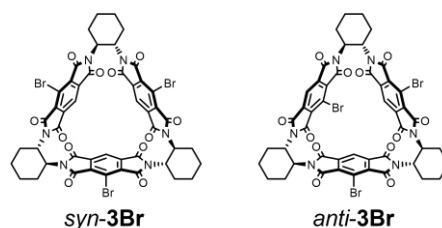
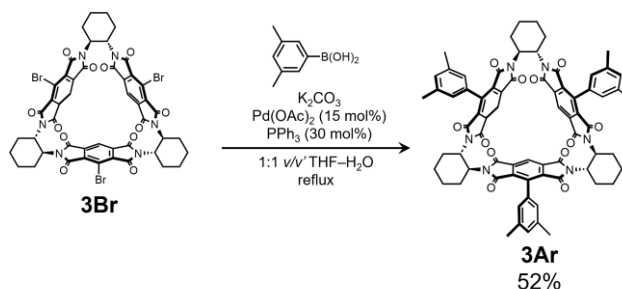


Figure 3.6 Structures of *syn*- and *anti*-**3Br**.

With the brominated molecular triangle in hand (possibly as a mixture of isomers) an analogous palladium catalysed Suzuki–Miyaura cross-coupling reaction as to that used to synthesise **6Ar** (Chapter 2) was completed between **3Br** and 3,5-dimethylbenzene boronic acid to form a tris-arylated macrocycle **3Ar** in a yield of 52% (Scheme 3.2). Macrocycle **3Ar** was isolated as a bright yellow solid following automated flash column chromatography (SiO_2 : 0–100% EtOAc in *n*-hexane) and

characterised using ^1H and ^{13}C NMR spectroscopy and APCI-MS (Supplementary Information, Sections 3.4.2 and 3.4.3).



Scheme 3.2 Synthesis of tris-aryl-substituted molecular triangle **3Ar** through a Suzuki-Miyaura coupling of 3,5-dimethylphenyl boronic acid with **3Br**.

The ^1H NMR spectrum of **3Ar** (Figure 3.7) is very similar to that of **6Ar** (Chapter 2) with the expected 3,5-dimethylphenyl proton environments in addition to the cyclohexane proton peaks for the molecular triangle backbone. Furthermore, analogous to the ^1H NMR spectrum for **3Br**, four aromatic proton environments are observed in the spectrum for **3Ar** (8.07, 8.05, 8.01 and 7.91 ppm), which indicates that the tris-arylated macrocycle could also exist as *syn*- and *anti*-isomers in solution. In contrast to **3Br**, in the ^1H NMR spectrum of **3Ar**, one of the aromatic proton environments is much more intense than the other three peaks, which would mean that the *syn*-isomer is the major component (81%) compared to the *anti*-conformer (19%). The proposed greater proportion of *syn*-**3Ar** (81%) in solution compared to the *anti*-isomer (19%) is the inverse of the ratio observed for *syn*- (25%) and *anti*-**3Br** (75%).

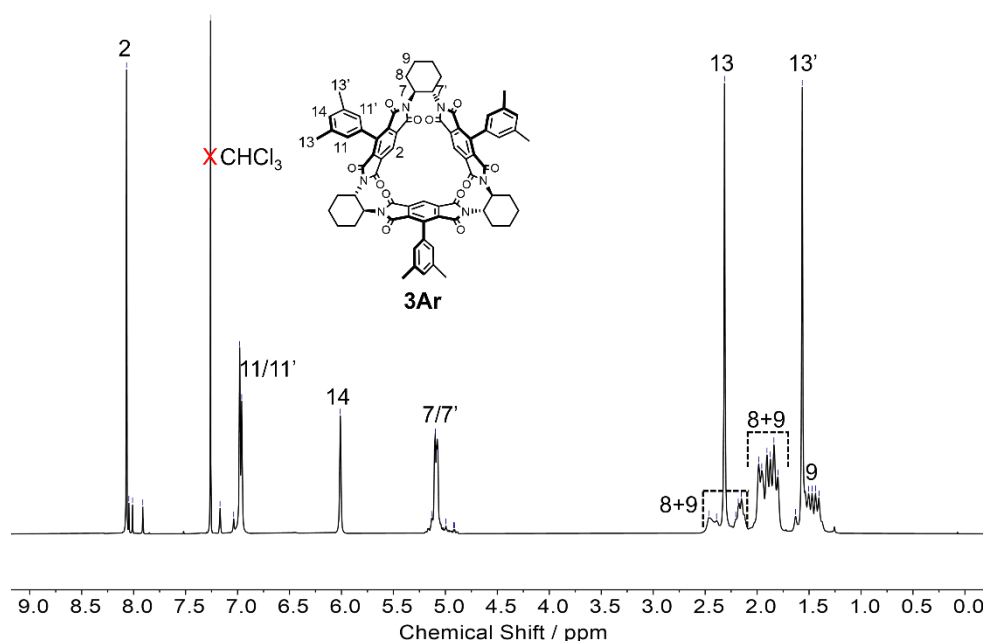


Figure 3.7 ^1H NMR (400 MHz, CDCl_3 , 298 K) spectrum of **3Ar**.

As discussed above, it was observed that **3Br** likely exists as a mixture of *syn*- and *anti*-isomers in solution through the observation of two macrocyclic species by ^1H NMR spectroscopy. This was confirmed to be the case in the solid state through X-ray diffraction of a single crystal grown by vapour diffusion of pentane into a solution of **3Br** in chloroform (Figure 3.8). In the crystal structure, two triangle molecules are present in the unit cell with both macrocycles containing disordered bromine atoms which is where the isomerisation occurs. One of the macrocycles contains a single disordered bromine atom which is present on either face of the molecular triangle throughout the single crystal. Furthermore, the remaining two bromine atoms that are not disordered are facing into opposite directions on the 3D macrocycle, which means that regardless of the position of the disordered bromine atom, this molecular triangle in the unit cell always exists as *anti*-**3Br** (Figure 3.8). Conversely, the second triangle molecule in the unit cell contains two disordered bromine atoms which can exist on either face of the macrocycle which means it is present as either the *syn*- (<10%) or *anti*-isomer (>90%) throughout the unit cell, where the % of each isomer has been calculated from the disorder in the diffraction pattern. The greater proportion of *anti*-**3Br** in the single crystal is consistent with the solution state data (^1H NMR spectroscopy) where the *syn*:*anti* ratio is 1:3.

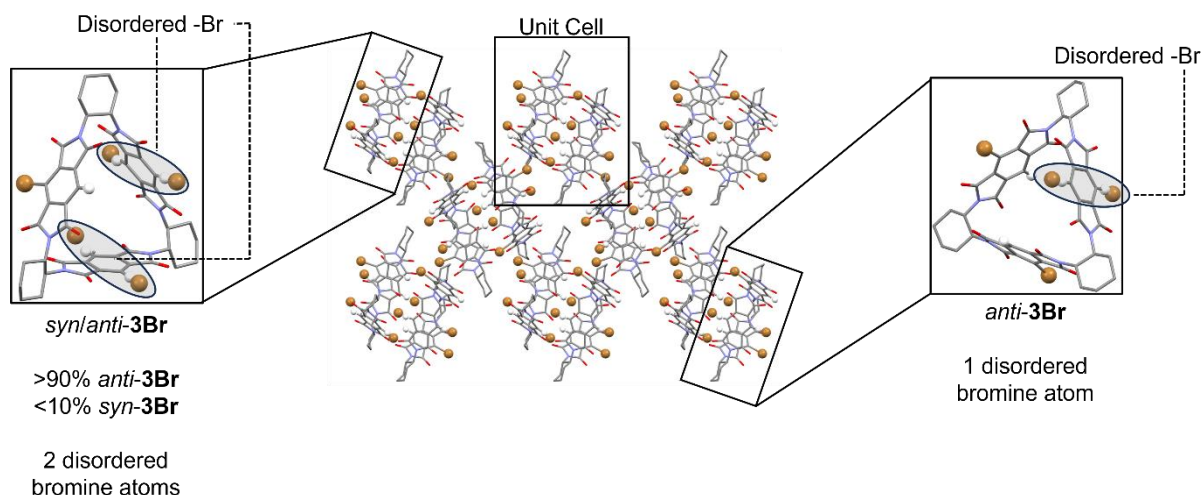


Figure 3.8 X-ray crystal structure of **3Br** showing supramolecular packing with two triangle molecules in unit cell. One triangle has two disordered bromine atoms that can exist as either *syn*- (<10%) or *anti*-**3Br** (>90%). The second triangle has one disordered bromine atom which exists as *anti*-**3Br** only. Cyclohexane hydrogen atoms omitted for clarity.

The structure of two polymorphs of tris-arylated molecular triangle **3Ar** were confirmed by X-ray diffraction of single crystals grown in either acetone (polymorph **3Ar**•2(CH₃)₂CO) or chloroform (polymorph **3Ar**•4CHCl₃, with two triangles in the unit cell **3Ar**•4CHCl₃ (1) and **3Ar**•4CHCl₃ (2)) (Figure 3.9). In both crystal structures, **3Ar** exists solely as the *syn*-isomer which is also consistent with the solution state data (^1H NMR spectroscopy) where the *syn*:*anti* ratio is 81:19. The preference for the *syn*-isomer in both solution and the solid state is surprising due to the steric hindrance and bulky nature of the 3,5-dimethylbenzene substituents. The aryl-groups on the PMDI core are twisted to minimise steric repulsion between the bulky substituents in the same manner as was observed for **6Ar** (Chapter 2). Furthermore, the position of the methyl groups on the aryl-substituents in *syn*-**3Ar** in the solid state

are pointing towards the benzene ring substituted on an adjacent PMDI unit in the same macrocycle (distances between 2.713–3.112 Å in the three triangle molecules across two crystal structures). Such intramolecular C-H $\cdots\pi$ interactions could be stabilising the sterically hindered structure of *syn*-**3Ar** as opposed to the *anti*-isomer. Furthermore, the presence of stabilising C-H $\cdots\pi$ interactions of one methyl group on each aryl substituent allowed for the respective CH₃ proton and carbon environments to be distinguished in the ¹H and ¹³C NMR spectra of *syn*-**3Ar** (Supplementary Information, Section 3.4.3, Figures S3.7–9). The donation of electron-density from the methyl group would deshield the protons and thus the CH₃ proton environment would be at a higher shift. Subsequent characterisation with ¹H-¹³C HSQC and HMBC 2D NMR spectroscopies allowed for the respective methyl carbon environments to be distinguished (Supplementary Information, Section 3.4.3, Figure S3.8 and S3.9).

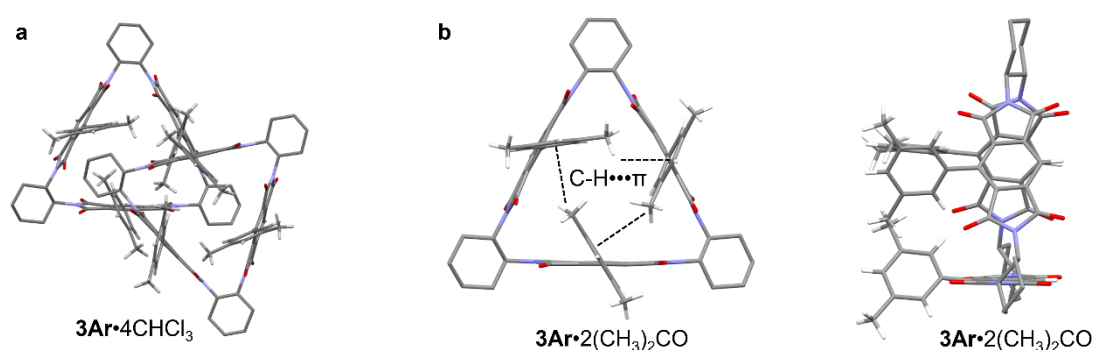


Figure 3.9 Unit cell of single crystal x-ray structures of (a) **3Ar•4CHCl₃** (two triangles in unit cell) and (b) **3Ar•2(CH₃)₂CO**, front view with C-H $\cdots\pi$ interactions shown and side view. Cyclohexane hydrogen atoms and solvent molecules have been omitted for clarity.

The structural parameters of tris-substituted molecular triangles, **3Br** and **3Ar** were also measured in the solid state to observe the effect of core-functionalisation on the distances and angles in the *syn*- and *anti*-macrocycles (Figure 3.10a). In the triangle molecules that exist as either *syn*- or *anti*-**3Br** in the single crystal unit cell (Figures 3.10b and c), the cavity distances within a macrocycle are quite variable (9.74, 9.55 and 9.34 Å, and 9.71, 9.60 and 9.54 Å for *syn/anti*-**3Br** and *anti*-**3Br** respectively). The angles between PMDI faces in a triangle molecule are all close to 60°, although the values are more variable in *anti*-**3Br** (61.9, 61.3 and 57.9°) than *syn/anti*-**3Br** (60.4, 59.4 and 60.5°). Furthermore, in both triangle molecules in the unit cell of **3Br**, the PMDI faces are bent (1.5–5.2°) where the greater bending angle is correlated with the larger cavity distances. In the structures of the three *syn*-**3Ar** triangle molecules in the solid state (**3Ar•2(CH₃)₂CO**, **3Ar•4CHCl₃** (1) and **3Ar•4CHCl₃** (2)) (Figures 3.10d–f) cavity distances of 9.60, 9.54 & 9.84 Å, 9.61, 9.53 & 9.61 Å and 9.69, 9.52 & 9.71 Å were observed. The larger of the three cavity distances is also correlated with a larger bend within PMDI units for *syn*-**3Ar**: 1.3–6.4°, 1.5–3.8° and 2.4–5.4° for **3Ar•2(CH₃)₂CO**, **3Ar•4CHCl₃** (1) and **3Ar•4CHCl₃** (2) respectively (Figures 3.10d–f). The dihedral angles (ϕ) between the 3,5-dimethylbenzene groups and PMDI faces in the three different macrocycles of **3Ar** are relatively similar 48.1–61.2°. Although in **3Ar•2(CH₃)₂CO** and **3Ar•4CHCl₃** the values are more consistent (54.1–57.6° and 52.8–57.1° respectively) with more variability in **3Ar•4CHCl₃** (2) (48.1–61.2°).

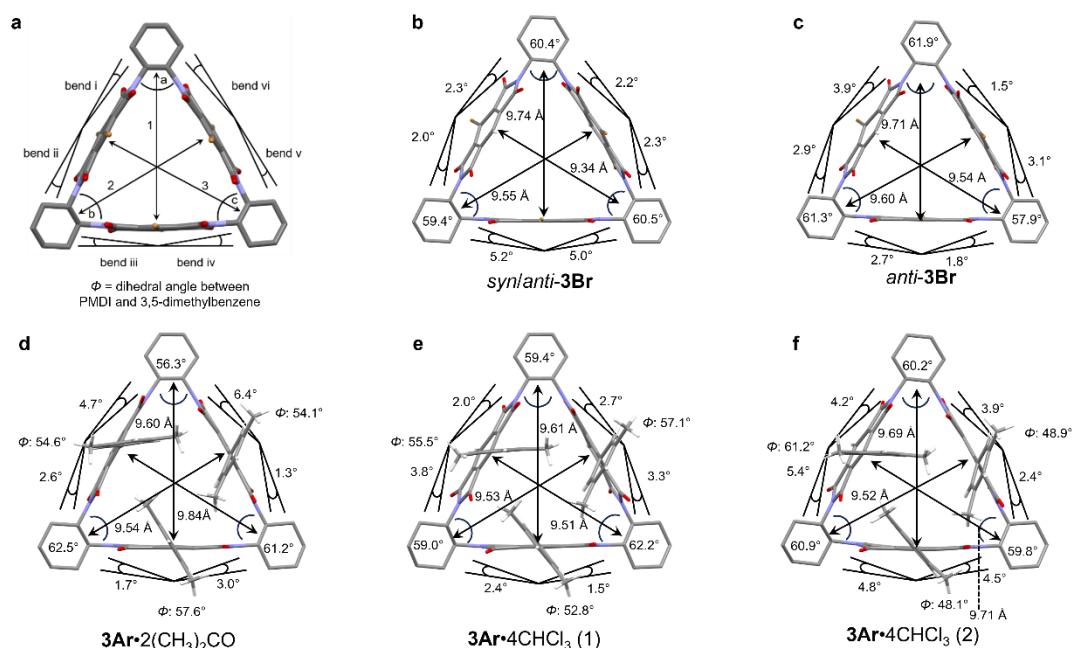


Figure 3.10 Crystal structures showing (a) structural parameters (distance, angle, bend and dihedral angle) for general macrocyclic structure for (b) *syn/anti-3Br*, (c) *anti-3Br*, (d) **3Ar•2(CH₃)₂CO**, (e) **3Ar•4CHCl₃ (1)** and (f) **3Ar•4CHCl₃ (2)**.

The structural parameters of *syn*- and *anti*-isomers of **3Br** and **3Ar** were also measured in geometry optimised macrocycles from DFT calculations at the B3LYP(D3-BJ)/def2svp level of theory in CH₂Cl₂ using the PCM model (Figure 3.11). The resulting measured distances and angles within each geometry optimised macrocycle are generally more consistent than the crystal structure data due to the absence of encapsulated or interacting solvent molecules that can influence the structure of the triangular geometry, which was also observed in the solid state and theoretical structural analyses conducted for **6H**, **6Br** and **6Ar** in Chapter 2. In the optimised structures of *syn*- and *anti-3Br* (Figures 3.11b and c) the cavity distances (9.54–9.58 Å), angles between PMDI faces (59.5–60.4°) and bends within individual PMDI units (0.7–1.2°) are consistent within each macrocycle and between each isomer. Conversely, more significant differences are observed between *syn*- and *anti-3Ar*. The structural parameters within *syn-3Ar* are consistent with its cavity distances (9.47–9.49 Å), angles (60.0–60.3°) and bends (2.0–4.0°) in a similar manner to *syn*- and *anti-3Br*. Whereas in *anti-3Ar*, the cavity distances and bends within PMDI faces are significantly more varied. Cavity distances of 9.05, 9.07 and 9.65 Å were measured along with pairs of bends of 5.5 and 5.9°, 0.8 and 4.0° and 3.6 and 0.0°. In a similar fashion to the solid-state structural parameters, a correlation is observed in the geometry optimised structures of *anti-3Ar*, where the shorter cavity distances (9.05 and 9.07 Å) are facing into PMDI units with lower bends (0.8 and 4.0° and 3.6 and 0.0°). The longer distance of 9.65 Å is therefore associated with the opposite PMDI face with increased bending, 5.5 and 5.9° respectively.

Furthermore, differences in the dihedral angles between PMDI faces and 3,5-dimethylbenzene substituents in the DFT calculated geometry optimised structures provides additional evidence for potential intramolecular C–H⋯π interactions. The three dihedral angles for *syn-3Ar* are relatively

similar (54.0, 53.3 and 52.5°) whereas the angles are more varied in *anti*-**3Br** (49.8, 57.7 and 62.3°). The similar dihedral angles in *syn*-**3Ar** could show that the three core-aryl substituents are all twisted to similar extents to minimise steric repulsion. It could also indicate that intramolecular CH $\cdots\pi$ interactions are three-way cooperative with the formation of three NCIs (average C-H $\cdots\pi$ distance = 2.71 Å). In *anti*-**3Br**, with only two 3,5-dimethylbenzene substituents on the same side of the macrocycle, only one C-H $\cdots\pi$ interaction (2.69 Å) can occur and therefore the absence of further interactions allows greater rotation to occur. The formation of three C-H $\cdots\pi$ interactions in *syn*-**3Ar** could stabilise the isomer with respect to *anti*-**3Ar** with the former isomer being 0.19 eV lower in energy and thus explain why *syn*-**3Ar** is the favoured conformation in the solution and solid states.

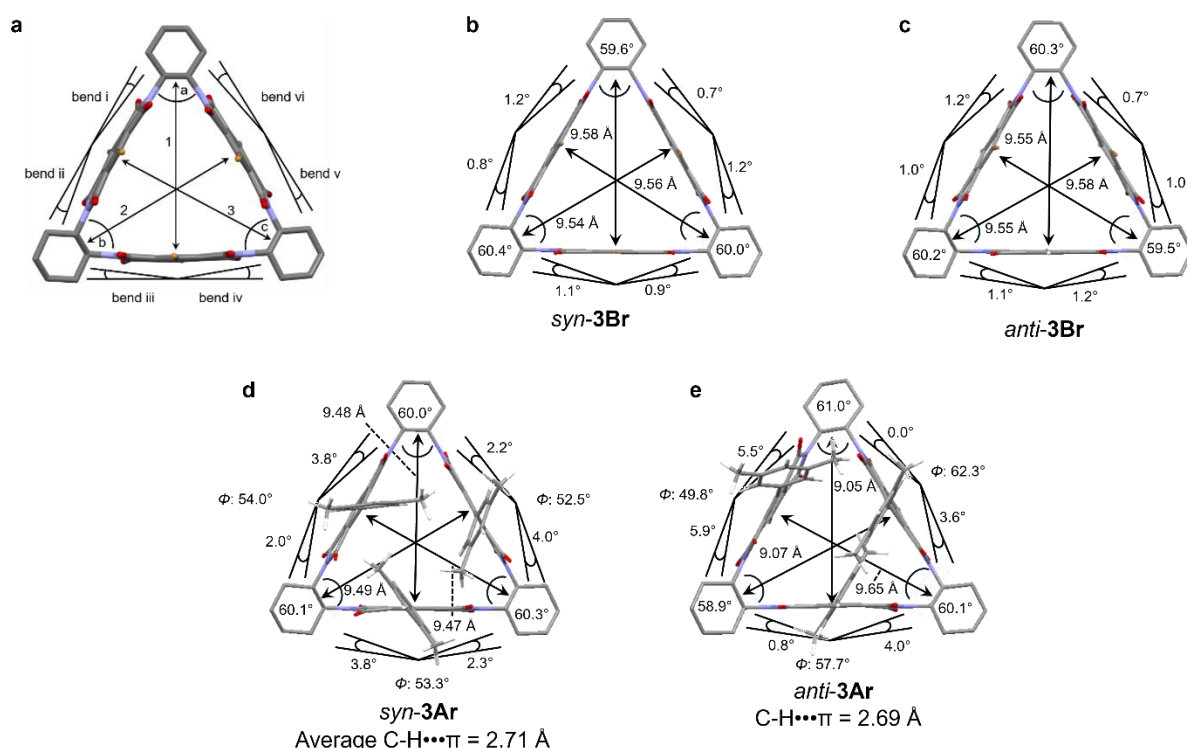


Figure 3.11 Geometry optimised DFT (DFT/B3LYP(D3-BJ)/def2svp/PCM(solvent = CH₂Cl₂) structures showing (a) structural parameters of general macrocyclic structure for (b) *syn*-**3Br**, (c) *anti*-**3Br**, (d) *syn*-**3Ar** and (e) *anti*-**3Ar**.

The completion of DFT calculations also allowed for the energy of the frontier molecular orbitals (FMOs) of *syn*-**3Br**, *anti*-**3Br**, *syn*-**3Ar** and *anti*-**3Ar** to be evaluated and compared to the unsubstituted macrocycle, **6H** (Chapter 2). The energies of the HOMO, HOMO–1, HOMO–2, LUMO, LUMO+1 and LUMO+2 were compared to observe any degeneracy in the energy levels (Figure 3.12). In *syn*- and *anti*-**3Br** (Figure 3.12a and b), the HOMO (–7.63 eV) is slightly destabilised and LUMO (–3.54 eV) stabilised compared to **6H** (HOMO: –7.70 eV and LUMO: –3.42 eV). However, the influence of tris-bromination on the HOMO and LUMO energies is not as significant as **6Br** (HOMO: –7.48 and LUMO: –3.65 eV). For *syn*/*anti*-**3Ar**, the HOMO (–6.47/–6.54 eV) and LUMO (–3.32/–3.34 eV) energies (Figure 3.12b and c), are destabilised with respect to **6H**, although not as significantly as in **6Ar** (–6.40 and –3.29 eV). These effects led to a narrowing of the band gap in *syn*/*anti*-**3Br** (4.09 eV)

and *syn/anti*-**3Ar** (3.15 and 3.20 eV) with respect to **6H** (4.28) eV, although less significantly compared with **6Br** (3.83 eV) and **6Ar** (3.11 eV) as discussed in Chapter 2.

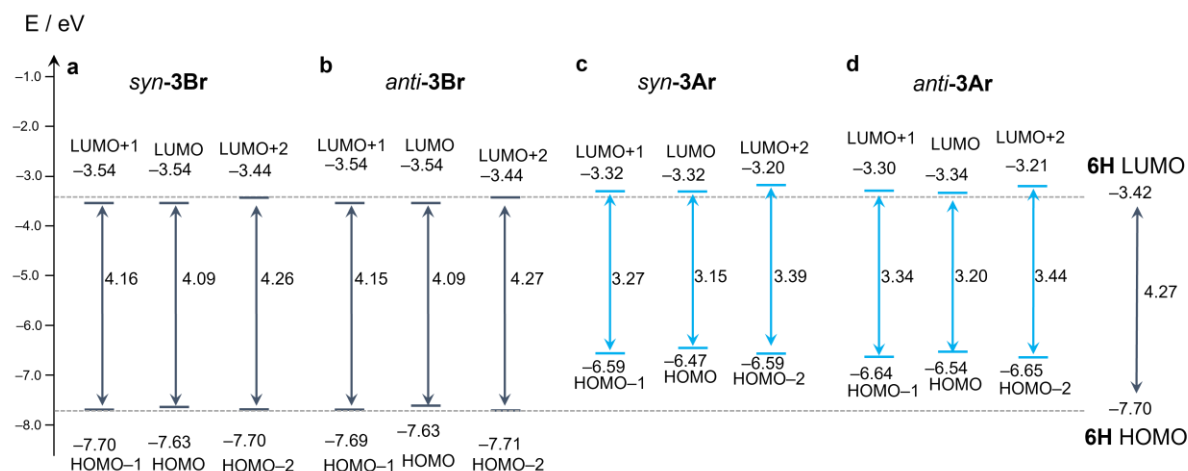


Figure 3.12 Energy levels of HOMO, HOMO–1, HOMO–2, LUMO, LUMO+1 and LUMO+2 from DFT calculations for (a) *syn*-**3Br**, (b) *anti*-**3Br**, (c) *syn*-**3Ar** and (d) *anti*-**3Ar**. Dashed line and additional arrow show data for **6H** for comparison. (B3LYP(D3-BJ)/def2svp/PCM (Solvent = CH₂Cl₂)).

In addition to influencing the energies of the FMOs and resulting bandgap in the same way as in **6Br** and **6Ar** (Chapter 2), tris-functionalisation of molecular triangles also affects the degeneracy of the HOMO and LUMO in *syn/anti*-**3Br** and *syn/anti*-**3Ar**. In **6H**, **6Br** and **6Ar**, the LUMO and LUMO+1 are doubly degenerate and the trend is observed in the same energy levels of *syn*-**3Br**, *anti*-**3Br** and *syn*-**3Ar**, whereas the LUMO and LUMO+1 are non-degenerate in *anti*-**3Ar**. In **6Br**, the HOMO–1 and HOMO–2 are degenerate and the same degeneracy is observed in the *syn*-isomers of **3Br** and **3Ar**. However, no such degeneracy is present in the HOMO, HOMO–1 and HOMO–2 of the *anti*-isomers of **3Br** and **3Ar** which is the same as for **6Ar** (Chapter 2). The loss of degeneracy of the HOMO and HOMO–1 energy levels from the *syn*- to *anti*-isomer of the tris-substituted molecular triangles could be due to the loss of rotational symmetry in the macrocycle.

The visual depictions of the FMOs for the *syn/anti*-isomers of **3Br** and **3Ar** (Supplementary Information, Figures S3.42 and S3.43) are analogous to those shown for core-functionalised molecular triangles **6Br** and **6Ar** (Chapter 2) where in the LUMOs, electron density is situated on the PMDI macrocycle backbone and in the HOMOs, electron density resides on the core-substituents (bromine atoms and 3,5-dimethylbenzene groups) and macrocycle core. Aromatic homoconjugation is also observed in the degenerate, asymmetric LUMOs of *syn/anti*-isomers of **3Br** and **3Ar** which provides evidence that core-functionalisation does not impact the presence of through-space electronic communication in molecular triangles.

Experimental values of the band gap of the mixtures of isomers (*syn-/anti*-) of **3Br** (3.43 eV) and **3Ar** (2.90 eV) were determined from absorption spectra of the molecular triangles in THF which agrees with the computational data that tris-functionalisation narrows the band gap compared with **6H** although not

as significantly as the analogous hexa-substituted macrocycles, **6Br** and **6Ar**. Concentration-dependent UV-vis studies of **3Br** and **3Ar** in CH₂Cl₂ were conducted (Supplementary Information, Figures S3.37 and S3.38) to determine the extinction coefficient, ϵ , with **3Ar** absorbing more light at the λ_{max} in solution ($\epsilon = 32,000 \text{ M}^{-1} \text{ cm}^{-1}$) compared to **3Br** ($\epsilon = 7550 \text{ M}^{-1} \text{ cm}^{-1}$). These results follow the trend observed between **6Br** and **6Ar** (Chapter 2), that with core-functionalisation of molecular triangles, symmetry selection rules for the electronic transitions are relaxed allowing for greater absorption of light at the λ_{max} .

The absorption spectra of the tris-functionalised molecular triangles (**3Br** and **3Ar**) are similar to their hexa-substituted analogues (**6Br** and **6Ar**, Chapter 2). As expected for absorption profiles of aromatic diimides, π – π^* transitions are present for **3Br** (325–350 nm) and **3Ar** (385–395 nm) are present in CHCl₃, DMF and THF, along with an additional smaller wavelength π – π^* transition (290–310 nm) in the spectrum of the tris-arylated macrocycle (**3Ar**). A red shift of absorption peaks with respect to the electronic transitions of the unsubstituted macrocycle **6H** upon tris-functionalisation is observed, however it occurs to a lesser extent compared with the hexa-substituted macrocycles (Chapter 2) due to fewer number of electron-donating and -withdrawing aryl groups and bromine atoms respectively. Furthermore, the decreased vibronic fine structure of the spectra for **3Ar** represents greater ability for rotation and vibration of the aryl core-substituents in the rigid, shape-persistent molecular triangles.

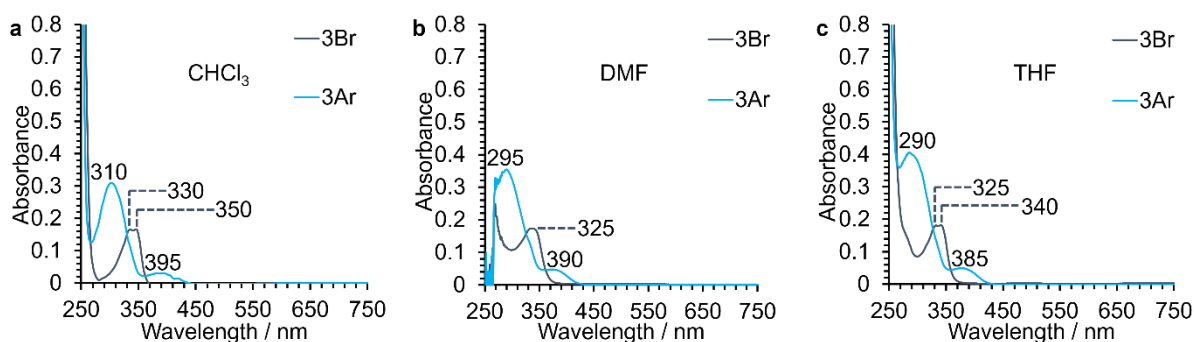


Figure 3.13 UV-vis spectra of **3Br** and **3Ar** (25 μM) in (a) CHCl₃, (b) DMF and (c) THF.

Experimental values for the LUMO energies for **3Br** and **3Ar** were also estimated from cyclic voltammograms of *syn/anti*-isomers of the macrocycles in THF (Figure 3.14a). Energy values of the experimental values for the LUMO of **3Br** and **3Ar** of -3.81 and -3.86 eV show a stabilisation compared with the experimental value for **6H** (-3.65 eV). The stabilisation of the LUMO is expected upon tris-bromination, although the effect is less significant than in **6Br** ($E_{\text{LUMO}} = -3.94$ eV). The stabilisation of the LUMO (-3.86 eV) upon the introduction of three electron-rich 3,5-dimethylbenzene groups is unexpected and is in conflict with the theoretical energy values. The tris-arylated molecular triangle is expected to be electron-rich and subsequently destabilising the LUMO as was modelled in the DFT calculations ($E_{\text{LUMO}} = -3.33$ eV) and seen in the hexa-arylated macrocycle **6Ar** (Chapter 2). Full comparison of the experimental and theoretically calculated energies and optical data can be found in Table 3.1.

In both cyclic and differential pulse voltammograms of **3Br** and **3Ar** (Figure 3.14a and b) the reduction peaks are split into multiple accessible redox-states due to cyclic aromatic homoconjugation around the tris-substituted molecular triangle in the same way as for **6H**, **6Br** and **6Ar** discussed in Chapter 2. These results provide evidence that tris-functionalisation of molecular triangles does not influence the ability of electrons to be delocalised around the macrocycle as was also seen in the visual depictions of the LUMO (Figure S3.42 and Figure S3.43).

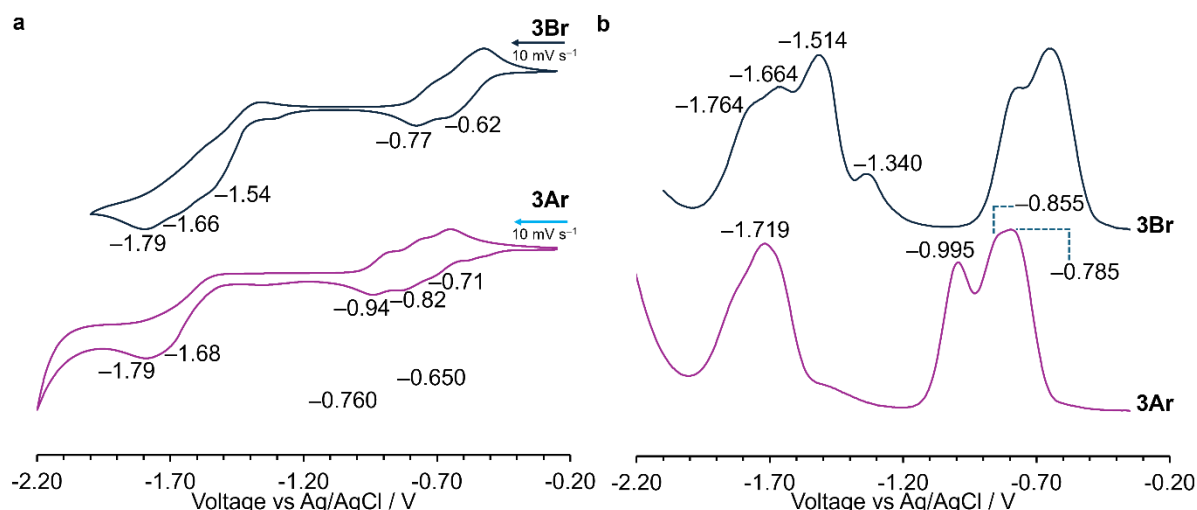


Figure 3.14 (a) CV and (b) DPV of **3Br** and **3Ar** in anhydrous, degassed THF (1 mM) with TBAPF₆ (0.1 M) as supporting electrolyte.

Table 3.1 Experimental and theoretical values from UV-vis spectroscopy, cyclic voltammetry and DFT calculations for molecular triangles **6H**, **3Br**, **6Br**, **3Ar** and **6Ar**.

	6H	3Br^h	6Br	3Ar^h	6Ar
^a λ_{max} / nm	320	344	368	299	302
^b ϵ / M ⁻¹ cm ⁻¹	5830	7550	10700	32000	35600
^c $E_{\text{g,opt}}$ / eV	3.68	3.43	3.25	2.90	2.76
^d $E_{1/2}$ / V	-0.72	-0.57	-0.42	-0.68	-0.78
^e E_{LUMO} (CV) / eV	-3.65	-3.81	-3.94	-3.86	-3.60
^f E_{HOMO} (Exp) / eV	-7.33	-7.24	-7.19	-6.76	-6.36
^g E_{LUMO} (DFT) / eV	-3.42	-3.54	-3.65	-3.33	-3.29
^g E_{HOMO} (DFT) / eV	-7.70	-7.63	-7.48	-6.51	-6.40
^g $E_{\text{g,DFT}}$ / eV	4.28	4.09	3.83	3.18	3.11

^aWavelength of maximum absorption in CH₂Cl₂. ^bMolar absorption coefficient in CH₂Cl₂ calculated at the λ_{max} . ^cOptical bandgap measured through onset wavelength of lowest energy transition in UV-vis spectrum of compound in THF. ^dHalf wave potential of first reductions of compounds in THF. ^eThe LUMO energy level was calculated from the onset of the first reduction potential in CV, using the equation $E_{\text{LUMO}} = [-e[E_{\text{onset, red}} - 0.50 + 4.8]]$ eV, where the oxidation potential of Fc/Fc⁺ against Ag/AgCl in THF with TBAPF₆ was found to be 0.50 V and 4.8 eV is the energy level of ferrocene below the vacuum level. ^f $E_{\text{HOMO}} = E_{\text{LUMO}} - E_{\text{g,opt}}$. ^gValues from DFT calculations (B3LYP(D3-BJ)/def2svp/PCM(solvent = CH₂Cl₂)). ^hAverage values from theoretical values for *syn*- and *anti*-isomer of **3Br** and **3Ar**.

The reduced states of **3Br**, *i.e.* the tris-radical anion ([**3Br**]^{3•-}) and hexa-anion ([**3Br**]⁶⁻), were formed after reduction with decamethylcobaltocene (CoCp*₂) and studied by UV-vis spectroscopy with the presence of free radicals confirmed by electron paramagnetic resonance (EPR) spectroscopy (Figure

3.15). The resulting absorption spectra upon titration of 0–3 equivalents of CoCp^*_2 revealed a pair of resolved red-shifted peaks at 650 and 695 nm, with the presence of free radicals confirmed by EPR spectroscopy indicating the reduction of **3Br** to $[\mathbf{3Br}]^{3\cdot-}$. Subsequent addition of an excess of CoCp^*_2 (>10 equiv.) led to the previously formed peaks to decrease in intensity and a new broad peak at 545 nm to be generated.

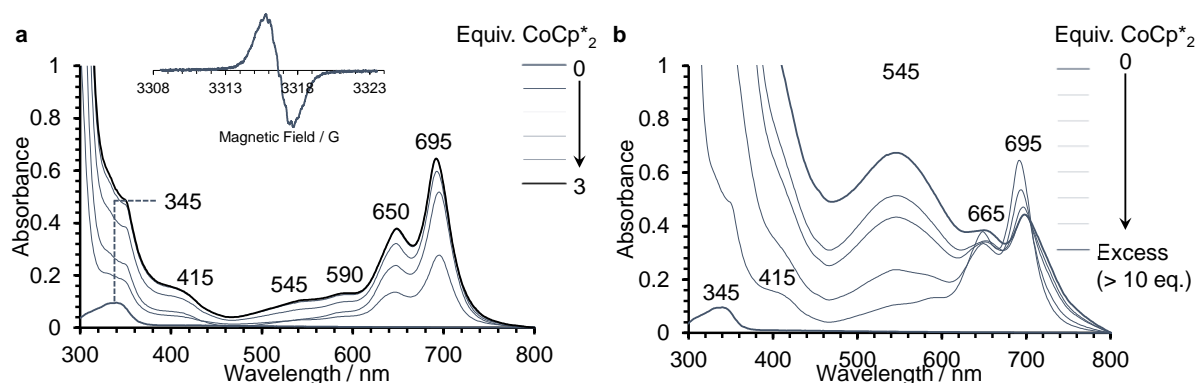


Figure 3.15 UV-vis spectra of reduced states of (a) **3Br** (0–3 eq. CoCp^*_2) and (b) **3Br** (0–>10 eq. CoCp^*_2) generated by chemical reduction with CoCp^*_2 in DMF. Inset: EPR spectra of tris-radical anion of (a) **3Br**.

The behaviour of **3Br** under reducing conditions (CoCp^*_2) is similar to **6H** and **6Br** (Chapter 2), with the absorption peaks representing $[\mathbf{3Br}]^{3\cdot-}$ (650 and 695 nm) being red-shifted with respect to the neutral state, to longer wavelengths than for $[\mathbf{6Br}]^{3\cdot-}$ (640 and 680 nm) but not to as long wavelengths as $[\mathbf{6H}]^{3\cdot-}$ (665 and 710 nm). Furthermore, upon subsequent reduction, from the tris-radical anion ($[\mathbf{3Br}]^{3\cdot-}$) to the hexa-anion $[\mathbf{3Br}]^{6-}$, the absorption peaks are blue-shifted to form a broad peak at 545 nm which is similar to the wavelengths for $[\mathbf{6H}]^{6-}$ (545 nm) and $[\mathbf{6Br}]^{6-}$ (550 nm).

3.2.2 DYNAMIC ATROPISOMERISM OF TRIS-SUBSTITUTED MOLECULAR TRIANGLES

In Section 3.2.1, it was hypothesised that **3Br** and **3Ar** existed as a mixture of *syn*- and *anti*-isomers in solution (^1H NMR spectroscopy) with both isomers of **3Br** also present in the solid state (X-ray diffraction). Due to the chiral nature of the (*R,R*) or (*S,S*)-*trans*-1,2-diaminocyclohexane linkers the two isomers of **3Br** might have different chiroptical properties including circularly polarised luminescence for use in OLEDs.⁴³ To be able to investigate the potential property differences between *syn*- and *anti*-**3Br**, attempts to separate the isomers by automatic flash chromatography and chiral HPLC were performed, albeit unsuccessfully. The inseparable nature of *syn*- and *anti*-**3Br** led to a hypothesis that the isomers could interconvert *via* rotation of a BrPMDI side-unit at room temperature – so called atropisomerism.

The potential rotation between *syn*- and *anti*-isomers of **3Br** was investigated using variable-temperature ^1H and ^1H - ^1H EXSY NMR spectroscopy ($\text{DMSO}-d_6$) (Figure 3.16). In $\text{DMSO}-d_6$ the ratio of *syn*:*anti* atropisomers of **3Br** are 23:77 (25 °C) and 13:37 (80 °C) which differs slightly to the ratio of 1:3 in CDCl_3 (80 °C). At temperatures above 80 °C the aromatic protons (7.92–7.81 ppm)

on the BrPMDI core begin to broaden and coalesce to one peak at 140 °C (Figure 3.16a, full spectrum in Supplementary Information, Section 3.4.5.1, Figure S3.18). The coalescence of aromatic proton environments indicates that rotation occurs at a rate faster than the NMR timescale and thus an average of the two species is observed. ^1H - ^1H EXSY NMR spectroscopy experiments at 80 °C were conducted to further confirm the interconversion between *syn*- and *anti*-**3Br**. The 2D experiments were completed at 80 °C as the four proton environments are still separate and visible but the rotation is still likely to occur more easily and thus exchange be observed in the EXSY NMR spectrum. Indeed, the 2D ^1H - ^1H EXSY NMR spectrum for **3Br** with a mixing time of 200 ms shows cross-peaks between the *syn*-proton and the three proton environments for the *anti*-isomer (Figure 3.16b).

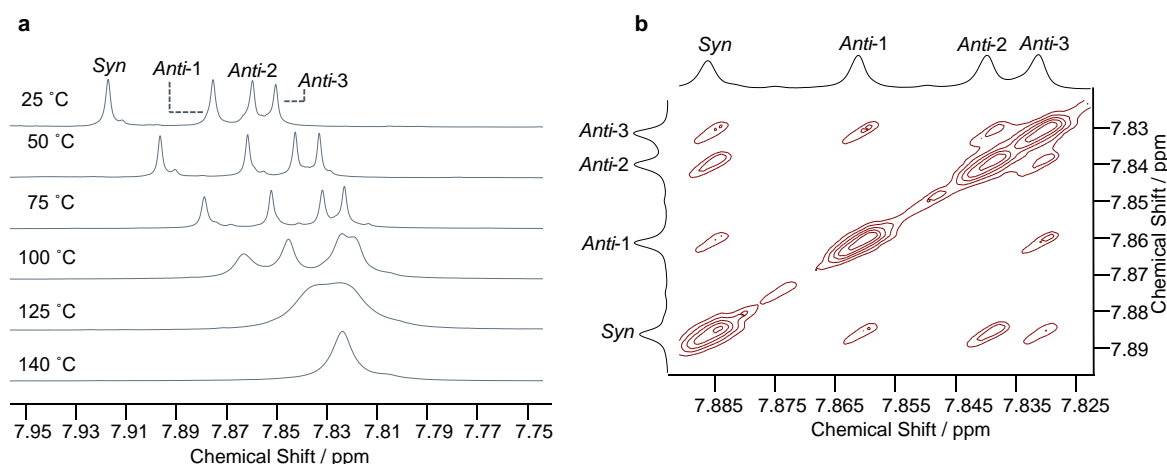


Figure 3.16 (a) Variable temperature ^1H NMR (600 MHz, $\text{DMSO-}d_6$, 25–140 °C) spectra and (b) ^1H - ^1H EXSY NMR (600 MHz, $\text{DMSO-}d_6$, 80 °C, mixing time = 200 ms) spectrum to study the atropisomerism of **3Br**.

Exchange peaks were also observed between *anti*-1 & *anti*-3 and *anti*-2 & *anti*-3 proton environments, with the notable absence of exchange between *anti*-1 & *anti*-2 protons. A graphical representation was used to represent the exchange between *syn*-**3Br** and different forms of *anti*-**3Br** to assist in the understanding and explanation for the absence of exchange between the *anti*-1 & *anti*-2 proton peaks. For example, in Figure 3.17, assume that white and blue circles represent a proton facing away and towards the plane of the triangle respectively. Considering the interconversion of a blue circle to a white circle as represented by the two *anti*-**3Br** representations at the top of the figure, this new white circle does not change its relationship within the macrocycle. *i.e.*, it still sees a white and blue circle. On the other hand, the already existing white circle is now surrounded by two blue circles (as opposed to a white and blue circle) and *vice versa* for the non-interconverting blue circle. Therefore, as the proton that has changed its direction (blue to white) does not change its environment, therefore one exchange peak will be absent. Whereas the other two circles, and thus proton environments, change their environment and thus exchange occurs with the presence of an exchange peak in the ^1H - ^1H EXSY NMR spectrum.

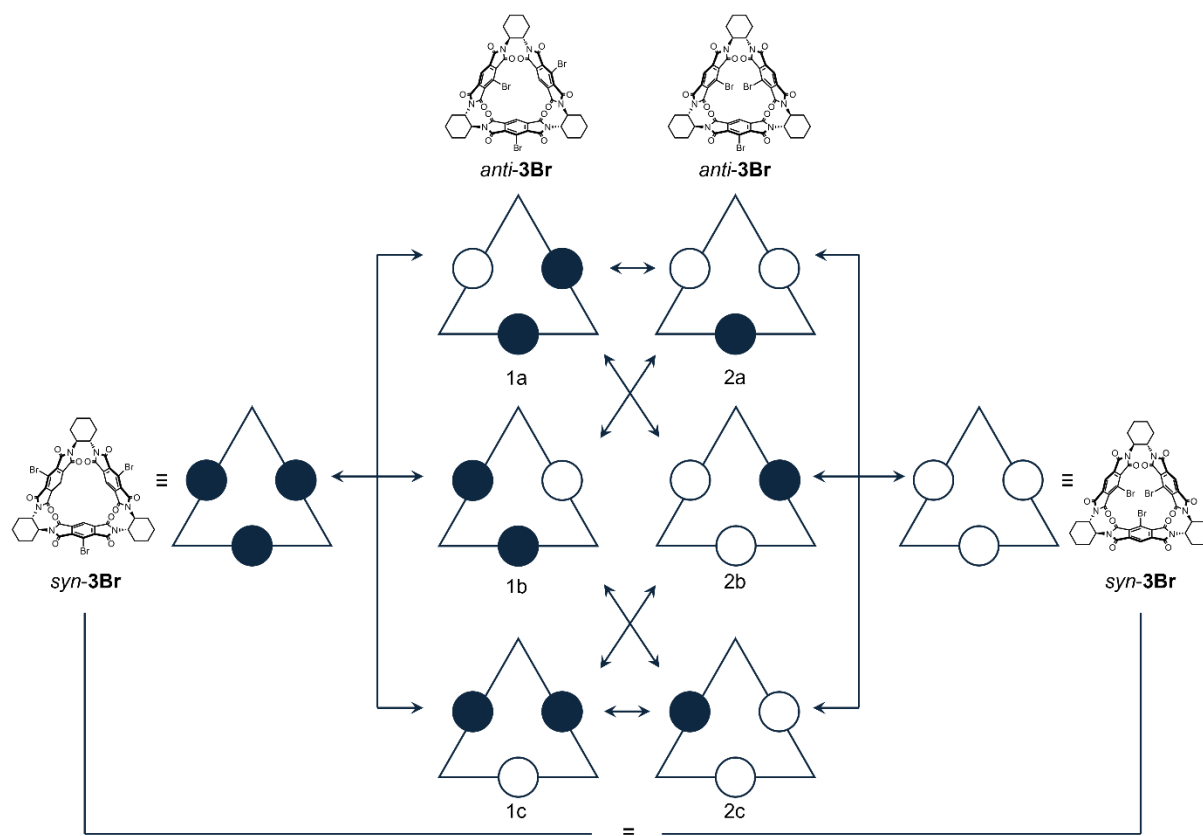


Figure 3.17 Representation of the interconversion between different forms of *syn-3Br* and *anti-3Br*.

^1H - ^1H EXSY NMR spectroscopy (Supplementary Information, Section 3.4.5.2, Figure S3.21) experiments were performed at a range of mixing times, with the cross and diagonal peaks in the resulting spectra integrated. The peak intensity ratio, r' was subsequently calculated and further manipulated with the mole fractions of the *syn*- and *anti*-isomers to give a value r which has a linear relationship with the mixing time.⁴⁴ Using the average exchange rate, the Gibbs energy of the transition state (ΔG^\ddagger), the half-life at 80 °C and the exchange rate and half-life at 25 °C were calculated, Table 3.2. Full details on the method and equations to calculation the exchange rate and other energetic and kinetic values are provided in the Supplementary Information, Section 3.4.5.2. The resulting calculated short half-life of atropisomers of **3Br** at room temperature, $96.3 \pm 1.6 \text{ s}^{-1}$, explains why it was not possible to separate the *syn*- and *anti*-isomers by column chromatography or HPLC as the two forms are readily interconverting on the minutes timescale.

Table 3.2 Kinetic and energetic values related to exchange rate calculated from the experimental data for **3Br**.

	3Br
Exchange rate (k_r) (80 °C) / s^{-1}	1.81 ± 0.03
Gibbs energy of transition state (ΔG^\ddagger) / kcal mol^{-1}	20.4 ± 0.3
Half-life ($t_{1/2}$) (80 °C) / s	0.383 ± 0.006
Exchange rate (k_r) (25 °C) / s^{-1}	0.00720 ± 0.00012
Half-life ($t_{1/2}$) (25 °C) / s	96.3 ± 1.6

The experimental energy barrier to rotation calculated *via* ^1H - ^1H EXSY NMR spectroscopy, 20.4 ± 0.3 kcal mol $^{-1}$, has been corroborated by transition state (TS) quantum chemical calculations (DFT/B3LYP(D3-BJ)/def2svp/ PCM (Solvent = CH $_2$ Cl $_2$). The atropisomerism of **3Br** was modelled, with the rotation between *syn*- and *anti*-isomers *via* two potential pathways where either the bromine or hydrogen atoms enter the cavity (Figure 3.18). As hypothesised, the TS calculations show that the initial barrier to rotation of BrPMDI units arise from the steric hinderance between carbonyl groups on adjacent PMDI faces. After the first transition state (TS1, Figure 3.18), an intermediate is reached where either the -Br or H-substituent is pointing directly into the cavity after a total 90° rotation (**Br-int** or **H-int**). Further rotation to the opposite atropisomer goes *via* a second transition state (TS2) due to further steric repulsion of diimide carbonyls. It was hypothesised that the large van der Waals radius of the bromine atom would hinder the rotation pathway *via* **Br-int** compared with the smaller hydrogen atom, **H-int**. Surprisingly, the IRC calculation indicates that the rotation containing an intra-annular bromine atom is energetically favourable compared to the intra-annular hydrogen rotation (18.3 and 22.2 kcal mol $^{-1}$ respectively). Therefore, there must be a favourable intramolecular halogen $\cdots\pi$ interaction in the transition state between the bromine substituent and the electron-deficient cavity of the macrocycle.

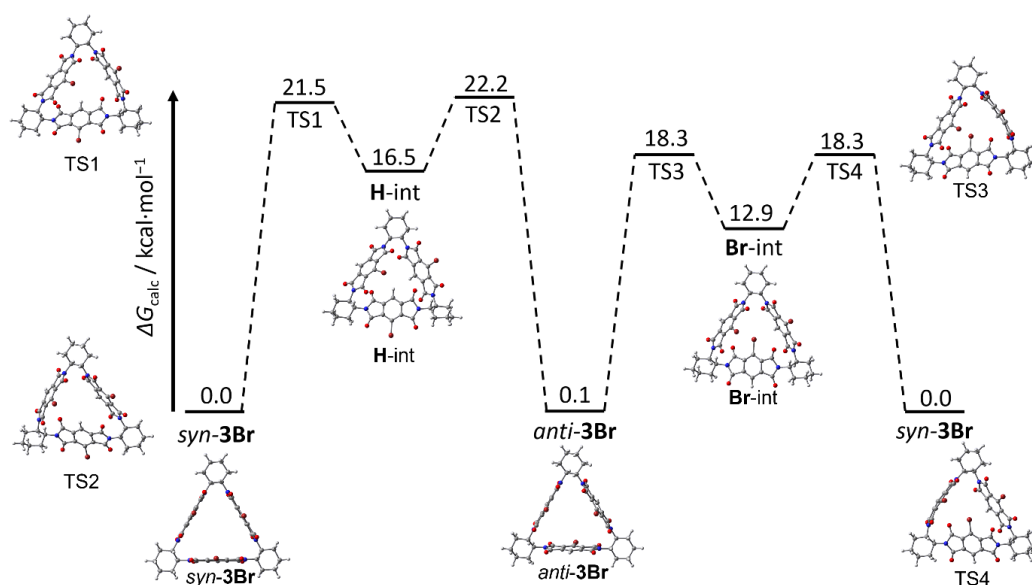


Figure 3.18 Internal Reaction Coordinate (IRC) DFT calculations (B3LYP(GD3BJ)/def2SVP/CH $_2$ Cl $_2$) modelling the rotation of a single BrPMDI unit from the *syn*-isomer to the *anti*-isomer and back to the *syn*-isomer *via* intra-annular hydrogen and intra-annular bromine intermediates.

This enhancement of rotation *via* an intramolecular halogen $\cdots\pi$ mediated pathway compared to the mechanism with an intra-annular hydrogen atom is significant because of the approximately 0.7 Å difference in van der Waals radius of the core-substituent atoms (H and Br).⁴⁵ Intuition of steric repulsion of functional groups led to the initial expectation that the intra-annular hydrogen pathway would be favoured on account of the reduced size of the atom. Thus, the average stabilisation of the transition state of 3.6 kcal mol $^{-1}$ (~14.9 kJ mol $^{-1}$) from the intra-annular bromine pathway was

unexpected. The potential stabilisation from halogen $\cdots\pi$ interactions in core-brominated molecular triangles (~ 14.9 kJ mol $^{-1}$) is greater than that observed in molecular balances of 7.9 kJ mol $^{-1}$ for bromine $\cdots\pi$ (from benzene) interactions.¹⁵ The stabilisation in the system from DFT calculations is around 1.9 times greater the previously reported values which could be due to the presence of two adjacent electron-deficient PMDI π -surfaces for Br $\cdots\pi$ interactions to occur in the transition state. Halogen $\cdots\pi$ interactions in the ground state have been shown to favour the least sterically hindered interaction, *e.g.* -H over -X or -X over -CH₃.¹⁴ This halogen $\cdots\pi$ mediated rotation in brominated molecular triangles allows for a comparison with that of enzymes in nature where similar interactions have been shown to play an important role for substrate selectivity with enzymes in drug discovery.⁴⁶ In the induced-fit binding model, enzymes are thought to undergo structural changes in their quaternary structure to enhance the binding of a substrate. This process is allowed to occur through the precise order of amino acids in the sequencing of the protein. In the computational modelling of the atropisomerism of **3Br**, a bending and rotation of the adjacent PMDI-unit to avoid electronic repulsion of carbonyl groups is observed to allow the bromine-substituent to enter the cavity. This remarkable adaptation and structural flexibility of the rigid, shape-persistent molecular triangles as well as the favourable interactions between the bromine substituent and the π -surface could be manipulated and utilised in the future as a synthetic mimic to enzymes and proteins.

To confirm the presence of the favourable intramolecular halogen $\cdots\pi$ mediated pathway in **3Br**, variable temperature ^1H and ^1H - ^1H EXSY NMR spectroscopy experiments were performed for **3Ar**. It was hypothesised that in the absence of a core-substituted bromine atom, rotation between *syn*-**3Ar** and *anti*-**3Ar** will be slower, as in the presence of the bulky 3,5-dimethylbenzene core-substituent, the rotation would only go *via* the **H-int** intermediate due to the large size of the aromatic group not being able to enter the cavity of the macrocycle.

As discussed in Section 3.2.1, room temperature ^1H NMR spectroscopy of **3Ar** revealed that the *syn*-isomer was preferred (81:19) compared with **3Br** where the *anti*-form was greater in proportion (*syn:anti* ratio 1:3) in CDCl₃. Indeed, as expected higher temperatures were required to observe broadening and merging of aromatic proton environments in the ^1H NMR spectrum (Figure 3.19a) compared with **3Br**, with full coalescence of **3Ar** aromatic protons not achieved at the maximum temperature of 140 °C in DMSO-*d*₆. ^1H - ^1H EXSY NMR spectroscopy (Figure 3.19b) was used to confirm interconversion of the *syn*- and *anti*-isomers through the exchange of proton environments. In DMSO-*d*₆, the order of *syn*- and *anti*-proton environments for **3Ar** in the aromatic region is different to **3Br**. However, the same proton exchanges are observed between the *syn*-environment with all three *anti*-environments and between two *anti*-environments (*anti*-1 and *anti*-2) in the same manner as for *syn*- and *anti*-**3Br** (Figure 3.16). Furthermore, in DMSO-*d*₆ the *syn:anti* ratio of atropisomers is 14:11 (25 °C) and 9:11 (80 °C) which is different to ratio of 81:19 in CDCl₃ (25 °C).

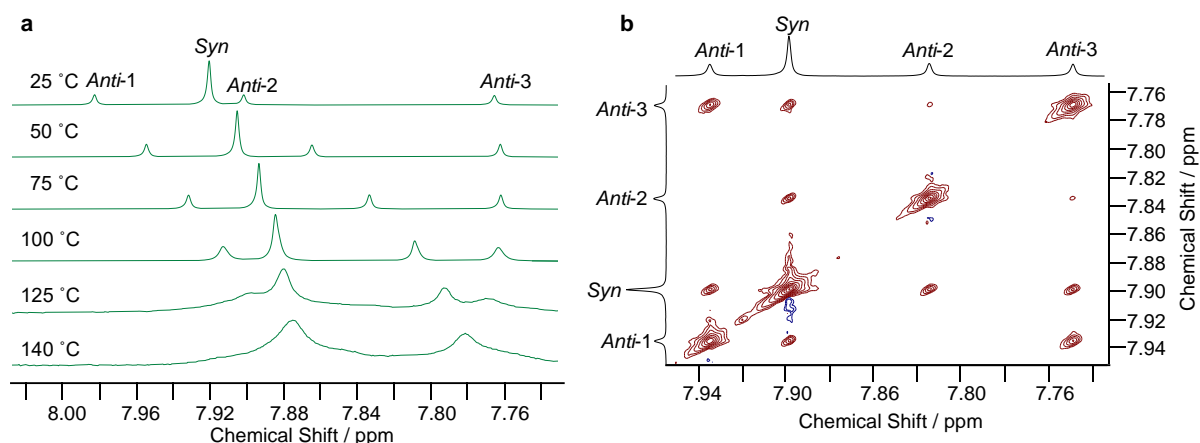


Figure 3.19 (a) Variable temperature ¹H NMR (600 MHz, DMSO-*d*₆, 25–140 °C) spectra and (b) ¹H-¹H EXSY NMR (600 MHz, DMSO-*d*₆, 80 °C, mixing time = 200 ms) spectrum to study the atropisomerism of **3Ar**.

In a similar manner to **3Br**, ¹H-¹H EXSY NMR spectroscopy experiments were repeated at a range of mixing times for **3Ar**, (Supplementary Information, Section 3.4.5.2, Figure S3.22), to calculate the average exchange rate, k_r , Gibbs energy, ΔG^\ddagger and half-life, $t_{1/2}$ (Table 3.3). The exchange rate at 80 °C for **3Ar** ($0.560 \pm 0.015 \text{ s}^{-1}$) is more than three times less than that for **3Br** ($1.81 \pm 0.03 \text{ s}^{-1}$), although this only accounts for a 0.8 kcal mol⁻¹ difference in transition state energy barrier, 21.2 ± 0.6 and 20.4 ± 0.3 kcal mol⁻¹ for **3Ar** and **3Br** respectively. These experimental values for the transition state energy barrier lie within the DFT calculated values for the hydrogen and bromine rotational pathways (Figure 3.18). The experimental value for the energy barrier for **3Br** could be greater than the calculated value experimentally as it is feasible for the rotation to go *via* either pathway especially at elevated temperatures (80 °C) and thus is an average of the two rotations *via* **Br**-int and **H**-int. However, as **3Ar** can only go *via* the intra-annular hydrogen route the experimental value (21.2 ± 0.6 kcal mol⁻¹) should be closer to the DFT calculated value. Despite this inaccuracy, the corresponding exchange rate and half-lives for rotation at room temperature (25 °C) for both **3Br** and **3Ar** show that isomers are interconverting at the minutes time scale which explains why separation of atropisomers has not been possible. LaPlante *et al.*⁴⁷ developed a qualitative guide and classification system to categorise potential pharmaceutical candidates that exist as atropisomers based on the torsion rotation energy barrier and thus rotation half-life to further understand their chirality and pharmacological properties. Using the LaPlante categorisation both **3Br** and **3Ar** would be labelled as ‘Class 2’ atropisomers based on an energy barrier of around 20 kcal mol⁻¹ and half-lives on the minutes timescale at room temperature.⁴⁷

Table 3.3 Kinetic and energetic values related to exchange rate calculated from the experimental data for **3Ar** and compared with **3Br**.

	3Ar	3Br
Exchange rate (k_r) (353 K) / s ⁻¹	0.560 ± 0.015	1.81 ± 0.03
Gibbs energy of transition state (ΔG^\ddagger) / kcal mol ⁻¹	21.2 ± 0.6	20.4 ± 0.3
Half-life (353 K)	1.24 ± 0.03	0.383 ± 0.006
Exchange rate (k_r) (298 K) / s ⁻¹	0.00179 ± 0.00005	0.00720 ± 0.00012
Half-life (298 K) / s	387 ± 10	96.3 ± 1.6

To provide further evidence that the atropisomerism in tris-brominated molecular triangles is catalysed by an intramolecular halogen $\cdots\pi$ interaction in the intermediate, further control experiments were completed using the hexa-substituted molecular triangles. We were able to take advantage of the presence of two diimide carbonyl environments (3 & 3') in the ^{13}C NMR spectra of molecular triangles, **6H**, **6Br** and **6Ar**, which occurs as a result of the 3D chiral nature of the macrocycles with the C=O bonds pointing in opposite planes as discussed in Chapter 2. Therefore, the rotation of the symmetric X_2PMDI -units (X = H, Br or Aryl group) were studied using ^{13}C - ^{13}C EXSY NMR spectroscopy, in order to observe exchange between the two carbonyl peaks (3 and 3'). The use of ^{13}C nuclei for the EXSY measurements added some extra complexity compared with using ^1H because of its low natural abundance and low receptivity thus requiring more scans and longer experiment times. Furthermore, carbonyls are known to have long T1 relaxation times and EXSY NMR spectroscopy experiments are required to have a delay at least five times longer than the T1 time. Therefore, the T1 relaxation times for the carbonyl peaks in **6H**, **6Br** and **6Ar** were required to be measured prior to the ^{13}C - ^{13}C EXSY measurements, (Supplementary Information, Section 3.4.5.3, Figures S3.24–26.). With the T1 relaxation times for the three symmetric macrocycles, **6H**, **6Br** and **6Ar**, calculated, ^{13}C - ^{13}C EXSY NMR spectroscopy experiments were conducted at 80 °C at a range of mixing times (Supplementary Information, Section 3.4.5.4, Figures S3.27–29), to compare the ratio of integrations of cross and diagonal peaks to assess the difference in rate of rotation between the three molecular triangles.

As expected, for **6Ar**, no cross-peaks are present in the EXSY spectrum at 80 °C, thus with no exchange of carbonyl environments, these experiments confirm that no rotation occurs due to the presence of large, bulky 3,5-dimethylbenzene core-substituents (Supplementary Information, Section 3.4.5.4, Figure S3.29). ^{13}C - ^{13}C EXSY NMR spectroscopy experiments at a range of mixing times for **6H**, display some exchange of carbonyl environments at 80 °C, whereas **6Br** showed more significant exchange with the cross peaks, (Supplementary Information, Section 3.4.5.4, Figures S3.27 and S3.28). Table 3.4 shows the ratio of the integrations of the diagonal and cross exchange peaks for **6H**, **6Br** and **6Ar** from the ^{13}C - ^{13}C EXSY NMR spectroscopy experiments at a range of mixing times. As would be expected, where there is exchange (**6H** and **6Br**) the proportion of cross exchange peaks increases with longer mixing time due to more time for rotation to occur. Whereas for **6Ar** no exchange peaks were observed and thus no rotation is occurring. Confirming the results seen by ^1H - ^1H EXSY NMR spectroscopy experiments for **3Br**, the hexa-brominated molecular triangle, **6Br** showed a greater proportion of cross peaks (smaller value in diagonal peak integration divided by cross peak integrations) compared with **6H**. These results show qualitatively that the rate of rotation in hexa-substituted molecular triangles goes in the order **6Br** > **6H** > **6Ar**. Quantitative evaluation of the ratio into an exchange rate and other kinetic parameters was completed for **6Br** where a linear relationship with mixing time is observed (Supplementary Information, Section 3.4.5.4, Figure S3.30), to give a rotation rate of $9.5 \pm 1.9 \text{ s}^{-1}$ at 80 °C and thus an energy barrier, ΔG^\ddagger , of $19 \pm 4 \text{ kcal mol}^{-1}$. Large errors are

present in both the exchange rate and energy barrier which is understandable given the nature of the ^{13}C - ^{13}C EXSY NMR spectroscopy experiments which leads to a qualitative interpretation of the results only compared with **6H** and **6Ar**. These qualitative results further confirm the conclusion from the ^1H - ^1H EXSY NMR spectroscopy results for **3Br** and **3Ar** that the presence of core-substituent bromine atoms enhance the rate of rotation in shape-persistent rigid macrocycles.

Table 3.4 Values of diagonal peak integration divided by cross peak integration from ^{13}C - ^{13}C EXSY NMR spectroscopy experiments for **6H**, **6Br** and **6Ar** at different mixing times 100, 125, 150, 175 and 200 ms.

Mixing Time / ms	6H	6Br	6Ar
100	77.02	16.39	No exchange
125	22.35 ^a	5.84	No exchange
150	49.38	5.37	No exchange
175	36.88	3.18	No exchange
200	Not Measured	1.91	Not Measured

^aProbable Outlier

3.2.3 HOST-GUEST COMPLEXATION OF MOLECULAR TRIANGLES

In Section 3.2.2, the influence of an intramolecular halogen $\cdots\pi$ interaction on the dynamic atropisomerism of the tris-brominated molecular triangle, **3Br** was discussed. Therefore, intermolecular halogen $\cdots\pi$ interactions were also investigated *via* host–guest chemistry (host–guest UV-vis spectroscopy and NMR spectroscopy titrations) between core-functionalised molecular triangles, (**6H**, **3Br**, **6Br**, **3Ar** and **6Ar**) and the electron-rich triiodide anion. Stoddart and coworkers³⁹ showed that the NDI based molecular triangle, **10**, discussed in Chapter 1, was able to form host–guest complexes with I_3^- through favourable anion $\cdots\pi$ interactions between the electron-rich guest and electron-deficient macrocycle with a binding constant of $25 \pm 2 \text{ M}^{-1}$ in CD_2Cl_2 determined by ^1H NMR spectroscopy. Therefore, it was hypothesised that the more electron-deficient **6Br**, **3Br** and **6H** molecular triangles would be more likely to form host–guest complexes compared to the more electron-rich **3Ar** and **6Ar**.

A single crystal of a host–guest complex of **6H** with the triiodide anion was obtained by the slow evaporation of diethyl ether into a chloroform solution of molecular triangle with tetrabutylammonium triiodide (1:7 ratio of **6H**: I_3^-). Despite using a seven-fold excess of guest, a relatively high proportion of free host and guest were observed in the unit cell of the crystal, one free **6H** macrocycle, five free I_3^- molecules, six tetrabutylammonium cation molecules and one host–guest complex, **6H** $\supset\text{I}_3^-$ (Figure 3.20a and b). Conversely, 1:1 host–guest complexes between **6Br** and $\text{TBA}\cdot\text{I}_3$ formed more readily upon vapour diffusion of diisopropylether into a 1:1.6 molar ratio solution of host and guest in chloroform, with two **6Br** $\supset\text{I}_3^-$ complexes present in the unit cell of the resulting crystal structure (Figure 3.20c and d). The large tetrabutylammonium cations are non-interacting with the molecular triangles and relatively separated from the triiodide counter-anions.

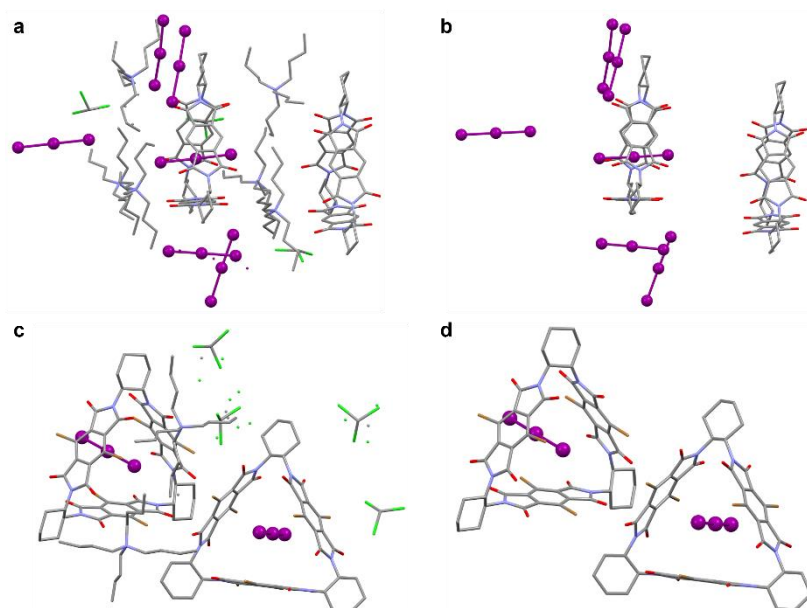


Figure 3.20 Unit cells of crystal structures containing host–guest complexes of molecular triangles with a triiodide anion for $2(\mathbf{6H}) \cdot 6(\text{I}_3^-) \cdot 6((\text{C}_4\text{H}_9)_4\text{N}^+) \cdot 3\text{CHCl}_3$ (a) with and (b) without solvent molecules and tetrabutylammonium cations and $2(\mathbf{6Br}) \cdot 2(\text{I}_3^-) \cdot 2((\text{C}_4\text{H}_9)_4\text{N}^+) \cdot 4\text{CHCl}_3$ (c) with and (d) without solvent molecules and tetrabutylammonium cations. Hydrogen atoms have been removed for clarity.

When observing the structural parameters of molecular triangles with and without encapsulated I_3^- (Figure 3.21), considerable bending is observed in Br_2PMDI units of $\mathbf{6Br} \supset \text{I}_3^-$ between the central benzene ring and the two 5-membered rings containing the diimides. In the unit cell of the host–guest complex between $\mathbf{6Br}$ and I_3^- , two complexes are present: $\mathbf{6Br} \supset \text{I}_3^-$ (1) and $\mathbf{6Br} \supset \text{I}_3^-$ (2), with both containing one face bent more considerably than the others, 7.6° & 7.6° and 5.1° & 6.0° respectively. It is hypothesised that the significant bending occurs to maximise anion $\cdots\pi$ interactions which consequently increases the cavity distance to 10.14 \AA and 9.90 \AA from the bent PMDI unit to the opposite cyclohexane linker for $\mathbf{6Br} \supset \text{I}_3^-$ (1) and $\mathbf{6Br} \supset \text{I}_3^-$ (2) respectively. Furthermore, the angle of the vertex between the other two, less bent PMDI units decreases upon the puckering of the opposite face (55.6° and 57.3° for $\mathbf{6Br} \supset \text{I}_3^-$ (1) and $\mathbf{6Br} \supset \text{I}_3^-$ (2) respectively). Conversely, despite one of the $\mathbf{6H}$ molecules in the unit cell encapsulating a triiodide anion ($\mathbf{6H} \supset \text{I}_3^-$), there is no significant difference in its structural properties compared with the free $\mathbf{6H}$ macrocycle. The similar cavity distances, angles and bends between $\mathbf{6H}$ and $\mathbf{6H} \supset \text{I}_3^-$ could indicate that non-covalent interactions between the anion and macrocycle are not occurring. Whereas the change in structure of the rigid, shape-persistent macrocycle upon complexation of I_3^- with $\mathbf{6Br}$ ($\mathbf{6Br} \supset \text{I}_3^-$ (1) and $\mathbf{6Br} \supset \text{I}_3^-$ (2)) compared with the free molecular triangle provides evidence that anion $\cdots\pi$ interactions could form between the electron-rich guest and electron-deficient host. In the host-guest complexes of $\mathbf{6Br}$ with I_3^- ($\mathbf{6Br} \supset \text{I}_3^-$ (1) and $\mathbf{6Br} \supset \text{I}_3^-$ (2)), a partially negatively charged terminal iodine⁴⁸ atoms sits in the centre of the macrocycle with the other two iodine atoms pointing out of the molecular triangle which could indicate that an interaction is occurring. Conversely, in $\mathbf{6H} \supset \text{I}_3^-$ the central iodine atom of the linear I_3^- chain sits in the centre of the cavity which could provide evidence for the absence of a NCI.

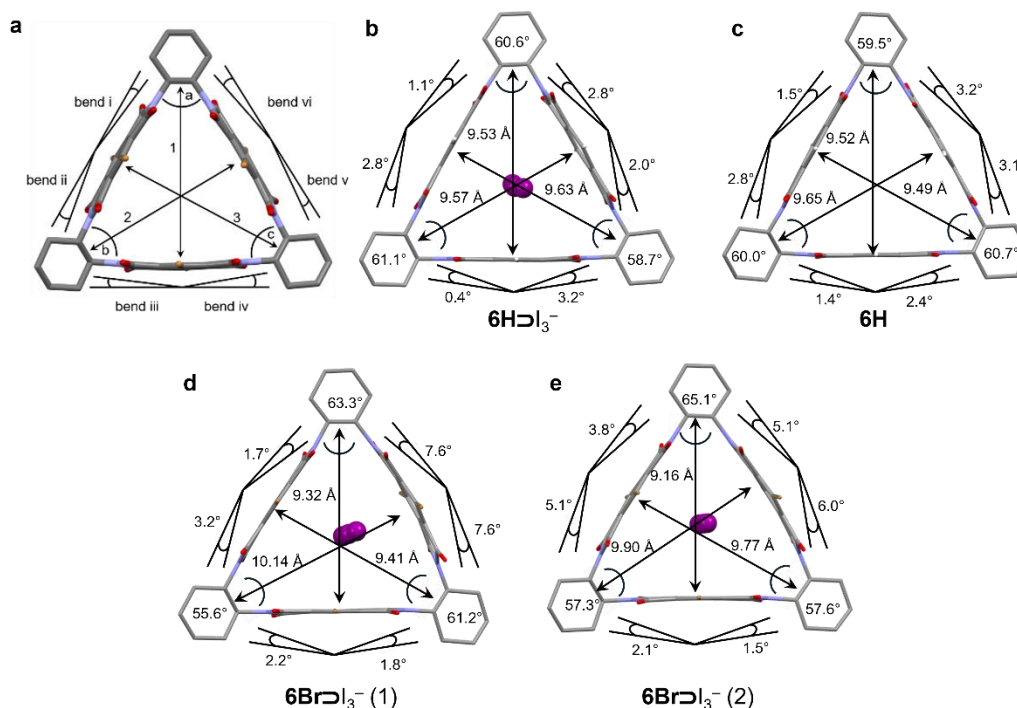


Figure 3.21 Molecular triangle molecules from host-guest crystal structures showing (a) structural parameters (distance, angle, bend and dihedral angle) for general macrocyclic structure for (b) $6\text{H}\supset\text{I}_3^-$, (c) 6H , (d) $6\text{Br}\supset\text{I}_3^-$ (1) and (e) $6\text{Br}\supset\text{I}_3^-$ (2). Cyclohexane hydrogen atoms have been omitted for clarity.

With the proof-of-concept of host–guest complexation of core-functionalised molecular triangles with the electron-rich I_3^- achieved, experiments to calculate the binding constants in solution were completed. Initially, UV-vis spectroscopy titrations of molecular triangles, 6H , 3Br and 6Br , with $\text{TBA}\cdot\text{I}_3$ in CH_2Cl_2 were attempted to quantify the change in wavelength of the $\pi\text{-}\pi^*$ transitions which could then be used find the binding constant (Supplementary Information, Section 3.4.6.2, Figures S3.39–41). Unfortunately, high intensity and broad absorption peaks at 297 and 365 nm were observed for $\text{TBA}\cdot\text{I}_3$ which overlapped with the peaks representing $\pi\text{-}\pi^*$ transitions at 310 and 320 nm, 334 and 344 nm and 354 and 370 nm for 6H , 3Br and 6Br respectively. The observed dark red colour observed upon dissolution of $\text{TBA}\cdot\text{I}_3$ in CH_2Cl_2 with absorption peaks at 297 and 365 nm is characteristic of the triiodide anion.⁴⁸ The dissociation of I_3^- to I_2 and I^- does occur in equilibrium, with an association constant of 600 M^{-1} favouring the polyiodide component.⁴⁹

As UV-vis spectroscopy titrations could not be used to monitor the binding of I_3^- with core-functionalised molecular triangles, NMR spectroscopy was used instead where the host–guest titrant solutions contained an excess of $\text{TBA}\cdot\text{I}_3$, so that the effect of the presence of I_2 and I^- were negligible.⁴⁹ For molecular triangles, 6H , 3Br and 3Ar , host–guest titrations were completed by monitoring the change in shift of the PMDI aromatic protons through ^1H NMR spectroscopy (Supplementary Information, Section 3.4.5.5, Figures S3.31–33). These protons were selected as these will be most influenced upon any anion $\cdots\pi$ interactions between I_3^- and the aromatic PMDI core. Upon increasing the guest I_3^- concentration, the signal ($\delta_{\text{H}} = 8.03\text{ ppm}$), associated with the PMDI proton of 6H , experienced an upfield shift to signify a binding interaction (presumed to be the formation of the

6H• I_3^- inclusion complex). However, upon addition of up to 250 equivalents of guest, the change in shift had not plateaued indicating that saturation of the host–guest complex had not been reached (Figure 3.22a). In the host–guest titrations for tris-functionalised molecular triangles, **3Br** and **3Ar**, aromatic proton peaks representing both *syn*- and *anti*-isomers were monitored by 1H NMR spectroscopy. A similar trend to that of **6H** was observed for both **3Br** and **3Ar** with an upfield shift of signals indicating host–guest inclusion complex formation. Although even with the presence of around 250 equivalents of guest, the change in shifts of the proton environments for both **3Br** and **3Ar** had not plateaued, again indicating that saturation of the host–guest complex had not been achieved (Figures 3.22.b and c). The results that host–guest complex saturation in solution was not reached for **6H**, **3Br** or **3Ar** indicates weak binding between the triiodide anion with these molecular triangles.

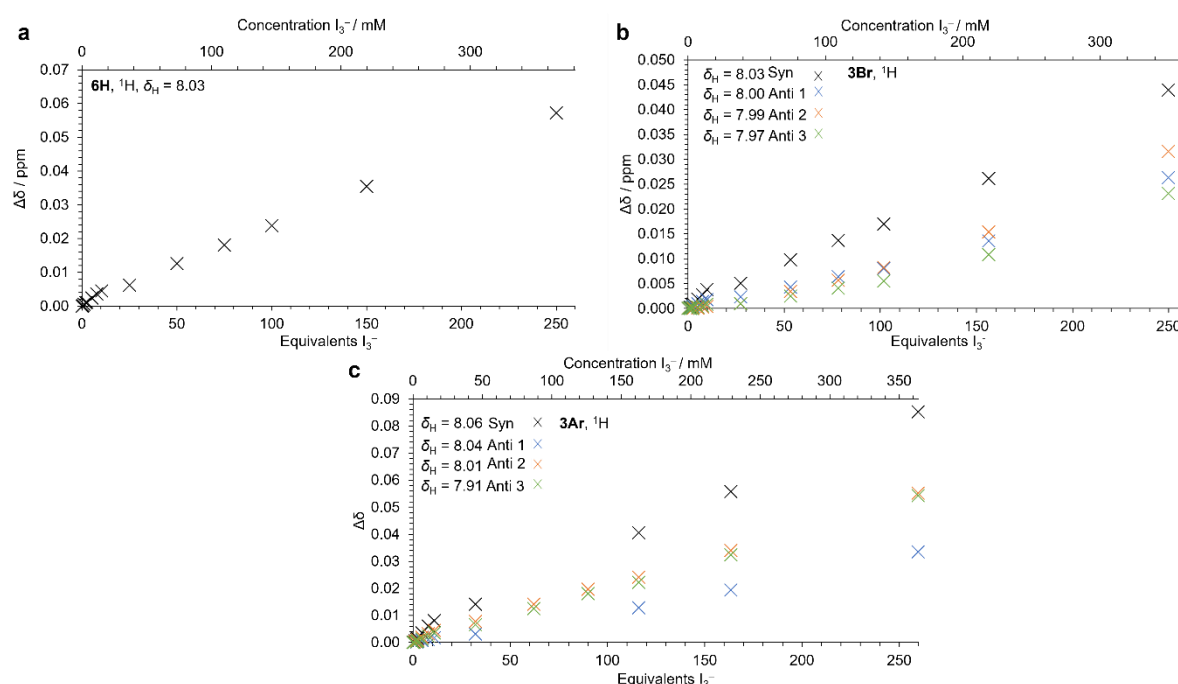


Figure 3.22 Graphs showing the change in shift of diagnostic protons vs equivalents/concentration of TBA• I_3 from 1H NMR (500 MHz, $CDCl_3$, 298 K) spectroscopy host–guest titrations for (a) **6H**, (b) **3Br** and (c) **3Ar**.

The hexa-substituted molecular triangles, **6Br** and **6Ar**, do not have any available PMDI protons to monitor by 1H NMR spectroscopy due to saturation of the aromatic core. Therefore, ^{13}C NMR spectroscopy was used to measure the binding between molecular triangle and guest with the change in shift of the carbon environment adjacent to the core-substituent monitored in the presence of increasing equivalents I_3^- guest (0–114 eq.) (Supplementary Information, Section 3.4.5.5, Figures S3.34–36). The host–guest behaviour of **6Ar** was similar to that of **6H**, **3Br** and **3Ar**, in that a plateau in the change of shift ($\delta_C = 129.9$ ppm) with increasing equivalents of guest was not achieved, indicating that saturation of the concentration of host–guest complex was not reached and thus the triiodide anion interacted weakly with the hexa-arylated macrocycle (Figure 3.23). Such a weak interaction between **6Ar** and I_3^- is not unexpected on account of the increased electron-density of the π -surface in the cavity from the

electron-donating 3,5-dimethylbenzene substituents. Binding constants are not given for **6H**, **3Br**, **3Ar** or **6Ar** as saturation of the host–guest complex was not achieved in the NMR spectroscopy titrations.

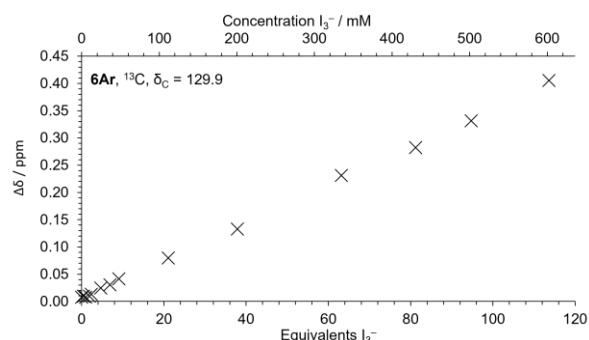


Figure 3.23 Graph showing the change in shift of diagnostic carbon vs equivalents/concentration of TBA•I₃ from ¹³C NMR (126 MHz, CDCl₃, 298 K) spectroscopy host guest titrations for **6Ar**.

Although molecular triangles **6H**, **3Br**, **3Ar** and **6Ar** exhibited weak binding with I₃[−], a more significant change in shift of the PMDI carbon ($\delta_{\text{C}} = 114.7$ ppm) for **6Br** was observed by ¹³C NMR spectroscopy host–guest titrations with the electron-rich triiodide anion. Upon increasing the concentration of the guest (I₃[−]) to 50 equivalents with respect to **6Br**, the downfield shift of the carbon signal reached a plateau, indicating that saturation of the host–guest complex, **6Br**⊃I₃[−], was achieved (Figure 3.24). Two host–guest titrations were completed for **6Br** so that an average association constant (K_{a}) could be calculated using the simulation software Bindfit.⁵⁰ For each trial (run 1 and run 2), two binding models were used modelling a 1:1 stoichiometry of host:guest, Nelder-Mead and L-BFGS-B and both models provided the same association constant and error within the respective runs, Table 3.5.

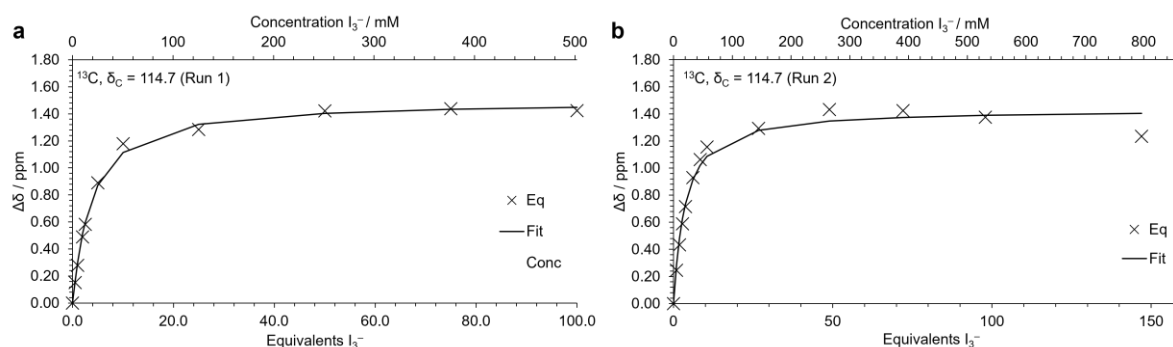


Figure 3.24 Graphs showing the change in shift of diagnostic carbons vs equivalents/concentration of TBA•I₃ from ¹³C NMR (126 MHz, CDCl₃, 298 K) spectroscopy host–guest titrations for **6Br** with (a) Run 1 and (b) Run 2. The graphs show experimental data points and a binding isotherm from a simulated binding model using Bindfit software.^{50–52}

Table 3.5 Association constants and error for ¹³C NMR host–guest titrations of **6Br** with I₃[−] using different fitting models and an average across two runs and two methods.

	Association Constant (K_{a}) / M ^{−1}
Run 1 – Nelder-Mead	63 ± 7
Run 1 – L-BFGS-B	63 ± 7
Run 2 – Nelder-Mead	59 ± 11
Run 2 – L-BFGS-B	59 ± 11
Average	61 ± 5

The calculated average binding constant, K_a for **6Br** with I_3^- , $61 \pm 5 \text{ M}^{-1}$ is greater than the literature value for NDI based molecular triangle **10** reported by Stoddart and coworkers in 2013, $25 \pm 2 \text{ M}^{-1}$.³⁹ These results indicate that although the unsubstituted PMDI molecular triangle **6H** binds weakly with I_3^- compared with the larger NDI macrocycle **10** on account of the decreased surface area of the electron-deficient aromatic cavity. However, with the introduction of six electron-withdrawing bromine atoms to the aromatic core of the PMDI based macrocycle, **6Br**, stronger anion $\cdots\pi$ interactions between the molecular triangle and triiodide anion can occur, overcoming the weaker binding of **6H** compared with the NDI macrocycle **10** (Figure 3.25).

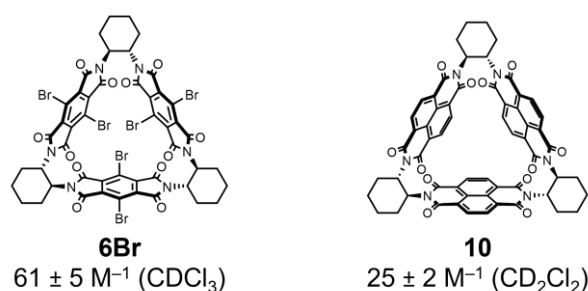


Figure 3.25 Comparison of the binding constant of PMDI based (**6Br**) and NDI based (**10**)³⁹ molecular triangles.

3.3 CONCLUSIONS

In this chapter, the role of the electron-deficient cavity of molecular triangles and its potential for non-covalent interactions has been investigated. These include intramolecular halogen $\cdots\pi$ interactions within the cavity of the electron-deficient macrocycles which can enhance the rate of rotation of PMDI walls in molecular triangles and intermolecular anion $\cdots\pi$ interactions in host–guest complexes. The synthesis and characterisation of tris-substituted molecular triangles **3Br** and **3Ar** are reported with these macrocycles having similar structural and optoelectronic properties as their hexa-functionalised analogues **6Br** and **6Ar**. Furthermore, **3Br** and **3Ar** exist as a mixture of *syn*- and *anti*-isomers in the solution state, with the conformers being able to interconvert which was shown using variable temperature ^1H NMR spectroscopy. The rate of rotation between these atropisomers was calculated using ^1H - ^1H EXSY NMR spectroscopy (**3Br**: $1.81 \pm 0.03 \text{ s}^{-1}$ and **3Ar**: $0.560 \pm 0.015 \text{ s}^{-1}$ at 80°C) which corresponds to half-lives of 96.3 ± 1.6 and $387 \pm 10 \text{ s}$ for **3Br** and **3Ar** respectively. IRC- and TS-DFT calculations indicate that the faster rotation of the brominated molecular triangle is due to a lower energy barrier through stabilisation *via* an intramolecular $\text{Br}\cdots\pi$ interaction inside the cavity of the molecular triangle. The potential for host–guest complexation between the electron-rich triiodide anion and core-substituted molecular triangles has been studied by growing single crystals for X-ray diffraction analysis and host–guest NMR spectroscopy titrations. The results from these experiments reveal that the most electron-deficient molecular triangle **6Br**, binds most strongly with I_3^- ($K_a = 61 \pm 5 \text{ M}^{-1}$ (CDCl_3)) which is greater than the previously reported NDI based molecular triangle **10**, $25 \pm 2 \text{ M}^{-1}$ (CD_2Cl_2). When host–guest complexes of **6Br** $\cdots I_3^-$ form in the solid state, the rigid, shape-persistent

molecular triangle changes its shape to maximise anion- π interactions through bending of a Br₂PMDI face. In this Chapter the role of both intra- and intermolecular interactions between halogen atoms and the π -surface of the cavity of molecular triangles in inducing a change in shape of the macrocycle is discussed. This flexible behaviour of molecular triangles to maximise non-covalent interactions is similar to the mode of action of enzymes upon binding of substrates in the induced fit model.

3.4 SUPPLEMENTARY INFORMATION

3.4.1 MATERIALS AND GENERAL METHODS

All chemicals and reagents were purchased from commercial suppliers (Sigma Aldrich, Fisher Scientific, Alfa Aesar, Fluorochem, Apollo Scientific or Tokyo Chemical Industry) and used without further purification unless otherwise stated. Anhydrous solvents were obtained from a neutral alumina Solvent Purification System under nitrogen and stored over activated (>250 °C at 0.01 mbar overnight) 3 Å molecular sieves under a dry Ar atmosphere.

Analytical thin-layer chromatography (TLC) was performed on silica gel 60 plates pre-loaded with F254 indicator (Sigma Aldrich) and visualised under UV light irradiation (254 and 365 nm). Automated flash column chromatography was performed using a Teledyne ISCO Combiflash NextGen 300+ with detectors using broad range UV-vis (200–800 nm) and evaporative light scattering (ELS) through N₂ gas and loaded on pre-filled RedisepTM Gold cartridges (normal phase: SiO₂) by dry loading from adsorbed celite. Nuclear magnetic resonance (NMR) spectra were recorded on either a JEOL ECS400D spectrometer (working frequency of 400 and 101 MHz for ¹H and ¹³C nuclei respectively), a Bruker AVIIIHD500 spectrometer (working frequency of 500 and 126 MHz for ¹H and ¹³C nuclei respectively) or a Bruker AVIIIHD600 spectrometer (working frequency of 600 and 151 MHz for ¹H and ¹³C nuclei respectively). Chemical shifts (δ) are reported in ppm relative to the signals corresponding to residual non-deuterated solvents (CDCl₃: δ_{H} 7.26 ppm, δ_{C} 77.16 ppm, (CD₃)₂SO: δ_{H} 2.50 ppm, δ_{C} 39.52 ppm, (CD₃)₂CO: δ_{H} 2.05 ppm, δ_{C} 206.62 ppm, 29.84 ppm). Coupling constants (J) are reported in Hertz (Hz) and ¹H multiplicities are reported in accordance with the following convention: s = singlet, d = doublet, t = triplet, q = quadruplet, p = pentet, m = multiplet. Assignment of ¹H and ¹³C NMR signals were accomplished with the aid of DEPT-135 and two-dimensional COSY, HSQC and HMBC NMR spectroscopies. NMR spectra were processed using MestReNova software, Version 14. High-resolution mass spectrometry was completed using a Bruker compact time-of-flight mass spectrometer using an atmospheric-pressure chemical ionisation (APCI) source.

Diffraction data were collected at 110 K (cooled with liquid N₂ using an Oxford Instruments Cryojel) on an Oxford Diffraction Supernova diffractometer (CuK α λ = 1.54184 Å) using a Cannon EOS CCD camera. A suitable crystal was selected and mounted (oil on 100 μ m mount) on a SuperNova Dual, Cu at home/near, Eos diffractometer. Diffractometer control, data collection, initial unit cell determination,

frame integration and unit cell refinement were carried out with ‘CrysAlisPro’.⁵³ Face-indexed absorption corrections were applied using spherical harmonics implemented in SCALE3 ABSPACK scaling algorithm.⁵⁴ OLEX2 was used for overall structure solution, refinement and preparation of computer graphics and publication data.⁵⁵ Within OLEX2, the structures were solved with the Superflip Structure solution program using ‘charge flipping’⁵⁶ or with the ShelXS/ShelXT structure solution programs using Direct Methods.⁵⁷ Refinement by full-matrix least-squares used the SHELXL-97 algorithm within OLEX2. All non-hydrogen atoms were refined anisotropically and hydrogen atoms were placed using a ‘riding model’ and included in the refinement at calculated positions. Visualisation, exploration, distance and angle measurement and image capture of crystal structures were completed using Mercury.⁵⁸

Solution-state absorption spectra were recorded using an Agilent Technologies Cary 5000 Series UV-Vis-NIR spectrophotometer or Shimadzu UV 1800 spectrophotometer using standard 10 mm path length UV-vis quartz cuvettes at room temperature using samples prepared in dry solvents.

Solution-state electrochemical experiments (cyclic voltammetry (CV) and differential pulse voltammetry (DPV)) were carried out using a Gamry Reference 3000 Potentiostat at room temperature with a standard three-electrode setup using Ar-purged freeze-pump-thawed sample solutions in anhydrous THF. Tetrabutylammonium hexafluorophosphate (TBAPF₆; 0.1 M) was recrystallized from hot EtOH and used as the supporting electrolyte. A glassy carbon working electrode (BASi; 0.071 cm²) was used where the electrode surface was polished routinely with 0.05 μm alumina–water slurry on a felt surface immediately before each use. A platinum wire counter electrode was used with an aqueous Ag/AgCl reference electrode which was routinely stored in an aqueous 3 M KCl solution.

Chemical reduction experiments were performed in an argon atmosphere using an MBraun UniLab Pro glove box (<0.1 ppm O₂ and H₂O content). Decamethylcobaltocene (CoCp*₂) was used as a single-electron reductant ($E_{1/2}(\text{CoCp}^*_2) = -1.3 \text{ V vs Fc}^+/\text{Fc}$) and titrated into analyte solutions prepared under a dry Ar atmosphere and using anhydrous, thoroughly degassed DMF solutions.

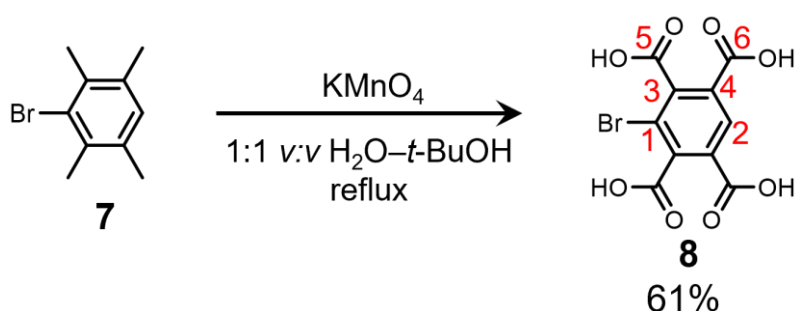
Electron paramagnetic spectroscopy (EPR) spectra were recorded at X-band on a Bruker EMX-Micro spectrometer using 0.1 G modulation amplitude. EPR samples were prepared and stored in an anaerobic glove box (MBraun UniLab Pro) under a dry Ar atmosphere in anhydrous and thoroughly degassed DMF solutions.

Theoretical density functional theory (DFT) ground state geometry optimisation and frequency calculations were performed using Gaussian 16 software,⁵⁹ on either Viking (University of York) or Hamilton (Durham University) High Performance Computer facilities. The calculations were carried out using Becke’s three-parameter exchange functional⁶⁰ with the gradient-corrected correlation formula of Lee, Yang and Parr (B3LYP)⁶¹ paired with the double zeta valence plus polarisation def2svp basis set,⁶² PCM solvation model (CH₂Cl₂) and dispersion corrections (D3BJ).⁶³ Optimised geometries

of the minimum energy ground state (GS), intermediate (I) and transition state (TS) were confirmed by carrying out frequency calculations to check for the presence and absence of negative vibrational frequencies in GS and TS (saddle points) structures respectively. A relaxed potential energy surface scan was conducted at 5° intervals to study the rotation of a BrPMDI unit between *syn*-**3Br** and *anti*-**3Br** and find transition state (TS) structures that were optimised *via* a geometry optimisation calculation. Intrinsic reaction coordinate (IRC) calculations were then performed to confirm that TS geometries identified lie on a potential surface linking the relevant energy minima.

3.4.2 SYNTHESIS

1-BROMOBENZENE-2,3,5,6-TETRACARBOXYLIC ACID (**8**)

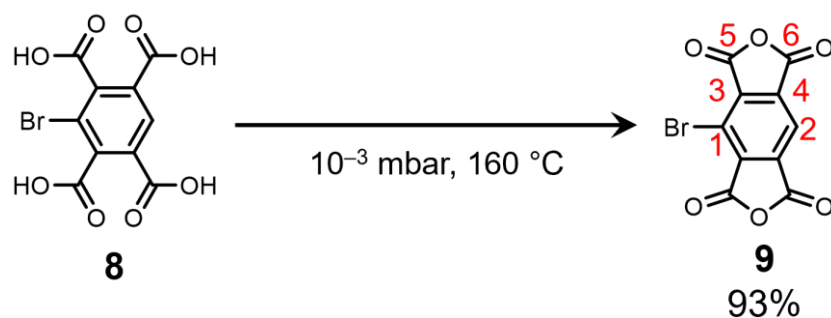


1-Bromo-2,3,5,6-tetramethylbenzene **7** (20.00 g, 93.8 mmol, 1.0 equiv.) was suspended in *t*-BuOH– H_2O (1:1 v/v, 350 mL) and stirred. Potassium permanganate (49.50 g, 313.2 mmol, 3.34 equiv.) was added and the reaction mixture heated at reflux for 4 hours at which point the pink colour of the solution had disappeared. The solution was cooled to rt and a second portion of potassium permanganate (49.50 g, 313.2 mmol, 3.34 equiv.) was added to the reaction mixture, which was then heated to reflux overnight at which point the pink colour of the solution had disappeared. The heating was removed and a third portion of potassium permanganate (49.50 g, 313.2 mmol, 3.34 equiv.) was added to the reaction mixture and heated to reflux for a further 24 hours at which point the solution was no longer pink. The reaction mixture was cooled to rt, absolute EtOH (40 mL) was added and the resulting mixture stirred for 20 min at which point it was filtered to remove insoluble MnO_2 salts and washed with H_2O . The filtrate was concentrated *in vacuo* and the resulting residue was dried at 80 °C in a vacuum oven (10^{-3} mbar) overnight. The dried crude material was dissolved in water and acidified with conc. HCl until a solution of pH = 1 was achieved. The solution was filtered of any insoluble precipitate, which was set aside for additional product recovery, before concentrating the filtrate *in vacuo*. The resulting residue was suspended in acetone and any insoluble salts were removed by filtration. The filtrate was concentrated *in vacuo* to give a first crop of the desired product **8** as a pale-yellow solid. Meanwhile, the insoluble precipitate from the acidification step was redissolved in water and the acidification followed by filtration procedure repeated to ultimately afford a second crop of the desired product **8** as

a pale-yellow solid. The isolated pale-yellow solids were combined and dried under high vacuum to afford **8** (18.95 g, 56.9 mmol, 61%).

^1H NMR (400 MHz, $(\text{CD}_3)_2\text{CO}$, 298 K): δ_{H} 8.70 (s, 1H^2). ^{13}C NMR (101 MHz, $(\text{CD}_3)_2\text{CO}$, 298 K): δ_{C} 167.1 (5), 164.6 (6), 143.4 (4), 132.2 (2), 130.3 (3), 118.3 (1). Spectroscopic data are consistent with the literature.⁴⁰

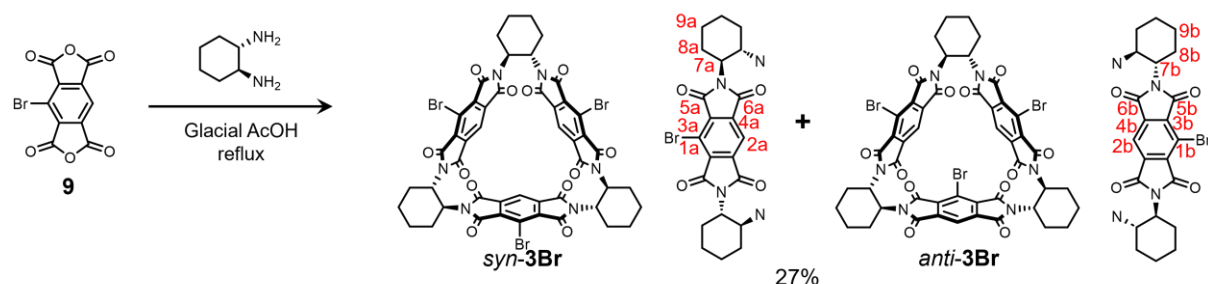
1-BROMOBENZENE-2,3,5,6-TETRACARBOXYLIC ANHYDRIDE (**9**)



1-Bromo-2,3,5,6-tetracarboxylic acid **8** (19.13 g, 57.44 mmol, 1.0 equiv.), as an unstirred powder in a beaker, was dehydrated in a vacuum oven under reduced pressure (10^{-3} mbar) at 160°C for 48 h to give anhydride **9** (15.85 g, 53.4 mmol, 93%) as a brown solid.

^1H NMR (400 MHz, $(\text{CD}_3)_2\text{CO}$, 298 K): δ_{H} 8.67 (s, 1H^2). ^{13}C NMR (101 MHz, $(\text{CD}_3)_2\text{CO}$, 298 K): δ_{C} 160.7 (6), 160.3 (5), 140.3 (3), 137.6 (4), 121.1 (2), 119.2 (1). Spectroscopic data are consistent with the literature.⁴⁰

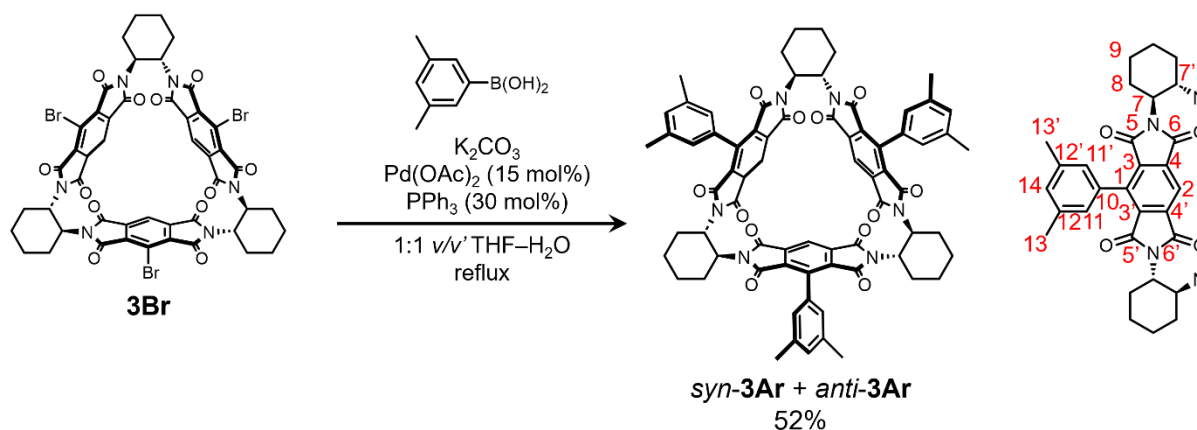
MOLECULAR TRIANGLE **3Br**



A solution of (*S,S*)-*trans*-1,2-diaminocyclohexane (0.19 g, 1.69 mmol, 1.01 equiv.) in AcOH (6 mL) was added to a stirring solution of 1-bromobenzene-2,3,5,6-tetracarboxylic anhydride **9** (0.50 g, 1.68 mmol, 1.00 equiv.) in AcOH (7.46 mL) and refluxed for 4 h. The reaction mixture was cooled to rt and concentrated *in vacuo* to give a red solid which was refluxed in CH_2Cl_2 (50 mL) for 2 h. The suspension was cooled to rt and the unwanted polymeric solid removed by filtration. The filtrate was concentrated *in vacuo* and the red solid subjected to automated flash column chromatography (SiO_2 : 0–100% Me_2CO in CH_2Cl_2) to give **3Br** (mixture of *syn*- and *anti*-atropisomers in a 1:3 ratio, 0.17 g, 0.15 mmol, 27%) as a white solid.

^1H NMR (400 MHz, CDCl_3 , 298 K): δ_{H} 8.05–7.95 (m, $6\text{H}^{1\text{a}+1\text{b}}$), 5.30–5.02 (m, $12\text{H}^{7\text{a}+7\text{b}}$), 2.13–1.80 (m, $36\text{H}^{8\text{a}+8\text{b}+9\text{a}+9\text{b}}$), 1.58–1.44 (m, $12\text{H}^{9\text{a}+9\text{b}}$). **^{13}C NMR** (101 MHz, CDCl_3 , 298 K): δ_{C} 164.7–163.0 ($5\text{a}+5\text{b}+6\text{a}+6\text{b}$), 138.4–137.5 ($3\text{a}+3\text{b}$), 134.6–134.0 ($4\text{a}+4\text{b}$), 117.8–117.3 ($2\text{a}+2\text{b}$), 116.6–116.1 ($1\text{a}+1\text{b}$), 51.9–51.1 ($7\text{a}+7\text{b}$), 31.6–30.0 ($8\text{a}+8\text{b}$), 25.3–24.5 ($9\text{a}+9\text{b}$). **APCI-MS** (+ve, CH_2Cl_2): calcd for $[M+\text{H}]^+$ m/z = 1122.9779, found 1122.9728.

MOLECULAR TRIANGLE **3Ar**

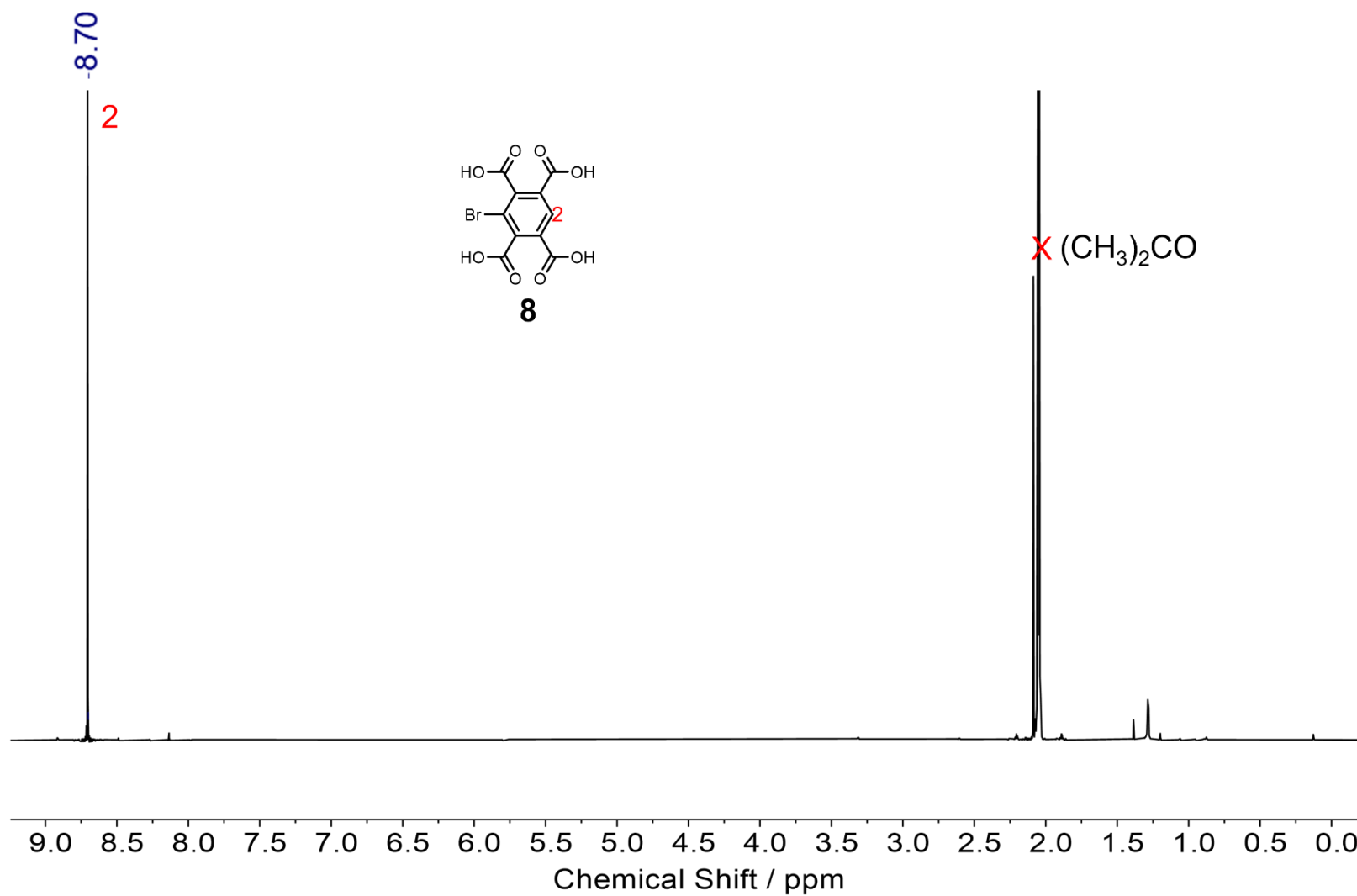


A round bottom flask was charged with **3Br** (200 mg, 0.18 mmol, 1.0 equiv.), 3,5-dimethylbenzene boronic acid (87.4 mg, 0.58 mmol, 3.28 equiv.), K_2CO_3 (73.7 mg, 0.53 mmol, 3.00 equiv.), $\text{Pd}(\text{OAc})_2$ (6.4 mg, 0.029 mmol, 0.16 equiv.) and PPh_3 (13.5 mg, 0.052 mmol, 0.29 equiv.) and cycled under N_2 atmosphere three times. A 1:1 v/v mixture of degassed $\text{THF-H}_2\text{O}$ (5.4 mL) was added under N_2 and the reaction mixture was heated to reflux overnight. The reaction mixture was then cooled to rt before adding CH_2Cl_2 (100 mL) and washing with saturated NaCl (2 x 100 mL). The organic layer was dried (MgSO_4) and filtered. The filtrate was concentrated *in vacuo* and the resulting solid purified by automated flash column chromatography (SiO_2 : 5–30% EtOAc in *n*-hexanes). The resulting yellow solid was recrystallised with acetone–heptane to afford pure **3Ar** (mixture of *syn*- and *anti*-atropisomers in a 81:19 ratio, 113 mg, 0.094 mmol, 52%) as a yellow solid.

* **^1H NMR** (400 MHz, CDCl_3 , 298 K): δ_{H} 8.07 (s, 3H^2), 6.97 (m, $6\text{H}^{11/11'}$), 6.01 (s, 3H^{14}), 5.14–5.04 (m, 6H^7), 2.31 (s, $9\text{H}^{13/13'}$), 2.08–1.79 (m, 18H^{8+9}), 1.57 (s, $9\text{H}^{13/13'}$), 1.52–1.38 (m, 6H^9). **^{13}C NMR** (101 MHz, CDCl_3 , 298 K): δ_{C} 165.6 ($6/6'$), 165.0 ($5/5'$), 164.8 ($5/5'$), 164.4 ($6/6'$), 140.0 (**10**), 137.9 ($12/12'$), 137.6 ($3/3'$), 137.3 ($3/3'$), 137.1 ($12/12'$), 133.1 ($4/4'$), 132.1 ($4/4'$), 131.7 ($11/11'$), 128.9 (**1**), 127.5 (**14**), 127.3 ($11/11'$), 117.3 (**2**), 51.4 ($7/7'$), 50.6 ($7/7'$), 30.6 (**8**), 25.1 (**9**), 21.4 (**13**), 20.0 (**13'**). **APCI-MS** (+ve, CH_2Cl_2): calcd for $[M+\text{H}]^+$ m/z = 1201.4342, found 1201.4320.

*Characterisation for *syn*-isomer only as major atropisomer. Peaks representing *anti*-**3Ar** are too low intensity for full characterisation.

3.4.3 CHARACTERISATION

Figure S3.1 ^1H NMR (400 MHz, Me_2CO , 298 K) spectrum of **8**.

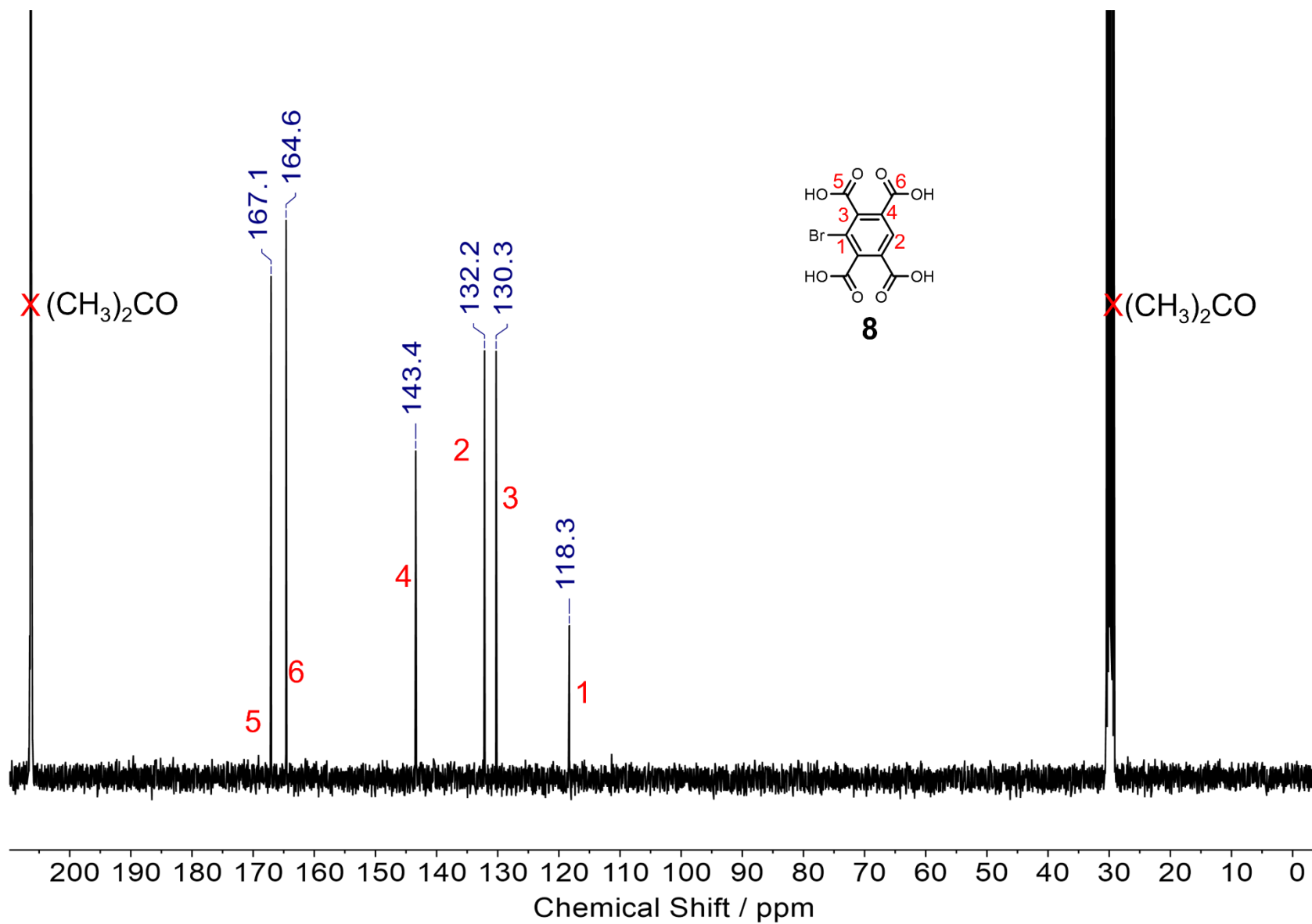


Figure S3.2 ^{13}C NMR (101 MHz, $(\text{CD}_3)_2\text{CO}$, 298 K) spectrum of **8**.

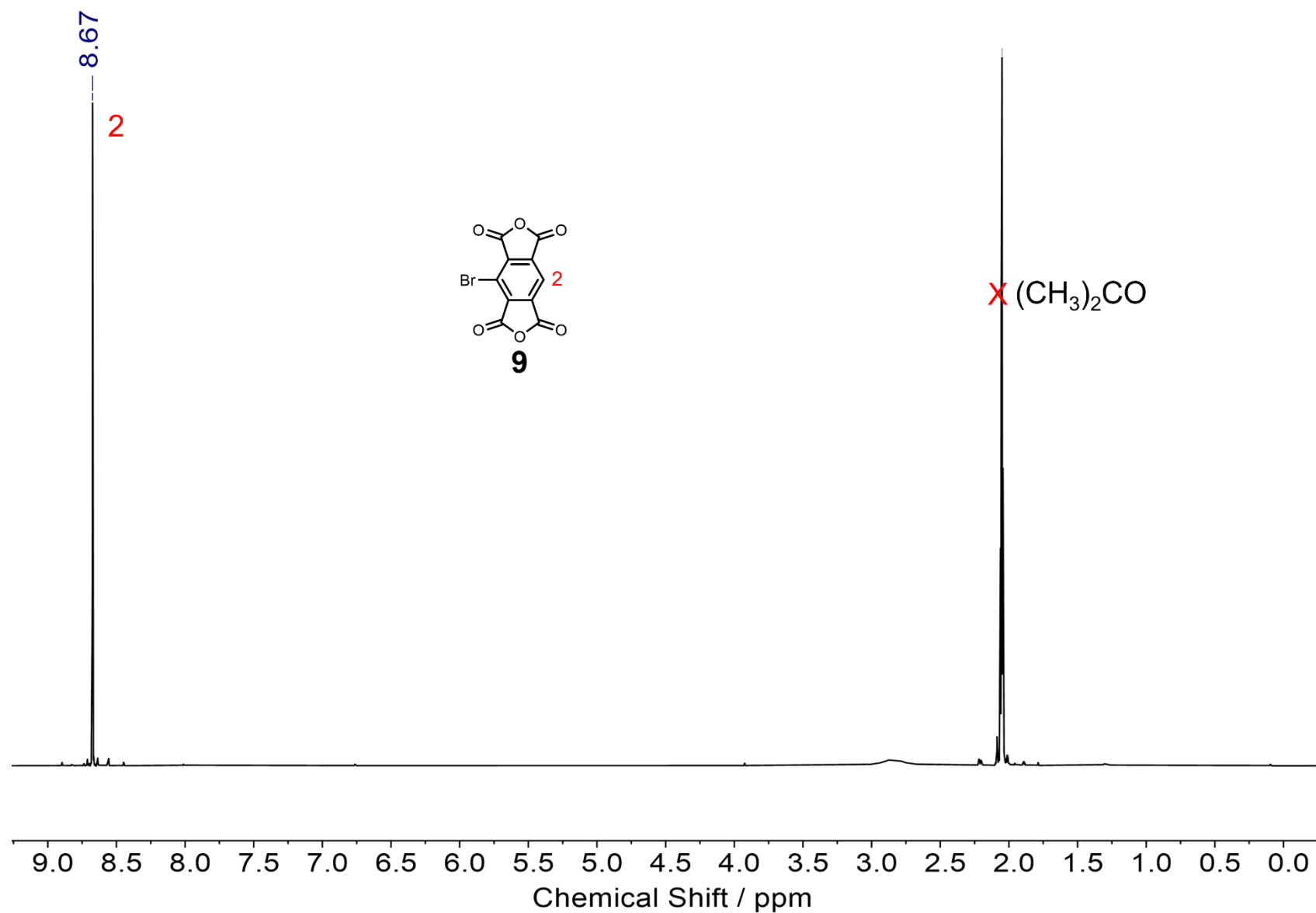


Figure S3.3 ^1H NMR (400 MHz, Me_2CO , 298 K) spectrum of **9**.

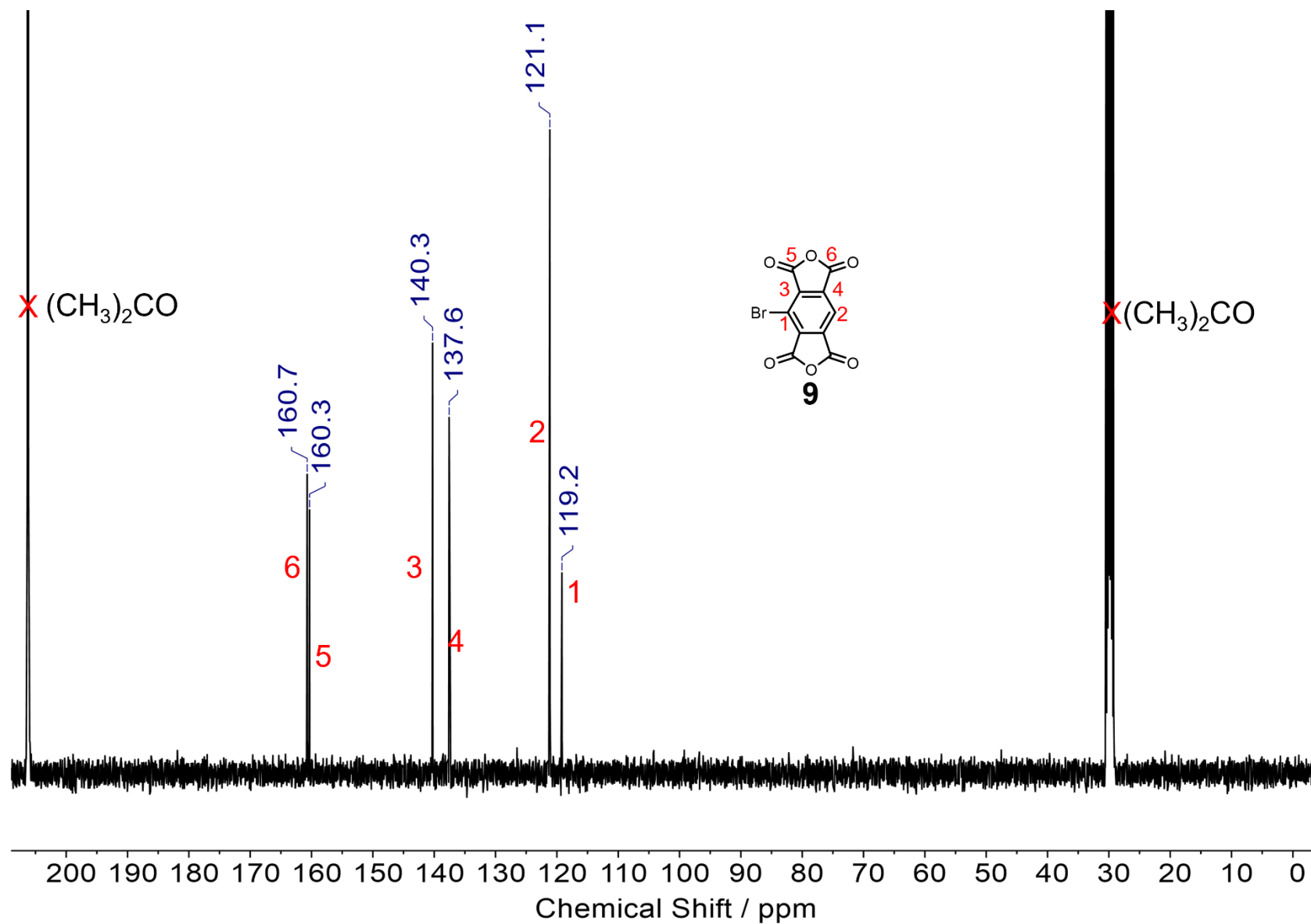
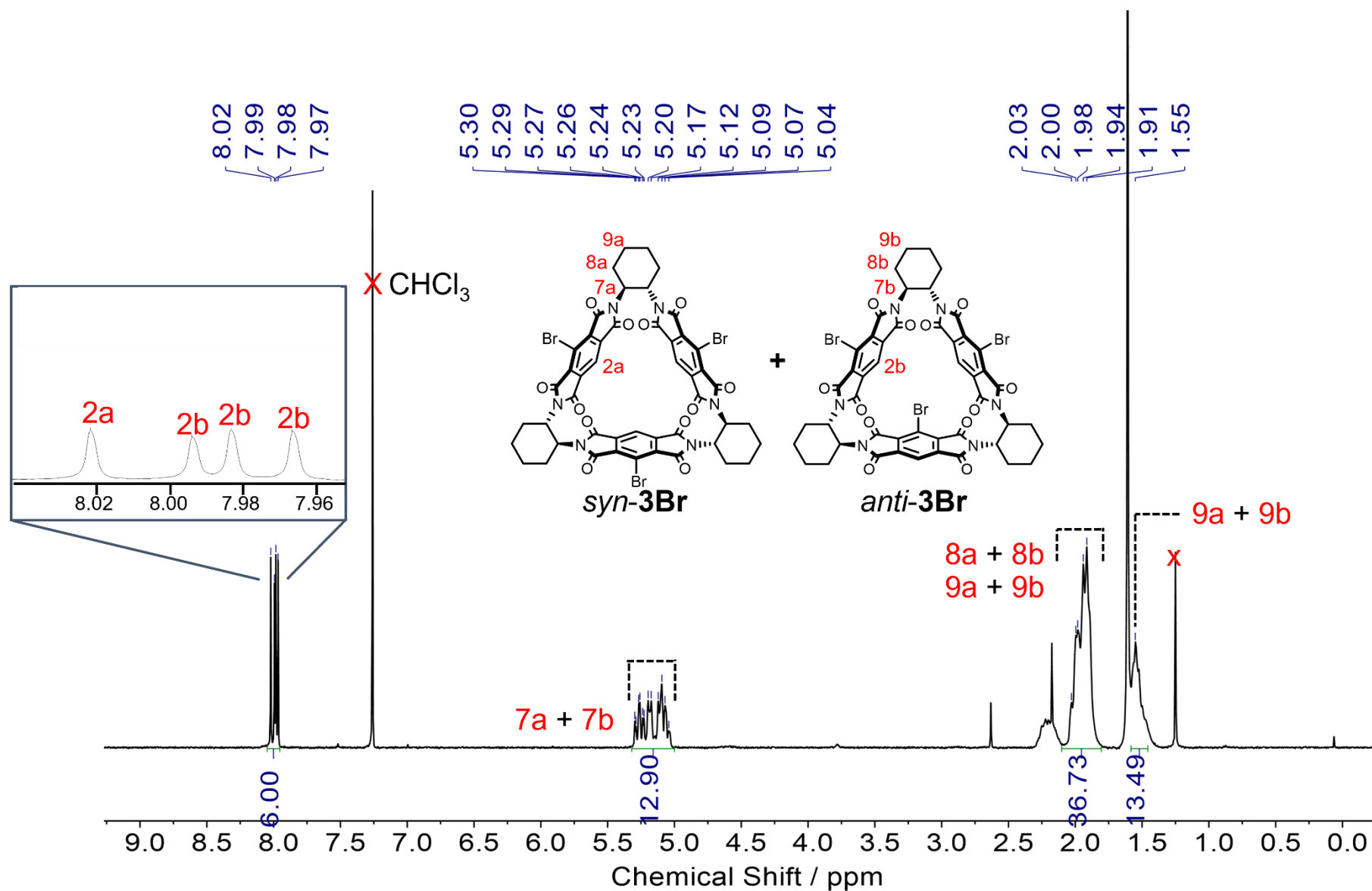
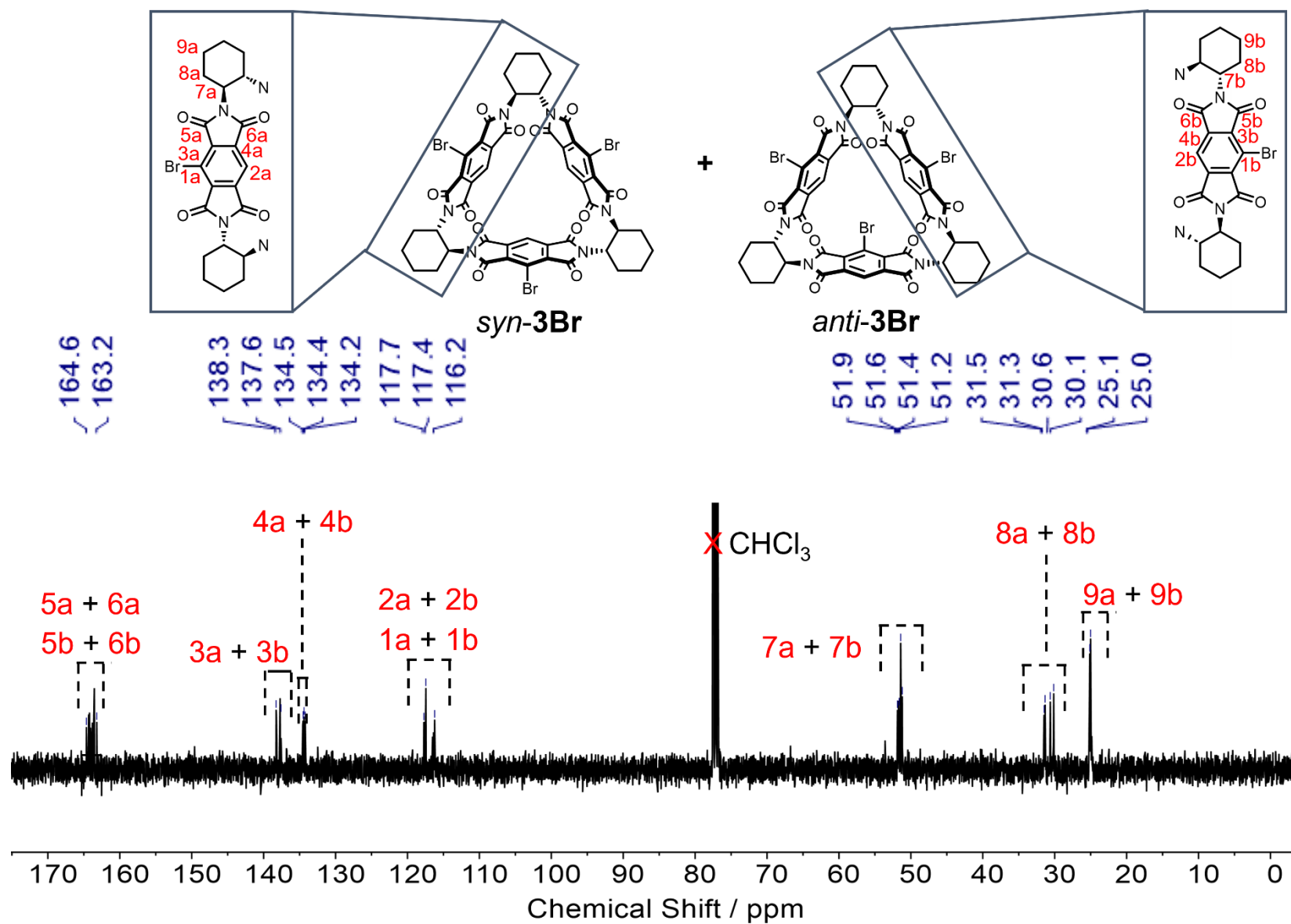
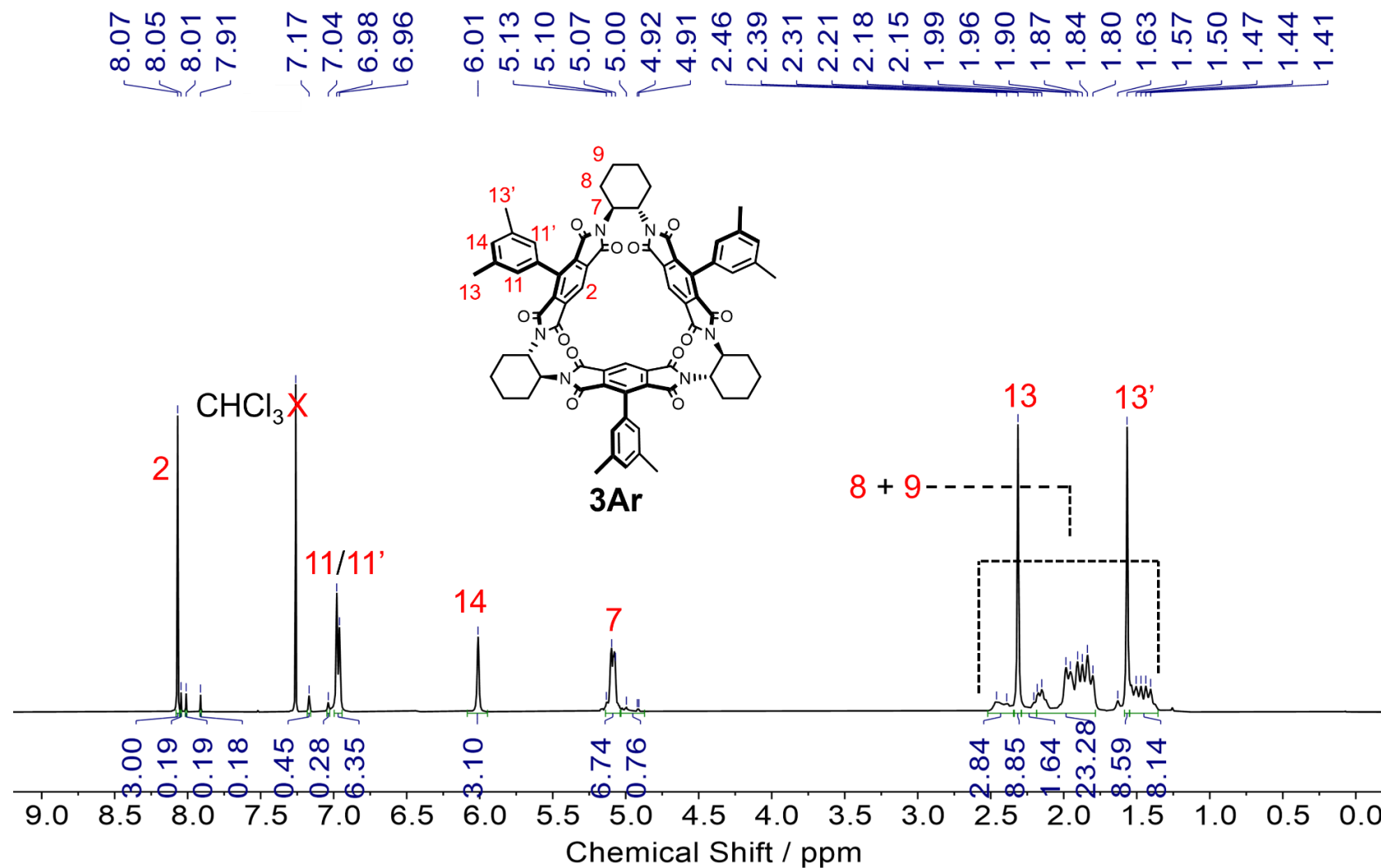


Figure S3.4 ^{13}C NMR (101 MHz, $(\text{CD}_3)_2\text{CO}$, 298 K) spectrum of **9**.


 Figure S3.5 ¹H NMR (400 MHz, CDCl₃, 298 K) spectrum of **3Br**.


 Figure S3.6 ¹³C NMR (101 MHz, CDCl₃, 298 K) spectrum of **3Br**.


 Figure S3.7 ¹H NMR (400 MHz, CDCl₃, 298 K) spectrum of **3Ar**.

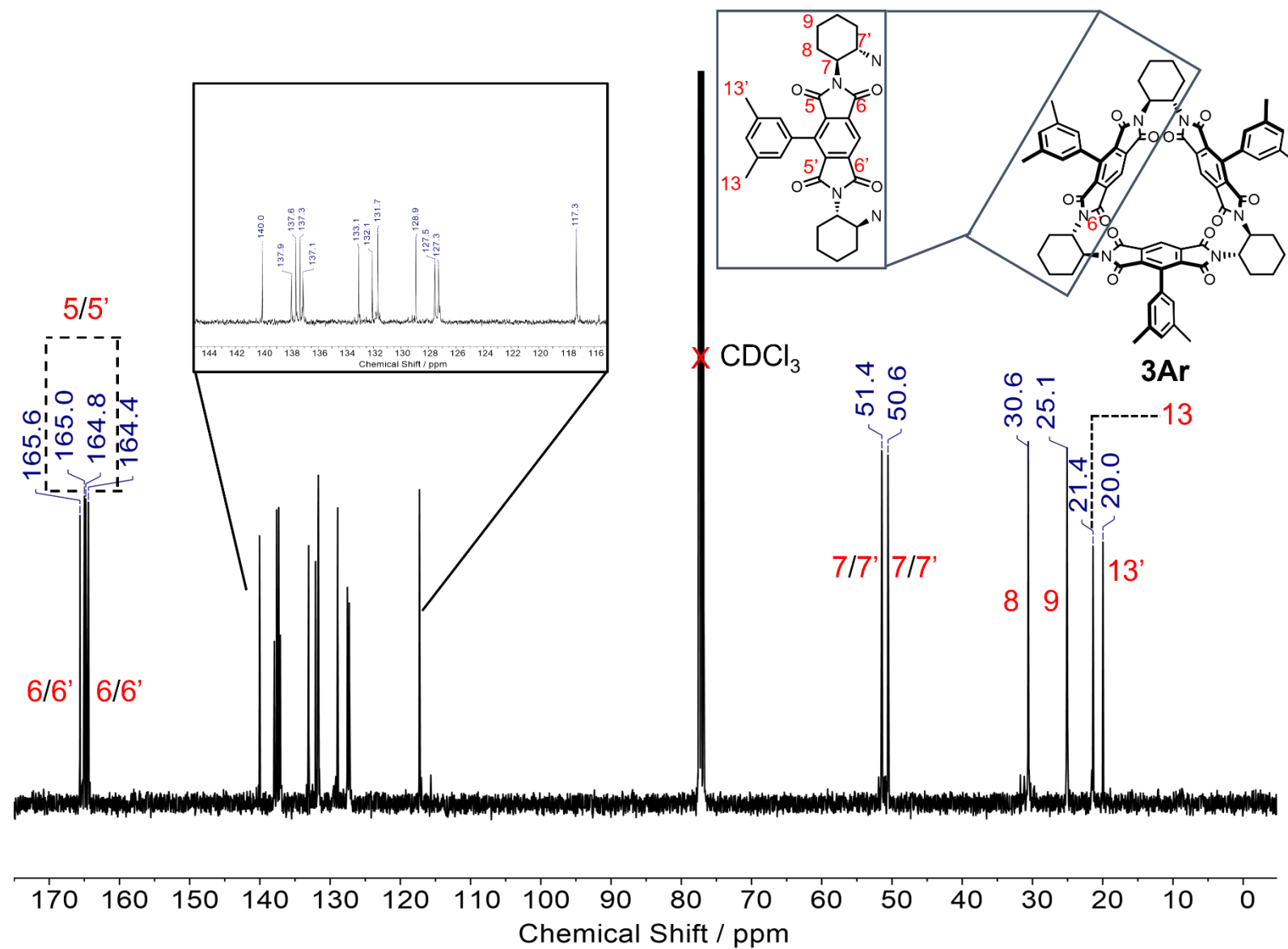
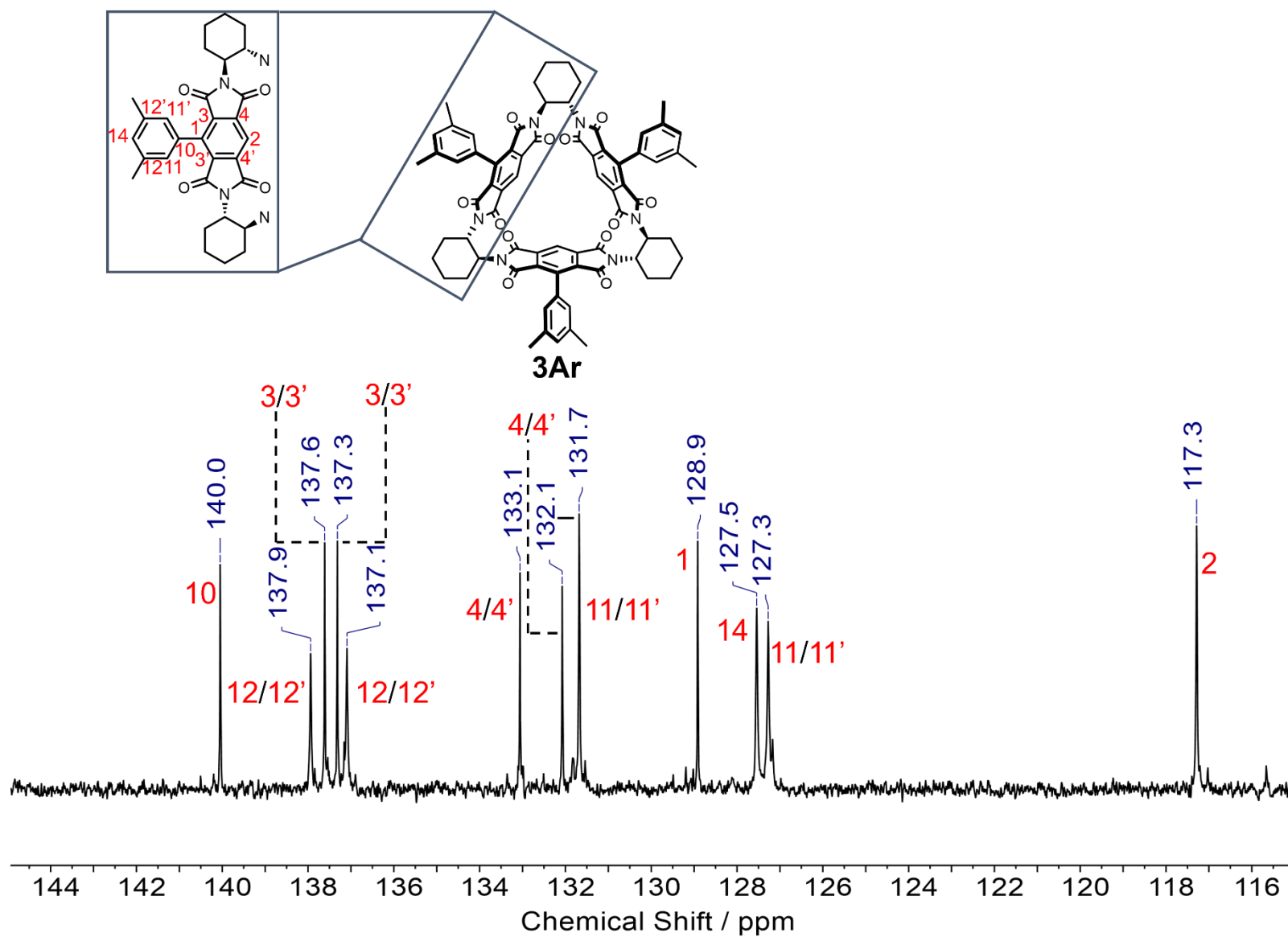


Figure S3.8 ^{13}C NMR (101 MHz, CDCl_3 , 298 K) spectrum of **3Ar**.

Figure S3.9 Inset of ^{13}C NMR (101 MHz, CDCl_3 , 298 K) spectrum of **3Ar**.

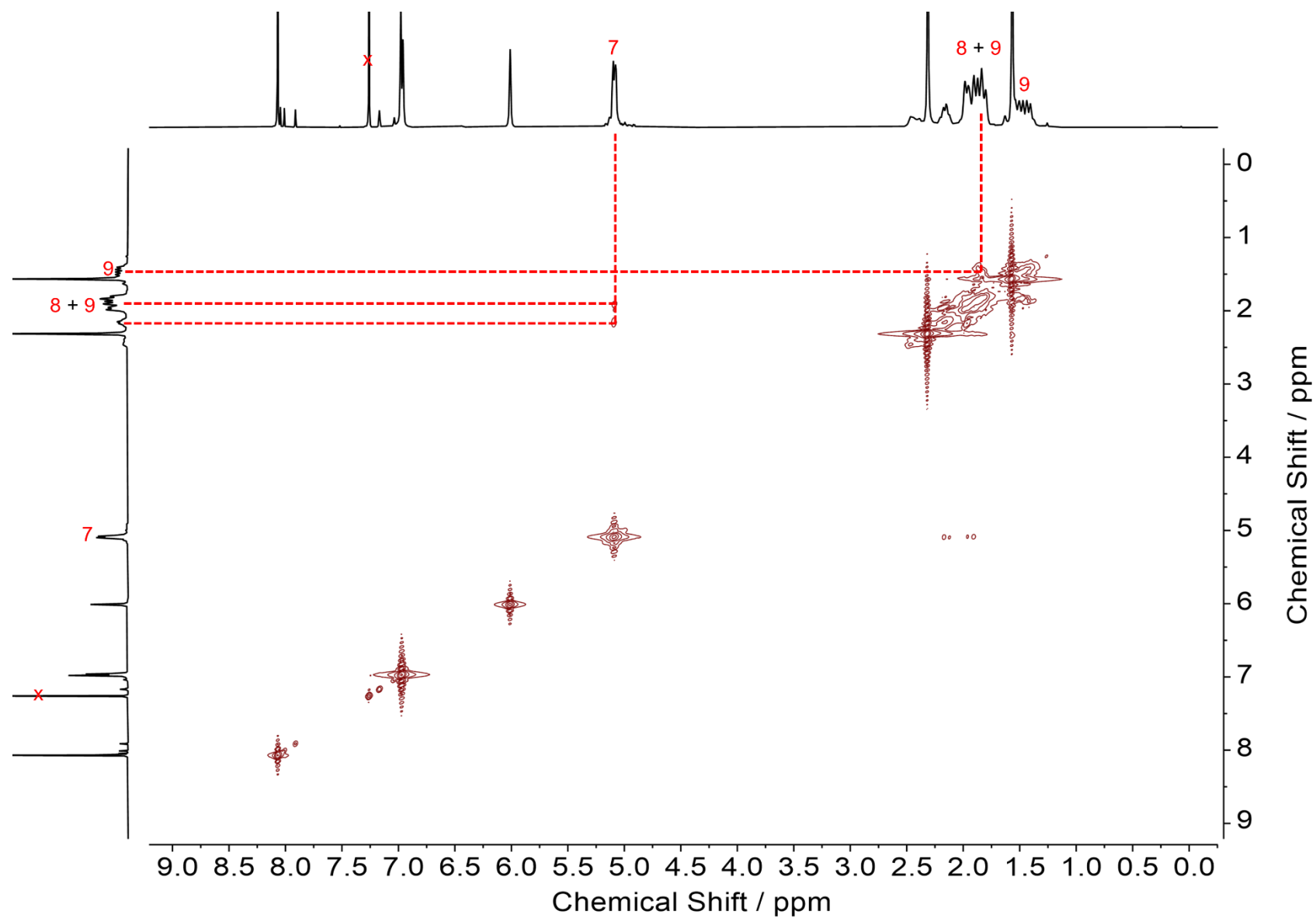


Figure S3.10 Annotated ^1H - ^1H COSY NMR (400 MHz, CDCl_3 , 298 K) spectrum of **3Ar**.

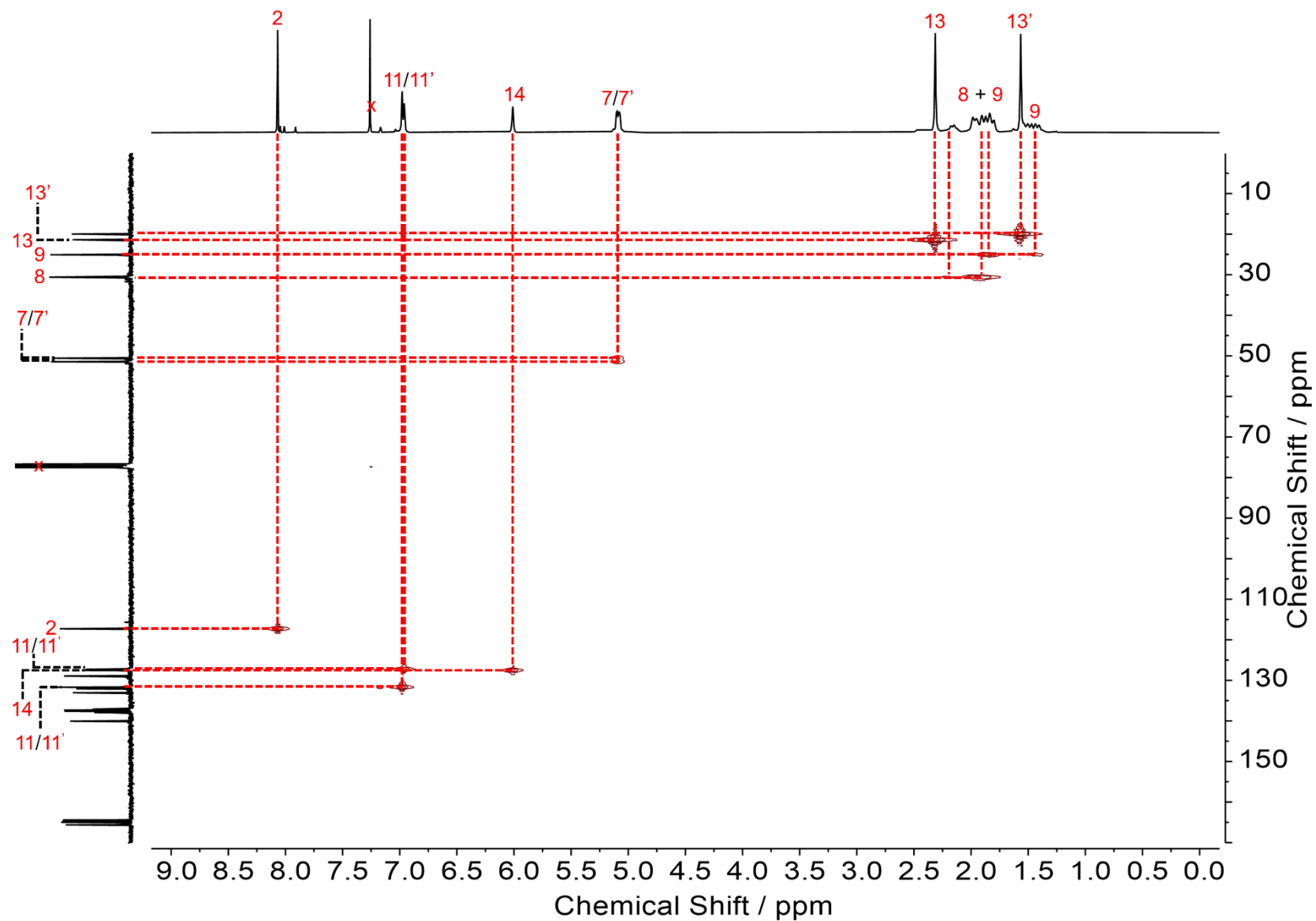


Figure S3.11 Annotated ^1H - ^{13}C HSQC NMR (400 MHz, CDCl_3 , 298 K) spectrum of **3Ar**.

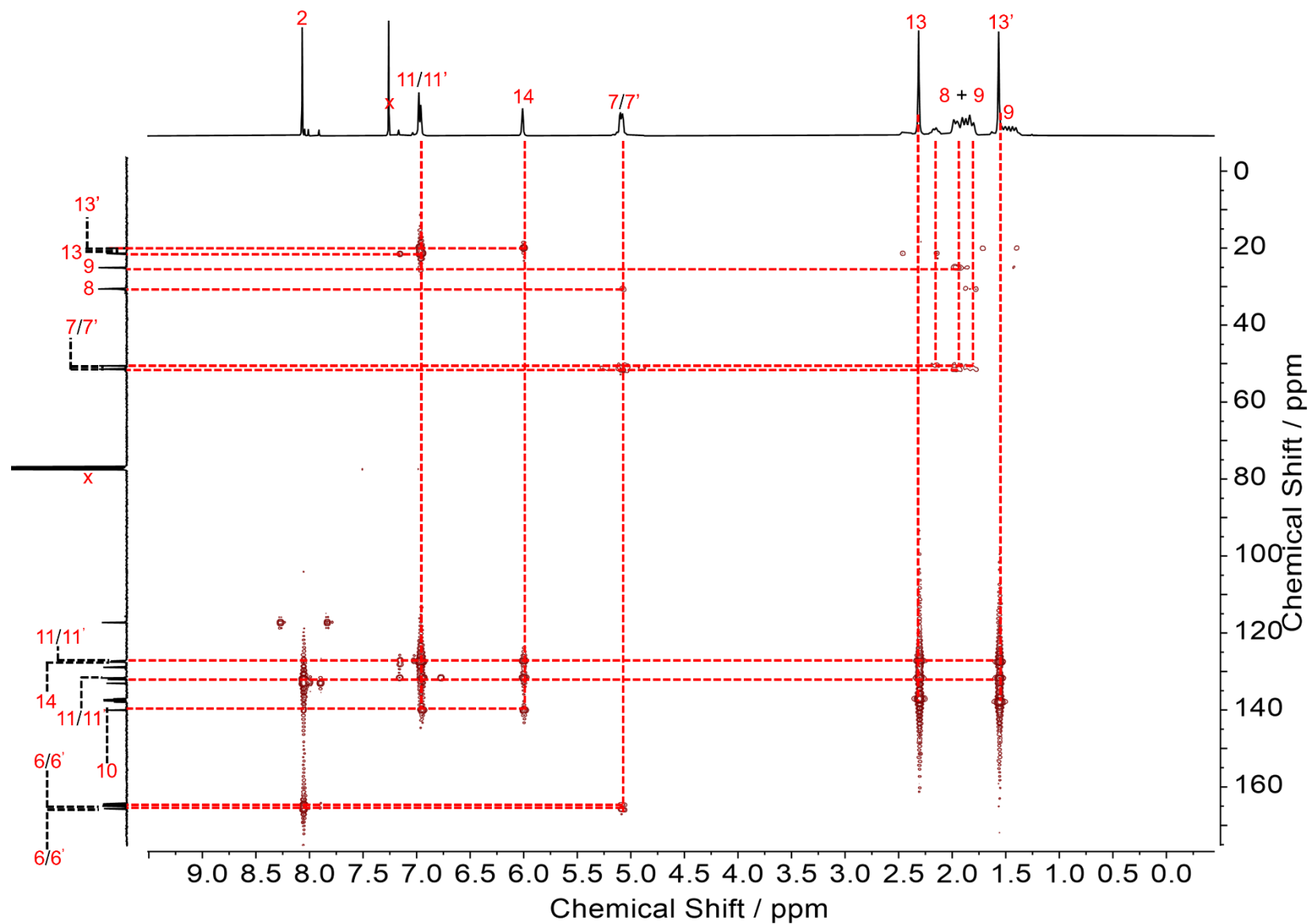


Figure S3.12 Annotated ^1H - ^{13}C HMBC NMR (400 MHz, CDCl_3 , 298 K) spectrum of **3Ar**.

3.4.4 SINGLE X-RAY CRYSTALLOGRAPHY

3.4.5.1 CRYSTAL STRUCTURE OF **3Br**

3Br•4CHCl₃

Single crystals of **3Br•4CHCl₃** suitable for X-ray diffraction were grown by solvent vapour diffusion of pentane into a solution of **3Br** (1.00 mg/mL) in chloroform. Crystal data for C_{55.65}H_{35.81}Br₃Cl_{11.58}N₆O₁₂ (M = 1630.70 g mol⁻¹): monoclinic, space group P2₁, *a* = 17.1895(4) Å, *b* = 18.1713(3) Å, *c* = 21.4755(5) Å, $\alpha = 90^\circ$, $\beta = 108.702(2)^\circ$, $\gamma = 90^\circ$, *V* = 6353.8(2) Å³, *Z* = 4, *T* = 110.00(10) K, $\mu(\text{Cu K}\alpha) = 7.388 \text{ mm}^{-1}$, $\rho_{\text{calc}} = 1.705 \text{ g cm}^{-3}$, 24606 reflections measured ($7.29^\circ \leq 2\theta \leq 134.146^\circ$), 16789 independent reflections (*R*_{int} = 0.0705, *R*_{sigma} = 0.1200) which were used in all calculations. The final *R*₁ was 0.0764 (*I* > 2σ(*I*)) and *wR*₂ was 0.2189 (all data).

The crystal exhibited disorder in both **3Br** and solvent molecules, where the disorder in macrocycle molecules led to the existence of a mixture of *syn*- and *anti*-isomers. One of the triangle molecules contained two disordered bromine atoms and existed as either *syn*- or *anti*-**3Br** throughout the single crystal. In this triangle molecule, two bromine atoms and one carbon atom were modelled in two positions with refined occupancies of 0.903:0.097(3) for Br2:Br2A and C21:C21A and 0.631:0.369(5) for Br3:Br3A. The second triangle molecule contained only one disordered bromine atom, and with the two fixed bromine atoms facing towards opposite directions, existed solely as *anti*-**3Br** in the single crystal. In this triangle molecule, the one bromine atom that was disordered was modelled with refined occupancies of 0.577:0.423(5) for Br6:Br6A. Three of the chloroform solvent molecules were disordered and modelled in two positions with refined occupancies of 0.563:0.437(14), 0.629:0.371(19) and 0.57:0.43(2), with the fourth chloroform molecule partially occupied with a refined occupancy of 0.676(9). A number of restraints and constraints were applied as follows: C-Cl bond lengths restrained to be 1.765 Å for Cl8A-C99A, Cl7A-C99A, Cl9-C99 and Cl8-C99. Atomic displacement parameters (ADPs) of pairs of close disordered atoms were constrained to be equal for C97 & C97A, C98 & C98A, C99 & C99A, Br2 & Br2A, Cl7 & Cl7A, Cl7a & Cl9, Cl8 & Cl8A, C21 & C21a. The ADP of atoms C21, C21A, C98, C98A were restrained to be approximately isotropic. Bond lengths for Br2-C22 and Br2A-C21A, Cl9-C21A and C23-C21A were restrained to be equal. In addition, there was disordered solvent molecules which could not be modelled using discrete atoms. This was instead modelled using a solvent mask with a predicted volume of 440 Å³ per unit cell containing 92 electrons which corresponds to an average of 1.5 pentane molecules and 0.5 chloroform molecules per unit cell.

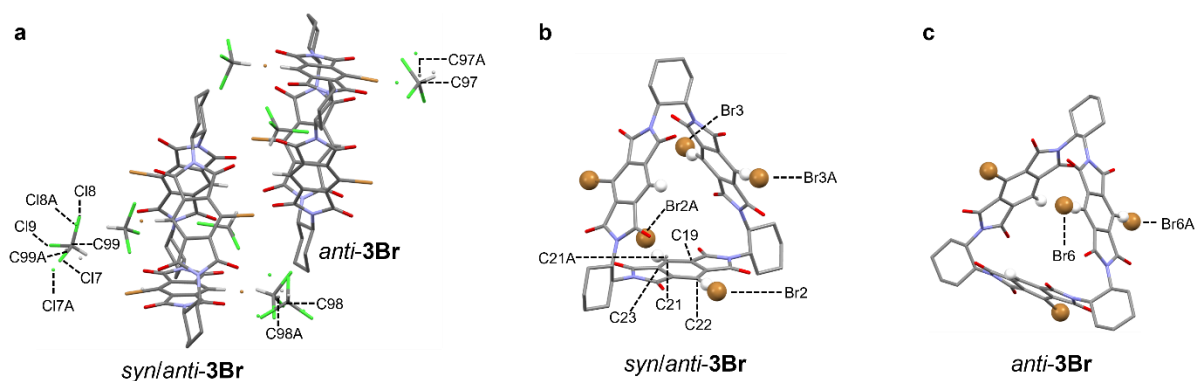


Figure S3.13 X-ray crystal structure of **3Br** showing (a) the unit cell with two triangle molecules and four chloroform solvent molecules, (b) one of the triangle molecules that exists as either *syn*- or *anti*-**3Br** (solvent molecules omitted for clarity) and (c) the second triangle molecule that exists solely as *anti*-**3Br** throughout the unit cell (solvent molecules omitted for clarity). Relevant triangle and solvent atom labels are shown where restraints have been made in crystal structure determination. Cyclohexane hydrogen atoms have been omitted for clarity.

3.4.5.2 CRYSTAL STRUCTURES OF **3Ar**

Two single crystal polymorphs of **3Ar** were obtained from Me_2CO or CHCl_3 solutions both crystallising as the thermodynamically preferred *syn*-**3Ar** isomer.

3Ar• $2(\text{CH}_3)_2\text{CO}$

Single crystals of **3Ar**• $2(\text{CH}_3)_2\text{CO}$ suitable for X-ray diffraction were grown by solvent vapour diffusion of n-hexane into a solution of **3Ar** (≈ 6 mg/mL) in acetone. Crystal data for $\text{C}_{78}\text{H}_{72}\text{N}_6\text{O}_{14}$ ($M = 1317.41$ g mol $^{-1}$): orthorhombic, space group $\text{P2}_12_12_1$, $a = 21.40944(14)$ Å, $b = 20.16344(15)$ Å, $c = 17.77505(12)$ Å, $\alpha = 90^\circ$, $\beta = 90^\circ$, $\gamma = 90^\circ$, $V = 7673.28(9)$ Å 3 , $Z = 4$, $T = 110.00(10)$ K, $\mu(\text{Cu K}\alpha) = 0.644$ mm $^{-1}$, $\rho_{\text{calc}} = 1.140$ g cm $^{-3}$, 29243 reflections measured ($7.812^\circ \leq 2\theta \leq 134.154^\circ$), 13137 independent reflections ($R_{\text{int}} = 0.0277$, $R_{\text{sigma}} = 0.0347$) which were used in all calculations. The final R_1 was 0.0281 ($I > 2\sigma(I)$) and wR_2 was 0.0723 (all data).

Two disordered acetone molecules were solvated in the single crystal. The encapsulated acetone molecule was modelled in two positions with refined occupancies of 0.937:0.063(2). The ADPs of pairs of disordered atoms were constrained to be equal (C73 & C73A, C74 & C74A, C75 & C75A, C76 & C76A, C77 & C77A and C78 & C78A). For the minor form the C-C bond lengths were restrained to be 1.5 angstroms and the C-C distance to 2.38 Å. One acetone was modelled in two positions with refined occupancies of 0.505:0.495(8). The ADPs of atoms C77 and C77A were constrained to be equal. A discrete atom model could not be obtained for the remaining solvent molecules, so they were modelled with a solvent mask instead. This gave a predicted electron count of 68 per asymmetric unit equivalent to two acetone molecules although the presence of pentane chains could not be discounted.

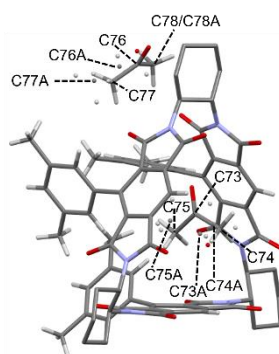


Figure S3.14 Unit cell of **3Ar**•2(CH₃)₂CO from x-ray crystal structure with relevant solvent atom labels given where restraints have been made in crystal structure determination. Cyclohexane hydrogen atoms have been omitted for clarity.

3Ar•4CHCl₃

Single crystals of **3Ar**•4CHCl₃ suitable for X-ray diffraction were grown by solvent vapour diffusion of pentane into a solution of **3Ar** (≈ 4 mg/mL) in chloroform. Crystal data for C_{153.86}H_{132.55}Cl_{23.81}N₁₂O₂₄ ($M = 3377.65$ g mol⁻¹): monoclinic, space group P2₁, $a = 17.43614(15)$ Å, $b = 20.88987(17)$ Å, $c = 22.10599(16)$ Å, $\alpha = 90^\circ$, $\beta = 95.6101(7)^\circ$, $\gamma = 90^\circ$, $V = 8025.70(11)$ Å³, $Z = 2$, $T = 110.00(10)$ K, $\mu(\text{Cu K}\alpha) = 4.283$ mm⁻¹, $\rho_{\text{calc}} = 1.398$ g cm⁻³, 53559 reflections measured ($7.478^\circ \leq 2\theta \leq 134.16^\circ$), 22329 independent reflections ($R_{\text{int}} = 0.0389$, $R_{\text{sigma}} = 0.0445$) which were used in all calculations. The final R_1 was 0.0489 ($I > 2\sigma(I)$) and wR_2 was 0.1327 (all data).

The asymmetric unit cell contained two triangle molecules plus a large amount of solvent. There were two ordered chloroform molecules situated within the cavity of the macrocycles, as well as four disordered chloroform molecules, six partially occupied chloroform molecules and a partially occupied pentane chain. For the first disordered chloroform molecule, the chlorine atoms were each modelled in two positions in a refined ratio of 0.6:0.4(2) with a common site for the carbon. C-Cl bond lengths were restrained to be equal and the Cl—Cl distances within each form restrained to be equal. The second disordered chloroform molecule was modelled in two positions with refined occupancies of 0.502:0.498(6). The ADPs of carbon atoms were constrained to be equal (C148 & C149). The third disordered chloroform molecule was modelled in two positions with refined occupancies of 0.692:0.308(9). The ADPs of carbon atoms were constrained to be equal (C150 & C151) as were two pairs of the chlorine atoms (Cl19 & Cl22, Cl20 & Cl23). The C-Cl bond lengths were restrained to be 1.76 Å. The fourth disordered chloroform molecule was modelled in two positions with refined occupancies of 0.529:0.471(6). The ADPs of carbon atoms were constrained to be equal (C152 & C153) and restrained to be approximately isotropic. Within one form, the C-Cl bond lengths were restrained to be equal (C152, Cl25-27).

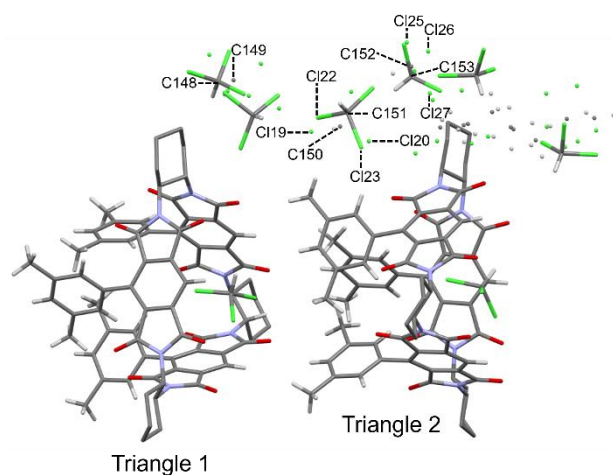


Figure S3.15 Unit cell of **3Ar•4CHCl₃** from x-ray crystal structure with relevant solvent atom labels given where restraints have been made in crystal structure determination. Cyclohexane hydrogen atoms have been omitted for clarity.

Table S3.1 Crystal structure data of tris-substituted molecular triangles (**3Br** and **3Ar**).

	3Br•CHCl₃	3Ar•2Me₂CO	3Ar•4CHCl₃
Empirical Formula	C _{55.65} H _{35.81} Br ₃ Cl _{11.58} N ₆ O ₁₂	C ₇₈ H ₇₂ N ₆ O ₁₄	C _{153.86} H _{132.55} Cl _{23.81} N ₁₂ O ₂₄
Formula Weight	1630.70	1317.41	3377.65
Temperature / K	110.00(10)	110.00(10)	110.00(10)
Crystal System	Monoclinic	Orthorhombic	Monoclinic
Space Group	P2 ₁	P2 ₁ 2 ₁ 2	P2 ₁
<i>a</i> / Å	17.1895(4)	21.40944(14)	17.43614(15)
<i>b</i> / Å	18.1713(3)	20.16344(15)	20.88987(17)
<i>c</i> / Å	21.4755(5)	17.77505(12)	22.10599(16)
α / °	90	90	90
β / °	108.702(2)	90	95.6101(7)
γ / °	90	90	90
Volume (<i>V</i>) / Å ³	6353.8(2)	7673.28(9)	8025.70(11)
<i>Z</i>	4	4	2
ρ_{calc} / g cm ⁻³	1.705	1.140	1.398
μ / mm ⁻¹	7.388	0.644	4.283
F(000)	3238.0	2776.0	3472.8
Crystal Size / mm ³	0.118 x	0.41 x	0.37 x
	0.048 x	0.167 x	0.27 x
	0.023	0.103	0.17
Radiation	Cu K α	Cu K α	Cu K α
	(λ = 1.54184)	(λ = 1.54184)	(λ = 1.54184)
2 θ range for data collection / °	7.29 to 134.146	7.812 to 134.154	7.478 to 134.16
	-20 \leq <i>h</i> \leq 20	-25 \leq <i>h</i> \leq 25	-18 \leq <i>h</i> \leq 20
Index Ranges	-16 \leq <i>k</i> \leq 21	-24 \leq <i>k</i> \leq 22	-24 \leq <i>k</i> \leq 23
	-22 \leq <i>l</i> \leq 25	-21 \leq <i>l</i> \leq 16	-21 \leq <i>l</i> \leq 26
Reflections Collected	24606	29243	53559
	16789	13137	22329
Independent Reflections	R _{int} = 0.0705	R _{int} = 0.0277	R _{int} = 0.0389
	R _{sigma} = 0.1200	R _{sigma} = 0.0347	R _{sigma} = 0.0445
Data/	16789 /	13137 /	22329 /
Restraints/	38 /	3 /	84 /
Parameters	1607	942	2179
Goodness-of-fit on F ²	1.025	0.981	1.019
Final R Indexes (<i>I</i> \geq 2 σ (<i>I</i>))	R ₁ = 0.0764	R ₁ = 0.0281	R ₁ = 0.0489
	wR ₂ = 0.2016	wR ₂ = 0.0714	wR ₂ = 0.1312
Final R Indexes (all data)	R ₁ = 0.0918	R ₁ = 0.0293	R ₁ = 0.0504
	wR ₂ = 0.2189	wR ₂ = 0.0723	wR ₂ = 0.1327
Largest diff. peak/hole / e Å ⁻³	1.29 / -0.81	0.16 / -0.14	0.73 / -0.69
Flack Parameter	0.00(3)	-0.03(5)	0.006(6)

3.4.4.2 HOST-GUEST CRYSTAL STRUCTURES

2(6H)•6(I₃[−])•6((C₄H₉)₄N⁺)•3CHCl₃

Single crystals of 2(6H)•6(I₃[−])•6((C₄H₉)₄N⁺)•3CHCl₃ suitable for X-ray diffraction were grown by solvent vapour diffusion of diethylether into a solution of 6H (1.12 mg/mL) and TBA•I₃ (5.6 mg/mL) in chloroform. Crystal data for C_{153.86}H_{132.55}Cl_{23.81}N₁₂O₂₄ (M = 3377.65 g mol^{−1}): monoclinic, space group P2₁, *a* = 17.46314(15) Å, *b* = 20.88987(17) Å, *c* = 22.10599(16) Å, *α* = 90°, *β* = 95.6101(7)°, *γ* = 90°, *V* = 8025.70(11) Å³, *Z* = 2, *T* = 110.00(10) K, *μ*(Cu Kα) = 4.283 mm^{−1}, *ρ*_{calc} = 1.398 g cm^{−3}, 53559 reflections measured (7.478° ≤ 2*θ* ≤ 134.16°), 22329 independent reflections (*R*_{int} = 0.0389, *R*_{sigma} = 0.0445) which were used in all calculations. The final *R*₁ was 0.0489 (*I* > 2σ(*I*)) and *wR*₂ was 0.1327 (all data).

The tetrabutylammonium cation containing butyl chain containing atoms C21–C24 was disordered with atoms C21, C22 and C23 modelled in a two-component system with 50:50 occupancy ratio. Triiodide molecule I4–I6 was disordered across two positions and modelled with a 0.82:0.18 occupancy ratio. Three triiodide anion molecules were disordered across two positions (I₃[−] molecules containing atoms I4–I6, I10–I12 and I16–I18) and they were subsequently modelled with a 0.82:0.18, 0.53:0.47 and 0.71:0.29 occupancy ratio respectively. For all disordered groups, SADI restraints were used to maintain consistent geometry between parts. The butyl chain containing atoms C17–C20 was modelled with DFIX, DANG and RIGU constraints to fix geometry.

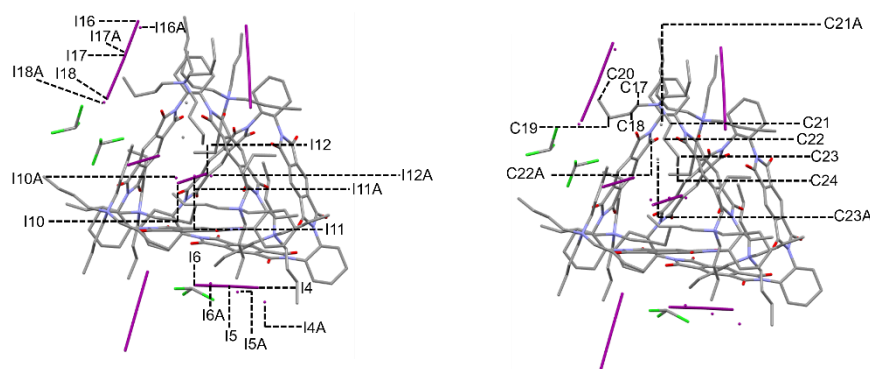


Figure S3.16 Unit cell of 2(6H)•6(I₃[−])•6((C₄H₉)₄N⁺)•3CHCl₃ from X-ray crystal structure with relevant atom labels given where restraints have been made in crystal structure determination. Hydrogen atoms have been omitted for clarity.

2(6Br)•2(I₃[−])•2((C₄H₉)₄N⁺)•4CHCl₃

Single crystals of 2(6Br)•2(I₃[−])•2((C₄H₉)₄N⁺)•4CHCl₃ suitable for X-ray diffraction were grown by solvent vapour diffusion of diisopropylether into a solution of 6Br (0.65 mg/mL) and TBA•I₃ (0.47 mg/mL) in chloroform. Crystal data for C₆₆H₆₈Br₆Cl₆I₃N₇O₁₂ (M = 2224.13 g mol^{−1}): monoclinic, space group P2₁, *a* = 18.3628(3) Å, *b* = 19.6026(3) Å, *c* = 21.9826(3) Å, *α* = 90°, *β* = 90.3125(12)°, *γ* = 90°, *V* = 7912.72(18) Å³, *Z* = 4, *T* = 110.00(10) K, *μ*(Cu Kα) = 15.225 mm^{−1}, *ρ*_{calc} = 1.867 g cm^{−3}, 30756 reflections measured (7.712° ≤ 2*θ* ≤ 134.158°), 20066 independent reflections (*R*_{int} = 0.00417,

$R_{\text{sigma}} = 0.0640$) which were used in all calculations. The final R_1 was 0.0475 ($I > 2\sigma(I)$) and wR_2 was 0.1219 (all data).

The terminal methyl group of one of the butyl chains from a tetrabutylammonium cation was disordered and modelled in two positions (C112 and C137) with refined occupancies of 0.56:0.44(7). The atomic displacement parameters (ADPs) of these carbon atoms were constrained to be equal and restrained to be approximately isotropic. Three of the chloroform solvent molecules were disordered, with two solvent molecules being modelled in two positions (containing atoms C130 & C131 and C132 & C133) with refined occupancies of 0.666:0.334(8) and 0.707:0.293(7) respectively. The third chloroform molecule was modelled in three positions (containing atoms C134, C135 & C136) with refined occupancies of 0.495(9):0.258(7):0.247(7) respectively. For the three disordered chloroform molecules, C-Cl bond lengths were restrained to be 1.73 Å and the Cl-Cl distances to 2.9 Å. The ADPs of proximal atoms were constrained to be equal (chlorine atoms Cl5 & Cl5A, Cl6 & Cl4A, Cl7 & Cl7A, Cl8 & Cl8A, Cl9 & Cl9A, Cl10 & Cl18, Cl11 & Cl15, Cl12 & Cl14, Cl13 & Cl16 & Cl17 and carbon atoms C130 & C131, C132 & C133, C134 & C135 & C136,). Chlorine atoms Cl5 and Cl5A were also constrained to have the same coordinates.

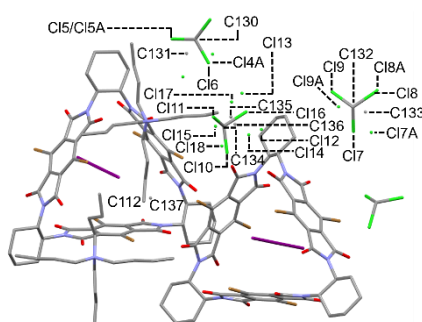


Figure S3.17 Unit cell of $2(\mathbf{6Br}) \cdot 2(\text{I}_3^-) \cdot 2((\text{C}_4\text{H}_9)_4\text{N}^+) \cdot 4\text{CHCl}_3$ from X-ray crystal structure with relevant atom labels given where restraints have been made in crystal structure determination. Hydrogen atoms have been omitted for clarity.

Table S3.2. Crystal structure data of host-guest complexes $2(\mathbf{6H}) \cdot 6(\text{I}_3^-) \cdot 6((\text{C}_4\text{H}_9)_4\text{N}^+) \cdot 3\text{CHCl}_3$ and $2(\mathbf{6Br}) \cdot 2(\text{I}_3^-) \cdot 2((\text{C}_4\text{H}_9)_4\text{N}^+) \cdot 4\text{CHCl}_3$.

	$2(\mathbf{6H}) \cdot 6(\text{I}_3^-) \cdot 6((\text{C}_4\text{H}_9)_4\text{N}^+) \cdot 3\text{CHCl}_3$	$2(\mathbf{6Br}) \cdot 2(\text{I}_3^-) \cdot 2((\text{C}_4\text{H}_9)_4\text{N}^+) \cdot 4\text{CHCl}_3$
Empirical Formula	$\text{C}_{153.86}\text{H}_{132.55}\text{Cl}_{23.81}\text{N}_{12}\text{O}_{24}$	$\text{C}_{66}\text{H}_{68}\text{Br}_6\text{Cl}_6\text{I}_3\text{N}_7\text{O}_{12}$
Formula Weight	3377.65	2224.13
Temperature / K	110.00(10)	110.00(10)
Crystal System	Monoclinic	Monoclinic
Space Group	P2_1	P2_1
$a / \text{\AA}$	17.46314(15)	18.3628(3)
$b / \text{\AA}$	20.88987(17)	19.6026(3)
$c / \text{\AA}$	22.10599(16)	21.9826(3)
$\alpha / ^\circ$	90	90
$\beta / ^\circ$	95.6101(7)	90.3125(12)
$\gamma / ^\circ$	90	90
Volume (V) / \AA^3	8025.70(11)	7912.72(18)
Z	2	4
$\rho_{\text{calc}} / \text{g cm}^{-3}$	1.398	1.867
μ / mm^{-1}	4.283	15.225
F(000)	3472.8	4320.0
Crystal Size / mm^3	0.37 x	0.125 x
	0.27 x	0.113 x
	0.17	0.058
Radiation	Cu $\text{K}\alpha$	Cu $\text{K}\alpha$
	($\lambda = 1.54184$)	($\lambda = 1.54184$)
2 θ range for data collection / $^\circ$	7.478 to 134.16	7.712 to 134.158
Index Ranges	$-18 \leq h \leq 20$	$-21 \leq h \leq 20$
	$-24 \leq k \leq 23$	$-17 \leq k \leq 23$
	$-21 \leq l \leq 26$	$-26 \leq l \leq 25$
Reflections Collected	53559	30756
Independent Reflections	22329	20066
	$R_{\text{int}} = 0.0389$	$R_{\text{int}} = 0.00417$
Data/ Restraints/ Parameters	$R_{\text{sigma}} = 0.0445$	$R_{\text{sigma}} = 0.0640$
	22329 /	20066 /
Goodness-of-fit on F^2	84 /	84 /
	2179	1876
Final R Indexes ($I \geq 2\sigma(I)$)	1.019	1.014
Final R Indexes (all data)	$R_1 = 0.0489$	$R_1 = 0.0475$
	$wR_2 = 0.1312$	$wR_2 = 0.1126$
Largest diff. peak/hole / e \AA^{-3}	$R_1 = 0.0504$	$R_1 = 0.0621$
	$wR_2 = 0.1327$	$wR_2 = 0.1219$
Flack Parameter	0.73 / -0.69	1.63 / -1.15
	0.006(6)	-0.014(4)

3.4.5 ADVANCED NMR SPECTROSCOPY

3.4.5.1 VARIABLE-TEMPERATURE NMR SPECTROSCOPY

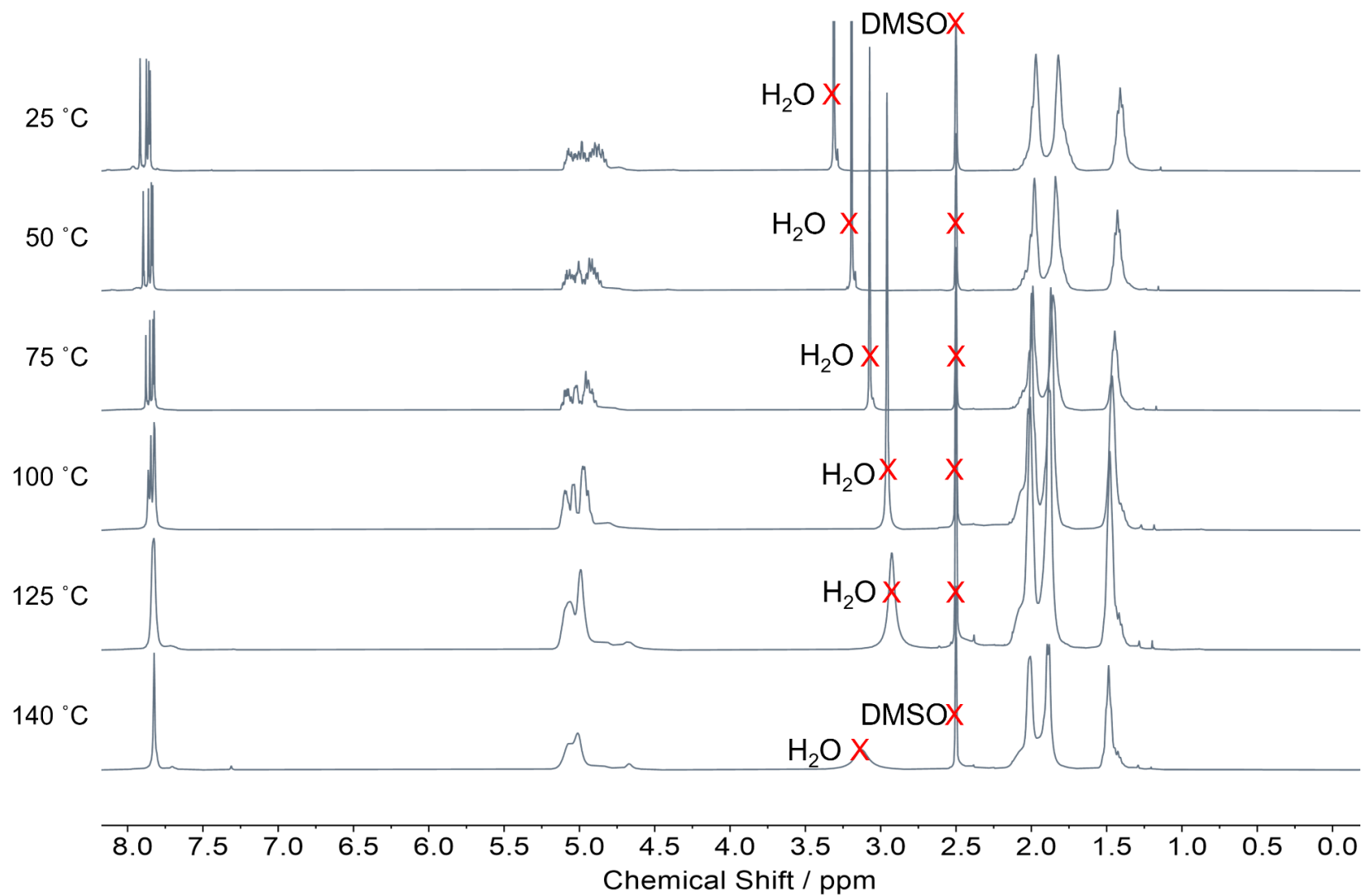


Figure S3.18 Variable temperature stacked ^1H NMR (600 MHz, $\text{DMSO-}d_6$, 25–140 °C) spectra for **3Br**.

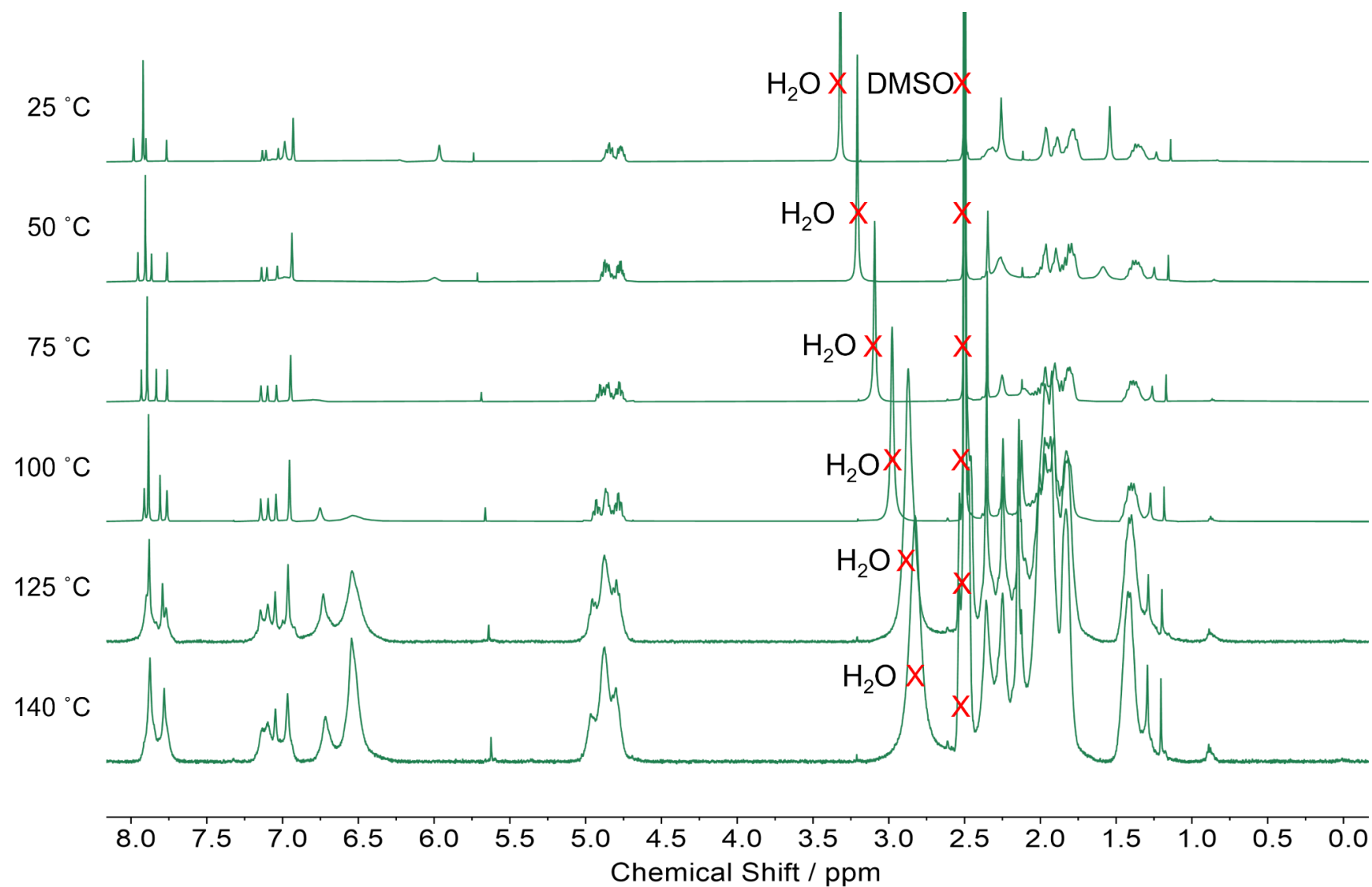


Figure S3.19 Variable temperature stacked ^1H NMR (600 MHz, $\text{DMSO-}d_6$, 25–140 °C) spectra for **3Ar**.

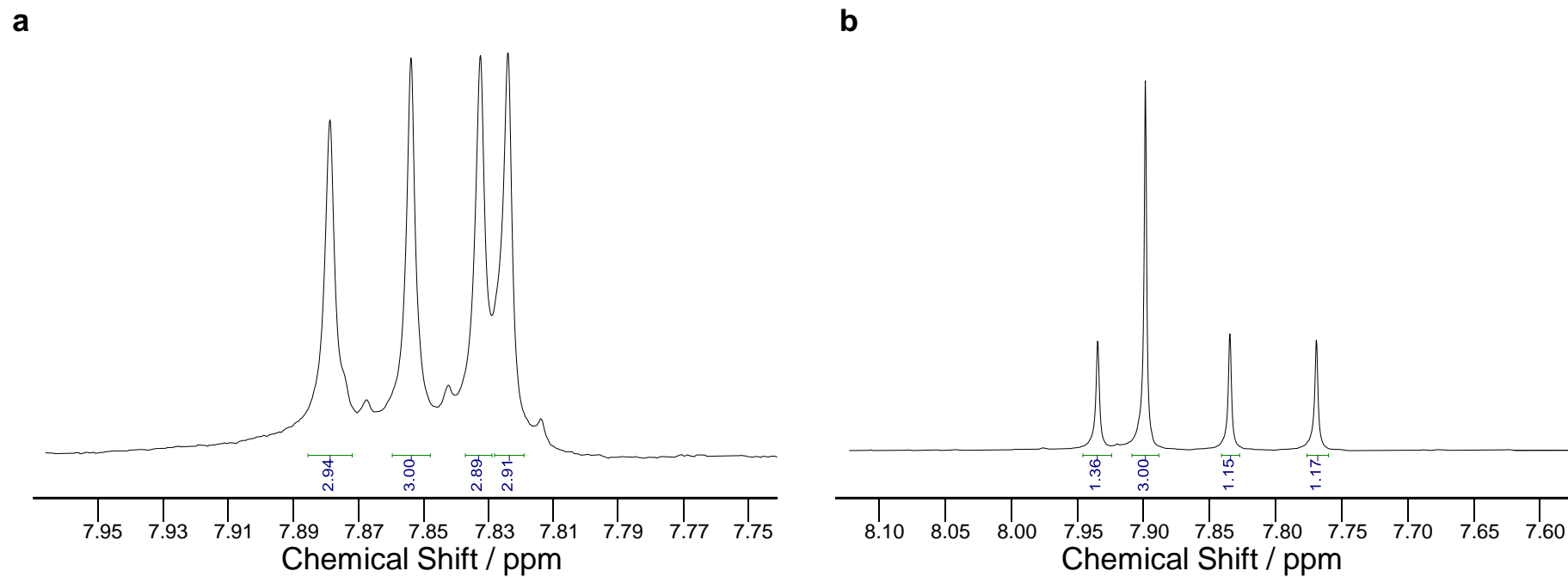


Figure S3.20 Zoomed in aromatic region of ^1H NMR (600 MHz, DMSO- d_6 , 80 $^\circ\text{C}$) spectra for (a) **3Br** (syn:anti = 13:37) and (b) **3Ar** (syn:anti = 9:11).

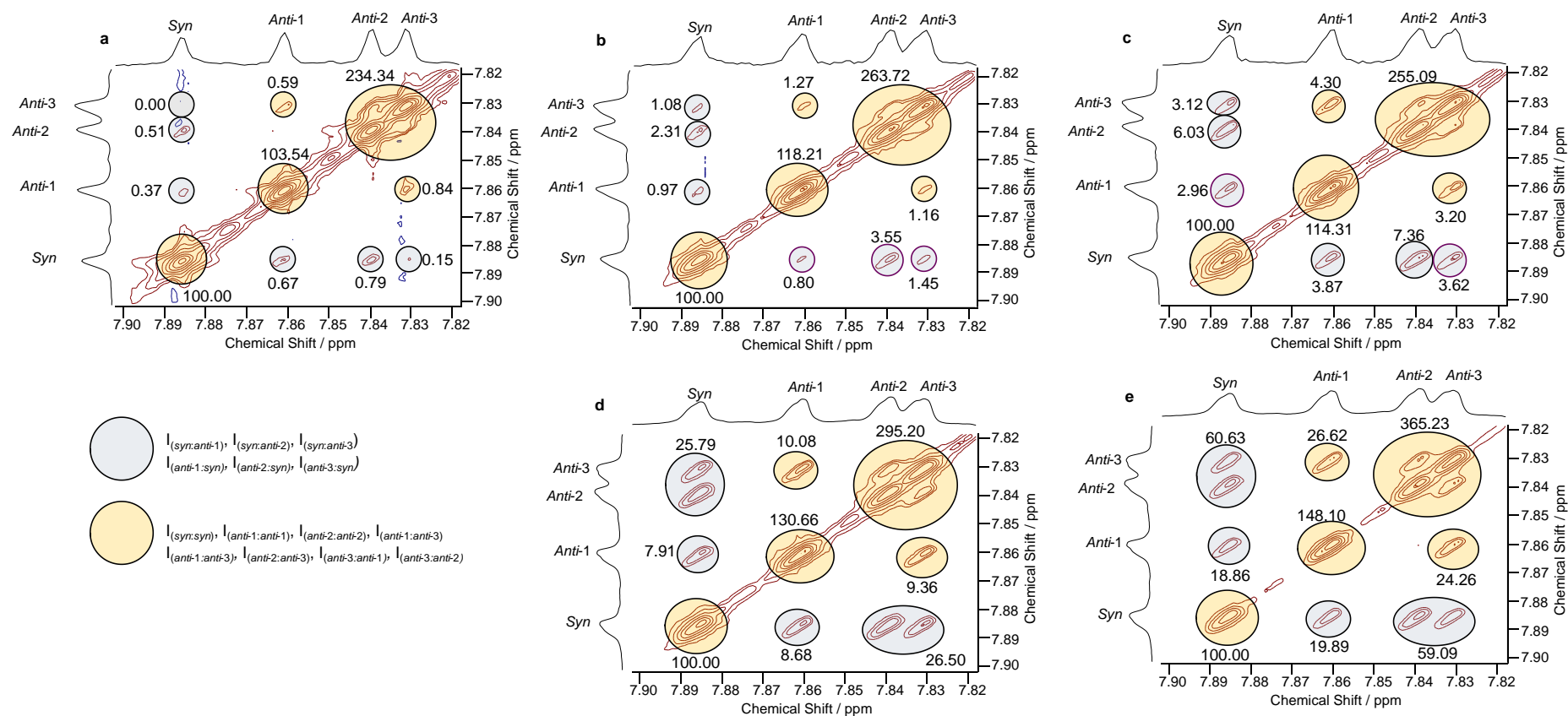
3.4.5.2 ^1H - ^1H EXSY NMR SPECTROSCOPY

Figure S3.21 ^1H - ^1H EXSY NMR (600 MHz, $\text{DMSO}-d_6$, 80 °C) spectra for **3Br** at (a) 20 ms, (b) 50 ms, (c) 100 ms, (d) 200 ms and (e) 400 ms, with representative regions of integration shown with their values.

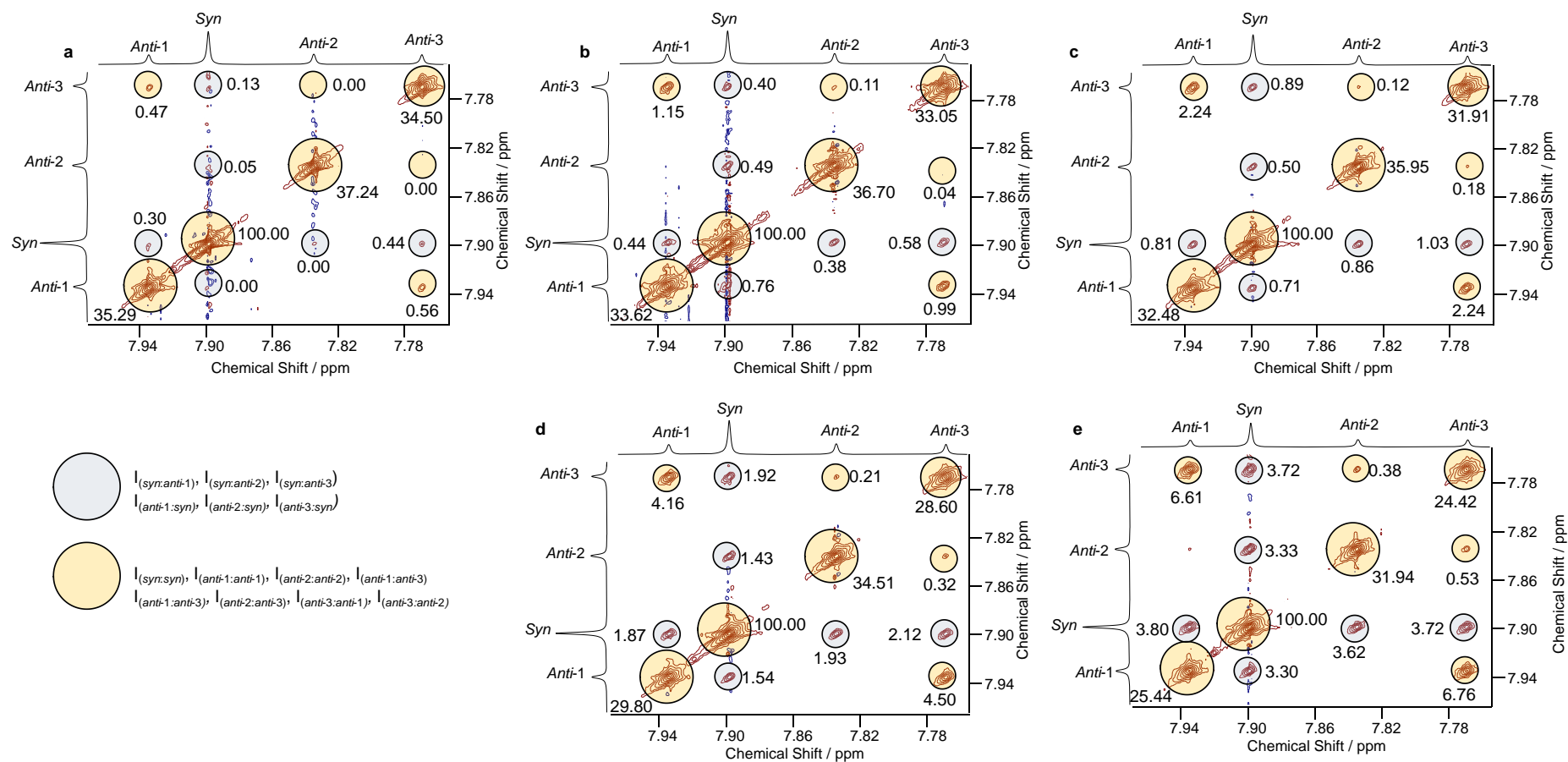


Figure S3.22 ^1H - ^1H EXSY NMR (600 MHz, $\text{DMSO}-d_6$, 80 °C) spectra for **3Ar** at (a) 20 ms, (b) 50 ms, (c) 100 ms, (d) 200 ms and (e) 400 ms, with representative regions of integration shown with their values.

Table S3.3 Data from ^1H - ^1H EXSY NMR spectroscopy for **3Br** (Figure S3.21) showing the integration intensities for all exchange processes and the resulting intensity ratio, r' , at a range of mixing times, 20, 50, 100, 200 and 400 ms.

Mixing Time / ms	20	40	100	200	400
$I_{\text{syn} \rightarrow \text{syn}}$	100.00	100.00	100.00	100.00	100.00
$I_{\text{anti-1} \rightarrow \text{anti-1}}$	103.54	118.21	114.31	130.66	148.10
$I_{\text{anti-2} \rightarrow \text{anti-2}}$	234.34	263.72	255.09	295.20	365.23
$I_{\text{anti-3} \rightarrow \text{anti-3}}$					
$I_{\text{anti-2} \rightarrow \text{anti-3}}$					
$I_{\text{anti-3} \rightarrow \text{anti-2}}$					
$I_{\text{anti-1} \rightarrow \text{anti-3}}$	0.59	1.27	4.30	10.08	26.62
$I_{\text{anti-3} \rightarrow \text{anti-1}}$	0.84	1.16	3.20	9.36	24.26
$I_{\text{syn} \rightarrow \text{anti-1}}$	0.37	0.97	2.96	7.91	18.86
$I_{\text{syn} \rightarrow \text{anti-2}}$	0.51	2.31	6.03	25.79	60.63
$I_{\text{syn} \rightarrow \text{anti-3}}$	0.00	1.08	3.12		
$I_{\text{anti-1} \rightarrow \text{syn}}$	0.67	0.80	3.87	8.68	19.89
$I_{\text{anti-2} \rightarrow \text{syn}}$	0.79	3.55	7.36	26.50	59.09
$I_{\text{anti-3} \rightarrow \text{syn}}$	0.15	1.45	3.62		
Total	439.31	484.36	476.90	545.30	664.21
Total	2.49	10.16	26.96	68.88	158.47
Peak intensity ratio r'	176.43	47.67	17.69	7.92	4.19

Table S3.4 Data from ^1H - ^1H EXSY NMR spectroscopy for **3Ar** (Figure S3.22) showing the integration intensities for all exchange processes and the resulting intensity ratio, r' , at a range of mixing times, 20, 50, 100, 200 and 400 ms.

Mixing Time / ms	20	40	100	200	400
$I_{\text{anti-1} \rightarrow \text{anti-1}}$	35.29	33.62	32.48	29.80	25.44
$I_{\text{syn} \rightarrow \text{syn}}$	100.00	100.00	100.00	100.00	100.00
$I_{\text{anti-2} \rightarrow \text{anti-2}}$	37.24	36.70	35.95	34.51	31.94
$I_{\text{anti-3} \rightarrow \text{anti-3}}$	34.50	33.05	31.91	28.60	24.42
$I_{\text{anti-1} \rightarrow \text{anti-3}}$	0.47	1.15	2.24	4.16	6.61
$I_{\text{anti-2} \rightarrow \text{anti-3}}$	0.00	0.11	0.12	0.21	0.38
$I_{\text{anti-3} \rightarrow \text{anti-1}}$	0.56	0.99	2.24	4.50	6.76
$I_{\text{anti-3} \rightarrow \text{anti-2}}$	0.00	0.04	0.18	0.32	0.53
$I_{\text{anti-1} \rightarrow \text{syn}}$	0.30	0.44	0.81	1.87	3.80
$I_{\text{anti-2} \rightarrow \text{syn}}$	0.00	0.38	0.86	1.93	3.62
$I_{\text{anti-3} \rightarrow \text{syn}}$	0.44	0.58	1.03	2.12	3.72
$I_{\text{syn} \rightarrow \text{anti-1}}$	0.00	0.76	0.71	1.54	3.30
$I_{\text{syn} \rightarrow \text{anti-2}}$	0.05	0.49	0.50	1.43	3.33
$I_{\text{syn} \rightarrow \text{anti-3}}$	0.13	0.40	0.89	1.92	3.72
Total	208.06	205.66	205.12	202.10	196.08
Total	0.92	3.05	4.80	10.81	21.49
Peak intensity ratio, r'	226.15	67.43	42.73	18.70	9.12

Calculations to find the exchange rate and other kinetic parameters were completed for **3Br** and **3Ar** following the method below. Using the integrations of each diagonal and cross peak, a peak intensity

ratio can be calculated (r'), Equation S3.1. Further manipulation of the peak intensity ratio, r' using the mole fractions of the *syn*- and *anti*-isomers was completed to give r , Equation S3.2. The exchange rate constant, k_r , can be related to r through the rate of exchange equation, Equation S3.3a, which can be further rearranged to give a relationship between r , and k_r , Equation S3.3b. From a graph of $\ln \frac{r+1}{r-1}$ vs t_m , the exchange rate, k_r is given from the gradient of the line.⁴⁴

$$\text{Peak intensity ratio } r' = \frac{I_{\text{syn:syn}} + I_{\text{anti-1:anti-1}} + I_{\text{anti-2:anti-2}} + I_{\text{anti-3:anti-3}} + I_{\text{anti-1:anti-3}} + I_{\text{anti-2:anti-3}} + I_{\text{anti-3:anti-1}} + I_{\text{anti-3:anti-2}}}{I_{\text{syn:anti-1}} + I_{\text{syn:anti-2}} + I_{\text{syn:anti-3}} + I_{\text{anti-1:syn}} + I_{\text{anti-2:syn}} + I_{\text{anti-3:syn}}} \quad (1)$$

Equation S3.1 Peak intensity ratio, S_r , calculated from the integrations of the diagonal and cross peaks.

$$r = 4(X_A)(X_B)r' - (X_A - X_B)^2 \quad (2)$$

where X_A = mole fraction of *syn*-isomer (*syn-3Br* = 0.26, *syn-3Ar* = 0.45) and X_B = mole fraction of *anti*-isomer (*anti-3Br* = 0.74, *anti-3Ar* = 0.55).

Equation S3.2 Value of r , calculated from peak intensity ratio r' and mole fractions (ratios) of *syn*- and *anti*-isomers at 80 °C in DMSO- d_6 .

$$(a) \quad k_r = \frac{1}{t_m} \ln \frac{r+1}{r-1} \quad (b) \quad \ln \frac{r+1}{r-1} = k_r t_m \quad (3)$$

Equation S3.3 (a) Rate of exchange equation, relating the exchange rate constant, k_r , function of r , and mixing time, t_m and (b) rearranged equation to give a linear relationship between r and t_m .

Using the gradient of the lines from the linear relationship between mixing time, t_m and a function of r , the exchange rate, k_r , for **3Br** and **3Ar** can be calculated. Using transition state theory, the rate of exchange can be related to the Gibbs energy through a modified Arrhenius equation (Equation S3.4). The modified Arrhenius equation can be rearranged to allow for the Gibbs energy of activation to be calculated for the exchange process from k_r (Equation S3.5). Furthermore, using the Arrhenius equation, half-lives for the rotation of **3Br** and **3Ar** at 353 and 298 K can be calculated (Table S3.5).

$$k_r = \frac{k_B T}{h} e^{-\frac{\Delta G^\ddagger}{RT}} \quad (4)$$

Equation S3.4 A modified Arrhenius equation for the rate of exchange, k_r , with Gibbs energy of the transition state for the rotation process.

$$\Delta G^\ddagger = -RT \ln \left(\frac{k_r h}{k_B T} \right) \quad (5)$$

Equation S3.5 A rearranged Arrhenius equation to give ΔG^\ddagger with respect to exchange rate.

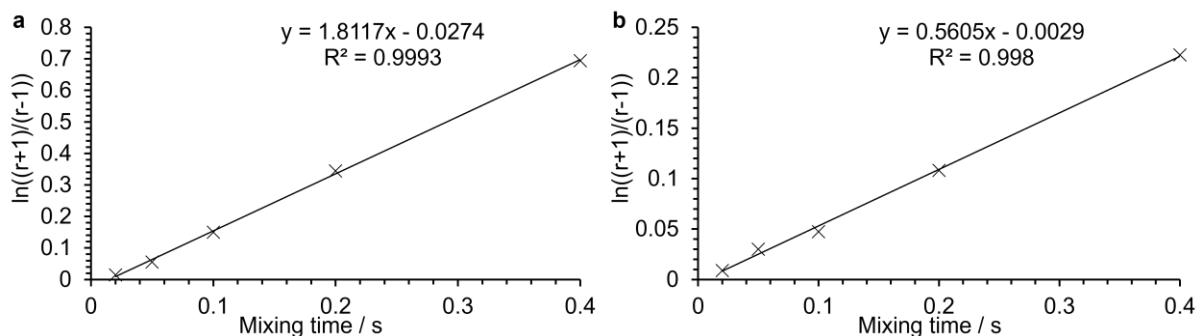


Figure S3.23 $\ln \frac{r+1}{r-1}$ vs mixing time, t_m graphs with line of best fit for the exchange of (a) **3Br** and (b) **3Ar**.

Table S3.5 Values for exchange rate, k_r , Gibbs energy, ΔG^\ddagger and half-life, $t_{1/2}$, at 353 and 298 K from ^1H - ^1H EXSY NMR spectroscopy experiments.

	3Br	3Ar
Exchange rate (k_r) (353 K) / s^{-1}	1.81 ± 0.03	0.560 ± 0.015
Gibbs energy of transition state (ΔG^\ddagger) / kcal mol^{-1}	20.4 ± 0.3	21.2 ± 0.6
Half-life (353 K) / s	0.383 ± 0.006	1.24 ± 0.03
Exchange rate (k_r) (298 K) / s^{-1}	0.00720 ± 0.00012	0.00179 ± 0.00005
Half-life (298 K) / s	96.3 ± 1.6	387 ± 10

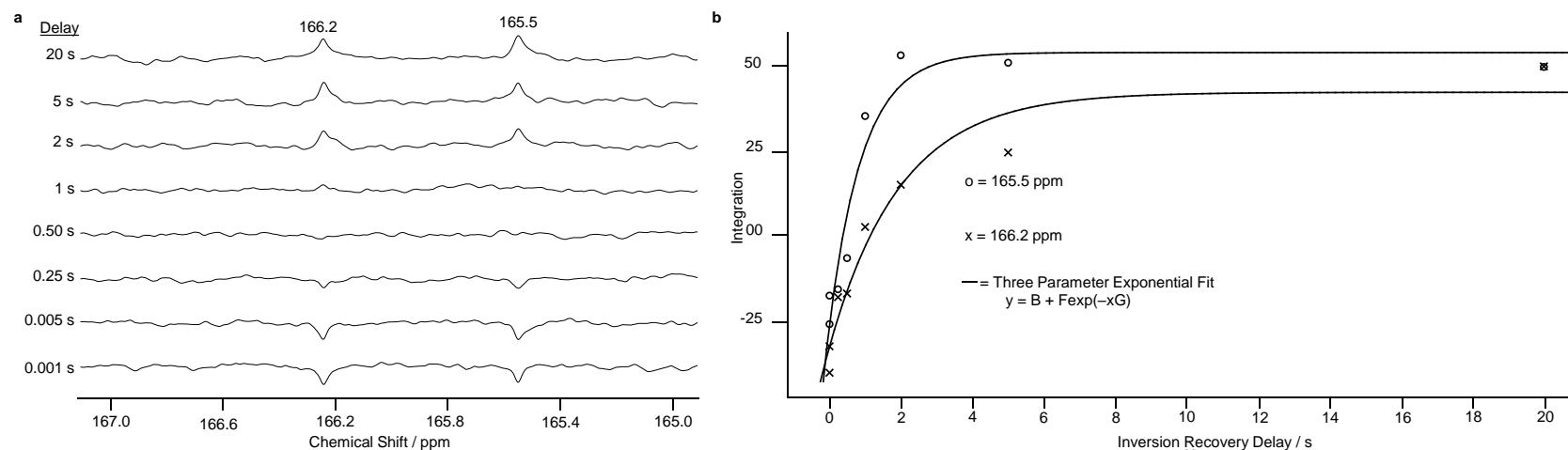
3.4.5.3 ^{13}C NMR SPECTROSCOPY T1 RELAXATION MEASUREMENTS

Figure S3.24 ^{13}C T1 relaxation measurements for **6H** using different inversion recovery delay times, (a) stacked ^{13}C NMR (600 MHz, DMSO- d_6 , 298 K) spectra for carbonyl peaks at 166.2 and 165.5 ppm. (b) Graph of integration vs inversion recovery delay time with three parameter fitting applied for carbonyl peaks at 166.2 and 165.5 ppm.

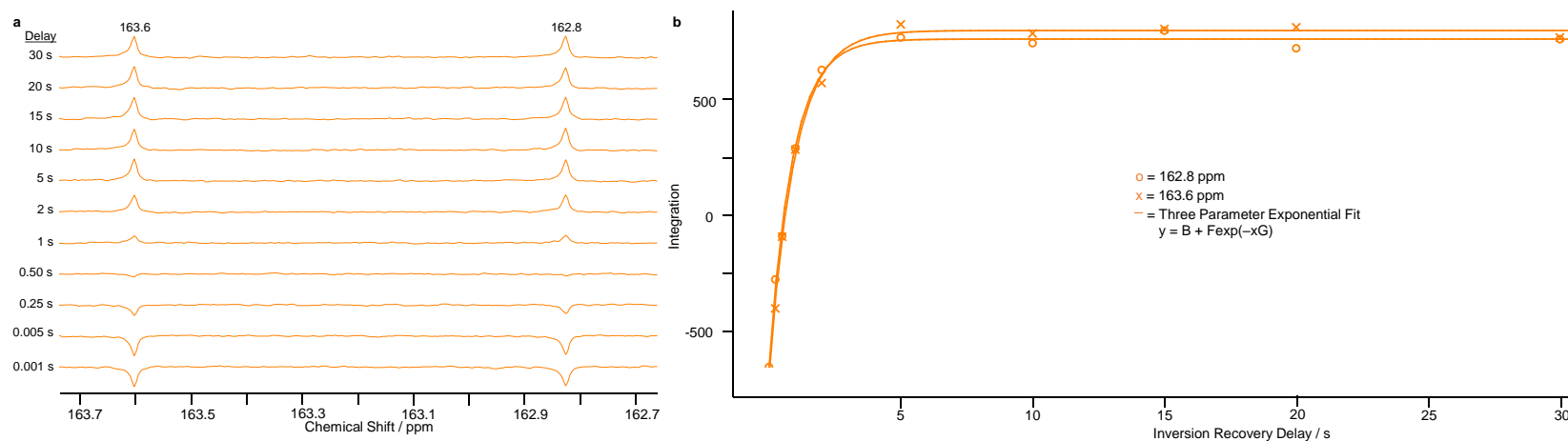


Figure S3.25 ^{13}C T1 relaxation measurements for **6Br** using different inversion recovery delay times, (a) stacked ^{13}C NMR (600 MHz, DMSO- d_6 , 298 K) spectra for carbonyl peaks at 163.6 and 162.8 ppm. (b) Graph of integration vs inversion recovery delay time with three parameter fitting applied for carbonyl peaks at 163.6 and 162.8 ppm.

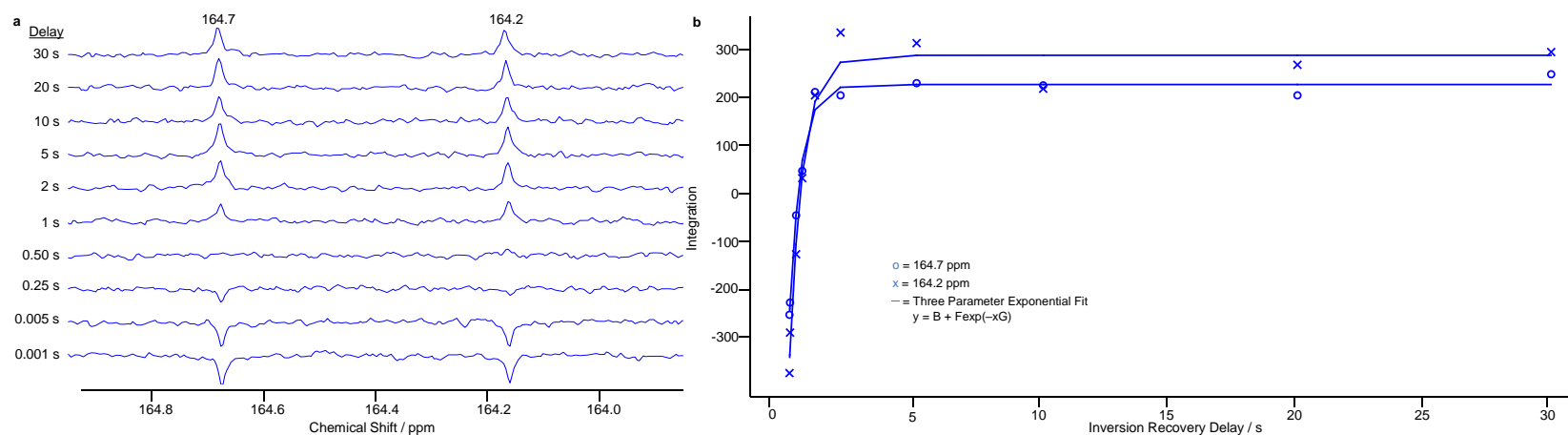


Figure S3.26 ^{13}C T1 relaxation measurements for **6Ar** using different inversion recovery delay times, (a) stacked ^{13}C NMR (600 MHz, DMSO- d_6 , 298 K) spectra for carbonyl peaks at 164.7 and 164.2 ppm. (b) Graph of integration vs inversion recovery delay time with three parameter fitting applied for carbonyl peaks at 164.7 and 164.2 ppm.

Table S3.6 Values from ^{13}C T1 relaxation measurements for **6H**, **6Br** and **6Ar** using a three-parameter exponential fit ($y = B + F \exp(-xG)$), where $T1 = 1/G$ for carbonyl peaks.

	Chemical Shift / ppm	B	F	G	T1 / s
6H	166.2	43.0076	-74.92	0.502492	1.99
	165.5	54.684	-80.4709	1.06031	0.94
6Br	163.6	798.233	-1503.34	1.01969	0.98
	162.8	761.2554	-1428.24	1.11895	0.89
6Ar	164.7	289.096	-629.004	1.88083	0.53
	164.2	228.345	-471.15	2.19431	0.46

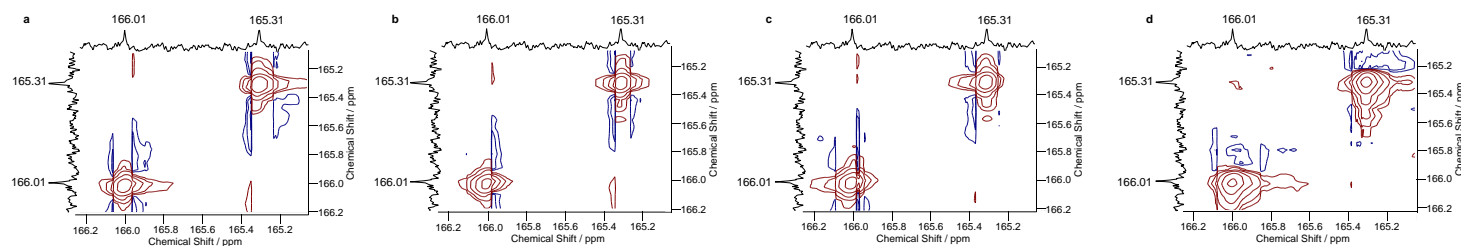
3.4.5.4 ^{13}C - ^{13}C EXSY NMR SPECTROSCOPY

Figure S3.27 ^{13}C - ^{13}C EXSY NMR (600 MHz, DMSO- d_6 , 80 °C) spectra for **6H** at (a) 100 ms, (b) 125 ms, (c) 150 ms and (d) 175 ms.

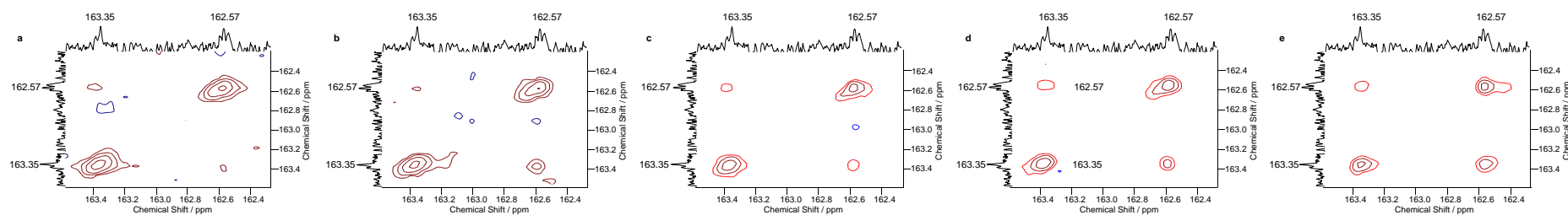


Figure S3.28 ^{13}C - ^{13}C EXSY NMR (600 MHz, DMSO- d_6 , 80 °C) spectra for **6Br** at (a) 100 ms, (b) 125 ms, (c) 150 ms, (d) 175 ms and (e) 200 ms.

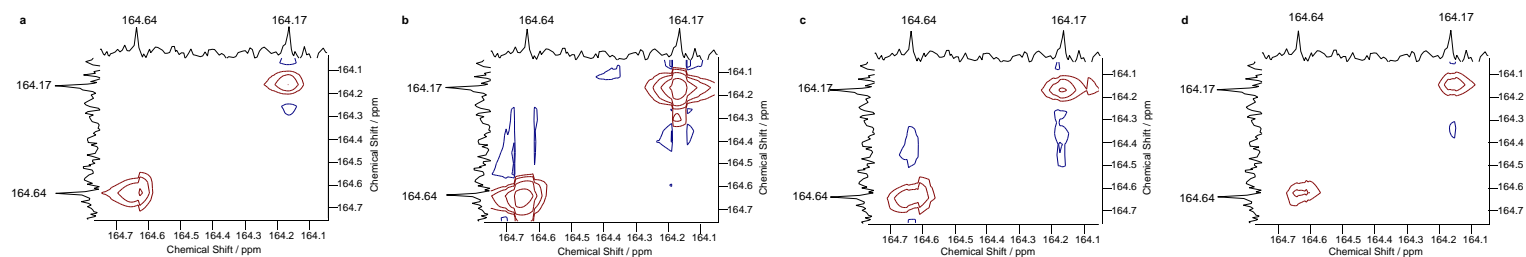


Figure S3.29 ^{13}C - ^{13}C EXSY NMR (600 MHz, DMSO- d_6 , 80 °C) spectra for **6Ar** at (a) 100 ms, (b) 125 ms, (c) 150 ms and (d) 175 ms.

The integration values of the cross peaks were divided by the integration of the diagonal peaks to give the peak intensity ratio, r' , Table S3.7 which is equal to the value of r for **6Br** as the mole fractions of the two forms were assumed to be equal ($X_A = X_B = 0.5$) as per Equation S3.2. The resulting values of a function of r were plotted against mixing time, t_m , using Equation S3.3b (Figure S3.30a), providing the exchange rate from the gradient of the line of best fit. The exchange rate, k_r , was then used to evaluate the Gibbs energy barrier of the transition state, ΔG^\ddagger (Equation S3.5) and half-lives at 353 and 298 K, Table S3.8.

Table S3.7 Values of peak intensity ratio, r' and thus r from ^{13}C - ^{13}C EXSY NMR spectroscopy experiments showing the ratio of cross and diagonal exchange peaks for **6H**, **6Br** and **6Ar** at different mixing times 100, 125, 150, 175 and 200 ms.

Mixing Time / ms	6H	6Br	6Ar
100	77.02	16.39	No exchange
125	22.35 ^a	5.84	No exchange
150	49.38	5.37	No exchange
175	36.88	3.18	No exchange
200	Not Measured	1.91	Not Measured

^aProbable Outlier

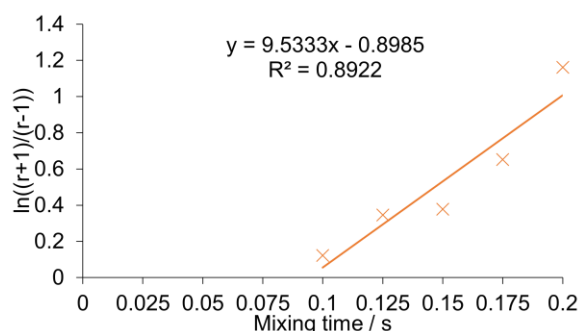


Figure S3.30 $\ln \frac{r+1}{r-1}$ vs mixing time, t_m graph with line of best fit for **6Br**.

Table S3.8 Values for exchange rate, k_r , Gibbs energy, ΔG^\ddagger and half-life, $t_{1/2}$, at 353 and 298 K from ^{13}C - ^{13}C EXSY NMR spectroscopy experiments for **6Br**.

	6Br
Exchange rate (k_r) (353 K) / s^{-1}	9.5 ± 1.9
Gibbs energy of transition state (ΔG^\ddagger) / kcal mol^{-1}	19 ± 4
Half-life (353 K) / s	0.069 ± 0.014
Exchange rate (k_r) (298 K) / s^{-1}	0.054 ± 0.011
Half-life (298 K) / s	13 ± 3

3.4.5.5 HOST–GUEST NMR SPECTROSCOPY TITRATIONS

The ability of molecular triangles, **6H**, **3Br**, **3Ar**, **6Br** and **6Ar** to host an electron-rich guest were studied by either ^1H or ^{13}C NMR spectroscopy titration depending on whether the macrocycle had a proton on the PMDI aromatic-core. The titrations were carried out by sequentially adding portions of a solution of guest (tetrabutylammonium triiodide) in CDCl_3 to a solution of host (molecular triangle) in CDCl_3 at room temperature. The concentrations of host and guest solutions used for each molecular triangle are shown in Table S3.9. Two guest solutions were prepared for low (≈ 0 –10 eq.) and high (≈ 25 –250 eq.) guest equivalents measurements. The guest solutions contained host at an equivalent concentration to the original solution to maintain a constant concentration of host in the NMR tube.

Table S3.9 Concentrations of host and guest solutions used in NMR titrations for molecular triangles, **6H**, **3Br**, **6Br**, **3Ar**, **6Ar**.

Host	NMR experiment	Host Concentration / mM	Guest Concentration / mM (Low)	Guest Concentration / mM (High)
6H	^1H	1.46	151.14	1598.96
3Br	^1H	1.40	151.04	1565.56
3Ar	^1H	1.64	162.37	1462.26
6Br	^{13}C	5.41	1049.56	1591.13
6Ar	^{13}C	5.28	1001.01	1001.01

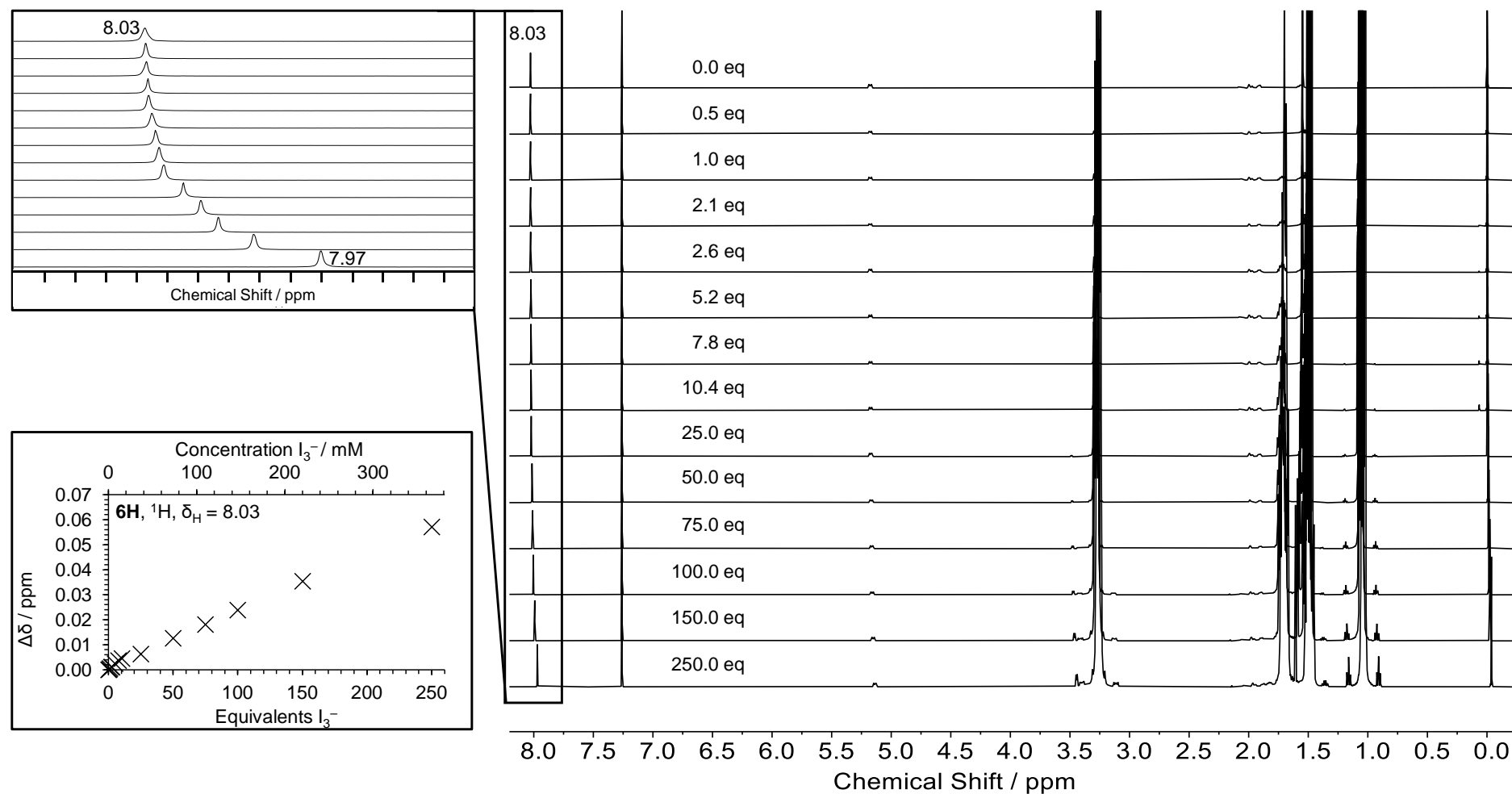


Figure S3.31 Stacked ^1H NMR (500 MHz, CDCl_3 , 298 K) spectra from host-guest titrations for **6H**. (Inset) showing carbon environment in which the change in shift is monitored and the change in shift plotted against guest equivalents/concentration with experimental data points.

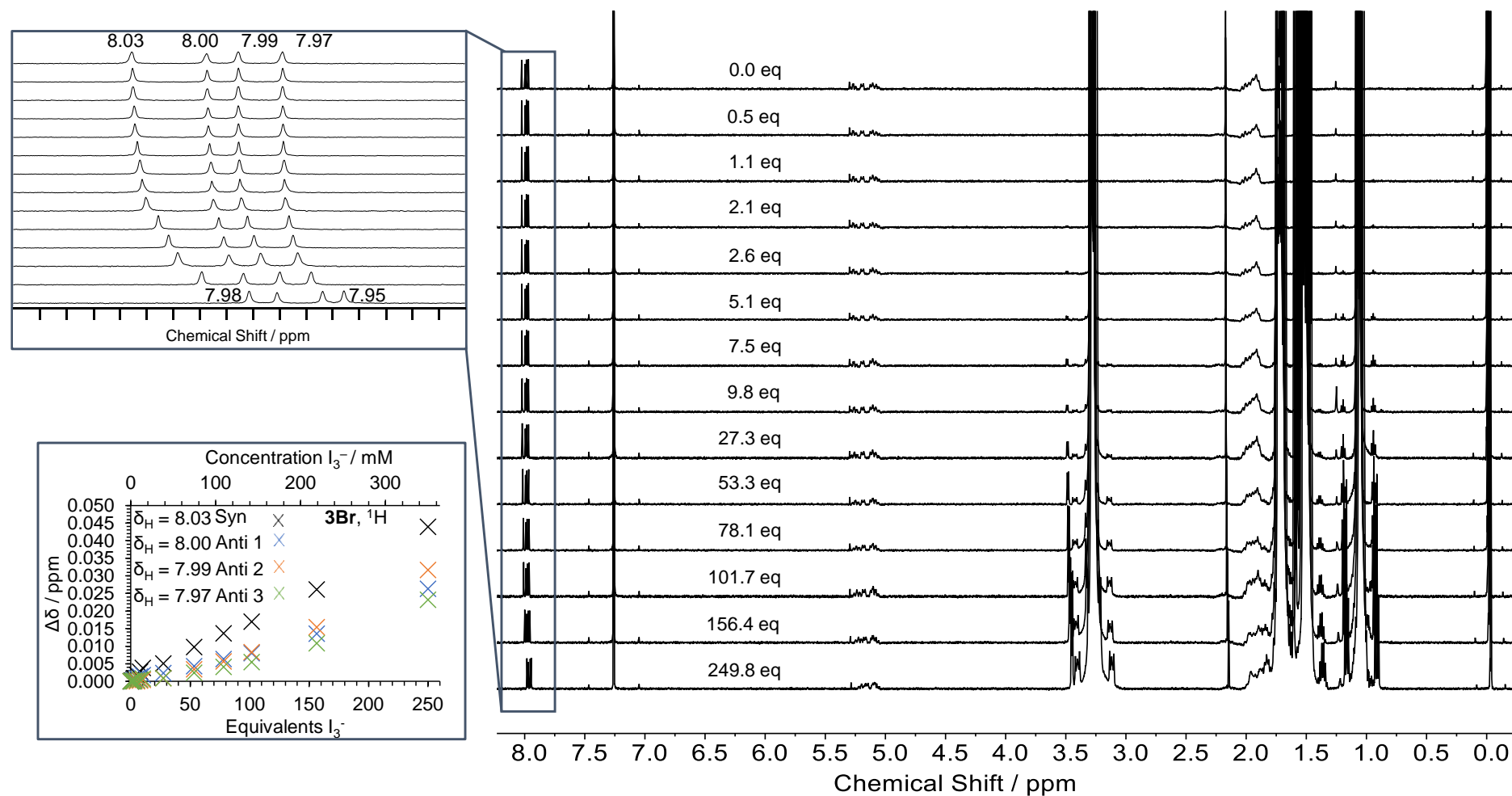


Figure S3.32 Stacked ^1H NMR (500 MHz, CDCl_3 , 298 K) spectra from host-guest titrations for **3Br**. (Inset) showing carbon environment in which the change in shift is monitored and the change in shift plotted against guest equivalents/concentration with experimental data points.

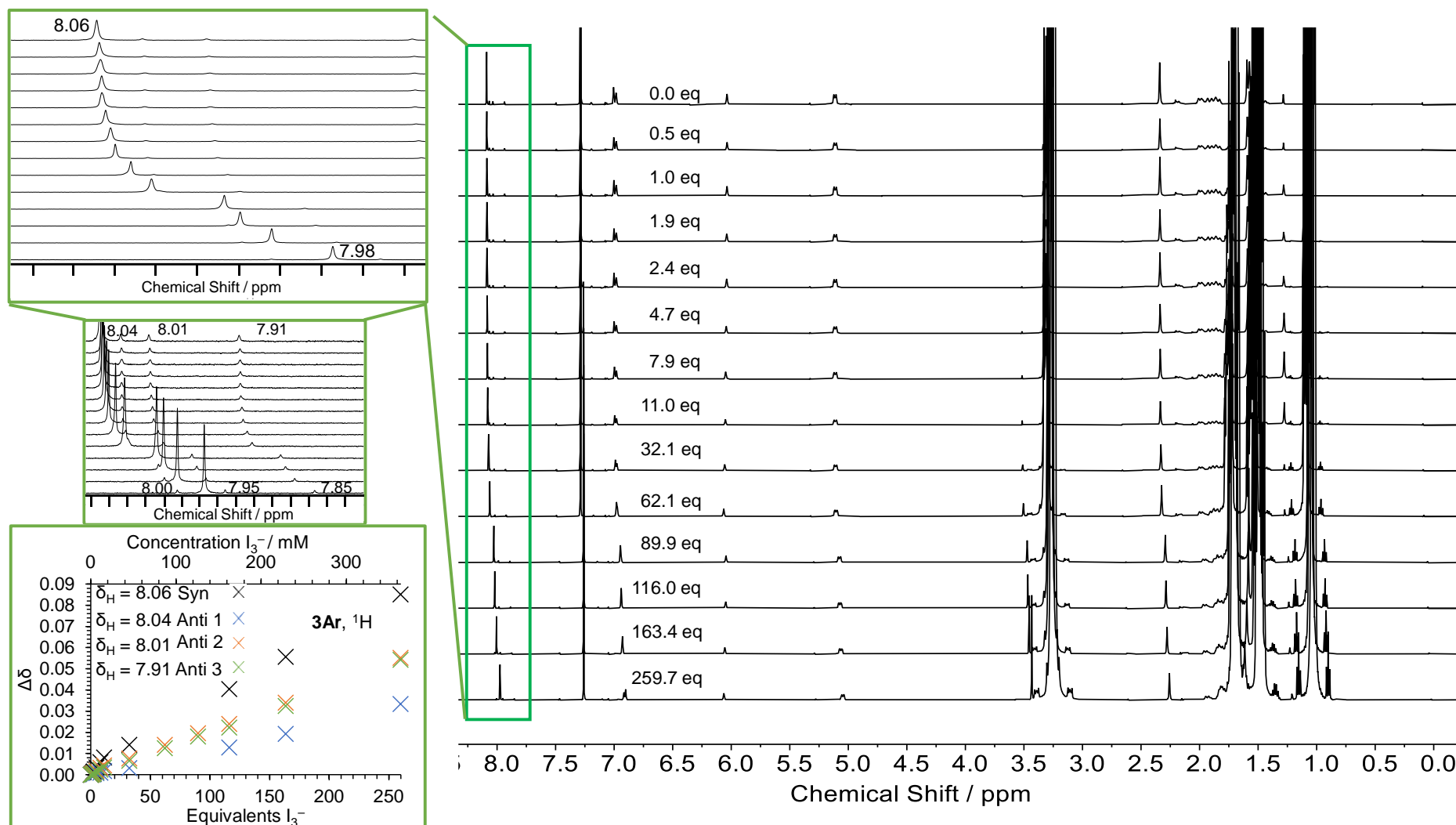


Figure S3.33 Stacked ^1H NMR (500 MHz, CDCl_3 , 298 K) spectra from host-guest titrations for **3Ar**. Inset showing carbon environment in which the change in shift is monitored and the change in shift plotted against guest equivalents/concentration with experimental data points.

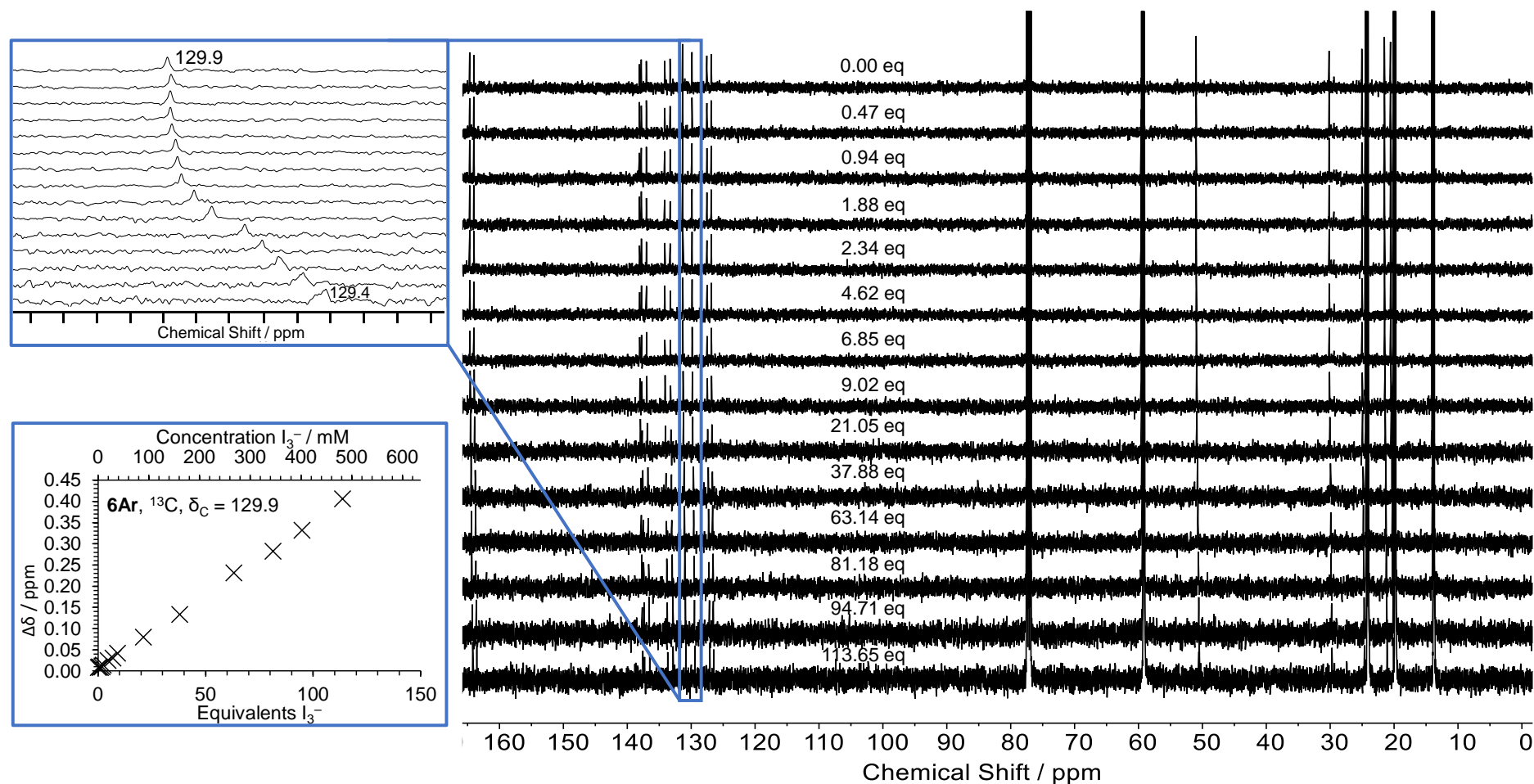


Figure S3.34 Stacked ^{13}C NMR (126 MHz, CDCl_3 , 298 K) spectra from host-guest titrations for **6Ar**. Inset showing carbon environment in which the change in shift is monitored and the change in shift plotted against guest equivalents/concentration with experimental data points.

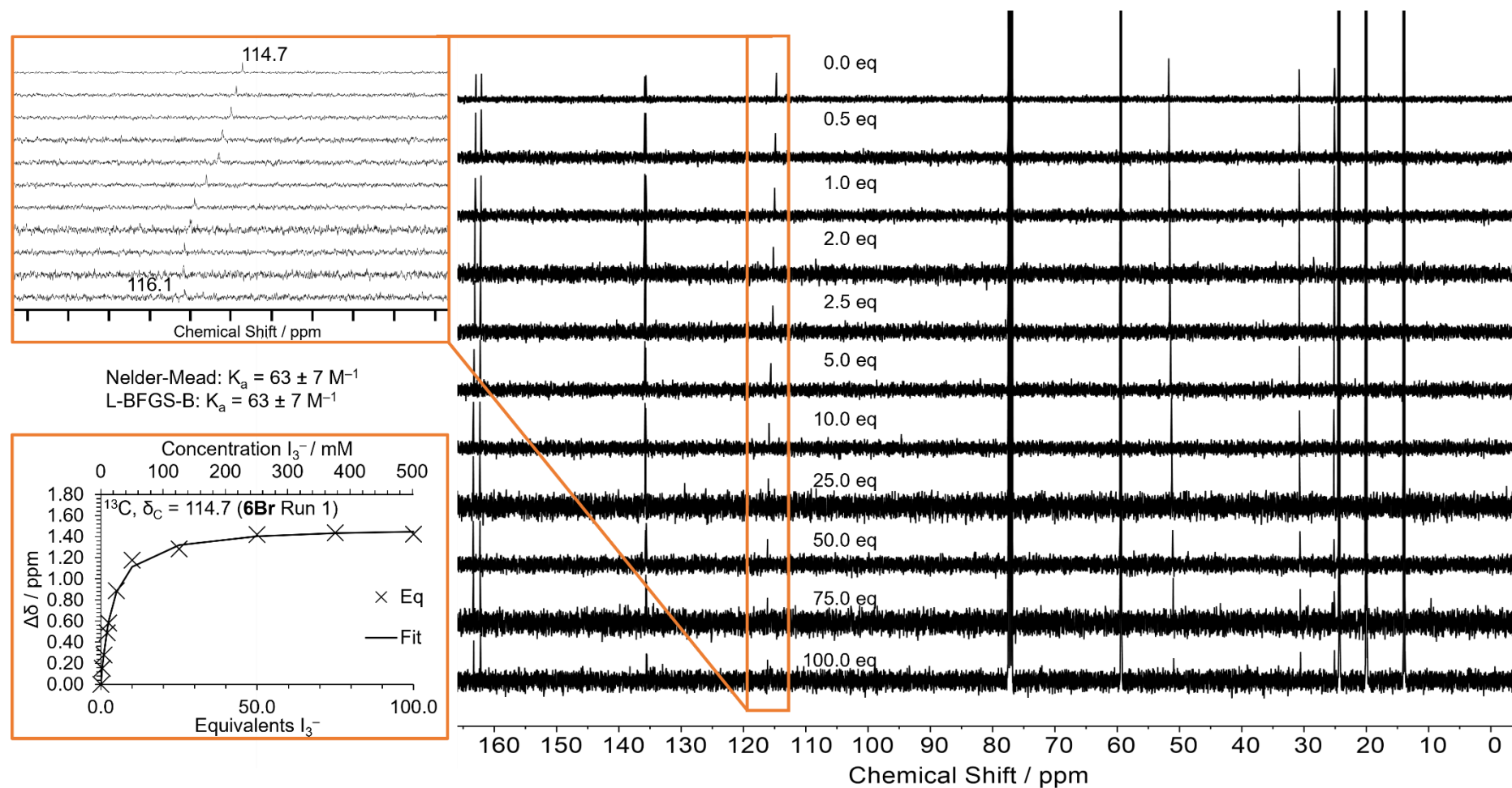


Figure S3.35 Stacked ^{13}C NMR (126 MHz, CDCl_3 , 298 K) spectra from host-guest titrations for **6Br** for run 1. (Inset) showing carbon environment in which the change in shift is monitored and the change in shift plotted against guest equivalents/concentration with experimental data points and a line showing the values for the least-squares regression fitting.

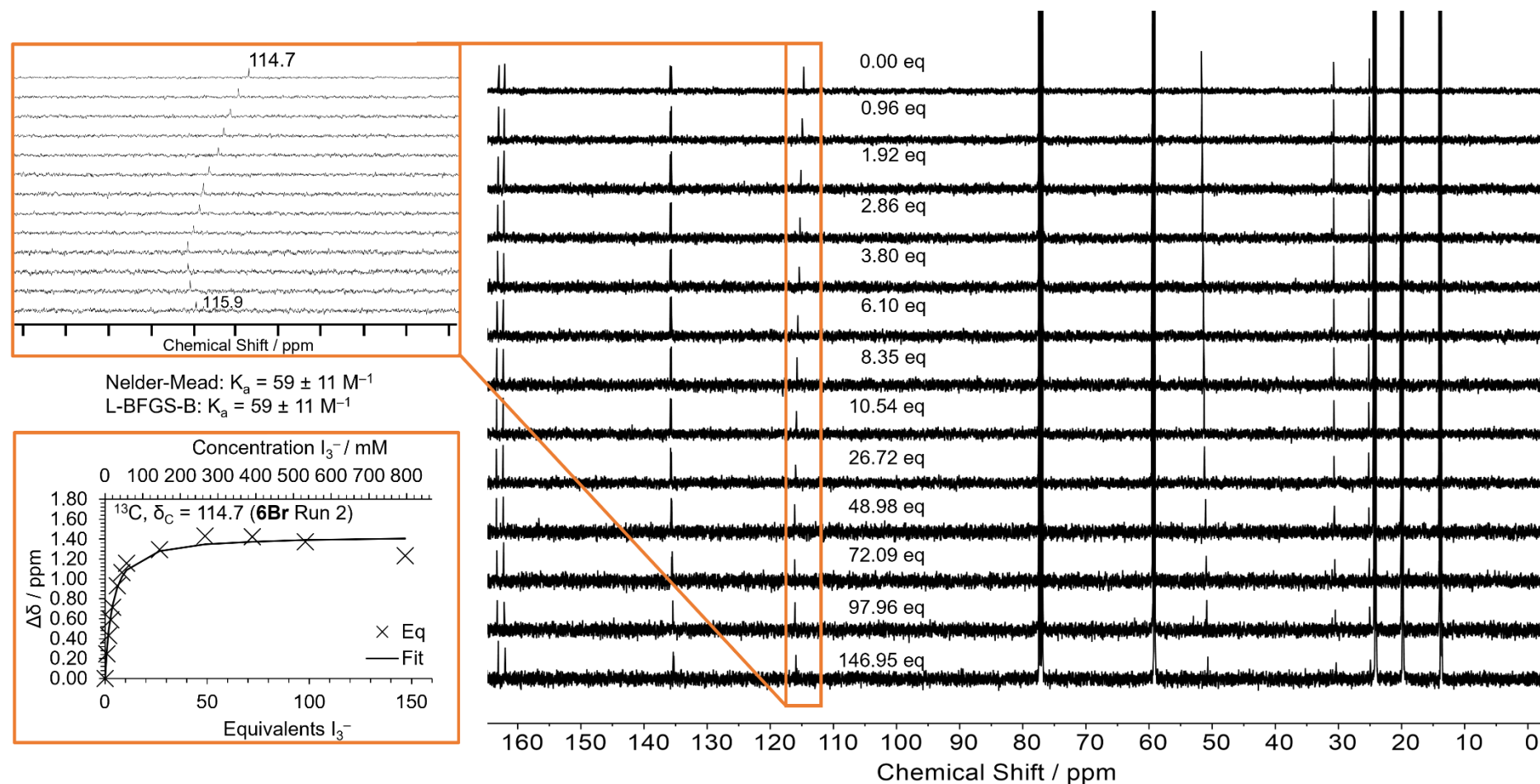


Figure S3.36 Stacked ^{13}C NMR (126 MHz, CDCl_3 , 298 K) spectra from host-guest titrations for **6Br** for run 2. (Inset) showing carbon environment in which the change in shift is monitored and the change in shift plotted against guest equivalents/concentration with experimental data points and a line showing the values for the least-squares regression fitting.

3.4.6 UV-VIS SPECTROSCOPY

3.4.6.1 CONCENTRATION-DEPENDENT UV-VIS SPECTROSCOPY

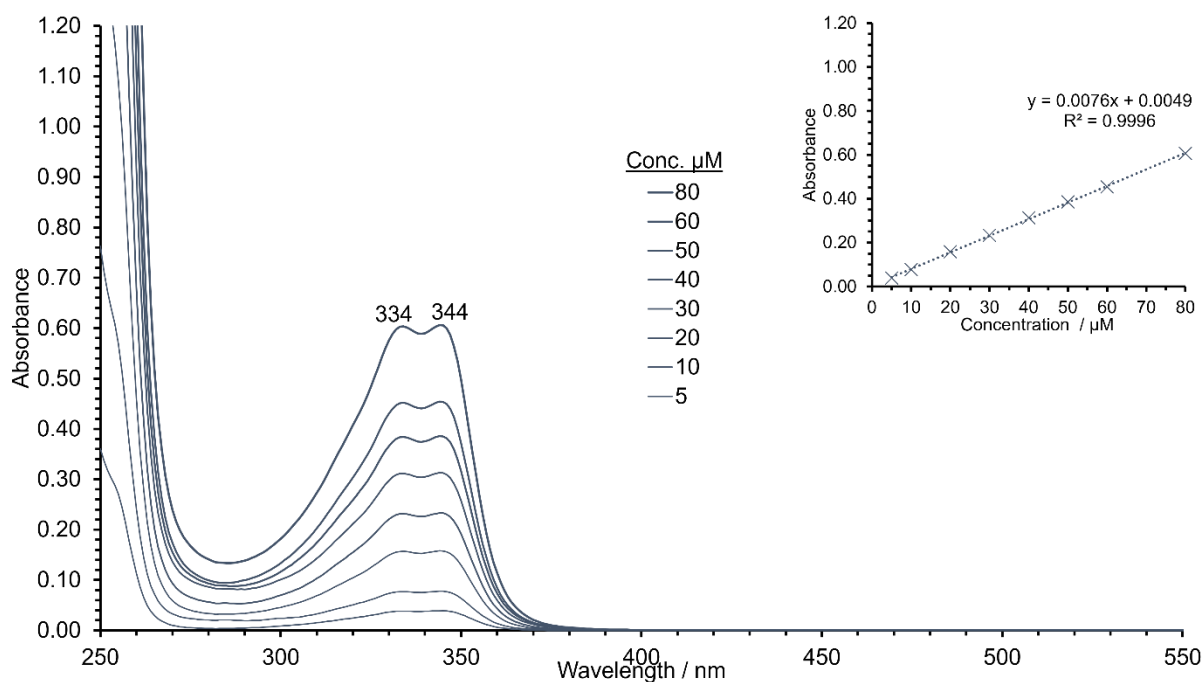


Figure S3.37 Concentration-dependent UV-vis spectrum of compound **3Br** in CH_2Cl_2 (80–5 μM). **Inset.** Beer-Lambert plot at 344 nm.

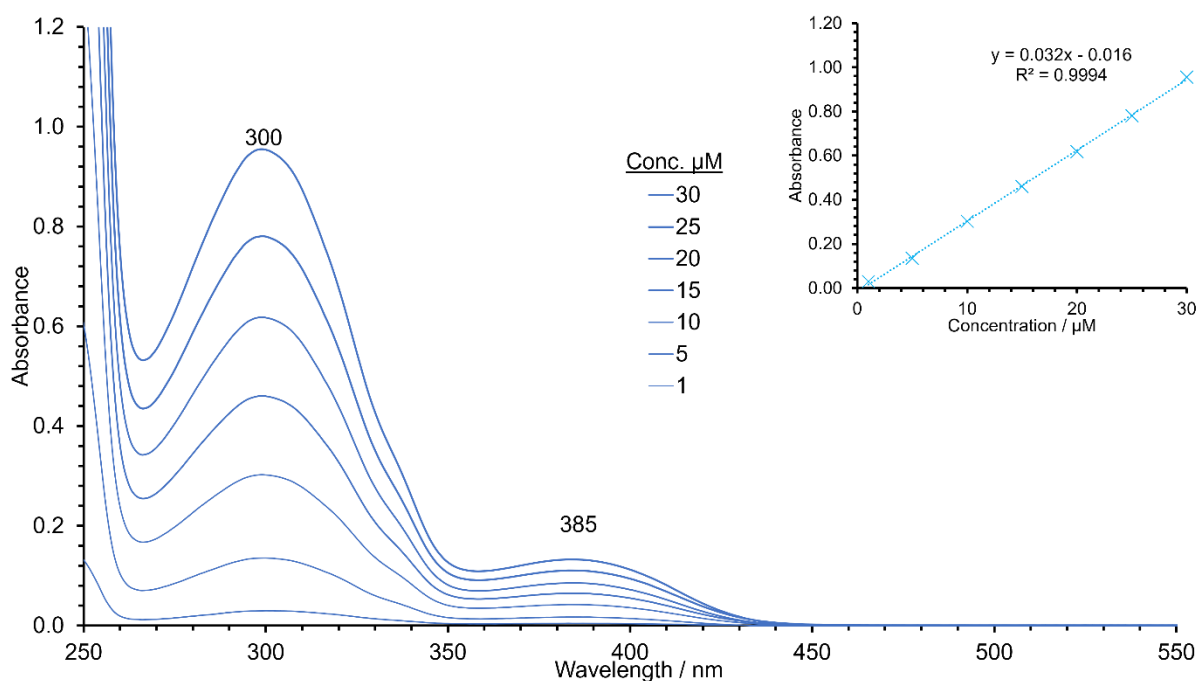


Figure S3.38 Concentration-dependent UV-vis spectrum of compound **3Ar** in CH_2Cl_2 (30–1 μM). **Inset.** Beer-Lambert plot at 299 nm.

3.4.6.2 HOST–GUEST UV-VIS SPECTROSCOPY TITRATIONS

The potential for molecular triangles **6H**, **3Br** and **6Br** to host the triiodide anion was investigated by UV-vis spectroscopy. The titrations were carried out by sequentially adding portions of a solution of

guest (tetrabutylammonium triiodide) in CH_2Cl_2 to a solution of host (molecular triangle) in CH_2Cl_2 at room temperature. The concentrations of host and guest solutions used for each molecular triangle are shown in Table S3.10.

Table S3.10 Concentrations of host and guest solutions used in UV-vis spectroscopy titrations for molecular triangles **6H**, **3Br** and **6Br**.

Host	Host Concentration / mM	Guest Concentration / mM
6H	0.17	18.69
3Br	0.13	13.97
6Br	0.09	9.96

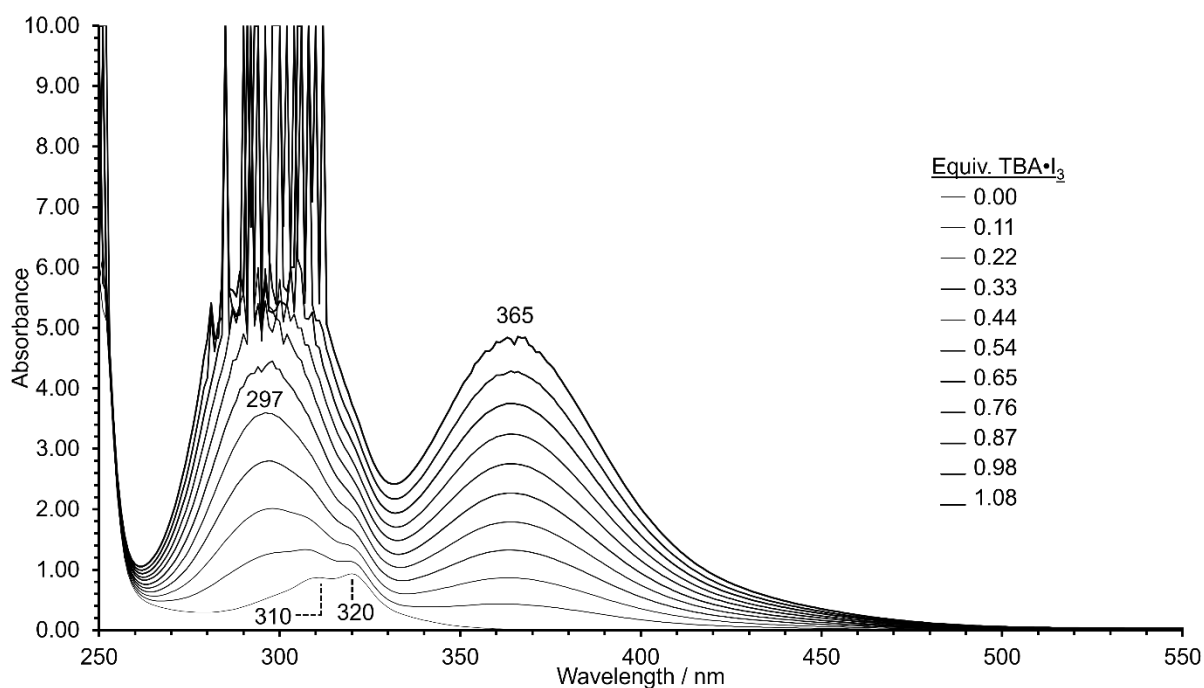


Figure S3.39 UV-vis spectra of a host–guest solution of **6H** with $\text{TBA}\cdot\text{I}_3$ in CH_2Cl_2 with increasing equivalents of guest.

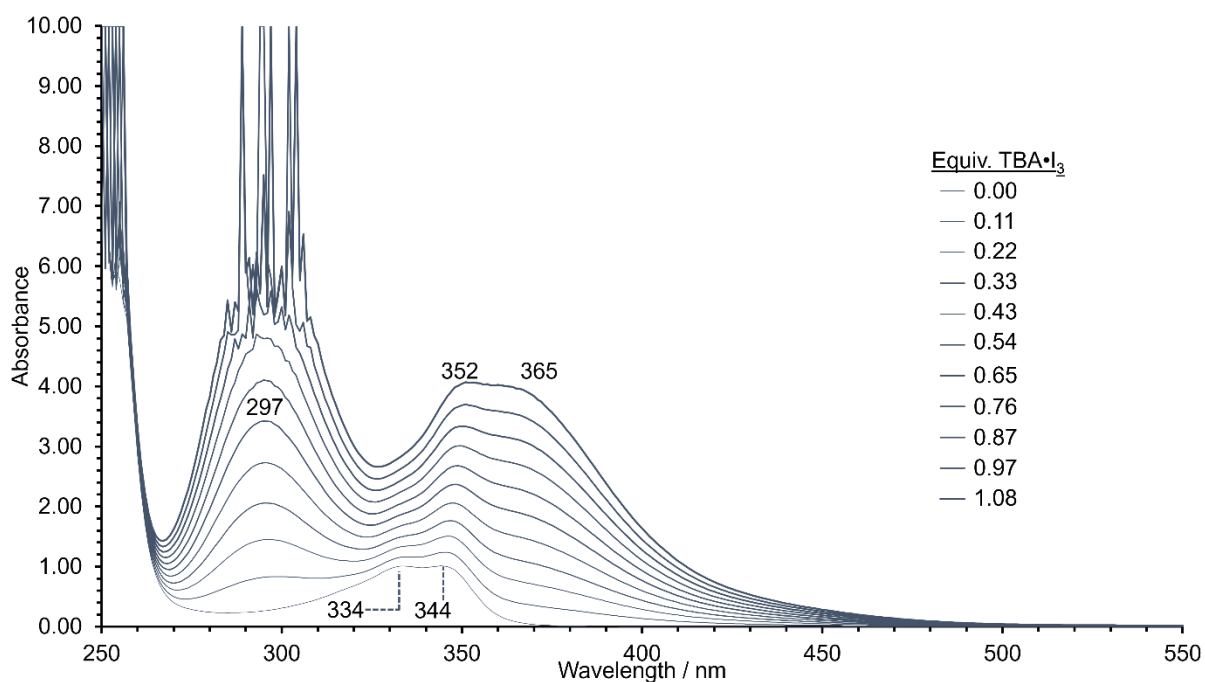


Figure S3.40 UV-vis spectra of a host-guest solution of **3Br** with $\text{TBA}\cdot\text{I}_3$ in CH_2Cl_2 with increasing equivalents of guest.

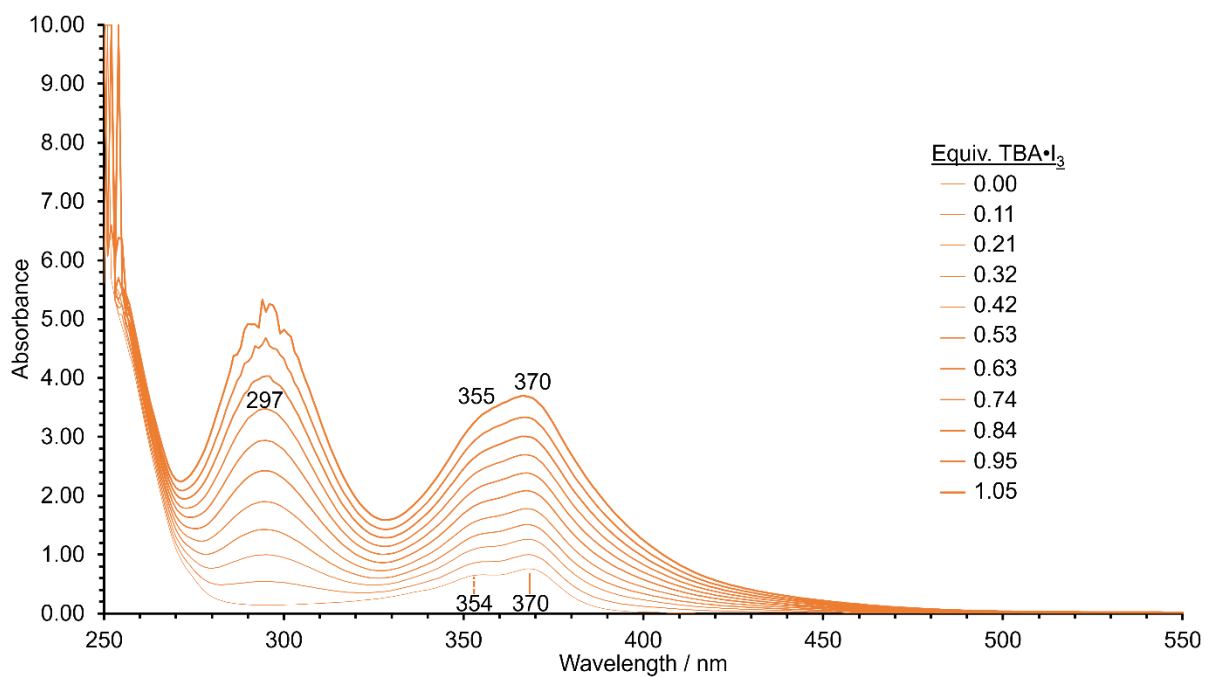


Figure S3.41 UV-vis spectra of a host-guest solution of **6Br** with $\text{TBA}\cdot\text{I}_3$ in CH_2Cl_2 with increasing equivalents of guest.

3.4.7 COMPUTATIONAL MODELLING

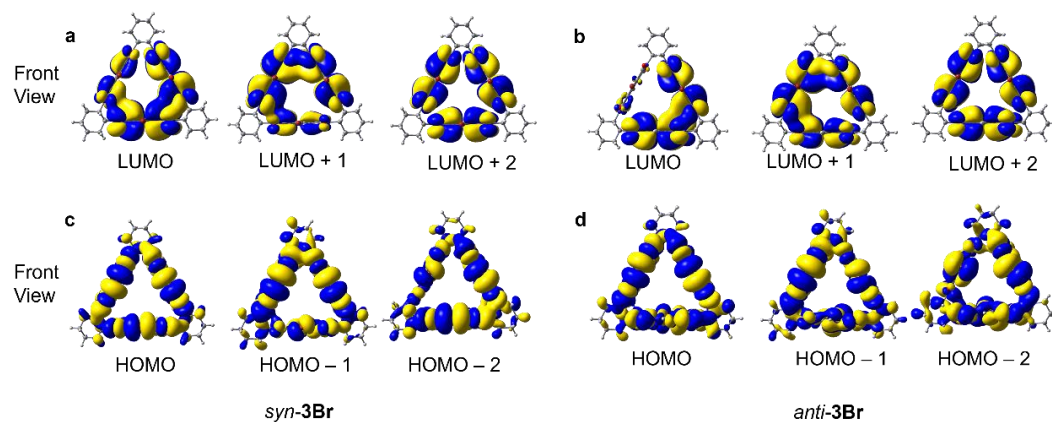


Figure S3.42 Visual depictions of the LUMO, LUMO+1 and LUMO+2 of (a) *syn-3Br* and (b) *anti-3Br* and HOMO, HOMO-1 and HOMO-2 of (c) *syn-3Br* and (d) *anti-3Br*. Isovalue = 0.05.

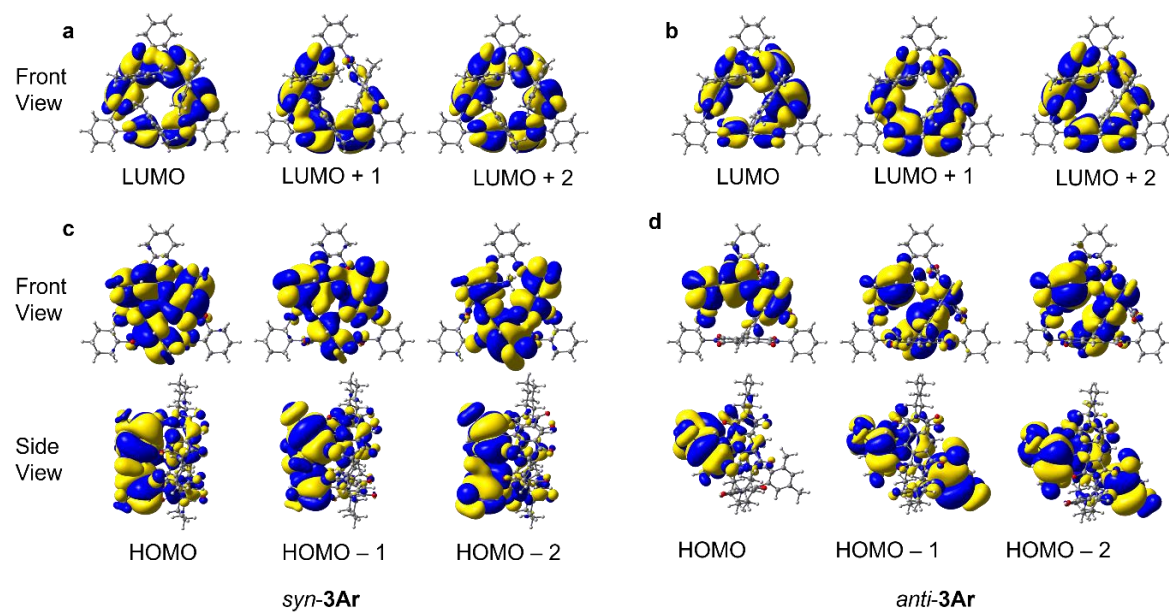


Figure S3.43 Visual depictions of the LUMO, LUMO+1 and LUMO+2 of (a) *syn*-3Ar and (b) *anti*-3Ar and HOMO, HOMO-1 and HOMO-2 of (c) *syn*-3Ar and (d) *anti*-3Ar from front and side views. Isovalue = 0.05.

Table S3.11 Cartesian coordinates of geometry-optimised structure of *syn*-**3Br** at the B3LYP-D3(BJ)/def2svp level of theory in CH₂Cl₂ (PCM solvent model).

C	5.616908	-8.1404	17.44707	C	6.655895	-8.08761	11.54654
H	5.39433	-9.20805	17.57242	C	7.04707	-9.20076	10.80933
C	4.844525	-7.6215	16.21557	C	7.603211	-9.24878	9.419092
H	5.040554	-6.54606	16.11089	N	7.871373	-10.5922	9.160652
C	7.884557	-9.21019	17.47628	N	5.339889	-8.20158	14.9713
C	9.281328	-8.76852	17.14727	O	7.58609	-12.6282	10.23388
C	10.49697	-9.46369	17.17175	O	5.214975	-10.4599	15.48637
C	11.63091	-8.73307	16.79594	O	5.61999	-6.21154	13.80209
C	13.07985	-9.12746	16.71678	O	7.787972	-8.32094	8.66404
C	12.90459	-6.90866	16.04324	C	7.451763	-11.1042	6.756711
C	11.53561	-7.38932	16.40746	H	6.528078	-11.6205	7.060165
C	10.33576	-6.68522	16.3839	H	7.185588	-10.0587	6.529746
C	9.219026	-7.41993	16.7693	C	8.068262	-11.7755	5.525533
C	7.792982	-6.97	16.85744	H	7.362244	-11.7281	4.681685
N	7.061851	-8.09066	17.24901	H	8.22987	-12.8459	5.743367
N	13.75756	-8.00378	16.22451	C	9.403389	-11.1299	5.141305
O	7.497079	-10.285	17.86239	H	9.223878	-10.0931	4.806235
O	13.59392	-10.1802	17.01171	H	9.856584	-11.6626	4.290634
O	13.23285	-5.80792	15.66891	C	10.38025	-11.1104	6.321285
O	7.351004	-5.86507	16.63648	H	11.30766	-10.583	6.050132
C	15.6869	-9.08048	15.06724	H	10.65739	-12.1388	6.605899
H	15.60138	-10.0182	15.63157	C	16.02941	-7.85872	17.24373
C	15.19105	-7.9243	15.9611	H	15.88611	-8.78947	17.81683
H	15.31337	-6.98255	15.40965	H	15.66198	-7.02872	17.86661
C	14.30114	-10.5412	13.57467	C	17.51057	-7.66644	16.90319
C	13.45709	-10.3284	12.35119	H	18.10718	-7.65014	17.82869
C	12.67632	-11.2197	11.60443	H	17.64383	-6.68096	16.423
C	12.0016	-10.6742	10.50537	C	18.01821	-8.76164	15.95986
C	11.09562	-11.3095	9.487264	H	17.99749	-9.73309	16.48453
C	11.25271	-9.04326	8.989683	H	19.0677	-8.57415	15.6838
C	12.10417	-9.31193	10.19027	C	17.15838	-8.85914	14.69577
C	12.8811	-8.41696	10.9194	H	17.24624	-7.93508	14.10101
C	13.55121	-8.97312	12.00444	H	17.49361	-9.69291	14.05996
C	14.45608	-8.29581	12.98786	C	5.162891	-7.38914	18.70471
N	14.8312	-9.27894	13.90225	H	5.414414	-6.32105	18.59864
N	10.66687	-10.2693	8.652083	H	5.722893	-7.77475	19.57048
O	14.51626	-11.5594	14.1838	C	3.655202	-7.56178	18.91341
O	10.78022	-12.4706	9.376044	H	3.33425	-6.99633	19.80225
O	11.08861	-7.99539	8.411412	H	3.440417	-8.62516	19.11978
O	14.7983	-7.13478	13.00092	C	2.861972	-7.11525	17.6812
C	8.440818	-11.1285	7.928776	H	2.98315	-6.02612	17.54455
H	8.678628	-12.1727	8.169762	H	1.786143	-7.29707	17.83055
C	9.745846	-10.4087	7.528666	C	3.338603	-7.83308	16.41462
H	9.50067	-9.37532	7.249922	H	2.806318	-7.45476	15.52841
C	7.494338	-11.4258	10.23061	H	3.131979	-8.91342	16.48682

C	6.97349	-10.5114	11.30153	H	12.95624	-7.35987	10.66212
C	6.480623	-10.782	12.5843	H	6.723694	-7.07165	11.15607
C	6.075957	-9.67102	13.33439	H	10.27508	-5.6383	16.0847
C	5.49901	-9.57084	14.71921	Br	12.52848	-13.0448	12.06167
C	5.695274	-7.41539	13.86887	Br	6.381991	-12.5384	13.26762
C	6.175167	-8.36997	12.82143	Br	10.59817	-11.2822	17.66564

Table S3.12 Cartesian coordinates of geometry-optimised structure of *anti*-**3Br** at the B3LYP-D3(BJ)/def2svp level of theory in CH₂Cl₂ (PCM solvent model).

C	5.627781	-8.13987	17.44927	C	6.669663	-8.09358	11.5567
H	5.437761	-9.21426	17.57323	C	7.056979	-9.20492	10.81478
C	4.836708	-7.64396	16.21982	C	7.613533	-9.24898	9.424585
H	5.00645	-6.56463	16.11049	N	7.875072	-10.5925	9.159698
C	7.926474	-9.13757	17.44603	N	5.341243	-8.2178	14.97625
C	9.300913	-8.64484	17.11989	O	7.578742	-12.6322	10.22275
C	10.50224	-9.3464	17.14871	O	5.216733	-10.4771	15.4857
C	11.61956	-8.60853	16.77082	O	5.633366	-6.22388	13.81629
C	13.04777	-9.05399	16.69313	O	7.802991	-8.31847	8.674049
C	12.94753	-6.82678	16.03096	C	7.449867	-11.0966	6.75492
C	11.55469	-7.26275	16.38344	H	6.525279	-11.6109	7.058927
C	10.34016	-6.56557	16.36984	H	7.186208	-10.0498	6.530552
C	9.20802	-7.29463	16.75363	C	8.062388	-11.7673	5.52141
C	7.764175	-6.89081	16.86769	H	7.355202	-11.7161	4.678761
N	7.070259	-8.04795	17.24617	H	8.221021	-12.8386	5.736977
N	13.76407	-7.95896	16.21111	C	9.398922	-11.1251	5.136206
O	7.597297	-10.2419	17.8087	H	9.222034	-10.0873	4.802936
O	13.50113	-10.1374	16.98546	H	9.849208	-11.6579	4.284055
O	13.33788	-5.74479	15.66841	C	10.3777	-11.1102	6.3147
O	7.265397	-5.80582	16.68357	H	11.30609	-10.5848	6.042871
C	15.67078	-9.09924	15.07913	H	10.65253	-12.1397	6.59739
H	15.55792	-10.0268	15.6555	C	16.03166	-7.86163	17.2425
C	15.20035	-7.91926	15.95486	H	15.8598	-8.78189	17.82506
H	15.35177	-6.98752	15.39422	H	15.68217	-7.01526	17.85349
C	14.28745	-10.5539	13.58045	C	17.51952	-7.71182	16.91005
C	13.45045	-10.3397	12.35234	H	18.11054	-7.70059	17.8392
C	12.67113	-11.2291	11.60185	H	17.68093	-6.7354	16.42013
C	12.00084	-10.6816	10.50116	C	18.00472	-8.82993	15.98194
C	11.09454	-11.314	9.481631	H	17.95666	-9.79464	16.51716
C	11.25931	-9.04827	8.984431	H	19.06012	-8.67198	15.70997
C	12.10756	-9.31946	10.1868	C	17.14971	-8.92058	14.7141
C	12.88464	-8.4267	10.91851	H	17.26466	-8.00654	14.10836
C	13.54921	-8.98473	12.00601	H	17.46691	-9.77047	14.09054
C	14.45238	-8.30971	12.99257	C	5.156377	-7.40456	18.71002
N	14.81838	-9.29292	13.91073	H	5.378661	-6.33006	18.60612
N	10.66979	-10.2725	8.646305	H	5.728847	-7.77719	19.57336
O	14.49694	-11.5724	14.19118	C	3.654382	-7.61719	18.92208
O	10.77558	-12.4741	9.370129	H	3.321534	-7.06302	19.81363

O	11.09982	-8.00014	8.405434	H	3.466993	-8.68638	19.12525
O	14.80005	-7.15036	13.00419	C	2.847311	-7.18668	17.69324
C	8.441023	-11.1262	7.925064	H	2.942605	-6.09474	17.55856
H	8.676864	-12.1717	8.162544	H	1.776457	-7.39402	17.84514
C	9.746957	-10.4086	7.524019	C	3.337027	-7.8917	16.42459
H	9.50366	-9.3743	7.246887	H	2.792752	-7.52632	15.54021
C	7.493143	-11.4294	10.22533	H	3.156753	-8.97655	16.49749
C	6.976234	-10.5176	11.30043	H	12.96336	-7.36972	10.66182
C	6.480152	-10.792	12.58114	H	6.742147	-7.07605	11.17115
C	6.079983	-9.68282	13.33632	Br	12.52007	-13.0549	12.05552
C	5.501353	-9.58622	14.72079	Br	6.369056	-12.5517	13.25419
C	5.704301	-7.42816	13.87871	H	10.56283	-10.395	17.44192
C	6.185336	-8.37992	12.82933	Br	10.23423	-4.75299	15.85491

Table S3.13 Cartesian coordinates of geometry-optimised structure of *syn*-**3Ar** at the B3LYP-D3(BJ)/def2svp level of theory in CH₂Cl₂ (PCM solvent model).

C	5.762582	-8.12806	17.55312	H	18.28047	-7.54459	17.52299
H	5.540401	-9.1965	17.67188	H	17.77492	-6.63183	16.09423
C	4.958081	-7.59357	16.34779	C	18.08775	-8.73923	15.71427
H	5.159685	-6.51901	16.2444	H	18.06544	-9.68554	16.28315
C	8.031908	-9.20544	17.46007	C	17.17616	-8.87002	14.49014
C	9.424897	-8.746	17.1321	H	17.26147	-7.97414	13.8539
C	10.64124	-9.45746	17.10638	H	17.46727	-9.7373	13.87753
C	11.74513	-8.68036	16.70187	C	5.347344	-7.39002	18.83158
C	13.21071	-9.02156	16.68014	H	5.602088	-6.32218	18.73209
C	12.97983	-6.84455	15.90042	H	5.9277	-7.78933	19.67769
C	11.62948	-7.34049	16.30767	C	3.844481	-7.55595	19.07807
C	10.42447	-6.64632	16.3343	H	3.550992	-7.00032	19.98256
C	9.336207	-7.39231	16.77383	H	3.627794	-8.62062	19.27591
C	7.917424	-6.94684	16.92272	C	3.021684	-7.08795	17.87334
N	7.200914	-8.07807	17.31246	H	3.149221	-5.9983	17.74648
N	13.85887	-7.90883	16.12275	H	1.948716	-7.26177	18.05076
O	7.639082	-10.3029	17.7794	C	3.456809	-7.79544	16.5862
O	13.7731	-10.014	17.08008	H	2.903131	-7.4034	15.71914
O	13.27882	-5.75634	15.46602	H	3.244487	-8.87473	16.65243
O	7.463771	-5.83801	16.74488	H	12.92852	-7.3701	10.5534
C	15.71602	-9.03978	14.92686	H	6.664515	-7.10751	11.21191
H	15.62815	-9.95481	15.52687	H	10.33907	-5.59994	16.03903
C	15.2789	-7.84231	15.79889	C	12.32985	-12.6304	12.02603
H	15.38323	-6.92382	15.20562	C	11.02927	-13.1246	12.20508
C	14.18165	-10.4889	13.56222	C	13.4242	-13.4934	12.16575
C	13.35821	-10.3064	12.31925	C	10.80892	-14.474	12.4984
C	12.52776	-11.2147	11.63363	H	10.17302	-12.4566	12.09757
C	11.87146	-10.6545	10.51997	C	13.23281	-14.8481	12.46252
C	11.02177	-11.3143	9.468089	H	14.43631	-13.1096	12.02659
C	11.13385	-9.04761	8.967423	C	11.92185	-15.3203	12.61163
C	11.99618	-9.30522	10.16202	H	11.76138	-16.38	12.83198

C	12.82175	-8.41614	10.84299	C	10.78201	-10.8939	17.4446
C	13.50533	-8.96926	11.9208	C	11.42138	-11.7559	16.54163
C	14.46691	-8.29567	12.84671	C	10.33127	-11.3907	18.67473
N	14.81148	-9.25257	13.80168	C	11.63355	-13.1012	16.86031
N	10.56505	-10.2816	8.636049	H	11.77752	-11.3758	15.58288
O	14.30748	-11.4644	14.26452	C	10.52754	-12.7333	19.01821
O	10.77813	-12.4869	9.303469	H	9.834386	-10.7213	19.37877
O	10.94719	-8.0026	8.388462	C	11.1891	-13.5672	18.10586
O	14.87513	-7.15655	12.79619	H	11.35676	-14.6156	18.37029
C	8.338931	-11.1913	8.01966	C	6.640678	-12.144	13.40829
H	8.616843	-12.2243	8.265401	C	7.310812	-12.3243	14.62687
C	9.606786	-10.4444	7.549616	C	5.947769	-13.2167	12.83302
H	9.325235	-9.4187	7.275954	C	7.276622	-13.5551	15.28984
C	7.566572	-11.4523	10.39733	H	7.852504	-11.4915	15.07853
C	7.027821	-10.5332	11.45646	C	5.899562	-14.4608	13.47335
C	6.623738	-10.8019	12.77873	H	5.42716	-13.0771	11.88409
C	6.205596	-9.65908	13.48837	C	6.556577	-14.6057	14.70303
C	5.580887	-9.5468	14.85239	H	6.514223	-15.571	15.21648
C	5.770297	-7.40026	13.98181	C	10.0058	-13.2762	20.32421
C	6.242822	-8.36827	12.94413	H	8.97184	-13.6442	20.20526
C	6.647279	-8.11132	11.63795	H	10.61401	-14.1197	20.6835
C	7.022398	-9.2389	10.91488	H	9.987897	-12.5023	21.10611
C	7.49637	-9.3094	9.498791	C	12.30077	-14.0219	15.87344
N	7.816094	-10.6476	9.268719	H	12.99238	-13.4744	15.2179
N	5.423707	-8.17421	15.0942	H	12.85331	-14.8259	16.38266
O	7.775394	-12.6416	10.44613	H	11.55377	-14.5007	15.2198
O	5.232531	-10.4221	15.60998	C	9.412209	-14.9955	12.70792
O	5.692397	-6.19621	13.90386	H	9.164465	-15.0288	13.78103
O	7.591542	-8.40381	8.700216	H	8.6645	-14.3527	12.22348
C	7.294875	-11.2126	6.8967	H	9.304201	-16.0193	12.31793
H	6.402655	-11.7523	7.250093	C	14.41249	-15.7669	12.65346
H	6.986084	-10.1792	6.669417	H	14.73396	-15.7697	13.70954
C	7.872844	-11.8814	5.64557	H	14.16468	-16.8045	12.38423
H	7.126228	-11.8675	4.836044	H	15.27616	-15.4479	12.05106
H	8.079036	-12.9433	5.868151	H	19.1295	-8.59039	15.38936
C	9.167293	-11.2	5.189672	H	15.85096	-6.87387	17.63975
H	8.939641	-10.1722	4.855636	C	5.186238	-15.6255	12.83525
H	9.592903	-11.7271	4.321399	H	4.812528	-16.3335	13.58987
C	10.20045	-11.1408	6.319205	H	4.336925	-15.2924	12.22013
H	11.09843	-10.5909	5.997808	H	5.87055	-16.1828	12.17216
H	10.51956	-12.1575	6.600128	C	8.017808	-13.7447	16.58647
C	16.17548	-7.73718	17.03854	H	9.034758	-14.1277	16.40247
H	16.04056	-8.63896	17.65726	H	8.12712	-12.7963	17.13066
C	17.64333	-7.59084	16.62586	H	7.509026	-14.4709	17.23846

Table S3.14 Cartesian coordinates of geometry-optimised structure of *anti-3Ar* at the B3LYP-D3(BJ)/def2svp level of theory in CH₂Cl₂ (PCM solvent model).

C	5.486955	-8.08226	17.58796	C	17.35453	-8.20356	17.25051
H	5.243324	-9.14319	17.72705	H	17.90583	-8.21909	18.20381
C	4.706944	-7.55644	16.3632	H	17.59034	-7.24088	16.76336
H	4.859785	-6.47209	16.29188	C	17.81446	-9.35281	16.34827
C	7.750562	-9.14682	17.74515	H	17.67776	-10.311	16.88006
C	9.132054	-8.7759	17.30706	H	18.89016	-9.2634	16.1295
C	10.32624	-9.46734	17.49236	C	17.02022	-9.38779	15.03961
C	11.45627	-8.81858	17.00247	H	17.22167	-8.47968	14.44823
C	12.87982	-9.28218	17.03353	H	17.31603	-10.2521	14.42517
C	12.80975	-7.21486	15.97132	C	5.04402	-7.31605	18.83949
C	11.40473	-7.57795	16.3503	H	5.28328	-6.24648	18.71695
C	10.19717	-6.89604	16.11329	H	5.614492	-7.6845	19.70577
C	9.069668	-7.53457	16.66013	C	3.539738	-7.51096	19.06276
C	7.656094	-7.03879	16.76927	H	3.213107	-6.93273	19.9413
N	6.929663	-8.07323	17.37402	H	3.350732	-8.57366	19.29602
N	13.6208	-8.28197	16.40309	C	2.721005	-7.11148	17.82964
O	7.385922	-10.1548	18.3049	H	2.800846	-6.02057	17.67795
O	13.3171	-10.3118	17.49799	H	1.653959	-7.32948	17.99317
O	13.22157	-6.22021	15.42456	C	3.210426	-7.82188	16.56203
O	7.198363	-5.96688	16.44614	H	2.661601	-7.45965	15.67929
C	15.51512	-9.47335	15.32173	H	3.038391	-8.90882	16.63507
H	15.30376	-10.4071	15.86111	H	12.983	-7.31105	11.0215
C	15.06608	-8.28817	16.203	H	6.213893	-6.86094	11.17635
H	15.27099	-7.35776	15.65714	H	10.37723	-10.4362	17.98918
C	14.0848	-10.7558	13.70824	C	12.39159	-12.7162	11.82019
C	13.36096	-10.4408	12.42829	C	13.51094	-13.5446	11.95926
C	12.56212	-11.2605	11.60574	C	11.10403	-13.2761	11.86038
C	11.92772	-10.5649	10.55675	C	13.36445	-14.9277	12.13155
C	11.10926	-11.0795	9.403415	H	14.5121	-13.1112	11.92022
C	11.16475	-8.76122	9.253629	C	10.92971	-14.652	12.02706
C	12.04345	-9.17762	10.38828	H	10.2261	-12.639	11.7494
C	12.87069	-8.38465	11.17685	C	7.112209	-11.7708	13.46304
C	13.53728	-9.07053	12.18652	C	6.486491	-12.9575	13.06107
C	14.49356	-8.52506	13.1976	C	7.989165	-11.7797	14.55407
N	14.72114	-9.5638	14.10162	C	6.715105	-14.1505	13.75493
N	10.62971	-9.94175	8.731972	H	5.804693	-12.9465	12.20834
O	14.12863	-11.7873	14.33595	C	8.243385	-12.9613	15.26103
O	10.90721	-12.2187	9.054706	H	8.470162	-10.8498	14.86816
O	10.93573	-7.64228	8.854043	C	10.07107	-5.6642	15.29647
O	14.98699	-7.42045	13.23403	C	10.74781	-4.48234	15.62717
C	8.398892	-10.7178	7.989187	C	9.234427	-5.6933	14.17363
H	8.662728	-11.7644	8.191398	C	10.58785	-3.33007	14.85087
C	9.690283	-9.95796	7.615794	H	11.39975	-4.45982	16.50167
H	9.434334	-8.90178	7.451187	C	9.057844	-4.55562	13.37638
C	7.735049	-11.0372	10.39183	H	8.710782	-6.61668	13.91439

C	7.127787	-10.1766	11.45792	C	12.07056	-15.4609	12.1606
C	6.820533	-10.4781	12.79522	C	7.592116	-14.1315	14.85098
C	6.238328	-9.40968	13.49824	C	9.739531	-3.38548	13.73271
C	5.645306	-9.39425	14.87702	H	9.605742	-2.48683	13.12336
C	5.416707	-7.26308	13.97721	H	11.94362	-16.5406	12.28528
C	6.040081	-8.14138	12.93797	H	7.772199	-15.0592	15.4018
C	6.370952	-7.84489	11.61803	C	9.16267	-12.9429	16.45543
C	6.91167	-8.90802	10.90026	H	10.14401	-12.5139	16.1961
C	7.37386	-8.93082	9.476728	H	8.733551	-12.3215	17.25912
N	7.839904	-10.2283	9.246449	H	9.32778	-13.9535	16.85495
N	5.234334	-8.07404	15.10543	C	6.063879	-15.4346	13.31043
O	8.083181	-12.1936	10.45082	H	6.688981	-15.9474	12.55916
O	5.504116	-10.3108	15.65293	H	5.926862	-16.13	14.1517
O	5.125296	-6.09231	13.89365	H	5.082934	-15.2507	12.8475
O	7.363939	-8.02244	8.676396	C	9.550479	-15.2574	12.05346
C	7.387977	-10.6706	6.836933	H	9.292795	-15.6096	13.06511
H	6.493222	-11.2429	7.127471	H	8.790224	-14.5241	11.75411
H	7.073219	-9.62787	6.675064	H	9.487631	-16.1265	11.37925
C	8.005133	-11.236	5.554657	C	14.58083	-15.8051	12.28887
H	7.274831	-11.174	4.732616	H	15.10942	-15.5787	13.23001
H	8.229597	-12.3076	5.699521	H	14.3114	-16.8709	12.30144
C	9.292969	-10.4947	5.183818	H	15.29986	-15.6425	11.46988
H	9.052563	-9.44409	4.94232	C	11.33244	-2.06273	15.18687
H	9.742122	-10.9324	4.278487	H	12.24878	-1.97481	14.57801
C	10.3048	-10.5303	6.3322	H	10.72085	-1.17049	14.98361
H	11.2049	-9.94819	6.080715	H	11.63681	-2.04147	16.24356
H	10.62579	-11.5667	6.521803	C	8.132108	-4.60291	12.18724
C	15.84889	-8.27461	17.52163	H	8.438481	-5.38638	11.47486
H	15.60933	-9.18457	18.09427	H	7.103508	-4.8353	12.50855
H	15.51822	-7.41227	18.12121	H	8.115371	-3.64427	11.64963

Table S3.15 Cartesian coordinates of geometry-optimised structure of **H-TS1** of **3Br** at the B3LYP-D3(BJ)/def2svp level of theory in CH₂Cl₂ (PCM solvent model).

C	-0.39757	5.31253	-0.12529	C	-0.39757	5.31253	-0.12529
H	-0.95401	5.19545	0.81526	H	-0.95401	5.19545	0.81526
C	-1.43048	5.31669	-1.30581	C	-1.43048	5.31669	-1.30581
H	-0.87163	5.18336	-2.24435	H	-0.87163	5.18336	-2.24435
C	1.96992	4.26387	0.2369	C	1.96992	4.26387	0.2369
C	2.60126	2.93489	-0.07146	C	2.60126	2.93489	-0.07146
C	3.89874	2.44441	0.14077	C	3.89874	2.44441	0.14077
C	4.13878	1.14282	-0.31799	C	4.13878	1.14282	-0.31799
C	5.3279	0.23765	-0.15857	C	5.3279	0.23765	-0.15857
C	3.74546	-0.87909	-1.43784	C	3.74546	-0.87909	-1.43784
C	3.15207	0.41441	-0.99687	C	3.15207	0.41441	-0.99687
C	1.8444	0.85686	-1.14298	C	1.8444	0.85686	-1.14298
C	1.61522	2.13191	-0.63779	C	1.61522	2.13191	-0.63779
C	0.3225	2.85314	-0.52414	C	0.3225	2.85314	-0.52414

N	0.6077	4.18998	-0.20205	N	0.6077	4.18998	-0.20205
N	5.03073	-0.9301	-0.89255	N	5.03073	-0.9301	-0.89255
O	2.516	5.18945	0.77967	O	2.516	5.18945	0.77967
O	6.32107	0.42677	0.49968	O	6.32107	0.42677	0.49968
O	3.22145	-1.73712	-2.11406	O	3.22145	-1.73712	-2.11406
O	-0.75495	2.31207	-0.61326	O	-0.75495	2.31207	-0.61326
C	5.44106	-2.99045	0.3829	C	5.44106	-2.99045	0.3829
H	5.60568	-2.34612	1.25883	H	5.60568	-2.34612	1.25883
C	5.80833	-2.17636	-0.88439	C	5.80833	-2.17636	-0.88439
H	5.45249	-2.74202	-1.75739	H	5.45249	-2.74202	-1.75739
C	3.0758	-2.52656	1.12301	C	3.0758	-2.52656	1.12301
C	1.71243	-2.98898	0.68733	C	1.71243	-2.98898	0.68733
C	0.42583	-2.61722	1.10367	C	0.42583	-2.61722	1.10367
C	-0.64305	-3.24943	0.45231	C	-0.64305	-3.24943	0.45231
C	-2.13198	-3.19147	0.68923	C	-2.13198	-3.19147	0.68923
C	-1.74281	-4.60082	-1.1152	C	-1.74281	-4.60082	-1.1152
C	-0.41775	-4.14846	-0.59836	C	-0.41775	-4.14846	-0.59836
C	0.85091	-4.52251	-1.02733	C	0.85091	-4.52251	-1.02733
C	1.89952	-3.92843	-0.33504	C	1.89952	-3.92843	-0.33504
C	3.36619	-4.11613	-0.54809	C	3.36619	-4.11613	-0.54809
N	4.00125	-3.27343	0.374	N	4.00125	-3.27343	0.374
N	-2.71167	-3.9965	-0.30394	N	-2.71167	-3.9965	-0.30394
O	3.36919	-1.66021	1.91359	O	3.36919	-1.66021	1.91359
O	-2.72391	-2.59754	1.55853	O	-2.72391	-2.59754	1.55853
O	-1.96767	-5.34871	-2.03811	O	-1.96767	-5.34871	-2.03811
O	3.90373	-4.83752	-1.35556	O	3.90373	-4.83752	-1.35556
C	-5.14282	-3.34044	0.01751	C	-5.14282	-3.34044	0.01751
H	-5.10579	-3.33023	1.11468	H	-5.10579	-3.33023	1.11468
C	-4.11984	-4.36317	-0.49947	C	-4.11984	-4.36317	-0.49947
H	-4.22816	-4.4398	-1.58967	H	-4.22816	-4.4398	-1.58967
C	-5.05145	-0.92627	0.56941	C	-5.05145	-0.92627	0.56941
C	-4.54394	0.31775	-0.08918	C	-4.54394	0.31775	-0.08918
C	-4.36508	1.60957	0.41608	C	-4.36508	1.60957	0.41608
C	-3.72319	2.5167	-0.43255	C	-3.72319	2.5167	-0.43255
C	-3.13673	3.86524	-0.1405	C	-3.13673	3.86524	-0.1405
C	-2.49909	3.26499	-2.28689	C	-2.49909	3.26499	-2.28689
C	-3.33544	2.15483	-1.72885	C	-3.33544	2.15483	-1.72885

Table S3.16 Cartesian coordinates of geometry-optimised structure of **H-Int** of **3Br** at the B3LYP-D3(BJ)/def2svp level of theory in CH₂Cl₂ (PCM solvent model).

C	-0.23999	5.41428	0.41478	C	-0.23999	5.41428	0.41478
H	-0.99388	5.10727	1.15233	H	-0.99388	5.10727	1.15233
C	-0.96027	5.55297	-0.96077	C	-0.96027	5.55297	-0.96077
H	-0.19417	5.50688	-1.74834	H	-0.19417	5.50688	-1.74834
C	2.10109	4.37725	0.05209	C	2.10109	4.37725	0.05209
C	2.60007	2.96256	-0.00224	C	2.60007	2.96256	-0.00224
C	3.89129	2.44734	-0.15959	C	3.89129	2.44734	-0.15959

C	3.97046	1.06442	-0.35699	C	3.97046	1.06442	-0.35699
C	5.15036	0.1367	-0.38748	C	5.15036	0.1367	-0.38748
C	3.25431	-1.08071	-0.91993	C	3.25431	-1.08071	-0.91993
C	2.81806	0.28175	-0.49612	C	2.81806	0.28175	-0.49612
C	1.53691	0.76218	-0.23646	C	1.53691	0.76218	-0.23646
C	1.48313	2.12124	0.06196	C	1.48313	2.12124	0.06196
C	0.3157	2.96032	0.46111	C	0.3157	2.96032	0.46111
N	0.72446	4.29655	0.35303	N	0.72446	4.29655	0.35303
N	4.64444	-1.12917	-0.75254	N	4.64444	-1.12917	-0.75254
O	2.73692	5.37739	-0.17321	O	2.73692	5.37739	-0.17321
O	6.29083	0.40492	-0.09999	O	6.29083	0.40492	-0.09999
O	2.55497	-1.97476	-1.34217	O	2.55497	-1.97476	-1.34217
O	-0.77138	2.57276	0.82756	O	-0.77138	2.57276	0.82756
C	5.24239	-3.13921	0.56473	C	5.24239	-3.13921	0.56473
H	5.43295	-2.409	1.36428	H	5.43295	-2.409	1.36428
C	5.39068	-2.40311	-0.80092	C	5.39068	-2.40311	-0.80092
H	4.87868	-3.01063	-1.56007	H	4.87868	-3.01063	-1.56007
C	2.90322	-2.8356	1.49059	C	2.90322	-2.8356	1.49059
C	1.54922	-3.37696	1.1138	C	1.54922	-3.37696	1.1138
C	0.25304	-2.95682	1.44766	C	0.25304	-2.95682	1.44766
C	-0.79854	-3.56698	0.74819	C	-0.79854	-3.56698	0.74819
C	-2.29393	-3.36171	0.8018	C	-2.29393	-3.36171	0.8018
C	-1.83424	-4.88236	-0.89262	C	-1.83424	-4.88236	-0.89262
C	-0.54292	-4.5237	-0.2436	C	-0.54292	-4.5237	-0.2436
C	0.73104	-4.96594	-0.57271	C	0.73104	-4.96594	-0.57271
C	1.75716	-4.36033	0.13948	C	1.75716	-4.36033	0.13948
C	3.21907	-4.479	-0.1173	C	3.21907	-4.479	-0.1173
N	3.84189	-3.5557	0.73037	N	3.84189	-3.5557	0.73037
N	-2.82408	-4.14969	-0.23084	N	-2.82408	-4.14969	-0.23084
O	3.17601	-1.91801	2.22832	O	3.17601	-1.91801	2.22832
O	-2.92676	-2.66736	1.56172	O	-2.92676	-2.66736	1.56172
O	-2.02075	-5.64056	-1.81618	O	-2.02075	-5.64056	-1.81618
O	3.76017	-5.18818	-0.93534	O	3.76017	-5.18818	-0.93534
C	-5.12441	-3.09704	-0.37715	C	-5.12441	-3.09704	-0.37715
H	-5.29549	-3.05953	0.70697	H	-5.29549	-3.05953	0.70697
C	-4.21007	-4.28858	-0.68265	C	-4.21007	-4.28858	-0.68265
H	-4.12596	-4.39293	-1.77321	H	-4.12596	-4.39293	-1.77321
C	-4.98492	-0.68263	0.07187	C	-4.98492	-0.68263	0.07187
C	-4.22078	0.49607	-0.43746	C	-4.22078	0.49607	-0.43746
C	-4.21434	1.82717	-0.01252	C	-4.21434	1.82717	-0.01252
C	-3.29444	2.66563	-0.64752	C	-3.29444	2.66563	-0.64752
C	-2.89832	4.07044	-0.32725	C	-2.89832	4.07044	-0.32725
C	-1.47331	3.29285	-1.98572	C	-1.47331	3.29285	-1.98572
C	-2.44414	2.19598	-1.65635	C	-2.44414	2.19598	-1.65635

Table S3.17 Cartesian coordinates of geometry-optimised structure of **H-TS2** of **3Br** at the B3LYP-D3(BJ)/def2svp level of theory in CH₂Cl₂ (PCM solvent model).

C	-4.89411	-3.25989	0.63017	C	-4.89411	-3.25989	0.63017
H	-4.34282	-3.69747	1.4745	H	-4.34282	-3.69747	1.4745
C	-4.41788	-3.97592	-0.65962	C	-4.41788	-3.97592	-0.65962
H	-4.80184	-3.41262	-1.523	H	-4.80184	-3.41262	-1.523
C	-5.14451	-0.79646	-0.06443	C	-5.14451	-0.79646	-0.06443
C	-4.2458	0.40336	0.05335	C	-4.2458	0.40336	0.05335
C	-4.4134	1.72969	-0.36593	C	-4.4134	1.72969	-0.36593
C	-3.28791	2.55753	-0.23199	C	-3.28791	2.55753	-0.23199
C	-3.06731	4.01033	-0.55104	C	-3.06731	4.01033	-0.55104
C	-1.04099	3.09177	0.02819	C	-1.04099	3.09177	0.02819
C	-2.07755	2.04979	0.23077	C	-2.07755	2.04979	0.23077
C	-1.90487	0.75406	0.70453	C	-1.90487	0.75406	0.70453
C	-3.04472	-0.03433	0.62868	C	-3.04472	-0.03433	0.62868
C	-3.21579	-1.45372	1.04772	C	-3.21579	-1.45372	1.04772
N	-4.47391	-1.85225	0.5888	N	-4.47391	-1.85225	0.5888
N	-1.69693	4.30231	-0.24436	N	-1.69693	4.30231	-0.24436
O	-6.20153	-0.87547	-0.64055	O	-6.20153	-0.87547	-0.64055
O	-3.89242	4.75906	-1.0067	O	-3.89242	4.75906	-1.0067
O	0.14495	2.85607	0.01642	O	0.14495	2.85607	0.01642
O	-2.42288	-2.14301	1.65075	O	-2.42288	-2.14301	1.65075
C	0.07676	5.9429	0.65901	C	0.07676	5.9429	0.65901
H	-0.33373	5.68907	1.64778	H	-0.33373	5.68907	1.64778
C	-1.02748	5.64476	-0.41473	C	-1.02748	5.64476	-0.41473
H	-0.54945	5.6506	-1.40471	H	-0.54945	5.6506	-1.40471
C	1.7231	4.2476	1.51967	C	1.7231	4.2476	1.51967
C	2.76055	3.3711	0.87429	C	2.76055	3.3711	0.87429
C	3.35438	2.18072	1.3115	C	3.35438	2.18072	1.3115
C	4.07128	1.4555	0.35062	C	4.07128	1.4555	0.35062
C	4.72229	0.09802	0.41022	C	4.72229	0.09802	0.41022
C	4.91923	0.8953	-1.76491	C	4.91923	0.8953	-1.76491
C	4.20354	1.92931	-0.96228	C	4.20354	1.92931	-0.96228
C	3.65013	3.12603	-1.40183	C	3.65013	3.12603	-1.40183
C	2.91116	3.81242	-0.4459	C	2.91116	3.81242	-0.4459
C	1.9828	4.96066	-0.67116	C	1.9828	4.96066	-0.67116
N	1.28885	5.13369	0.51965	N	1.28885	5.13369	0.51965
N	5.14328	-0.17892	-0.89647	N	5.14328	-0.17892	-0.89647
O	1.2823	4.21161	2.64262	O	1.2823	4.21161	2.64262
O	4.85733	-0.6349	1.36228	O	4.85733	-0.6349	1.36228
O	5.24726	0.94337	-2.92698	O	5.24726	0.94337	-2.92698
O	1.81471	5.57922	-1.70099	O	1.81471	5.57922	-1.70099
C	5.19645	-2.6871	-0.79092	C	5.19645	-2.6871	-0.79092
H	5.46271	-2.7357	0.27264	H	5.46271	-2.7357	0.27264
C	5.78507	-1.39596	-1.37961	C	5.78507	-1.39596	-1.37961
H	5.59687	-1.38477	-2.46127	H	5.59687	-1.38477	-2.46127
C	3.08512	-3.54325	0.17095	C	3.08512	-3.54325	0.17095

C	1.62877	-3.52978	-0.18046	C	1.62877	-3.52978	-0.18046
C	0.53707	-4.1784	0.40798	C	0.53707	-4.1784	0.40798
C	-0.70663	-3.95633	-0.19316	C	-0.70663	-3.95633	-0.19316
C	-2.06749	-4.48269	0.15312	C	-2.06749	-4.48269	0.15312
C	-2.30045	-3.02442	-1.64342	C	-2.30045	-3.02442	-1.64342
C	-0.84282	-3.10754	-1.29997	C	-0.84282	-3.10754	-1.29997

Table S3.18 Cartesian coordinates of geometry-optimised structure of **Br-TS1** of **3Br** at the B3LYP-D3(BJ)/def2svp level of theory in CH₂Cl₂ (PCM solvent model).

C	-2.20153	5.06168	0.14106	C	-2.20153	5.06168	0.14106
H	-2.68641	4.82188	1.09848	H	-2.68641	4.82188	1.09848
C	-3.19319	4.70328	-1.0172	C	-3.19319	4.70328	-1.0172
H	-2.65181	4.80796	-1.96974	H	-2.65181	4.80796	-1.96974
C	-0.65804	2.99819	-0.29921	C	-0.65804	2.99819	-0.29921
C	0.81468	2.79176	-0.37543	C	0.81468	2.79176	-0.37543
C	1.56051	1.73402	-0.90629	C	1.56051	1.73402	-0.90629
C	2.9422	1.82563	-0.71832	C	2.9422	1.82563	-0.71832
C	4.05504	0.9418	-1.18069	C	4.05504	0.9418	-1.18069
C	4.96244	2.53847	0.23983	C	4.96244	2.53847	0.23983
C	3.50988	2.85208	0.05042	C	3.50988	2.85208	0.05042
C	2.7741	3.91351	0.56843	C	2.7741	3.91351	0.56843
C	1.40969	3.86132	0.28935	C	1.40969	3.86132	0.28935
C	0.33091	4.83592	0.65156	C	0.33091	4.83592	0.65156
N	-0.88147	4.33436	0.09999	N	-0.88147	4.33436	0.09999
N	5.21917	1.4035	-0.54422	N	5.21917	1.4035	-0.54422
O	-1.47713	2.12801	-0.45813	O	-1.47713	2.12801	-0.45813
O	4.00329	-0.00027	-1.9374	O	4.00329	-0.00027	-1.9374
O	5.7436	3.11898	0.95613	O	5.7436	3.11898	0.95613
O	0.49292	5.8262	1.32242	O	0.49292	5.8262	1.32242
C	6.35863	-0.36508	0.718	C	6.35863	-0.36508	0.718
H	6.23404	0.25749	1.61614	H	6.23404	0.25749	1.61614
C	6.43326	0.57916	-0.50925	C	6.43326	0.57916	-0.50925
H	6.38536	-0.04308	-1.4143	H	6.38536	-0.04308	-1.4143
C	3.97178	-0.84924	1.35574	C	3.97178	-0.84924	1.35574
C	2.89504	-1.76395	0.84283	C	2.89504	-1.76395	0.84283
C	1.5484	-1.90887	1.20486	C	1.5484	-1.90887	1.20486
C	0.81895	-2.87628	0.4998	C	0.81895	-2.87628	0.4998
C	-0.58027	-3.40544	0.69079	C	-0.58027	-3.40544	0.69079
C	0.35843	-4.48865	-1.13635	C	0.35843	-4.48865	-1.13635
C	1.3971	-3.58383	-0.56164	C	1.3971	-3.58383	-0.56164
C	2.72613	-3.43908	-0.94493	C	2.72613	-3.43908	-0.94493
C	3.45515	-2.52905	-0.18881	C	3.45515	-2.52905	-0.18881
C	4.89579	-2.15773	-0.33018	C	4.89579	-2.15773	-0.33018
N	5.13564	-1.17053	0.63587	N	5.13564	-1.17053	0.63587
N	-0.78383	-4.33804	-0.33891	N	-0.78383	-4.33804	-0.33891
O	3.89391	0.03121	2.18079	O	3.89391	0.03121	2.18079
O	-1.36973	-3.12	1.55911	O	-1.36973	-3.12	1.55911

O	0.45732	-5.22828	-2.08758	O	0.45732	-5.22828	-2.08758
O	5.69607	-2.60435	-1.11791	O	5.69607	-2.60435	-1.11791
C	-3.2749	-4.7281	-0.036	C	-3.2749	-4.7281	-0.036
H	-3.2448	-4.74759	1.06121	H	-3.2448	-4.74759	1.06121
C	-1.9265	-5.23062	-0.57403	C	-1.9265	-5.23062	-0.57403
H	-1.99401	-5.29928	-1.66808	H	-1.99401	-5.29928	-1.66808
C	-4.14413	-2.49765	0.60978	C	-4.14413	-2.49765	0.60978
C	-4.17256	-1.13066	0.00202	C	-4.17256	-1.13066	0.00202
C	-4.49925	0.10955	0.5601	C	-4.49925	0.10955	0.5601
C	-4.27396	1.22637	-0.25068	C	-4.27396	1.22637	-0.25068
C	-4.2206	2.68408	0.10248	C	-4.2206	2.68408	0.10248
C	-3.46522	2.452	-2.07772	C	-3.46522	2.452	-2.07772
C	-3.80669	1.08916	-1.56404	C	-3.80669	1.08916	-1.56404

Table S3.19 Cartesian coordinates of geometry-optimised structure of **Br-Int** of **3Br** at the B3LYP-D3(BJ)/def2svp level of theory in CH₂Cl₂ (PCM solvent model).

C	3.40187	-4.61951	0.35674	C	3.40187	-4.61951	0.35674
H	3.80465	-3.98123	1.15536	H	3.80465	-3.98123	1.15536
C	4.11587	-4.21723	-0.97045	C	4.11587	-4.21723	-0.97045
H	3.52173	-4.61238	-1.80746	H	3.52173	-4.61238	-1.80746
C	1.496	-2.97544	0.39722	C	1.496	-2.97544	0.39722
C	0.05102	-2.98933	0.02022	C	0.05102	-2.98933	0.02022
C	-0.84158	-1.95768	-0.28575	C	-0.84158	-1.95768	-0.28575
C	-2.1705	-2.34665	-0.47678	C	-2.1705	-2.34665	-0.47678
C	-3.37632	-1.58017	-0.91034	C	-3.37632	-1.58017	-0.91034
C	-4.08047	-3.69226	-0.27517	C	-4.08047	-3.69226	-0.27517
C	-2.58165	-3.6682	-0.26921	C	-2.58165	-3.6682	-0.26921
C	-1.68705	-4.71649	-0.07147	C	-1.68705	-4.71649	-0.07147
C	-0.3525	-4.32827	0.0169	C	-0.3525	-4.32827	0.0169
C	0.87834	-5.182	0.07801	C	0.87834	-5.182	0.07801
N	1.9585	-4.2992	0.27945	N	1.9585	-4.2992	0.27945
N	-4.49025	-2.40013	-0.6558	N	-4.49025	-2.40013	-0.6558
O	2.14692	-2.03249	0.78275	O	2.14692	-2.03249	0.78275
O	-3.41227	-0.48451	-1.42054	O	-3.41227	-0.48451	-1.42054
O	-4.77596	-4.63197	0.02752	O	-4.77596	-4.63197	0.02752
O	0.91176	-6.38105	-0.05997	O	0.91176	-6.38105	-0.05997
C	-6.20943	-1.05125	0.53104	C	-6.20943	-1.05125	0.53104
H	-5.94885	-1.663	1.4072	H	-5.94885	-1.663	1.4072
C	-5.867	-1.87168	-0.7479	C	-5.867	-1.87168	-0.7479
H	-5.85613	-1.17172	-1.59527	H	-5.85613	-1.17172	-1.59527
C	-4.25546	0.25303	1.48392	C	-4.25546	0.25303	1.48392
C	-3.48901	1.47146	1.04009	C	-3.48901	1.47146	1.04009
C	-2.26898	2.01229	1.47292	C	-2.26898	2.01229	1.47292
C	-1.72279	3.02972	0.67699	C	-1.72279	3.02972	0.67699
C	-0.42367	3.79315	0.77447	C	-0.42367	3.79315	0.77447
C	-1.51055	4.46636	-1.16633	C	-1.51055	4.46636	-1.16633
C	-2.3803	3.46916	-0.48079	C	-2.3803	3.46916	-0.48079

C	-3.61199	2.98031	-0.89505	C	-3.61199	2.98031	-0.89505
C	-4.13445	1.97129	-0.097	C	-4.13445	1.97129	-0.097
C	-5.34373	1.14244	-0.36562	C	-5.34373	1.14244	-0.36562
N	-5.34627	0.13436	0.60548	N	-5.34627	0.13436	0.60548
N	-0.359	4.58577	-0.38173	N	-0.359	4.58577	-0.38173
O	-3.99017	-0.53479	2.36095	O	-3.99017	-0.53479	2.36095
O	0.41121	3.74811	1.64683	O	0.41121	3.74811	1.64683
O	-1.7276	5.06674	-2.19323	O	-1.7276	5.06674	-2.19323
O	-6.14567	1.2842	-1.26038	O	-6.14567	1.2842	-1.26038
C	2.10107	5.16554	-0.36182	C	2.10107	5.16554	-0.36182
H	2.17778	5.25403	0.72954	H	2.17778	5.25403	0.72954
C	0.67443	5.54045	-0.78247	C	0.67443	5.54045	-0.78247
H	0.62352	5.5414	-1.8793	H	0.62352	5.5414	-1.8793
C	3.38373	3.14021	0.22764	C	3.38373	3.14021	0.22764
C	3.57759	1.76186	-0.32006	C	3.57759	1.76186	-0.32006
C	4.31979	0.68365	0.16981	C	4.31979	0.68365	0.16981
C	4.19449	-0.51597	-0.53664	C	4.19449	-0.51597	-0.53664
C	4.69194	-1.88563	-0.19929	C	4.69194	-1.88563	-0.19929
C	3.29323	-2.07176	-2.04363	C	3.29323	-2.07176	-2.04363
C	3.37942	-0.6202	-1.67038	C	3.37942	-0.6202	-1.67038

Table S3.20 Cartesian coordinates of geometry-optimised structure of **Br-TS2** of **3Br** at the B3LYP-D3(BJ)/def2svp level of theory in CH₂Cl₂ (PCM solvent model).

C	5.65505	-2.48029	0.3027	C	5.65505	-2.48029	0.3027
H	5.73309	-1.83389	1.18831	H	5.73309	-1.83389	1.18831
C	5.92611	-1.60312	-0.94593	C	5.92611	-1.60312	-0.94593
H	5.68404	-2.19941	-1.83828	H	5.68404	-2.19941	-1.83828
C	3.23682	-2.13927	0.83121	C	3.23682	-2.13927	0.83121
C	1.94666	-2.72139	0.35415	C	1.94666	-2.72139	0.35415
C	0.63501	-2.25305	0.46753	C	0.63501	-2.25305	0.46753
C	-0.34666	-3.10286	-0.05384	C	-0.34666	-3.10286	-0.05384
C	-1.81125	-2.90056	-0.22413	C	-1.81125	-2.90056	-0.22413
C	-1.32522	-4.99683	-1.01554	C	-1.32522	-4.99683	-1.01554
C	-0.03798	-4.33173	-0.63251	C	-0.03798	-4.33173	-0.63251
C	1.2715	-4.76475	-0.83405	C	1.2715	-4.76475	-0.83405
C	2.24613	-3.90694	-0.33267	C	2.24613	-3.90694	-0.33267
C	3.7363	-4.00081	-0.46322	C	3.7363	-4.00081	-0.46322
N	4.25784	-2.92904	0.27682	N	4.25784	-2.92904	0.27682
N	-2.37835	-4.14417	-0.57761	N	-2.37835	-4.14417	-0.57761
O	3.40914	-1.17835	1.54472	O	3.40914	-1.17835	1.54472
O	-2.35919	-1.82787	-0.16972	O	-2.35919	-1.82787	-0.16972
O	-1.40901	-6.03765	-1.62077	O	-1.40901	-6.03765	-1.62077
O	4.35885	-4.80969	-1.11019	O	4.35885	-4.80969	-1.11019
C	-4.76637	-3.78087	0.37045	C	-4.76637	-3.78087	0.37045
H	-4.33904	-3.97959	1.36488	H	-4.33904	-3.97959	1.36488
C	-3.84667	-4.46812	-0.69565	C	-3.84667	-4.46812	-0.69565
H	-4.17981	-4.15036	-1.69463	H	-4.17981	-4.15036	-1.69463

C	-4.43022	-1.48537	1.31964	C	-4.43022	-1.48537	1.31964
C	-4.32782	-0.10949	0.72619	C	-4.32782	-0.10949	0.72619
C	-3.70881	1.04749	1.21359	C	-3.70881	1.04749	1.21359
C	-3.52755	2.08723	0.29299	C	-3.52755	2.08723	0.29299
C	-2.79826	3.39922	0.4097	C	-2.79826	3.39922	0.4097
C	-3.53891	3.18013	-1.78343	C	-3.53891	3.18013	-1.78343
C	-3.97513	1.96831	-1.03028	C	-3.97513	1.96831	-1.03028
C	-4.61482	0.83622	-1.52145	C	-4.61482	0.83622	-1.52145
C	-4.7526	-0.19971	-0.60533	C	-4.7526	-0.19971	-0.60533
C	-5.1107	-1.62235	-0.8934	C	-5.1107	-1.62235	-0.8934
N	-4.85927	-2.32514	0.27752	N	-4.85927	-2.32514	0.27752
N	-2.80169	3.95097	-0.87705	N	-2.80169	3.95097	-0.87705
O	-4.1652	-1.85909	2.43609	O	-4.1652	-1.85909	2.43609
O	-2.28839	3.89634	1.38704	O	-2.28839	3.89634	1.38704
O	-3.75495	3.46318	-2.93816	O	-3.75495	3.46318	-2.93816
O	-5.47652	-2.09122	-1.9504	O	-5.47652	-2.09122	-1.9504
C	-0.76747	5.40503	-0.68969	C	-0.76747	5.40503	-0.68969
H	-0.89313	5.6132	0.38033	H	-0.89313	5.6132	0.38033
C	-2.15657	5.1851	-1.30774	C	-2.15657	5.1851	-1.30774
H	-2.04368	5.06267	-2.39299	H	-2.04368	5.06267	-2.39299
C	1.12426	4.11481	0.24494	C	1.12426	4.11481	0.24494
C	1.95859	2.93749	-0.15851	C	1.95859	2.93749	-0.15851
C	3.13308	2.41397	0.39401	C	3.13308	2.41397	0.39401
C	3.69409	1.32246	-0.27745	C	3.69409	1.32246	-0.27745
C	4.9493	0.5468	-0.00718	C	4.9493	0.5468	-0.00718
C	3.87468	-0.43567	-1.82165	C	3.87468	-0.43567	-1.82165
C	3.07589	0.76148	-1.4032	C	3.07589	0.76148	-1.4032

3.5. REFERENCES

- (1) Chen, K.; Arnold, F. H. Engineering New Catalytic Activities in Enzymes. *Nat. Catal.* **2020**, *3*, 203–213.
- (2) Knowles, R. R.; Jacobsen, E. N. Attractive Noncovalent Interactions in Asymmetric Catalysis: Links between Enzymes and Small Molecule Catalysts. *Proc. Natl. Acad. Sci.* **2010**, *107*, 20678–20685.
- (3) Jena, S.; Dutta, J.; Tulsiyan, K. D.; Sahu, A. K.; Choudhury, S. S.; Biswal, H. S. Noncovalent Interactions in Proteins and Nucleic Acids: Beyond Hydrogen Bonding and π -Stacking. *Chem. Soc. Rev.* **2022**, *51*, 4261–4286.
- (4) Aliev, A. E.; Motherwell, W. B. Some Recent Advances in the Design and Use of Molecular Balances for the Experimental Quantification of Intramolecular Noncovalent Interactions of π Systems. *Chem. – Eur. J.* **2019**, *25*, 10516–10530.
- (5) Mati, I. K.; Cockroft, S. L. Molecular Balances for Quantifying Non-Covalent Interactions. *Chem. Soc. Rev.* **2010**, *39*, 4195–4205.
- (6) Paliwal, S.; Geib, S.; Wilcox, C. S. Molecular Torsion Balance for Weak Molecular Recognition Forces. Effects of “Tilted-T” Edge-to-Face Aromatic Interactions on Conformational Selection and Solid-State Structure. *J. Am. Chem. Soc.* **1994**, *116*, 4497–4498.

- (7) Motherwell, W. B.; Moïse, J.; Aliev, A. E.; Nič, M.; Coles, S. J.; Horton, P. N.; Hursthouse, M. B.; Chessari, G.; Hunter, C. A.; Vinter, J. G. Noncovalent Functional-Group–Arene Interactions. *Angew. Chem. Int. Ed.* **2007**, *46*, 7823–7826.
- (8) Li, P.; Vik, E. C.; Shimizu, K. D. N-Arylimide Molecular Balances: A Comprehensive Platform for Studying Aromatic Interactions in Solution. *Acc. Chem. Res.* **2020**, *53*, 2705–2714.
- (9) Elmi, A.; Cockroft, S. L. Quantifying Interactions and Solvent Effects Using Molecular Balances and Model Complexes. *Acc. Chem. Res.* **2021**, *54*, 92–103.
- (10) Burns, R. J.; Mati, I. K.; Muchowska, K. B.; Adam, C.; Cockroft, S. L. Quantifying Through-Space Substituent Effects. *Angew. Chem. Int. Ed.* **2020**, *59*, 16717–16724.
- (11) Kim, E.; Paliwal, S.; Wilcox, C. S. Measurements of Molecular Electrostatic Field Effects in Edge-to-Face Aromatic Interactions and CH- π Interactions with Implications for Protein Folding and Molecular Recognition. *J. Am. Chem. Soc.* **1998**, *120*, 11192–11193.
- (12) Aliev, A. E.; Arendorf, J. R. T.; Pavlakos, I.; Moreno, R. B.; Porter, M. J.; Rzepa, H. S.; Motherwell, W. B. Surfing π Clouds for Noncovalent Interactions: Arenes versus Alkenes. *Angew. Chem. Int. Ed.* **2015**, *54*, 551–555.
- (13) Motherwell, W. B.; Moreno, R. B.; Pavlakos, I.; Arendorf, J. R. T.; Arif, T.; Tizzard, G. J.; Coles, S. J.; Aliev, A. E. Noncovalent Interactions of π Systems with Sulfur: The Atomic Chameleon of Molecular Recognition. *Angew. Chem. Int. Ed.* **2018**, *57*, 1193–1198.
- (14) Jian, J.; Poater, J.; White, P. B.; McKenzie, C. J.; Bickelhaupt, F. M.; Mecinović, J. Probing Halogen- π versus CH- π Interactions in Molecular Balance. *Org. Lett.* **2020**, *22*, 7870–7873.
- (15) Sun, H.; Horatscheck, A.; Martos, V.; Bartetzko, M.; Uhrig, U.; Lentz, D.; Schmieder, P.; Nazaré, M. Direct Experimental Evidence for Halogen–Aryl π Interactions in Solution from Molecular Torsion Balances. *Angew. Chem. Int. Ed.* **2017**, *56*, 6454–6458.
- (16) Li, P.; Vik, E. C.; Maier, J. M.; Karki, I.; Strickland, S. M. S.; Umana, J. M.; Smith, M. D.; Pellechia, P. J.; Shimizu, K. D. Electrostatically Driven CO- π Aromatic Interactions. *J. Am. Chem. Soc.* **2019**, *141*, 12513–12517.
- (17) Vik, E. C.; Li, P.; Madukwe, D. O.; Karki, I.; Tibbetts, G. S.; Shimizu, K. D. Analysis of the Orbital and Electrostatic Contributions to the Lone Pair–Aromatic Interaction Using Molecular Rotors. *Org. Lett.* **2021**, *23*, 8179–8182.
- (18) Carroll, W. R.; Pellechia, P.; Shimizu, K. D. A Rigid Molecular Balance for Measuring Face-to-Face Arene–Arene Interactions. *Org. Lett.* **2008**, *10*, 3547–3550.
- (19) Pascoe, D. J.; Ling, K. B.; Cockroft, S. L. The Origin of Chalcogen-Bonding Interactions. *J. Am. Chem. Soc.* **2017**, *139*, 15160–15167.
- (20) Cockroft, S. L.; Hunter, C. A. Desolvation Tips the Balance: Solvent Effects on Aromatic Interactions. *Chem. Commun.* **2006**, 3806–3808.
- (21) Mati, I. K.; Adam, C.; Cockroft, S. L. Seeing through Solvent Effects Using Molecular Balances. *Chem. Sci.* **2013**, *4*, 3965–3972.
- (22) Ōki, M. Recent Advances in Atropisomerism. In *Topics in Stereochemistry*; John Wiley & Sons, Ltd, 1983; pp 1–81.
- (23) Zask, A.; Murphy, J.; Ellestad, G. A. Biological Stereoselectivity of Atropisomeric Natural Products and Drugs. *Chirality* **2013**, *25*, 265–274.

- (24) Smyth, J. E.; Butler, N. M.; Keller, P. A. A Twist of Nature – the Significance of Atropisomers in Biological Systems. *Nat. Prod. Rep.* **2015**, *32*, 1562–1583.
- (25) Clayden, J.; Moran, W. J.; Edwards, P. J.; LaPlante, S. R. The Challenge of Atropisomerism in Drug Discovery. *Angew. Chem. Int. Ed.* **2009**, *48*, 6398–6401.
- (26) LaPlante, S. R.; Fader, L. D.; Fandrick, K. R.; Fandrick, D. R.; Hucke, O.; Kemper, R.; Miller, S. P. F.; Edwards, P. J. Assessing Atropisomer Axial Chirality in Drug Discovery and Development. *J. Med. Chem.* **2011**, *54*, 7005–7022.
- (27) Borsley, S.; Kreidt, E.; Leigh, D. A.; Roberts, B. M. W. Autonomous Fuelled Directional Rotation about a Covalent Single Bond. *Nature* **2022**, *604*, 80–85.
- (28) Yang, F.; Liu, C.; Yin, D.; Xu, Y.; Wu, M.; Wei, W. Atropisomer-Based Construction of Macrocyclic Hosts That Selectively Recognize Tryptophan from Standard Amino Acids. *Chem. Commun.* **2019**, *55*, 14335–14338.
- (29) Ogoshi, T.; Yamagishi, T.; Nakamoto, Y. Pillar-Shaped Macrocyclic Hosts Pillar[n]Arenes: New Key Players for Supramolecular Chemistry. *Chem. Rev.* **2016**, *116*, 7937–8002.
- (30) Xue, M.; Yang, Y.; Chi, X.; Zhang, Z.; Huang, F. Pillararenes, A New Class of Macrocycles for Supramolecular Chemistry. *Acc. Chem. Res.* **2012**, *45*, 1294–1308.
- (31) Ogoshi, T.; Kanai, S.; Fujinami, S.; Yamagishi, T.; Nakamoto, Y. Para-Bridged Symmetrical Pillar[5]Arenes: Their Lewis Acid Catalyzed Synthesis and Host–Guest Property. *J. Am. Chem. Soc.* **2008**, *130*, 5022–5023.
- (32) Ogoshi, T.; Kitajima, K.; Aoki, T.; Fujinami, S.; Yamagishi, T.; Nakamoto, Y. Synthesis and Conformational Characteristics of Alkyl-Substituted Pillar[5]Arenes. *J. Org. Chem.* **2010**, *75*, 3268–3273.
- (33) Ogoshi, T.; Masaki, K.; Shiga, R.; Kitajima, K.; Yamagishi, T. Planar-Chiral Macrocyclic Host Pillar[5]Arene: No Rotation of Units and Isolation of Enantiomers by Introducing Bulky Substituents. *Org. Lett.* **2011**, *13*, 1264–1266.
- (34) Ogoshi, T.; Demachi, K.; Masaki, K.; Yamagishi, T. Diastereoselective Synthesis of Meso - Pillar[6]Arenes by Bridging between Hydroquinone Units in an Alternating up-and-down Manner. *Chem. Commun.* **2013**, *49*, 3952–3954.
- (35) Ogoshi, T.; Kitajima, K.; Aoki, T.; Yamagishi, T.; Nakamoto, Y. Effect of an Intramolecular Hydrogen Bond Belt and Complexation with the Guest on the Rotation Behavior of Phenolic Units in Pillar[5]Arenes. *J. Phys. Chem. Lett.* **2010**, *1*, 817–821.
- (36) Chen, J.-F.; Ding, J.-D.; Wei, T.-B. Pillararenes: Fascinating Planar Chiral Macrocyclic Arenes. *Chem. Commun.* **2021**, *57*, 9029–9039.
- (37) Nalluri, S. K. M.; Liu, Z.; Wu, Y.; Hermann, K. R.; Samanta, A.; Kim, D. J.; Krzyaniak, M. D.; Wasielewski, M. R.; Stoddart, J. F. Chiral Redox-Active Isosceles Triangles. *J. Am. Chem. Soc.* **2016**, *138*, 5968–5977.
- (38) Wang, Y.; Wu, H.; Stoddart, J. F. Molecular Triangles: A New Class of Macrocycles. *Acc. Chem. Res.* **2021**, *54*, 2027–2039.
- (39) Schneebeli, S. T.; Frasconi, M.; Liu, Z.; Wu, Y.; Gardner, D. M.; Strutt, N. L.; Cheng, C.; Carmieli, R.; Wasielewski, M. R.; Stoddart, J. F. Electron Sharing and Anion– π Recognition in Molecular Triangular Prisms. *Angew. Chem. Int. Ed.* **2013**, *52*, 13100–13104.

- (40) Wu, Y.; Han, J.-M.; Hong, M.; Krzyaniak, M. D.; Blackburn, A. K.; Fernando, I. R.; Cao, D. D.; Wasielewski, M. R.; Stoddart, J. F. X-Shaped Oligomeric Pyromellitimide Polyradicals. *J. Am. Chem. Soc.* **2018**, *140*, 515–523.
- (41) Hoffman, W. B. Production of Pyromellitic Diimide. US 2937189A. **1957**.
- (42) Gawroński, J.; Brzostowska, M.; Gawrońska, K.; Koput, J.; Rychlewska, U.; Skowronek, P.; Nordén, B. Novel Chiral Pyromellitimide (1,2,4,5-Benzenetetracarboxydiimide) Dimers and Trimers: Exploring Their Structure, Electronic Transitions, and Exciton Coupling. *Chem. – Eur. J.* **2002**, *8*, 2484–2494.
- (43) Deng, Y.; Wang, M.; Zhuang, Y.; Liu, S.; Huang, W.; Zhao, Q. Circularly Polarized Luminescence from Organic Micro-/Nano-Structures. *Light Sci. Appl.* **2021**, *10*, 76.
- (44) Perrin, C. L.; Dwyer, T. J. Application of Two-Dimensional NMR to Kinetics of Chemical Exchange. *Chem. Rev.* **1990**, *90*, 935–967.
- (45) Batsanov, S. S. Van Der Waals Radii of Elements. *Inorg. Mater.* **2001**, *37*, 871–885.
- (46) Shah, M. B.; Liu, J.; Zhang, Q.; Stout, C. D.; Halpert, J. R. Halogen– π Interactions in the Cytochrome P450 Active Site: Structural Insights into Human CYP2B6 Substrate Selectivity. *ACS Chem. Biol.* **2017**, *12*, 1204–1210.
- (47) LaPlante, S. R.; Edwards, P. J.; Fader, L. D.; Jakalian, A.; Hucke, O. Revealing Atropisomer Axial Chirality in Drug Discovery. *ChemMedChem* **2011**, *6*, 505–513.
- (48) Svensson, P. H.; Kloo, L. Synthesis, Structure, and Bonding in Polyiodide and Metal Iodide–Iodine Systems. *Chem. Rev.* **2003**, *103*, 1649–1684.
- (49) Burgess, A. E.; Davidson, J. C. A Kinetic–Equilibrium Study of a Triiodide Concentration Maximum Formed by the Persulfate–Iodide Reaction. *J. Chem. Educ.* **2012**, *89*, 814–816.
- (50) *BindFit v0.5 | Supramolecular*. <http://app.supramolecular.org/bindfit/> (accessed 2023-11-15).
- (51) Hibbert, D. B.; Thordarson, P. The Death of the Job Plot, Transparency, Open Science and Online Tools, Uncertainty Estimation Methods and Other Developments in Supramolecular Chemistry Data Analysis. *Chem. Commun.* **2016**, *52*, 12792–12805.
- (52) Thordarson, P. Determining Association Constants from Titration Experiments in Supramolecular Chemistry. *Chem. Soc. Rev.* **2011**, *40*, 1305–1323.
- (53) CrysAlisPro. CrysAlisPro, Oxford Diffraction Ltd. Version 1.171.34.40.
- (54) Empirical Absorption Correction Using Spherical Harmonics, Implemented in SCALE3 ABSPACK Scaling Algorithm within CrysAlisPro Software. Scale3, Oxford Diffraction Ltd. Version 1.171.34.40.
- (55) Dolomanov, O. V.; Bourhis, L. J.; Gildea, R. J.; Howard, J. a. K.; Puschmann, H. OLEX2: A Complete Structure Solution, Refinement and Analysis Program. *J. Appl. Crystallogr.* **2009**, *42*, 339–341.
- (56) Sheldrick, G. M. A Short History of SHELX. *Acta Crystallogr. A* **2008**, *64*, 112–122.
- (57) Sheldrick, G. M. SHELXT – Integrated Space-Group and Crystal-Structure Determination. *Acta Crystallogr. Sect. Found. Adv.* **2015**, *71*, 3–8.

- (58) Macrae, C. F.; Sovago, I.; Cottrell, S. J.; Galek, P. T. A.; McCabe, P.; Pidcock, E.; Platings, M.; Shields, G. P.; Stevens, J. S.; Towler, M.; Wood, P. A. Mercury 4.0: From Visualization to Analysis, Design and Prediction. *J. Appl. Crystallogr.* **2020**, *53*, 226–235.
- (59) Frisch, M. J.; Trucks, G. W.; Schlegel, H. B.; Scuseria, G. E.; Robb, M. A.; Cheeseman, J. R.; Scalmani, G.; Barone, V.; Petersson, G. A.; Nakatsuji, H.; Li, X.; Caricato, M.; Marenich, A. V.; Bloino, J.; Janesko, B. G.; Gomperts, R.; Mennucci, B.; Hratchian, H. P.; Ortiz, J. V.; Izmaylov, A. F.; Sonnenberg, J. L.; Williams; Ding, F.; Lipparini, F.; Egidi, F.; Goings, J.; Peng, B.; Petrone, A.; Henderson, T.; Ranasinghe, D.; Zakrzewski, V. G.; Gao, J.; Rega, N.; Zheng, G.; Liang, W.; Hada, M.; Ehara, M.; Toyota, K.; Fukuda, R.; Hasegawa, J.; Ishida, M.; Nakajima, T.; Honda, Y.; Kitao, O.; Nakai, H.; Vreven, T.; Throssell, K.; Montgomery Jr., J. A.; Peralta, J. E.; Ogliaro, F.; Bearpark, M. J.; Heyd, J. J.; Brothers, E. N.; Kudin, K. N.; Staroverov, V. N.; Keith, T. A.; Kobayashi, R.; Normand, J.; Raghavachari, K.; Rendell, A. P.; Burant, J. C.; Iyengar, S. S.; Tomasi, J.; Cossi, M.; Millam, J. M.; Klene, M.; Adamo, C.; Cammi, R.; Ochterski, J. W.; Martin, R. L.; Morokuma, K.; Farkas, O.; Foresman, J. B.; Fox, D. J. Gaussian 16 Rev. A.03, 2016.
- (60) Becke, A. D. Density-functional Thermochemistry. III. The Role of Exact Exchange. *J. Chem. Phys.* **1993**, *98*, 5648–5652.
- (61) Lee, C.; Yang, W.; Parr, R. G. Development of the Colle-Salvetti Correlation-Energy Formula into a Functional of the Electron Density. *Phys. Rev. B* **1988**, *37*, 785–789.
- (62) Weigend, F. Accurate Coulomb-Fitting Basis Sets for H to Rn. *Phys. Chem. Chem. Phys.* **2006**, *8*, 1057.
- (63) Grimme, S.; Ehrlich, S.; Goerigk, L. Effect of the Damping Function in Dispersion Corrected Density Functional Theory. *J. Comput. Chem.* **2011**, *32*, 1456–1465.

CHAPTER 4 |

PHOTOACTIVITY OF CORE-SUBSTITUTED MOLECULAR TRIANGLES

SYNOPSIS

Light-emitting compounds play a key role in modern life including for bioimaging and electronic device applications. The luminescent properties of aromatic diimides (ADIs) are well studied, with the emission of perylene diimide (PDI) contributing to its use as a common dye and as a standard for fluorescent quantum yield measurements. Although, to ‘turn on’ the emission of pyromellitic diimides (PMDIs) core-substitution of the aromatic core is required. The introduction of halogen atoms to the PMDI core has been shown to induce phosphorescence on account of enhanced intersystem crossing (ISC) due to the heavy atom effect. Alternatively, functionalisation of the PMDI aromatic core with hydroxy-groups ‘turns on’ emission with excited state intramolecular proton transfer (ESIPT) occurring where both tautomers (*via* a keto-enol tautomerisation) are emissive in the excited state.

In this Chapter, investigations into the photoactivity of core-brominated molecular triangles are outlined. A photochemical transformation of **6Br** in DMF upon irradiation with UV-light is observed through a colour change (colourless to pink) and the generation of new peaks in absorption spectra which are attributed to the formation of a partially core-hydroxylated molecular triangle. Furthermore, the luminescent properties of core-brominated molecular triangles, **3Br** and **6Br**, are investigated in the solid state with the emission of the macrocycles occurring *via* room-temperature phosphorescence. This Chapter also presents some preliminary synthetic attempts to optimise a bromine to hydroxy functional group transformation in PMDI small molecules through reaction with CsF in dioxane. The application of these reaction conditions to a Br₂PMDI compound are shown to form partially hydroxylated mono-hydroxy-mono-bromo PMDI units. In addition to being emissive, these asymmetric hydroxy-bromo PMDI units could be used for orthogonal reactivity towards further aromatic core extension in the future. Therefore, the photoactivity of electron-deficient core-substituted molecular triangles is not only beneficial for the luminescent properties of the macrocycles but can also be used in the further core-extension of the aromatic core.

Acknowledgements

FHNA acknowledges support from (i) Dr Andrew Danos and Professor Andy Monkman for completing photophysical experiments at Durham University.

4.1 INTRODUCTION

Organic luminophores which can emit light through the relaxation of excited states on the nanosecond to second timescale have applications in fluorescent bioimaging,¹ in organic light-emitting diodes (OLEDs)² and for studying non-covalent interactions (NCIs) *e.g.*, host–guest complexation.³ Organic luminescent materials have become more attractive compared to their inorganic counterparts due to their decreased toxicity, higher synthetic versatility, and lower cost.⁴ The phenomenon of fluorescence was first reported in 1565, with further studies leading to the current accepted explanation where absorbance of light to excite an electron from the S_0 ground state to a higher electronic state is followed by relaxation back to the ground state by emission of light.⁵ Despite, a history of nearly 500 years, new luminescent phenomena in organic compounds are still being discovered and studied for potential applications in the 21st century, *e.g.*, aggregation-induced emission (AIE),⁶ room-temperature phosphorescence (RTP),^{7,8} thermally-activated delayed fluorescence,⁹ excited-state intramolecular proton transfer (ESIPT),^{10,11} and circularly polarised luminescence (CPL).¹² These different emissive processes all rely on the electronic structure of molecules and the various mechanisms of relaxation and spin interconversions that can occur in the excited state as shown by the Jablonski diagram (Figure 4.1).

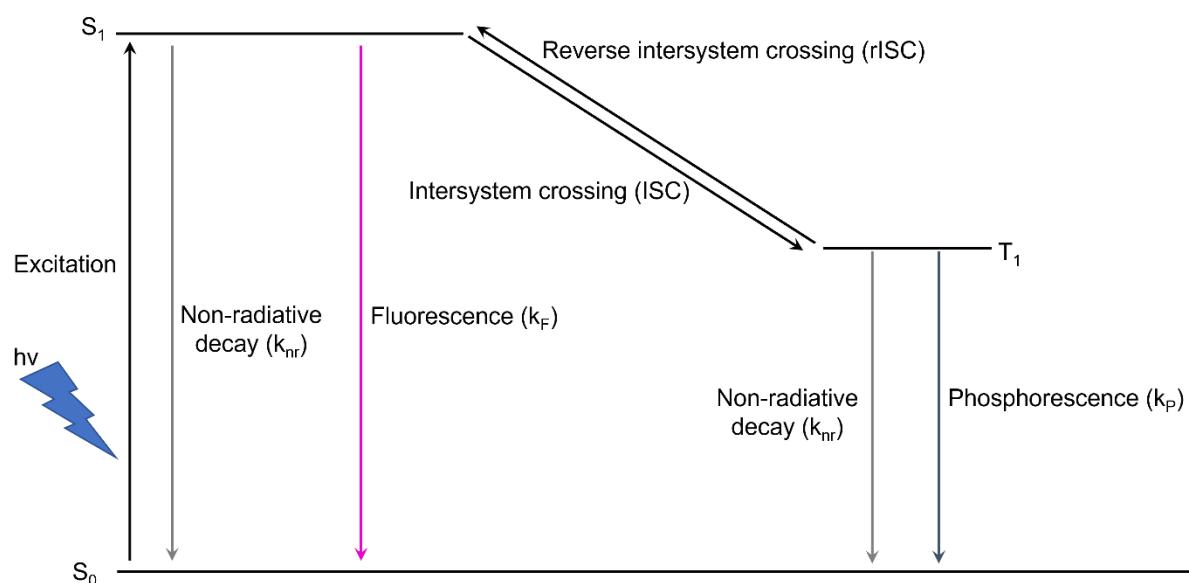


Figure 4.1 Jablonski diagram showing the excitation of a molecule from the ground state (S_0) to the first singlet excited state (S_1) and subsequent relaxation processes (non-radiative decay and fluorescence) and intersystem crossing to the first triplet excited state (T_1) which can decay non-radiatively or *via* phosphorescence or return to the S_1 state through reverse intersystem crossing.

The synthetic versatility and redox-active nature of aromatic diimides (ADIs), such as pyromellitic, naphthalene and perylene diimides (PMDI, NDI and PDI respectively), makes them attractive organic compounds for use as functional materials in electronic devices.^{13,14} Additionally, PDIs have been used widely in dyes and pigments,¹⁵ and due to their efficient emission with a quantum yield (the ratio of emitted photons compared with the number of photons used in excitation), ϕ , close to unity they are used as standards for calculating the quantum yields of new luminophores.¹⁶ However, aggregation of

PDI molecules by $\pi \cdots \pi$ interactions in the solid state leads to emission quenching (e.g. in PDI **1**). Nalluri *et al.*¹⁷ hypothesised that the aggregation-caused quenching (ACQ) of PDI molecules could be reduced through the incorporation of the luminophore into isosceles molecular triangles (**2** and **3**), where one PDI unit is connected to two NDI or PMDI units by chiral (*R,R*)- or (*S,S*)-*trans*-1,2-diaminocyclohexane linkers (Figure 4.2a–c). The non-equilateral triangular geometry of the macrocycle could disrupt any potential long-range $\pi \cdots \pi$ interactions, whilst the vibrational and rotational motion of the emissive PDI units would be restricted to decrease the non-radiative decay and thus enhance the quantum yield. High fluorescent quantum yields were observed for both macrocycles **2** (CH_2Cl_2 : 100%, MeCN: 96%, PhMe: 100%) and **3** (CH_2Cl_2 : 100%, MeCN: 96% and PhMe: 63%) in the solution state with the reference monomeric PDI **1** as a standard. The decreased quantum yield for **3** in PhMe was attributed to ACQ from intermolecular $\pi \cdots \pi$ interactions between the macrocycle and aromatic solvent. Although the quantum yield of molecular triangles **2** and **3** diminish in the solid state (*i.e.*, in neat thin films or as powders) compared to in solution, they are still fairly emissive (**2**: $\phi_{\text{powder}} = 4\%$, $\phi_{\text{film}} = 2\%$, **3**: $\phi_{\text{powder}} = 3\%$, $\phi_{\text{film}} = 2\%$). The solid-state quantum yields of emission of macrocycles **2** and **3** are also greater than the monomeric PDI reference **1** ($\phi_{\text{powder}} = 0.1\%$, $\phi_{\text{film}} = 0.2\%$) which suggests that the incorporation of the luminophore into a macrocycle does indeed reduce ACQ and non-radiative decay to improve the luminescence.¹⁷

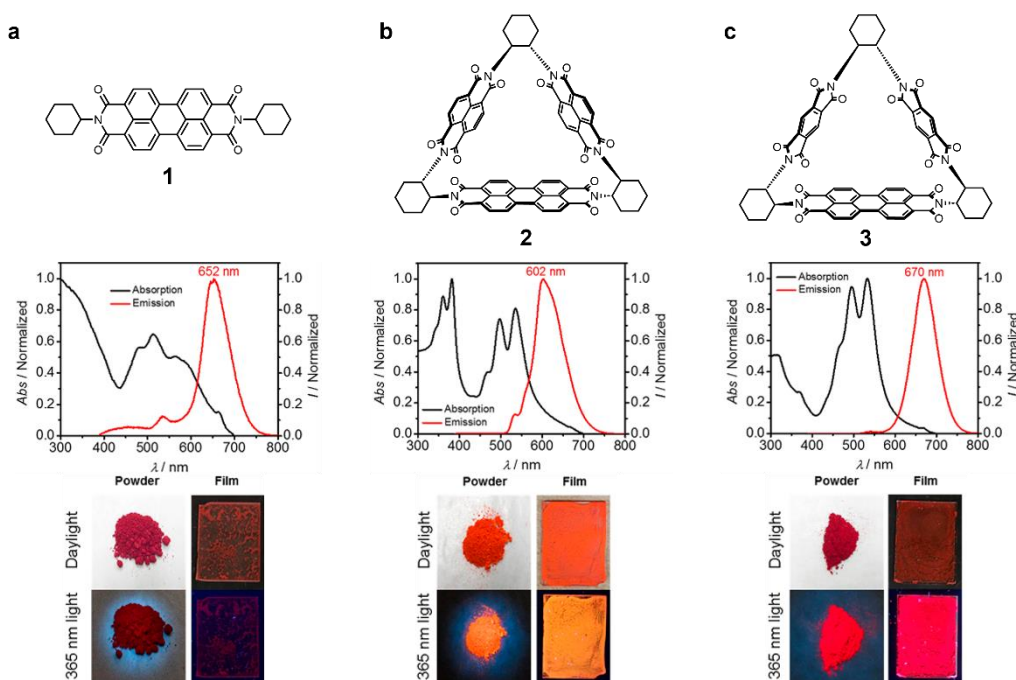


Figure 4.2 Chemical structure, emission and absorption spectra and images of powders and thin film in daylight and 365 nm light for macrocycles (a) **1**, (b) **2** and (c) **3**. Figure reproduced from Reference 17.¹⁷

Conversely, PMDIs are not inherently emissive with luminescence ‘turned on’ upon core-functionalisation with halogens,^{8,10} electron-rich donors,⁹ or hydroxy-groups.^{10,11} The emissive properties of core-halogenated and -hydroxylated PMDI molecules occurs as a result of RTP and ESIPT mechanistic processes respectively. The functionality of core-halogenated PMDI small molecules

makes them attractive candidates for RTP due to the ability of carbonyls and halogen atoms to facilitate spin-forbidden ISC from the S_1 to T_1 excited states (Figure 4.1). Subsequently, lower energy phosphorescent emission is promoted (T_1 to S_0) at longer wavelengths to relax to the ground state which occurs over a longer timescale (ms) on account of it being spin-forbidden process ($\Delta S \neq 0$).⁸ Indeed, Kanosue and Ando,⁷ have shown that the introduction of a single halogen atom (bromine or iodine) on the aromatic core of PMDI small molecules ‘turns on’ red and orange emission in compounds **4** and **5** respectively (Figure 4.3a and b) with a large Stokes shift indicating phosphorescence. However, relatively low quantum yields for **4** ($\phi = 1\%$) and **5** ($\phi = 2\%$) in CHCl_3 solutions were measured although still greater than the unsubstituted PMDI model compound **6** ($\phi = <0.1\%$). Shorter emission lifetimes than expected for spin-forbidden phosphorescence were also observed (**4**: $\tau = 7.1$ ns and **5**: $\tau = 13.0$ ns) which was attributed to vibrational and rotational motion of the excited states in solution enhancing non-radiative decay and thus quenching of emission.⁷

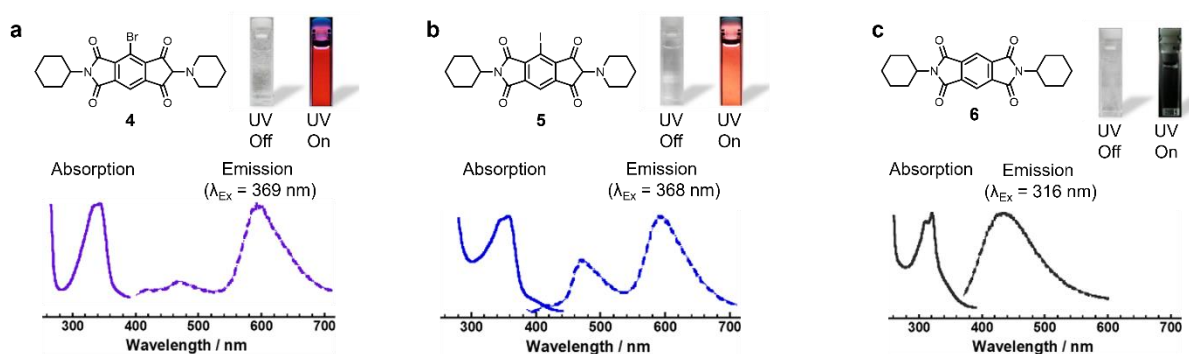


Figure 4.3 Chemical structures, absorption and emission spectra and colour of CHCl_3 solutions with UV-light (365 nm) off and on for PMDI compounds (a) **4**, (b) **5** and (c) **6**. Figure reproduced and replicated from Reference 7.⁷

A common strategy to avoid non-radiative decay from vibrational and rotational motion is ‘freezing’ the phosphors into the solid state (*i.e.*, crystals or polymer matrices). Garain *et al.*⁸ used these methods to enhance phosphorescence in dibromo- and diiodo- PMDI derivatives **7** and **8** (Figure 4.4) that display weak fluorescent emission (400–550 nm) in the solution state (THF) with short lifetimes (<1 ns). When the THF solutions were frozen at 77 K, the emission was red-shifted to 425–700 nm indicating lower energy phosphorescence which led the authors to investigate the luminescence of the halogenated PMDI molecules in the solid state through the formation of different wt% poly(methylmethacrylate) (PMMA) matrices, drop-casted thin films and crystals. Indeed, long-lived phosphorescent emission with considerable quantum yields was observed in the solid state, with tuning of the emission wavelength possible through increasing the wt% of compound in PMMA matrices and aggregation in thin films and supramolecular packing *via* halogen $\cdots\pi$, $\pi\cdots\pi$ and halogen $\cdots\text{O}=\text{C}$ interactions.⁸

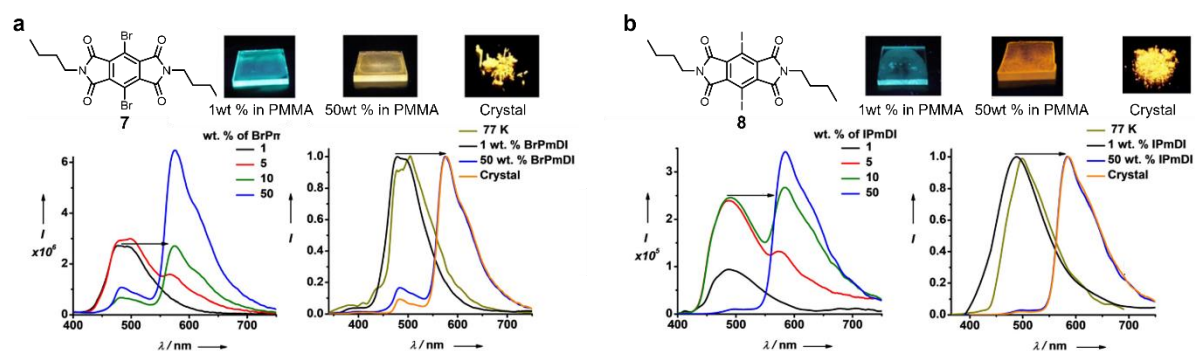


Figure 4.4 Chemical structures, emission spectra (1, 5, 10 and 50 wt% in PMMA, THF solution at 77 K and in single crystal) and colour of emission in solid state UV-light (365 nm) for PMDI compounds (a) **7** and (b) **8**. Figure reproduced and replicated from Reference 8.⁸

Table 4.1 Quantum yields (ϕ) of di-brominated **7** and di-iodinated **8** in the solid state (1 and 50 wt% in PMMA and crystals).⁸

	7		8	
	ϕ (Air) / %	ϕ (Vacuum) / %	ϕ (Air) / %	ϕ (Vacuum) / %
1 wt% in PMMA	18	54.7	2	2.4
50 wt% in PMMA	17.5	23.5	30	45.9
Crystal	26	28.7	48	68.2

An alternative method to ‘turn on’ emission in PMDI compounds is core-functionalisation with hydroxy-groups, where the 1,3-position relationship of -OH and C=O groups provides an optimal geometry for an intramolecular hydrogen-bond to form a stabilised planar six-membered ring. The non-covalent -OH \cdots O=C interaction facilitates intramolecular proton transfer in the excited state *via* an ESIPT process thus prompting a keto-enol tautomerisation (Figure 4.5c). In the case of a mono-hydroxylated PMDI compound **9**, relaxation to the ground state occurs from the ketone tautomer which is evidenced by a large Stokes shift (10356 cm⁻¹) between the absorption (369 nm) and emission (592 nm) peaks (Figure 4.5a). The orange colour of the relaxation of the ketone tautomer in a CHCl₃ solution occurs with a relatively high quantum yield (19.4 %) which indicates a fast ESIPT process to enhance the photon efficiency of the emission.¹¹ Furthermore, in di-hydroxylated PMDI **10**, dual-wavelength emission is observed at 457 and 641 nm after excitation at 430 nm. These two emission peaks with small (1374 cm⁻¹) and large (7655 cm⁻¹) Stokes shift represent relaxation to the ground state from the excited states of the enol and keto tautomers respectively. The blue and red emission from enol and keto tautomers can be tuned using solvent effects to disrupt or enhance intramolecular H-bonding (Figure 4.5.b). In solvents with no H-bonding capability (*e.g.*, CHCl₃), intramolecular H-bonds are favoured and thus efficient ESIPT occurs with subsequent relaxation to the ground state *via* red emission with a quantum yield of 16%. Whereas in solvents which can participate in H-bonding (*e.g.* TFA), there is competition between inter- and intramolecular interactions. When intermolecular interactions occur, the resulting absence of a stabilising six-membered ring from intramolecular H-bonding hinders any ESIPT process thus enhancing blue emission from the enol tautomer.¹⁰

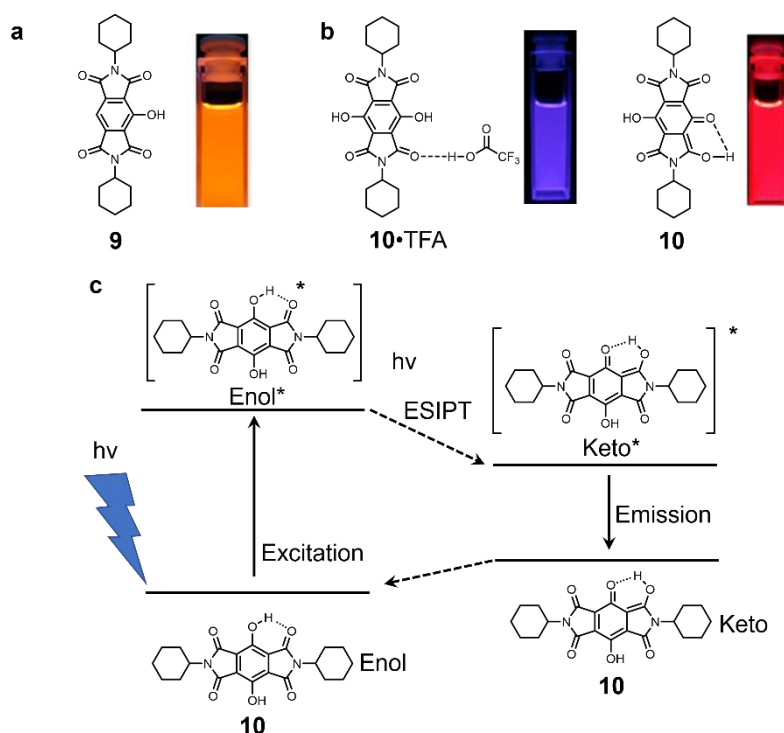
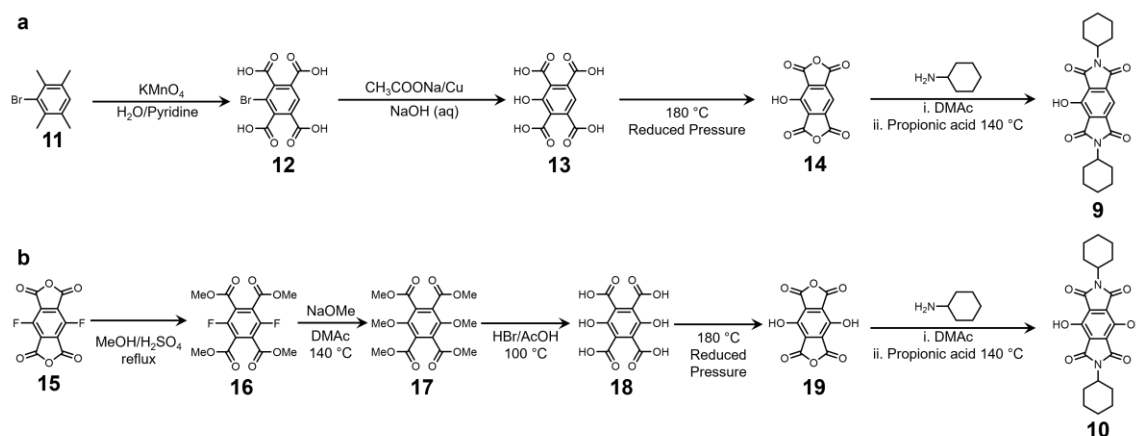


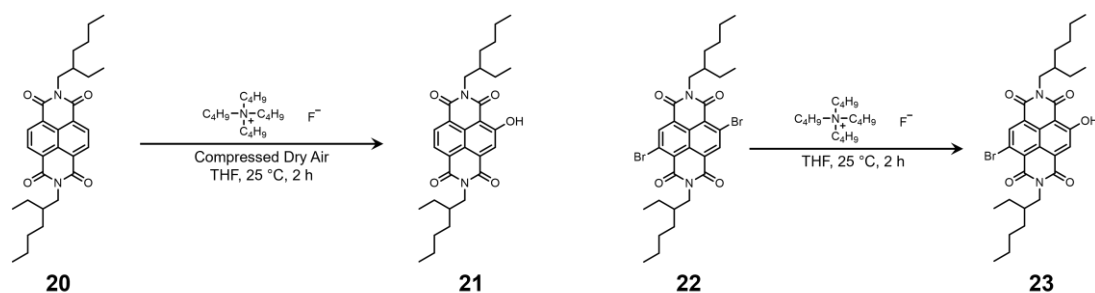
Figure 4.5 Structure and emission colour of core-hydroxylated PMDI compounds (a) **9** and (b) **10** with intermolecular (with TFA) and intramolecular H-bonding. (c) Keto-enol tautomerisation involved in the ESIPT process of compound **10**. Figure reproduced from References 10 and 11.^{10,11}

Various methods for the preparation of core-hydroxylated ADIs have been shown including (i) conventional syntheses^{10,11} and (ii) *via* radical anion formation.^{18,19} The synthesis of mono- and di-hydroxy-PMDI compounds (**9** and **10**) (Scheme 4.1) are different up until the formation of key hydroxybenzene tetracarboxylic precursors (**13** and **18**) at which point the syntheses align: (i) ring-closing by dehydration under reduced pressure at 180 °C followed by (ii) condensation with cyclohexylamine.^{10,11} The synthesis of the mono-hydroxylated acid **13** begins with 1-bromodurene (**11**) which is oxidised to acid **12** using KMnO_4 followed by a functional group transformation from -Br to -OH using NaOAc, aqueous NaOH and a copper catalyst.¹¹ Conversely, the synthesis of acidic precursor **18** uses a different approach as it begins with difluoro anhydride **15** which, when treated with MeOH and H_2SO_4 , forms tetramethylester **16** and subsequent reaction with NaOMe yields dimethoxy tetramethylester **17**. The key hydroxylation step is then performed by acidification with HBr in AcOH to form the hydroxy precursor **18**.¹⁰



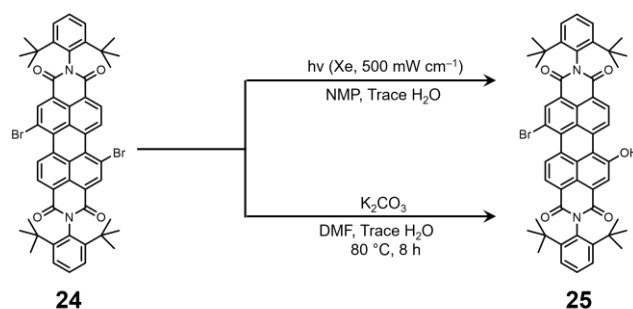
Scheme 4.1 Conventional literature synthesis of mono- and di-hydroxy-PMDI compounds (a) **9**¹¹ and (b) **10**.¹⁰

Alternative methods have been used to synthesise core-hydroxylated NDIs and PDIs utilising the electron-deficiency of the π -surface. Tam and Xu,¹⁸ showed that the aromatic core of NDIs **20** and **22** could be substituted with a hydroxy group under reducing conditions with tetrabutylammonium fluoride (TBAF \cdot 3H₂O) in polar aprotic solvents *e.g.*, THF (Scheme 4.2). The authors hypothesised that the transformations occurred as a result of electron transfer from electron-rich hydroxide ions to the aromatic naphthalene π -surface *via* a radical anion mechanism. The hydroxide ions are present as a result of deprotonation of water molecules in the hydrated salt by basic F[−] ions. In the case of the formation of NDI **23**, further hydroxylation does not occur as the electron-donating -OH increases the electron-density of the π -surface and prevents further electron transfer and subsequent substitution from a second OH[−] group.



Scheme 4.2 Reaction scheme for the hydroxylation of NDIs **20** and **22** to **21** and **23** under reducing conditions with TBAF.¹⁸

Furthermore, a similar core-hydroxylation of a dibrominated PDI **24** has been presented to form mono-bromo-mono-hydroxy **25** in electron-rich polar solvents (*e.g.*, NMP or DMF) *via* (i) irradiation with UV-light¹⁹ or (ii) conventional synthesis by reaction with H₂O in DMF at 80 °C (Scheme 4.3).²⁰ Zhang *et al.*,¹⁹ hypothesised that the formation of hydroxylated **25** after irradiation with UV-light occurs as a result of the deprotonation of residual H₂O molecules by the electron-rich basic solvent (DMF or NMP) and PET from hydroxide anions to the electron-deficient PDI π -surface. The presence of hydroxide anions subsequently leads to a bromine to hydroxy transformation potentially *via* a mechanism involving radicals to form PDI **25**.



Scheme 4.3 Reaction conditions for the synthesis of Br-PDI-OH, **25**, from dibrominated **24**, by irradiation with a xenon lamp (500 mW cm^{-1}) in DMF for 45 minutes or conventional heating ($80 \text{ } ^\circ\text{C}$) with K_2CO_3 in DMF for 8 hours.^{19,20}

This Chapter pursues these photoactive properties of functionalised ADIs within rigid shape-persistent molecular triangles in combination with the cyclic aromatic homoconjugation of the macrocycles. The optical and luminescent properties of core-substituted PMDI-based molecular triangles (Figure 4.6) are discussed through (i) the photochemical behaviour of **6Br** by the irradiation of UV-light, (ii) the solution- and solid-state emission of core-brominated molecular triangles (**3Br** and **6Br**) and (iii) progress towards the synthesis of core-hydroxylated molecular triangles using a post-synthetic functionalisation method. It was hypothesised that the incorporation of brominated and hydroxylated luminophores into a rigid, shape-persistent macrocycle would enhance the emission by reducing non-radiative decay *via* vibrational and rotational motion as exhibited by the isosceles triangles discussed above.¹⁷ The use of the chiral (*R,R*)- or (*S,S*)-*trans*-1,2-diaminocyclohexane linkers means that the molecular triangles possess helical chirality²¹ which could be utilised for CPL properties.¹²

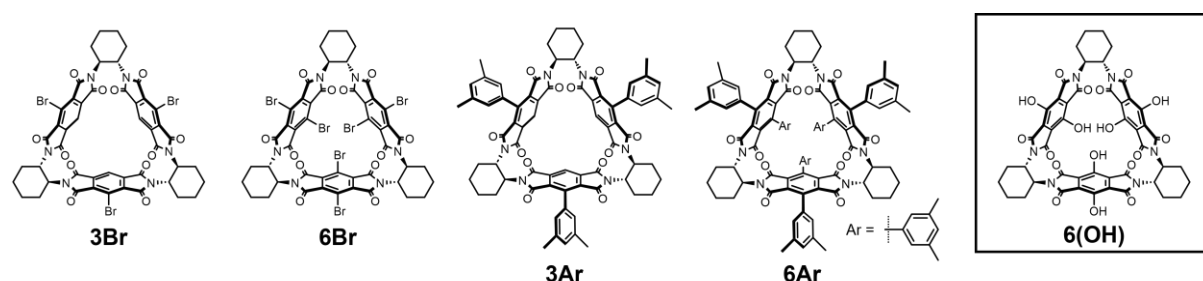


Figure 4.6. Chemical structures of core-functionalised molecular triangles, **3Br**, **6Br**, **3Ar** and **6Ar**, and the structure of core-hydroxylated macrocycle **6(OH)** which synthetic progress towards is discussed in this chapter.

4.2. RESULTS AND DISCUSSION

4.2.1. THE PHOTO-ACTIVE BEHAVIOUR OF 6Br IN DMF

During initial optical property analysis of molecular triangles, **6H**, **3Br**, **6Br**, **3Ar** and **6Ar** described in Chapters 2 and 3 in a range of solvents (CHCl_3 , THF and DMF) an intriguing observation was made after 24 hours as the solution of **6Br** in DMF that was left out under ambient light had turned a pink colour from its original colourless state. Notably, the colour change only occurred in the brominated macrocycles (**3Br** and **6Br**) and in electron-rich DMF. This surprising discovery led to a series of experiments to understand the colour change and the conditions under which it occurs. Initially, absorption spectra of all core-functionalised molecular triangles in CHCl_3 and DMF were repeated at 0 and 24 hours at 25 μM (Figure 4.7), with a new broad peak at 520 nm formed in the spectrum for **6Br** in DMF after 24 h. Similarly, a lower energy peak at 500 nm was also observed for **3Br** in DMF after 24 hours (500 nm). In DMF solutions where no colour change occurred (**6H**, **3Ar** and **6Ar**), no new peaks evolved after 24 hours with no colour changes and no new peaks formed in CHCl_3 solutions of any molecular triangle (**6H**, **3Br**, **6Br**, **3Ar** and **6Ar**) either.

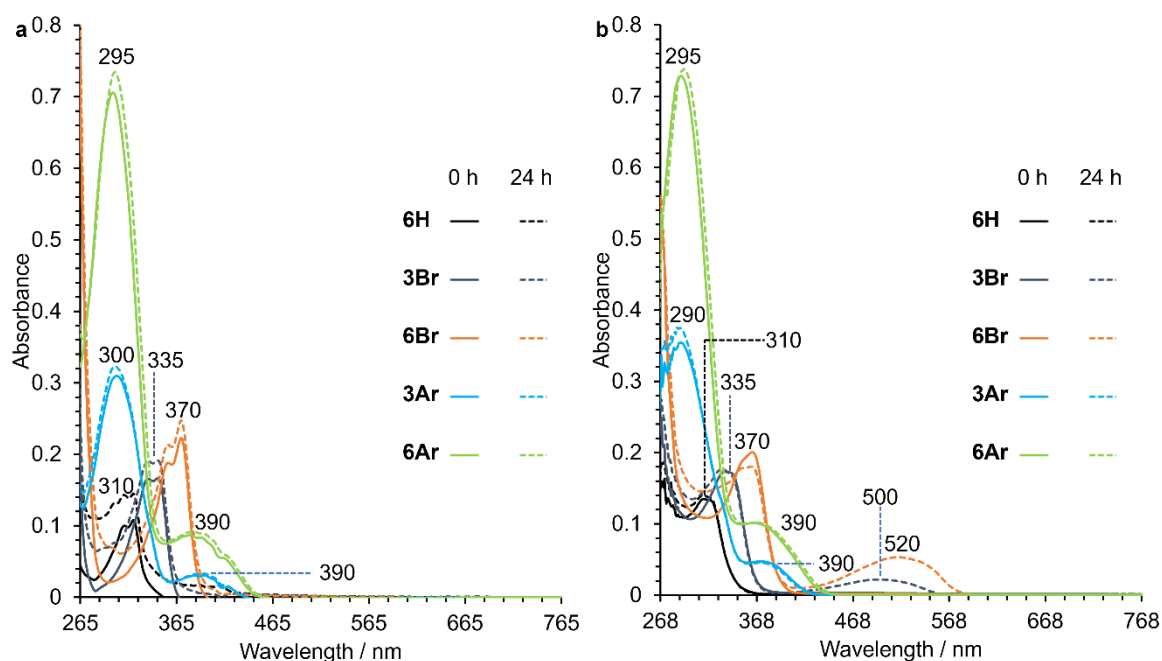


Figure 4.7 UV-vis spectra of core-functionalised molecular triangles (**6H**, **3Br**, **6Br**, **3Ar** and **6Ar**) in (a) CHCl_3 and (b) DMF at 25 μM at time = 0 and 24 h.

Subsequently, a potential concentration effect (25–200 μM) on the formation of the new peaks for **3Br** and **6Br** in DMF was probed by repeating absorption spectroscopy experiments at 0 and 24 hours (Figure 4.8) with new absorption bands evolving after 24 hours at all concentrations (25–200 μM). Significantly, the peaks at 500 and 525 nm for **3Br** after 24 h are more than two-times less intense than the low energy peaks at 515 and 545 nm for **6Br** (Table 4.2). The evolution of the longer wavelength

peaks in the UV-vis spectra for **3Br** and **6Br** does appear to be concentration dependent although not in a linear relationship and thus does not conform with the Beer-Lambert law.

Table 4.2 Absorbance values (A.U.) of **3Br** and **6Br** at 0 and 24 h at a range of wavelengths and concentrations (25–200 μM).

			200 μM	150 μM	100 μM	75 μM	50 μM	25 μM
3Br	340 nm	0 h	1.400	0.992	0.641	0.537	0.379	0.180
		24 h	1.400	0.989	0.640	0.535	0.385	0.183
	500 nm	0 h	0.005	0.002	0.001	0.001	0.001	0.001
		24 h	0.045	0.034	0.025	0.027	0.017	0.012
	525 nm	0 h	0.005	0.002	0.001	0.001	0.001	0.001
		24 h	0.041	0.031	0.023	0.026	0.015	0.012
6Br	365 nm	0 h	1.426	1.127	0.710	0.515	0.361	0.175
		24 h	1.503	1.088	0.677	0.489	0.334	0.149
	515 nm	0 h	0.021	0.020	0.013	0.010	0.008	0.009
		24 h	0.197	0.219	0.197	0.182	0.15	0.153
	545 nm	0 h	0.023	0.022	0.015	0.012	0.010	0.011
		24 h	0.235	0.242	0.231	0.213	0.170	0.168

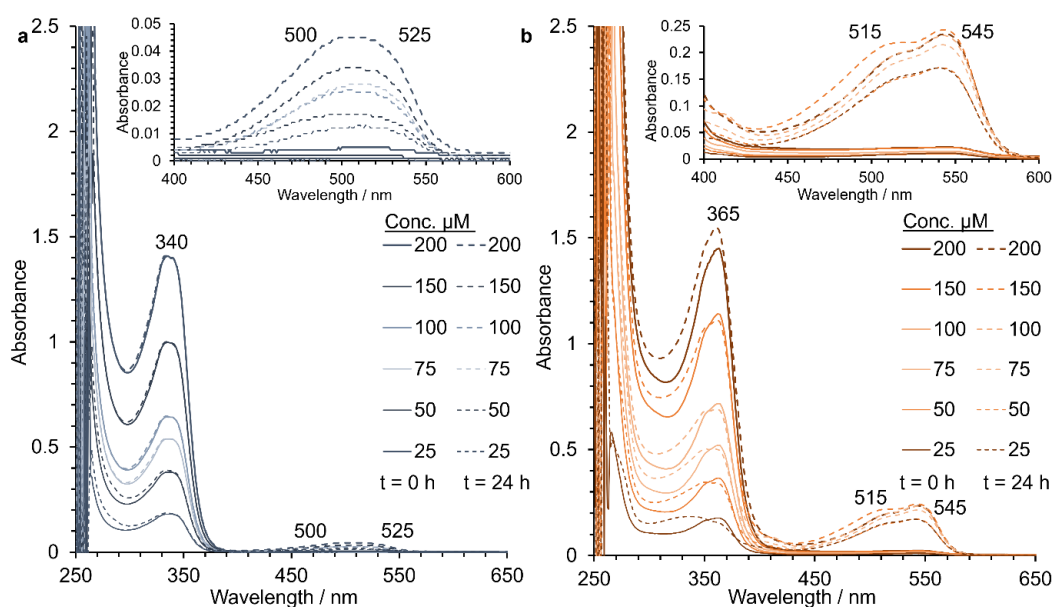


Figure 4.8 UV-vis spectra of core-brominated molecular triangles, (a) **3Br** and (b) **6Br** at time = 0 and 24 h. at a range of concentrations (200–25 μM) in DMF.

Notably, when DMF samples of **6Br** were kept in the dark, the pink colour evolved much more slowly, suggesting the presence of a photoactivated process. To confirm this hypothesis, absorption kinetic experiments of samples maintained under ambient light and dark conditions at room temperature over a 24 h period were performed. The graphs in Figure 4.9 show quantifiably that the growth of the new peaks at 515 and 545 nm are enhanced under ambient light compared with a solution that is kept in darkness. For example, after 48 hours, the peak at 515 nm has an intensity of 0.3 A.U. in the solution

kept under ambient light whereas the solution kept under darkness has an intensity of 0.037 A.U., an almost 10-fold decrease in absorption intensity. Furthermore, for the sample kept under ambient light, the intensity ratio of the peaks at 515 and 545 nm changes over time from 0 to 48 hours. When the lower energy peaks are first observed and grow in, the intensity of the peak at 545 nm is slightly higher than the peak at 515 nm (Figure 4.9c). However, the ratio of the peaks shifts towards the latter times (> 24 h), the absorbance at 515 nm is slightly higher than at 545 nm. The change in ratio of absorbance intensity of the peaks at 515 and 545 nm over time could indicate the photochemical transformation that is occurring involves a two-step process over time.

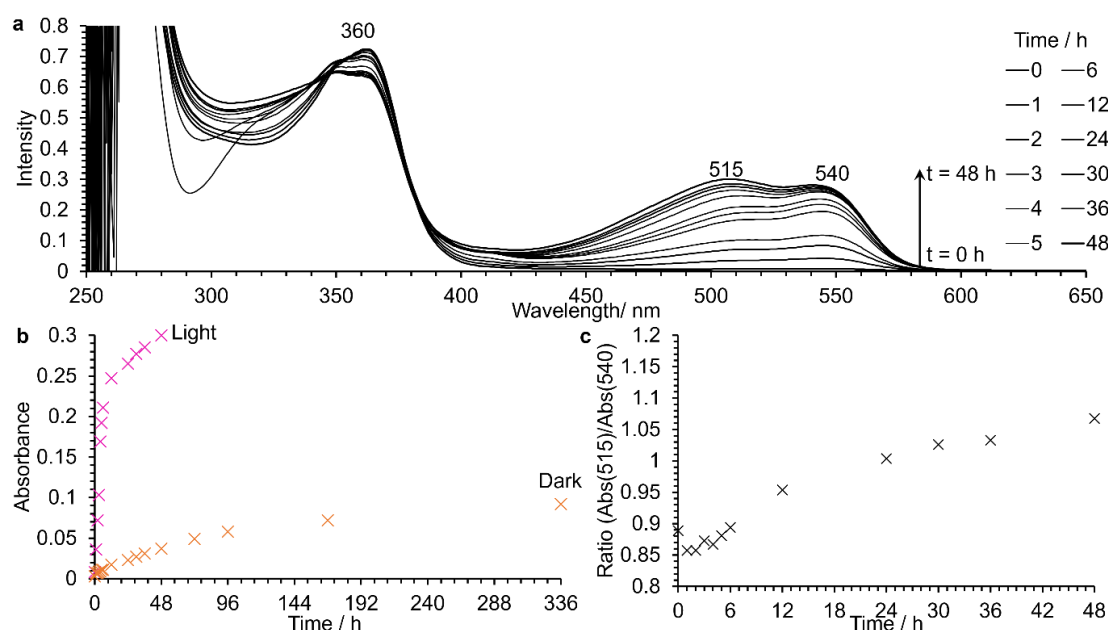


Figure 4.9 (a) UV-vis spectra of **6Br** in DMF (100 μ M) at regular time periods (0–48 h) for a sample kept under ambient light. Plots showing (b) the intensity of the peak at 515 nm over time under ambient light (0–48 h) and dark (0–336 h) and (c) the ratio intensity of the absorbance peaks at 515 and 545 nm for the sample kept under ambient light.

Furthermore, when irradiating samples of **3Br** and **6Br** with 365 nm UV-light (from a UV torch) in 5-minute portions, the colour change and subsequent growth of lower energy peaks between 500 and 550 nm is accelerated (Figure 4.10). The formation of peaks in **3Br** is less significant than in **6Br** as has been observed previously in Figure 4.10, and as expected, no new absorption is developed in the non-brominated macrocycle, **6H**. In addition, the ratio of the higher energy π - π^* transitions and the newly formed peaks at 515 and 545 nm for **6Br** is roughly 2:1 after 40 minutes of exposure to UV-light. Conversely, it is only after 48 hours aging in ambient light conditions that the intensity of the lower energy transitions reach a similar 2:1 ratio with the π - π^* transition at 365 nm.

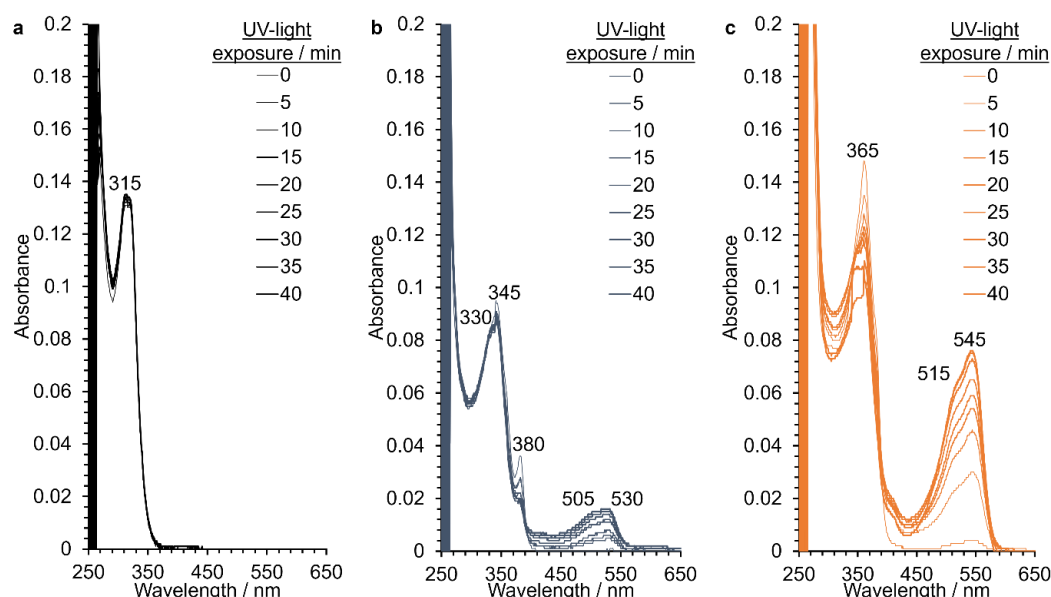


Figure 4.10 UV-vis spectra of (a) **6H**, (b) **3Br** and (c) **6Br** (10 μ M in DMF) after exposure to UV-light in 5-minute periods.

With the understanding of the conditions required for the colour-change and growth of lower-energy electronic transitions improved, the cause of the phenomena were investigated. It was hypothesised that the changes were as a result of a PET or charge-transfer process from the electron-rich *N,N*-dimethylformamide molecules which can interact with the electron-deficient π -surface of the core-brominated molecular triangles or an influence of the high polarity of the DMF solvent as discussed by Saha and coworkers.^{22,23} Crystals of **6Br** in DMF were attempted to be grown to provide potential evidence of a charge-transfer interaction between the electron-deficient and electron-rich components although proved to be unsuccessful. Instead, the photoactive behaviour of **6Br** in DMF was compared to that of NDI and PDI compounds. Interestingly, the absorption spectrum of **6Br** after exposure to UV-light for 40 minutes (Figure 4.10c), is similar to those of Br-NDI-OH **23**¹⁸ and Br-PDI-OH **25**¹⁹ after reacting with TBAF or irradiation with UV-light respectively as discussed in Section 4.1 (Figure 4.11). Br₂NDI **22** shows two absorption peaks (500–600 nm) in the presence of the reducing agent in THF whilst two new peaks (700–800 nm) evolve in the spectrum of Br₂PDI **24** after irradiation with UV-light which was attributed to the formation of Br-NDI-OH **23** and Br-PDI-OH **25** respectively. Therefore, it was hypothesised that the photochemical transformation of **6Br** in DMF could be as a result of a -Br to -OH functional group transformation to form **3(OH)3Br**.

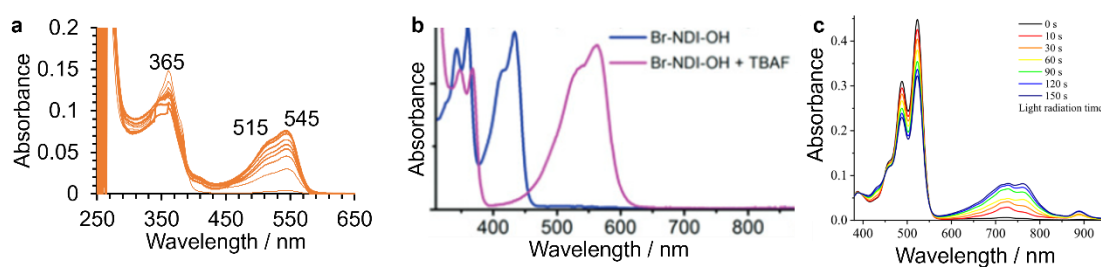
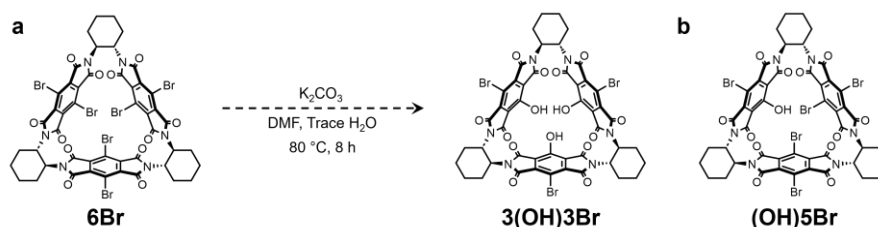


Figure 4.11 Comparison of absorption spectra of (a) **6Br** in DMF after irradiation with UV-light (0–40 min), (b) Br-NDI-OH **23** formed from reacting Br₂NDI **22** with TBAF in THF¹⁸ and (c) Br-PDI-OH **25** after irradiation of Br₂PDI **24** with UV-light in NMP.¹⁹ Figure reproduced from References 18 and 19 respectively.^{18,19}

To investigate whether the photochemical transformation that occurs when **6Br** in DMF is irradiated with UV-light is indeed a -Br to -OH conversion, a conventional synthesis of **3(OH)3Br** was attempted. The conditions for the conventional synthesis of Br-PDI-OH **25** from Br₂PDI **24** as shown by Dong *et al.*²⁰ (Scheme 4.3) were replicated by heating **6Br** with K₂CO₃ in DMF with trace H₂O at 80 °C overnight (Scheme 4.4a). Upon evaporation of the reaction solvent, the crude solid was purified by automated flash chromatography (EtOAc 0–100% in n-hexane), washing with MeOH and HCl (1 M) to isolate a red solid. Characterisation of the red solid by ¹H NMR spectroscopy (Figure 4.12) showed a proton environment at 5.14 ppm which is indicative of a molecular triangle, in particular the cyclohexane proton adjacent to the diimide although full product identification by NMR spectroscopy was not possible. However, analysis by HR-MS revealed the presence of the mass of a core-functionalised molecular triangle with one hydroxy group and five bromine atoms (**(OH)5Br**) (HR-MS: [M + H]⁺, expected = 1294.7939, found = 1294.7292). However, the isolated red solid which contained the compound (**(OH)5Br**) remained impure by thin-layer chromatography (TLC).



Scheme 4.4 (a) Expected synthesis of tris-hydroxy **3(OH)3Br** and (b) structure of mono-hydroxy-penta-bromo (**(OH)5Br**), the mass of which was identified by HR-MS following the reaction.

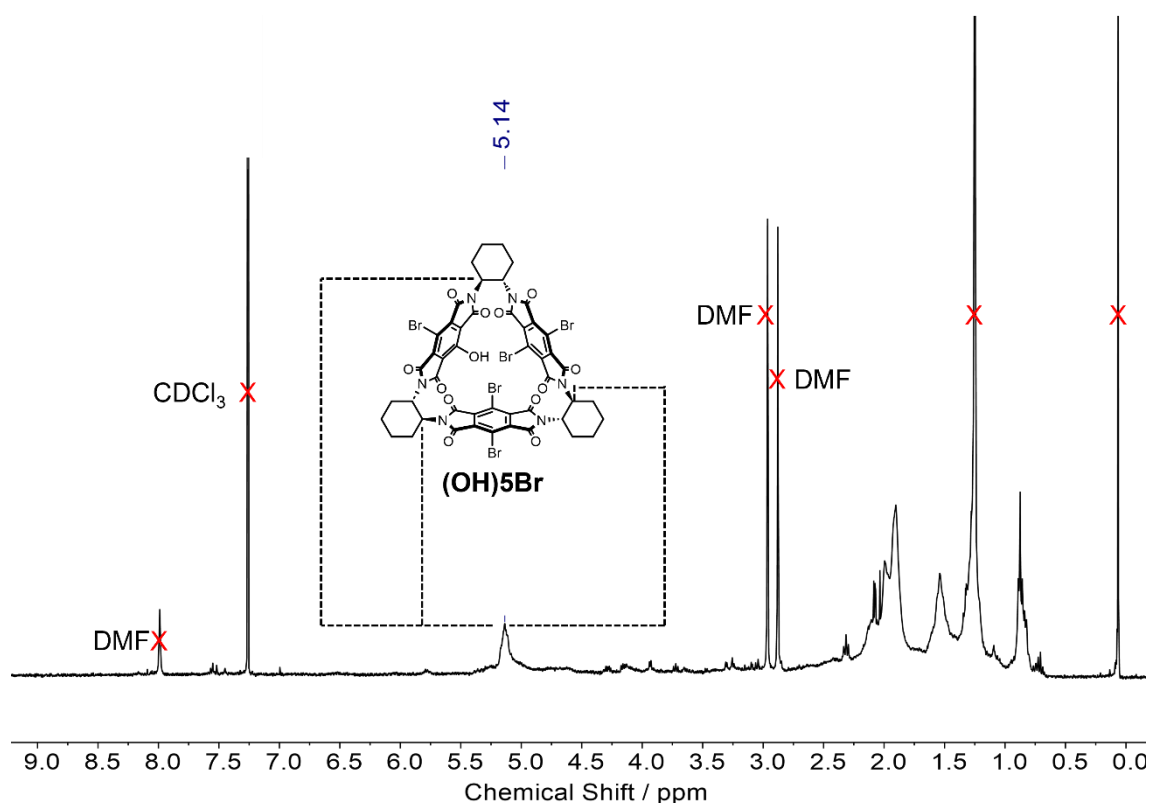


Figure 4.12 ¹H NMR (400 MHz, CDCl₃, 298 K) spectrum of red solid containing impure (**(OH)5Br**).

Although the isolated solid containing **(OH)5Br** was impure, the absorption and emission spectra of the sample were measured and compared with **6Br** in DMF after irradiation with UV-light. These experiments were completed despite the impurities to assess a proof-of-concept for the emissive properties of a core-hydroxylated molecular triangle. Furthermore, the reaction of **6Br** with water for the bromine to hydroxy transformation (Scheme 4.4.a) was completed in DMF solvent, with no measures taken to shield the reaction mixture from light. Therefore, it could be that the resulting identification of **(OH)5Br** *via* HR-MS is as a result of the exposure of **6Br** to light during the overnight reaction. Nonetheless, if **(OH)5Br** was generated from a photochemical reaction the absorption and emission spectra are still interesting to study for potential ESIPT properties. Previously, the isolation and identification of a core-hydroxylated molecular triangle or other macrocyclic species by HR-MS and ^1H NMR spectroscopy directly after irradiation of **6Br** in DMF with UV-light by HR-MS had been attempted, all-be-it unsuccessfully.

Solutions of impure **(OH)5Br** (around 0.3 mg mL^{-1}) were prepared and diluted five-fold and ten-fold in CH_2Cl_2 and DMF respectively and studied by UV-vis spectroscopy (Figure 4.13). In the UV-vis spectra in Figure 4.13, characteristic $\pi\text{-}\pi^*$ transitions between 300–400 nm for ADIs are observed in addition to longer wavelength peaks between 450–550 nm. The observed lower energy transitions are similar to that observed for the hydroxy NDI (**23**) and PDI (**25**) compounds reported in the literature and discussed above (Figure 4.11) and most significantly are in the same region as the absorption peaks that develop upon irradiation of **6Br** in DMF with UV-light.

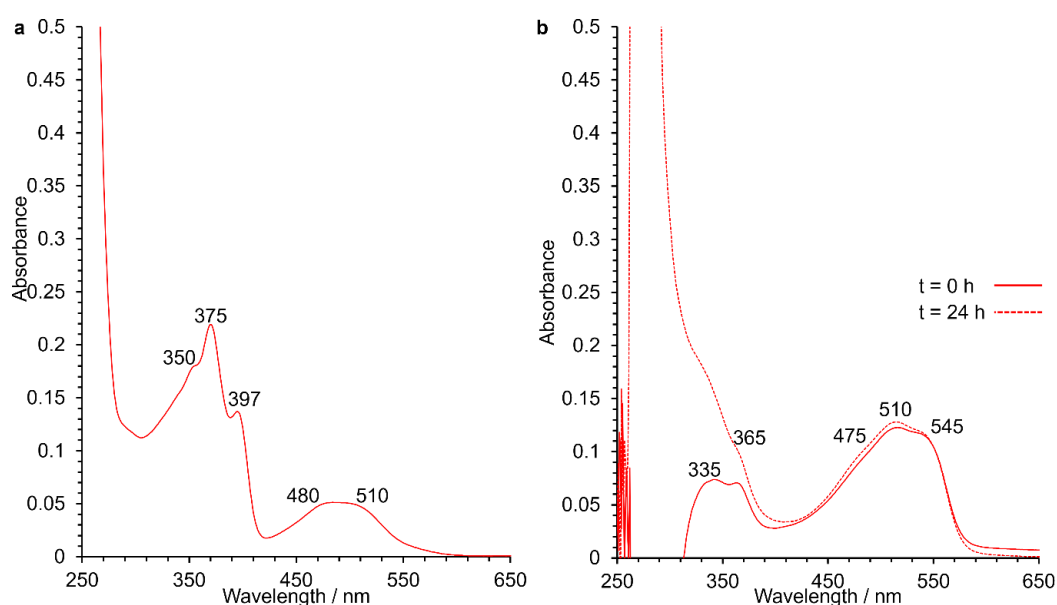


Figure 4.13 UV-vis spectra of impure **(OH)5Br** in (a) CH_2Cl_2 (*c.a.* 0.06 mg mL^{-1}) and (b) DMF (*c.a.* 0.03 mg mL^{-1}) at time, $t = 0$ and 24 h.

If indeed the phenomenon that occurs in **6Br** in DMF upon exposure to UV-light is a bromine to hydroxy group transformation, the resulting core-hydroxylated compound would be expected to be emissive and ESIPT active as discussed in the introduction and shown by Ando and coworkers.^{10,11} Therefore, the

fluorescent properties of **6Br** (before and after exposure to UV-light) and the impure **(OH)5Br** (visibly fluorescent under 366 nm UV light) were investigated. Initially, the emission and excitation spectra of **6Br** and impure **(OH)5Br** in CH_2Cl_2 were studied. The emission profile for the sample of impure **(OH)5Br** in CH_2Cl_2 is different to **6Br** with peaks red shifted for the hydroxy-substituted compound. Upon exciting the $\pi\text{-}\pi^*$ transition of **6Br** at 380 nm, emission peaks at 435 and 465 nm were observed (Figure 4.14a). Conversely, after exciting impure **(OH)5Br** at 410 nm (representing the $\pi\text{-}\pi^*$ transition) (Figure 4.14b), three emission peaks at 510, 560 and 610 nm are revealed. The different wavelengths of emission between **6Br** and impure **(OH)5Br** in CH_2Cl_2 indicates that a new emissive species was formed in the reaction of **6Br** with H_2O and K_2CO_3 in DMF at 80 °C. In addition, exciting the sample at 530 nm ($\lambda_{\text{Abs}} = 510 \text{ nm}$) yields a single broad and featureless emission band at 560 nm. The resulting excitation spectrum of the emission at 560 nm reveals peaks that match the analogous absorption profile at 375, 400 and 510 nm. Furthermore, the intensity of the emission from exciting impure **(OH)5Br** at 530 nm is at-least 3-fold greater than exciting the same sample at 410 nm and of **6Br** in CH_2Cl_2 .

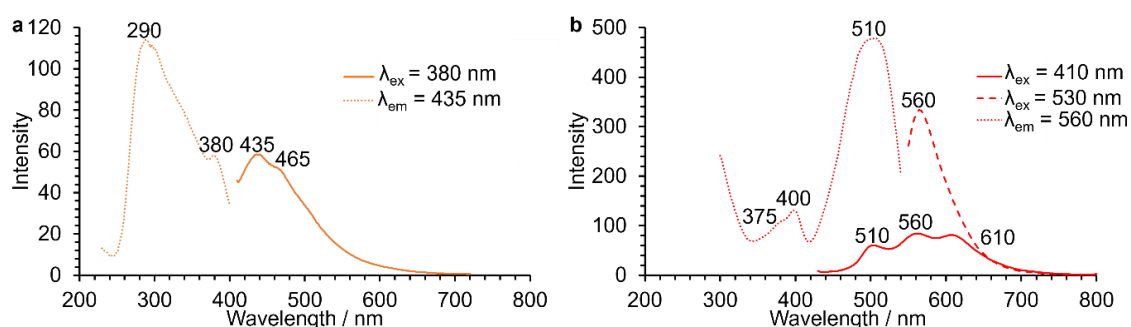


Figure 4.14 Emission and excitation spectra of (a) **6Br** (50 μM) and (b) impure **(OH)5Br** (c.a. 0.06 mg mL^{-1}) in CH_2Cl_2 .

Furthermore, the emission and excitation spectra of **6Br** in DMF were measured, before and after aging with UV-light (Figure 4.15) to investigate whether the photochemical transformation yields a fluorescent species which could be a core-hydroxylated molecular triangle. In the emission spectrum for **6Br** in DMF at $t = 0 \text{ h}$ (Figure 4.15a), a single emission at 435 or 570 nm is observed when the macrocycle is excited at 380 or 500 nm respectively. Subsequently, after 30 minutes irradiation with UV-light (Figure 4.15b), the same emission peaks remain, however, when the sample is excited at 380 nm, a second emission at 570 nm also occurs. The emission at 570 nm (after being excited at 500 nm) increases in intensity 2-fold after irradiation with UV-light which is likely as a result of greater absorption at 500 nm after aging **6Br** in DMF. The increased emission after aging with UV-light indicates that the photochemical transformation does indeed produce a more emissive species which could be as a result of the presence of a core-hydroxylated molecular triangle.

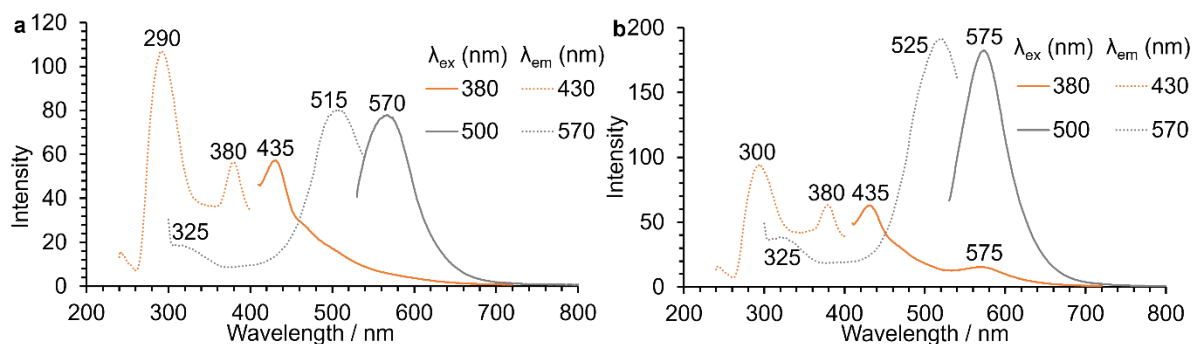


Figure 4.15 Emission and excitation spectra of **6Br** (50 μM) in DMF, (a) at $t = 0$ h and (b) after 30 mins irradiation with UV-light.

No change in emission profile is observed for a solution of impure **(OH)5Br** in DMF before and after aging for 24 hours in ambient light (Figure 4.16a and b). The intensity of the emission of the sample before and after aging in ambient light for 24 hours stay the same, with the emission at 575 nm ($\lambda_{\text{ex}} = 500$ nm) more intense than for **6Br** in DMF after irradiation with UV-light ($\lambda_{\text{ex}} = 500$ nm). The emission profile of the impure sample of **(OH)5Br** is similar to **6Br** in DMF after irradiation with UV-light, where upon exciting the sample at 380 nm, two high intensity emission peaks at 420 and 440 nm are observed with a shoulder at 580 nm. Furthermore, when the lower energy transition at 500 nm for impure **(OH)5Br** is excited, a single, lower energy emission at 580 nm occurs. The similar wavelength of emission of impure **(OH)5Br** and **6Br** after irradiation with UV-light could mean that the luminophores responsible are the same species, *i.e.* a core-hydroxylated molecular triangle such as **(OH)5Br**.

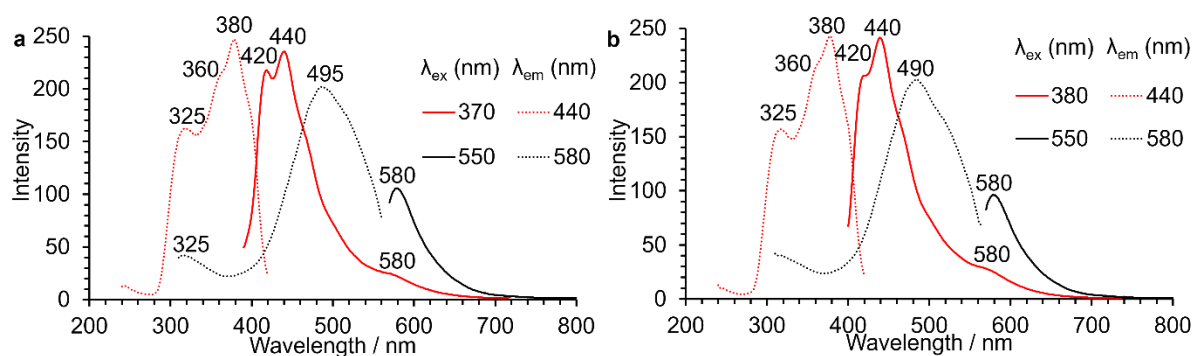


Figure 4.16 Emission and excitation spectra of impure **(OH)5Br** (around 0.06 mg mL^{-1}) in DMF, (a) at $t = 0$ h and (b) after 24 h aging in visible light.

These results of increased intensity of emission of **6Br** after irradiation with UV-light and similar behaviour to impure **(OH)5Br** shows that the photochemical transformation could provide a useful method for synthesising core-hydroxylated molecular triangles. Although further studies to confirm the identity of the emissive compound are required *e.g.* NMR spectroscopy and growing single crystals for structure determination. The isolation of a pure core-hydroxylated molecular triangle is required to confirm the hypothesis. Furthermore, the emission peaks at 570 and 580 nm for **6Br** and impure **(OH)5Br** are in a similar region to mono-hydroxy PMDI **2** (592 nm),¹¹ di-hydroxy PMDI **3** (641

nm)¹⁰ and Br-PDI-OH **26** (around 575 nm)²⁰ which shows that the photoactivity of core-brominated ADIs are similar.

4.2.2 ROOM-TEMPERATURE PHOSPHORESCENCE OF BROMINATED MOLECULAR TRIANGLES

In Section 4.2.1 the sample of **(OH)5Br** exhibited increased emission compared to **6Br** in CH₂Cl₂ and DMF. Subsequently, the solution-state emission of **6H**, **3Br** and **6Br** in degassed THF (Figure 4.17a–c) and degassed CHCl₃, (Figure 4.17d–f) was measured. The normalised emission spectra of **6H** in THF and CHCl₃ (Figure 4.17a and d) show single intense emission peaks at 370 nm and 400 & 415 nm when excited at the wavelength of the π - π^* absorption ($\lambda_{\text{ex}} = 330$ nm). In the emission spectrum of **3Br** in THF, a single sharp emission peak at 390 nm is observed ($\lambda_{\text{ex}} = 350$ nm) with the presence of additional emission peaks at 415, 470 and 520 nm observed in CHCl₃ (Figure 4.17e). The emissive behaviour of **6Br** in CHCl₃ (Figure 4.17f) exhibits four well-defined emission peaks at 415, 440, 470 and 500 nm ($\lambda_{\text{ex}} = 375$ nm) with the intensity decreasing towards longer wavelengths. Similar behaviour is observed in THF (Figure 4.17c) with emission peaks at 430, 470 and 500 nm ($\lambda_{\text{ex}} = 375$ nm) although the intensity of emission is greater at the latter peaks. The larger Stokes shift of emission in **6Br** could indicate room-temperature phosphorescence (RTP) in accordance with the Jablonski diagram (Figure 4.1). Relaxation from the T₁ excited state can occur after intersystem crossing (ISC) from the S₁ state which occurs at longer wavelengths (smaller energy gap) and with a longer lifetime (spin forbidden process, $\Delta S \neq 0$). Similar longer wavelength RTP emission was also observed for compounds containing Br₂PMDI units by George and coworkers in the solid state.^{8,12}

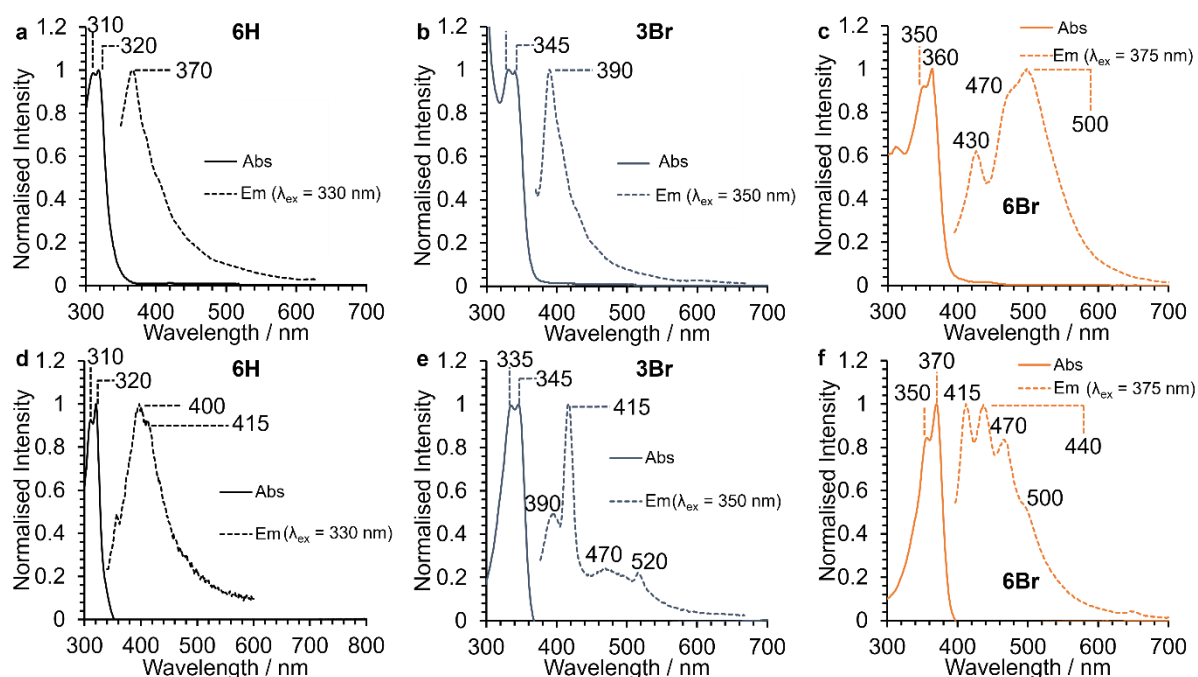


Figure 4.17 UV-vis absorption and emission spectra of (a) **6H**, (b) **3Br** and (c) **6Br** in THF (25 μ M) and (d) **6H**, (e) **3Br** and (f) **6Br** in CHCl₃ (10 μ M).

To investigate the potential RTP emission of **6Br**, the solution and solid-state emission of core-brominated molecular triangles was studied in collaboration with Dr Andrew Danos and Professor Andy Monkman at Durham University. The vibrational and rotational motion of the macrocycles was reduced so that the non-radiative decay would be decreased and thus luminescent relaxation would be enhanced. Such effect was achieved by comparing emission wavelengths and lifetimes in the solution state (50 μM , CHCl_3) to thin films (drop-casted 1 wt% solutions of macrocycle in a PMMA matrix) at room temperature and then when the films were cooled to 80 K.

Two-dimensional contour plots were used to show the intensity of emission at different wavelengths (350–650 nm) across different time scales (0.1 ns to 0.1 s) for molecular triangles (**6H**, **3Br** and **6Br**) in solution (50 μM , CHCl_3) at rt and in thin films (1 wt% in PMMA) at rt and 80 K. When the emission of the sample cannot be distinguished from the integrated baseline signal, the contour plot is unreadable with the data for these regions being disregarded. These contour plots were then extracted vertically across different emission wavelengths at different time points to show the wavelength of the emission peaks. Alternatively, the contour plot could be extracted horizontally to show how the emission intensity integrated at all wavelengths changes over time which provides an insight into the type of luminescence (fluorescence or phosphorescence) that is occurring.

The contour plot for **6H** (Figure 4.18a) in solution at rt only shows emission at short lifetimes (10^{-10} to 10^{-8} s) which is indicative of fluorescent emission from the S_1 excited state. The relevant wavelength vs intensity graph (Figure 4.18.d) shows emission peaks at 433 and 465 nm. When **6H** is incorporated into a thin film (1% in PMMA) emission is red-shifted compared with in solution and is observed at longer timescales (10^{-8} s) at rt and 80 K (Figure 4.18.b and c). At rt, the emission of **6H** (1 wt% in PMMA) occurs at 471 nm and 487 nm at 8.00×10^{-10} s and 5.01×10^{-2} s respectively (Figure 4.18.e) and at 80 K at 8.00×10^{-10} s and 1.00×10^{-1} s the emission peaks are at 473 and 493 nm (Figure 4.18f). Although, the contour plots for **6H** show that the emission continues in the thin films at longer times (10^{-2} s), the lifetime graphs for **6H** (Figure 4.18g–i) show a single prompt fluorescence at short lifetimes (10^{-9} to 10^{-7} s) only in solution (rt) and in drop-casted polymer matrix thin films (rt and 80 K). The absence of longer lifetime phosphorescent emission in **6H** is unsurprising as there are no core-substituted bromine atoms on the molecular triangle to enhance ISC from the S_1 to the T_1 excited state and subsequent spin-forbidden, T_1 to S_0 relaxation.

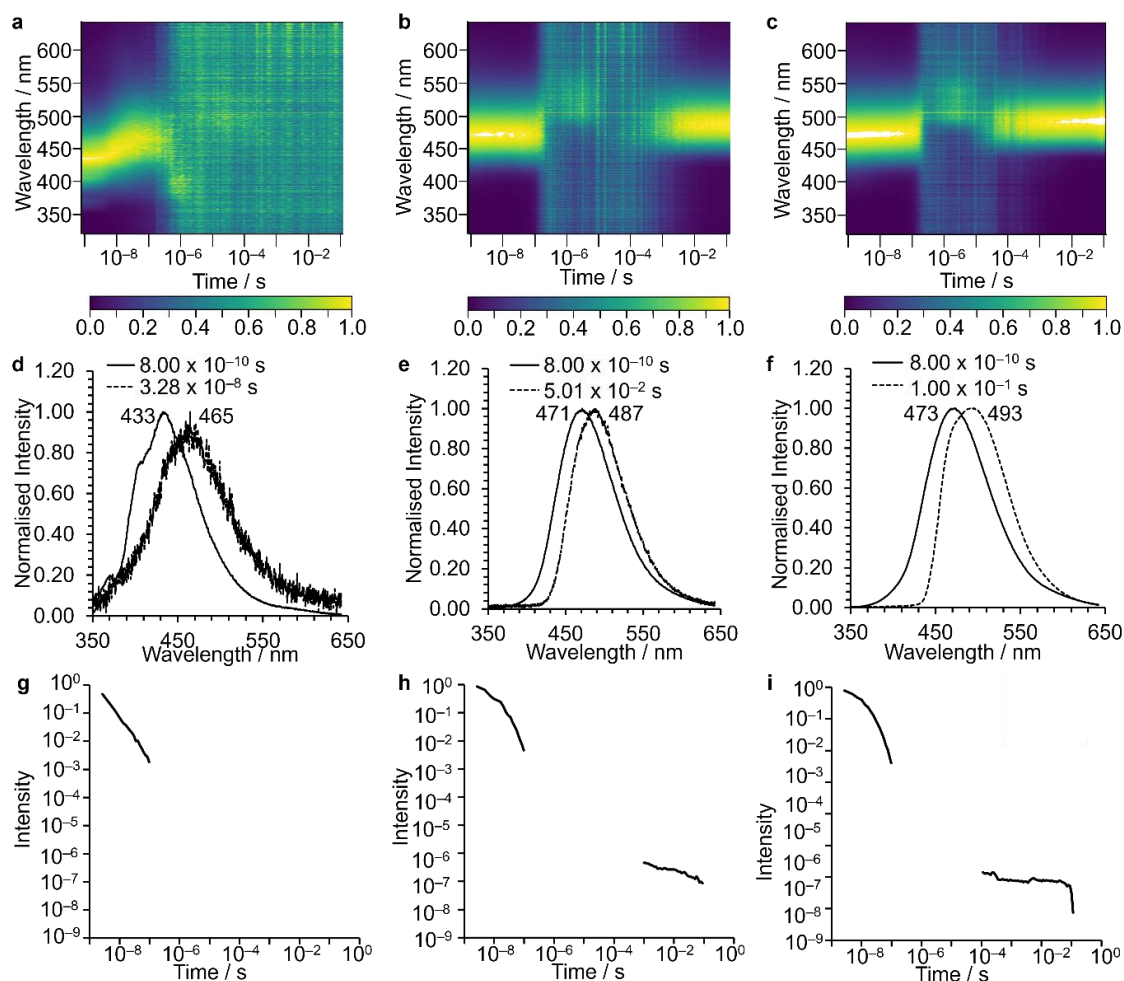


Figure 4.18 Emission ($\lambda_{\text{ex}} = 355$ nm) contour plots of **6H** in (a) solution (50 μM , CHCl_3) at rt and drop-casted films (1% in PMMA) at (b) rt and (c) 80 K. Intensity vs wavelength graphs at certain time points extracted from contour plots for **6H** in (d) solution (50 μM , CHCl_3) and drop-casted films (1% in PMMA) at (e) rt and (f) 80 K. Emission lifetime decay profiles from integrating emission from all wavelengths from 10^{-9} to 10^{-1} s for **6H** in (g) solution (50 μM) and drop-casted films (1% in PMMA) at (h) rt and (i) 80 K.

Upon the addition of three bromine atoms to the aromatic core of the PMDI based molecular triangle in **3Br**, the emissive behaviour (Figure 4.19) changes compared with **6H**. The emission peaks for **3Br** are red-shifted with respect to **6H**, although there is not any significant difference in the wavelength of emission between solution (50 μM , CHCl_3) at rt and in drop-casted thin films (1 wt% in PMMA) at rt and 80 K (Figure 4.19d–e). For the solution of **3Br** (50 μM , CHCl_3) at rt, the emission of **3Br** occurs at 478 and 483 nm at 8.00×10^{-10} s and 3.28×10^{-8} s respectively. Similarly, the drop-casted thin film of **3Br** (1 wt% in PMMA) at rt emits at 473 nm (8.00×10^{-10} s) and 480 nm (5.01×10^{-2} s) with no significant change at 80 K, 474 nm (8.00×10^{-10} s) and 492 nm (1.00×10^{-2} s). In the solid state, the emission continues to longer time frames (10^{-2} s) which was confirmed in the lifetime graphs (Figure 4.19g–i). For **3Br** in solution at rt (Figure 4.19g) a single emissive process at short timescales is observed representing relaxation to the ground state *via* prompt fluorescence. Whereas in 1 wt% PMMA thin films of **3Br** at rt and 80 K, two emissive processes are observed, an initial prompt fluorescence at 10^{-9} s followed by a second relaxation at longer timescales (10^{-5} to 10^{-2} s). This second emission at

longer timescales in the solid state represents spin-forbidden phosphorescence and is maintained for an increased duration at 80 K compared with at rt.

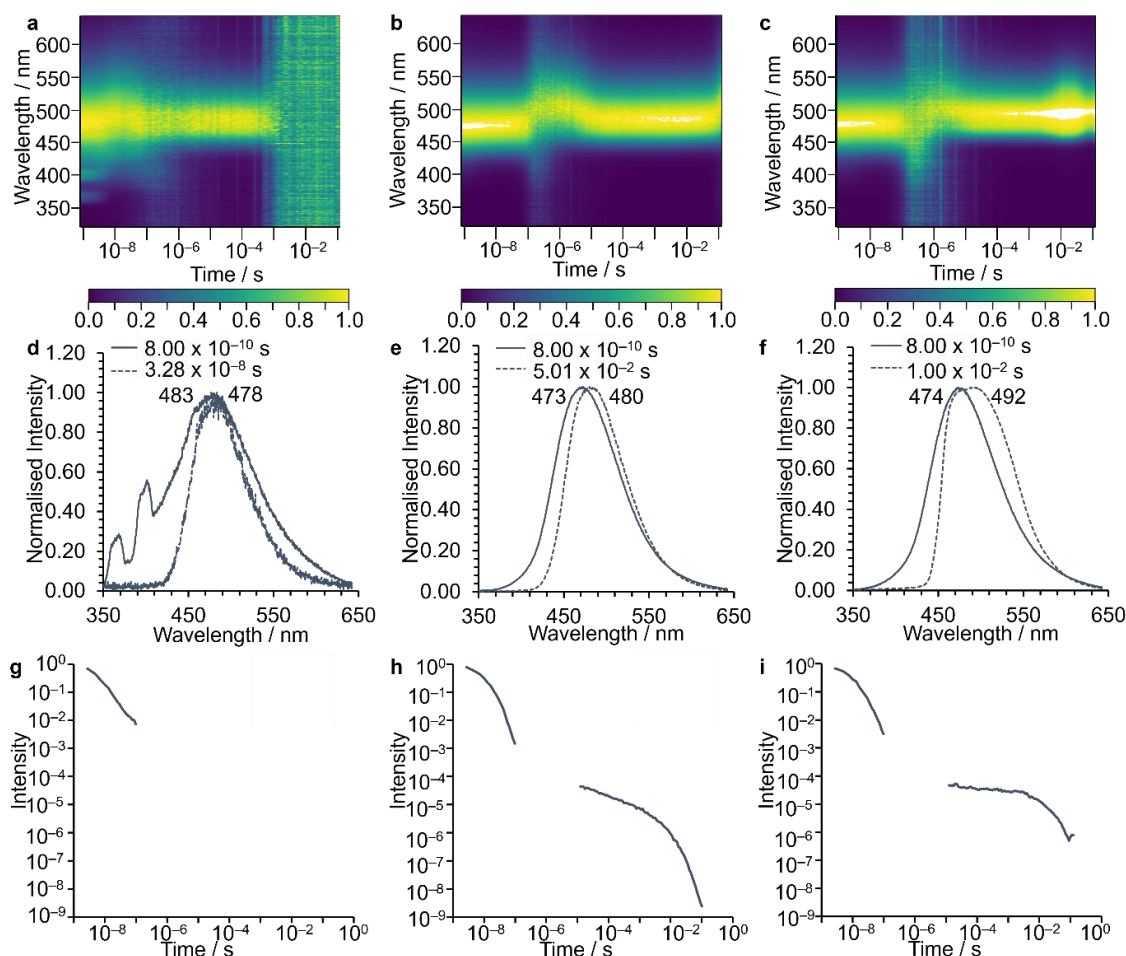


Figure 4.19 Emission ($\lambda_{\text{ex}} = 355$ nm) contour plots of **3Br** in (a) solution (50 μM , CHCl_3) at rt and drop-casted films (1% in PMMA) at (b) rt and (c) 80 K. Intensity vs wavelength graphs at certain time points extracted from contour plots for **3Br** in (d) solution (50 μM , CHCl_3) and drop-casted films (1% in PMMA) at (e) rt and (f) 80 K. Emission lifetime decay profiles from integrating emission from all wavelengths from 10^{-9} to 10^{-1} s for **3Br** in (g) solution (50 μM) and drop-casted films (1% in PMMA) at (h) rt and (i) 80 K.

The contour plots for **6Br** (Figure 4.20a–c) in solution (50 μM , CHCl_3) at rt and in the solid state in 1 wt% PMMA thin films at rt and 80 K show two emission bands from 0.1 ns to 0.1 s. The emission wavelengths are red-shifted upon decreasing motion of the molecules from the solution to solid state with peaks at 431 nm (8.00×10^{-10} s) and 470 nm (1.11×10^{-6} s) for **6Br** in CHCl_3 (50 μM) at rt (Figure 4.20d). Although the emission for **6Br** in 1 wt% PMMA thin films are similar upon cooling with peaks at 471 nm (8.00×10^{-10} s and 1.00×10^{-3} s) and 491 nm (2.996×10^{-8} s) at rt (Figure 4.20e) and 471 nm (8.00×10^{-10} s) and 498 nm (7.08×10^{-3} s) at 80 K (Figure 4.20f). The lifetime graphs for **6Br** in the solution (rt) and solid state (rt and 80K) (Figure 4.20g–i) shows two emissive processes. For **6Br** in solution (50 μM , CHCl_3) (Figure 4.20g), the first emission process occurs at short timescales (10^{-9} to 10^{-8} s) with the second emission taking place between 10^{-7} to 10^{-5} s. In the solid state (1 wt% **6Br** in PMMA) at rt and 80 K (Figure 4.20h and i), the first emissive process also occurs at short timescales (10^{-9} to 10^{-7} s) as a result of prompt fluorescence and the second emission at longer timescales (10^{-6} to

10^{-2} s) compared to the solution state occurring as a result of spin-forbidden phosphorescence. The presence of two emission processes in the solution state for **6Br**, albeit at shorter timescales than in the solid state, could represent the increased ability for ISC and phosphorescence to occur when the vibrational and rotational motion of the phosphors is restricted within the shape-persistent, rigid molecular triangle.

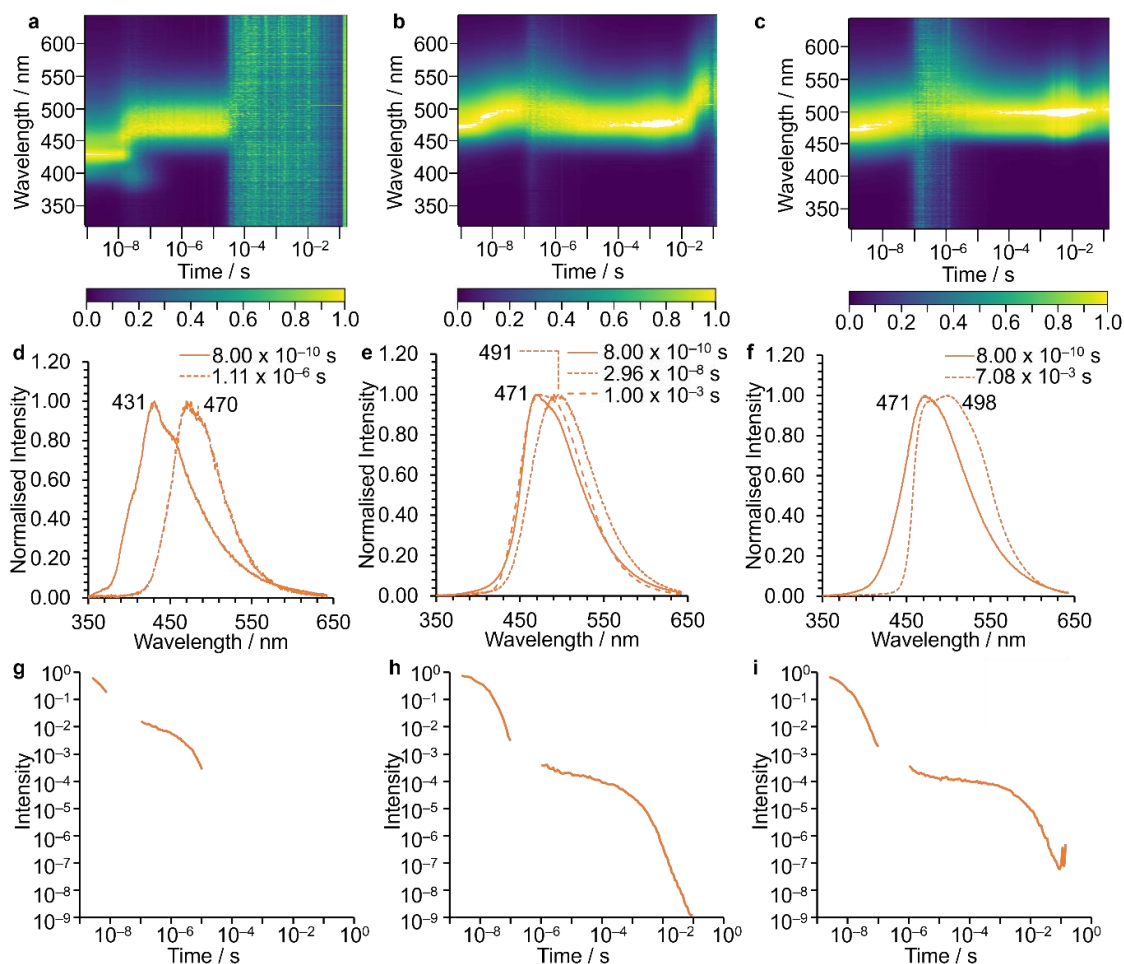


Figure 4.20 Emission ($\lambda_{\text{ex}} = 355$ nm) contour plots of **6Br** in (a) solution (50 μM , CHCl_3) at rt and drop-casted films (1% in PMMA) at (b) rt and (c) 80 K. Intensity vs wavelength graphs at certain time points extracted from contour plots for **6Br** in (d) solution (50 μM , CHCl_3) and drop-casted films (1% in PMMA) at (e) rt and (f) 80 K. Emission lifetime decay profiles from integrating emission from all wavelengths from 10^{-9} to 10^{-1} s for **6Br** in (g) solution (50 μM) and drop-casted films (1% in PMMA) at (h) rt and (i) 80 K.

Molecular triangles are weakly emissive in CHCl_3 solution such that reliable photoluminescent quantum yields (PLQY) could not be measured whether under air or nitrogen. On the other hand, PLQYs (albeit still weak) could be established from thin films of **6H**, **3Br** and **6Br** under nitrogen and air (Table 4.3). As phosphorescent emission is quenched by O_2 molecules, quantum yield measurements were completed under nitrogen to maximise the long lifetime relaxation. The PLQY measurements were then repeated in air to allow for the phosphorescent emission to be quenched with the resulting difference in PLQY values in nitrogen and air representing the contribution to emission from phosphorescence only. The measured quantum yields are all low and within experimental error (around 5%) which meant that

the phosphorescent quantum yield could not be determined reliably. Despite this, there is a trend for increasing quantum yield (in both air and nitrogen) as the number of core-substituted bromine atoms increased from **3Br** to **6Br**.

Table 4.3 Emission quantum yields (ϕ) in nitrogen and air for **6H**, **3Br** and **6Br** (1 wt% in PMMA), $\lambda_{\text{ex}} = 330$ nm.

ϕ %	6H	3Br	6Br
Nitrogen	1.7	1.5	2.2
Air	0.7	1.5	1.8

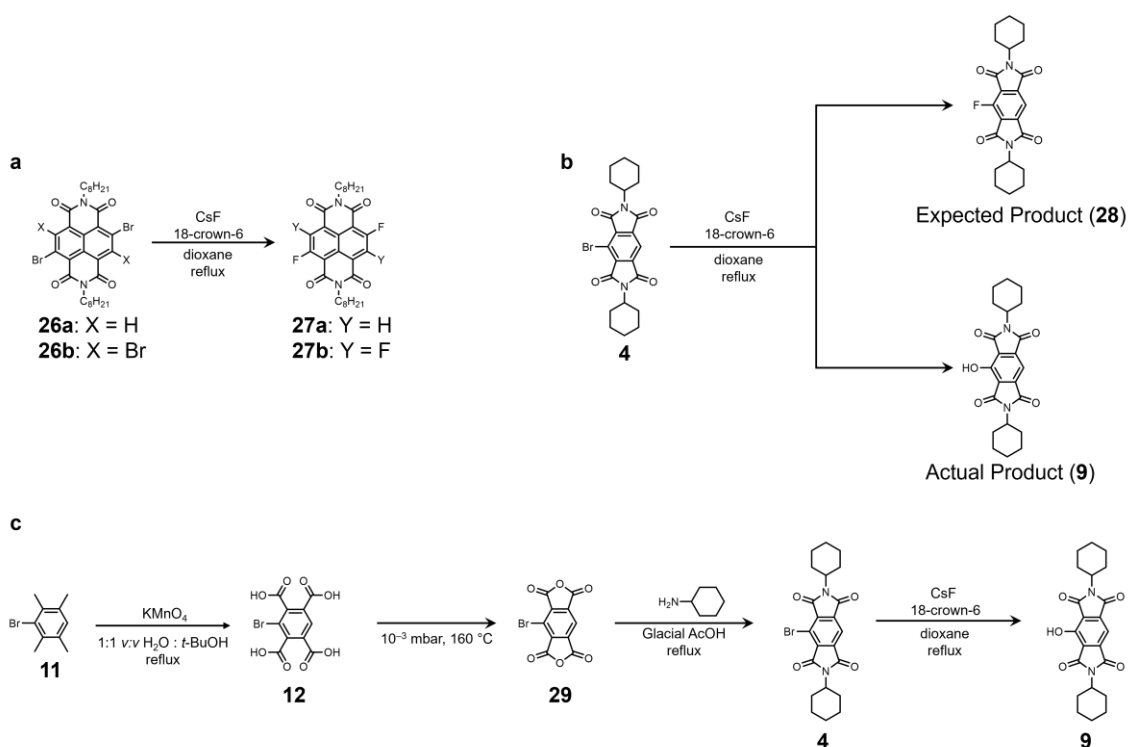
The results discussed in this Section show that the core-substitution of the PMDI based molecular triangle with three (**3Br**) or six (**6Br**) bromine atoms does affect the luminescence of the macrocycles. In particular, in the solid state (1 wt% in PMMA), long-lived emission is observed at longer wavelengths for **3Br** and **6Br** compared with **6H** which indicates that the presence of the heavy halogen atoms does enhance ISC from S_1 to T_1 excited states and thus enhance phosphorescence. Unfortunately, the molecular triangles were weakly emissive in solution and solid states which led to very low PLQY values for **6H**, **3Br** and **6Br**.

4.2.3. TOWARDS THE SYNTHESIS OF EMISSIVE CORE-HYDROXYLATED MOLECULAR TRIANGLES

As part of the general aims within this Thesis to synthesise new core-functionalised molecular triangles and study their structural and optoelectronic properties, a post-synthetic functionalisation reaction to install fluorine atoms onto the PMDI core was investigated. Yuan *et al.*²⁴ had previously shown that core-brominated NDIs **26a** and **26b** could be transformed to their fluorinated analogues (**27a** and **27b**) by refluxing in anhydrous dioxane with CsF and 18-crown-6 in a catalytic quantity (Scheme 4.5a). These reaction conditions were initially applied to a mono-brominated PMDI model compound (**4**) to assess the applicability of the transformation towards core-fluorinated molecular triangles (Scheme 4.5b). Upon aqueous work up of the reaction mixture from the reaction of compound **4** with CsF and 18-crown-6 in anhydrous dioxane, an orange solid was isolated which was fluorescent in solution. Characterisation of the product by ^1H NMR spectroscopy (Figure 4.21) and mass spectrometry did not reveal the desired fluorinated compound **28**, showing instead the formation of mono-hydroxylated PMDI **9**, through comparison with the literature characterisation.¹¹

The serendipitous discovery of a bromine to hydroxy transformation on a PMDI core is attractive due the position of the -OH group adjacent to two diimide carbonyls, allowing for ESIPT to occur *via* a keto-enol tautomerisation with subsequent relaxation to the ground state *via* fluorescent emission. The post-synthetic functionalisation from core-brominated to core-hydroxylated PMDI compounds using caesium fluoride is attractive due to its simplicity after imide formation and potential applicability to a

wide scope of brominated ADIs including core-brominated molecular triangles **3Br** and **6Br**. The overall synthetic scheme for the preparation of mono-hydroxy **9** via the CsF mediated reaction (Scheme 4.5c) is not too dissimilar to the previous literature protocol discussed in Section 4.1 (Scheme 4.1a),¹¹ with the major difference being the step at which the -Br to -OH functional group transformation occurs. The hydroxylation method used by Kanosue *et al.*,¹¹ (NaOAc, Cu and NaOH (aq)) for compound **9** is required to occur prior to imide formation to prevent the potential hydrolysis of the diimide in the presence of hydroxide ions. It was envisioned that a general protocol for the core-hydroxylation of a wide range of brominated PMDI compounds without the potential risk of imide hydrolysis would be attractive. Such a functional group transformation could be used to synthesise core-hydroxylated molecular triangles to study the synergistic effect of cyclic aromatic homoconjugation with emission of the ESIPT active chromophores.



Scheme 4.5 (a) Literature conditions for halide metathesis exchange of bromine atoms with fluorine atoms on an NDI aromatic core.²⁴ (b) Applying the literature halide metathesis exchange conditions to a brominated PMDI compound **4** showing the expected fluorinated product (**28**) and the actual isolated hydroxylated product (**9**). (c) Proposed synthesis of hydroxy **9** via a CsF mediated -Br to -OH transformation.

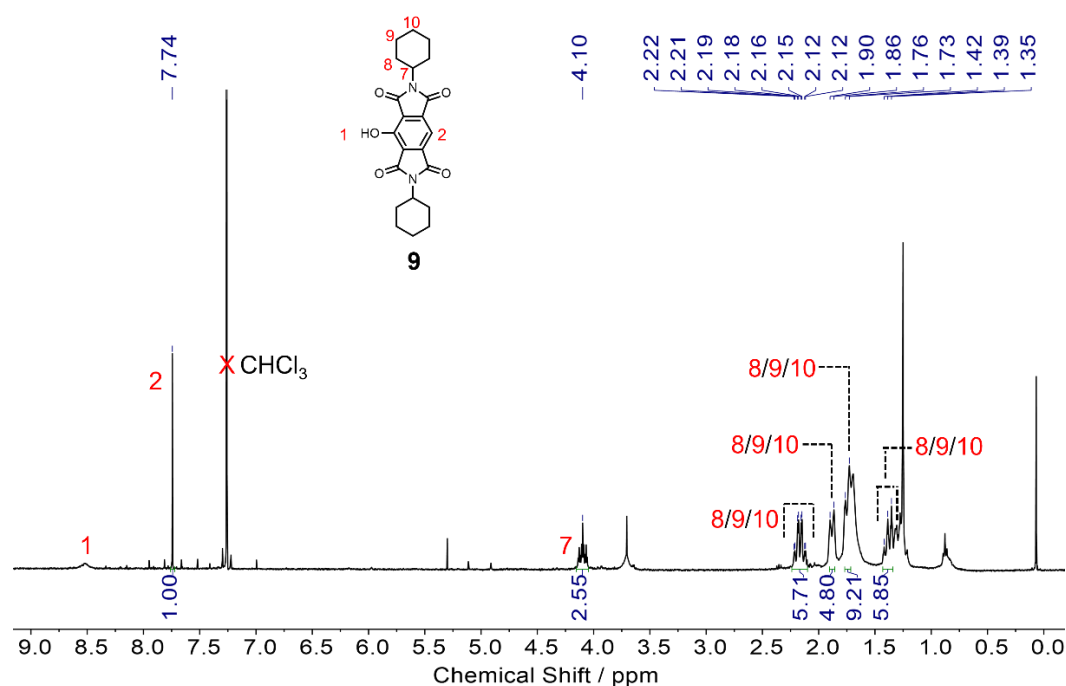


Figure 4.21 ^1H NMR (400 MHz, CDCl_3 , 298 K) spectrum of hydroxy **9** isolated from the reaction shown in Scheme 4.5b.

The reaction conditions using the conversion of mono-brominated PMDI model compound **4** to mono-hydroxy **9** were optimised to improve the understanding of the transformation before attempting the post-synthetic hydroxylation of **3Br** or **6Br** using CsF. The reaction of brominated **4** with CsF was initially attempted two times (Entries 1 and 2, Table 4.4) with different proportions of starting material (SM) and product **9** (P) in the crude ^1H NMR spectra (Figure 4.22). The % proportions of bromo **4** and hydroxy **9** were calculated by integrating the peaks at 8.15 ppm (SM) and 7.74 ppm (P) respectively in the ^1H NMR spectrum and dividing by the total integration of peaks between 7.60–8.40 ppm. Additional proton environments in the aromatic region (7.60–8.40 ppm) were observed and integrated as potential side products of the reaction. Upon diluting the concentration of the limiting reagent (**4**) in dioxane by a factor of six (Entry 3, Table 4.4), full consumption of the starting material was observed with a proportion of 81% of hydroxylated **9** subsequently observed in the ^1H NMR spectrum of the crude product (Figure 4.22).

Table 4.4 Reaction conditions for the conversion of mono-brominated **4** to mono-hydroxy **9** with % proportions of SM and P from ^1H NMR spectra (Figure 4.22).

Entry	9 / Equiv.	CsF / Equiv.	18-crown-6 / Equiv.	Concentration of 4 in dioxane / M	% Proportion of 4 (SM)	% Proportion of 9 (P)
1	1.0	15.07	0.14	0.150	28	64
2	1.0	15.25	0.06	0.150	81	16
3	1.0	14.99	0.06	0.024	0	81

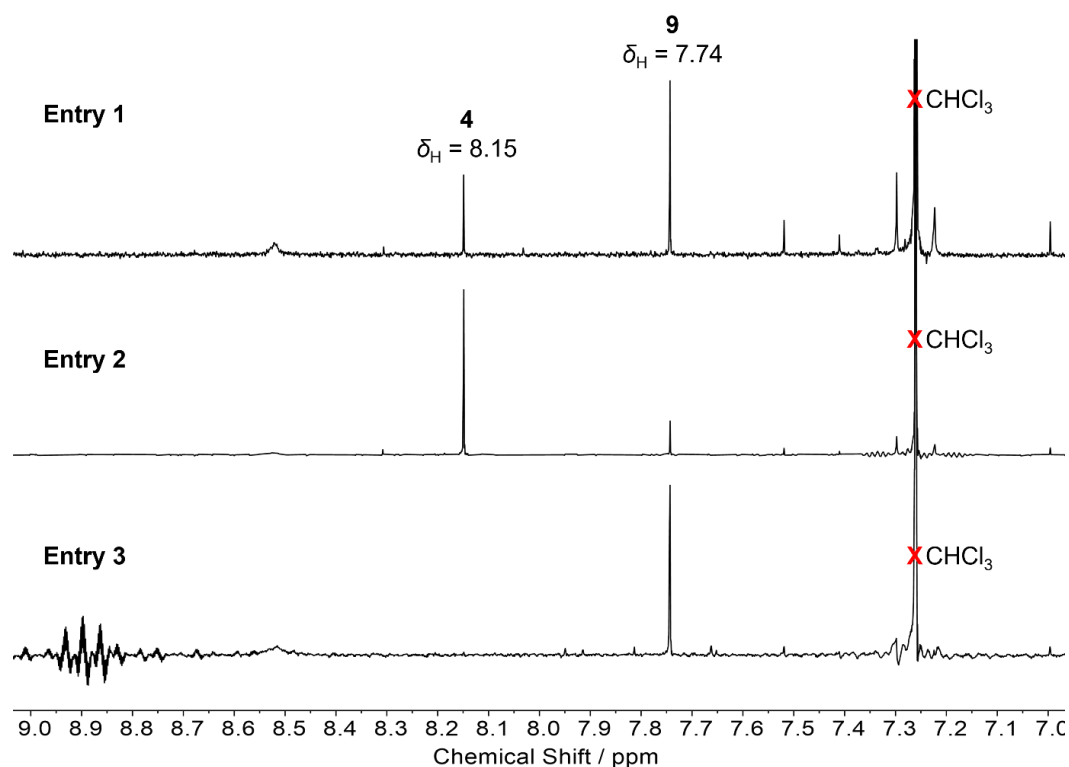
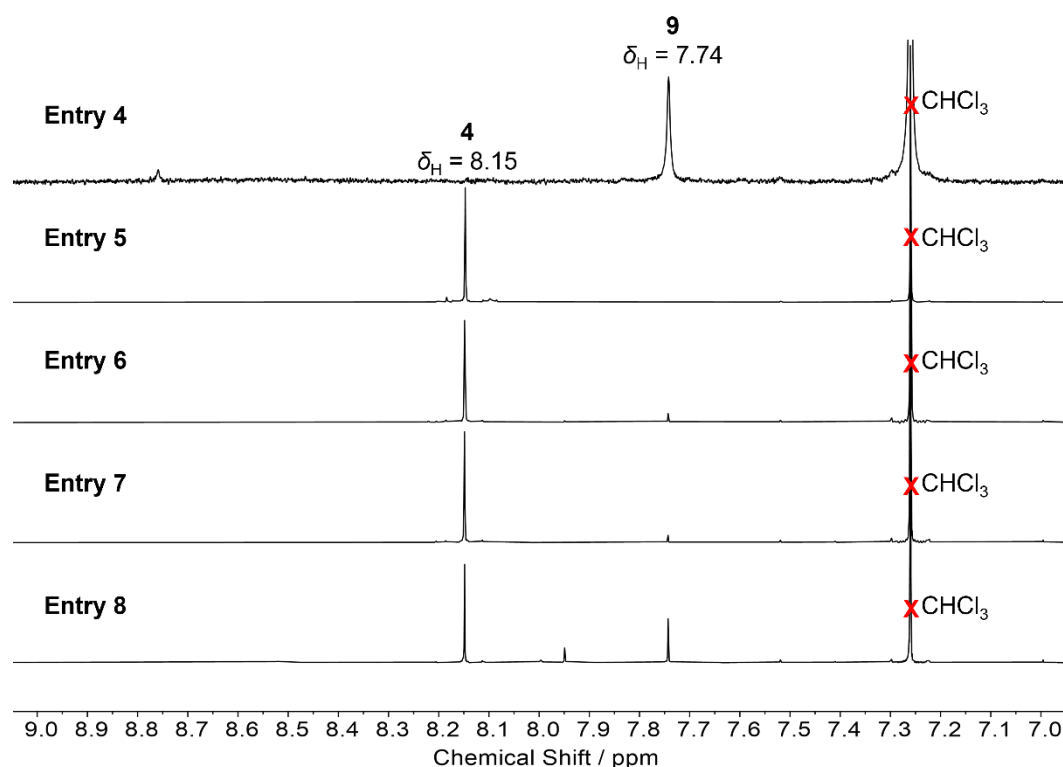


Figure 4.22 Stacked partial ¹H NMR (400 MHz, CDCl₃, 298 K) spectra of crude product from the transformation of brominated **4** to hydroxy **9** shown in Entries 1–3, Table 4.4.

After the full consumption of starting material **4** (Entry 3, Table 4.4), efforts into optimising the reaction conditions for the sole synthesis of hydroxy **9** were made. Initially, the role and effect of the presence of different reagents was investigated by omitting either CsF (Entry 4, Table 4.5) or 18-crown-6 (Entry 5, Table 4.5). Full consumption of starting material **4** to the desired product **9** was achieved in the absence of 18-crown-6 (Entry 4, Table 4.5), which indicates that the crown ether was not essential to the successful hydroxylation of the PMDI core. However, when CsF was omitted (Entry 5, Table 4.5), a small consumption of starting material **4** was observed with no generation of the product (**9**) showing that the base was vital to the -Br to -OH transformation. Subsequently, the stoichiometry of CsF used in the reaction was varied to optimise the equivalents of the key reagent (Entries 6–8, Table 4.5) with 18-crown-6 not used as a result of it not being required for the successful synthesis of hydroxy **9**. Low consumption of starting material **4** and low conversion to the target compound **9** was achieved in the presence of 3.13 and 5.14 equivalents of CsF respectively (Entries 6 and 7, Table 4.5). Although, upon increasing the equivalents of CsF to 9.74 equivalents the consumption of the starting material **4** was greater along with the generation of product **9** (Entry 8, Table 4.5), albeit still smaller than 14.82 equiv. of CsF. Therefore, it was determined that the original stoichiometry of *c.a.* 15 equivalents of CsF with respect to brominated **4** was optimal for the transformation of the bromine atom to a hydroxy group.

Table 4.5 Reaction conditions for the conversion of mono-brominated **4** to mono-hydroxy **9** with % proportions of SM and P from ^1H NMR spectra (Figure 4.23).

Entry	CsF / Equiv.	18-crown-6 / Equiv.	Concentration of 4 in dioxane / M	% Proportion of 4	% Proportion of 9
4	14.82	-	0.024	0	100
5	-	0.06	0.024	78	0
6	3.13	-	0.025	76	7
7	5.14	-	0.025	87	5
8	9.74	-	0.025	57	25

**Figure 4.23** Stacked partial ^1H NMR (400 MHz, CDCl_3 , 298 K) spectra of crude product from the transformation of brominated **4** to hydroxy **9** shown in Entries 4–8, Table 4.5.

Subsequently, brominated PMDI **4** in dioxane was diluted two-, three- and four-fold compared with the 100% conversion reaction where the concentration was 0.024 M (Entry 4, Table 4.5) to explore the optimal concentration of the limiting reagent (**4**) (Entries 9–11, Table 4.6). When the concentration of **4** was diluted to 0.012, 0.008 and 0.006 M (Entries 9–11, Table 4.6), only small amounts of the starting material remained after the reaction, although the proportion of hydroxy **9** in the ^1H NMR spectrum of the crude product (Figure 4.24) was not particularly high (max 67%), compared with when the concentration of **4** was 0.024 M. The high consumption of starting material **4** but lower proportion of product **9** is due to a new peak at 7.94 ppm which is increasingly prevalent at lower concentrations. The new species with a proton environment at 7.94 ppm could be a side product or intermediate although its structure is unknown. Therefore, the optimal concentration of limiting reagent **9** in dioxane was 0.024 M with reactions at more dilute concentrations giving increased amounts of the unidentified

species in addition to the expected product **9**. Therefore, all further reactions to hydroxy **9** were completed at concentrations of 0.024 M of bromo **4** in dioxane.

Table 4.6 Reaction conditions for the conversion of mono-brominated **4** to mono-hydroxy **9** with % proportions of SM and P from ^1H NMR spectra (Figure 4.24).

Entry	Concentration of 4 in dioxane / M	% Proportion of 4	% Proportion of 9
9	0.012	2	67
10	0.008	15	54
11	0.006	11	65

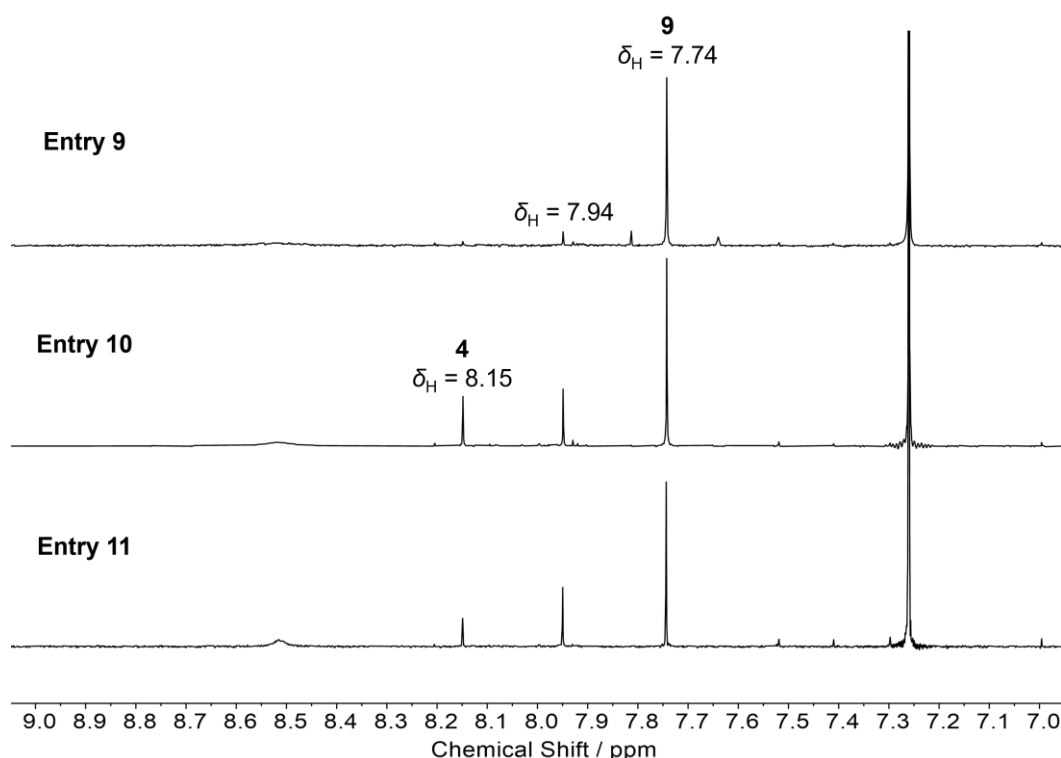


Figure 4.24 Stacked partial ^1H NMR (400 MHz, CDCl_3 , 298 K) spectra of crude product from the transformation of brominated **4** to hydroxy **9** shown in Entries 9–11, Table 4.6.

Thus far, the transformation of brominated **4** to hydroxy **9** had been trialed 11 times with varying consumption of starting material and conversion to product on each occasion as observed in ^1H NMR spectra of the crude products after workup. In considering the potential mechanism of the functional group transformation of a bromine atom to a hydroxy group, the presence of a reactive hydroxy-based species is required. The source of the -OH group could be either the hygroscopic CsF base or water contamination from the dioxane solvent as residual water was eliminated from the reaction glassware by flame-drying before use. In the core-hydroxylation of NDIs shown by Tam and Xu¹⁸ and discussed in Section 4.1, the reducing agent tetrabutylammonium fluoride ($\text{TBAF} \cdot 3\text{H}_2\text{O}$) is used with the hydrated water molecules being deprotonated by the F^- ions, with the resulting hydroxy ions able to react with the electron deficient π -surface.

To investigate the influence of water on the -Br to -OH transformation from **4** to **9**, the previously optimised reaction conditions (Entry 4, Table 4.5) were repeated using different dioxane sources (dried over molecular sieves, anhydrous and reagent grade) whilst monitoring the water content by Karl-Fischer titrations. Furthermore, the CsF was either used untreated or after drying under vacuum at 120 °C for 18 h to observe the influence of the presence of H₂O from the hygroscopic base on the -Br to -OH functional group transformation. When the CsF was used untreated (Entries 12 and 13, Table 4.7), high consumption of starting material was observed in the ¹H NMR spectra (Figure 4.25), although conversion to hydroxy **9** was lower at higher water content, with the %proportion of **9** being 81% (26 ppm) and 59% (51 ppm) respectively. The decreased amount of hydroxy **9** (Entry 13, Table 4.7) was on account of additional aromatic proton environments in the ¹H NMR spectrum (Figure 4.25) of the crude product, in particular a more prominent peak at 8.03 ppm. Furthermore, when the CsF was dried prior to use with 70 ppm water in the dioxane (Entries 14 and 15, Table 4.7) the consumption of starting material **4** was varied, although lower than when CsF was untreated (Entries 12 and 13, Table 4.7). Despite increased conversion of starting material in Entry 15 compared with Entry 14 (Table 4.7), the proportion of product **9** is not increased by the same amount, this is because the side-product represented by a proton environment at 8.03 ppm is more significant. These results show that the presence of water from the hygroscopic base is important for the successful conversion of brominated **4** to hydroxy **9** where even if consumption of the starting material is high, the formation of a side-product ($\delta_{\text{H}} = 8.03$ ppm) occurs as well as conversion to the desired product (**9**).

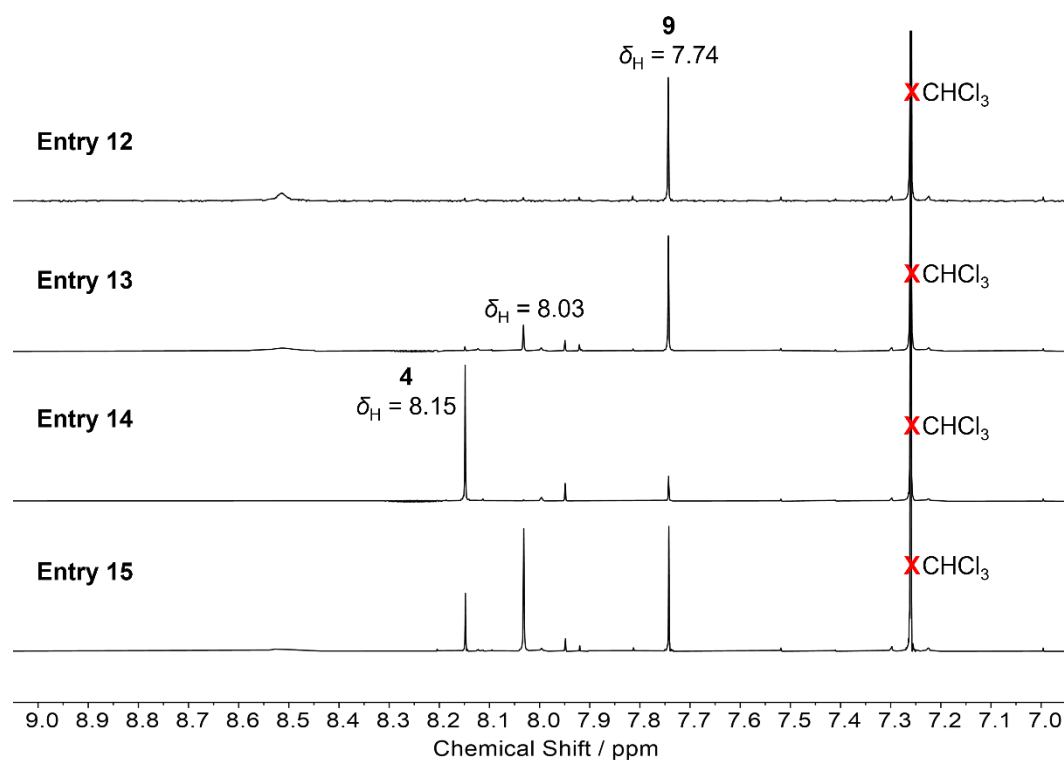


Figure 4.25 Stacked partial ¹H NMR (400 MHz, CDCl₃, 298 K) spectra of crude product from the transformation of brominated **4** to hydroxy **9** shown in Entries 12–15, Table 4.7.

Table 4.7 Reaction conditions for the conversion of mono-brominated **4** to mono-hydroxy **9** with % proportions of SM and P from ^1H NMR spectra (Figure 4.25).

Entry	Treatment of CsF	H ₂ O Content in Dioxane / ppm	% Proportion of 4	% Proportion of 9
12	-	26	2	81
13	-	51	2	59
14	Dried (120 °C, <i>in vacuo</i> , 18 h)	70	67	12
15	Dried (120 °C, <i>in vacuo</i> , 18 h)	70	14	29

Having observed a decrease in quantity of hydroxy **9** upon drying the CsF, the quality of the base was considered. The CsF used thus far was not handled in any specific manner and had already been opened prior to this reaction screening. Therefore, a fresh sample of CsF was purchased and subsequently always handled under a flow of argon. The -Br to -OH functional group transformation was repeated six times with the new sample of CsF with different quantities of water in the dioxane (Entries 17–20, Table 4.8) and in two cases drying the hygroscopic base before use (Entries 20 and 21, Table 4.8). In all of the entries in Table 4.8, relatively high consumption of starting material **4** is achieved with the maximum proportion remaining in the crude product being 32% in Entry 21, Table 4.8. (Figure 4.26). Despite high consumption of starting material, a maximum proportion of the desired hydroxy product **9** of 52% is observed in the ^1H NMR spectra (Figure 4.26) in Entry 18, Table 4.8. These relatively low conversions to the hydroxylated product (**9**) is once again due to the presence of a significant quantity of the side-product represented by a proton environment at 8.03 ppm (Figure 4.26). These results show that when using the fresh sample of CsF handled under a flow of argon, brominated **4** is consumed but with considerable conversion to side products ($\delta_{\text{H}} = 8.03$ ppm) as well as the desired product **9**. This could be due to less hydrated salt in the fresh sample of the hygroscopic CsF base when it is handled under argon in a controlled environment. This observation is similar to that observed in Entries 14 and 15 (Table 4.7) when the older sample of CsF was dried under vacuum at 120 °C. These results therefore indicate that in a similar manner to when TBAF•3H₂O was used in the core-hydroxylation of NDIs,¹⁸ the presence of basic water molecules from the hygroscopic CsF base is required for the successful conversion to the desired core-hydroxylated PMDI **9**.

Table 4.8 Reaction conditions for the conversion of mono-brominated **4** to mono-hydroxy **9** with % proportions of SM and P from ^1H NMR spectra (Figure 4.26).

Entry	Treatment of CsF	H ₂ O Content in Dioxane / ppm	% Proportion of 4	% Proportion of 9
16	-	26	10	12
17	-	51	2	52
18	-	62	14	19
19	-	189	17	28
20	Dried (120 °C, <i>in vacuo</i> , 18 h)	70	32	15
21	Dried (120 °C, <i>in vacuo</i> , 18 h)	70	3	23

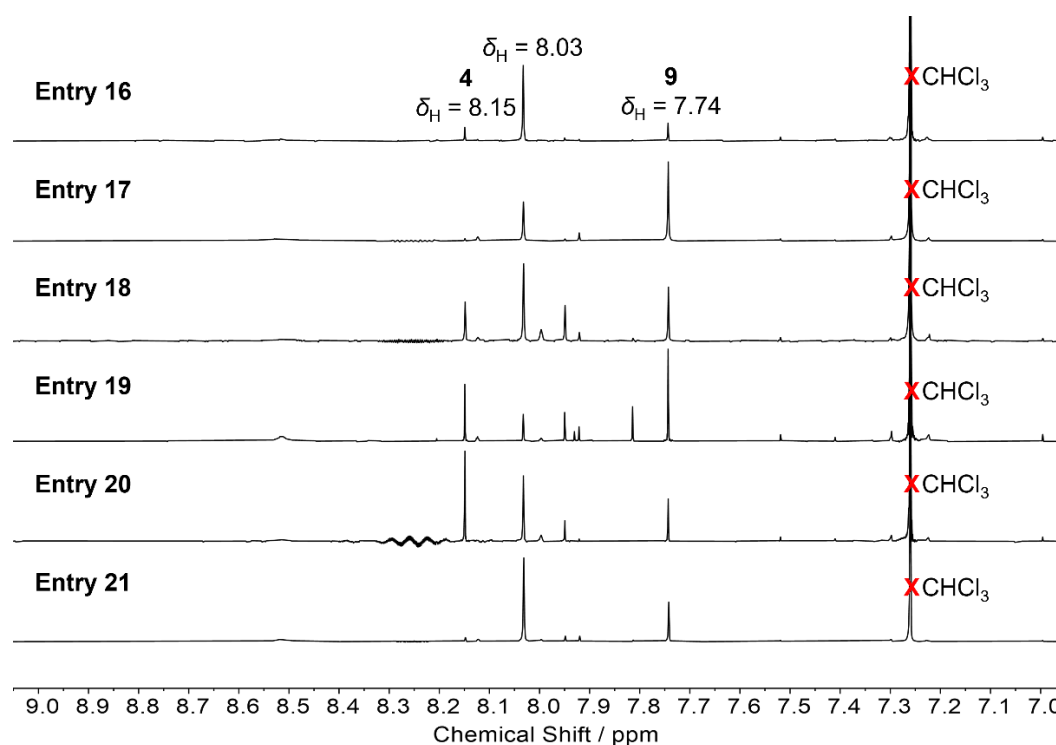
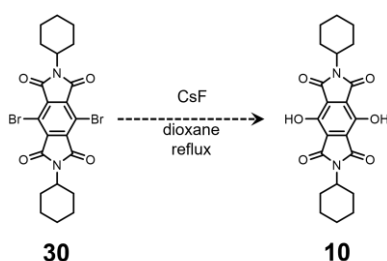


Figure 4.26 Stacked partial ^1H NMR (400 MHz, CDCl_3 , 298 K) spectra of crude product from the transformation of brominated **4** to hydroxy **9** shown in Entries 16–21, Table 4.8.

The reaction screening had shown that the role of the CsF was important to the -Br to -OH functional group transformation with the hygroscopic nature of the base potentially deprotonating water molecules that were present as a result of abstraction of moisture from the air. As the crude reaction materials often contained a mixture of starting material, product and other unidentified side products, the crude solids from Entries 13, 14, 15, 17, 18, 20 and 21 were combined and subjected to automated flash column chromatography. Co-elution of product and starting material occurred in different fractions throughout the separation, which meant that pure hydroxy **9** was not isolated. Despite the incomplete isolation of pure mono-hydroxy **9**, the reaction conditions were used in the attempt to synthesise dihydroxy **10** (30 equiv. CsF, conc. of **30** = 0.025 M) (Scheme 4.6). Upon aqueous workup, a red crude solid was isolated although analysis by ^1H NMR spectroscopy and mass spectrometry did not reveal the expected dihydroxy product (**10**).



Scheme 4.6 Proposed synthesis for core-hydroxylation of dibrominated PMDI **30** to hydroxy **10**.

The reactant in Scheme 4.6. (di-bromo **30**) contains a Br_2PMDI unit which could be mono-hydroxylated upon reaction with CsF to form an asymmetric Br(OH)PMDI unit, in a similar manner to that shown by Tam and Xu¹⁸ where Br_2NDI **22** formed Br(OH)NDI **23** when reacted with $\text{TBAF} \cdot 3\text{H}_2\text{O}$ (Scheme

4.2). The addition of the second hydroxyl group to the partially hydroxylated NDI **23** was prevented on account of the increased electron density. Indeed, when revisiting the high-resolution mass spectra for the red crude solid isolated from the reaction of dibrominated **30** with CsF (Scheme 4.6.), the exact mass for compound **31** (Figure 4.27.), HR-MS $[M + H^+]$ expected = 475.086311, found = 475.088095, was observed. If the Br₂PMDI units in **6Br** were to react in a similar manner, asymmetric mono-hydroxy-mono-brominated PMDI units could occur to form **3(OH)3Br**, **2(OH)4Br** and **(OH)5Br** (Figure 4.27.). Such potential products would be attractive on account of their emissive ESIPT behaviour as well as their orthogonal reactivity for further post-synthetic functionalisation. For example, the hydroxy group could be used as a nucleophile in substitution reactions with the bromine atom subsequently used to enable oxidative addition in transition metal cross-couplings. The dual reactivity of the partially hydroxylated partially brominated compounds could potentially allow for the access of further core-functionalised and extended molecular triangles.

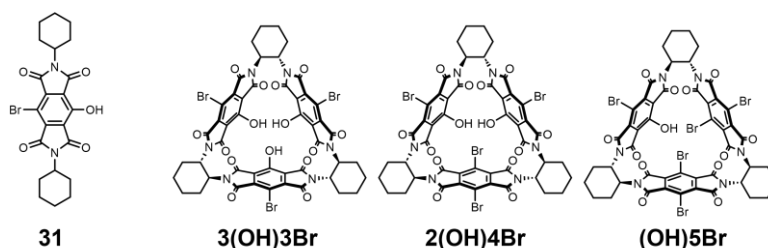


Figure 4.27 The observed actual product, **31** from reacting dibrominated **30** with CsF and the hypothesised multiply hydroxylated products, **3(OH)3Br**, **2(OH)4Br** and **(OH)5Br** from reacting hexa-brominated **6Br** with CsF.

4.3 CONCLUSIONS

In this Chapter, the photoactivity of core-functionalised molecular triangles have been investigated through (i) photochemical and conventional synthetic methods to generate core-hydroxylated molecular triangles and (ii) luminescence of core-brominated **3Br** and **6Br** in the solution and solid states.

The hexa-brominated molecular triangle **6Br** was shown to undergo a photochemical transformation in DMF which was observed by a colour change from colourless to pink and the generation of new peaks at longer wavelengths upon exposure to ambient- or irradiation with UV-light. The photochemical transformation was attributed to a partial core-hydroxylation of **6Br** which was further confirmed by the generation of **(OH)5Br** by reacting the brominated macrocycle with water in DMF. Both the impure **(OH)5Br** and **6Br** after irradiation with UV-light showed increase emission compared with the unreacted brominated macrocycle. Similarly, progress was made to synthesise core-hydroxylated PMDI compounds with CsF in dioxane. The transformation was discovered serendipitously when attempting to synthesise core-fluorinated analogues and subsequent reaction screening showed that the presence of water from the hygroscopic CsF base was required for the generation of the desired core-hydroxylated PMDI product. Upon application of the optimised reaction conditions to a Br₂PMDI compound (**30**) partial hydroxylation was observed to form a (OH)BrPMDI compound (**31**). Such a transformation is

attractive with the resulting compound not only being emissive due to the presence of the ESIPT active hydroxy group but also the orthogonal reactivity of the two substituents. If this was applied to synthesise partially hydroxylated brominated molecular triangles (**3(OH)3Br**, **2(OH)4Br** or **(OH)5Br**) further core-functionalisation of the macrocycle *via* two synthetic routes could be achieved towards triangular nanoprisms.

The introduction of bromine atoms to the aromatic core of PMDI based molecular triangles (**3Br** and **6Br**) has also been shown to ‘turn on’ emission in the macrocycles compared with the unsubstituted **6H**. The presence of the bromine atoms enhances intersystem crossing (ISC) from the S_1 to T_1 excited states on account of the heavy atom effect. Steady-state and time-resolved emission experiments show that **3Br** and **6Br** exhibit fluorescence in the solution at rt with longer wavelength phosphorescence more prevalent in the solid state at rt and 80 K, whereas as expected, the non-halogenated macrocycle **6H** did not show any phosphorescent properties. The phosphorescent properties of the helical molecular triangles (**3Br** and **6Br**) could allow for CPL to be studied for application in optical devices. Although the low PLQYs of the macrocycles (< 2.2%) means that molecular triangles with greater luminescence *e.g.*, the core-hydroxylated macrocycles, should be pursued and studied instead.

4.4 SUPPLEMENTARY INFORMATION

4.4.1 MATERIALS AND GENERAL METHODS

All chemicals and reagents were purchased from commercial suppliers (Sigma Aldrich, Fisher Scientific, Alfa Aesar, Fluorochem, Apollo Scientific or Tokyo Chemical Industry) and used without further purification unless otherwise stated. Anhydrous solvents were obtained from a neutral alumina Solvent Purification System under nitrogen and stored over activated (>250 °C at 0.01 mbar overnight) 3 Å molecular sieves under a dry Ar atmosphere. CsF was either used fresh from the bottle, handled under a flow of argon or after being dried under vacuum at 120 °C for 18 h. Molecular triangles **6H**, **3Br**, **6Br**, **3Ar** and **6Ar** were synthesised according to procedures given in Chapters 2 and 3.

Analytical thin-layer chromatography (TLC) was performed on silica gel 60 plates pre-loaded with F254 indicator (Sigma Aldrich) and visualised under UV light irradiation (254 and 365 nm). Automated flash column chromatography was performed using a Teledyne ISCO Combiflash NextGen 300+ with detectors using broad range UV-vis (200–800 nm) and evaporative light scattering (ELS) through N_2 gas and loaded on pre-filled RedisepTM Gold cartridges (normal phase: SiO_2) by dry loading from adsorbed celite. Nuclear magnetic resonance (NMR) spectra were recorded on a Jeol ECS400D spectrometer (working frequency of 400 and 101 MHz for 1H and ^{13}C nuclei respectively). Chemical shifts (δ) are reported in ppm relative to the signals corresponding to residual non-deuterated solvents ($CDCl_3$: δ_H 7.26 ppm, δ_C 77.16 ppm, $(CD_3)_2SO$: δ_H 2.50 ppm, δ_C 39.52 ppm, $(CD_3)_2CO$: δ_H 2.05 ppm, δ_C 206.62 ppm, 29.84 ppm). Coupling constants (J) are reported in Hertz (Hz) and 1H multiplicities are

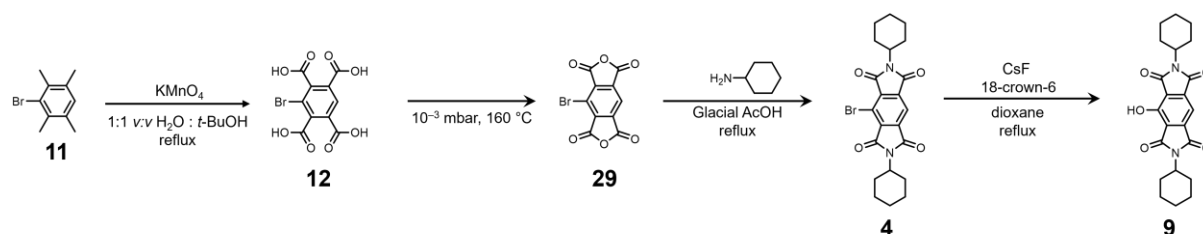
reported in accordance with the following convention: s = singlet, d = doublet, t = triplet, q = quadruplet, p = pentet, m = multiplet. NMR spectra were processed using MestReNova software, Version 14. High-resolution mass spectrometry was completed using a Bruker compact time-of-flight mass spectrometer using either an atmospheric-pressure chemical ionisation (APCI) or electrospray ionisation (ESI) source.

Solution-state absorption spectra were recorded using an Agilent Technologies Cary 5000 Series UV-Vis-NIR spectrophotometer or Shimadzu UV 1800 spectrophotometer using standard 10 mm path length UV-vis quartz cuvettes at room temperature. Solution-state fluorescence spectroscopy was carried out using a Hitachi F-4500 fluorimeter equipped with a 150 W Xe lamp using standard photoluminescence quartz cuvettes. Samples for solution-state fluorescence spectroscopy had an optical density (O.D. < 0.3) and prepared in dry solvents.

Emission spectra of thin films and solutions carried out in the Department of Physics, Durham University were collected using a Horiba-Jobin Yvon Fluorolog-3 spectrofluorometer equipped with a 450 W Xe lamp as the light source. PLQYs were measured using a calibrated Quanta-φ integrating sphere with coupled Jobin Yvon FluoroLog-3 spectrometer and analysed using FluorEssence software.

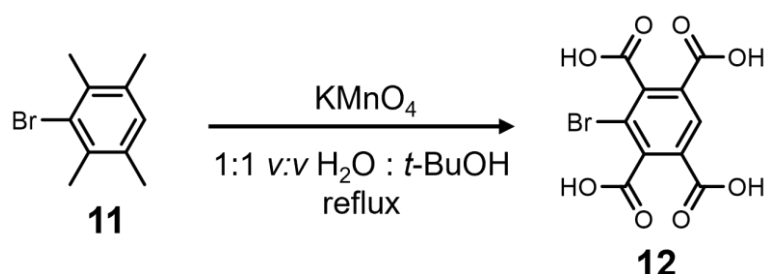
4.4.2 SYNTHESIS

PROPOSED SYNTHESIS OF MONO-HYDROXY PMDI COMPOUND (9)

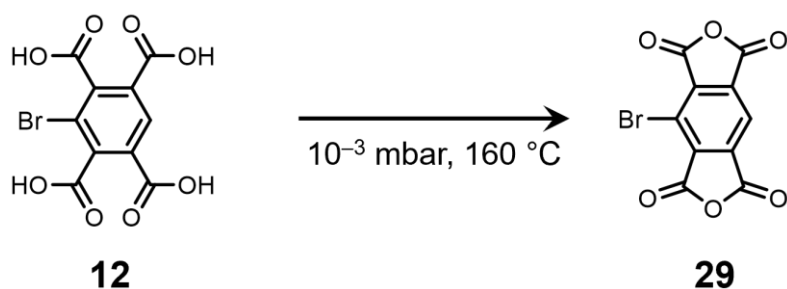


Scheme S4.1 Proposed synthesis of mono-hydroxy PMDI compound **9**.

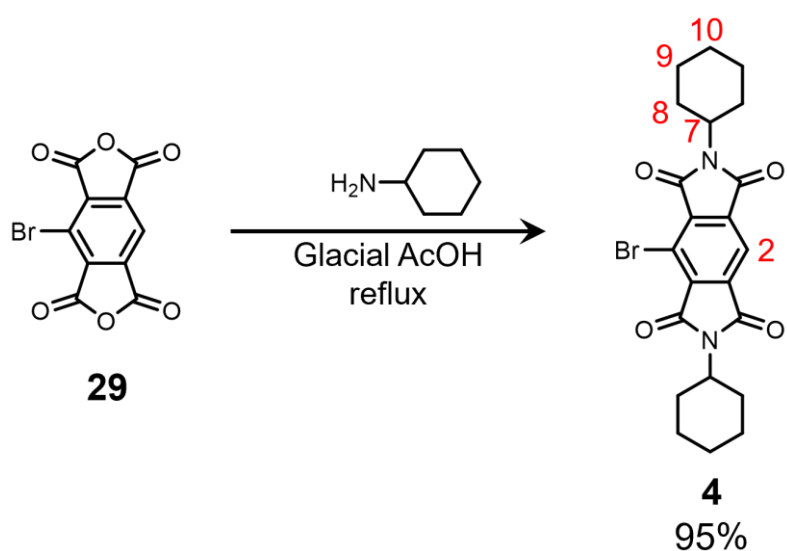
1-BROMOBENZENE-2,3,5,6-TETRACARBOXYLIC ACID (12)



Synthesis of 1-bromobenzene-2,3,5,6-tetracarboxylic acid (**12**) was completed as described in Chapter 3.

1-BROMOBENZENE-2,3,5,6-TETRACARBOXYLIC ANHYDRIDE (29)

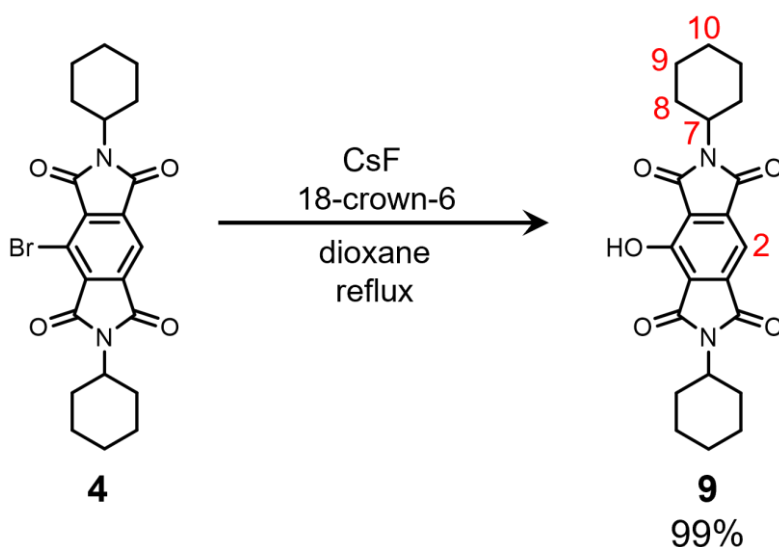
Synthesis of 1-bromobenzene-2,3,5,6-tetracarboxylic anhydride (**29**) was completed as described in Chapter 3.

N-CYCLOHEXYLAMINE 1-BROMOBENZENE-2,3,5,6-TETRACARBOXYLIC DIIMIDE (4)

Cyclohexylamine (0.19 g, 1.89 mmol, 2.25 equiv.) was added to a stirring solution of anhydride **29** (0.25 g, 0.84 mmol, 1.0 equiv.) in glacial AcOH (5 mL) for 1 h. The reaction mixture was then refluxed overnight, the suspension was cooled to room temperature and the colourless precipitate isolated by filtration, washed with H₂O (3 x 50 mL) and MeOH (3 x 50 mL) and dried *in vacuo* to give the desired product **4** (0.37 g, 0.81 mmol, 95%) as a colourless solid.

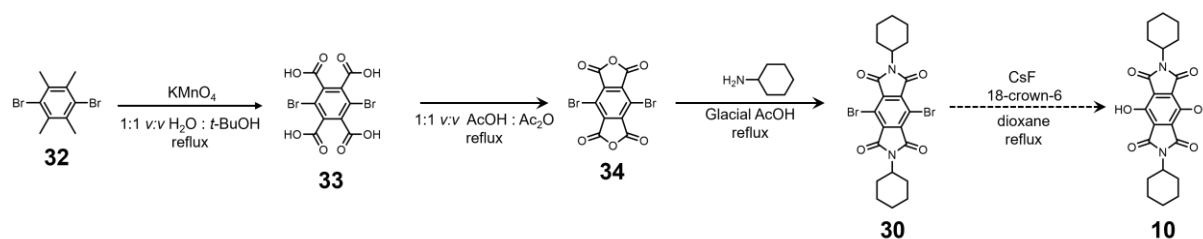
¹H NMR (CDCl₃, 400 MHz, 298 K): δ_{H} 8.14 (s, 1H²), 4.15 (tt, $J_{\text{ax}} = 14 \text{ Hz}$, $J_{\text{eq}} = 4 \text{ Hz}$, 2H⁷), 2.20 (qd, $J = 12 \text{ MHz}$, $J = 4 \text{ MHz}$, 4H^{8/9/10}), 1.94–1.84 (m, 4H^{8/9/10}), 1.79–1.71 (m, 5H^{8/9/10}), 1.46–1.26 (m, 7H^{8/9/10}).

APCI-MS (+ve, CH₂Cl₂): calcd for $[M+H]^+$ $m/z = 459.0914$, found 459.0901. Spectroscopic data are consistent with the literature.⁷

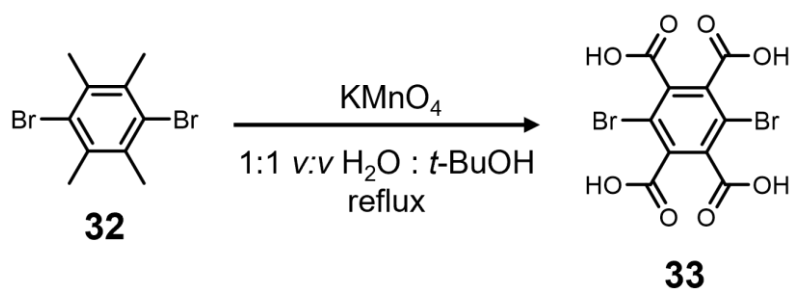
N-CYCLOHEXYLAMINE 1-HYDROXYBENZENE-2,3,5,6-TETRACARBOXYLIC DIIMIDE (9)

A 25 mL RBF was flame-dried and mono-bromo **4** (0.10 g, 0.22 mmol, 1.0 equiv.), CsF (0.50 g, 3.29 mmol, 14.99 equiv.) and 18-crown-6 (0.0028 g, 0.01 mmol, 0.05 equiv.) were added. The flask was evacuated and purged with Ar gas three times. Dioxane (9 mL) was added and the off-white suspension stirred heated to reflux (110 °C) for 18 h. The orange solution was cooled to room temperature and deionised water (25 mL) was added and extracted with CH₂Cl₂ (3 x 50 mL). The organic layers were combined, dried (Na₂SO₄), filtered and the filtrate concentrated *in vacuo* to give the product **9** (0.085 g, 0.21 mmol, 99%) as an orange solid.

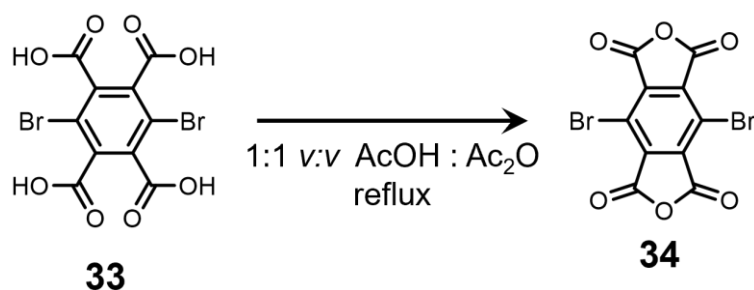
¹H NMR (CDCl₃, 400 MHz, 298 K): δ_{H} 7.74 (s, 1H²), 4.10 (t, J = 12 Hz, 2H⁷), 2.16 (q, J = 16 Hz, 4H^{8/9/10}), 1.92–1.83 (m, 6H^{8/9/10}), 1.79–1.71 (m, 6H^{8/9/10}), 1.44–1.33 (m, 4H^{8/9/10}). ESI-MS (–ve, CH₂Cl₂): calcd for $[M-H]^-$ m/z = 395.1612, found 395.1610. Spectroscopic data are consistent with the literature.¹¹

PROPOSED SYNTHESIS OF DI-HYDROXY PMDI COMPOUND (10)

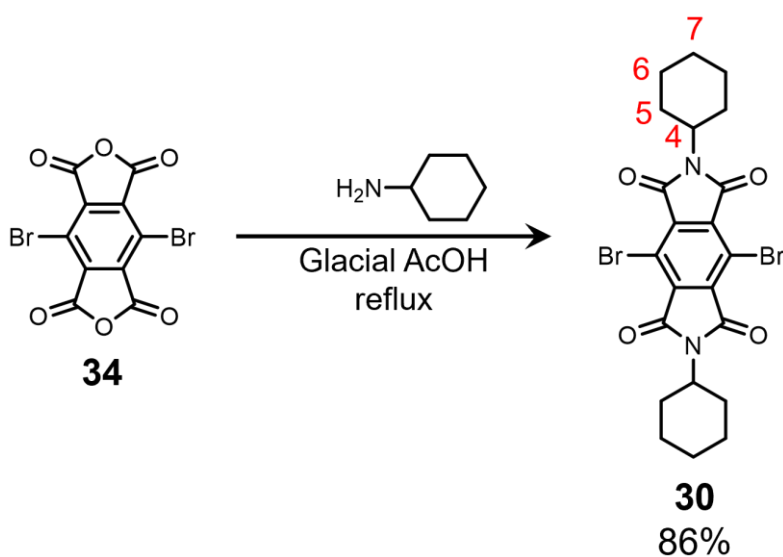
Scheme S4.2. Proposed synthesis of di-hydroxy PMDI compound **10**.

1,4-DIBROMOBENZENE-2,3,5,6-TETRACARBOXYLIC ACID (33)

Synthesis of 1,4-dibromobenzene-2,3,5,6-tetracarboxylic acid (**33**) was completed as described in Chapter 2.

1,4-DIBROMOBENZENE-2,3,5,6-TETRACARBOXYLIC ANHYDRIDE (34)

Synthesis of 1,4-dibromobenzene-2,3,5,6-tetracarboxylic anhydride (**34**) was completed as described in Chapter 2.

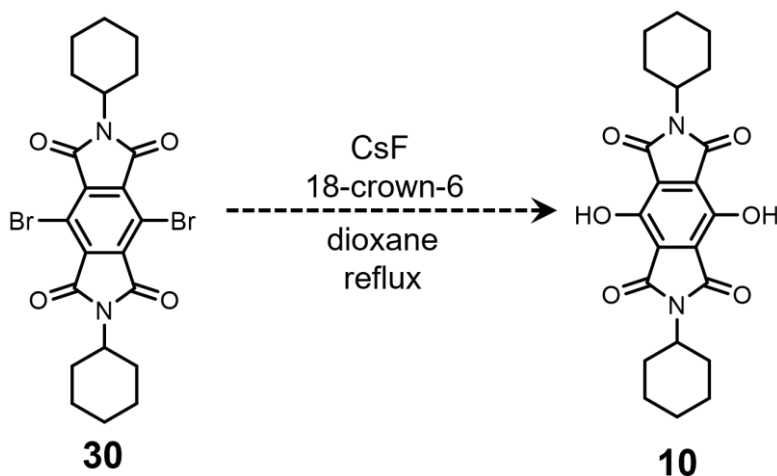
***N*-CYCLOHEXYLAMINE 1,4-DIBROMOBENZENE-2,3,5,6-TETRACARBOXYLIC DIIMIDE (30)**

Cyclohexylamine (0.27 g, 2.73 mmol, 2.05 eq.) was added to a stirring solution of anhydride **34** (0.50 g, 1.33 mmol, 1.0 equiv.) in glacial AcOH (8 mL) for 1 h. The brown reaction mixture was then refluxed

overnight to form a dark red solution. The brown suspension was cooled to room temperature and the off-white precipitate isolated by filtration to give product **30** (0.62 g, 1.15 mmol, 86%).

^1H NMR (CDCl_3 , 400 MHz, 298 K): δ_{H} 4.27–4.04 (m, 2H^4), 2.26–2.16 (m, $4\text{H}^{5/6/7}$), 1.94–1.70 (m, $12\text{H}^{5/6/7}$), 1.41–1.35 (m, $4\text{H}^{5/6/7}$). APCI-MS (+ve, CH_2Cl_2): calcd for $[\text{M}+\text{H}]^+$ m/z = 537.0019, found 537.0037.

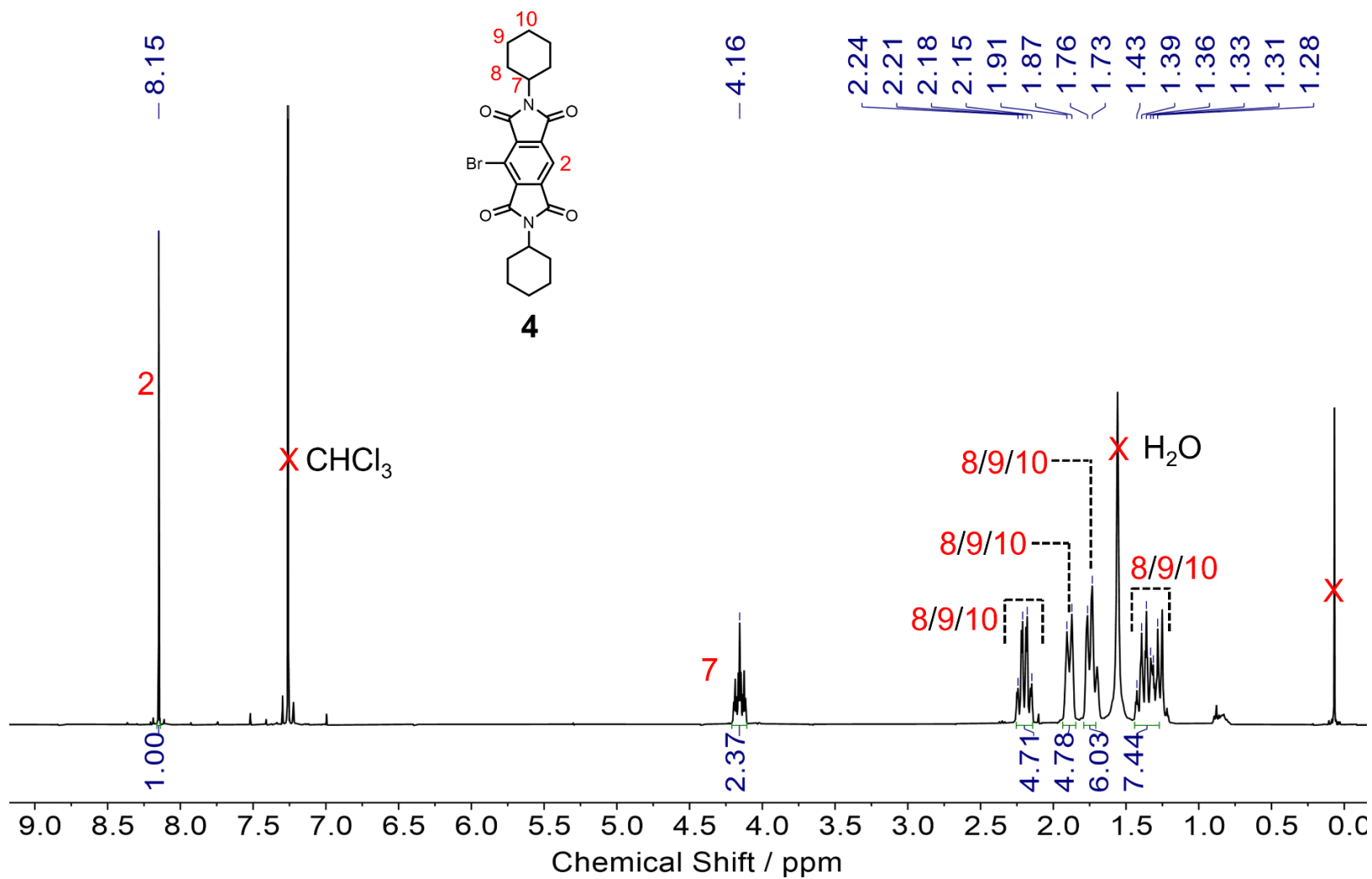
N-CYCLOHEXYLAMINE 1,4-DIHYDROXYBENZENE-2,3,5,6-TETRACARBOXYLIC DIIMIDE (10)

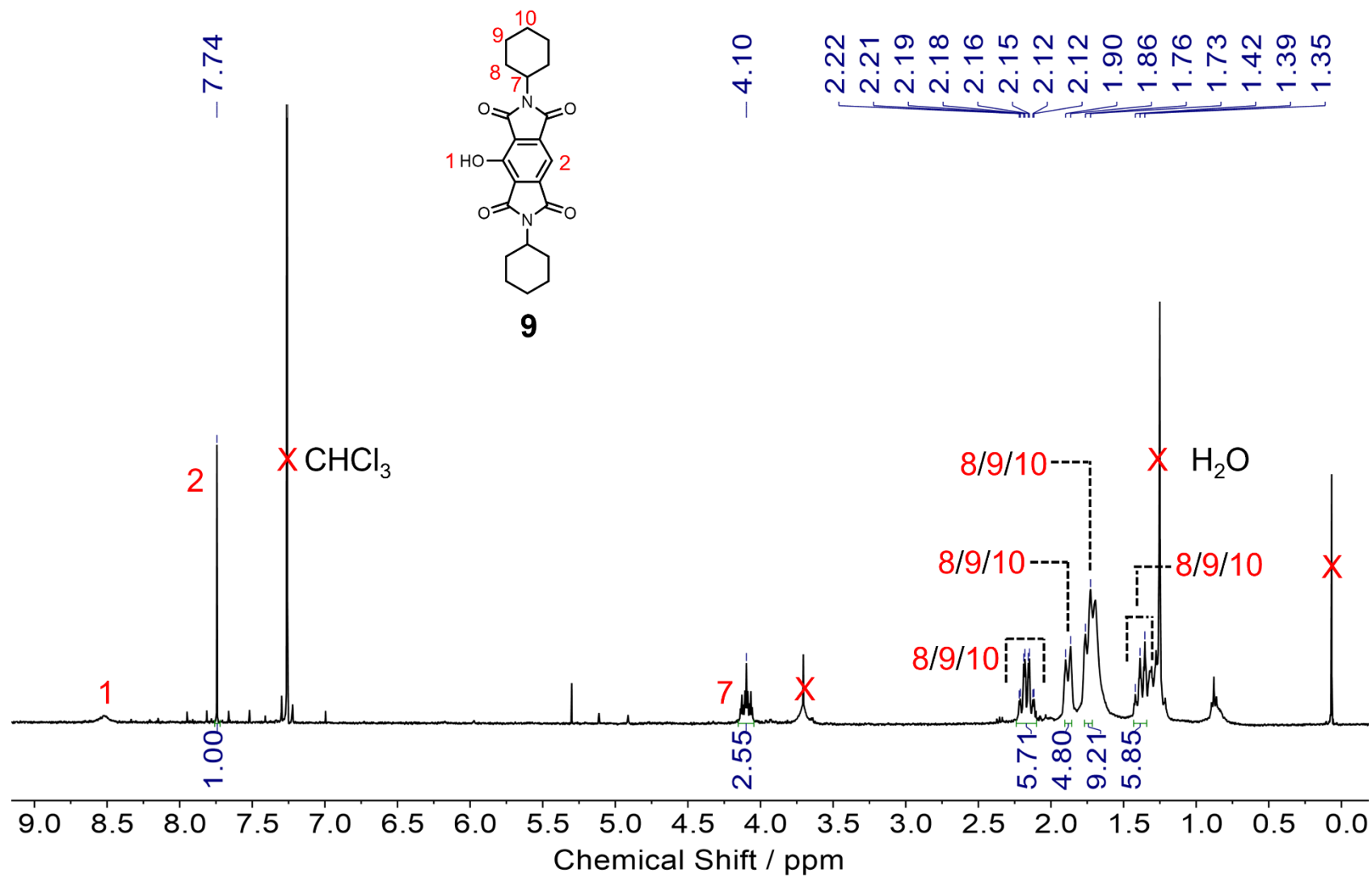


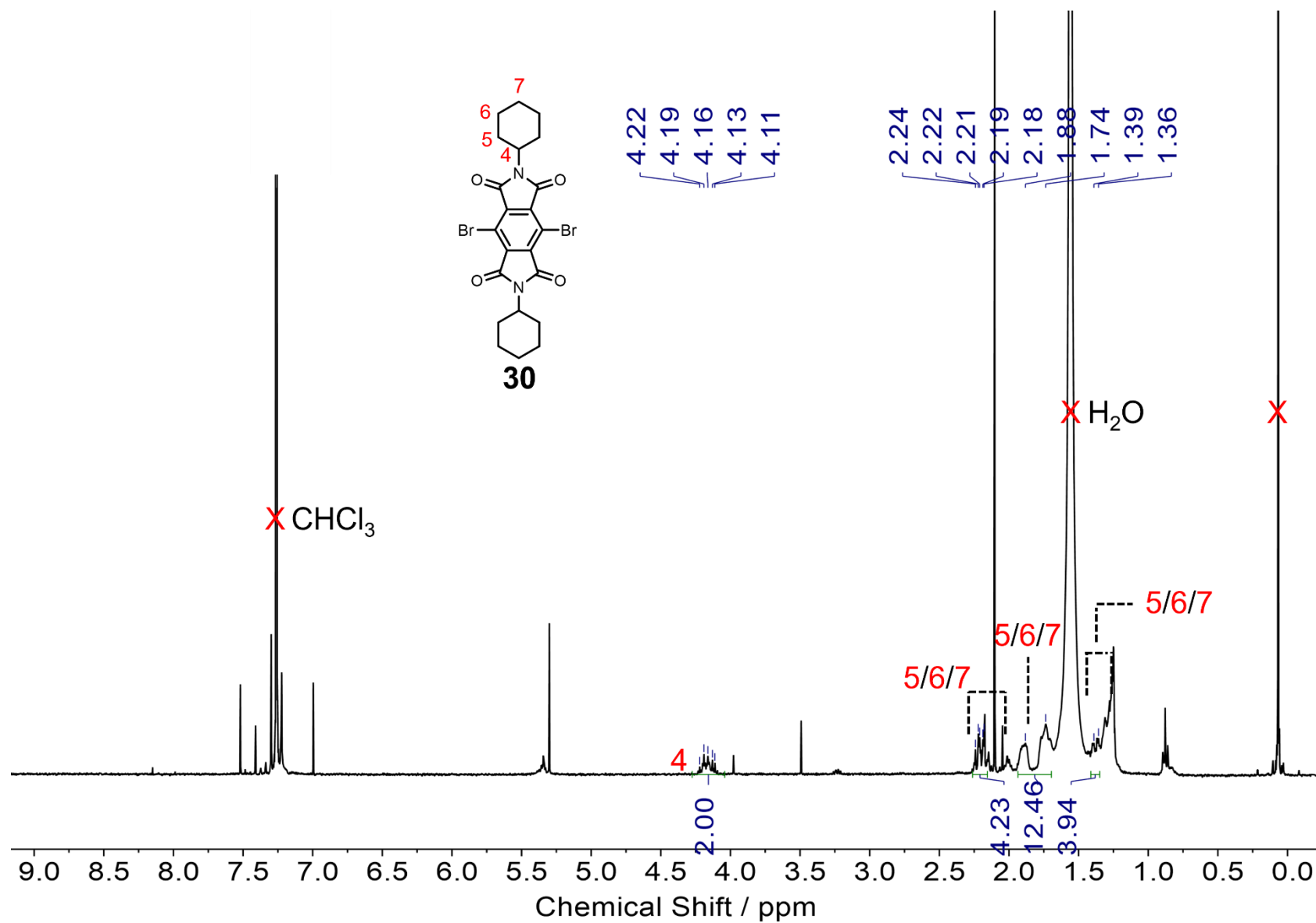
Di-bromo **30** (21 mg, 0.038 mmol, 1.0 equiv.) and CsF (0.17 g, 1.12 mmol, 29.37 equiv.) were combined and evacuated and purged with Ar gas three times. Dioxane (1.5 mL) was added and the off-white suspension stirred heated to reflux (105 °C) for 18 h. The red suspension was cooled to room temperature, deionised water (10 mL) was added and extracted with CH_2Cl_2 (3 x 10 mL). The organic layers were combined, dried (Na_2SO_4), filtered and the filtrate concentrated *in vacuo* to give a red crude solid.

Upon characterisation of the crude red solid by ^1H NMR spectroscopy and HR-MS the expected product **10** was not identified. However, the mono-hydroxylated product **31** was identified in the high-resolution mass spectrum, HR-MS $[\text{M} + \text{H}^+]$ expected = 475.086311, found = 475.088095.

4.4.3 CHARACTERISATION

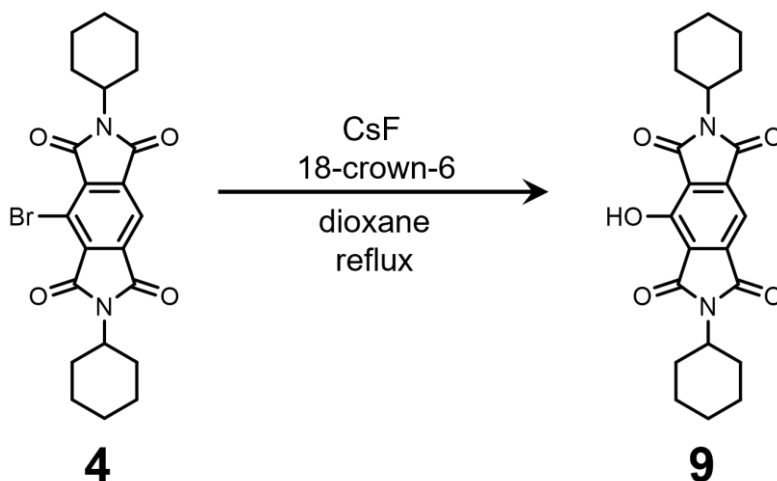
Figure S4.1 ^1H NMR (400 MHz, CDCl_3 , 298 K) spectrum of **4**.

Figure S4.2 ^1H NMR (400 MHz, CDCl_3 , 298 K) spectrum of **9**.

Figure S4.3 ^1H NMR (400 MHz, CDCl_3 , 298 K) spectrum of **30**.

4.4.4 REACTION SCREENING OF TRANSFORMATION OF MONO-BROMINATED **4** TO MONO-HYDROXYLATED **9**

GENERAL SYNTHETIC METHOD



All reagents were added to a reaction vessel and evacuated and purged with Ar gas three times. Dioxane was added and the off-white suspension stirred heated to reflux (110 °C) for 18 h. The solution was cooled to room temperature and deionised water was added and the product was extracted with CH₂Cl₂ (three portions). The organic layers were combined, dried (Na₂SO₄), filtered and the filtrate concentrated *in vacuo* to give the crude product containing mono-hydroxy **9**.

Table 4.4 Entry 1: **4** (0.10 g, 0.22 mmol, 1.00 equiv.), CsF (0.50 g, 3.29 mmol, 15.1 equiv.), 18-Crown-6 (8 mg, 0.03 mmol, 0.14 equiv.) and anhydrous dioxane (1.45 mL, 0.15 M with respect to compound **4**).

Table 4.4 Entry 2: **4** (0.10 g, 0.22 mmol, 1.00 equiv.), CsF (0.50 g, 3.32 mmol, 15.3 equiv.), 18-Crown-6 (4 mg, 0.01 mmol, 0.06 equiv.) and anhydrous dioxane (1.45 mL, 0.15 M with respect to compound **4**).

Table 4.4 Entry 3: **4** (0.10 g, 0.22 mmol, 1.00 equiv.), CsF (0.50 g, 3.32 mmol, 15.0 equiv.), 18-Crown-6 (3 mg, 0.01 mmol, 0.05 equiv.) and anhydrous dioxane (9 mL, 0.024 M with respect to compound **4**).

Table 4.5 Entry 4: **4** (20 mg, 0.04 mmol, 1.00 equiv.), CsF (99 mg, 0.65 mmol, 14.8 equiv.) and anhydrous dioxane (1.8 mL, 0.024 M with respect to compound **4**).

Table 4.5 Entry 5: **4** (20 mg, 0.04 mmol, 1.00 equiv.), 18-Crown-6 (0.7 mg, 0.003 mmol, 0.06 equiv.) and anhydrous dioxane (1.8 mL, 0.024 M with respect to compound **4**).

Table 4.5 Entry 6: **4** (20 mg, 0.04 mmol, 1.00 equiv.), CsF (21 mg, 0.14 mmol, 3.1 equiv.) and anhydrous dioxane (1.8 mL, 0.025 M with respect to compound **4**).

Table 4.5 Entry 7: **4** (20 mg, 0.04 mmol, 1.00 equiv.), CsF (35 mg, 0.23 mmol, 5.1 equiv.) and anhydrous dioxane (1.8 mL, 0.025 M with respect to compound **4**).

Table 4.5 Entry 8: **4** (20 mg, 0.04 mmol, 1.00 equiv.), CsF (66 mg, 0.43 mmol, 9.7 equiv.) and anhydrous dioxane (1.8 mL, 0.025 M with respect to compound **4**).

Table 4.6 Entry 9: **4** (20 mg, 0.04 mmol, 1.00 equiv.), CsF (0.10 g, 0.66 mmol, 15.3 equiv.) and anhydrous dioxane (3.6 mL, 0.012 M with respect to compound **4**).

Table 4.6 Entry 10: **4** (20 mg, 0.04 mmol, 1.00 equiv.), CsF (0.10 g, 0.68 mmol, 15.5 equiv.) and anhydrous dioxane (5.4 mL, 0.008 M with respect to compound **4**).

Table 4.6 Entry 11: **4** (20 mg, 0.04 mmol, 1.00 equiv.), CsF (0.10 g, 0.66 mmol, 15.0 equiv.) and anhydrous dioxane (7.2 mL, 0.006 M with respect to compound **4**).

Table 4.7 Entry 12: **4** (20 mg, 0.04 mmol, 1.00 equiv.), CsF (0.10 g, 0.66 mmol, 15.3 equiv.) and anhydrous dioxane (1.8 mL, 0.024 M with respect to compound **4**).

Table 4.7 Entry 13: **4** (20 mg, 0.04 mmol, 1.00 equiv.), CsF (0.10 g, 0.67 mmol, 15.6 equiv.) and reagent grade dioxane (1.8 mL, 0.024 M with respect to compound **4**).

Table 4.7 Entry 14: **4** (20 mg, 0.04 mmol, 1.00 equiv.), dried (*in vacuo*, 120 °C) CsF (0.10 g, 0.66 mmol, 14.9 equiv.) and reagent grade dioxane (1.8 mL, 0.024 M with respect to compound **4**).

Table 4.7 Entry 15: **4** (20 mg, 0.04 mmol, 1.00 equiv.), dried (*in vacuo*, 120 °C) CsF (0.10 g, 0.65 mmol, 15.2 equiv.) and anhydrous dioxane (1.8 mL, 0.024 M with respect to compound **4**).

Table 4.8 Entry 16: **4** (19 mg, 0.04 mmol, 1.00 equiv.), CsF (94 mg, 0.62 mmol, 14.7 equiv.) and anhydrous dioxane (1.8 mL, 0.023 M with respect to compound **4**).

Table 4.8 Entry 17: **4** (33 mg, 0.07 mmol, 1.00 equiv.), CsF (0.16 g, 1.04 mmol, 14.7 equiv.) and reagent grade dioxane (2.9 mL, 0.024 M with respect to compound **4**).

Table 4.8 Entry 18: **4** (25 mg, 0.05 mmol, 1.00 equiv.), CsF (0.13 g, 0.85 mmol, 15.5 equiv.) and anhydrous dioxane (2.4 mL, 0.023 M with respect to compound **4**).

Table 4.8 Entry 19: **4** (23 mg, 0.05 mmol, 1.00 equiv.), CsF (0.11 g, 0.74 mmol, 15.0 equiv.) and anhydrous dioxane (1.8 mL, 0.027 M with respect to compound **4**).

Table 4.8 Entry 20: **4** (18 mg, 0.04 mmol, 1.00 equiv.), dried (*in vacuo*, 120 °C) CsF (92 mg, 0.60 mmol, 15.2 equiv.) and reagent grade dioxane (1.65 mL, 0.024 M with respect to compound **4**).

Table 4.8 Entry 21: **4** (25 mg, 0.05 mmol, 1.00 equiv.), dried (*in vacuo*, 120 °C) CsF (0.13 g, 0.84 mmol, 15.4 equiv.) and anhydrous dioxane (2.3 mL, 0.024 M with respect to compound **4**).

The percentage proportions of starting material (SM) mono-bromo **4** and desired product (P) mono-hydroxy **9** were calculated from the ratio of the integrals in the ^1H NMR spectra of the crude product. The proton environment for compound **9** (δ_{H} 7.74 ppm) was integrated and normalised to 1.00 and the starting material compound **4** (δ_{H} 8.15 ppm) was integrated with respect to δ_{H} 7.74 ppm. All other aromatic proton environments between 7.60–8.40 ppm were integrated with respect to δ_{H} 7.74 ppm. The ratio of δ_{H} 7.74 ppm or δ_{H} 8.15 ppm and δ_{H} 7.60–8.40 was calculated to give the respective %proportions.

Table S4.1 Table showing the % conversion of transformation of mono-bromo **4** to mono-hydroxy **9** based on the relative ratio of the integrations in the ^1H NMR spectrum of the crude product.

Entry	Integration of 4 (δ_{H} 8.15 ppm)	Integration of 9 (δ_{H} 7.74 ppm)	Integration aromatic region (δ_{H} 7.60–8.40 ppm)	% Proportion of 4	% Proportion of 9
1	0.44	1.00	1.56	28	64
2	4.98	1.00	6.13	81	16
3	0.00	1.00	1.24	0	81
4	0.00	1.00	1.00	0	100
5	16.42	0.00	21.15	78	0
6	10.61	1.00	14.03	76	7
7	16.45	1.00	18.85	87	5
8	2.31	1.00	4.05	57	25
9	0.03	1.00	1.50	2	67
10	0.28	1.00	1.85	15	54
11	0.17	1.00	1.55	11	65
12	0.02	1.00	1.24	2	81
13	0.04	1.00	1.70	2	59
14	5.41	1.00	8.03	67	12
15	0.48	1.00	3.50	14	29
16	0.81	1.00	8.31	10	12
17	0.04	1.00	1.91	2	52
18	0.75	1.00	5.39	14	19
19	0.63	1.00	3.61	17	28
20	2.11	1.00	6.64	32	15
21	0.12	1.00	4.41	3	23

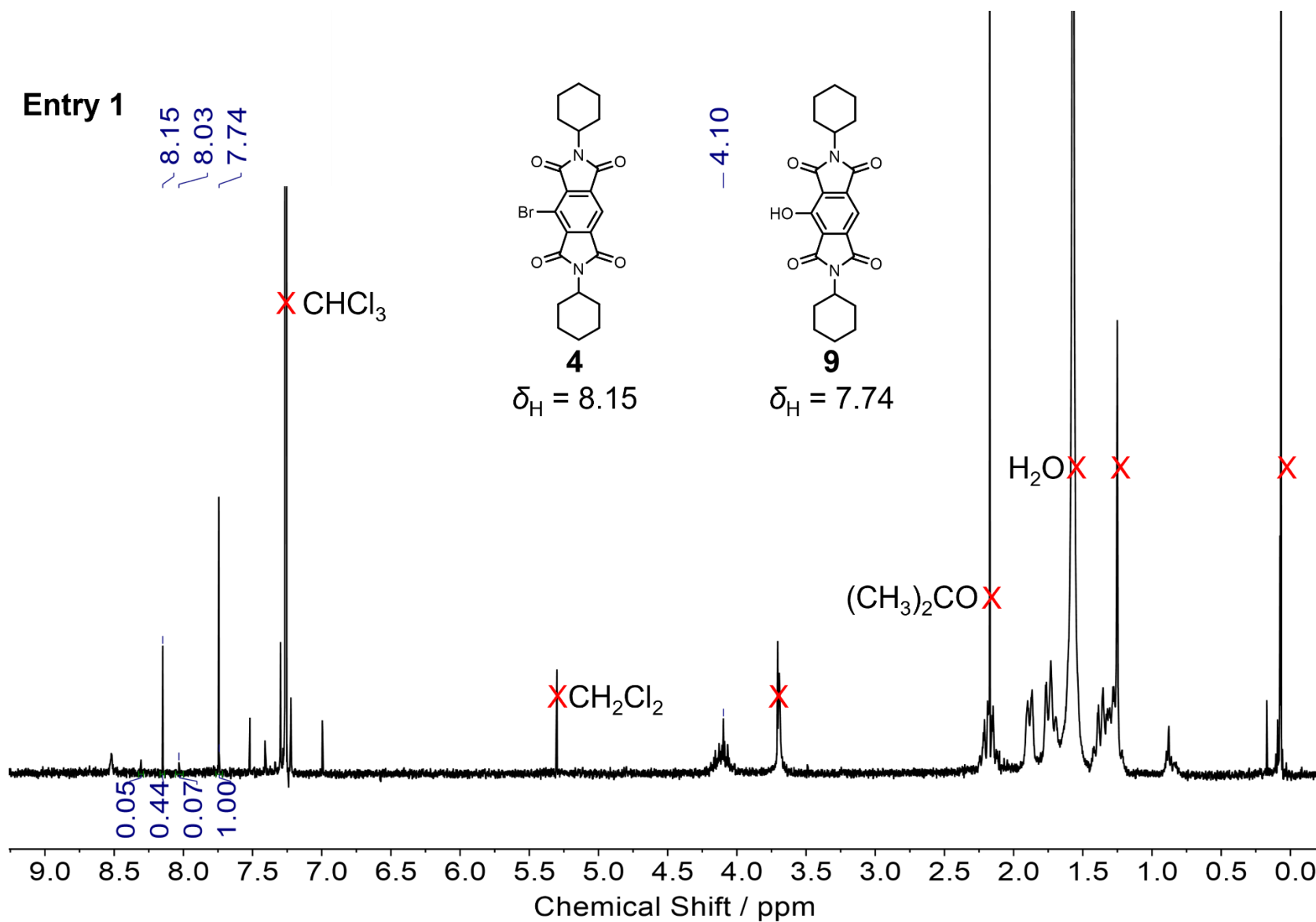


Figure S4.4 ^1H NMR (400 MHz, CDCl_3 , 298 K) spectrum of crude product containing mono-hydroxy **9** and mono-bromo **4** from the reaction discussed in Entry 1, Table 4.4.

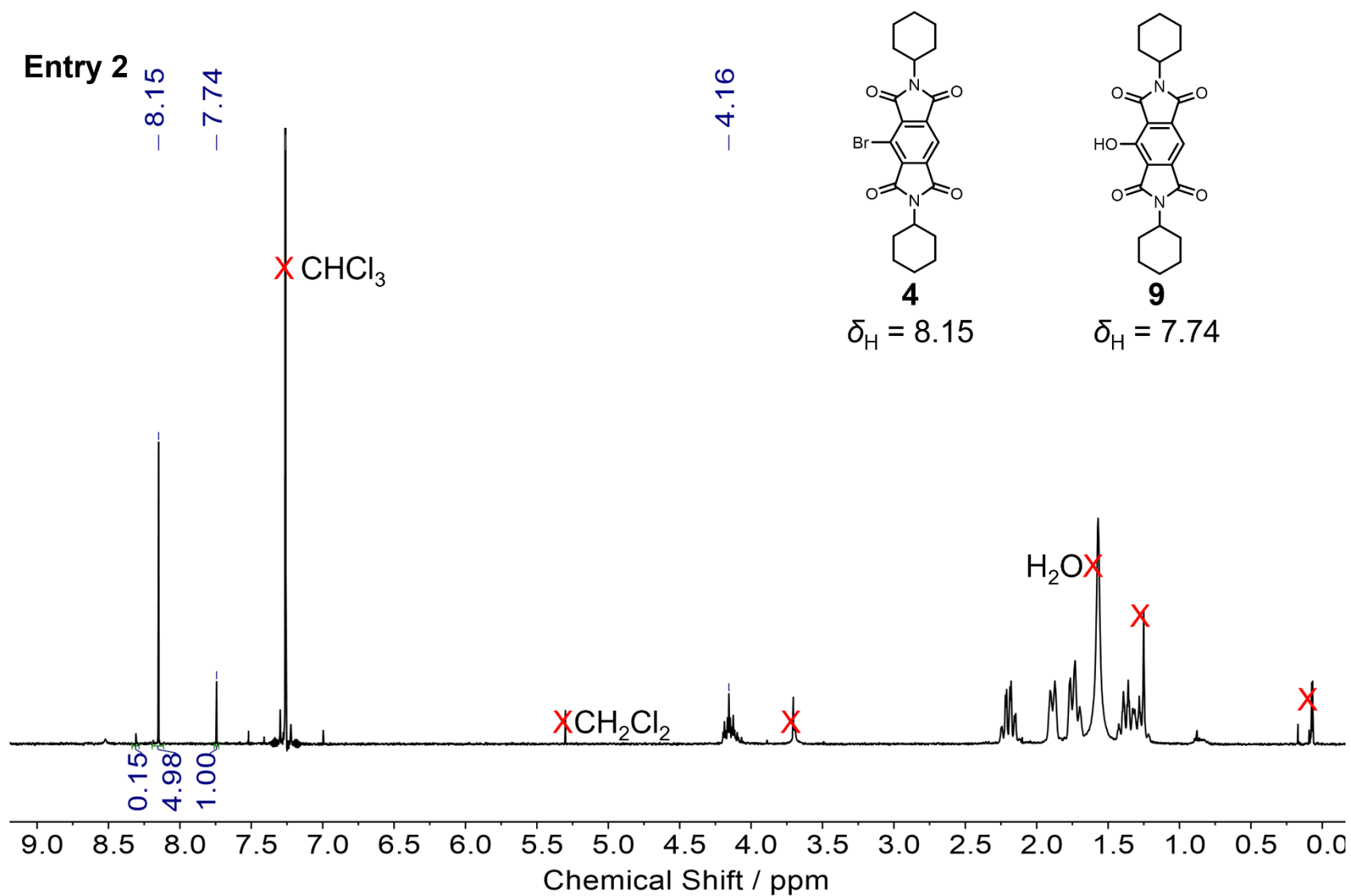


Figure S4.5 ^1H NMR (400 MHz, CDCl_3 , 298 K) spectrum of crude product containing mono-hydroxy **9** and mono-bromo **4** from the reaction discussed in Entry 2, Table 4.4.

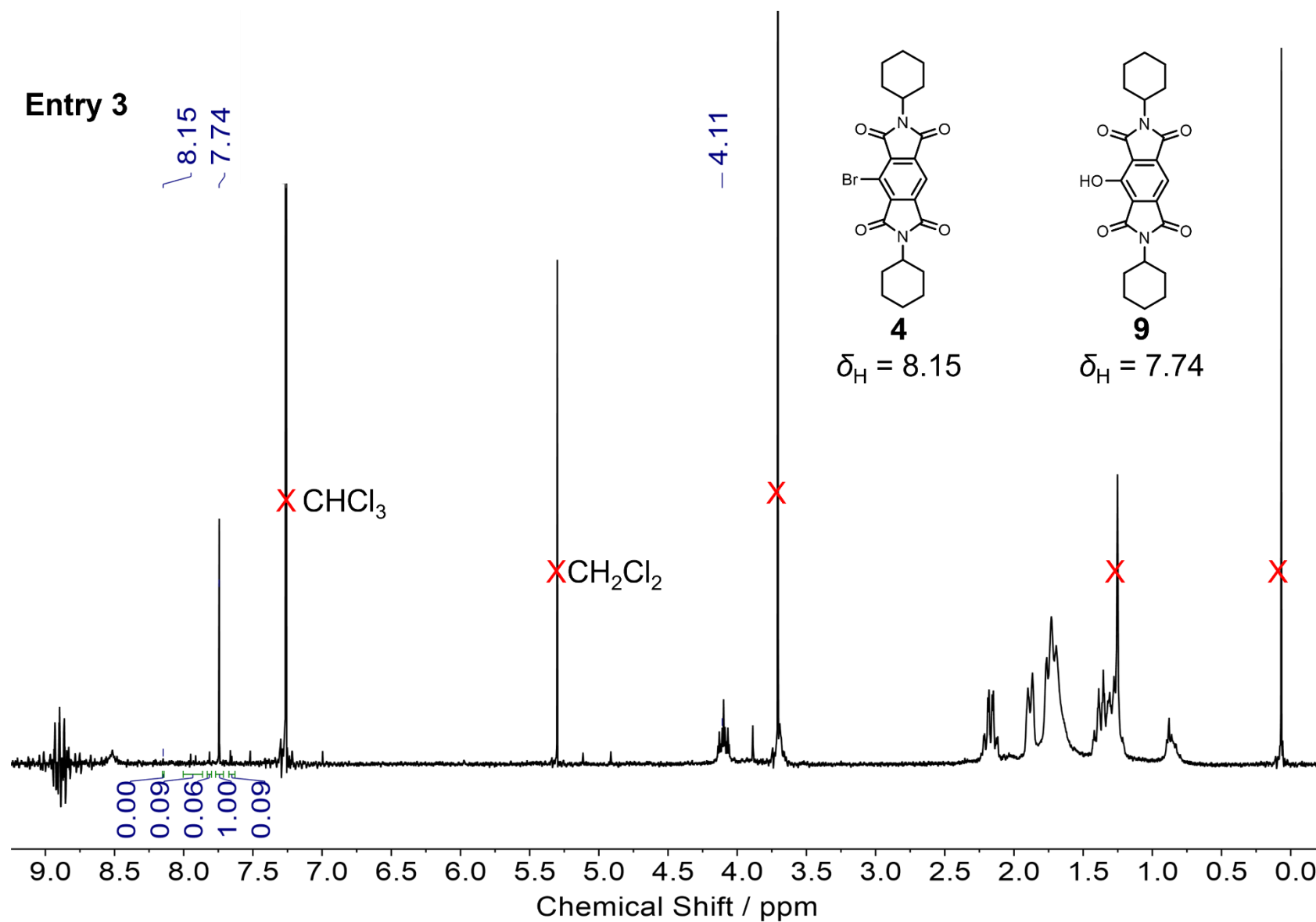


Figure S4.6 ^1H NMR (400 MHz, CDCl_3 , 298 K) spectrum of crude product containing mono-hydroxy **9** and mono-bromo **4** from the reaction discussed in Entry 3, Table 4.4.

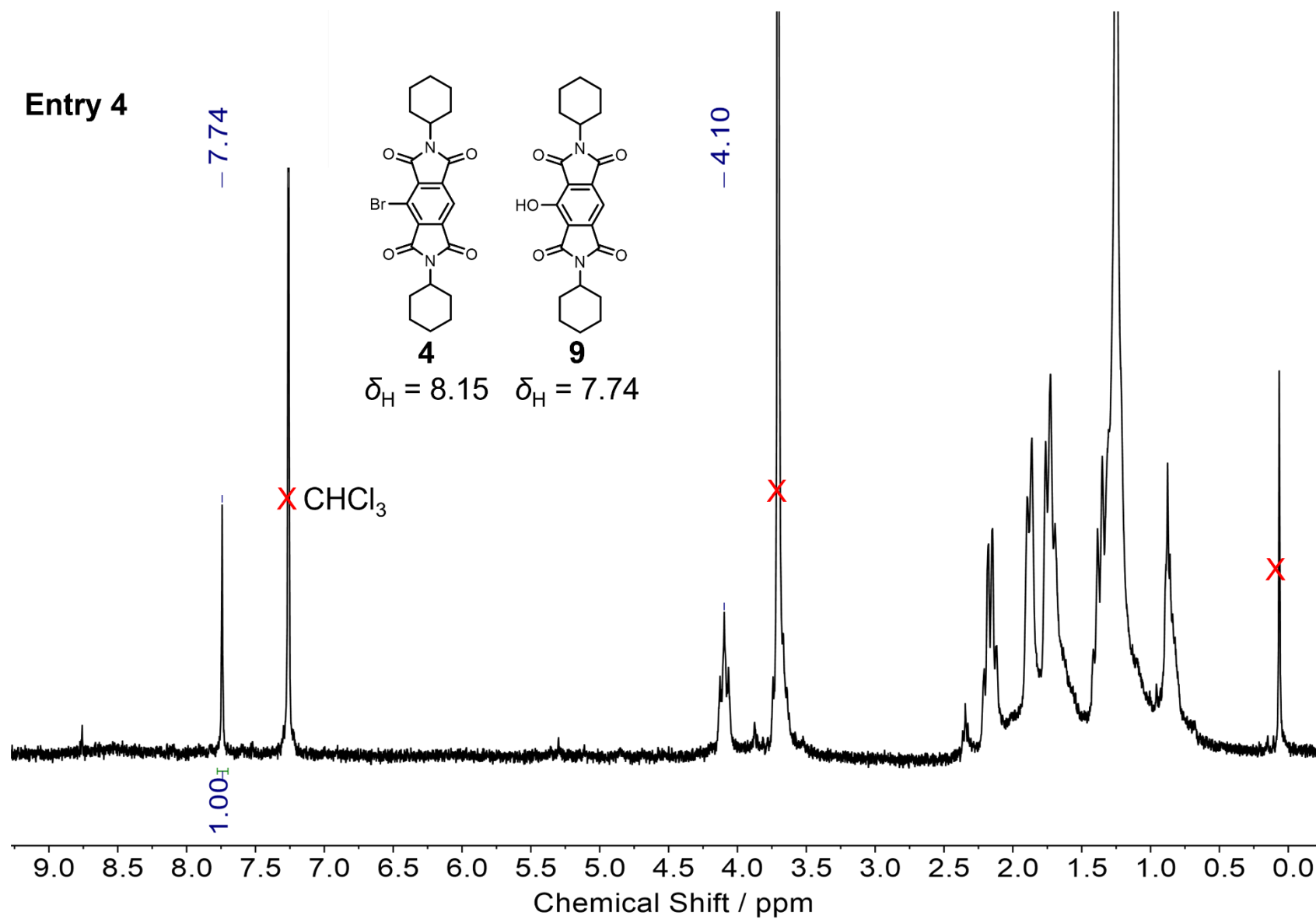


Figure S4.7 ^1H NMR (400 MHz, CDCl_3 , 298 K) spectrum of crude product containing mono-hydroxy **9** and mono-bromo **4** from the reaction discussed in Entry 4, Table 4.5.

Entry 5

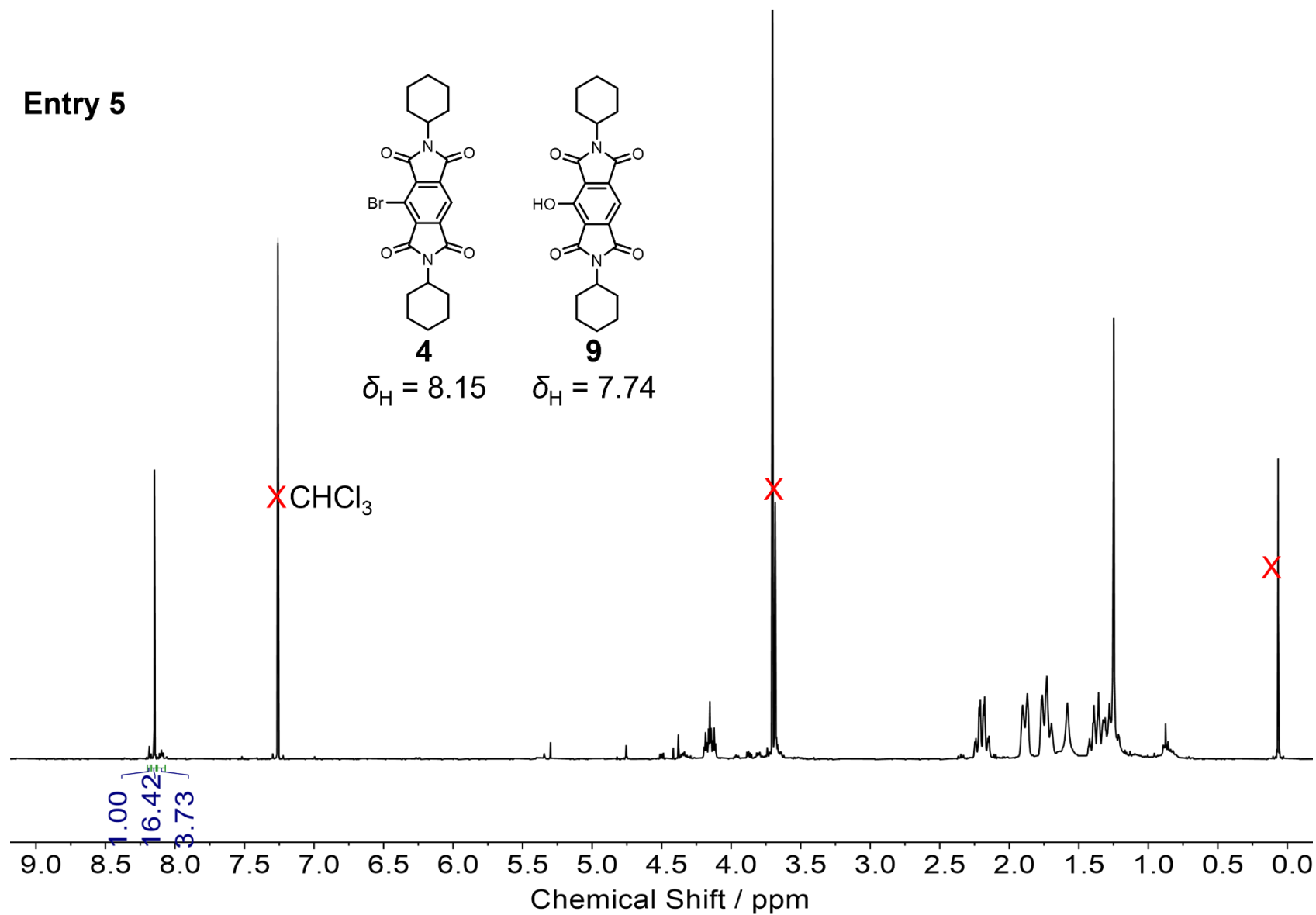


Figure S4.8 ^1H NMR (400 MHz, CDCl_3 , 298 K) spectrum of crude product containing mono-hydroxy **9** and mono-bromo **4** from the reaction discussed in Entry 5, Table 4.5.

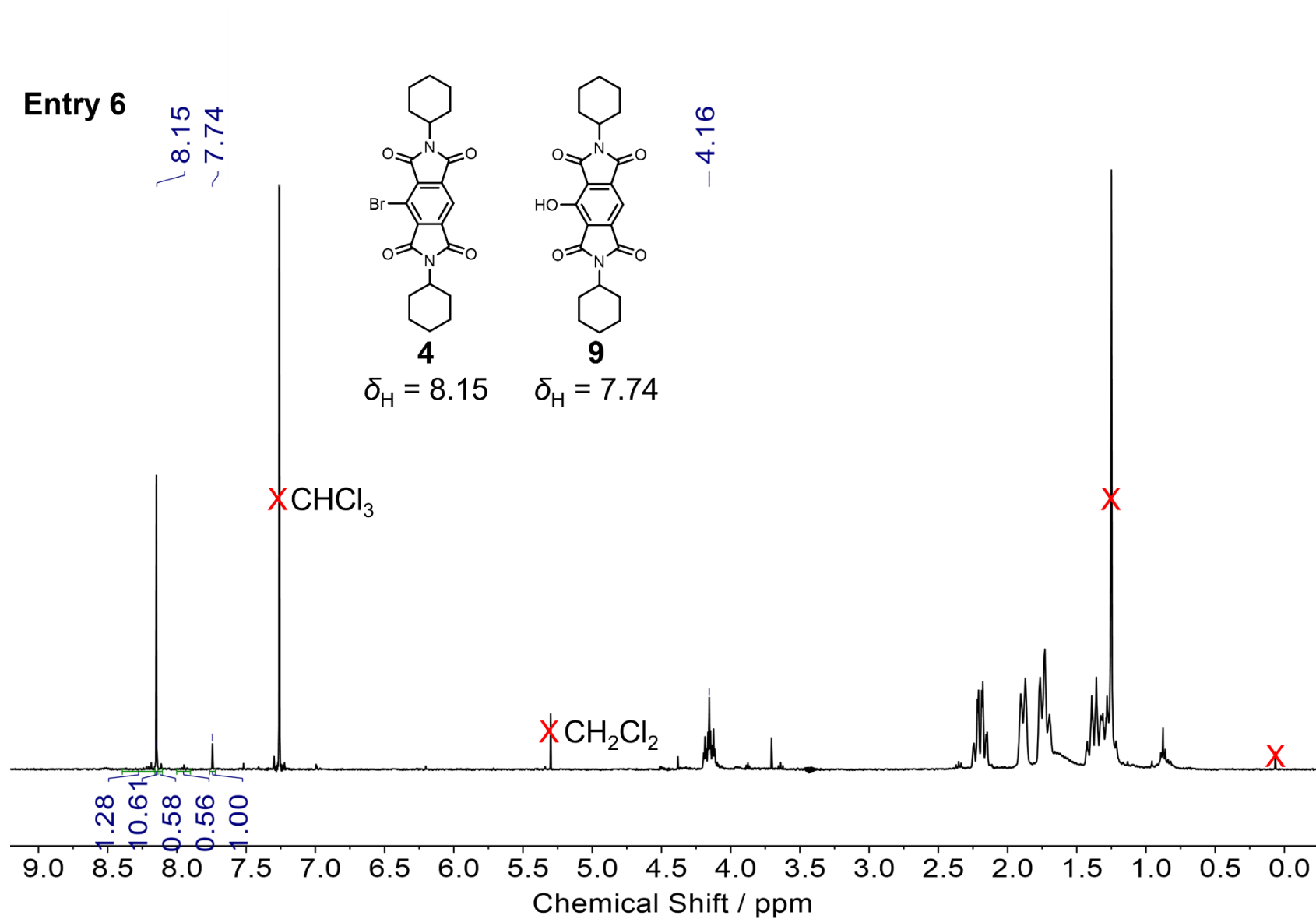


Figure S4.9 ^1H NMR (400 MHz, CDCl_3 , 298 K) spectrum of crude product containing mono-hydroxy **9** and mono-bromo **4** from the reaction discussed in Entry 6, Table 4.5.

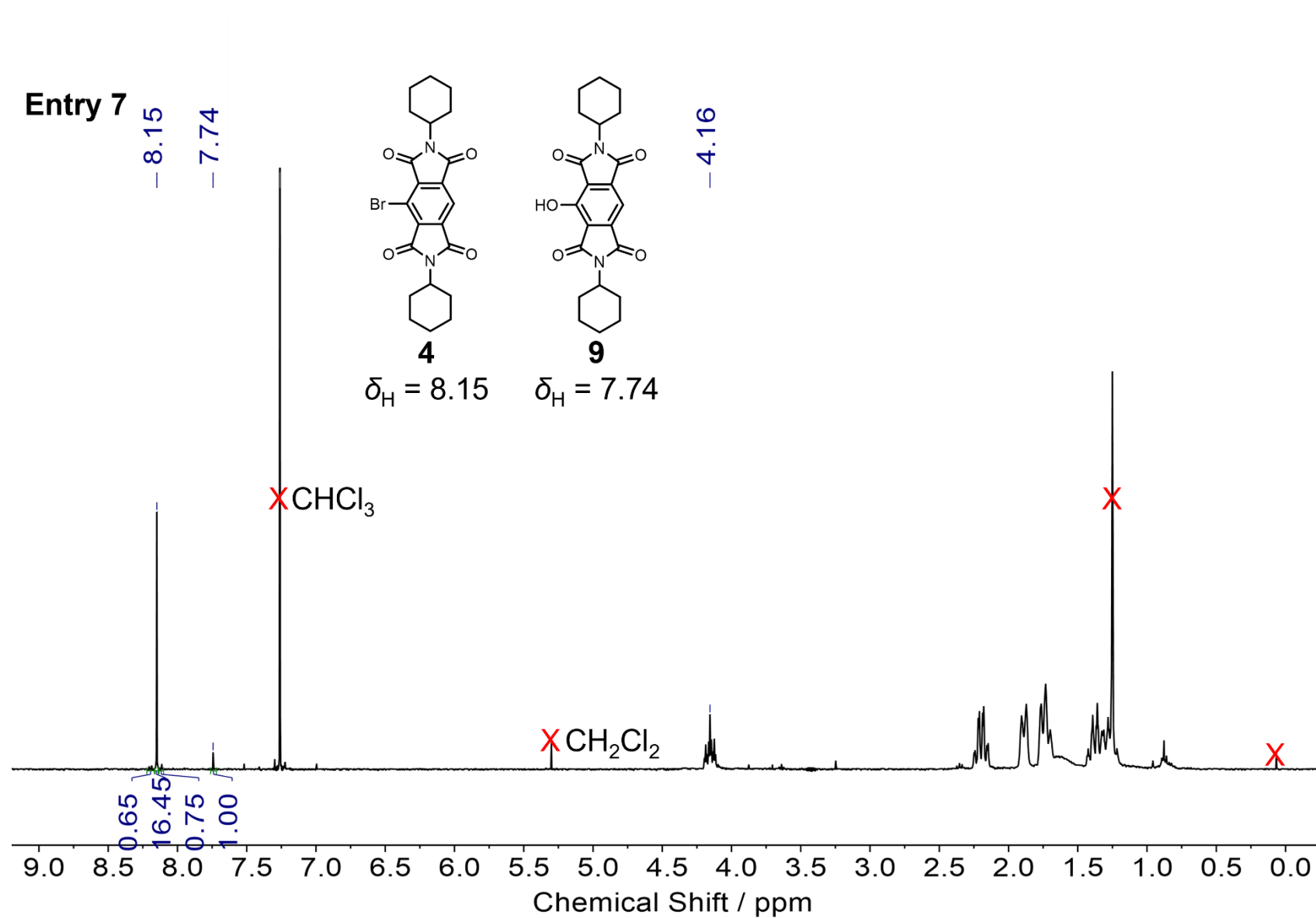


Figure S4.10 ^1H NMR (400 MHz, CDCl_3 , 298 K) spectrum of crude product containing mono-hydroxy **9** and mono-bromo **4** from the reaction discussed in Entry 7, Table 4.5.

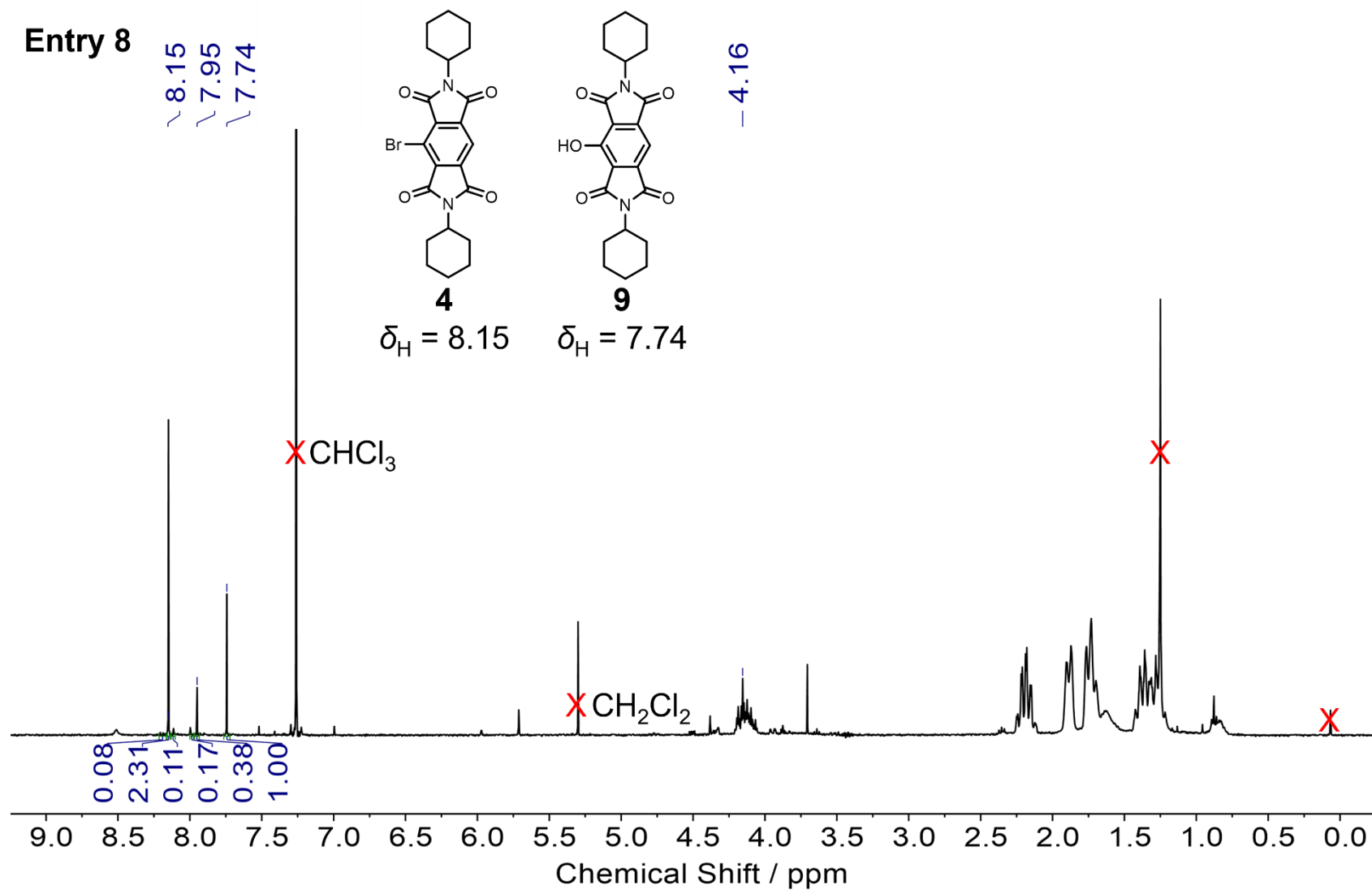


Figure S4.11 ¹H NMR (400 MHz, CDCl₃, 298 K) spectrum of crude product containing mono-hydroxy **9** and mono-bromo **4** from the reaction discussed in Entry 8, Table 4.5.

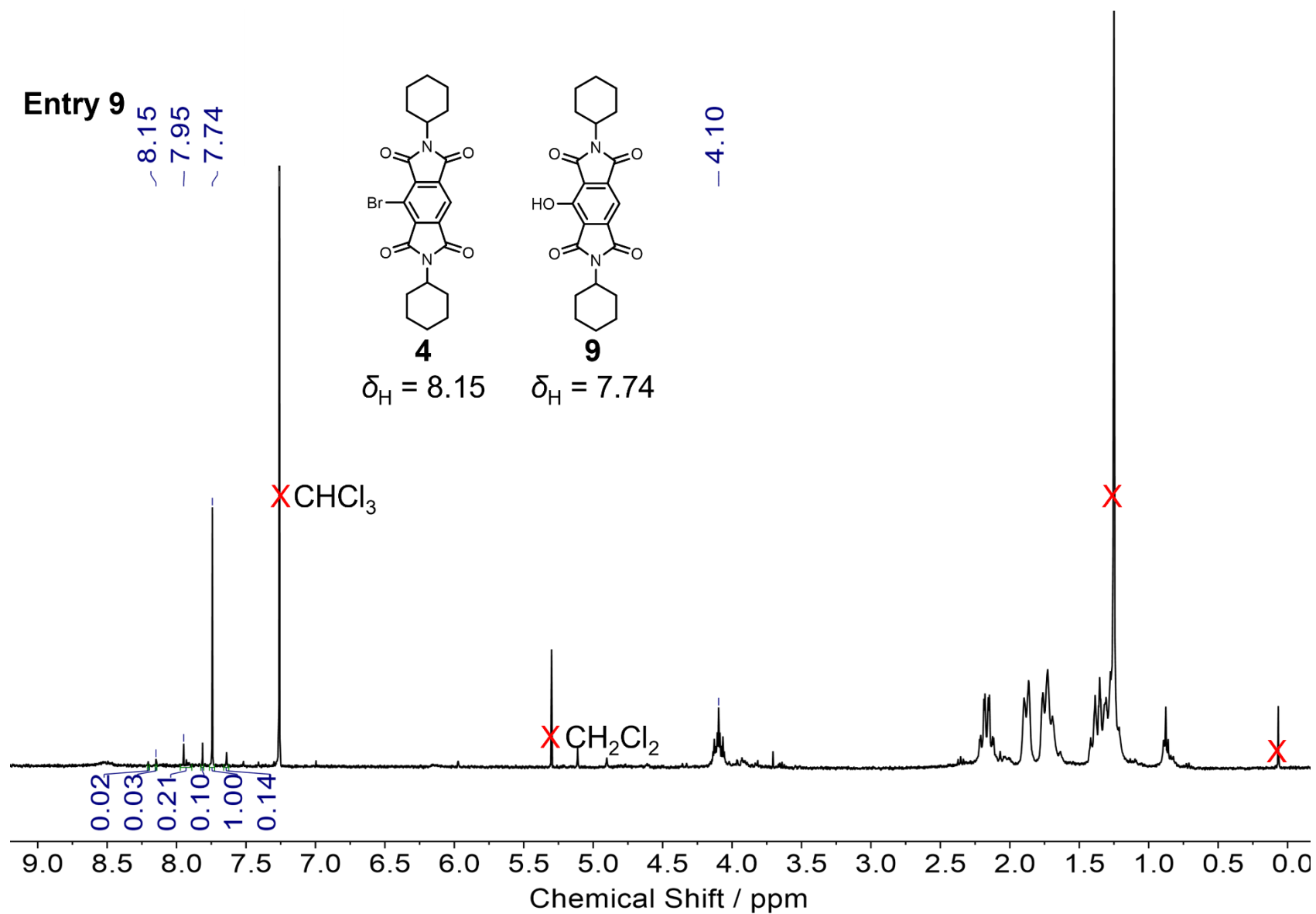


Figure S4.12 ¹H NMR (400 MHz, CDCl₃, 298 K) spectrum of crude product containing mono-hydroxy **9** and mono-bromo **4** from the reaction discussed in Entry 9, Table 4.6.

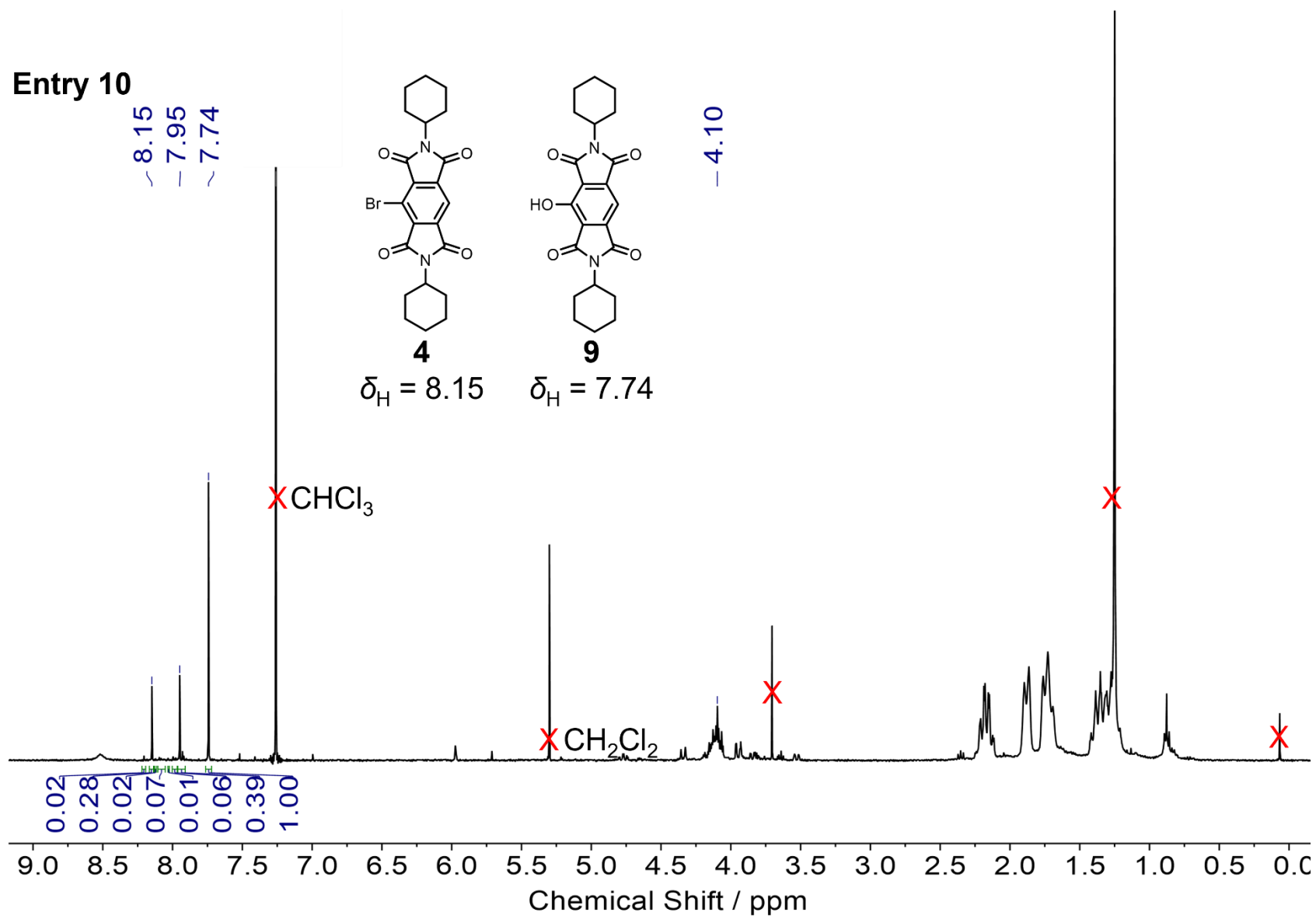


Figure S4.13 ¹H NMR (400 MHz, CDCl₃, 298 K) spectrum of crude product containing mono-hydroxy **9** and mono-bromo **4** from the reaction discussed in Entry 10, Table 4.6.

Entry 11

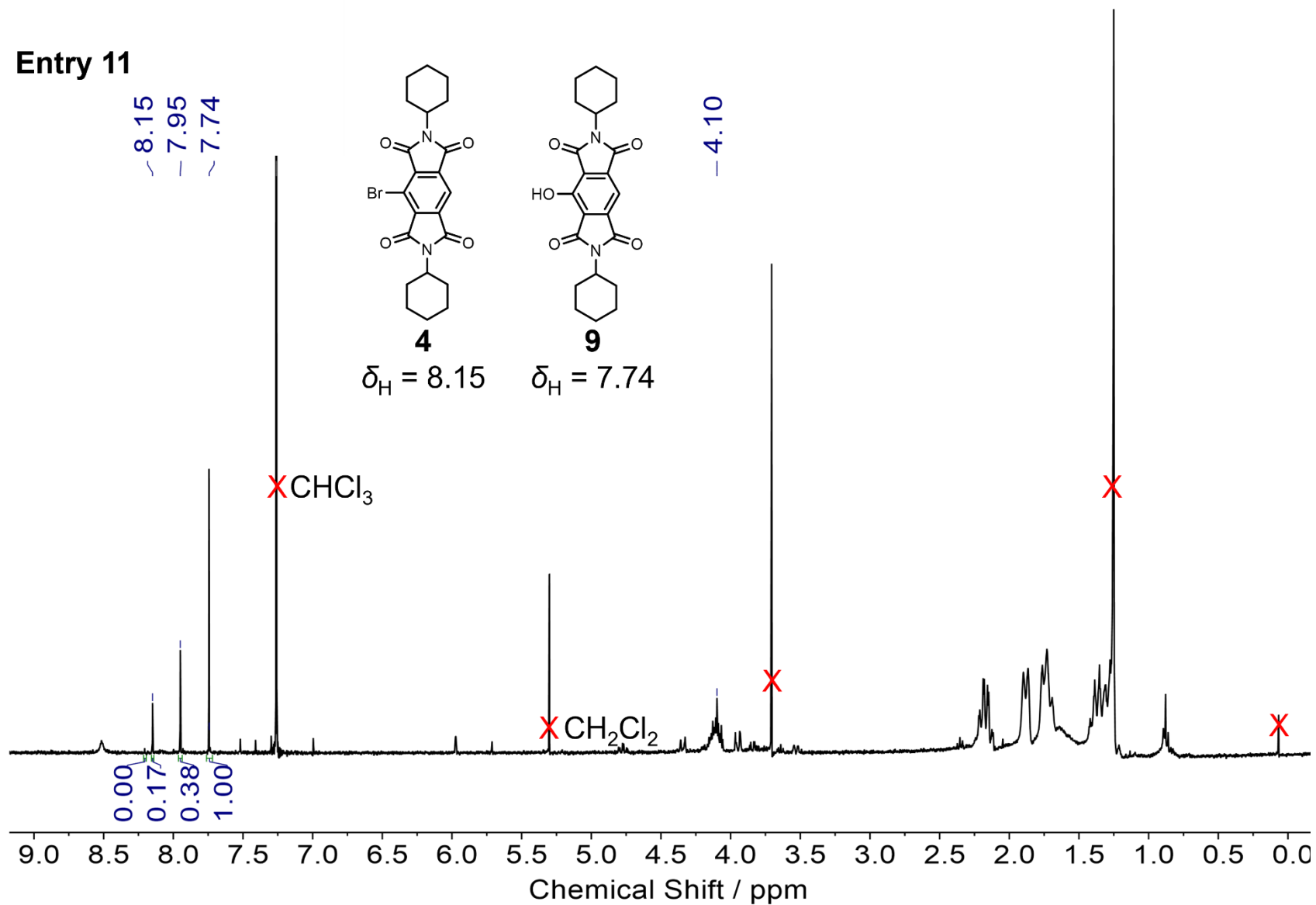


Figure S4.14 ^1H NMR (400 MHz, CDCl_3 , 298 K) spectrum of crude product containing mono-hydroxy **9** and mono-bromo **4** from the reaction discussed in Entry 11, Table 4.6.

Entry 12

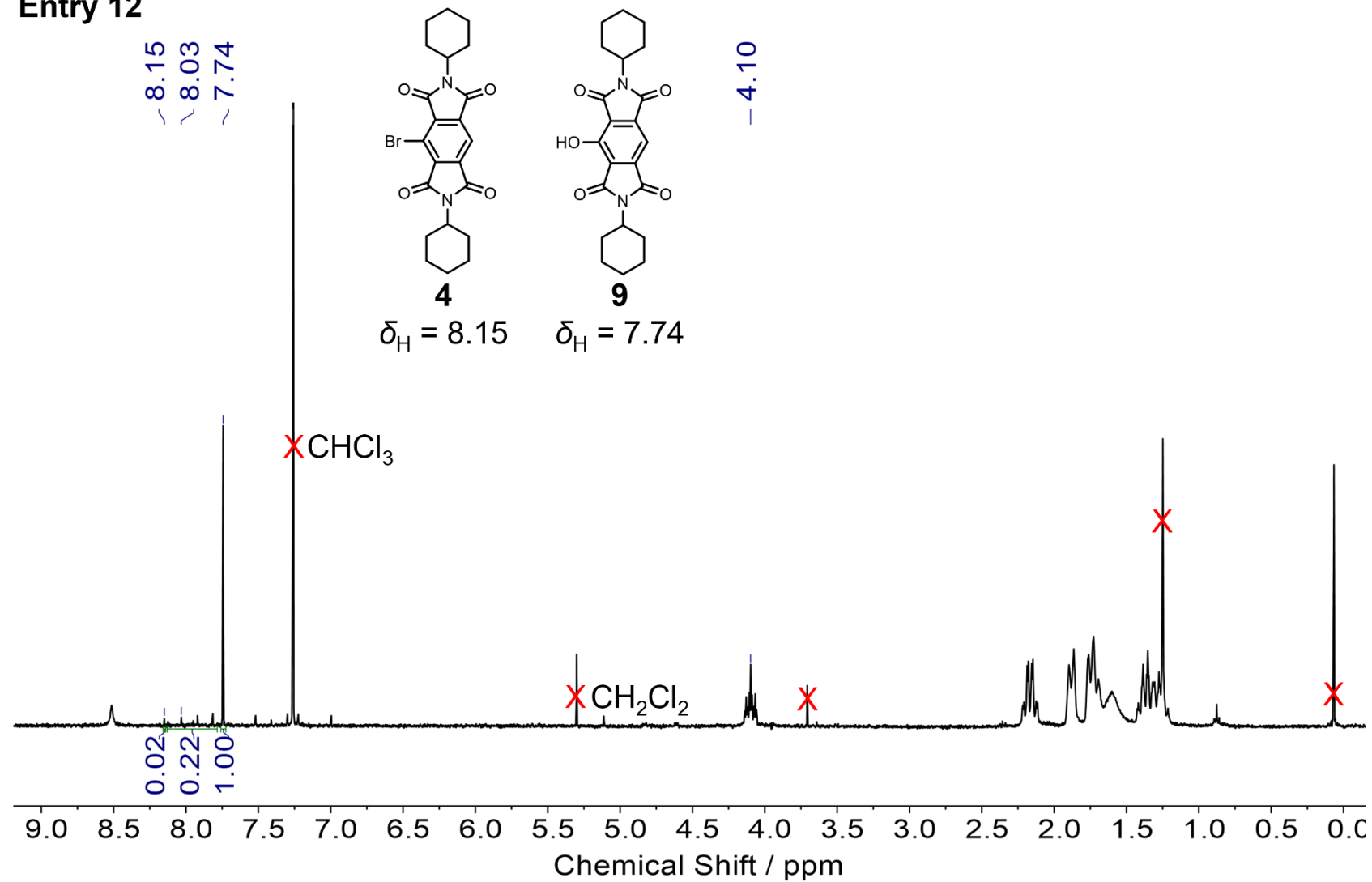


Figure 4.15 ^1H NMR (400 MHz, CDCl_3 , 298 K) spectrum of crude product containing mono-hydroxy **9** and mono-bromo **4** from the reaction discussed in Entry 12, Table 4.7.

Entry 13

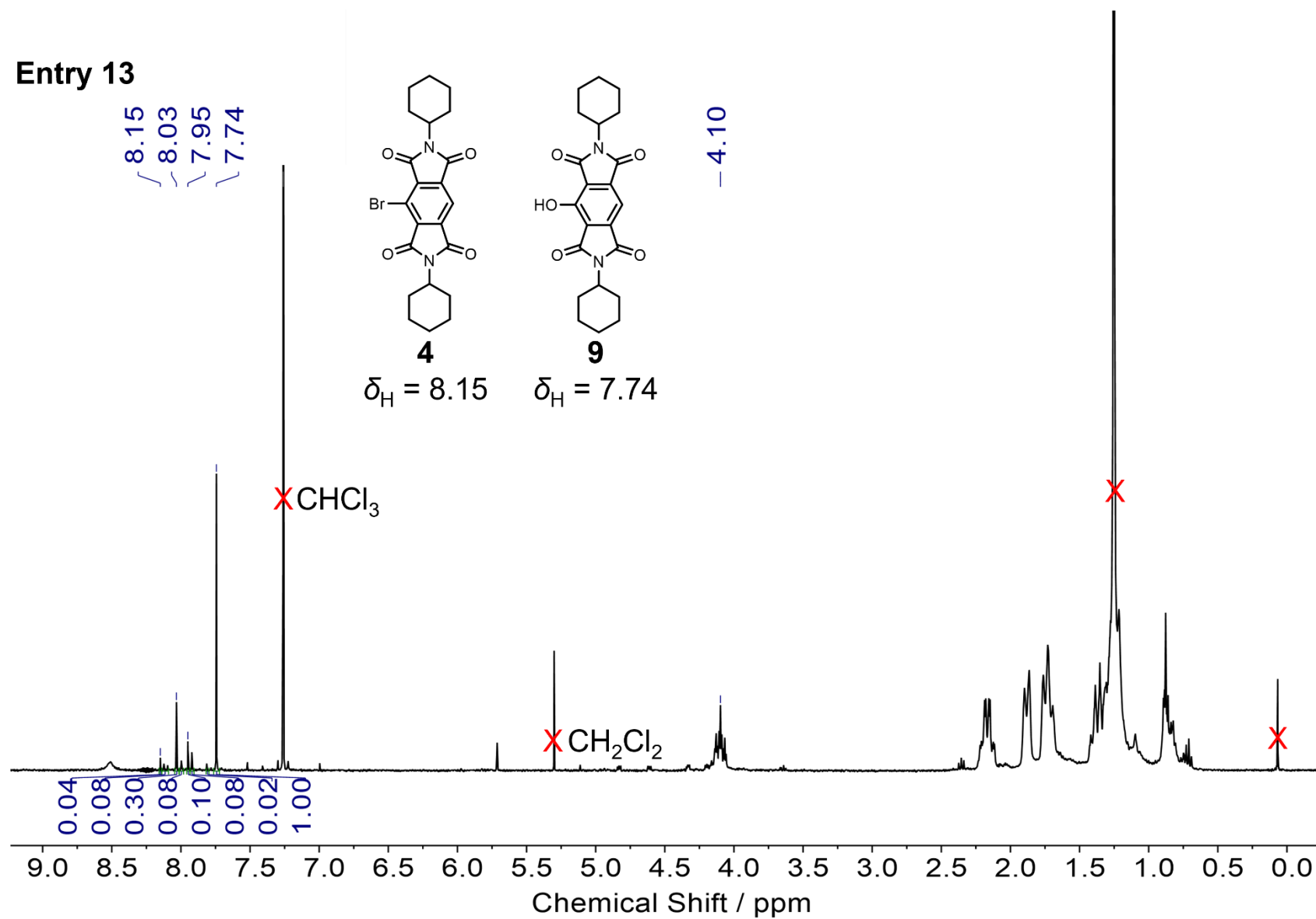


Figure S4.16 ^1H NMR (400 MHz, CDCl_3 , 298 K) spectrum of crude product containing mono-hydroxy **9** and mono-bromo **4** from the reaction discussed in Entry 13, Table 4.7.

Entry 14

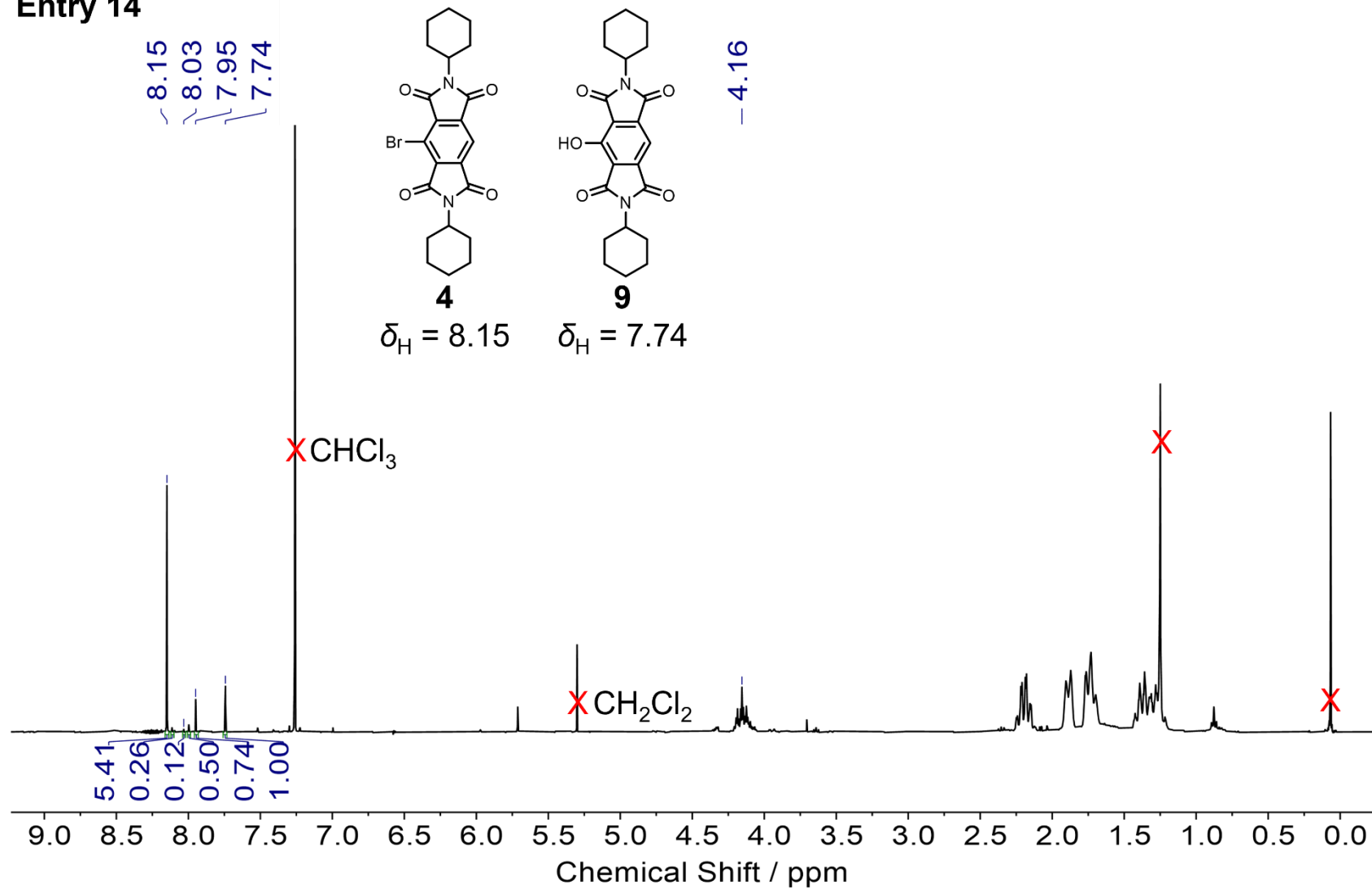


Figure S4.17 ^1H NMR (400 MHz, CDCl_3 , 298 K) spectrum of crude product containing mono-hydroxy **9** and mono-bromo **4** from the reaction discussed in Entry 14, Table 4.7.

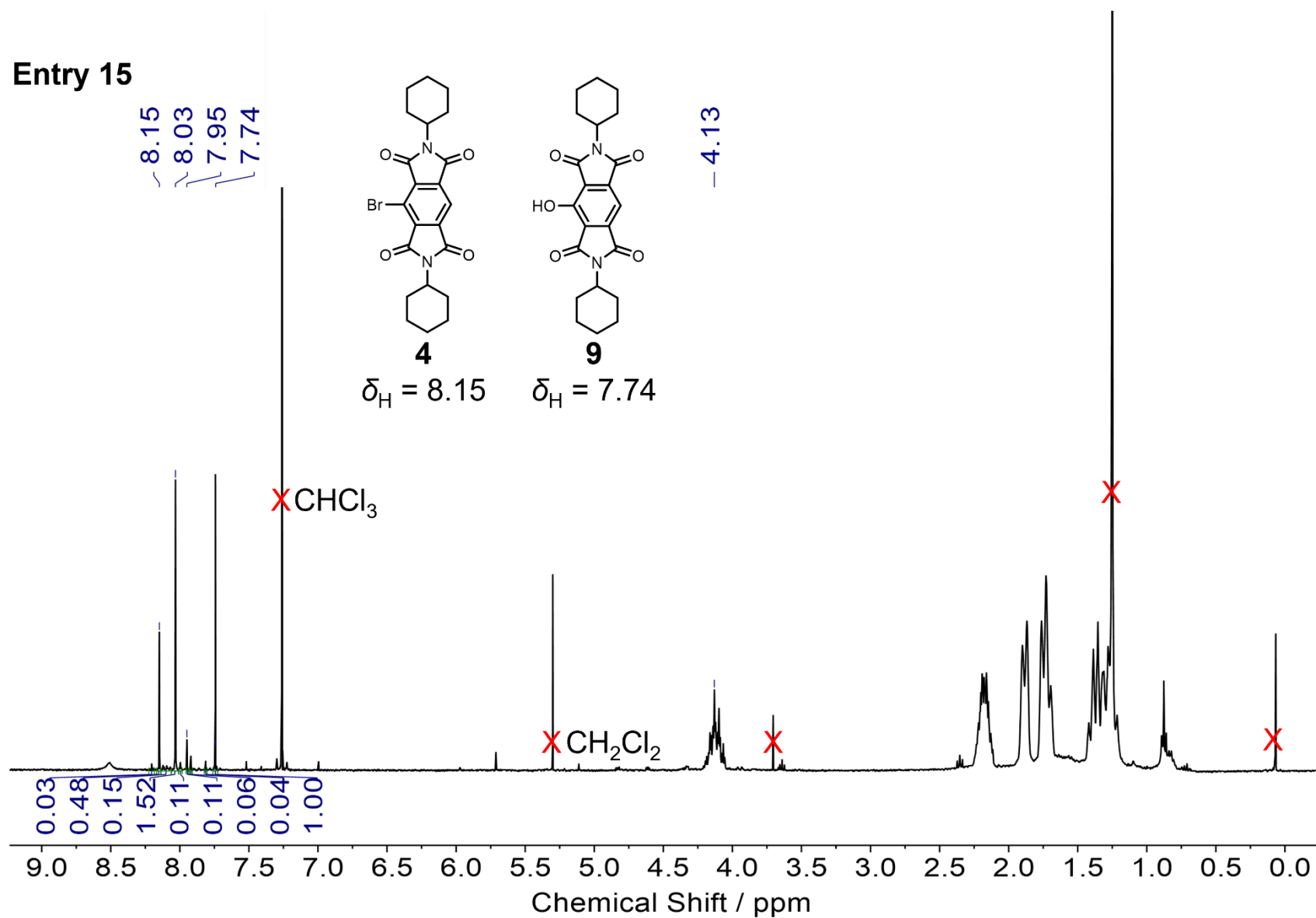


Figure S4.18 ^1H NMR (400 MHz, CDCl_3 , 298 K) spectrum of crude product containing mono-hydroxy **9** and mono-bromo **4** from the reaction discussed in Entry 15, Table 4.7.

Entry 16

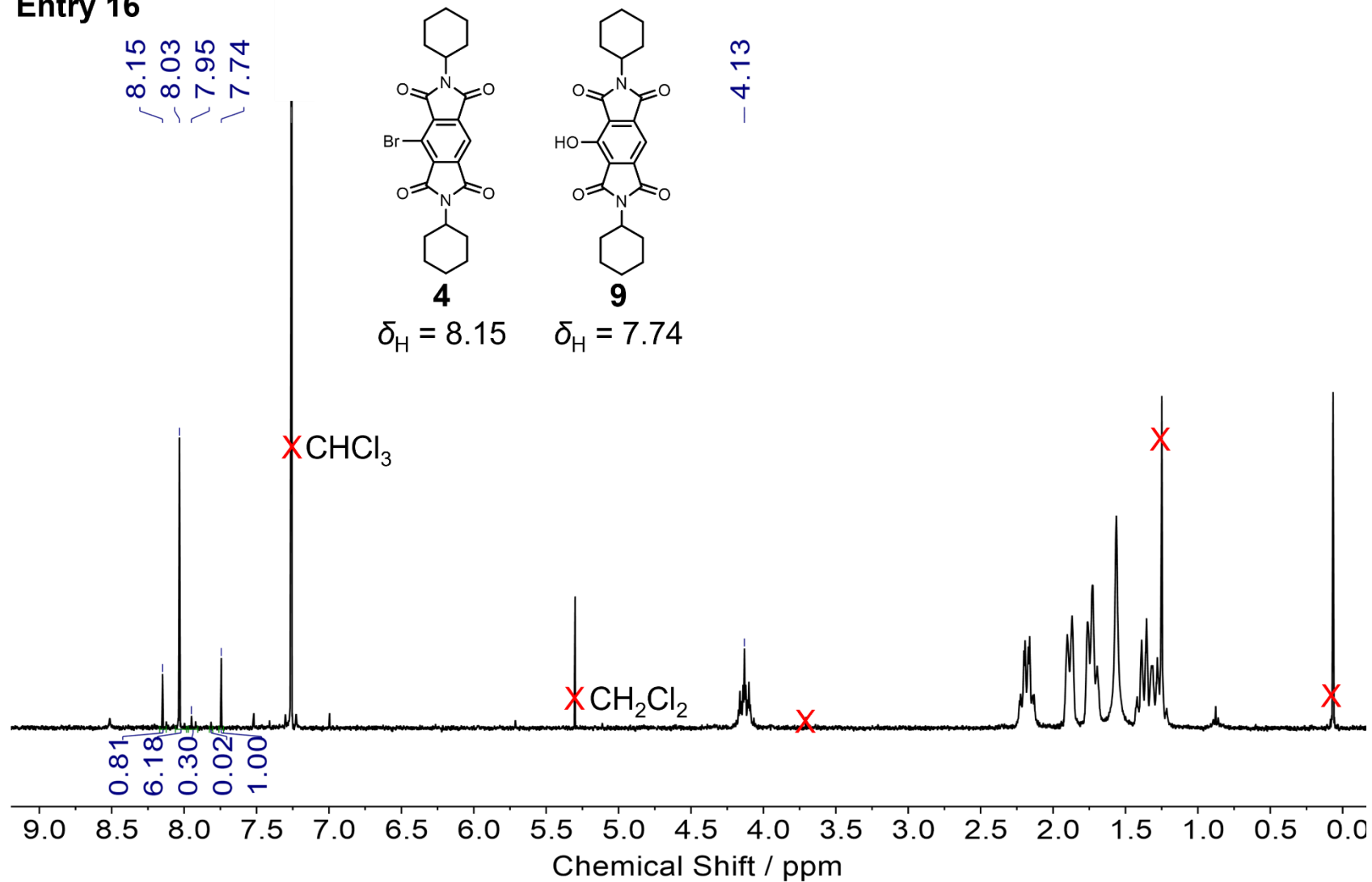


Figure S4.19 ^1H NMR (400 MHz, CDCl_3 , 298 K) spectrum of crude product containing mono-hydroxy **9** and mono-bromo **4** from the reaction discussed in Entry 16, Table 4.8.

Entry 17

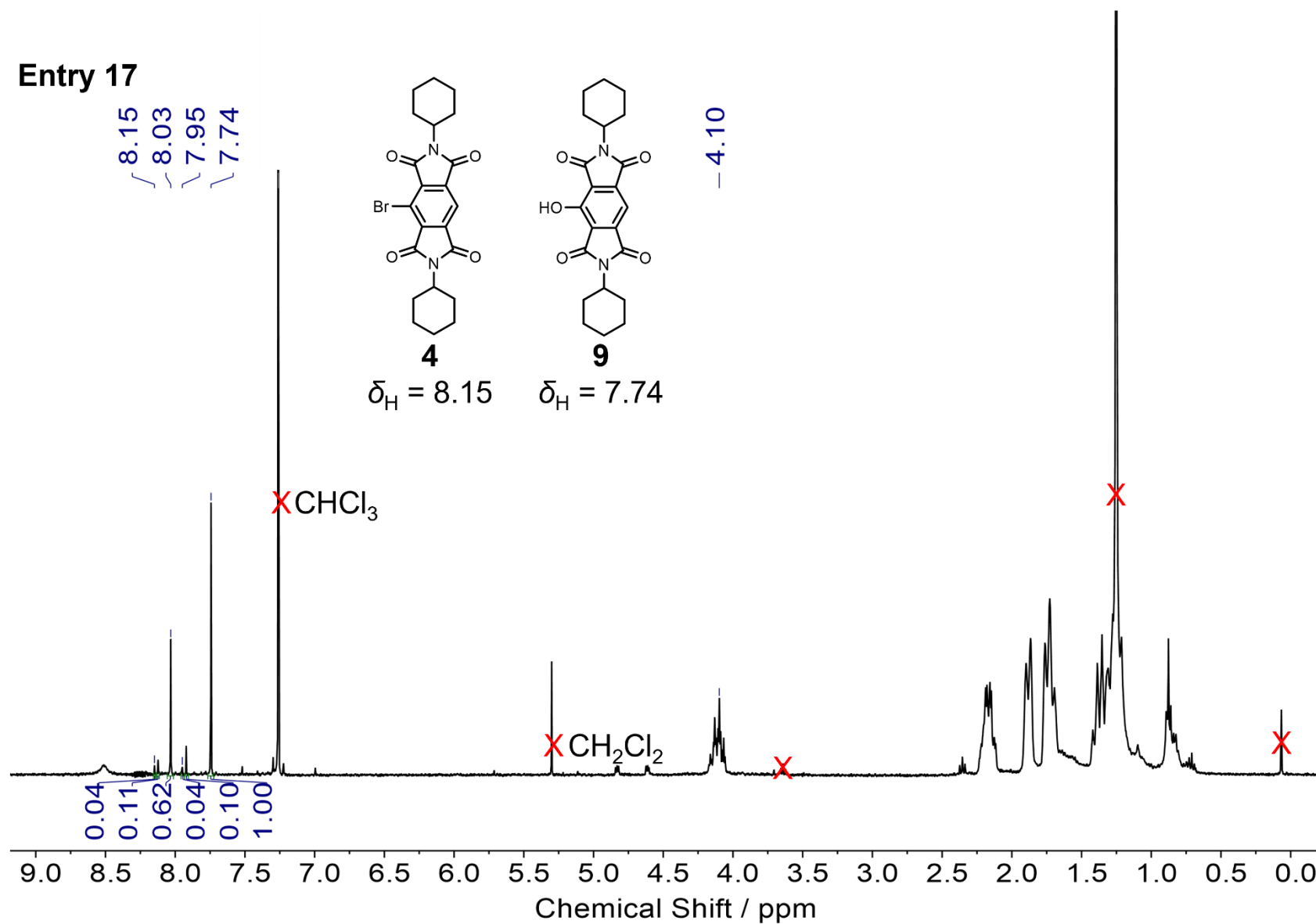


Figure S4.20 ^1H NMR (400 MHz, CDCl_3 , 298 K) spectrum of crude product containing mono-hydroxy **9** and mono-bromo **4** from the reaction discussed in Entry 17, Table 4.8.

Entry 18

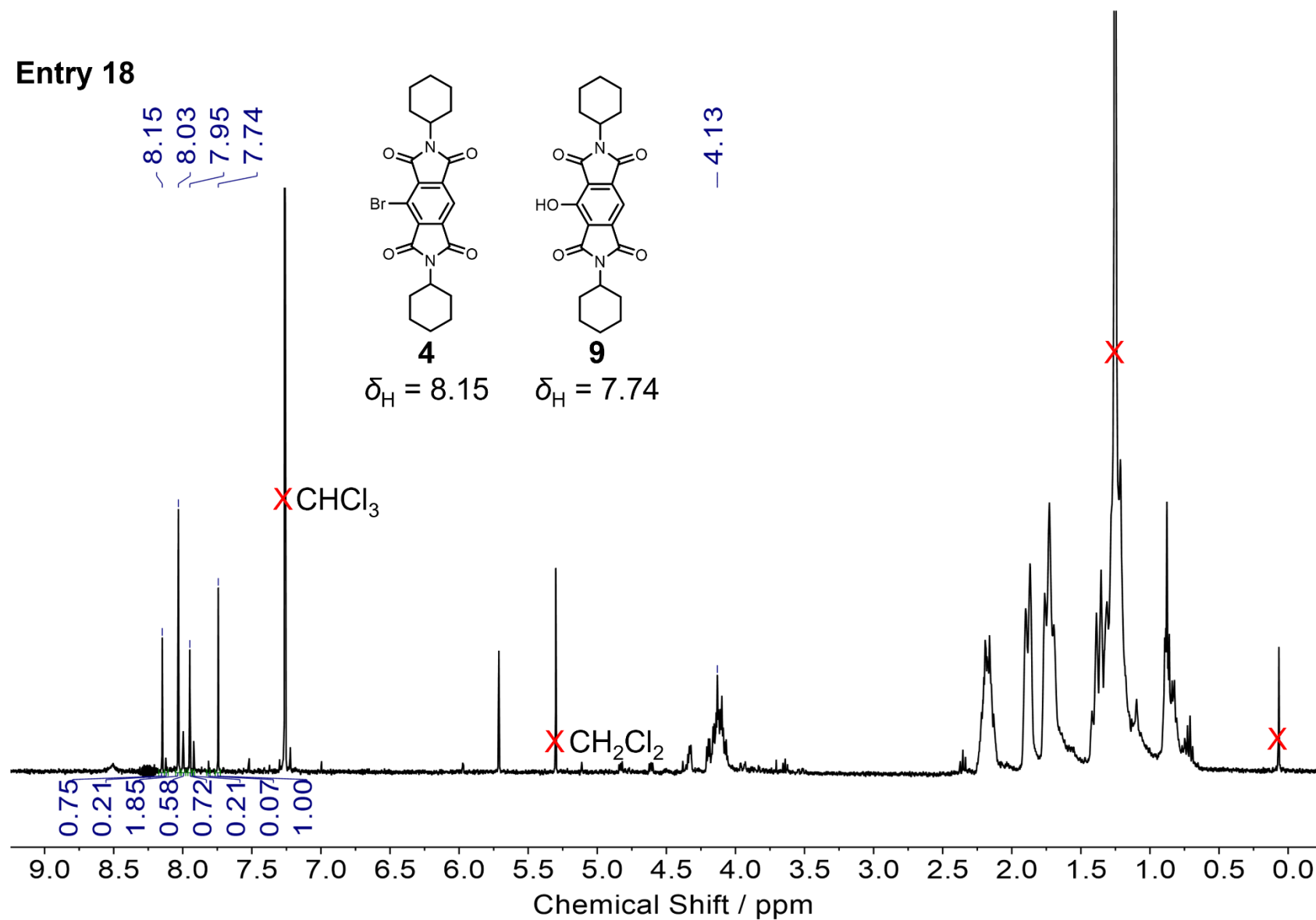


Figure S4.21 ^1H NMR (400 MHz, CDCl_3 , 298 K) spectrum of crude product containing mono-hydroxy **9** and mono-bromo **4** from the reaction discussed in Entry 18, Table 4.8.

Entry 19

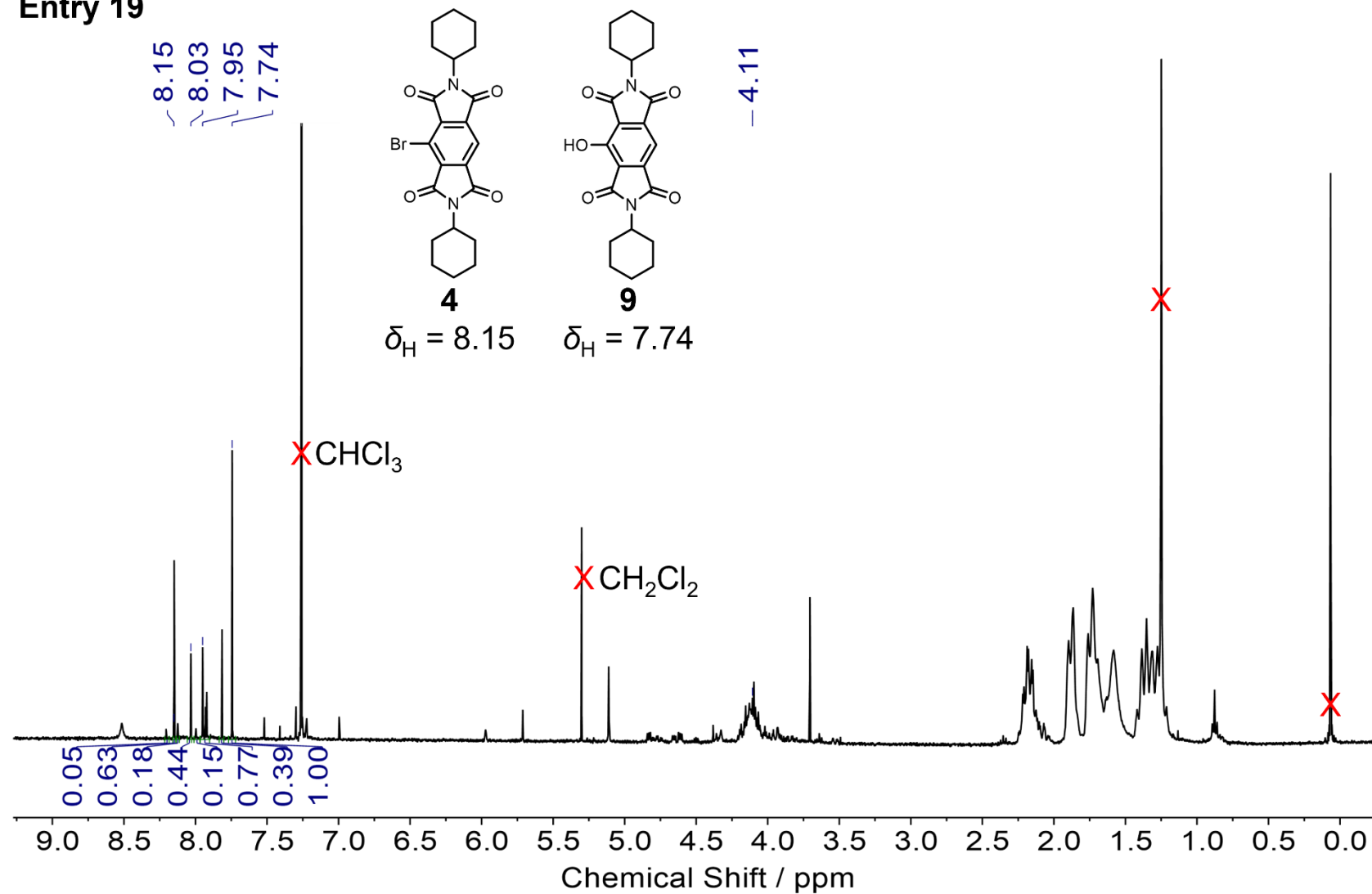


Figure S4.22 ^1H NMR (400 MHz, CDCl_3 , 298 K) spectrum of crude product containing mono-hydroxy **9** and mono-bromo **4** from the reaction discussed in Entry 19, Table 4.8.

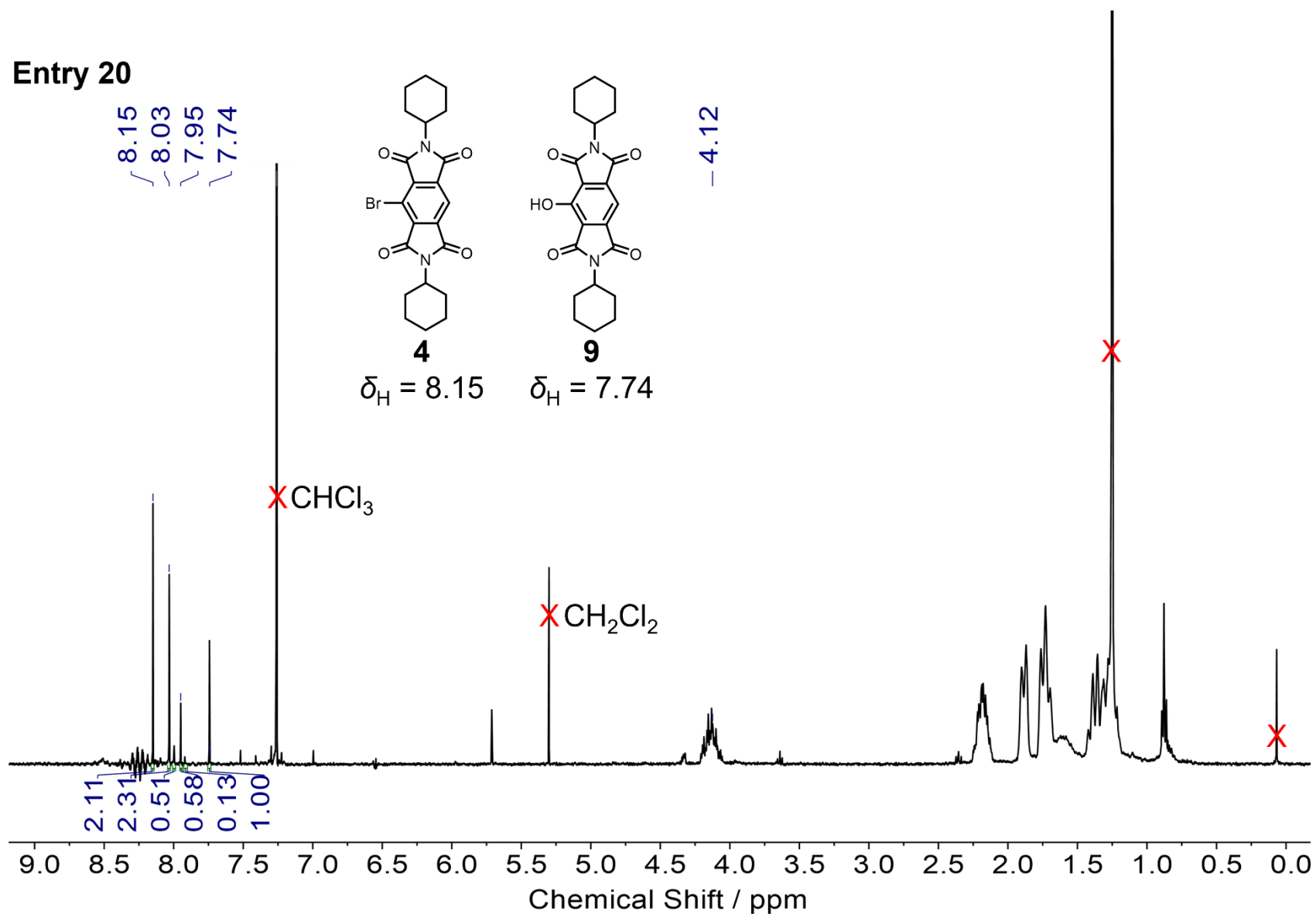


Figure S4.23 ^1H NMR (400 MHz, CDCl_3 , 298 K) spectrum of crude product containing mono-hydroxy **9** and mono-bromo **4** from the reaction discussed in Entry 20, Table 4.8.

Entry 21

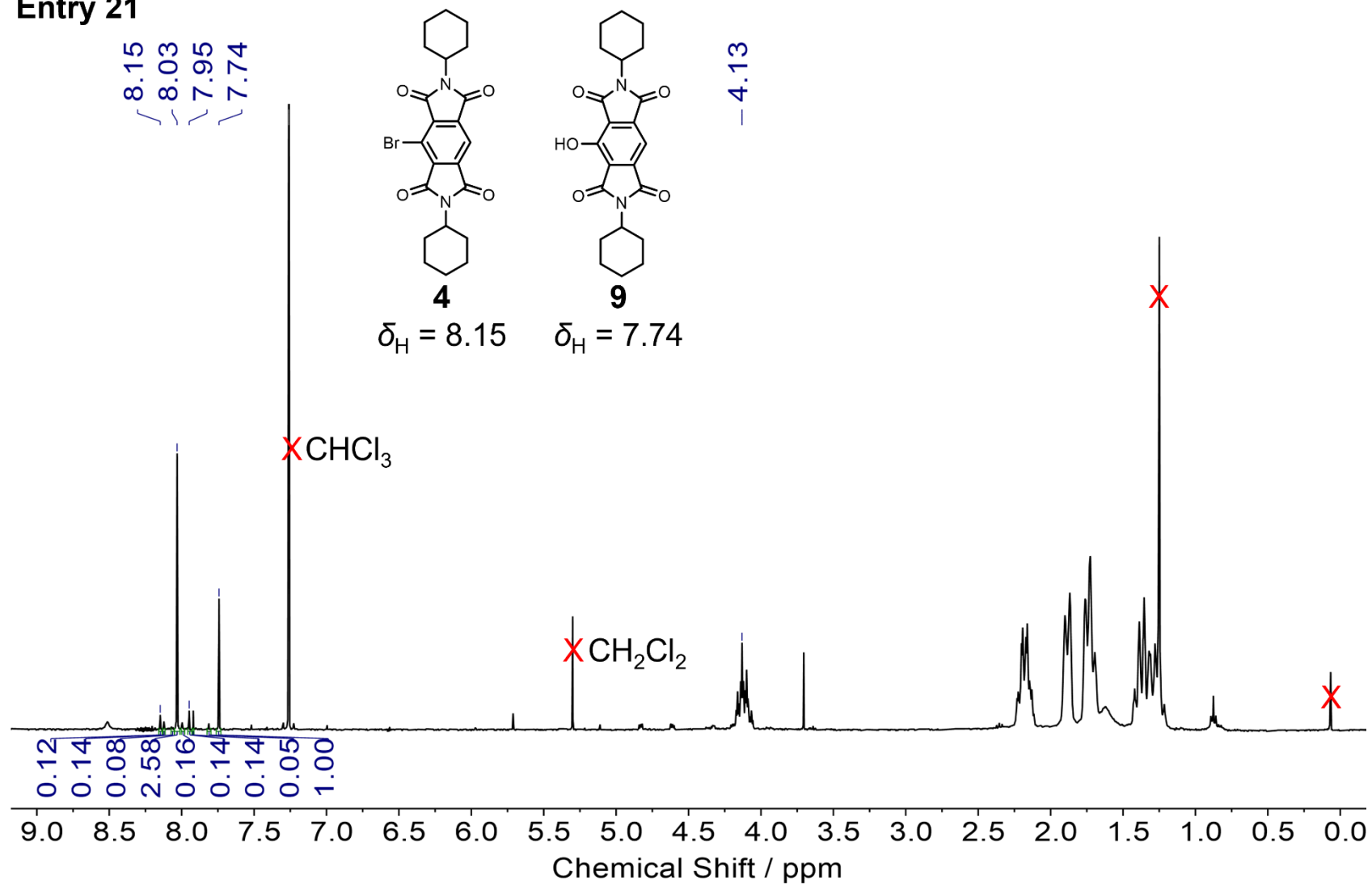


Figure S4.24 ^1H NMR (400 MHz, CDCl_3 , 298 K) spectrum of crude product containing mono-hydroxy **9** and mono-bromo **4** from the reaction discussed in Entry 21, Table 4.8.

4.5 REFERENCES

- (1) Gao, P.; Pan, W.; Li, N.; Tang, B. Fluorescent Probes for Organelle-Targeted Bioactive Species Imaging. *Chem. Sci.* **2019**, *10*, 6035–6071.
- (2) Hong, G.; Gan, X.; Leonhardt, C.; Zhang, Z.; Seibert, J.; Busch, J. M.; Bräse, S. A Brief History of OLEDs—Emitter Development and Industry Milestones. *Adv. Mater.* **2021**, *33*, 2005630.
- (3) Beer, P. D.; Barendt, T. A.; Lim, J. Y. C. *Supramolecular Chemistry: Fundamentals and Applications*; Oxford University Press, 2022.
- (4) Sun, H.; Zhu, L. Achieving Purely Organic Room Temperature Phosphorescence in Aqueous Solution. *Aggregate* **2023**, *4*, e253.
- (5) Czarnik, A. W. Supramolecular Chemistry, Fluorescence, and Sensing. In *Fluorescent Chemosensors for Ion and Molecule Recognition*; ACS Symposium Series; American Chemical Society, 1993; Vol. 538, pp 1–9.
- (6) Luo, J.; Xie, Z.; Lam, J. W. Y.; Cheng, L.; Tang, B. Z.; Chen, H.; Qiu, C.; Kwok, H. S.; Zhan, X.; Liu, Y.; Zhu, D. Aggregation-Induced Emission of 1-Methyl-1,2,3,4,5-Pentaphenylsilole. *Chem. Commun.* **2001**, 1740–1741.
- (7) Kanosue, K.; Ando, S. Polyimides with Heavy Halogens Exhibiting Room-Temperature Phosphorescence with Very Large Stokes Shifts. *ACS Macro Lett.* **2016**, *5*, 1301–1305.
- (8) Garain, S.; Kuila, S.; Garain, B. C.; Kataria, M.; Borah, A.; Pati, S. K.; George, S. J. Arylene Diimide Phosphors: Aggregation Modulated Twin Room Temperature Phosphorescence from Pyromellitic Diimides. *Angew. Chem. Int. Ed.* **2021**, *60*, 12323–12327.
- (9) Kuila, S.; Garain, S.; Banappanavar, G.; Garain, B. C.; Kabra, D.; Pati, S. K.; George, S. J. Ambient Room Temperature Phosphorescence and Thermally Activated Delayed Fluorescence from a Core-Substituted Pyromellitic Diimide Derivative. *J. Phys. Chem. B* **2021**, *125*, 4520–4526.
- (10) Kanosue, K.; Shimosaka, T.; Wakita, J.; Ando, S. Polyimide and Imide Compound Exhibiting Bright Red Fluorescence with Very Large Stokes Shifts via Excited-State Intramolecular Proton Transfer. *Macromolecules* **2015**, *48*, 1777–1785.
- (11) Kanosue, K.; Augulis, R.; Peckus, D.; Karpicz, R.; Tamulevičius, T.; Tamulevičius, S.; Gulbinas, V.; Ando, S. Polyimide and Imide Compound Exhibiting Bright Red Fluorescence with Very Large Stokes Shifts via Excited-State Intramolecular Proton Transfer II. Ultrafast Proton Transfer Dynamics in the Excited State. *Macromolecules* **2016**, *49*, 1848–1857.
- (12) Garain, S.; Sarkar, S.; Chandra Garain, B.; Pati, S. K.; George, S. J. Chiral Arylene Diimide Phosphors: Circularly Polarized Ambient Phosphorescence from Bischromophoric Pyromellitic Diimides. *Angew. Chem. Int. Ed.* **2022**, *61*, e202115773.
- (13) Suraru, S.-L.; Würthner, F. Strategies for the Synthesis of Functional Naphthalene Diimides. *Angew. Chem. Int. Ed.* **2014**, *53*, 7428–7448.
- (14) Würthner, F.; Ahmed, S.; Thalacker, C.; Debaerdemaeker, T. Core-Substituted Naphthalene Bisimides: New Fluorophors with Tunable Emission Wavelength for FRET Studies. *Chem. – Eur. J.* **2002**, *8*, 4742–4750.
- (15) Würthner, F. Perylene Bisimide Dyes as Versatile Building Blocks for Functional Supramolecular Architectures. *Chem Commun* **2004**, 1564–1579.

- (16) Langhals, H.; Karolin, J.; Johansson, L. B.-Å. Spectroscopic Properties of New and Convenient Standards for Measuring Fluorescence Quantum Yields. *J. Chem. Soc. Faraday Trans.* **1998**, *94*, 2919–2922.
- (17) Mohan Nalluri, S. K.; Zhou, J.; Cheng, T.; Liu, Z.; Nguyen, M. T.; Chen, T.; Patel, H. A.; Krzyaniak, M. D.; Goddard, W. A. I.; Wasielewski, M. R.; Stoddart, J. F. Discrete Dimers of Redox-Active and Fluorescent Perylene Diimide-Based Rigid Isosceles Triangles in the Solid State. *J. Am. Chem. Soc.* **2019**, *141*, 1290–1303.
- (18) Tam, T. L. D.; Xu, J. W. The Role of Fluoride in Anion– π Interaction with Naphthalene Diimide. *Chem. Commun.* **2019**, *55*, 6225–6228.
- (19) Zhang, J.; Liu, J.; Yin, G.; Hou, W.; Zhang, H. Photoinduced Nucleophilic Substitution Reaction of 1,7-Dibromo-Perylene Diimide to Form 1-Bromo-7-Hydroxyl Perylene Diimide. *Tetrahedron* **2023**, *134*, 133319.
- (20) Dong, D.; Yin, G.; Hou, W.; Dong, D.; Zhang, C.; Liu, L.; Liang, B.; Zhang, H. Perylene Diimide Radical Anion Constructed by Hydrogen Bonds and Its Colorimetric Chemodosimeter for the Rapid Detection of Fe³⁺. *J. Mol. Struct.* **2021**, *1224*, 129038.
- (21) Wang, Y.; Wu, H.; Stoddart, J. F. Molecular Triangles: A New Class of Macrocycles. *Acc. Chem. Res.* **2021**, *54*, 2027–2039.
- (22) Saha, S. Anion-Induced Electron Transfer. *Acc. Chem. Res.* **2018**, *51*, 2225–2236.
- (23) Guha, S.; Goodson, F. S.; Corson, L. J.; Saha, S. Boundaries of Anion/Naphthalenediimide Interactions: From Anion– π Interactions to Anion-Induced Charge-Transfer and Electron-Transfer Phenomena. *J. Am. Chem. Soc.* **2012**, *134*, 13679–13691.
- (24) Yuan, Z.; Ma, Y.; Geßner, T.; Li, M.; Chen, L.; Eustachi, M.; Weitz, R. T.; Li, C.; Müllen, K. Core-Fluorinated Naphthalene Diimides: Synthesis, Characterization, and Application in n-Type Organic Field-Effect Transistors. *Org. Lett.* **2016**, *18*, 456–459.

CHAPTER 5 |

REDOX-ACTIVE MACROCYCLES FOR POROUS,
THIN-FILM ORGANIC SEMICONDUCTORS

SYNOPSIS

The increasing demand for electronic devices and continually advancing technologies requires electro-active materials to be (i) low costing, (ii) lightweight and (iii) readily available. These requirements have been sought to be addressed by the development of organic semiconducting devices containing electron-rich *p*-type and/or electron-deficient *n*-type materials. Aromatic diimides have been studied for application as *n*-type organic semiconductors on account of their ability to accept two electrons and assemble in different morphologies to optimise $\pi \cdots \pi$ interactions. Furthermore, unsubstituted molecular triangles based on aromatic diimides have previously been studied for potential applications as optical materials and cathodic materials in lithium-ion batteries. In Chapters 2, 3 and 4, the effects of core-substitution on the fundamental structural and optoelectronic properties of molecular triangles were described with the resulting ability of core-functionalised molecular triangles to (i) assemble in crystalline frameworks, (ii) accept electrons and (iii) encapsulate electron-rich guests envisioned to make them suitable compounds for use as *n*-type organic semiconductors for application in ion-gated transistors or photovoltaic devices. This Chapter details the initial experiments conducted during a two-month Japan Society for the Promotion of Science (JSPS) Summer PhD Exchange Fellowship which marked the beginning of a collaboration between the Avestro group at the University of York, UK, the Ariga group at the National Institute for Materials Science (NIMS), Japan and the Akamatsu group at Tottori University, Japan. The fabrication of monolayer thin films of core-functionalised molecular triangles, **6H**, **3Br 6Br**, **3Ar** and **6Ar** at the air-water interface is presented and subsequent investigations to characterise the potential configuration of assembly using π -*A* isotherms and X-ray reflectivity (XRR) experiments. Furthermore, the characterisation of the electronic structure of core-functionalised molecular triangles in monolayer and drop-casted thin films following chemical and electrochemical reduction was sought to confirm the generation of the reduced states. Lastly, the structure of crystalline thin films of electron-rich polymers (PBTTT, PDCBT and PQT) doped with electron-deficient **6Br** were investigated by X-ray diffraction to exploit its potential applicability as an acceptor material for organic solar cells.

ACKNOWLEDGEMENTS

FHNA acknowledges support from (i) Masaki Ishii, Dr Yu Yamashita and the Supermolecules Group at the National Institute for Materials Science (NIMS), Japan for their guidance and assistance in completing the fabrication and property analysis of thin films outlined in this Chapter, (ii) Professor Katsuhiko Ariga for being the host researcher at NIMS, Japan and (iii) Dr Masa Akamatsu for arranging and facilitating the collaboration between research groups at the University of York, UK and NIMS, Japan.

5.1 INTRODUCTION

Ever since the discovery of (i) conjugated organic complexes of perylene and bromine by Akamatu *et al.* in 1954¹ and (ii) conjugated organic polymers by Heeger, MacDiarmid and Shirakawa in the 1970s,^{2,3} organic semiconducting (OSC) materials have been considered as the future of electronics, to potentially replace their inorganic counterparts due to their low-cost, light weight, availability and functional versatility⁴ with potential applications in light-emitting diodes,⁵ vertical phototransistors,⁶ field-effect transistors (FETs),⁷ ion gated transistors⁸ and photovoltaic devices.⁹ Ion-gated transistors are of interest due to their low resistance to conductivity enabled through the mass transport of ions across a permeable membrane (Figure 5.1a.)⁸ while photovoltaic devices are attractive on account of their ability to utilise the renewable, inexhaustible energy source of the sun to absorb photons to generate excitons for the transport of a charge (Figure 5.1b)⁹ respectively. The active layer in a photovoltaic device is commonly a bulk heterojunction (BHJ) layer which contains a blend of *p*- and *n*-type materials. Crystalline thin films of the *p*-type polymer poly-(2,5-bis(3-tetradecylthiophene-2-yl)thieno[3,2-b]thiophene (PBTtT) have been explored for use in BHJs where the lamellar structure of interdigitated polymer chains allows for the encapsulation of a range of functionalised fullerene electron acceptors in a 1:1 ratio on account of through-space charge-transfer interactions with the electron-rich polymer, Figure 5.1c.^{10,11}

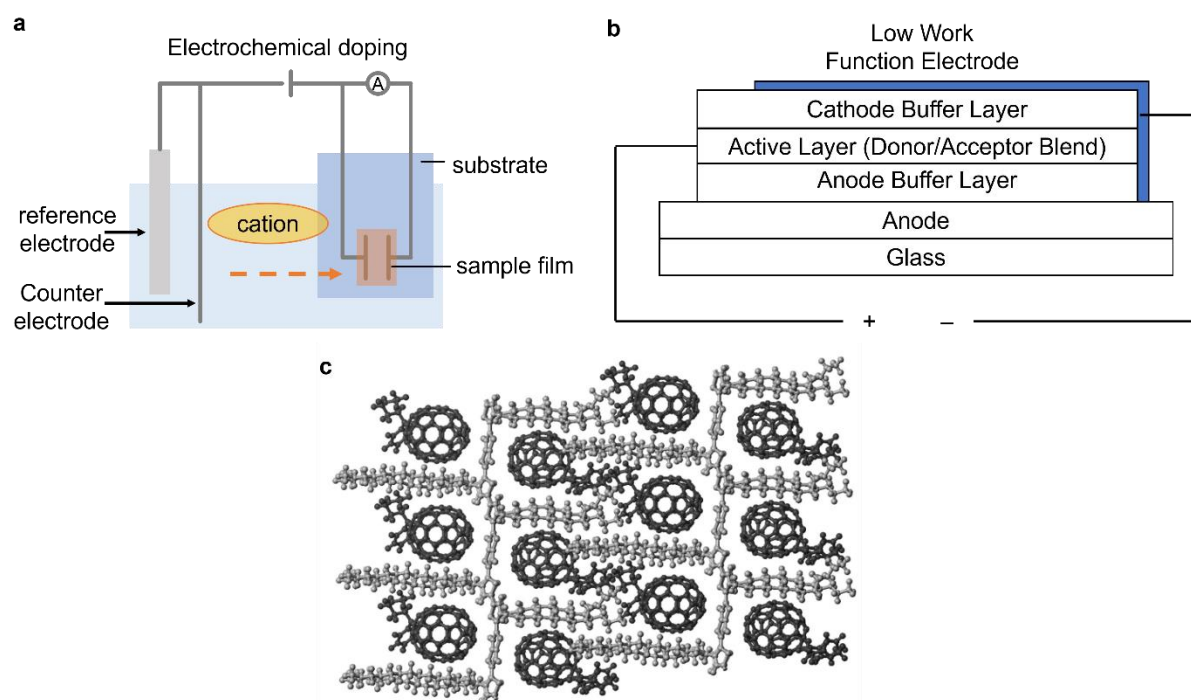


Figure 5.1 Schematics of (a) an ion-gated transistor⁸, (b) a normal architecture bulk heterojunction (BHJ) photovoltaic device⁹ and (c) encapsulation of fullerene within the lamellar structure of interdigitated PBTtT polymer chains (reproduced from Reference 11).¹¹

The utilisation of through-space delocalisation of electrons *via* π -orbital overlap in OSCs has allowed for the tuning of optoelectronic properties through precise molecular design, high synthetic versatility

and low synthetic cost.^{6,12} Electron-deficient *n*-type OSCs that carry a charge by accepting electrons are attractive materials due to their water and air stability when the LUMO is below -4.0 eV.¹³ The solid-state packing of *n*-type materials such as tetracyanoquinodimethane (TCNQ) small molecules and electron-deficient polymers has allowed for the realisation of efficient charge transport in OSCs (>0.1 cm² V⁻¹ s⁻¹) matching well-explored *p*-channel electron-rich systems.¹⁴⁻¹⁷ Aromatic diimides (ADIs) including pyromellitic (PMDI), naphthalene (NDI) and perylene diimides (PDI) are ideal candidates for supramolecular *n*-type organic semiconductors due to their highly electron deficient π -surface, redox-active nature as two-electron acceptors and their ability to pack in the solid state through $\pi\cdots\pi$ contacts typically in a herringbone morphology due to aromatic quadrupole interactions. Indeed, ADI small molecules have been studied as *n*-type OSCs showing efficient charge mobility making them attractive materials for use in organic electronic devices. For example thin-film transistors (TFTs) consisting of unsubstituted ADI small molecules have been fabricated where the packing of the aromatic π -surfaces in the solid state enables electron transport with charge mobilities of 0.079, 0.02 and 0.6 cm² V⁻¹ s⁻¹ for PMDI,¹⁸ NDI¹⁹ and PDI²⁰ respectively. Recent developments for ion-gated transistors have involved using an electrolyte solution and porous OSC thin film to increase capacitance and enhance ion penetration and transport compared with devices using a solid gate dielectric and non-permeable conducting surface.²¹ Porous crystalline thin films of thiophene-based polymers or perylene diimide small molecules have previously been studied with fast ion intercalation and high charge carrier densities.^{22,23} The structures of these porous crystalline thin films are attractive as they can balance efficient hole transport *via* through-space $\pi\cdots\pi$ interactions enabled through the packing of the polymer chains whilst maintaining seamless ion transport throughout the permeable structure.²⁴ New structural designs and strategies to balance these competing effects are sought to fabricate devices with increased capacitance, with one method being the swelling of polymers upon the addition of water in thin films to increase ion transport.²⁴

In Chapters 2 and 3, the ability of core-functionalised molecular triangles to (i) accept electrons to form negatively charged anions, which are stabilised by cyclic aromatic homoconjugation, (ii) encapsulate anions to form host-guest complexes and (iii) form porous assemblies in the solid state (Figure 5.2a and b) was discussed. An alternative supramolecular packing structure of core-functionalised molecular triangles was also envisioned where intermolecular $\pi\cdots\pi$ interactions between macrocycles form a porous 2D tessellated nanosheet (Figure 5.2c). These structural and electrochemical properties of 3D macrocyclic core-functionalised molecular triangles could make them ideal candidates for use as *n*-type OSCs in ion-gated transistors on account of their ability to facilitate the diffusion of ions throughout the porous framework whilst facilitating electron mobility through the $\pi\cdots\pi$ packing of the PMDI faces.

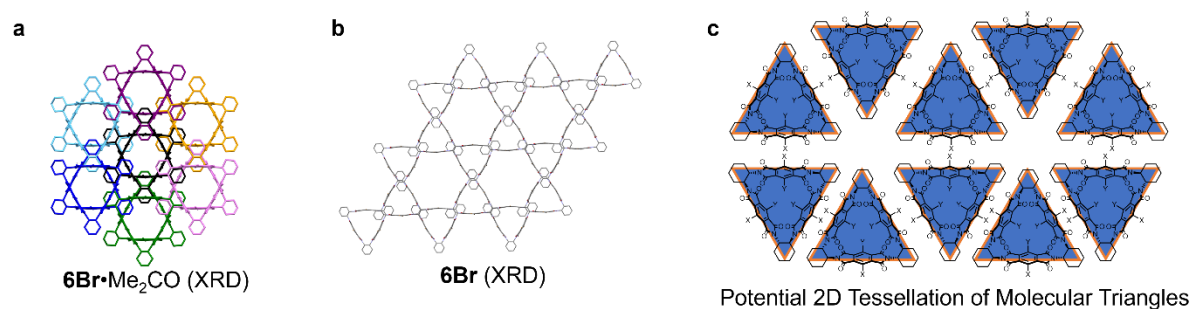


Figure 5.2 X-ray crystal structures of **6Br** in (a) Me₂CO and (b) CH₂Cl₂ discussed in Chapter 2 and (c) potential 2D tessellation of core-functionalised molecular triangles.

In this Chapter, research that was completed as part of a two-month Japan Society for the Promotion of Science (JSPS) Summer PhD Exchange Fellowship (June–August 2023) is presented. The JSPS Fellowship marked the beginning of an ongoing collaboration between the Avestro group at the University of York, UK, the Ariga group at the National Institute for Materials Science (NIMS), Japan and the Akamatsu group at Tottori University, Japan. This Chapter presents preliminary results regarding the suitability of core-functionalised molecular triangles for application as organic semiconducting materials in ion-gated transistors through the fabrication and structural and property analysis of core-functionalised molecular triangle thin films. Furthermore, the ability of the highly electron-deficient **6Br** macrocycle to be used as an *n*-type dopant with electron-rich *p*-type polymers *e.g.* PBTTT are explored in a similar manner to fullerene electron acceptors for potential use as BHJs in photovoltaic solar cells.^{10,11} It was hypothesised that the molecular triangle **6Br** would be encapsulated within the interdigitated lamellar structure of electron-rich polymers (Figure 5.3). The potential encapsulation of the electron-deficient macrocycle in the supramolecular packing of three different *p*-type polymers is studied through wide-angle X-ray scattering (WAXS) and X-ray diffraction (XRD) experiments with the impact on the crystalline phases of the thin films also investigated.

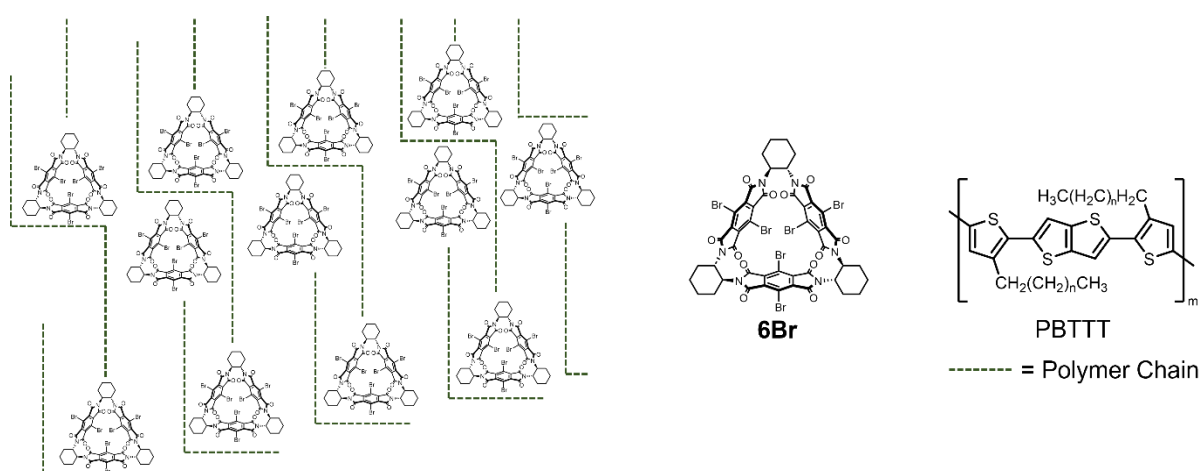


Figure 5.3 Representation of potential encapsulation of **6Br** within interdigitated PBTTT polymer chains with chemical structures of **6Br** and generic PBTTT polymer with *m* number of monomer units and *n* number of CH₂ groups in alkyl chains.

5.2 RESULTS AND DISCUSSION

5.2.1 STRUCTURAL PROPERTIES OF MOLECULAR TRIANGLE THIN FILMS

Initially, the behaviour and self-assembly of core-functionalised molecular triangles at the air–water interface was investigated prior to thin film fabrication from the water surface in a Langmuir–Blodgett (LB) trough. Solutions of core-functionalised molecular triangles (**6H**, **3Br**, **6Br**, **3Ar** and **6Ar**) in chloroform ($\approx 0.5 \text{ mg mL}^{-1}$) were dispersed onto a water surface and the solvent allowed to evaporate at room temperature. A layer of macrocycles was formed on the water surface with subsequent compression in the LB trough causing a change in surface pressure π (mN m^{-1}) which was plotted against molecular area, A (nm^2) (Figure 5.4). The x-axis represents the changing area that each macrocycle molecule can occupy on the water surface (mm^2) which was calculated using the area of the trough (mm^2) and number of molecules n that were dispersed in solution (Equation 5.1). The value of n could be calculated from the concentration (g mL^{-1}) and volume (mL) of the chloroform solution, molecular mass (g mol^{-1}) of the specific molecular triangle (**6H**, **3Br**, **6Br**, **3Ar** or **6Ar**) and Avogadro's constant N_A (mol^{-1}) (Equation 5.2).

$$\text{Molecular Area (mm}^2\text{)} = \frac{\text{Area (mm}^2\text{)}}{\text{no. of molecules}} \quad (\text{Eqn 5.1})$$

$$\text{where no. of molecules} = \frac{\text{conc (g mL}^{-1}\text{)} \times \text{vol (mL)} \times N_A \text{ mol}^{-1}}{Mr (\text{g mol}^{-1})} \quad (\text{Eqn 5.2})$$

During the compression of the layer of macrocycles on the water surface, the surface pressure increases when the molecules are in close contact and with subsequent further reduction in molecular area the surface pressure increases drastically. The onset of surface pressure in the π – A isotherm represents the cross-sectional molecular area which is the molecular area of the compound in the optimal assembly of the thin film. At molecular areas below the cross-sectional molecular area, the surface pressure increases when the assembly of molecular triangles is compressed such that the optimal assembly of the macrocycles is no longer possible at the air–water interface within the LB trough. The π – A isotherms were recorded three times for all five molecular triangles with an average onset of surface pressure calculated for **6H** (0.81 nm^2), **3Br** (0.89 nm^2), **6Br** (0.94 nm^2), **3Ar** (1.50 nm^2) and **6Ar** (1.66 nm^2) upon reducing the molecular area by compression of the trough from 2.5 nm^2 towards 0 nm^2 . The cross-sectional molecular area is larger in the core-arylated molecular triangles (**3Ar** and **6Ar**) compared with **6H**, **3Br** and **6Br**. Although the difference in cross-sectional molecular area within the two groups of macrocycles **6H** & **6Br** (0.15 nm^2) and **3Ar** & **6Ar** (0.16 nm^2) is minimal.

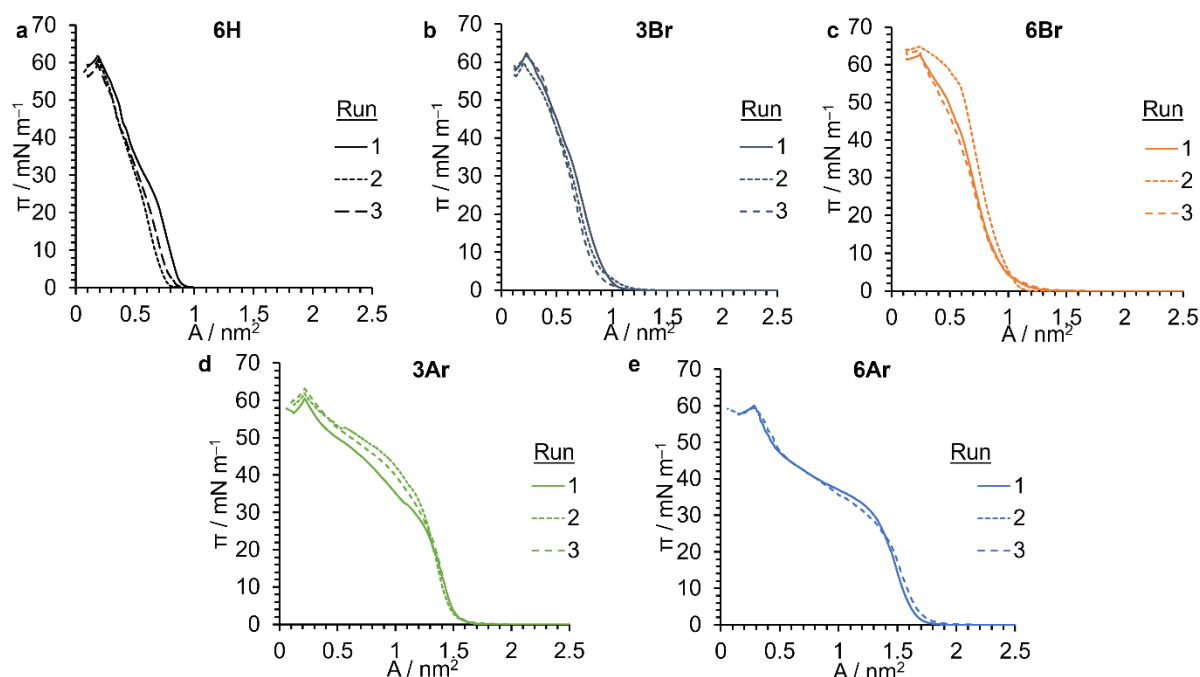


Figure 5.4 π - A isotherms of molecular triangles (a) **6H**, (b) **3Br**, (c) **6Br**, (d) **3Ar** and (e) **6Ar**.

In visualising the potential assembly of molecular triangles at the air–water interface, there are two possible configurations: (i) ‘standing upright’ (configuration *a*) or (ii) ‘lying flat’ (configuration *b*) (Figures 5.5a and b) on account of maximising $\pi \cdots \pi$ interactions between adjacent macrocycles. The cross-sectional molecular area of the macrocycles at the air–water interface in these configurations was estimated from geometry optimised structures of the molecular triangles using density functional theory (DFT) calculations at the B3LYP(D3-BJ)/def2svp level of theory in CH_2Cl_2 (PCM solvent model) (Figure 5.5c and d) presented in Chapters 2 and 3. The molecular areas of the macrocycles in the two conformations were estimated by measuring the actual N–N distance along a PMDI face in nm. The same N–N distance was measured in a screenshot of the molecule in the same conformation in mm. The scale factor for the translation of the actual and screenshot N–N distance was calculated so that the actual area of the macrocycle in the two conformations (nm^2) could be scaled from the area of the molecule in the image screenshot (mm^2). The estimated theoretical molecular area of the molecular triangles when assembled in configuration *a* is slightly more complicated as a result of the alternating up and down nature of the macrocycles. This complication led to an estimation that two molecules occupy roughly the area of one macrocycle at the air–water interface. Therefore, the molecular area of one macrocycle when assembled in configuration *a* is half the estimated area of the PMDI face (Figure 5.5c). The resulting theoretical molecular area of configurations *a* and *b* (Table 5.1) were compared to the experimental cross-sectional areas calculated from the π - A isotherm (Figure 5.4). For all of the molecular triangles (**6H**, **3Br**, **6Br**, **3Ar** and **6Ar**) the theoretical area is larger in configuration *b* compared with configuration *a* as a result of the more efficient assembly of the macrocycles in the ‘Standing Upright’ formation at the air–water interface. The molecular area of all of the macrocycles in configuration *a* are more similar to the experimental average cross-sectional molecular area

calculated from the π - A isotherms. The close similarity of these results indicates that the molecular triangles are likely to assemble according to configuration *a* compared with configuration *b*. The largest discrepancy between the average cross-sectional area and molecular area in configuration *a* occurs for **3Ar**. This difference could be as a result of the estimations involved in the calculations of the theoretical molecular from the geometry optimised structures.

Table 5.1 Comparison of the experimental average cross-sectional area with theoretical molecular area in configuration *a* and *b* estimated from DFT geometry optimised structures (DFT/B3LYP(D3-BJ)/def2svp in CH₂Cl₂ (PCM solvent model)).

	Experimental	Theoretical	
	Average Cross-Sectional Molecular Area / nm ²	Configuration <i>a</i> / nm ²	Configuration <i>b</i> / nm ²
6H	0.81	0.67	2.51
3Br	0.89	0.79	2.49
6Br	0.94	0.86	2.57
3Ar	1.50	1.05	2.76
6Ar	1.66	1.55	2.97

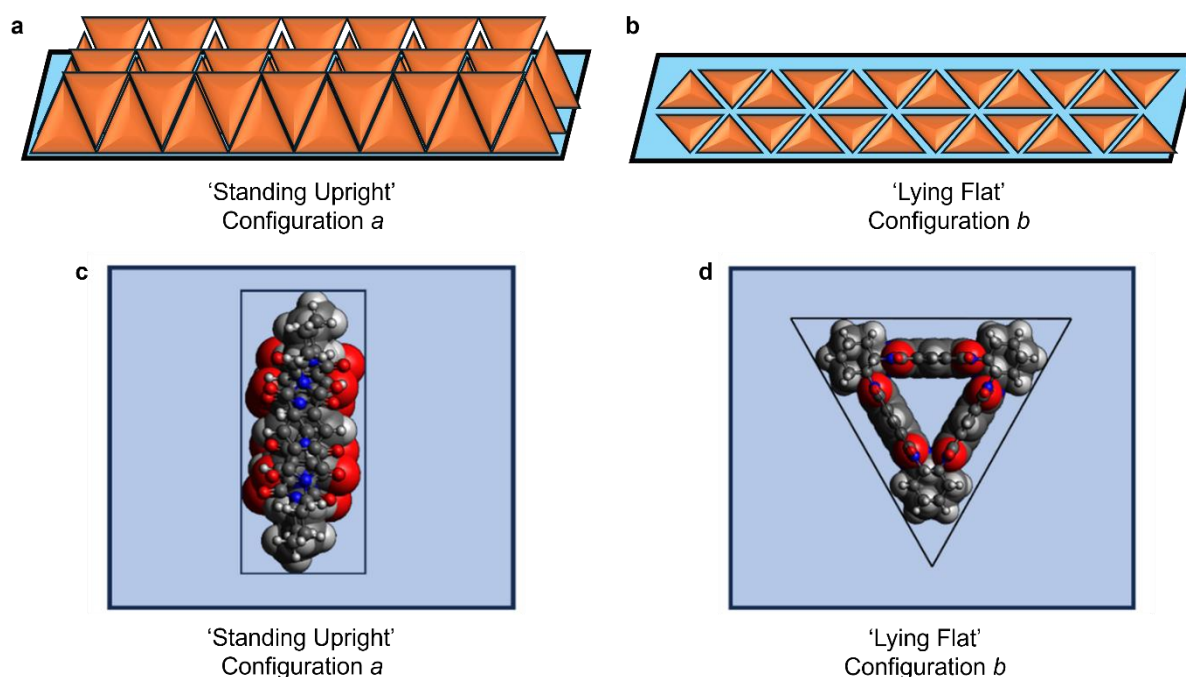


Figure 5.5 Representation of the two potential configurations of molecular triangle assemblies in a monolayer: (a) 'standing upright' configuration *a* or (b) 'lying flat' configuration *b*. Representative areas used to estimate the molecular area of **6H** in (c) configuration *a* and (d) configuration *b* from DFT geometry optimised structures (DFT/B3LYP(D3-BJ)/def2svp in CH₂Cl₂ (PCM solvent model)).

Once the π - A isotherms for the five molecular triangles at the air–water interface were measured, the same method was used to attempt to fabricate thin films of **6H**, **3Br**, **6Br**, **3Ar** and **6Ar** on a glass surface. To fabricate thin films at the air–water interface, a glass substrate was submerged in the water-filled LB trough and the macrocycles compressed until the surface pressure reached 15 mN m⁻¹.

The compression of the layer of molecular triangles was stopped when the surface pressure reached 15 mN m^{-1} as beyond that the pressure exerted on the thin films can cause deformities in the assembly of the macrocycles. The substrate was then slowly lifted from the water filled LB trough with molecules adhering to the surface as it was removed to form a thin film on the glass surface.

Structural analysis of the molecular triangle thin films formed at the air–water interface was completed using X-ray reflectivity (XRR) with the aim to use the resulting diffraction pattern to determine of the surface roughness and film-thickness of the respective thin films.²⁵ The presence of peaks (fringes) in XRR diffraction patterns is used to characterise thin films, with increasing number of fringe peaks indicating a more uniform thin film. In the XRR curves of **6H**, **3Br**, **6Br** and the clean glass substrate (control), a smooth featureless line is observed, whereas in the curves for **3Ar** and **6Ar**, a single fringe peak is observed at 2θ angles of 5.70° and 5.18° respectively, Figure 5.6. The fringe peak in the XRR curves for thin films of **3Ar** and **6Ar** below 10° indicates the presence of macrocycle on the glass substrate, Figure 5.6. Although, the presence of a single peak in the diffraction pattern indicates that the X-rays are reflected off a rough, non-uniform thin film.²⁶

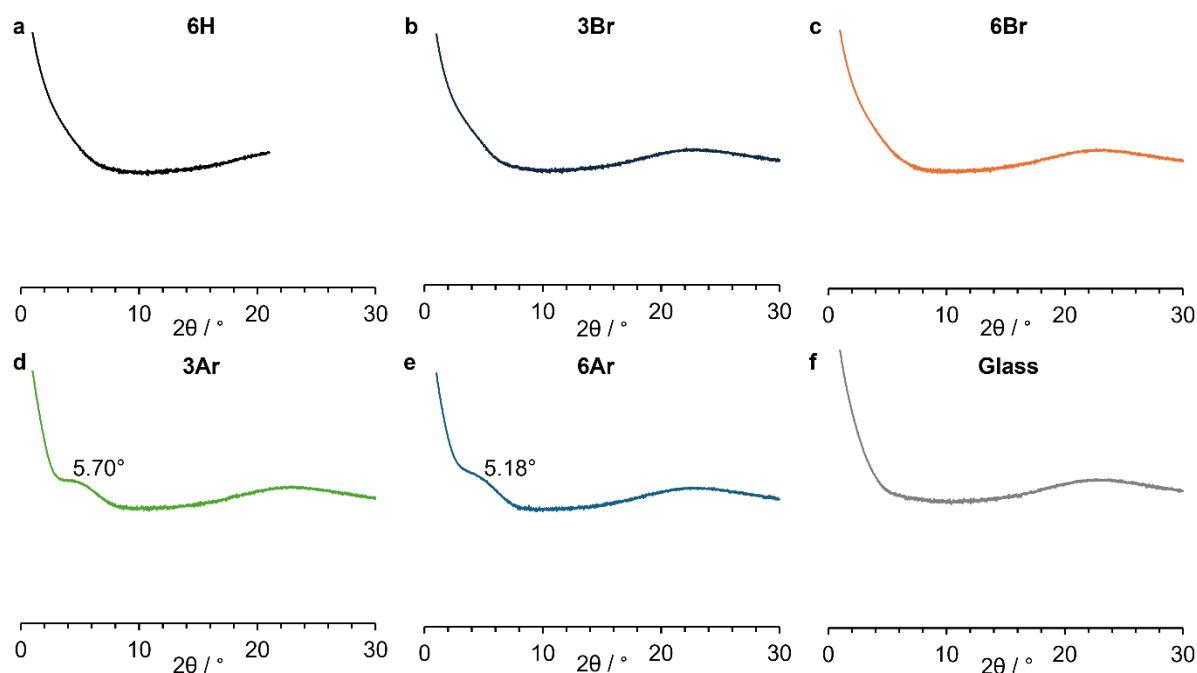


Figure 5.6 XRR diffraction data of LB thin films comprising (a) **6H**, (b) **3Br**, (c) **6Br**, (d) **3Ar**, (e) **6Ar** on glass substrates. (f) XRR diffraction of pristine glass substrate as a control.

The lack of a difference in XRR patterns of **6H**, **3Br** and **6Br** with the control glass substrate indicates that the molecular triangle films are too thin to be observed using XRR or are not crystalline. The crystallinity of the thin films could have been confirmed by powder X-ray diffraction (pXRD) prior to the XRR measurement. Alternatively, macrocycles **6H**, **3Br** and **6Br** could interact weakly with the glass substrate leading to poor adhesion between molecular triangle and surface and thus little material is present in the thin films. The core-arylated molecular triangles could interact more strongly with the

substrate on account of the 3,5-dimethyl-benzene substituents increasing the surface area for van der Waals interactions between macrocycle and the glass surface. If the lack of fringe peak in the XRR curves for **6H**, **3Br** and **6Br** is due to poor adhesion of the molecular triangle to the substrate, the surface could instead be coated with a self-assembled monolayer (SAM) *e.g.* an aromatic surface appended with organophosphonate group, where the phosphonate group would be able to interact with the glass. The SAM containing aromatic surfaces such as anthracene would subsequently provide greater functionality for increased non-covalent interactions ($\pi\cdots\pi$ contacts) between the substrate and the core-functionalised molecular triangles.²⁸

5.2.2. OPTOELECTRONIC PROPERTIES OF MOLECULAR TRIANGLE THIN FILMS

As formation of thin films of **6H**, **3Br** and **6Br** on glass surfaces could not be confirmed using XRR due to the absence of any fringe peaks, UV-vis spectroscopy was used instead to confirm the deposition of macrocycle material onto a quartz substrate at the air–water interface. The absorption spectra of thin films of core-functionalised molecular triangles, **6H**, **3Br**, **6Br**, **3Ar** and **6Ar** (Figure 5.7) show the presence of $\pi\text{-}\pi^*$ (>300 nm) electronic transitions at the same wavelengths as in the solution state (Chapters 2 and 3). The same wavelength of absorption peaks in UV-vis spectra for core-functionalised molecular triangles in thin films and solution confirms the deposition of material onto the quartz surface and that aggregation effects in the solid state are not influencing the energy of the electronic transitions. Additional higher intensity $\pi\text{-}\pi^*$ transitions between 240–250 nm are also observed in the thin films for all macrocycles. These higher energy $\pi\text{-}\pi^*$ transitions are not observed in solution due to the solvent cut-off wavelength. Furthermore, the absorption spectra of core-arylated macrocycles, **3Ar** and **6Ar**, have better resolution compared to **6H**, **3Br** and **6Br**. The improved resolution of absorption spectra for thin films of the core-arylated molecular triangles occurs as a result of the higher molar extinction coefficient of **3Ar** ($32000\text{ M}^{-1}\text{ cm}^{-1}$) and **6Ar** ($35600\text{ M}^{-1}\text{ cm}^{-1}$) compared with **6H** ($5830\text{ M}^{-1}\text{ cm}^{-1}$), **3Br** ($7550\text{ M}^{-1}\text{ cm}^{-1}$) and **6Br** ($10700\text{ M}^{-1}\text{ cm}^{-1}$) in CH_2Cl_2 (Chapters 2 and 3). Although attribution of the improved resolution for **3Ar** and **6Ar** to higher molar extinction coefficients is assuming equal loading of the molecular triangles onto the glass substrate.

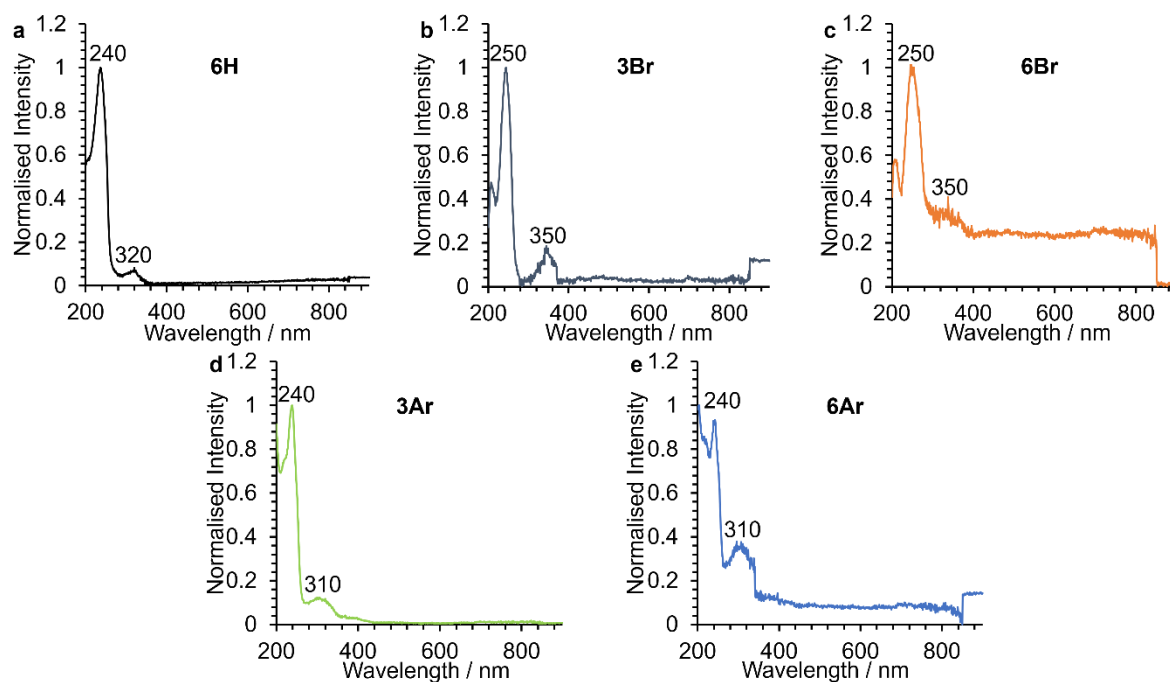


Figure 5.7 Normalised UV-vis absorption spectra of monolayer thin films formed from the air-water interface using a LB trough of (a) **6H**, (b) **3Br**, (c) **6Br**, (d) **3Ar** and (e) **6Ar** on a quartz substrate.

To assess the suitability of core-functionalised molecular triangles for use in organic semiconducting devices, their ability to be reduced using chemical and electrochemical methods was investigated, with UV-vis spectroscopy used to identify the reduced states. In Chapters 2 and 3, UV-vis spectra (Figures 2.16 and 3.15) of the reduced states of **6H**, **3Br** and **6Br** after reduction with decamethylcobaltocene were characterised with new absorption peaks being generated at longer wavelengths upon the formation of the tris-radical anion (645 to 710 nm). Subsequently, upon further reduction the new absorption peaks were blue shifted to 550 nm representing the formation of the hexa-anion. Therefore, similar absorption peaks were expected to be observed in the solid state of reduced states of monolayer thin films of core-functionalised molecular triangles.

As part of the collaboration with the Supermolecules group at NIMS, Japan during the JSPS fellowship, a novel set of reducing conditions developed by the collaborators were used to attempt the chemical reduction of thin films of core-functionalised molecular triangles **6H**, **3Br**, **6Br**, **3Ar** and **6Ar**. These reducing conditions developed at NIMS, Japan are unpublished so the details cannot be discussed although the estimated reduction potential of the reductant was ≈ -0.56 V vs Ag/AgCl. To confirm the required reduction potentials for thin films or core-functionalised molecular triangles, solid-state electrochemical experiments were attempted. Unfortunately, a representative cyclic voltammogram could not be obtained despite varying the solvent (H_2O and MeCN). Instead, comparing the estimated reduction potential of the chemical reductant (≈ -0.56 V vs Ag/AgCl) with the solution-state data in THF (Chapters 2 and 3) shows that the most electron-deficient molecular triangle **6Br** only would be reduced to the mono-radical anion ($[\mathbf{6Br}]^{\cdot-}$), $E_{\text{red}} = -0.47$ V vs Ag/AgCl as measured by cyclic voltammetry (CV). Nonetheless, out of scientific curiosity, thin films of core-functionalised molecular

triangles (**6H**, **3Br**, **6Br**, **3Ar** and **6Ar**) fabricated on quartz substrates at the air–water interface were submerged in the reductant solution for 30 seconds. The absorption spectrum of the thin films before and after exposure to the reducing solution were measured to investigate the effect of the chemical reductant on the core-functionalised molecular triangles (Figure 5.8.).

For molecular triangles **6H**, **3Br** and **6Br** (Figure 5.8a–c) upon exposure to reducing conditions the peaks for the π - π^* transitions between 300–400 nm are absent with no peaks formed at longer wavelengths (500–700 nm) representing the radical anion and anionic reduced states as expected from the solution-state data (Chapter 2, Figure 2.16. and Chapter 3, Figure 3.15.). The π - π^* transitions for **3Ar** (310 nm) and **6Ar** (305 and 370 nm) are also absent in the absorption spectra (Figure 5.8d and e) after exposure to the chemical reductant for 30 s, although the higher intensity, higher energy π - π^* transitions are red shifted from 235 to 270 nm and 245 to 275 nm for the tris- and hexa-arylated macrocycles respectively. Changes in the UV region cannot be due to chemical reduction to the radical anion owing to the insufficient reduction applied from the chemical reductant (≈ -0.5 V) compared with the solution-state (THF) reduction potentials of **3Ar** (-0.71 V vs Ag/AgCl) and **6Ar** (-0.84 V vs Ag/AgCl) (Chapter 2, Figure 2.14a and Chapter 3, Figure 3.14a). Therefore, this change is more likely to do with a chemical transformation between the components of the chemical reductant and molecular triangle (**3Ar** and **6Ar**). As **6Br** had the lowest solution-state reduction potential, its thin film was submerged in the chemical reduction solution for an additional hour although the absorption spectrum remained featureless. These results show that the chemical reductant with estimated reduction potential of -0.56 V vs Ag/AgCl is insufficient to reduce the core-functionalised molecular triangles, including the most electron-deficient macrocycle **6Br** which had a first reduction potential of -0.47 V vs Ag/AgCl in THF (Chapter 2).

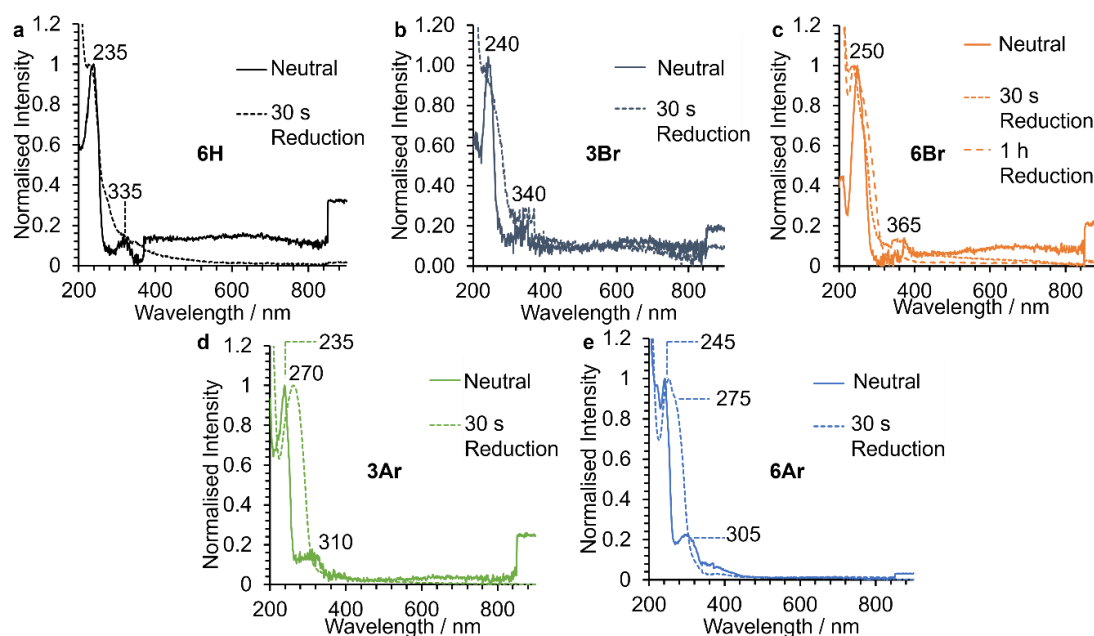


Figure 5.8 Absorption spectra of thin films of (a) **6H**, (b) **3Br**, (c) **6Br**, (d) **3Ar** and (e) **6Ar** in the neutral state and after exposure to the chemical reductant solution.

The absorption spectra of core-arylated molecular triangle thin films (**3Ar** and **6Ar**) were most well-resolved compared to **6H**, **3Br** and **6Br** and therefore electrochemical reduction experiments were conducted on **3Ar** and **6Ar** thin films through the application of a potential. Thin films of **3Ar** and **6Ar** were fabricated at the air–water interface onto ITO coated glass using the protocol discussed above and in the Supplementary Information, Section 5.4.2. ITO coated glass substrates were required to be used in electrochemical experiments to act as the working electrode within a standard three-electrode setup (Ag/AgCl reference electrode and platinum wire counter electrode). Two thin films of **3Ar** and **6Ar** each were prepared and a potential of -0.5 or -0.7 V applied in an aqueous electrolyte solution containing potassium chloride (0.1 M) and bis(triphenylphosphoranylidene) (0.96 mM) for 5 mins (conditions for the electrochemical experiments were supplied by collaborators at NIMS, Japan). The applied voltages in the electrochemical experiments were limited by the narrow electroactive window of the aqueous electrolyte solutions. Despite the applied potentials (-0.5 and -0.7 V vs Ag/AgCl) being less negative than the first reduction potential in THF for **3Ar** (-0.71 V vs Ag/AgCl, Figure 3.14.a, Chapter 3) and **6Ar** (-0.84 V vs Ag/AgCl, Figure 2.14.a, Chapter 2), the electrochemical experiments were still pursued in the off chance that the reduced species could be detected by absorption spectroscopy, Figures 5.9 and 5.10.

The absorption spectra of thin films of **3Ar** and **6Ar** formed at the air–water interface on ITO coated glass before and after applying a potential of -0.5 or -0.7 V vs Ag/AgCl (Figure 5.9.a–d) are inconsistent with negative absorbances. The absence of consistent absorption spectra could be as a result of the low loading of **3Ar** and **6Ar** onto the ITO coated glass from the air–water interface. The maximum mass of **3Ar** and **6Ar** that could be deposited onto the glass surface was 0.0265 mg and 0.0260 mg respectively based on dispersion of 50 μ L of CHCl_3 solutions (**3Ar** 0.530 mg mL $^{-1}$ and **6Ar** 0.520 mg mL $^{-1}$). Furthermore, as quartz substrates were not used with ITO coated glass required for use as the working electrode, less UV-light was transmitted through the substrate and thus the intensity of the absorption peaks were reduced. The presence of negative absorption peaks could be as a result of improper baseline correction of the ITO coated glass substrate. In the UV-vis spectrometer, to measure the solid-state absorption spectra, the glass substrates were fixed to the cuvette holder through adhesion with tape. However, there was not a uniform procedure to ensure that the substrate was positioned in the exact same location for each measurement. This could have led to sub-optimal positioning of the substrate with respect to the beam of light during baseline and sample measurements. Subsequently, when the baseline absorption intensities were subtracted from the sample values at all wavelengths, a negative absorption might evolve if the sample substrate was positioned differently to the initial baseline glass slide. Therefore, a sample holder should be used in the future which can ensure that the glass substrates are positioned in the same position for each measurement to allow for proper baseline corrections to be applied.

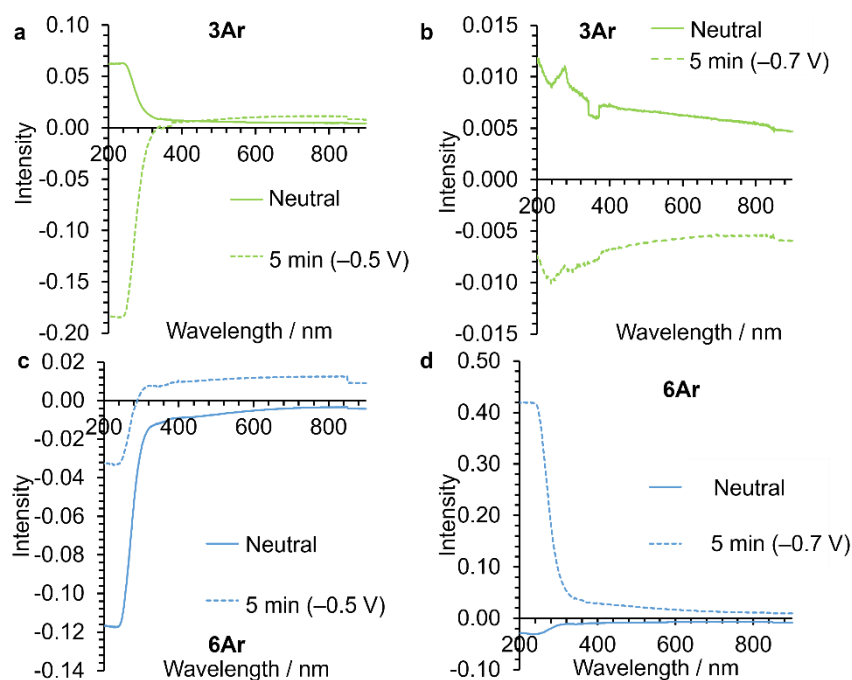


Figure 5.9 Absorption spectra of molecular triangle thin films on ITO coated glass formed at the air–water interface before and after applying a potential (–0.5 or –0.7 V vs Ag/AgCl) for 5 mins (a) **3Ar** at –0.5 V, (b) **3Ar** at –0.7 V, (c) **6Ar** at –0.5 V and (d) **6Ar** at –0.7 V.

Drop-casting was subsequently used as an alternative method of thin film fabrication to increase the loading of molecular triangle and ensure coverage of solid material onto the ITO coated glass substrate for electrochemical experiments. Drop-casted films were prepared by dispersing 100 μL of CHCl_3 solution (**3Ar**: 0.48 mg mL^{-1} and **6Ar**: 0.49 mg mL^{-1}) onto the ITO coated glass substrate and allowing the solvent to evaporate at room temperature (> 15 mins) to give loadings of 0.048 mg and 0.049 mg for **3Ar** and **6Ar** respectively. Two drop-casted thin films of **3Ar** and **6Ar** each were prepared with absorption spectra measured before and after applying a potential of –0.5 or –0.7 V vs Ag/AgCl (Figure 5.10). For the drop-casted thin film of **6Ar** a potential of –0.7 V vs Ag/AgCl was also applied for an additional hour to see if there would be any change in absorption. Unfortunately, the absorption spectra for the drop-casted films of **3Ar** and **6Ar** gave inconsistent results with negative absorbances in a similar manner to thin films formed at the air–water interface (Figure 5.9), with the expected $\pi\text{-}\pi^*$ transitions not observed. The lack of consistency in the absorption spectra for drop-casted thin films of **3Ar** and **6Ar** could be accounted for by the loss of deposited material from the ITO coated glass substrate. This was evidenced by the appearance of insoluble solid material at the bottom of the aqueous electrolyte solution after the electrochemical experiment.

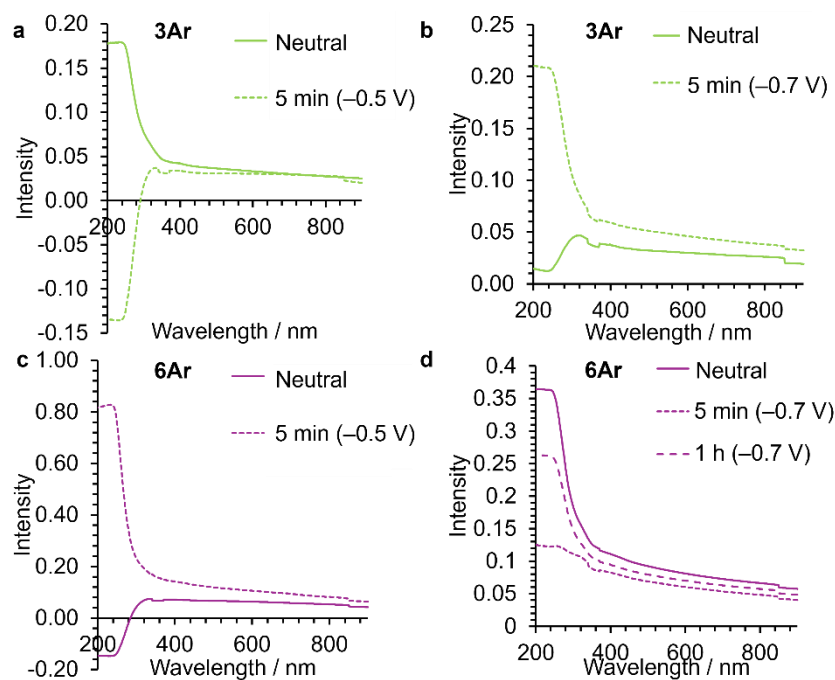


Figure 5.10 Absorption spectra of molecular triangle thin films on ITO coated glass formed by drop-casting before and after applying a potential for 5 mins (or 1h): (a) **3Ar** at -0.5 V, (b) **3Ar** at -0.7 V, (c) **6Ar** at -0.5 V and (d) **6Ar** at -0.7 V.

Acknowledging from the **3Ar** and **6Ar** films that *c.a.* 0.05 mg is not sufficient to observe a signal (and considering their relatively high molar absorptivities compared to **6Br**) a series of increasingly loaded thin films of **6Br** (**6Br-1**, **6Br-2**, **6Br-3** and **6Br-4**) were prepared on ITO by drop casting 100, 200, 300 and 400 μL (using portions of 100 μL solutions) of a 0.548 mg mL^{-1} solution of **6Br** in CHCl_3 (Table 5.2).

Table 5.2 Volume and mass loadings of **6Br** (0.548 mg mL^{-1} in CHCl_3) in different drop-casted thin films **6Br-1**, **6Br-2**, **6Br-3** and **6Br-4**.

	6Br-1	6Br-2	6Br-3	6Br-4
Volume / μL	100	200	300	400
Mass / mg	0.0548	0.1096	0.1644	0.2192

In all of the absorption spectra of the neutral drop-casted thin films, **6Br-1**, **6Br-2**, **6Br-3** and **6Br-4** (Figure 5.11) an absorption at 380 nm is observed representing the $\pi\text{-}\pi^*$ electronic transition of the macrocycle which is the same wavelength as in solution (Figure 2.13., Chapter 2). The intensity of the $\pi\text{-}\pi^*$ absorption peak in **6Br-1** is around 0.015 A.U. with the same peak in **6Br-2**, **6Br-3** and **6Br-4** more intense occurring at roughly equal intensity (≈ 0.15 A.U.). The equal intensity absorption of **6Br-2**, **6Br-3** and **6Br-4** indicates a similar quantity of solid on the surface which may occur as a result of inadvertent removal of material from the ITO coated glass to the aqueous electrolyte solution as observed visually during the electrochemical experiments. For **6Br-1**, upon application of a potential for 5 minutes the intensity of the $\pi\text{-}\pi^*$ absorption decreases in intensity with a lower energy, broad peak forming at 540 nm (-0.5 V vs Ag/AgCl) and 605 nm (-0.7 V vs Ag/AgCl). The wavelengths of the new peaks following electrochemical reduction occur at similar wavelengths to the reduced states of **6Br** in

solution ($[\mathbf{6Br}]^{3+}$: 645 and 680 nm and $[\mathbf{6Br}]^{6-}$: 550 nm, Chapter 2). In thin films **6Br-2**, **6Br-3** and **6Br-4**, no lower energy peaks representing the reduced states of the macrocycle were observed (Figure 5.11.b–d) suggesting that electrochemical reduction does not occur which could be due to the thicker layer of macrocycle hindering the role of the ITO coated glass surface as the working electrode.

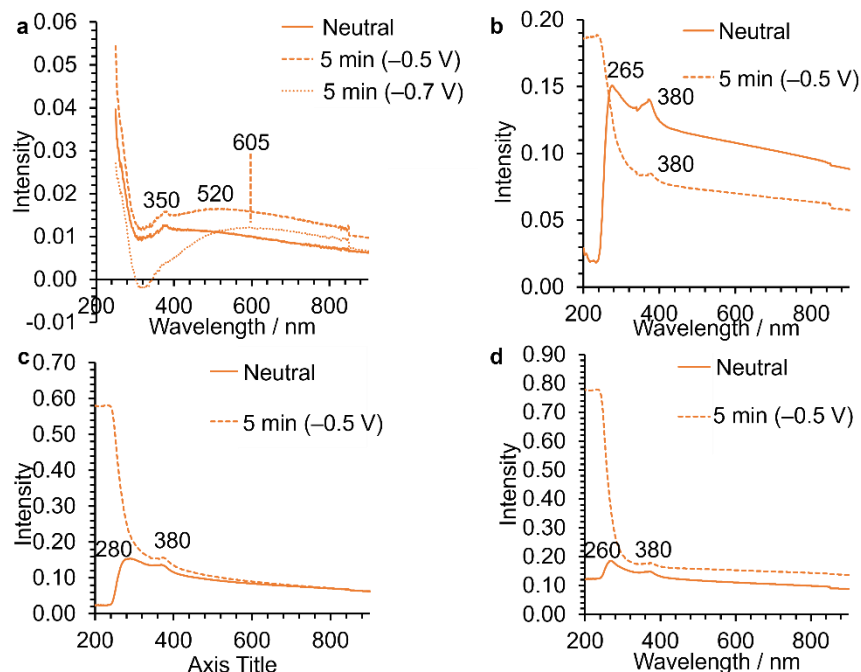


Figure 5.11 Absorption spectra of **6Br** drop-casted thin films on ITO covered glass substrate for (a) **6Br-1**, (b) **6Br-2**, (c) **6Br-3** and (d) **6Br-4** before and after applying a potential (–0.5 or –0.7 V vs Ag/AgCl).

The evolution of broad absorption peaks in a similar region to the reduced states of **6Br** upon the electrochemical reduction of thin film **6Br-1** provides initial evidence that the electron-deficient macrocycle in the solid state might be suitable for use in ion-gated transistor devices. One of the attractive properties of **6Br** for use as a semi-permeable membrane in an ion-gated transistor was the 2D tessellated assembly of the macrocycles to allow for the selective transport of ions. A disadvantage of the drop-casting method is that the resulting thin films can lack uniformity with little control over thickness.²⁹ Therefore, future experiments to assess the suitability of molecular triangles in organic semiconducting devices could use alternative fabrication methods such as blade-coating to make the thin films, or additional post-fabrication treatment such as annealing.

5.2.3 DOPING ELECTRON-RICH *N*-TYPE POLYMERS WITH ELECTRON-DEFICIENT **6Br**

Alongside studying the properties of core-functionalised molecular triangles in thin films, an alternative method to utilise the attractive assembly, redox-active and host-guest abilities of the electron-deficient **6Br** was pursued by incorporating the macrocycle into crystalline thin films of electron-rich polymers for application in bulk heterojunction photovoltaic devices. Three electron-rich polymers were used that have been shown to form crystalline thin films for use as *p*-type materials for the transport of electrons in organic semiconductors.^{30,31} The three electron-rich polymers used were: (i) poly[2,5-bis(3-

tetradecylthiophen-2-yl)thieno[3,2-*b*]thiophene] (PBTTT), (ii) poly[2,2'''-bis[[2-butyl-octyl)oxy]carbonyl]-[2,2':5',2'':5'',2'''-quarterthiophene]-5,5'''-diyl] (PDCBT) or (iii) poly(3,3'''-didodecyl[2,2':5',2'':5'',2'''-quarterthiophene]-5,5'''-diyl] (PQT), Figure 5.12.^{30,31} When these *p*-type polymers are mixed with *n*-type electron-acceptors, the resulting fabricated crystalline thin films can be used as effective materials for use as bulk heterojunction layers in photovoltaic devices for use in solar cells.³² Solutions containing polymer (PBTTT, PDCBT or PQT, 0.5 wt%) with and without **6Br** (0.5 wt%) in *o*-1,2-dichlorobenzene were heated at 180 °C for an hour. Thin films of the mixtures were then formed on glass substrates using spin coating (2000 RPM for 1 minute) and annealed at 180 °C under vacuum for 1 h. The resulting crystalline thin films were studied using wide-angle X-ray scattering (WAXS) and grazing incidence X-ray diffraction (GIXRD).

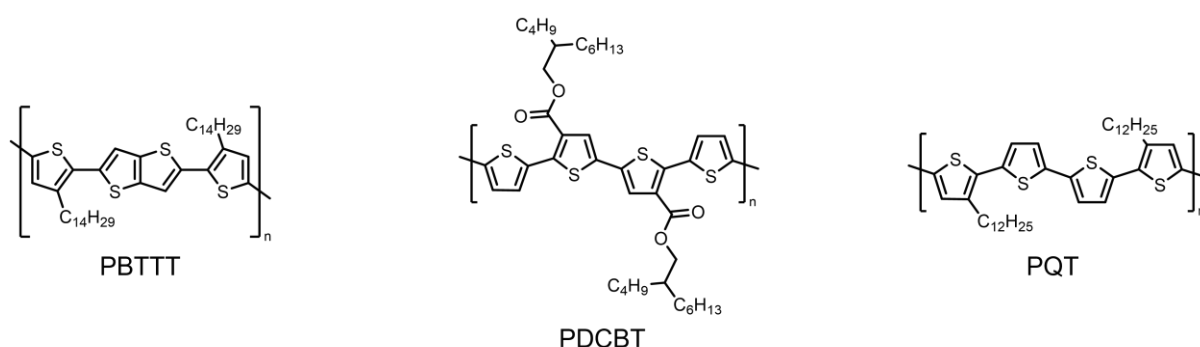


Figure 5.12 Chemical structures of PBTTT, PDCBT and PQT polymers used in mixtures with **6Br**.

In the WAXS images for crystalline thin films of PBTTT:**6Br**, PDCBT:**6Br**, and PQT:**6Br** (Figure 5.13a–c) no clear scattering peaks are observed, although the scattering patterns formed upon reducing the 2D images by azimuthally integrating regions in the out-of-plane (around 0°) (Figure 5.13d–f) and in-plane (around 90°) (Figure 5.13g–i) directions can be used to study how the crystalline phases of the polymer thin films change upon blending with **6Br**. In the out-of-plane direction for crystalline thin films of PBTTT and PDCBT polymer only, sharp peaks at 2θ values of 3.17°, 4.58° & 8.85° and 3.11°, 4.88° & 9.27° are observed respectively. Whereas the out-of-plane WAXS pattern for PQT has increased signal-to-noise with peaks at 3.08° & 4.55°. Upon blending PBTTT and PDCBT with **6Br** the polymer peaks are unchanged with additional new peaks at 5.90° and 5.76° for PBTTT:**6Br** and PDCBT:**6Br** respectively in the out-of-plane scattering pattern. However, for PQT:**6Br** the out of plane WAXS pattern is more different to the solely polymer thin film with the absence of the 4.55° peak and a new peak at 5.66° although the peak at 3.08° is still present. The unchanged 2θ angles of the polymer peaks upon doping with **6Br** in the out-of-plane WAXS patterns indicates that no change in the crystalline phase of the thin films is detected. Similarly, the scattering patterns in the in-plane direction for the polymers (PBTTT, PDCBT or PQT) are very similar and do not change significantly upon doping with **6Br** which further indicates that any change in the crystalline phase upon encapsulation of the macrocycle cannot be detected by WAXS.

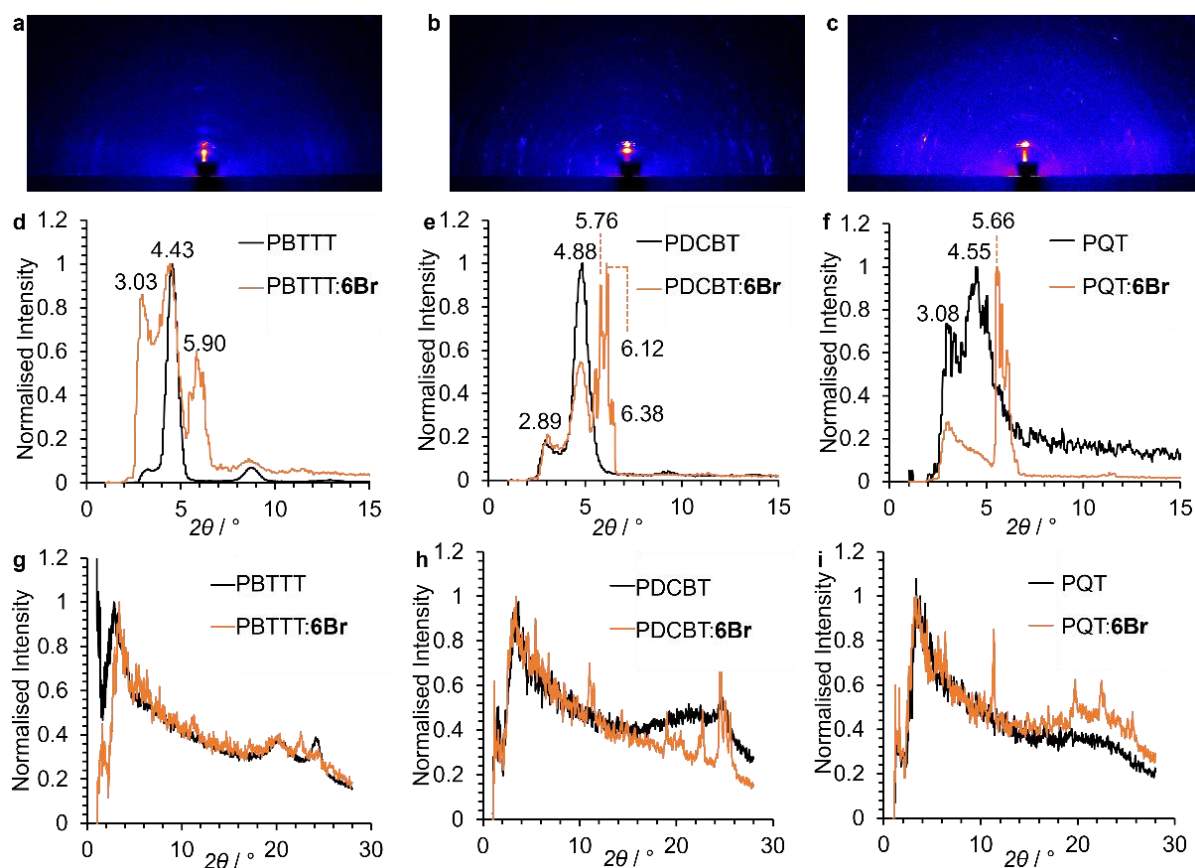


Figure 5.13 WAXS images of polymer blends with **6Br** (a) PBTBT:6Br, (b) PDCBT:6Br and (c) PQT:6Br. Out of plane WAXS patterns for polymer blends with and without **6Br** for (d) PBTBT, (e) PDCBT and (f) PQT. In plane WAXS patterns for polymer blends with and without **6Br** for (g) PBTBT, (h) PDCBT and (i) PQT.

Experiments using GIXRD were also completed to inspect any potential change in the crystalline phases of the polymer chains and macrocycle upon doping of PBTBT and PDCBT with **6Br** (Figure 5.14a and b). The GIXRD patterns for crystalline polymer thin films contain peaks at 4.34° and 4.12° for PDCBT and PBTBT respectively corresponding to crystalline phases. Furthermore, a broad peak is observed above 20° for both PDCBT and PBTBT as a result of an amorphous phase in the thin film. Upon doping the polymers (PDCBT and PBTBT) with **6Br**, the GIXRD patterns show a series of sharp, distinct peaks around 10° , 16° and 21° . The presence of these new peaks represents a change in the crystalline phase in the thin film upon doping the polymers with **6Br**. As the 2θ angles of the sharp distinct peaks are similar regardless of the polymer (PDCBT or PBTBT) they could be attributed to the crystalline phase of the **6Br** dopant. Subsequently, the GIXRD patterns of PDCBT:6Br and PBTBT:6Br were compared with simulated pXRD patterns for **6Br** crystals (**6Br**•Me₂CO and **6Br**, Chapter 2) to assess the nature of the crystalline phase of the macrocycle (Figure 5.14 c and d). The simulated diffraction patterns for single-crystals of **6Br** are distinctly different to the GIXRD patterns thus confirming a different crystalline phase of the macrocycle upon blending with electron-rich *p*-type polymers which could occur as a result of encapsulation or a new polymorph of the molecular triangle from the spin-coating fabrication method.

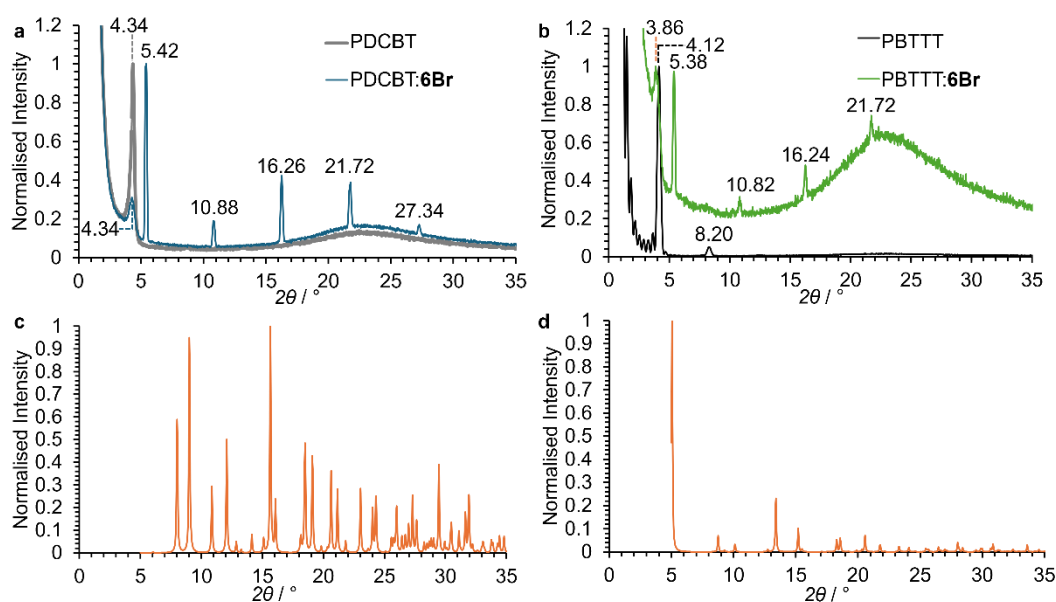


Figure 5.14 GIXRD patterns for (a) PDCBT and PDCBT:**6Br** and (b) PBTTT and PBTTT:**6Br**. Simulated powder XRD (pXRD) patterns for **6Br** crystals from Chapter 2 (c) **6Br**:Me₂CO and (d) **6Br**.

Furthermore, in the GIXRD patterns for PDCBT:**6Br** and PBTTT:**6Br** the amorphous broad peaks for above 20° are unchanged, while the 2θ angle for the crystalline phase of the PDCBT polymer chains remains unchanged (4.34°). Conversely, the diffraction peak for PBTTT polymer after doping with **6Br** (PBTTT:**6Br**) moves to a lower angle from 4.12° to 3.86°. The change in peak position for the PBTTT polymer crystalline phase indicates a change in d -spacing of the lamellar structure of the intercalated polymer chains which could be calculated using Bragg's law (Equation 5.3) using the value for the 2θ peak for the polymer and λ (Cu K α = 1.5418 Å).

$$d = \frac{\lambda}{2 \sin(\theta)} \quad (\text{Eqn 5.3})$$

An increase of the d -spacing from PBTTT (21.45 Å) to PBTTT:**6Br** (22.89 Å) indicates the incorporation of the macrocycle within the cavity of the intercalated polymer chains to disrupt the packing of the lamellar structure of the crystalline thin film in a similar manner to that shown for the fullerene electron-acceptor with electron-rich polymers.^{10,11} Whereas no change in the d -spacing of PDCBT chains in PDCBT:**6Br** was observed (Table 5.3), although the large spacing could mean that the macrocycle can be encapsulated without disrupting the intercalating polymer chains.

Table 5.3 Experimental values for the 2θ angle and d -spacing in PDCBT and PBTTT with and without **6Br** dopant.

	PDCBT	PDCBT: 6Br	PBTTT	PBTTT: 6Br
$2\theta / ^\circ$	4.34	4.34	4.12	3.86
$d / \text{\AA}$	40.72	40.72	21.45	22.89

The insertion of electron-deficient n -type **6Br** macrocycles into the crystalline assembly of p -type electron-rich PBTTT polymer chains could lead to the incorporation of the crystalline thin films as

active layers in bulk heterojunction photovoltaic devices for use in solar cells in the future. To confirm the encapsulation of the macrocycles within the packing of the polymer chains, the chemical composition of the films could be established by elemental and surface analysis of the thin films *via* energy dispersive X-ray microanalysis and electron microscopy. Prior to application in devices, optimisation of the conditions for thin film fabrication is required which could be achieved by either varying (i) the ratio of *p*- and *n*-type material in the spin coated solution or (ii) the fabrication method, *i.e.* stamping to a glass surface from the air-water interface.

5.3 CONCLUSIONS

In this Chapter, the suitability of core-functionalised molecular triangles for use in organic semiconductors (OSCs) has been studied by fabricating thin films of core-functionalised molecular triangles (**6H**, **3Br**, **6Br**, **3Ar** and **6Ar**) and investigating their structural and optoelectronic properties. It was hypothesised that the supramolecular packing of molecular triangles to form 2D networks combined with the redox-active nature of the macrocycles would make them ideal candidates for use in ion-gated transistors to facilitate ion and electron transport.

The assembly of the macrocycles at the air–water interface was studied in π -*A* isotherms with the onset of surface pressure being the cross-sectional molecular area. The experimental molecular area for core-functionalised molecular triangles were compared with the theoretical values calculated from geometry optimised structures from DFT calculations (Chapters 2 and 3) in two potential modes of assembly (i) standing upright (configuration *a*) and (ii) lying flat (configuration *b*). The values of the experimental molecular area for all molecular triangles are more similar to the theoretical values in configuration *a*, indicating that the macrocycles could potentially prefer to assemble in a ‘standing upright’ morphology. X-ray reflectivity experiments of thin films on glass substrates were conducted with a single fringe peak present in the curves for **3Ar** and **6Ar** indicating a rough film. Conversely, no difference between the curves for **6H**, **3Br** and **6Br** and a clean glass substrate was observed which indicates that the films were too thin or the macrocycles interacted weakly with the surface. Despite the absence of any reflectance peaks in the XRR patterns of **6H**, **3Br** and **6Br** the deposition of the core-functionalised molecular triangles to a quartz surface was confirmed using absorption spectroscopy with the same electronic transitions observed in the solid state as in solution (Chapters 2 and 3). Notably, upon electrochemical reduction of a drop-casted thin film of **6Br**, the intensity of the π - π^* transition (380 nm) in the absorption spectrum decreased in favour of broader, lower energy peaks at 520 and 605 nm indicating the potential presence of the reduced species.

An alternative approach investigated was the doping of electron-rich *p*-type polymers (PBTTT, PDCBT and PQT), which are known for the formation of crystalline thin films in photovoltaic devices, with the electron-deficient **6Br** macrocycle. The presence of a series of new sharp well-defined peaks in the

GIXRD pattern of the polymers (PDCBT and PBTTT) upon doping with **6Br** indicates the formation of a new crystalline phase of the molecular triangle which is independent of the polymer type. The peak pattern and 2θ angles of the new crystalline phase of **6Br** is different to the simulated pXRD patterns generated for the two crystal structures of the molecular triangle discussed in Chapter 2 which indicates that a new polymorph of electron-deficient macrocycle is formed upon spin coating. The new polymorph of **6Br** could be as a result of encapsulation of the macrocycle within the supramolecular intercalation of polymer chains. An increase in the lamellar d -spacing of PBTTT chains upon doping with **6Br** was calculated from the 2θ angle of the polymer peak in the GIXRD pattern. The increased d -spacing indicates disruption of the packing of the intercalated polymer chains upon doping with the macrocycle and the formation of a new crystalline phase.

The initial experiments in this collaboration during the JSPS fellowship investigating the suitability of core-functionalised molecular triangle for use in ion-gated transistors discussed in this Chapter, show that the macrocycles can be fabricated into thin films and studied by absorption spectroscopy for identification of reduced states generated by electrochemical reduction. However, the thin films of the macrocycles are not inherently smooth as shown by XRR and interact weakly with glass substrates. Therefore, a second-generation of core-functionalised molecular triangles could be synthesised with polar functional groups (*i.e.* -COOH) to interact with the glass surface. Furthermore, the functionality of core-substituents on molecular triangles could be tuned intentionally to influence the assembly of macrocycles into the 2D tessellated porous framework (configuration *b*) at the air–water interface. Such preferential assembly could be enforced through asymmetric core-substitution or the favourable formation of a *syn*-isomer of a tris-substituted macrocycle. One side of the 3D macrocycle would be functionalised with polar, hydrophilic functional groups such as carboxylic acids, alcohols or phosphates and the opposite side functionalised with hydrophobic groups such as alkyl chains, Figure 5.15a. The asymmetric nature of the core-substituents could be used to induce a 2D tessellated assembly of the macrocycles into the ‘lying flat’ configuration with the hydrophobic functional groups pointing into the water and/or the hydrophobic substituents facing the opposite direction towards the air, Figure 5.15b.

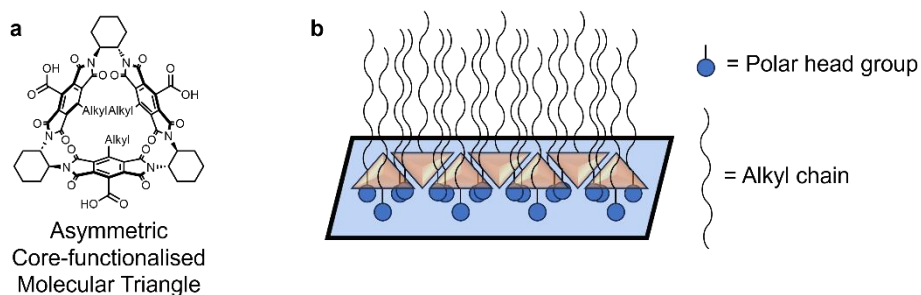


Figure 5.15 (a) Hypothetical asymmetric core-functionalised molecular triangles with substituted with three carboxylic acid groups and three hydrophobic alkyl chains. (b) Hypothetical assembly of the asymmetric core-functionalised molecular triangle at the air–water interface with polar head groups pointing into the water and hydrophobic alkyl chains pointing into the air.

5.4 SUPPLEMENTARY INFORMATION

5.4.1 Materials and General Methods

Core-functionalised molecular triangles **6H**, **3Br**, **6Br**, **3Ar** and **6Ar** were synthesised according to the procedures in Chapters 2 and 3. Electrolyte salts for electrochemical reduction were purchased from: TCI (lithium bis(trifluoromethanesulfonyl)imide and tetrabutylammonium bromide), Nacalai Tesque (potassium chloride) and Fujifilm wako (bis(triphenylphosphoranylidene)ammonium chloride). Polymers PBTTT and PQT-C12 were purchased from Sigma-Aldrich and PDCBT was purchased from Solaris Chem. Chloroform and acetone were purchased from Kanto chemical, isopropanol and ethanol were purchased from Nacalai Tesque and *o*-1,2-dichlorobenzene was purchased from TCI.

EAGLE XG[®] glass for thin film fabrication and XRD measurements was purchased from CORNING Corporation and ITO-coated glass was purchased from Sigma-Aldrich. Prior to thin film fabrication, substrates were treated by sonicating in acetone and chloroform for 5 minutes, removal of residual solvent by rinsing with isopropanol and then removal of residual organics using an ultraviolet-ozone (UV-O₃) process. Deionised (DI) water used in Langmuir-Blodgett experiments and aqueous solutions was prepared through the distillation and deionisation of water using an ELGA Purelab Option R7 Flex water purifier (resistance: 18 MΩ cm⁻¹).

X-ray diffraction data (XRR, WAXS and GIXRD) were collected using a RIGAKU SmartLab with a MicroMax-007HF X-ray generator using Cu K α radiation ($\lambda = 0.15418$ nm) in conjunction with a 0.1 mm thick EAGLE XG[®] glass substrate to reduce scattering. Thin films of molecular triangles were studied by XRR measurements. Thin films of polymers (PBTTT, PDCBT and PQT) with and without **6Br**, were studied by WAXS and GIXRD.

UV-vis absorption spectra were recorded from specimens on quartz or ITO-coated glass substrates using a JASCO V-670 UV-Vis spectrophotometer.

Chemical reduction was completed using novel conditions developed by the Supermolecules group at the National Institute for Materials Science. Exact conditions for chemical reduction are kept confidential by request of the collaborator. Absorption spectra of core-functionalised molecular triangle monolayers on quartz substrates were recorded before and after submersion of the thin films in the reductant solution for 30 seconds or 1 h.

Monolayer and drop-casted thin films of **3Ar**, **6Ar** and **6Br** on ITO coated glass substrates were reduced electrochemically at room temperature using an ALS electrochemical analyser model 850D with a standard three-electrode setup: Ag/AgCl reference electrode, platinum wire counter electrode and ITO working electrode. Aqueous electrolyte solutions were used containing either: (i) tetrabutylammonium bromide (TBABr) (0.1 M) for **6Br**-1 drop-casted thin film, (ii) lithium

bis(trifluoromethanesulfonyl)imide (LiTFSI) (0.1 M) for drop-casted thin films **6Br-2**, **6Br-3** and **6Br-4** and (iii) potassium chloride (KCl) (0.1 M) and bis(triphenylphosphoranylidene)ammonium chloride (0.96 mM) for **3Ar** and **6Ar** monolayers and drop-casted thin films.

5.4.2 ASSEMBLY OF CORE-FUNCTIONALISED MOLECULAR TRIANGLES INTO THIN FILMS

STUDYING THE ASSEMBLY OF MOLECULAR TRIANGLES AT THE AIR–WATER INTERFACE

Solutions for investigating the behaviour of core-functionalised molecular triangles at the air–water interface were prepared by dissolving in the specific macrocycle in chloroform. Surface pressure π (mN m^{-1}) vs molecular area A (nm^2) (π - A) isotherms were measured by dispersing 50 μL of molecular triangle solution in CHCl_3 onto a DI water surface at 19.5 °C and left for 15 minutes to allow for solvent evaporation. The layer of molecules was compressed using the Langmuir Blodgett (LB) method through a Kibron MicroTrough X-L/LB which measured the resulting change in surface pressure using the Wilhelmy plate method.³³ The trough has a working area of 150 x 60 mm^2 (9.00 x 10³ mm^2).

Table S5.1 Concentrations of solutions (mg mL^{-1}) used to study the assembly of molecular triangles at the air–water interface.

Molecular Triangle	Concentration / mg mL^{-1}
6H	0.464
3Br	0.480
6Br	0.548
3Ar	0.530
6Ar	0.520

THIN FILM FABRICATION OF MOLECULAR TRIANGLES AT THE AIR–WATER INTERFACE

LB monolayer thin films were formed by submerging the desired substrate (EAGLE XG[®] glass, quartz or ITO coated glass) into the DI water surface (19.5 °C) and spreading 50 μL of molecular triangle CHCl_3 solution. The solvent was allowed to evaporate for 15 minutes and the layer of molecules compressed using a Kibron MicroTrough X-L/LB until a surface pressure of 15 mN m^{-1} was reached. The substrate was slowly removed from the water to deposit the monolayer onto the surface.

Table S5.2 Concentrations of solutions (mg mL^{-1}) used to fabricate thin films of molecular triangles on EAGLE XG[®] glass, quartz or ITO coated glass substrates at the air–water interface.

Molecular Triangle	Concentration / mg mL^{-1}
6H	0.464
3Br	0.480
6Br	0.548
3Ar	0.530
6Ar	0.520

FABRICATION OF DROP-CASTED THIN FILMS OF MOLECULAR TRIANGLES

Drop-casted thin films of **6Br**, **3Ar** and **6Ar** were prepared by dispersing CHCl_3 solution containing macrocycle onto an ITO coated glass substrate and left at room temperature for more than 15 minutes to allow the solvent to evaporate.

Table S5.3 Concentrations (mg mL^{-1}), volumes (mL) and mass loadings (mg) to fabricate thin films of molecular triangles on ITO coated glass substrates by drop-casting.

Molecular Triangle Thin Film	Concentration / mg mL^{-1}	Volume / mL	Mass / mg
6Br -1	0.548	0.1	0.0548
6Br -2	0.548	0.2	0.1096
6Br -3	0.548	0.3	0.1644
6Br -4	0.548	0.4	0.2192
3Ar	0.480	0.1	0.0480
6Ar	0.490	0.1	0.0490

FABRICATION OF SPIN-COATED THIN FILMS OF MOLECULAR TRIANGLES

A 1:1 *w/w* solution of **6Br** and the requisite polymer (PBTtT, PDCBT or PQT) was prepared in *o*-1,2-dichlorobenzene (*o*-DCB) (see Table S5.4. for exact masses) to achieve a final concentration of around 0.5 wt% for each component. Control solutions of polymer (PDCBT or PQT) only (around 0.5 wt%, Table S5.4.) were prepared in *o*-DCB. The solutions were stirred at 180 °C for 1 hour with thin films fabricated by spin coating (2000 rpm for 1 minute) the respective hot *o*-DCB solution onto EAGLE XG[®] glass substrates. The resulting films were annealed in a vacuum oven at 180 °C for 1 h and then cooled slowly to room temperature.

Table S5.4 Mass and weight % of **6Br** and polymers (PBTtT, PDCBT and PQT) in *o*-DCB solutions for thin film fabrication by spin-coating (2000 rpm for 1 minute).

	6Br / mg (overall wt%)	Polymer / mg (overall wt%)	<i>o</i> -DCB / mg
6Br :PBTtT	1.00 (0.48)	0.99 (0.48)	205.02
6Br :PDCBT	0.99 (0.49)	0.98 (0.49)	199.97
6Br :PQT	1.04 (0.51)	1.15 (0.56)	203.18
PDCBT	—	0.99 (0.49)	199.32
PQT	—	0.99 (0.49)	200.36

5.5 REFERENCES

- (1) Akamatu, H.; Inokuchi, H.; Matsunaga, Y. Electrical Conductivity of the Perylene–Bromine Complex. *Nature* **1954**, *173*, 168–169.
- (2) Shirakawa, H.; Louis, E. J.; MacDiarmid, A. G.; Chiang, C. K.; Heeger, A. J. Synthesis of Electrically Conducting Organic Polymers: Halogen Derivatives of Polyacetylene, $(\text{CH})_x$. *J. Chem. Soc. Chem. Commun.* **1977**, 578–580.

- (3) Chiang, C. K.; Druy, M. A.; Gau, S. C.; Heeger, A. J.; Louis, E. J.; MacDiarmid, A. G.; Park, Y. W.; Shirakawa, H. Synthesis of Highly Conducting Films of Derivatives of Polyacetylene, (CH)_x. *J. Am. Chem. Soc.* **1978**, *100*, 1013–1015.
- (4) Zhang, Q.; Hu, W.; Sirringhaus, H.; Müllen, K. Recent Progress in Emerging Organic Semiconductors. *Adv. Mater.* **2022**, *34*, 2108701.
- (5) Duc Pham, H.; Hu, H.; Wong, F.-L.; Lee, C.-S.; Chen, W.-C.; Feron, K.; Manzhos, S.; Wang, H.; Motta, N.; Ming Lam, Y.; Sonar, P. Acene-Based Organic Semiconductors for Organic Light-Emitting Diodes and Perovskite Solar Cells. *J. Mater. Chem. C* **2018**, *6*, 9017–9029.
- (6) Yao, Y.; Ou, Q.; Wang, K.; Peng, H.; Fang, F.; Shi, Y.; Wang, Y.; Asperilla, D. I.; Shuai, Z.; Samorì, P. Supramolecular Engineering of Charge Transfer in Wide Bandgap Organic Semiconductors with Enhanced Visible-to-NIR Photoresponse. *Nat. Commun.* **2021**, *12*, 3667.
- (7) Operamolla, A.; Farinola, G. M. Molecular and Supramolecular Architectures of Organic Semiconductors for Field-Effect Transistor Devices and Sensors: A Synthetic Chemical Perspective. *Eur. J. Org. Chem.* **2011**, *2011*, 423–450.
- (8) Tybrandt, K.; Forchheimer, R.; Berggren, M. Logic Gates Based on Ion Transistors. *Nat. Commun.* **2012**, *3*, 871.
- (9) Rafique, S.; Abdullah, S. M.; Sulaiman, K.; Iwamoto, M. Fundamentals of Bulk Heterojunction Organic Solar Cells: An Overview of Stability/Degradation Issues and Strategies for Improvement. *Renew. Sustain. Energy Rev.* **2018**, *84*, 43–53.
- (10) Mayer, A. C.; Toney, M. F.; Scully, S. R.; Rivnay, J.; Brabec, C. J.; Scharber, M.; Koppe, M.; Heeney, M.; McCulloch, I.; McGehee, M. D. Bimolecular Crystals of Fullerenes in Conjugated Polymers and the Implications of Molecular Mixing for Solar Cells. *Adv. Funct. Mater.* **2009**, *19*, 1173–1179.
- (11) Cates, N.; Cho, E.; Gysel, R.; Risko, C.; Coropceanu, V.; Miller, C. E.; Sweetnam, S.; Sellinger, A.; Heeney, M.; McCulloch, I.; Brédas, J.-L.; Toney, M. F.; McGehee, M. D. Factors Governing Intercalation of Fullerenes and Other Small Molecules Between the Side Chains of Semiconducting Polymers Used in Solar Cells. *Adv. Energy Mater.* **2012**, *2*, 1208–1217.
- (12) Coropceanu, V.; Cornil, J.; da Silva Filho, D. A.; Olivier, Y.; Silbey, R.; Brédas, J.-L. Charge Transport in Organic Semiconductors. *Chem. Rev.* **2007**, *107*, 926–952.
- (13) Okamoto, T.; Kumagai, S.; Fukuzaki, E.; Ishii, H.; Watanabe, G.; Niitsu, N.; Annaka, T.; Yamagishi, M.; Tani, Y.; Sugiura, H.; Watanabe, T.; Watanabe, S.; Takeya, J. Robust, High-Performance n-Type Organic Semiconductors. *Sci. Adv.* **2020**, *6*, eaaz0632.
- (14) Long, R. E.; Sparks, R. A.; Trueblood, K. N. The Crystal and Molecular Structure of 7,7,8,8-Tetracyanoquinodimethane. *Acta Crystallogr.* **1965**, *18*, 932–939.
- (15) Mandal, A.; Choudhury, A.; Kumar, R.; Iyer, P. K.; Mal, P. Exploring the Semiconductor Properties of a Charge Transfer Cocrystal of 1-Aminopyrene and TCNQ. *CrystEngComm* **2020**, *22*, 720–727.
- (16) Menard, E.; Podzorov, V.; Hur, S.-H.; Gaur, A.; Gershenson, M. E.; Rogers, J. A. High-Performance n- and p-Type Single-Crystal Organic Transistors with Free-Space Gate Dielectrics. *Adv. Mater.* **2004**, *16*, 2097–2101.
- (17) Yan, H.; Chen, Z.; Zheng, Y.; Newman, C.; Quinn, J. R.; Dötz, F.; Kastler, M.; Facchetti, A. A High-Mobility Electron-Transporting Polymer for Printed Transistors. *Nature* **2009**, *457*, 679–686.

- (18) Zheng, Q.; Huang, J.; Sarjeant, A.; Katz, H. E. Pyromellitic Diimides: Minimal Cores for High Mobility n-Channel Transistor Semiconductors. *J. Am. Chem. Soc.* **2008**, *130*, 14410–14411.
- (19) Palai, A. K.; Kim, S.; Shim, H.; Cho, S.; Kumar, A.; Kwon, J.; Park, S.-U.; Pyo, S. N-Type Small Aromatic Core Diimides Flanked with Electron Donating Thienylethyl Moieties and Electrical Responses in Organic Devices. *RSC Adv* **2014**, *4*, 41476–41482.
- (20) Malenfant, P. R. L.; Dimitrakopoulos, C. D.; Gelorme, J. D.; Kosbar, L. L.; Graham, T. O.; Curioni, A.; Andreoni, W. N-Type Organic Thin-Film Transistor with High Field-Effect Mobility Based on a N,N'-Dialkyl-3,4,9,10-Perylene Tetracarboxylic Diimide Derivative. *Appl. Phys. Lett.* **2002**, *80*, 2517–2519.
- (21) Sun, H.; Gerasimov, J.; Berggren, M.; Fabiano, S. N-Type Organic Electrochemical Transistors: Materials and Challenges. *J. Mater. Chem. C* **2018**, *6*, 11778–11784.
- (22) Huang, L.; Wang, Z.; Chen, J.; Wang, B.; Chen, Y.; Huang, W.; Chi, L.; Marks, T. J.; Facchetti, A. Porous Semiconducting Polymers Enable High-Performance Electrochemical Transistors. *Adv. Mater.* **2021**, *33*, 2007041.
- (23) Panzer, M. J.; Frisbie, C. D. Polymer Electrolyte Gate Dielectric Reveals Finite Windows of High Conductivity in Organic Thin Film Transistors at High Charge Carrier Densities. *J. Am. Chem. Soc.* **2005**, *127*, 6960–6961.
- (24) Rivnay, J.; Leleux, P.; Ferro, M.; Sessolo, M.; Williamson, A.; Koutsouras, D. A.; Khodagholy, D.; Ramuz, M.; Strakosas, X.; Owens, R. M.; Benar, C.; Badier, J.-M.; Bernard, C.; Malliaras, G. G. High-Performance Transistors for Bioelectronics through Tuning of Channel Thickness. *Sci. Adv.* **2015**, *1*, e1400251.
- (25) Chason, E.; Mayer, T. M. Thin Film and Surface Characterization by Specular X-Ray Reflectivity. *Crit. Rev. Solid State Mater. Sci.* **1997**, *22*, 1–67.
- (26) Carmichael, A. J.; Hardacre, C.; Holbrey, J. D.; Nieuwenhuyzen, M.; Seddon, K. R. Molecular Layering and Local Order in Thin Films of 1-Alkyl-3-Methylimidazolium Ionic Liquids Using X-Ray Reflectivity. *Mol. Phys.* **2001**, *99*, 795–800.
- (27) Sheng, Y.; Tang, X.; Peng, E.; Xue, J. Graphene Oxide Based Fluorescent Nanocomposites for Cellular Imaging. *J. Mater. Chem. B* **2013**, *1*, 512–521.
- (28) Liao, K.-C.; Ismail, A. G.; Kreplak, L.; Schwartz, J.; Hill, I. G. Designed Organophosphonate Self-Assembled Monolayers Enhance Device Performance of Pentacene-Based Organic Thin-Film Transistors. *Adv. Mater.* **2010**, *22*, 3081–3085.
- (29) Yunus, Y.; Mahadzir, N. A.; Mohamed Ansari, M. N.; Tg Abd Aziz, T. H.; Mohd Afdzaluddin, A.; Anwar, H.; Wang, M.; Ismail, A. G. Review of the Common Deposition Methods of Thin-Film Pentacene, Its Derivatives, and Their Performance. *Polymers* **2022**, *14*, 1112.
- (30) Northrup, J. E. Atomic and Electronic Structure of Polymer Organic Semiconductors: P3HT, PQT, and PBTTT. *Phys. Rev. B* **2007**, *76*, 245202.
- (31) Liang, Z.; Li, M.; Wang, Q.; Qin, Y.; Stuard, S. J.; Peng, Z.; Deng, Y.; Ade, H.; Ye, L.; Geng, Y. Optimization Requirements of Efficient Polythiophene:Nonfullerene Organic Solar Cells. *Joule* **2020**, *4*, 1278–1295.
- (32) Facchetti, A. π -Conjugated Polymers for Organic Electronics and Photovoltaic Cell Applications. *Chem. Mater.* **2011**, *23*, 733–758.

- (33) Volpe, C. D.; Siboni, S. The Wilhelmy Method: A Critical and Practical Review. *Surf. Innov.* **2018**, 6, 120–132.

CHAPTER 6 |

SUMMARY AND OUTLOOK

This Thesis has investigated the consequence of core-substitution of pyromellitic diimide (PMDI) based molecular triangles with three or six bromine atoms or 3,5-dimethylbenzene groups on the structural and optoelectronic properties of the cyclic aromatic homoconjugated macrocycles. The combined effects of macrocyclisation and core-substitution on the properties of the redox-active PMDI faces is realised through experimental and theoretical studies on the dynamic structural, electrochemical and optical properties in core-functionalised molecular triangles and presented in Chapters 2–5.

Chapter 1 explores the different methods of electron delocalisation *via* through-bond and through-space conjugation in organic macrocycles, with a particular focus on the less commonly explored aromatic homoconjugation. A new term of cyclic aromatic homoconjugation is introduced which occurs when through-space electronic communication across non-conjugating sp^3 centres occurs in macrocycles, with the most commonly studied class of compound exhibiting this property being the molecular triangles. The rigid, shape-persistent molecular triangles **1**, **2** and **6H**, Figure 6.1, composed of three aromatic diimide (ADI) faces linked by three chiral (*R,R*)- or (*S,S*)-*trans*-1,2-diaminocyclohexane groups have been developed over the last 22 years with the cyclic aromatic homoconjugation being shown to introduce favourable redox-active, structural and optical properties to the macrocycles. However, the large majority of molecular triangles that have been studied have comprised of core unsubstituted ADI faces, which is surprising given that core functionalisation of PMDIs, naphthalene diimides (NDIs) and perylene diimides (PDIs) have been shown to also promote attractive supramolecular and optoelectronic properties in the monomeric small molecules. Core-substitution of PMDIs in macrocycles can allow for further π -extension *via* cross-coupling reactions towards carbon nanotube like structures. In 2023, the first example of a core-functionalised PMDI based molecular triangle (**6Br**, Figure 6.1) was presented, where the addition of six bromine atoms to the aromatic faces influences the supramolecular assembly of the macrocycle in the solid-state, with the resulting hydrogen-bonded organic framework showing selective adsorption of benzene over cyclohexane. However, the influence of core-bromination on the optoelectronic properties of the PMDI based molecular triangle was not explored. The aim of this introductory Chapter was to show the effect of cyclic aromatic homoconjugation in macrocycles, especially molecular triangles and to highlight the benefits that could be achieved upon core-functionalisation of the aromatic core.

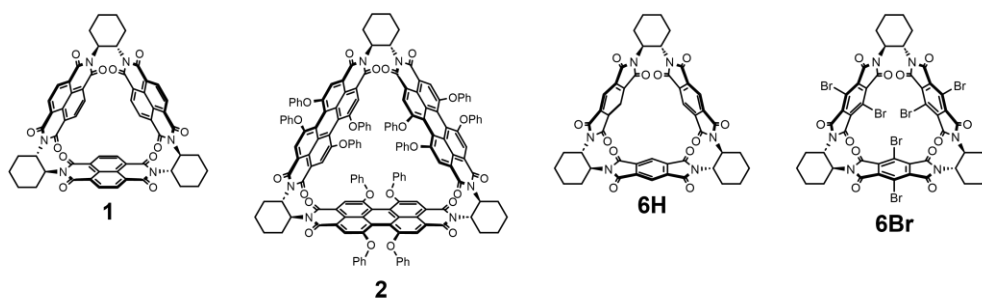


Figure 6.1 Cyclic aromatic homoconjugated macrocycles in NDI-based **1**, PDI-based **2** and PMDI-based **6H** and **6Br** molecular triangles.

In Chapter 2, an alternative synthesis of the hexa-brominated PMDI based molecular triangle **6Br** is presented and the first example of post-synthetic functionalisation *via* a palladium catalysed Suzuki-Miyaura cross-coupling reaction is reported to prepare a hexa-arylated macrocycle **6Ar**, where the aryl groups are 3,5-dimethylbenzene substituents, Figure 6.2a. Subsequently, the structural and optoelectronic properties of core-functionalised molecular triangles are investigated and compared with the unsubstituted, original PMDI based macrocycle by growing single crystals for X-ray diffraction, theoretical DFT calculations, absorption spectroscopy, cyclic voltammetry (CV) and spectroelectrochemistry. The addition of six electron-withdrawing bromine atoms in **6Br** increases the electron-deficiency of the macrocycle with electrochemical reduction by application of a potential achieved at less negative potentials. Whereas core-substitution with electron-donating 3,5-dimethylbenzene groups in **6Ar** increases the electron-density of the molecular triangle with electrochemical reduction occurring at more negative potentials observed by CV. Furthermore, core-functionalisation of the molecular triangles was shown not to influence the cyclic aromatic homoconjugation in the core-functionalised molecular triangles with splitting of the reduction peaks observed by CV and differential pulse voltammetry (DPV) in both **6Br** and **6Ar** representing electron delocalisation around the macrocycle. Notably, a new polymorph of **6Br** in the solid-state was observed where $C=O \cdots Br$ interactions between the molecular triangle and solvated acetone molecules induces supramolecular assembly into a hexagonal array of 1D channels of macrocycles, Figure 6.2b. Furthermore, the structure of **6Ar** in the solid-state shows that the extension of the aromatic core begins to resemble a carbon nanotube structure, Figure 6.2c. The initial post-synthetic functionalisation of **6Br** to **6Ar** enables a visualisation and proof of concept of oligomerisation of molecular triangles into nanoprisms chains *via* Suzuki-Miyaura Pd catalysed cross-coupling reactions in the future. In triangular nanoprisms, cyclic aromatic homoconjugation around the macrocycle and through-bond conjugation along the π -extended core-substituents could occur in a similar manner to polymeric cycloparaphenylenes discussed in Chapter 1.

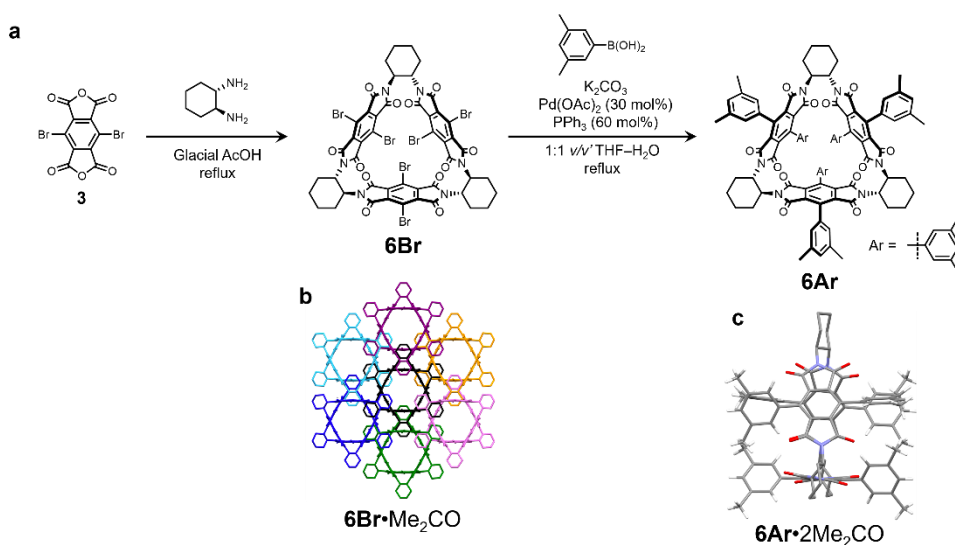


Figure 6.2 (a) Synthesis of **6Br** and **6Ar**. X-ray crystal structures of (b) **6Br**·Me₂CO and (c) **6Ar**·2Me₂CO.

In Chapter 3, asymmetric molecular triangles composed of mono-substituted PMDI faces are synthesised with Suzuki-Miyaura cross-coupling of the tris-brominated **3Br** with 3,5-dimethylbenzene substituents yielding a tris-arylated macrocycle **3Ar**. These tris-brominated and -arylated molecular triangles show similar optoelectronic properties as the hexa-functionalised macrocycles in Chapter 2, although the effect of core-substitution is less significant as a result of half the number of bromine atoms or 3,5-dimethylbenzene groups. Most notably, **3Br** and **3Ar** were shown to exist as a mixture of *syn*- and *anti*-isomers in solution, with separation of the different conformers not possible as a result of interconversion by rotation. The rotation between the *syn*- and *anti*-conformers of **3Br** and **3Ar** respectively (Figure 6.3) were visualised using variable temperature ^1H NMR spectroscopy *via* coalescence of the PMDI aromatic protons at temperatures greater than 125 $^{\circ}\text{C}$. Further ^1H - ^1H EXSY NMR spectroscopy experiments at a variety of mixing times at 80 $^{\circ}\text{C}$ revealed rates of rotation of $1.81 \pm 0.03 \text{ s}^{-1}$ for **3Br** and $0.560 \pm 0.015 \text{ s}^{-1}$ for **3Ar**, Figure 6.3. The increased rate of rotation in **3Br** compared with **3Ar** was shown by DFT calculations to be as a result of an intramolecular $\text{Br} \cdots \pi$ interaction lowering the energy barrier of the interconversion pathway *via* an intra-annular bromine atom (18.3 kcal mol^{-1}) compared with the route where the PMDI hydrogen-substituent enters the cavity of the macrocycle (21.5 kcal mol^{-1}). The lowering of the energy barrier of rotation by a favourable $\text{Br} \cdots \pi$ interaction by 3.2 kcal mol^{-1} shows that this system could be used as a transition state molecular balance with asymmetric core-substitution with other halogens or functional groups allowing for the strength of other non-covalent interactions to be measured. Intermolecular halogen $\cdots \pi$ interactions have also been studied through host-guest chemistry of the core-functionalised molecular triangles with the electron-rich triiodide anion (I_3^-). The most electron-deficient macrocycle, **6Br** exhibited the greatest binding with I_3^- ($61 \pm 5 \text{ M}^{-1}$) with the single crystal of the host-guest complex **6Br** $\supset\text{I}_3^-$ showing significant bending of a Br_2PMDI face to optimise the anion $\cdots \pi$ interaction. The remarkable flexible dynamic structural properties of the rigid shape-persistent molecular triangles to maximise intra- and intermolecular halogen $\cdots \pi$ interactions with the cyclic aromatic homoconjugated cavity could allow these systems to be used as enzyme mimics through the similarity to the induced fit model for the binding of substrates.

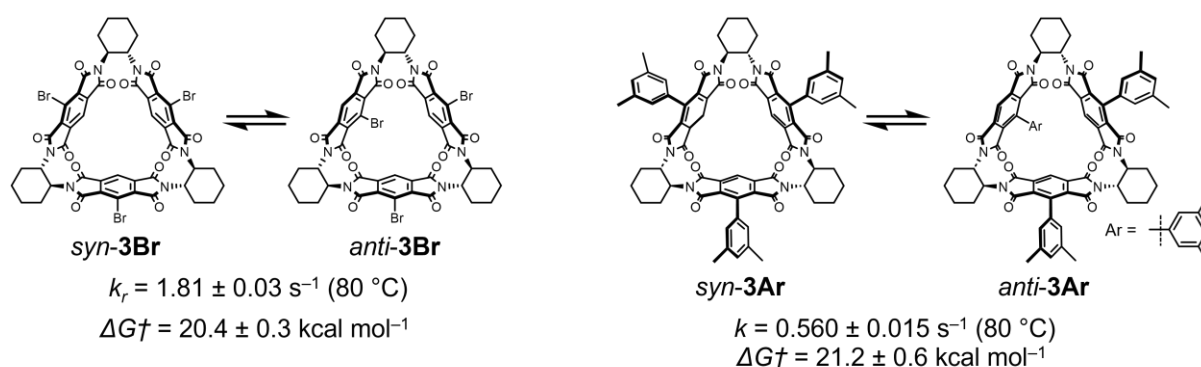


Figure 6.3 Atropisomerism between *syn*- and *anti*-isomers of **3Br** and **3Ar** with exchange rates and energy barrier calculated from ^1H - ^1H EXSY NMR spectroscopy analysis.

In Chapter 4, the photoactive behaviour of core-brominated molecular triangles is investigated with efforts to synthesise core-hydroxylated molecular triangles and PMDI compounds by irradiation with UV-light and by reaction with CsF pursued. The photochemical transformation of **6Br** to a partially core-hydroxylated-brominated molecular in DMF was serendipitously discovered by the observation that the colourless solution turned a deep pink colour after 24 hours. Subsequent studies into the colour change showed the generation of new absorption peaks by UV-vis spectroscopy with the growth of these lower energy electronic transitions accelerated under ambient and UV-light, Figures 6.4c and d. The photochemical transformation of **6Br** in DMF increased the luminescent properties of the macrocycle which exhibited the same emissive behaviour as an impure sample of **(OH)5Br**, Figure 6.4b. The luminescence of the partially core-hydroxylated molecular triangle could be as a result of ESIPT activity with the aromatic hydroxy group and diimide carbonyl. Furthermore, a similar -Br to -OH hydroxylation functional group transformation was discovered for a BrPMDI monomeric model compound through reaction with CsF in dioxane, Figure 6.4a. Reaction screening showed that the hygroscopic nature of the CsF was key to the generation of the desired hydroxy PMDI compound where if the base was dried prior to use the conversion to the target molecule was decreased. The application of these hydroxylation reaction conditions to a Br₂PMDI small molecule showed the generation of a mono-hydroxy-mono-brominated compound in the absence of the di-hydroxylated species. The incorporation of hydroxy groups onto the cyclic aromatic homoconjugated molecular triangle framework was desirable to ‘turn on’ luminescence whilst the potential asymmetric mono-hydroxy-mono-brominated functionalisation of the PMDI would be attractive towards further functionalisation. The orthogonal reactivity of the hydroxy and bromine substituents towards S_NAr and palladium catalysed cross-coupling reactions respectively would allow for core-extension in two directions *via* different synthetic pathways.

Furthermore, the luminescent properties of **6H**, **3Br** and **6Br** in the solution and solid states were investigated. In the solid state, where vibrational and rotational motion was restricted, long lifetime room temperature phosphorescence (RTP) was observed for **3Br** and **6Br**. Although, low quantum yields for RTP were measured in the solid state, an increase in the emission efficiency was observed in **6Br** compared with **3Br** as a result of the increased influence of the heavy halogen effect to enhance intersystem crossing from the S₁ to T₁ excited state and subsequent relaxation *via* phosphorescence. The results in this Chapter show that the luminescence of PMDI based molecular triangles can be ‘turned on’ through the addition of hydroxy or bromine core substituents and most notably, can be achieved using photochemical or conventional synthetic methods. Although the RTP emission of **3Br** and **6Br** was relatively weak, the combination of ESIPT active core-hydroxylated PMDI faces with the cyclic aromatic homoconjugated π -system in molecular triangles remains an attractive goal for pursuit of luminescent macrocycles.

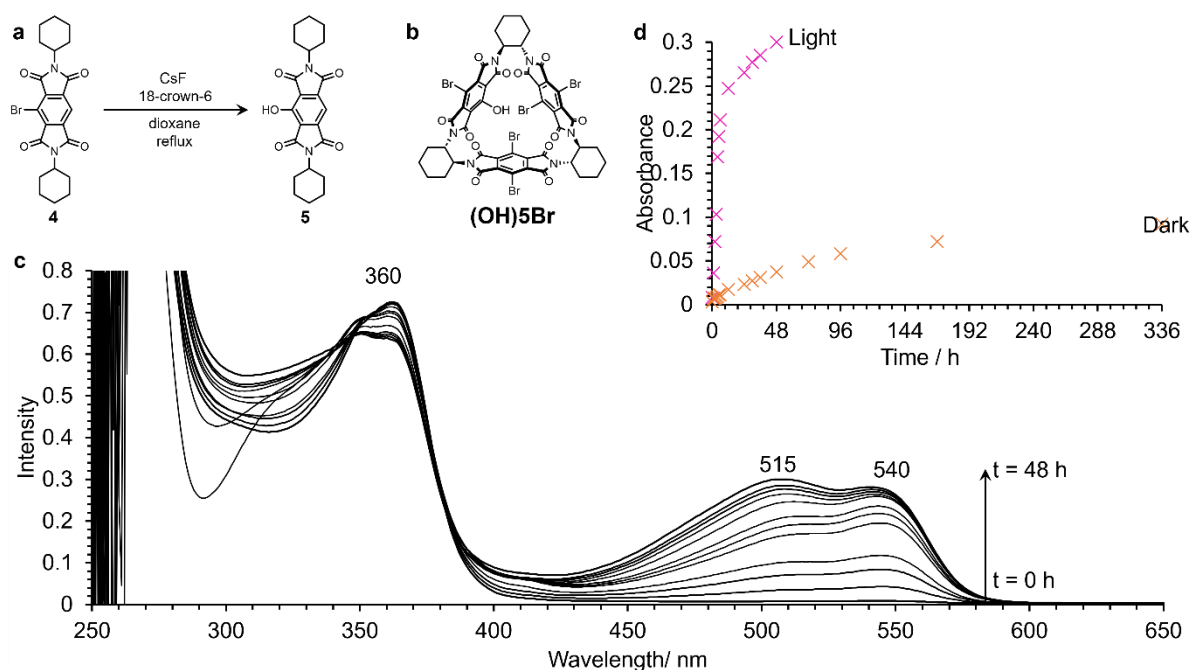


Figure 6.4 (a) Synthesis of hydroxy-substituted **5** from bromo-PMDI compound **4**. (b) Structure of partially hydroxylated brominated molecular triangle (OH)**5Br** which could contribute to (c) the growth of new absorption peaks at 515 and 540 nm when **6Br** is dissolved in DMF with (d) the evolution of the new peaks at 515 and 540 nm is enhanced when the solution of **6Br** in DMF is exposed to ambient light compared to being kept in the dark.

In Chapter 5, research conducted during a two-month PhD Exchange Fellowship funded by the Japan Society for the Promotion of Science in collaboration with researchers at the National Institute for Materials Science, Japan is presented and discussed. The structural and optoelectronic properties of the core-functionalised molecular triangles (**6H**, **3Br**, **6Br**, **3Ar** and **6Ar**) in thin films were studied to assess their suitability for application as *n*-type organic semiconductor (OSC) materials. It was envisioned that OSCs containing core-functionalised molecular triangle thin films would be appropriate for use in ion-gated transistors on account of their redox-active nature, supramolecular packing in the solid state to form porous frameworks, *e.g.* potential 2D tessellation in Figure 6.5a, and ability to encapsulate electron-rich guests. The assembly of the core-functionalised molecular triangles at the air-water interface was studied using a Langmuir-Blodgett trough. The resulting experimentally measured molecular area was compared with the theoretical values calculated from the geometry optimised DFT structures (Chapters 2 and 3) in two configurations (*a* and *b*), Figures 6.5c and d. The experimental molecular area of the molecular triangles were more similar to the theoretical values in configuration *a* which potentially indicated preferential assembly in the ‘standing upright’ morphology. The core-functionalised molecular triangle thin films prepared at the air–water interface were transferred to glass substrates for structural analysis by X-ray reflectivity experiments where a single fringe peak was observed for **3Ar** and **6Ar** respectively which indicates the presence of a thin film, albeit likely rough. No diagnostic fringe peaks for **6H**, **3Br** or **6Br** were observed with the reflectivity patterns being similar to that of the glass control. Although thin films of **6H**, **3Br** and **6Br** could not be identified by XRR experiments, deposition of macrocyclic material for all molecular triangles was

confirmed by absorption spectroscopy. Upon exposure of a drop-casted thin film of **6Br** to a potential, the characteristic π - π^* transition at 380 nm in the UV-vis spectrum decreased in intensity in favour for a broad peak at longer wavelengths which could indicate electrochemical reduction towards the radical anion and anionic species. The difficulty in fabricating and studying the structure of thin films of core-functionalised molecular triangles shows that future macrocycles investigated in the ongoing collaboration should be prepared with intentional synthetic design for use as OSCs. A second generation of core-substituted molecular triangles should utilise polar functional groups (*i.e.* -COOH) that will enhance the interaction of the macrocycles with glass substrates. Alternatively, the asymmetric nature of the tris-substituted molecular triangles in the *syn*-conformation could influence the assembly of the macrocycle at the air–water interface. Tris-substitution with hydrophilic or hydrophobic functional groups could favour the tessellation of the macrocycles into 2D nanosheets which is attractive for use in ion-gated transistors.

An alternative approach of doping electron-rich *p*-type polymers (PBTTT, PDCBT and PQT) with the most electron-deficient molecular triangle **6Br** and fabricating into spin-coated thin films was also studied in Chapter 5. Structural analysis of spin-coated thin films of PBTTT:**6Br** and PDCBT:**6Br** by GIXRD reveal a new crystalline phase compared with the undoped polymer samples. The presence of distinct diffraction peaks for **6Br** which are different to simulated patterns of the macrocycle in single crystals indicates that a new crystalline polymorph of the molecular triangle is formed. An increase in the lamellar *d*-spacing between the polymer chains is also observed upon doping with **6Br**. The greater *d*-spacing could mean that the new crystalline phase of the macrocycle is a polymorph where the molecular triangle is incorporated within the supramolecular structure of the intercalated polymer chains, *e.g.* the schematic in Figure 6.5b. The blending of *p*-type electron-rich polymers and the electron-deficient *n*-type molecular triangle **6Br** in thin films could be incorporated into bulk heterojunction layers for light-harvesting applications in photovoltaic devices.

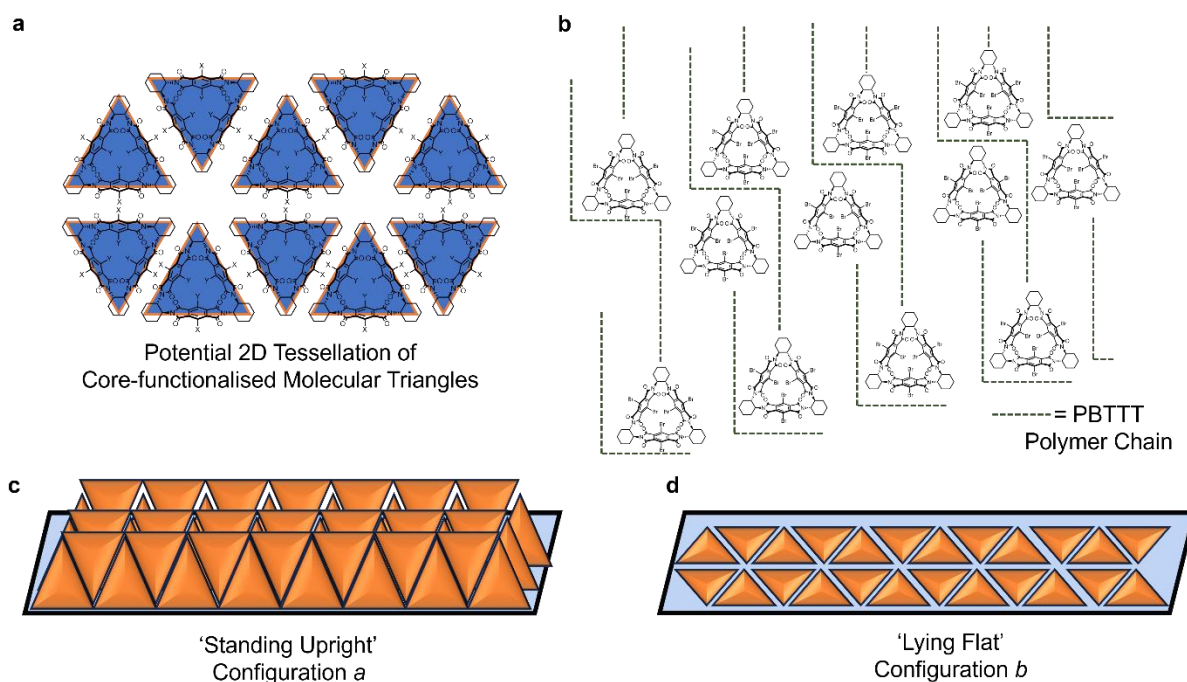


Figure 6.5 Potential (a) 2D tessellation of core-functionalised molecular triangles and (b) incorporation of **6Br** into crystalline lamellar framework of PBTtT polymer chains. Hypothetical assembly of molecular triangles at the air-water interface in (c) ‘Standing Upright’ and (d) ‘Lying Flat’ configurations.

This Thesis has provided an in-depth study into the effect of core-functionalisation on the structural, dynamic and optoelectronic properties of a PMDI based molecular triangle. The results show that not only can the scope of this relatively new class of macrocycle be increased by core-functionalisation, but new unexpected properties can also emerge such as the dynamic atropisomerism of the asymmetric tris-substituted molecular triangles. The presence of reactive bromine atoms at the aromatic core allows for further post-synthetic functionalisation *via* palladium cross-coupling reactions to occur. The potential pool of core-substituted molecular triangles is therefore extremely vast with the ability to utilise the functional macrocycles in a range of supramolecular applications. Core-substituted aromatic diimides (ADIs) have been well studied in the literature and now, combined with cyclic aromatic homoconjugated redox-active molecular triangles, the potential properties and applications are endless.